Interactions magmas-détachements : Du terrain (Mer Egée, Grèce) à l'expérimentation

Aurélien Rabillard

Centre Val de Loire UNIVERSITÉ

UNIVERSITÉ D'ORLÉANS

UNIVERSITE D'ORLEANS

ÉCOLE DOCTORALE
ENERGIE, MATERIAUX, SCIENCES DE LA TERRE ET DE L'UNIVERS

Institut des Sciences de la Terre d'Orléans

THÈSE présentée par :

Aurélien RABILLARD

soutenue le : **19 Décembre 2017**

pour obtenir le grade de : **Docteur de l'université d'Orléans**

Discipline : Sciences de la Terre et de l'Univers

Interactions magmas-détachements: du terrain (Mer Égée, Grèce) à l'expérimentation

THÈSE dirigée par :

Laurent Arbaret	Maître de conférences (HDR), Université d'Orléans
Laurent Jolivet	Professeur, Université Pierre et Marie Curie

RAPPORTEURS :

Michel de Saint-Blanquat	DR CNRS, Université de Toulouse
Micha Bystricky	Maître de conférences, Université de Toulouse

---

JURY:

Bruno Scaillet	DR CNRS, Université d'Orléans (Président)
Loïc Labrousse	Professeur, Université Pierre et Marie Curie
Didier Laporte	DR CNRS, Université Clermont-Ferrand
Micha Bystricky	Maître de conférences, Université de Toulouse
Michel de Saint-Blanquat	DR CNRS, Université de Toulouse
Laurent Arbaret	Maître de conférences, Université d'Orléans
Laurent Jolivet	Professeur, Université Pierre et Marie Curie

"Geology holds the keys of one of the kingdoms of nature;
and it cannot be said that a science which extends our knowledge [...]
over a third part of nature, holds a low place among intellectual employments."

William Buckland (1784-1856)

Sommaire

Chapitre I

Introduction générale

Sommaire

Les motivations à l'origine de ce mémoire

L'une des principales propriétés intrinsèques de la lithosphère continentale, lorsqu'elle est soumise aux contraintes tectoniques, réside sans doute dans sa capacité à concentrer et accumuler localement la déformation au cours du temps. Ce comportement mécanique, relevant du phénomène de localisation de la déformation, se révèle être une tendance commune à de nombreux évènements tectoniques et ce, quel que soit le champ de contrainte (i.e., compressif, extensif) ou même le régime de déformation associé (i.e., cassant, ductile). La localisation de la déformation ne se rapporte pas strictement à la croûte supérieure cassante, dans laquelle la déformation est par nature localisée, mais se matérialise également dans les portions de la croûte continentale où la déformation ductile prévaut, bien que cette dernière soit par définition distribuée. Le caractère localisé de la déformation ductile se manifeste à de multiples échelles spatiales, depuis la simple bande de cisaillement d'épaisseur millimétrique jusqu'au couloir de déformation de grande ampleur que représentent les zones de cisaillement d'échelle plurikilométrique. Évaluer les modalités d'initiation et de développement de ces zones de forte accumulation de la déformation constitue l'un des axes majeurs de la recherche en géosciences, tant pour ses enjeux économiques que pour ses implications fondamentales. Intérêts économiques, par le rôle de drain que peuvent jouer ces structures ductiles/cassantes pour la percolation de fluides minéralisateurs et le piégeage de métaux, mais aussi fondamentaux, par l'importance que représentent ces zones de déformation localisée pour la reconstitution cinématique de blocs continentaux et l'élaboration de modèles rhéologiques de la lithosphère.

C'est autour de cet objectif global que s'articule le projet de recherche ERC RHEOLITH (RHEOlogie de la LITHosphère), dans lequel je me suis greffé depuis mes débuts en tant que doctorant. Dans le cadre de ce projet, je me suis plus modestement focalisé sur **les liens intimes qui unissent le phénomène de localisation de la déformation et le magmatisme intrusif**, avec pour objets d'étude les dômes métamorphiques extensifs (ou MCCs pour « Metamorphic Core Complexes » en anglais) et leurs détachements associés. Il arrive en effet que ces discontinuités tectoniques extensives d'échelle crustale, considérées comme les témoins d'une localisation progressive de la déformation, soient étroitement associées à des corps magmatiques syn-extensifs. Les processus à l'origine de cette interaction ne sont encore aujourd'hui que partiellement décryptés. Plus précisément, l'enjeu sera ici (1) **d'évaluer l'impact du magmatisme sur la dynamique de dômes métamorphiques extensifs,** et (2) **d'identifier les possibles mécanismes gouvernant l'initiation d'une déformation localisée au sein de corps magmatiques en cours de cristallisation et estimer leur capacité à localiser la déformation à plus grande échelle, tel le long des détachements crustaux.** La recherche des vecteurs de localisation de la déformation sera abordée sous deux angles différents, mais complémentaires. La première approche consistera à caractériser l'état de déformation finie au sein de granitoïdes cycladiques (Mer Égée, Grèce), corps intrusifs placés au cœur de dômes métamorphiques extensifs et en étroite association avec des détachements crustaux. Outre la mise en œuvre d'études structurales et microstructurales

systématiques, avec la détermination de la cinématique de la déformation, l'application de méthodes de quantification des fabriques permettront de mettre en évidence des gradients d'intensité de la déformation et de contraindre les relations entre les différentes fabriques développées et l'évolution de la déformation (i.e., magmatique, ductile, cataclastique). La seconde approche sera quant à elle expérimentale. Il s'agira de déterminer le comportement structural de suspensions magmatiques face à un état de contrainte donné, depuis les stades précoces de la cristallisation jusqu'à la quasi-solidification. L'étude comparative entre les éventuelles fabriques et structures se développant au cours des expériences de déformation et celles enregistrées sur le terrain permettront *in fine* de mieux appréhender les mécanismes à l'origine de la localisation de la déformation au sein de corps magmatiques partiellement cristallisés.

Après une brève description du concept de MCC et de ses principales caractéristiques morphologiques et tectono-métamorphiques, la suite de ce chapitre introductif sera consacrée aux divers modèles d'interaction qui ont été conceptualisés ces dernières décennies pour expliquer le lien spatio-temporel entre le développement de détachements et le magmatisme intrusif. Il sera ensuite relayé les quelques hypothèses concernant les mécanismes précurseurs de la déformation localisée dans les complexes magmatiques en cours de consolidation Enfin, le choix des Cyclades comme zone d'étude sera finalement justifié, en soulevant notamment les quelques éléments de controverse qui existent dans la bibliographie quant au rôle du magmatisme dans la dynamique des MCCs cycladiques.

1. Les dômes métamorphiques extensifs & magmatisme associé

1.1. Les dômes métamorphiques extensifs & leurs détachements associés

Dans les domaines de croûte continentale amincie, en particulier au sein de régions marquées par une extension post-orogénique, le développement de dômes métamorphiques extensifs (ou MCCs pour « Metamorphic Core Complexes » en anglais) incarne un processus tectonique majeur par lequel des roches métamorphiques profondément enfouies sont efficacement exhumées vers des niveaux de la croûte supérieure [*Whithney et al.*, 2013]. Historiquement, le concept de MCC fut développé à la fin des années 70 après plus d'une décennie d'observations de terrain dans la région du Basin & Range (i.e., la Cordillère Nord-Américaine ; *Davis & Coney* [1979]; *Crittenden et al.* [1980]; Armstrong [1982]; Figures I-1). Ce concept fut par la suite élargi à de nombreux autres domaines continentaux, tels qu'en mer Égée [*Lister et al.*, 1984; *Avigad & Garfunkel*, 1989], en Papouasie-Nouvelle-Guinée [*Hill*, 1987; 1991], en Nouvelle-Zélande [*Gibson*, 1990] ou plus récemment en Asie de l'Est [*Davis et al.*, 1996; *Faure et al.*, 1996].

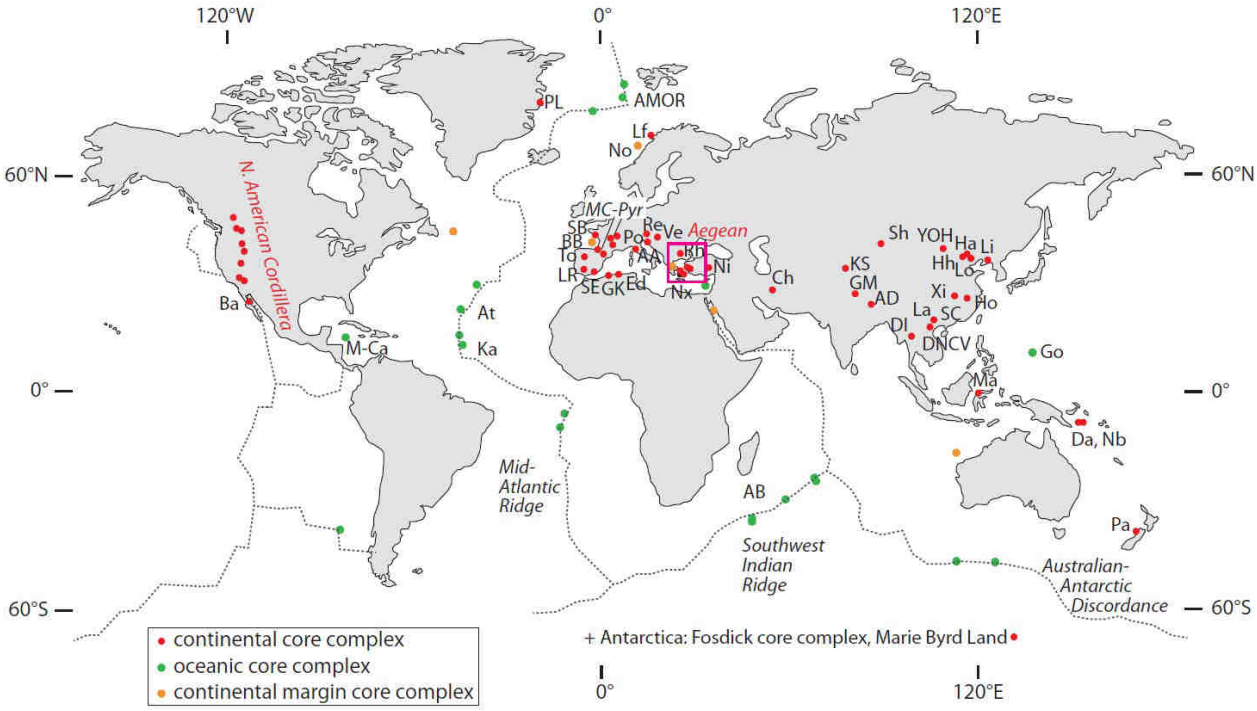

Figure I-1: *répartition au travers du globe des dômes métamorphiques extensifs (MCCs), d'après Whitney et al. [2013]. Les points rouges correspondent au MCCs se développant dans les domaines continentaux.*

1.1.1. Caractéristiques morphologiques, métamorphiques & structurales

Avec près de 40 années de données structurales et géophysiques accumulées, la suite de cette section ne prétend aucunement décrire de manière exhaustive les caractéristiques morphologiques et tectono-métamorphiques de MCCs, tant elles sont diverses (Figure I-2). Il est néanmoins possible d'en dégager quelques-unes. L'une des caractéristiques majeures d'un

MCC est, par définition, sa forme de dôme. Ces dômes structuraux sont en général coiffés par un seul détachement (i.e., une faille normale à faible pendage, <30°) ou, plus rarement, par un système de détachements [*Spencer*, 1984; *Lister & Davis*, 1989]. Dans les cas de MCCs les plus couramment rencontrés, le plan de détachement délimite deux unités aux caractéristiques métamorphiques et structurales bien distinctes.

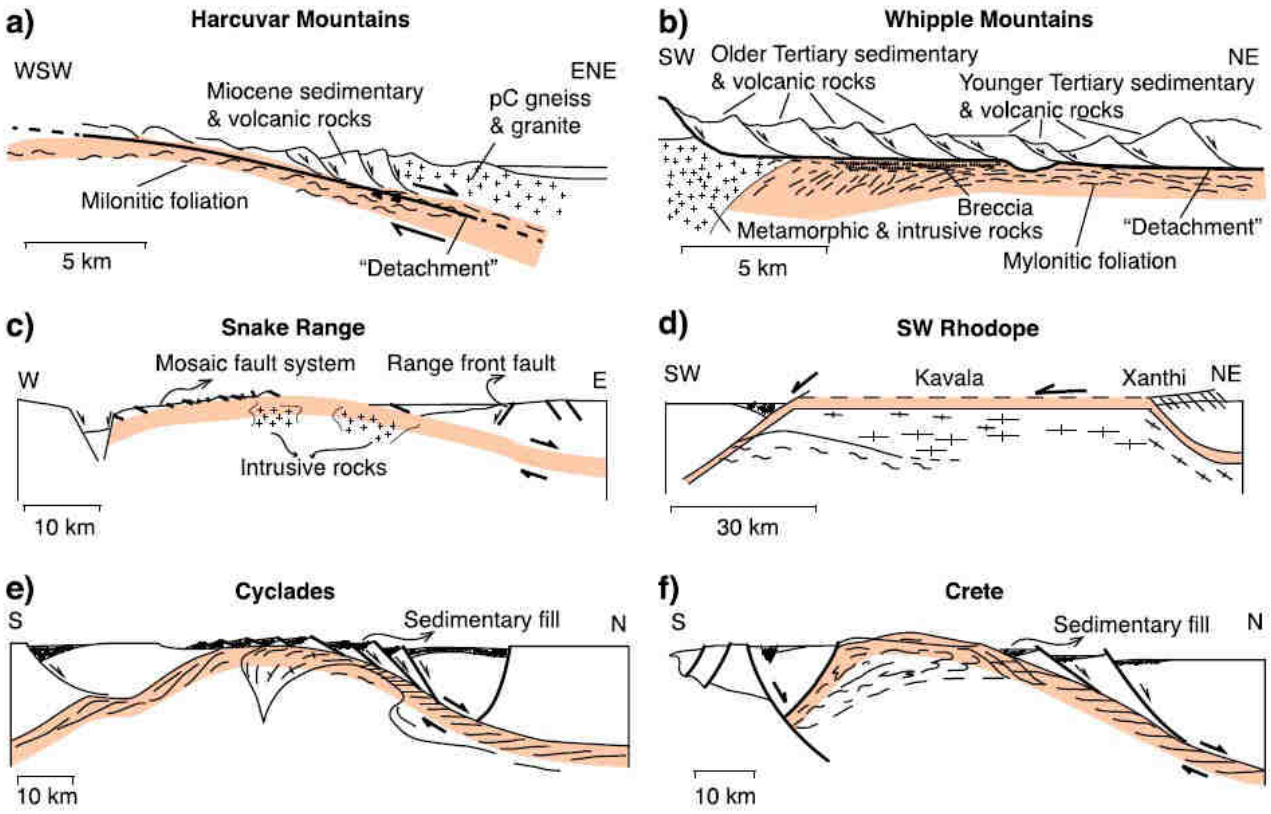

Figure I-2 : *Coupes de dômes métamorphiques extensifs avec leurs détachements associés, élaborées à partir d'observations de terrain et de reconstructions géophysiques dans les domaines continentaux du Basin & Range et de l'Égée, montrant ainsi la diversité architecturale de ces dômes structuraux. (a) Harcuvar montains [Buck, 1988] ; (b) Whipple Mountains [Buck, 1988] ; (c) Snake Range [Miller et al., 1983] ; (d) Massif du Rhodope (Grèce-Bulgarie) [Gautier et al., 1999] ; (e) Cyclades (Mer Égée, Grèce) [Gautier et al., 1999] ; Crète (Mer Égée, Grèce) [Gautier et al., 1999]. Les bandes de couleur beige représentent pour chaque coupe la zone de cisaillement ductile associée au plan de détachement. Notez également les occurrences magmatiques au cœur de dômes (coupes b, c et e). Figure issue de Wu & Lavier [2016].*

Au mur du détachement (i.e., au sein de l'unité inférieure), les roches constitutives du dôme structural se voient affectées par une déformation ductile qui tend à s'intensifier à l'approche du contact tectonique ; zone coloriée en beige sur la Figure I-2. Le long de ce gradient, il est ainsi possible d'observer le passage progressif d'une déformation ductile discrète – préservant dès lors partiellement au cœur du dôme le protolithe ou éventuellement des roches déformées lors d'une phase tectonique antérieure – à une déformation (ultra)mylonitique au niveau de la carapace du dôme. La mylonitisation est le plus souvent contemporaine d'un métamorphisme rétrograde de type schiste vert et/ou amphibolitique. La

trace d'un métamorphisme haute pression et basse température (H*P*-B*T*), sans rééquilibrage thermique, peut être également retrouvée au cœur du dôme. La préservation de paragenèses dans le faciès schistes bleus, voire dans le faciès des éclogites, témoigne de l'enfouissement de ces roches dans une zone de subduction, préalablement à leur exhumation. Juste au-dessous du plan de détachement, la déformation ductile peut être finalement reprise par un jeu de failles à fort pendage ou bien encore par une déformation (ultra)cataclastique. Le plan de faille arbore quant à lui divers indices de déplacement dans le régime cassant (e.g., stries, corrugations). L'unité supérieure, au toit du détachement, se distingue quant à elle par des dépôts sédimentaires syn-tectoniques ou bien des roches de bas grade métamorphique (Figure I-2). Contrairement à l'unité inférieure, la déformation ductile y est quasi-absente. Si tel est le cas, elle se limite uniquement sur les premiers mètres d'épaisseur juste au-dessus du plan de détachement. Seules des brèches ou des failles à fort pendage sont donc en général perceptibles. Les failles de grande envergure s'enracinent le plus souvent le long du plan de détachement, telles des failles listriques. Ces failles pendent dans la même direction que le plan de détachement, dessinant ainsi des blocs basculés (Figure I-2).

En résumé, les critères cinématiques de la déformation et le saut métamorphique de part et d'autre des détachements attestent du caractère extensif de dômes métamorphiques extensifs. Les failles faiblement pentées doivent être ainsi considérées comme des accidents à cinématique normale d'échelle crustale impliquant des déplacements de plusieurs kilomètres [e.g., *Crittenden et al.*, 1980; *Davis & Coney*, 1979; *Lister & Davis*, 1989].

1.1.2. Détachements crustaux & localisation de la déformation

Comme en témoignent les éléments structuraux à l'instant exposés, les détachements incarnent le parfait exemple d'une intense concentration de la déformation. Ces discontinuités tectoniques d'échelle crustale, inhérentes au développement de dômes métamorphiques extensifs, sont ainsi l'expression de l'état fini du phénomène de localisation de la déformation. Bien qu'ils soient parfois observés à l'affleurement comme des structures purement cassantes, les détachements semblent nucléer dans leur grande majorité telle une zone de cisaillement ductile et évoluer dans les stades ultimes de leur développement comme une faille à faible pendage. Du fait de leur style structural si particulier, les détachements ont suscité à la fois curiosité et scepticisme, soulevant notamment un certain nombre de questions fondamentales (e.g., contradictions avec la mécanique andersonienne). Depuis l'émergence du concept de MCC, une partie de la communauté scientifique s'est alors attachée à contraindre les processus responsables de leur nucléation. Un des modèles les plus populaires est celui initialement développé par *Buck* [1988] et *Lavier et al.* [1999], i.e., le modèle du « rolling-hinge » dans lequel toutes les failles normales à faible pendage sont considérées comme des discontinuités tectoniques initialement fortement pentées et progressivement basculées pendant le processus d'extension. Ce modèle fut repris de multiples fois dans de nombreux exemples de terrain, tels que dans la Montagne Noire [*Van den Driessche & Brun,* 1992] ou dans les Cyclades (Mer Égée, Grèce) [*Gautier & Brun*, 1994b; *Brun et al.,* 2017]. Il est pourtant aujourd'hui admis que la présence initiale d'hétérogénéités (mécaniques, thermo-mécaniques ou de densité) dans un volume soumis à des contraintes tectoniques peut également constituer un vecteur efficace de

localisation de la déformation le long de plans peu pentées [e.g., *Le Pourhiet et al.*, 2004; *Jolivet et al.*, 2004b; *Huet et al.*, 2011a; 2011b; *Labrousse et al.*, 2016; *Duretz et al.*, 2016]. Quelle que soit leur origine, ces hétérogénéités occasionnent en effet dans l'espace une non-linéarité de la résistance mécanique nécessaire à la localisation de la déformation. Néanmoins, évaluer dans un cas précis la nature de ces hétérogénéités s'avère être en pratique le plus souvent un exercice délicat. La croûte continentale est en effet un milieu architecturalement complexe dans lequel coexistent à toute échelle spatiale de multiples anisotropies ou instabilités transitoires susceptibles de localiser la déformation (e.g., variations texturales et de compositions minéralogiques ; présence de phases mécaniquement faibles tels que les micas ; contacts lithologiques ; magmatisme syn-extensif ; migmatitisation ; héritage tectonique). De ce fait, tester la sensibilité du phénomène de localisation de la déformation faces aux hétérogénéités présentes aux différentes échelles spatiales peut devenir quelque peu difficile et nécessite en général la mutualisation de diverses approches (e.g., terrain, datations radiométriques, modélisation, expérimentation).

1.2. Modèles d'interaction entre détachements crustaux & magmatisme intrusif

Dans ces domaines continentaux où l'extension s'accommode préférentiellement sous forme de MCCs, il arrive bien souvent que l'exhumation des roches métamorphiques de la croûte inférieure s'accompagne d'épisodes de migmatitisation et de remontées magmatiques. Les témoins de corps intrusifs au cœur de dômes métamorphiques, en étroite interaction avec des détachements crustaux, ne sont pas rare dans la nature (e.g., coupes géologiques (b), (c) et (e) de la Figure I-2). De telles occurrences ont été en effet identifiées dans la région du Basin & Range [e.g., *Davis & Coney*, 1979; *Hyndman*, 1980; *Dallmeyer et al.*, 1986; *Lee Armstrong & Ward*, 1991; *Vanderhaeghe & Teyssier*, 1997; *Campbell-Stone et al.*, 2000], en Asie de l'Est [e.g., *Davis et al.*, 1996; *Faure et al.*, 1996; *Shu et al.*, 1998; *Webb et al.*, 1999; *Lin & Wang*, 2006; *Lin et al.*, 2008; *Charles et al.*, 2011, 2013], en Papouasie-Nouvelle-Guinée [*Bladwin et al.*, 1993 ; *Lister & Baldwin*, 1993], dans la région méditerranéenne [e.g., *Dinter & Royden*, 1993; *Bozkurt & Park*, 1994; *Daniel & Jolivet*, 1995; *Hetzel et al.*, 1995; *Whitney & Dilek*, 1997; *Jolivet et al.*, 1998; *Rossetti et al.*, 1999], ou bien encore plus spécifiquement en mer Égée [*Faure et al.*, 1991; *Lee & Lister*, 1992; *Gautier et al.*, 1993; *Grasemann & Petrakakis*, 2007; *Jolivet et al.*, 2010; *Denèle et al.*, 2011]. Au cours de ces quatre dernières décennies, un certain nombre d'études se sont donc attelées à évaluer les processus géologiques par lesquels des épisodes magmatiques auraient pu être gémotriquement associées à l'activité de détachements crustaux au cours des histoires d'exhumation. Selon les contraintes temporelles obtenues (i.e., âges de mise en place des corps intrusifs et du métamorphisme rétrograde), divers modèles d'interaction ont été conceptualisés.

1.2.1. Le magmatisme comme vecteur de l'extension post-orogénique

Le magmatisme intrusif est communément considéré comme un processus d'importance majeure à même de modifier transitoirement et localement les propriétés physiques initiales de son milieu. Lorsque les datations radiométriques tendent à démontrer des

épisodes magmatiques synchrones des premiers stades d'exhumation de roches crustales, ou bien légèrement antérieurs (i.e, en phase tardi-orogénique), il est dès lors supposé que la présence de magmas au sein d'une croûte continentale sur-épaissie pourrait incarner un processus favorisant le développement de MCCs [e.g., *Carr*, 1992; *Baldwin et al.*, 1993; *Hill et al.*, 1995]. Il est en effet possible que des forts gradients thermiques en base de croûte et l'accumulation de produits magmatiques extraits de la fusion partielle puissent introduire de manière drastique un affaiblissement mécanique des roches environnantes ; ceci facilitant le fluage latéral de la croûte inférieure ductile tout en contribuant à l'exhumation de portions crustales sous forme de dômes [e.g., *Armstrong*, 1982; *Coney & Harms*, 1984; *Gans*, 1987; *Brown & Dallmeyer*, 1996; *MacCready et al.*, 1997; *Vanderhaeghe & Teyssier*, 2001; *Vanderhaeghe*, 2012]. En parallèle, la déformation se localiserait au toit d'intrusions magmatiques, donnant finalement lieu au développement de détachement crustaux. Cette hypothèse fut également étayée par des modélisations analogiques (Figure I-3) [e.g., *Brun et al.*, 1994; 2017], puis plus tard testée par des simulations thermo-mécaniques à l'échelle lithosphérique [e.g., *Tirel et al.*, 2004, 2008].

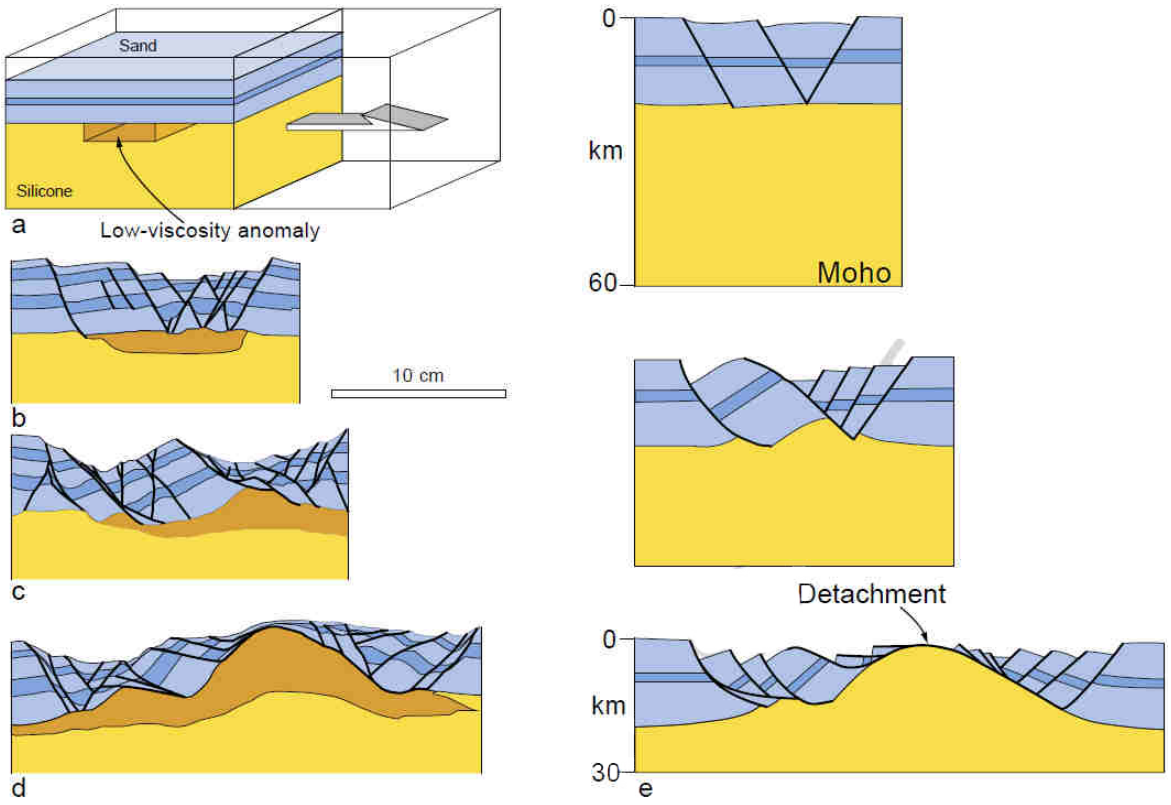

Figure I-3 : *modélisation analogique du développement d'un dôme métamorphique extensif dans un système ductile-cassant à deux couches, figure issue de Brun et al. [2017] et modifiée de Brun et al. [1994]. La couches supérieure et inférieure incarnent respectivement la croûte supérieure cassante et la croûte inférieure ductile (a) Boîte de départ ; notez la présence d'une anomalie de faible viscosité sous la couche s cassante, symbolisant la présence de magmas partiellement cristallisés. (b) à (d) évolution en coupe du modèle analogique ; avec l'augmentation de la quantité d'extension, la couche inférieure ductile flux latéralement mais également verticalement dans la zone où se localise l'anomalie de viscosité. Un détachement se localise progressivement au toit de l'anomalie. (e) Modèle général du développement d'un dôme métamorphique extensif et son détachement associé résumant le modèle analogique.*

1.2.2. Le magmatisme comme conséquence de l'amincissement crustal

L'initiation de détachements crustaux comme conséquence de l'activité magmatique, bien qu'il s'agisse d'une instabilité thermomécanique, est souvent soumise à controverse. Les âges de mise en place de ces intrusions ne semblent pas toujours coïncider avec le stade précoce du développement de MCCs (i.e., âges du métamorphisme rétrograde lié à l'exhumation des roches crustales), mais plutôt se limiter à leur histoire tardive. Dans un tel contexte, le magmatisme ne peut alors être regardé comme un réel candidat pour la genèse de MCCs, mais serait au contraire le produit d'un environnement thermique plus chaud au cours de l'amincissement lithosphérique. L'arrivée de flux mantelliques toroïdaux (i.e., dans un plan horizontal) et/ou poloïdaux (i.e., dans un plan vertical) sous la croûte continentale amincie est une hypothèse à l'origine de la fusion partielle et la production de magmas en base de croûte [e.g., *Jolivet et al.*, 2015; Menant et al., 2016a]. Selon d'autres auteurs, la migmatitisation et l'extraction de liquides silicatés seraient juste la conséquence de l'amincissement crustal et le phénomène de décompression qui lui est associé [e.g., *Teyssier & Whitney*, 2002; *Whitney et al.*, 2004b; *Teyssier et al.*, 2005]. Il est alors possible d'imaginer que la migration des magmas au travers de la croûte soit en partie guidée par des gradients de pression négatifs engendrés par l'extension et des zones d'intense concentration de la déformation, telles des zones de détachement, jusqu'à finalement atteindre le cœur de dômes métamorphiques déjà formés [e.g., *Fletcher et al.*, 1995; *Vanderhaeghe*, 1999; *Bonini et al.*, 2001]. Dans ce modèle, le magmatisme revêt un caractère totalement passif vis-à-vis de la tectonique extensive. Les détachements, en activité, se comportent comme des barrières mécaniques au-dessous desquelles les magmas en ascension sont piégés, stockés et tout simplement déformés au cours de leur cristallisation et leur refroidissement ultérieur. Néanmoins, ce modèle reste relativement simple dans sa conception. Une fois accumulés le long de zones de détachement, les magmas peuvent à leur tour perturber la structure thermique, le régime de déformation et l'architecture des dômes métamorphiques. C'est en tout cas ce que soutiennent certains auteurs pour expliquer la structure arquée de détachements [e.g., *Lister & Baldwin*, 1993] ou bien la présence de systèmes de détachements [e.g., *Daniel & Jolivet*, 1995] en étroite interaction avec des corps magmatiques (Figure I-4).

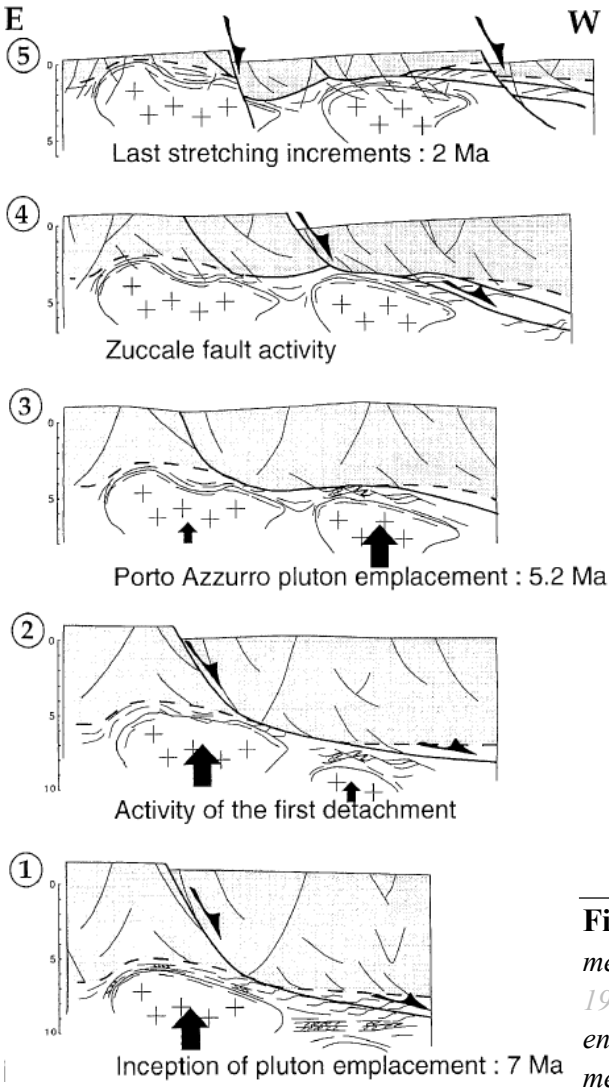

Figure I-4 : *schéma d'évolution en coupe E-O du dôme métamorphique de l'île d'Elbe [e.g., Daniel & Jolivet, 1995]. Les détachements se développent séquentiellement en raison d'arrivées magmatiques au cœur du dôme métamorphique.*

1.3. Magmatisme & mécanismes à l'origine de la localisation de la déformation

Comme évoqué à l'instant, les évènements magmatiques au sein d'une croûte continentale soumise à des contraintes tectoniques peuvent éventuellement favoriser le développement de MCCs (Figure I-3) ou bien impacter leur dynamique avec successivement une redistribution, puis une localisation de la déformation le long de détachements crustaux nouvellement formés (Figure I-4). Naturellement, ces scenarii ne tiennent pas uniquement compte des contraintes radiométriques ou de l'architecture des MCCs, mais s'appuient également sur les résultats expérimentaux acquis à la fin du siècle dernier. Par leur caractère faiblement visqueux (Figure I-5) [e.g., *Lejeune & Richet*, 1995; *Vigneresse et al.*, 1996], les corps magmatiques en cours de consolidation seraient en effet capables de générer avec leur encaissant des interfaces à rhéologie contrastée, le long desquelles la localisation de la déformation serait efficacement stimulée [e.g., *Lynch & Morgan*, 1987; *Pavlis*, 1996].

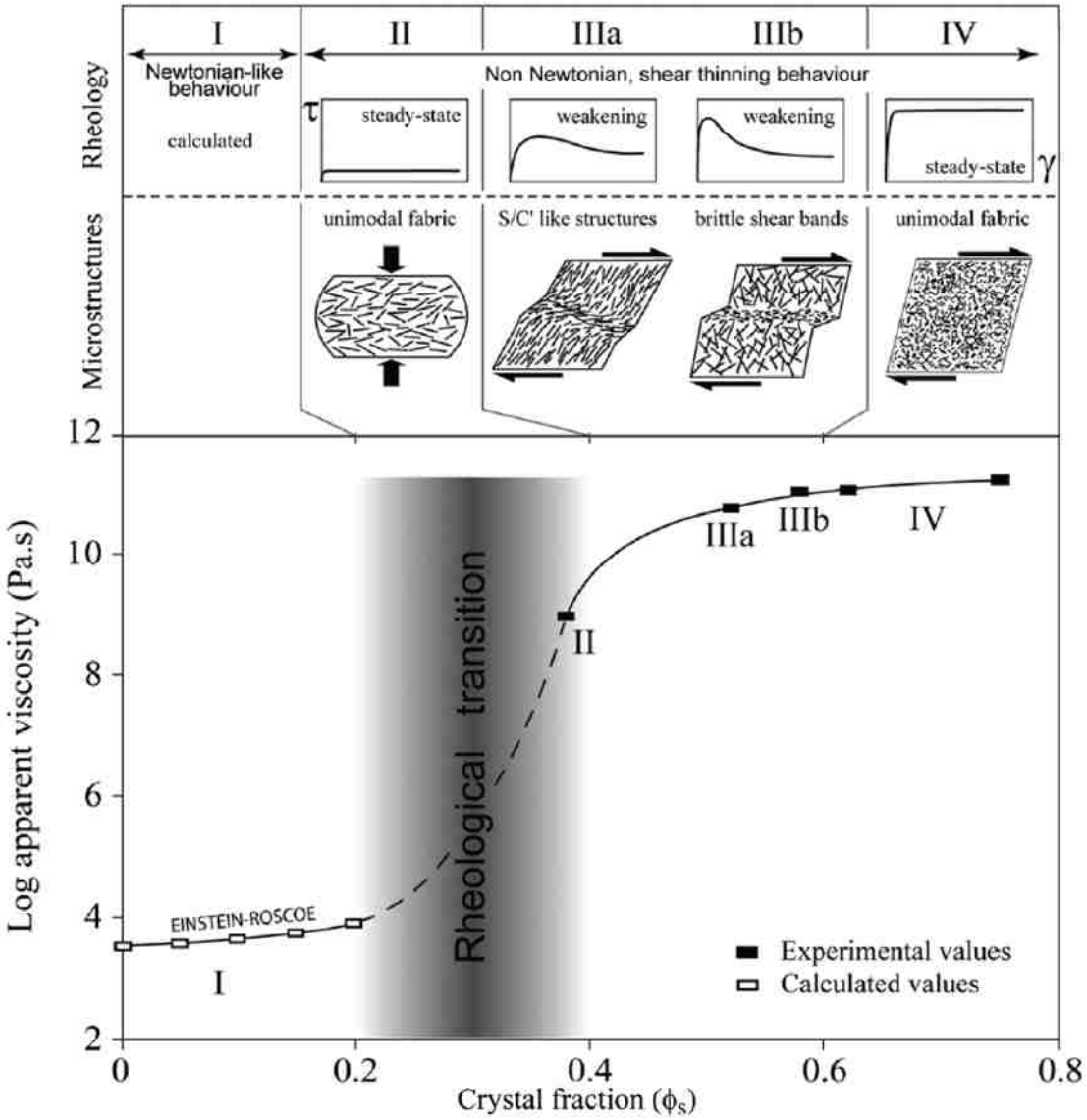

Figure I-5: *évolution du comportement rhéologique et structurale en fonction du taux de cristallinité d'une suspension magmatique, d'après Picard et al. [2013]. En bas : viscosité apparente en fonction de la fraction cristalline ϕ_s. En haut : croquis du illustrant l'évolution des microstructures développées avec le taux de cristallinité et le comportement rhéologique correspondant.*

Si de nombreux auteurs s'accordent à expliquer le rôle majeur des interfaces magma-encaissant dans l'initiation d'une déformation localisée, ce mécanisme ne peut être en réalité considéré à lui seul comme suffisant pour expliquer l'évolution de la déformation à l'approche de détachements crustaux et la manière dont elle se localise au sein même de granitoïdes syn-tectoniques. Nombreux sont les exemples naturels montrant en bordure de corps intrusifs des gradients d'intensité de la déformation, préservant ainsi sur de larges portions un continuum de la déformation depuis une structuration syn-magmatique (i.e., fabriques cristallines sans surimposition significative d'une déformation à l'état solide) jusqu'à une déformation ductile pénétrative. Ce simple constat laisse donc supposer que le phénomène de localisation de la déformation ne relève pas strictement de contrastes rhéologiques abrupts le long de contacts intrusifs, mais résulte également d'une non-linéarité de la résistance mécanique au sein même de complexes magmatiques au cours de leur cristallisation et leur refroidissement.

1.3.1. Les filons syn-plutoniques

Les hétérogénéités compositionnelles planaires (i.e., filons syn-plutoniques) peuvent être une hypothèse à l'origine d'une localisation de la déformation (Figure I-6) [e.g., *Christiansen & Pollard*, 1997; *Pennacchioni*, 2005; *Pennacchioni & Mancktelow*, 2007; *Mancktelow & Pennacchioni,* 2013]. L'injection de magmas sous forme de filon au sein d'un corps magmatique peut en effet introduire des forts gradients de la résistance mécanique et ainsi agir comme des sites préférentiels pour la nucléation d'une déformation localisée, à l'instar du processus opérant aux interfaces entre les corps magmatiques et leur encaissant.

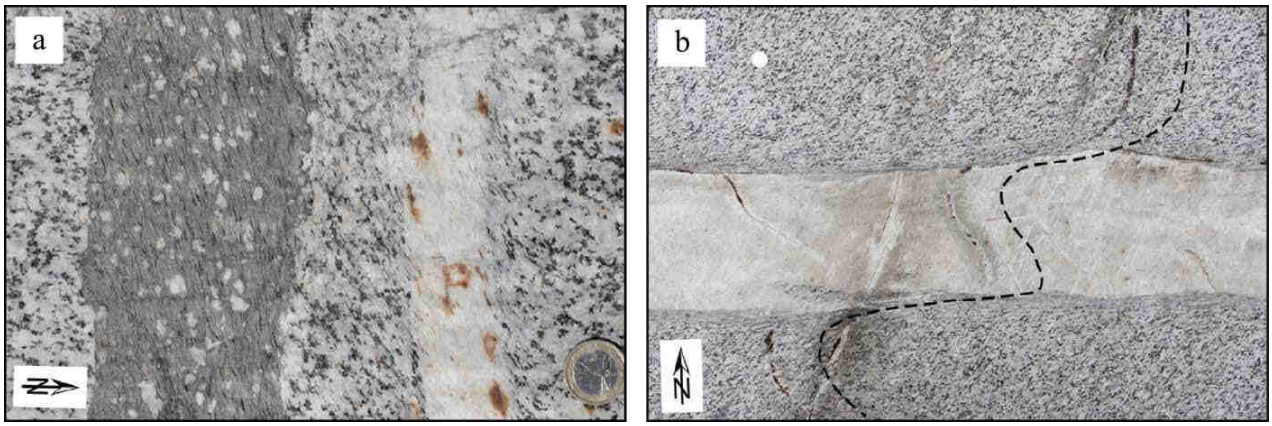

Figure I-6: *injections magmatiques au sein d'une granodiorite et phénomène de localisation de la déformation associé ; clichés issus de Mancktelow & Pennacchioni [2013]. (a) exemple de deux filons (à gauche : lamprophyre ; à droite : aplite) le long desquels la déformation s'accommode et se distribue de manière différente. Dans le cas du filon de lamprophyre, la déformation se distribue de façon homogène au sein même de ce filon ; la granodiorite au contact de ce filon n'est pas affectée par la déformation. Dans le cas du filon d'aplite, la déformation se concentre à l'inverse essentiellement au niveau de ses épontes. Ce constat est encore plus flagrant sur le cliché (b), montrant clairement une localisation de la déformation à l'interface granodiorite-aplite, avec en particulier une forte concentration de la déformation dans la granodiorite. La veine de quartz-calcite (indiquée par la ligne en pointillé) agit comme un marqueur passif délimitant la distribution hétérogène de la déformation.*

Selon le comportement rhéologique des roches magmatiques en présence, la déformation s'accommode et se distribue de diverses façons. Mancktelow & Pennacchioni [2013] ont par exemple mis en évidence des comportements de la déformation ductile bien distincts suivant la nature compositionnelle de filons au sein d'un même corps granodioritique (Figure I-6). Dans le cas d'un lamprophyre, la déformation tend à se concentrer au cœur du filon, tandis que la texture magmatique de l'hôte granodioritique le long du contact est relativement préservée (Figure I-6a). À l'inverse, dans le cas d'une aplite, la déformation se concentre préférentiellement à l'interface entre ce filon et le corps granodioritique (Figure I-6b). Si ces observations de terrain montrent clairement une relation étroite entre la présence de filons syn-plutoniques et le phénomène de localisation de la déformation, elles ne peuvent en revanche contraindre le stade (i.e., magmatique, tardi-magmatique, sub-solidus) durant lequel cette déformation localisée s'est initiée. D'autre part, dans les conditions magmatiques, le comportement rhéologique des magmas ne dépend pas exclusivement de leur composition mais aussi de nombreux autres propriétés intrinsèques de magmas (e.g., taux de cristallinités, quantité de volatils, homogénéité texturale) et paramètres extrinsèques (température, pression différentielle, vitesse de la déformation).

1.3.2. L'effet des textures magmatiques

Les inhomogénéités texturales, ou plus simplement les propriétés de la texture en elle-même (i.e., distribution de taille et de forme des cristaux mais aussi la manière dont ils s'agencent dans le liquide silicaté), sont considérées par quelques études comme un facteur susceptible de produire à leur échelle spatiale des chutes de la résistance mécanique et de permettre le développement de structures semi-pénétratives à localisées [e.g., *Tikoff & Teyssier*, 1994; *Arbaret et al.*, 2007; *Picard,* 2009; *Picard et al.*, 2011; 2013]. Alors que les témoins structuraux d'une déformation localisée le long filons syn-plutoniques sont sur le terrain perceptibles, identifier à l'affleurement l'effet des propriétés d'une texture sur le degré de localisation de la déformation s'avère être un exercice pour le moins délicat. Seuls les états de déformation finie sont observables et les témoins de l'état initial anté-déformation – donc de textures magmatiques – sont partiellement à totalement effacés par les derniers incréments de la déformation. Avec les études structurales, l'outil expérimental est considéré comme l'une des voies capables de fournir des contraintes supplémentaires sur la structuration progressive de magmas partiellement cristallisés et ainsi de mieux appréhender les conséquences mécaniques que pourraient entraîner les inhomogénéités texturales. Malgré la littérature abondante sur la rhéologie des magmas, peu d'études ont prêté attention au comportement structural de suspensions magmatiques [*Arbaret et al.*, 2007; *Picard*, 2009; *Forien et al.*, 2011; *Laumonier et al.*, 2011; *Picard et al.*, 2011, 2013; *Cordonnier et al.*, 2012; *Okumura et al.*, 2016].

Les quelques résultats expérimentaux de *Picard et al.* [2011, 2013] ont en particulier montré que le développement de fabriques cristallines et de structures semi-pénétratives à localisées est intimement lié aux propriétés texturales de la suspension magmatique, notamment dans les conditions de moyenne à forte fraction cristalline (Figure I-5). Au-delà de 20% vol. de particules solides, la rhéologie des suspensions magmatiques évolue vers un

comportement rhéologique non-newtonien (Figure I-5) [*Caricchi et al*., 2007; *Champallier et al*., 2008; *Picard et al*., 2013]. Le comportement rhéologique passe d'un système en écoulement contrôlé par les propriétés du liquide en une suspension solide capable de transmettre les contraintes, ce traduisant ainsi par une augmentation non-linéaire de la viscosité apparente. Avec l'augmentation de la fraction cristalline, les comportements rhéologiques et/ou structuraux des suspensions magmatiques évoluent. Dans leurs expériences, *Picard et al.* [2013] ont en particulier définit deux principaux seuils rhéologiques. Dans la gamme de cristallinité de 20-40% vol. (domaine II, Figure I-5), des fabriques pénétratives se développent par rotation et translation des particules anisométriques, permettant la stabilisation de la contrainte avec la déformation. Au-delà de ces 40% vol., le comportement rhéologique change (i.e., adoucissement généralisé avec la déformation) et quelques bandes semi-pénétratives à localisées se forment (domaine II, Figure I-5). Ce changement de comportement rhéologique et structural est lié à la taille et la forme des cristaux, mais également à leur distribution spatiale ainsi que leurs interactions mutuelles au sein du liquide silicaté lors de la déformation.

Ces études, bien qu'essentielles à la compréhension du comportement rhéologique et/ou structural de magmas partiellement cristallisés, ne sont pas forcément représentatives de la complexité chimique ou texturale de magmas naturels. La quasi-totalité des études expérimentales de ces dernières années ont été en effet réalisées sur des matériaux analogiques ou des systèmes silicatés synthétiques simplifiés [e.g., *Arbaret et al.*, 2007; *Caricchi et al.*, 2007; *Champallier et al.*, 2008; *Mueller et al.*, 2010; *Cimarelli et al.*, 2011; *Forien et al.*, 2011; *Laumonier et al*., 2011; *Picard et al.*, 2011; 2013; *Moitra & Gonnermann*, 2015].

2. Les Cyclades (Mer Égée, Grèce) : un terrain de jeu adéquat

L'archipel des Cyclades, appartenant aux îles grecques de la mer Égée (Figure I-7), apparait comme étant une cible privilégiée pour l'étude des processus contrôlant la localisation de la déformation le long de détachements crustaux et leurs interactions avec le magmatisme intrusif. Si les structures et les cinématiques associées sont bien contraintes dans les Cyclades, peu d'études se sont en revanche focalisées sur l'évolution et la distribution de la déformation dans les corps magmatiques.

2.1. L'extension arrière-arc en Égée

Le bassin égéen, domaine arrière-arc le plus à l'est de la Méditerranée (Figure I-7), s'est formé au niveau de la plaque supérieure de la zone de subduction hellénique [*Le Pichon & Angelier*, 1981]. Comme la plupart des domaines continentaux soumis à un régime extensif, la région égéenne a connu une histoire tectonique complexe, produisant des hétérogénéités thermomécaniques dans la croûte, tels de grands chevauchements, des détachements, de la fusion partielle ou même du magmatisme intrusif [*Jolivet & Brun*, 2010; *Royden & Papanikolaou*, 2011; *Jolivet et al.*, 2013]. En raison de la convergence entre les plaques Afrique et Eurasie depuis le Crétacé supérieur (Figure I-8), le domaine arrière-arc égéen a été au préalable occupé par la ceinture Hellénides-Taurides, un prisme orogénique polygénique construit par l'accrétion progressive de portions crustales à affinité océanique et continentale

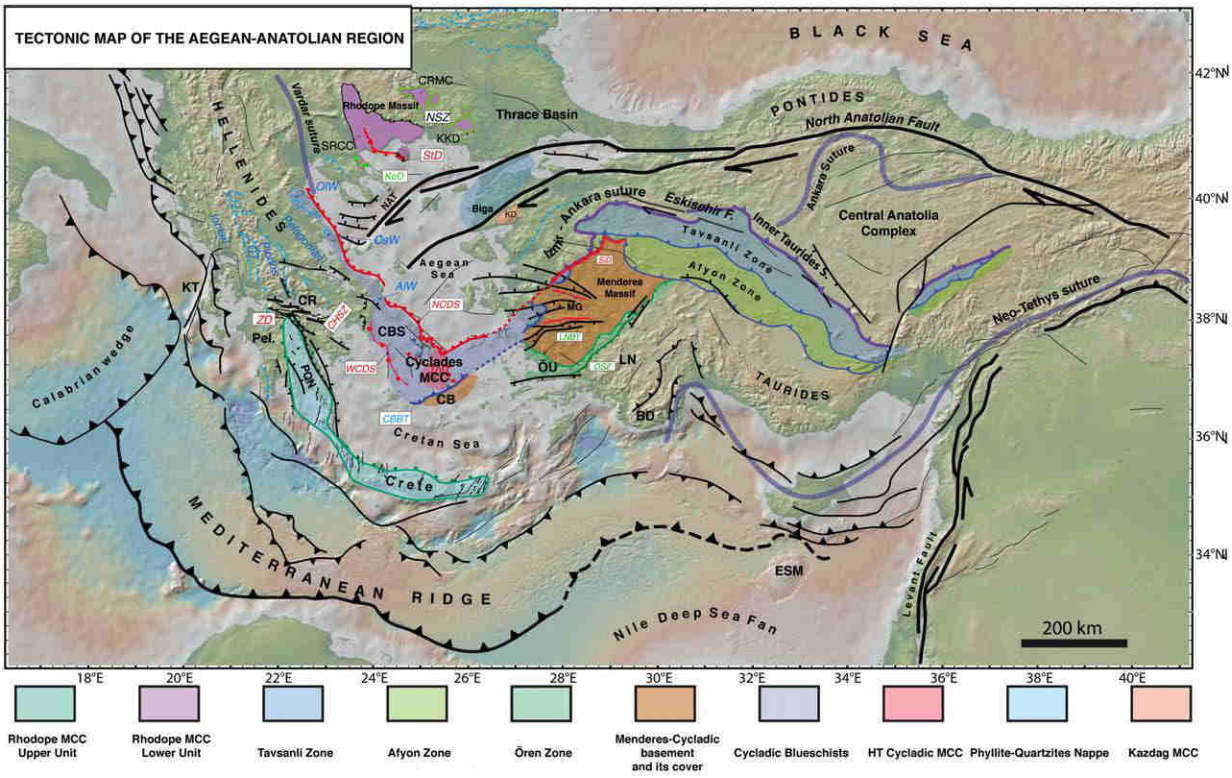

Figure I-7: *carte tectonique de la Méditerranée orientale montrant les principales structures actives (lignes noires), les principales zones de suture océanique (lignes épaisses violettes ou bleues), les principaux chevauchements constituant la chaîne des Hellénides-Taurides (lignes fines bleues), les principales structures extensives à faible pendage (i.e. détachements, lignes rouges). D'après Jolivet et al. [2013].*

[*Aubouin*, 1958; *Jacobshagen et al.*, 1978; *Bonneau*, 1984; *van Hinsbergen et al.*, 2005; *Ring et al.*, 2010]. L'empilement de nappes à vergence sud qui en résulte a permis successivement d'enclencher des processus d'enfouissement et d'exhumation syn-orogénique à haute pression-basse température (H*P*-L*T*) sous des chevauchements et des détachements crustaux, respectivement [*Jolivet et al.*, 1994, 2003, *Ring et al.*, 2007a, 2007b; *Brun & Faccenna*, 2008; *Huet et al.*, 2009]. Depuis l'Eocène moyen (~45 Ma, Figure I-8), la croûte Hellénique sur-épaissie fut d'abord soumise à une tectonique extensive en lien avec une éventuelle délamination lithosphérique tandis que la zone de subduction hellénique est restée relativement statique ou reculait lentement vers le sud, permettant ainsi le développement de MCCs dans le Rhodope, région septentrionale du domaine Égéen (*Burg* [2012] et les articles référencés). En réponse au retrait plus rapide vers le sud du panneau plongeant hellénique depuis 30-35 Ma (Figure I-8), la plaque supérieure eurasienne a subi une extension arrière-arc [*Jolivet & Faccenna*, 2000], jusqu'à atteindre l'architecture tectonique actuelle du domaine égéen avec un prisme d'accrétion arqué (i.e. Ride Méditerranéenne, Figure I-7). L'extension arrière-arc est aujourd'hui active autour de la Mer Égée, i.e., la Turquie Occidentale, le rift de Corinthe, la région Sud du Péloponnèse et la Crète [*Jackson*, 1994; *Hatzfeld et al.*, 2000; *Goldsworthy et al.*, 2002]. L'absence quasi-totale d'activité sismique en Mer Égée – seulement présente sous l'arc volcanique égéen [*Bohnhoff et al.*, 2004, 2006; *Dimitriadis et al.*, 2009] –, suggère que cette région se comporte actuellement tel un bloc rigide.

2.2. Les dômes métamorphiques extensifs cycladiques

Dans l'archipel des Cyclades, située au cœur de la mer Égée (Figures I-7 et I-9), l'extension arrière-arc est manifeste de l'Oligocène au Miocène (Figure I-10) [*Jolivet & Faccenna*, 2000; *Jolivet & Brun*, 2010; *Ring et al.*, 2010]. Au cours de cette période, le retrait du panneau plongeant et le changement du régime de contrainte associé ont probablement été accompagnés d'une délamination lithosphérique et d'une déchirure du panneau plongeant; tout cela étant également contemporain d'un état thermique plus chaud dans la lithosphère, d'une fusion partielle de la croûte inférieure en extension et de la formation de multiples MCCs [*Lister et al.*, 1984; *Gautier et al.*, 1993; *Gautier & Brun*, 1994a, 1994b; *Keay et al.*, 2001; *Vanderhaeghe*, 2004; *Pe-Piper & Piper*, 2006; *Ersoy & Palmer*, 2013; *Jolivet et al.*, 2013, *Menant et al.*, 2016a, 2016b]. Plus précisément, la formation des MCCs cycladiques et des détachements associés ont conduit à l'exhumation progressive des parties les plus profondes du prisme orogénique hellénique (i.e., le socle continental cycladique et l'unité des schistes bleus cycladiques, voir plus loin pour plus de précision, Figure I-9). Cette exhumation fut contemporaine d'un métamorphisme rétrograde de types schistes vert et amphibolitique. Ce métamorphisme s'est surimposé à un métamorphisme H*P*-L*T* d'âge Eocène (Figure I-10). Au nord et au centre des Cyclades, l'exhumation est accommodée respectivement par le North Cycladic Detachment System (NCDS) [*Jolivet et al.*, 2010; *Lecomte et al.*, 2010] et le Naxos–Paros Detachment System (NPDS) [*Gautier et al.*, 1993; *Brichau et al.*, 2006], deux systèmes de détachement crustaux à cinématique vers le nord (Figure I-9). À l'échelle de l'Égée, le NCDS s'étend sur plus de 200 km depuis Evia jusqu'aux îles cycladiques les plus septentrionales (Andros, Tinos et Mykonos), voire même plus à l'est sur l'île d'Ikaria [*Jolivet et al.*, 2010]. Dans les Cyclades occidentales, une grande partie de l'exhumation fut accommodée par le West Cycladic Detachment System (WCDS), une série de détachements à vergence opposée et à cinématique vers le sud-ouest (Figure I-9). Ce système de détachements affleure depuis Lavrion (Grèce continentale) [*Skarpelis*, 2007; *Krohe et al.*, 2010; *Berger et al.*, 2013] jusqu'au îles cycladiques occidentales (Kythnos, Kea and Serifos) [*Iglseder et al.*, 2011; *Grasemann et al.*, 2012; *Rice et al.*, 2012]. Une extension possible vers le sud-est du WCDS est proposée au large des îles de Sifnos et Folegandros [*Ring et al.*, 2011; *Augier et al.*, 2015b; *Roche et al.*, 2016]. Plus à l'est, sur les îles de Sikinos et Ios (Figure I-9), une déformation ductile top-S est également reconnue, d'abord interprétée comme étant le reflet d'une zone de cisaillement extensive (i.e., le South Cyclades Shear Zone, SCSZ) [*Lister et al.*, 1984; *Vandenberg & Lister*, 1996; *Baldwin & Lister*, 1998; *Forster & Lister*, 2009], mais plutôt vu aujourd'hui comme un évènement chevauchant d'âge Eocène repris au cours l'Oligocène par une déformation extensive top-N [*Huet et al.*, 2009; *Augier et al.*, 2015b].

L'histoire tardive de l'exhumation est principalement accommodée par des incréments cassants de la déformation le long des détachements, remontant ainsi vers la surface trois unités principales [*Bonneau*, 1984; *Jolivet et al.*, 2004a; *Jolivet & Brun*, 2010; *Ring et al.*, 2010]. De bas en haut de la pile tectonique (Figure I-9), on reconnaîtra (1) le socle continental cycladique, constitué principalement de para- et orthogneiss équilibrés dans les conditions métamorphiques de type amphibolitique d'âge Varisque ou même pré-Varique [*Henjes-Kunst & Kreuzer*, 1982; *Andriessen et al.*, 1987; *Keay & Lister*, 2002]. Affleurant dans certaines fenêtres tectoniques

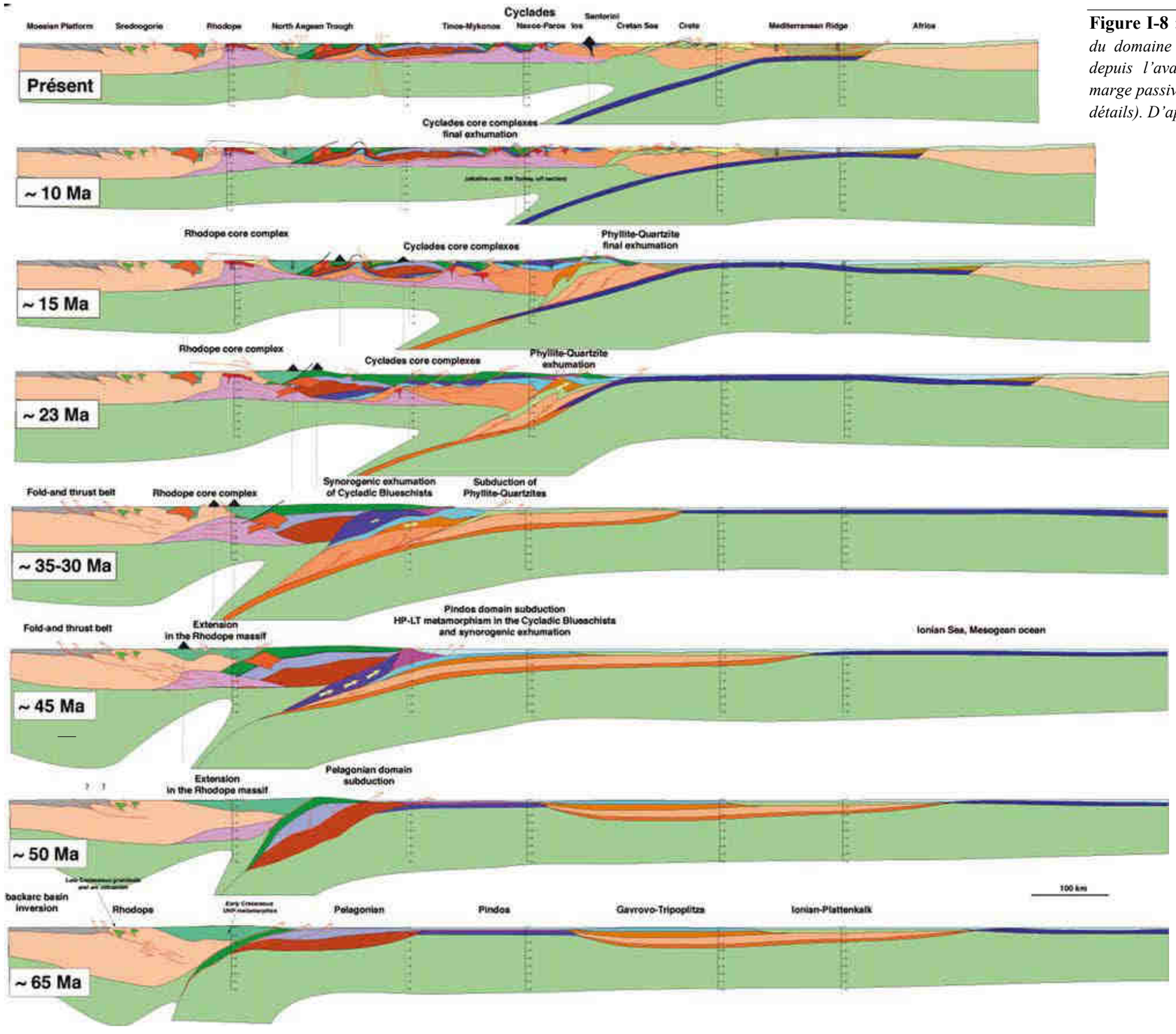

Figure I-8 : *Reconstructions tectoniques en coupes N-S du domaine égéen depuis 65 Ma jusqu'à aujourd'hui, depuis l'avant-pays des Balkans au nord jusqu'à la marge passive africaine au sud (voir le texte pour plus de détails). D'après Jolivet & Brun [2010].*

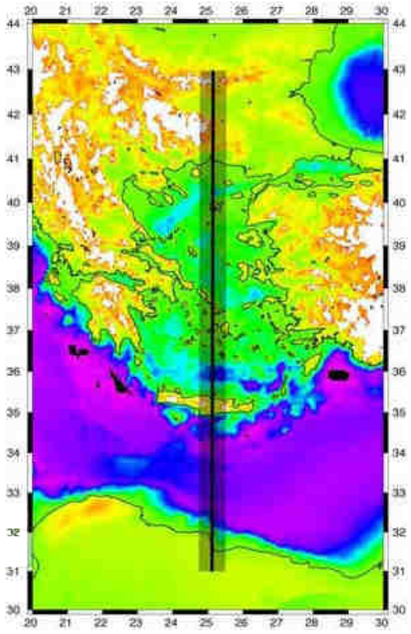

(Naxos, Paros, Ikaria, Ios, Ios, Sikinos, Serifos et Mykonos-Delos), le socle cycladique contient localement une couverture de métapelites et de marbres [*Dürr et al.*, 1978; *Ring et al.*, 1999; *Grasemann & Petrakakis*, 2007]. Le socle continental cycladique est positionné structuralement sous (2) l'unité des schistes bleus cycladiques, une unité méta-volcanosédimentaire dominée par une séquence de schistes et de marbres contenant quelques boudins de métabasite [*Blake et al.*, 1981; *Reinecke et al.*, 1982; *Avigad & Garfunkel*, 1989; *Keiter et al.*, 2004]. Alors que le socle continental cycladique et l'unité des schistes bleus cycladiques ont tous deux été soumis à un événement de H*P*-L*T* au cours de l'Éocène [*Andriessen et al.*, 1979; *Wijbrans & McDougall*, 1986, 1988; *Maluski et al.*, 1987; *Bröcker et al.*, 1993; *Trotet et al.*, 2001a; *Parra et al.*, 2002; *Groppo et al.*, 2009; *Huet et al.*, 2015], l'unité supérieure cycladique (3) est dépourvue de reliques de H*P*-L*T,* laissant penser que cette unité ne fut pas enfouie au sein de la zone de subduction hellénique. Lithologiquement hétérogène, l'unité supérieure cycladique n'affleure qu'au niveau de klippes. Elle comprend un socle continental (amphibolites, gneiss) qui préserve les âges du métamorphisme H*T* Crétacé et une couverture sédimentaire Permienne à Mésozoïque obductée par une série ophiolitique (i.e.,. serpentinite, gabbros, basaltes) [*Altherr et al.*, 1994; *Patzak et al.*, 1994; *Katzir et al.*, 1996; *Papanikolaou*, 2009; *Martha et al.*, 2016]. Cette pile tectonique est fréquemment bordée par des bassins sédimentaires remplis de dépôts détritiques marins et continentaux [*Sanchez-Gomez et al.*, 2002; *Kuhlemann et al.*, 2004]. Les clastes des unités cycladiques sous-jacentes sont couramment observés, indiquant des dépôts syn-tectoniques [*Kuhlemann et al.*, 2004; *Lecomte et al.*, 2010].

2.3. Place du magmatisme intrusif dans l'extion arrière-arc

Au cours de l'évolution tardive de l'exhumation des roches crustales, plusieurs granitoïdes syn-tectoniques se sont mis en place au cœur des MCCs Cycladiques à des niveaux de croûte supérieure [*Gautier et al.*, 1993; *Bröcker & Franz*, 1994; *Lucas*, 1999; *Pe-Piper*, 2000; *St. Seymour et al.*, 2009; *Cao et al.*, 2017]. Les âges de mise en place de ces granitoïdes ((U-Th) / Pb sur zircon) révèle des histoires de cristallisation allant de 15 à 9 Ma (Figure I-10) [*Keay*, 1998; *Keay et al.*, 2001; *Brichau et al.*, 2007, 2008; *Iglseder et al.*, 2009; *Bolhar et al.*, 2010], un intervalle de temps relativement court durant lequel un magmatisme de type-I et -S migre depuis le NNE des Cyclades (Tinos, Mykonos-Delos, Ikaria) vers le SO (Serifos), en passant par le centre des Cyclades (Naxos, Paros). Les intrusions de type-S sont principalement associées aux dômes migmatitiques et presque systématiquement plus âgées que les intrusions de type-I spatialement associées. Les granitoïdes de type-I sont placés sous des détachements d'échelle crustale (Figure I-9). Leur pétrologie englobent un large spectre de compositions modales et certains d'entre eux constituent des intrusions composites à grande échelle [*Altherr et al.*, 1982; *Pe-Piper et al.*, 1997; *Altherr & Siebel*, 2002; *Iglseder et al.*, 2009; *Denèle et al.*, 2011]. Il est également intéressant de noter que ces corps intrusifs sont généralement issus d'un mélange entre une fusion partielle de la croûte et de magmas dérivés du manteau dans des proportions fluctuantes, comme documenté par des études géochimiques [*Altherr et al.*, 1988; *Altherr & Siebel*, 2002; *Pe-Piper & Piper*, 2006; *Stouraiti et al.*, 2010; *Bolhar et al.*, 2012]. À l'affleurement, les reliques d'une source présumée mantellique et l'interaction de magmas de

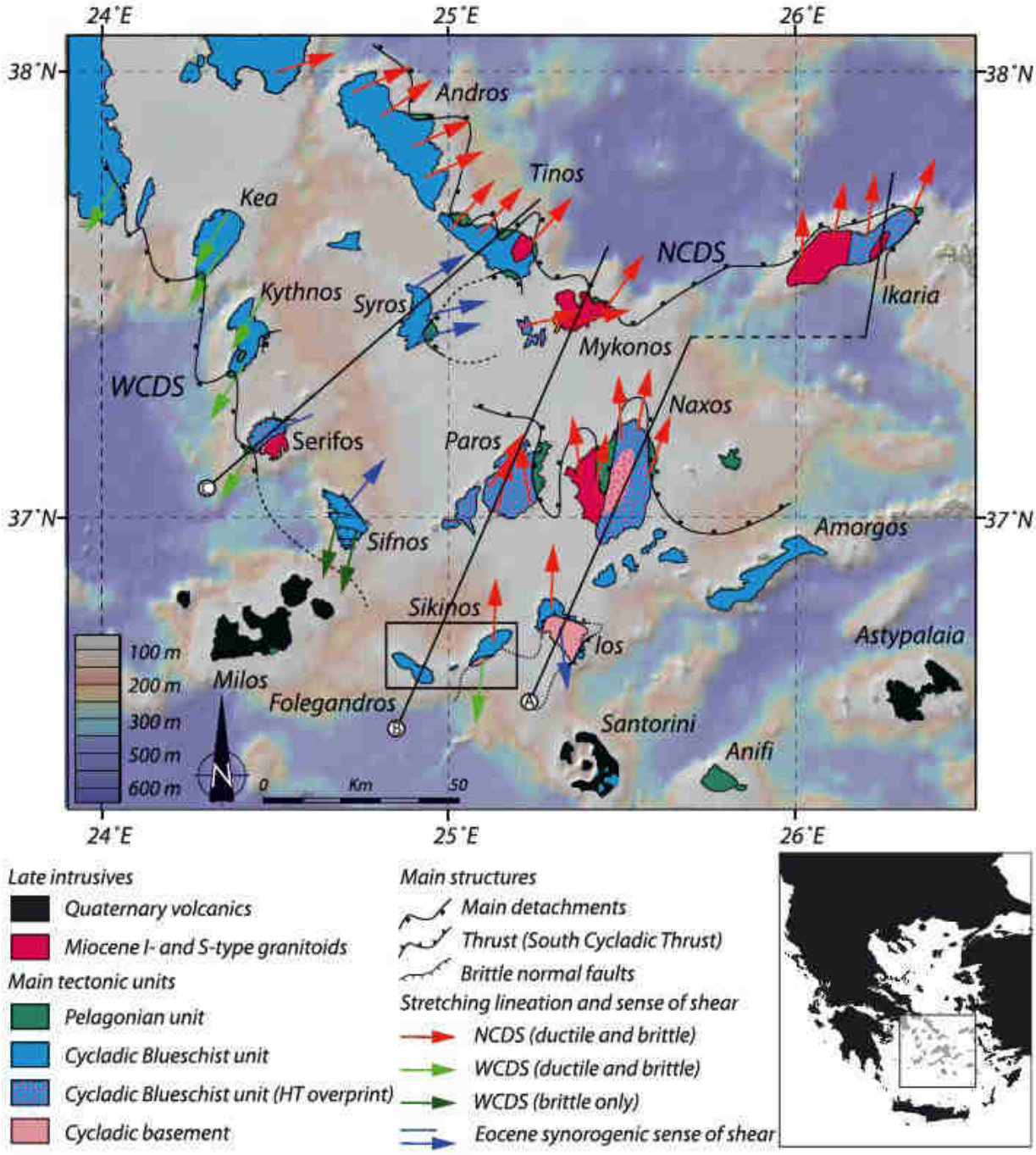

Figure I-9: *carte tectonique du domaine cycladique, d'après Augier et al. [2015b]. A l'echelle du dmaine, notez la relation spatiale entre les granitoïdes de type-I (i.e., Tinos, Mykonos-Delos-Rhenia, Ikaria, Naxos et Serifos) et les systèmes de détachements (NCDS, WCDS et NPDS). NCDS: North Cycladic Detachment System. NPDS: Naxos–Paros Detachment System. WCDS: West Cycladic Detachment System. SCSZ: South Cyclades Shear Zone. VD: Vari detachment.*

compositions hétérogènes lors du refroidissement des intrusions peuvent être également montrées par des occurrences d'enclaves mafiques et des filons syn-plutoniques au sein de corps magmatiques plus felsiques [e.g., *Avigad et al.*, 1998; *Koukouvelas & Kokkalas*, 2003; *Denèle et al.*, 2011]. Par conséquent, la variation de leurs caractéristiques pétrographiques et géochimiques a conduit certains auteurs à suggérer une mise en place incrémentale de plusieurs

injections magmatiques, une suggestion en quelque sorte corroborée par les spectres d'âge multimodaux (i.e., (U-Th)/Pb sur zircons) obtenus à partir des granitoïdes de type-I.

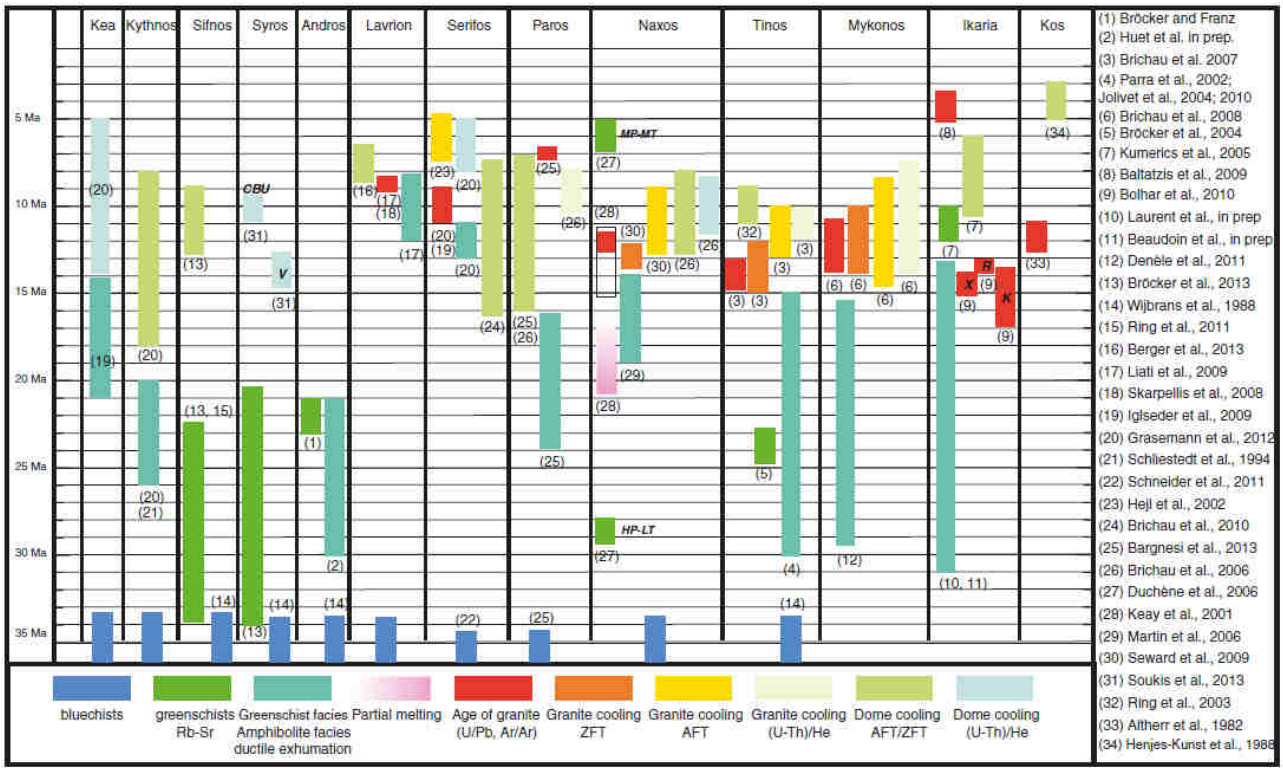

Figure I-10: *compilation des âges radiométriques disponibles dans les îles cycladiques où le développement de dômes métamorphiques extensifs et leurs systèmes de détachement associés (c. -à-d. NCDS, NPDS et WCDS) sont spatialement associés à une activité magmatique. Notez que les épisodes magmatiques sont tardifs par rapport au métamorphisme rétrograde de type schiste vert. Le côté droit de la figure comprend toutes les références. D'après Jolivet et al. [2015].*

Malgré les progrès significatifs dans la compréhension géologique des Cyclades, aucun consensus n'a encore été atteint sur les mécanismes responsables de l'association étroite entre corps magmatiques et détachements crustaux. En raison des âges de mise en place tardives des intrusions par rapport aux âges du métamorphisme rétrograde, la plupart des contributions ont conclu que le magmatisme ne semble ni être un vecteur efficace pour le développement des MCC ni un précurseur de localisation de la déformation le long des détachements, et que certains d'entre eux n'auraient servi que de marqueurs passifs de l'extension crustale [*Brichau et al.*, 2007, 2008; *Bolhar et al.*, 2010]. En ce sens, les détachement auraient plutôt favorisé des voies préférentielles pour le transport du magma à travers la croûte, tandis que la mise en place de corps intrusifs serait contrôlée par des détachements actifs [*Brichau et al.*, 2007, 2008; *Bolhar et al.*, 2010]. Bien que reconnaissant la logique de cette dernière proposition, certaines études sur le terrain ont suggéré de manière alternative un rôle plus important de l'activité magmatique dans la redistribution et la localisation de la déformation, en favorisant notamment la nucléation de nouvelles zones de détachement [*Jolivet et al.*, 2010; *Denèle et al.*, 2011].

3. Ce que vous trouverez dans ce mémoire

Chapitre II – ***Structuration d'un granitoïde sous un détachement d'échelle crustale : le dôme métamorphique de Naxos (Cyclades, Grèce)***. Ce second volet s'attache à caractériser la distribution et l'évolution de la déformation au sein d'un corps magmatique syn-extensif placé sous un détachement d'échelle crustale. L'étude comprend (1) des données structurales, (2) des observations microstructurales, (3) des analyses tomographiques par absorption de rayon X qui permettront de quantifier l'intensité de la fabrique de forme minéralogique en 2-D et 3-D d'échantillons, et enfin (4) des mesures d'orientations préférentielles d'axes cristallographiques du quartz par EBSD (en anglais *Electron BackScattered Diffraction)* afin de remonter à d'éventuels mécanismes de déformation plastique.

Chapitre III – ***Interactions entre magmatisme et un système de détachements : le dôme métamorphique extensif de Serifos (Cyclades, Grèce)***. Ce troisième volet vise à reconstituer l'architecture globale du dôme métamorphique de Serifos et d'en extraire un modèle d'interaction entre détachements et magmatisme intrusif. Ce travail comporte ainsi une étude structurale couvrant l'ensemble du dôme et le corps intrusif, des observations microstructurales et des mesures d'anisotropie de susceptibilité magnétique (ASM).

Chapitre IV – ***Comment le magmatisme syn-extensif a-t-il impacté l'évolution tardive des dômes métamorphiques cycladiques***. Ce quatrième volet se propose d'évaluer à l'échelle de l'ensemble du domaine des Cyclades l'impact du magmatisme intrusif sur la dynamique des dômes métamorphiques extensifs (MCCs). Rédigé sous la forme d'un arcticle de synthèse, le chapitre englobe une étude comparative des cinq dômes métamorphiques extensifs où les complexes plutoniques affleurent à proximité de détachements (Tinos, Mykonos-Delos-Rhenia, Ikaria, Naxos et Serifos). Cette synthèse intègre ainsi les observations terrain, analyses et discussions des précédents chapitres ainsi qu'un certain nombre d'éléments clés de la littérature accumulés ces dernières décennies (âges radiométriques, caractéristiques tectono-métamorphiques, cinématiques)

Chapitre V – ***Déformation expérimentale de magmas granodioritiques de faible à forte cristallinité***. Ce cinquième volet ambitionne d'évaluer, sous l'effet d'un cisaillement simple simulé par un mouvement de torsion, le comportement structural de suspensions magmatiques chimiquement et texturalement proches de systèmes naturels, et finalement d'en déduire de possibles mécanismes à l'origine de la localisation de la déformation au sein de magmas ne comportant initialement aucune hétérogénéité forte (e.g., enclaves). Les expériences de synthèse ont ainsi couvert une gamme de cristallinité allant depuis quelques pourcents jusqu'à la quasi solidification. Ces mêmes produits expérimentaux ont été ensuite déformés au sein d'une presse de type Paterson dans des conditions de pression (300 MPa) et température (800, 750, 700 ou 650°C) identiques à celles imposées durant leur synthèse en autoclave.

Références bibliographiques

Altherr, R., Kreuzer, H., Lenz, H., Wendt, I., Harre, W., & Dürr, S. (1994). Further evidence for a Late Cretaceous low-pressure/high-temperature terrane in the Cyclades, Greece. *Chemie Der Erde*, *54*, 319–328.

Altherr, R., Henjes-Kunst, F., Matthews, A., Friedrichsen, H., & Hansen, B. T. (1988). O-Sr isotopic variations in Miocene granitoids from the Aegean: evidence for an origin by combined assimilation and fractional crystallization. *Contributions to Mineralogy and Petrology*, *100*(4), 528–541. https://doi.org/10.1007/BF00371381

Altherr, R., Kreuzer, H., Wendt, I., Lenz, H., Wagner, G. A., Keller, J., … Höhndorf, A. (1982). A late Oligocene/early Miocene high temperature belt in the Attic-Cycladic crystalline complex (SE Pelagonian, Greece). *Geologisches Jahrbuch*, *E23*, 97–164.

Altherr, R., & Siebel, W. (2002). I-type plutonism in a continental back-arc setting: Miocene granitoids and monzonites from the central Aegean Sea, Greece. *Contributions to Mineralogy and Petrology*, *143*(4), 397–415. https://doi.org/10.1007/s00410-002-0352-y

Andriessen, P. A. M., Banga, G., & Hebeda, E. H. (1987). Isotopic age study of pre-Alpine rocks in the basal units on Naxos, Sikinos and Ios, Greek Cyclades., *66*, 3–14.

Andriessen, P. A. M., Boelrijk, N. A. I. M., Hebeda, E. H., Priem, H. N. A., Verdurnen, E. A. T., & Verschure, R. H. (1979). Dating the events of metamorphism and granitic magmatism in the Alpine orogen of Naxos (Cyclades, Greece). *Contributions to Mineralogy and Petrology*, *69*(3), 215–225. https://doi.org/10.1007/BF00372323

Arbaret, L., Bystricky, M., & Champallier, R. (2007). Microstructures and rheology of hydrous synthetic magmatic suspensions deformed in torsion at high pressure. *Journal of Geophysical Research*, *112*(B10), 1–24. https://doi.org/10.1029/2006JB004856

Armstrong, R. L. (1982). Cordilleran Metamorphic Core Complexes -- From Arizona to Southern Canada. *Annual Review of Earth and Planetary Sciences*, *10*(1), 129–154. https://doi.org/10.1146/annurev.ea.10.050182.001021

Aubouin, J. (1959). *Contribution à l'étude de la Grèce septentrionale; les confins de l'Epire et de la Thessalie* (Ph.D thesis). Univ. Paris, France.

Augier, R., Jolivet, L., Gadenne, L., Lahfid, A., & Driussi, O. (2015). Exhumation kinematics of the Cycladic Blueschists unit and back-arc extension, insight from the Southern Cyclades (Sikinos and Folegandros Islands, Greece). *Tectonics*, *34*(1), 152–185. https://doi.org/10.1002/2014TC003664

Augier, R., Choulet, F., Faure, M., & Turrillot, P. (2015). A turning-point in the evolution of the Variscan orogen: the ca. 325 Ma regional partial-melting event of the coastal South Armorican domain (South Brittany and Vendée, France). *Bulletin de La Société Géologique de France*, *186*(2–3), 63–91. https://doi.org/10.2113/gssgfbull.186.2-3.63

Avigad, D., & Garfunkel, Z. (1989). Low-angle faults above and below a blueschist belt - Tinos Island, Cyclades, Greece. *Terra Nova*, *1*(2), 182–187. https://doi.org/10.1111/j.1365-3121.1989.tb00350.x

Avigad, D., Baer, G., & Heimann, A. (1998). Block rotations and continental extension in the central Aegean Sea: palaeomagnetic and structural evidence from Tinos and Mykonos (Cyclades, Greece). *Earth and Planetary Science Letters*, *157*(1–2), 23–40. https://doi.org/10.1016/S0012-821X(98)00024-7

Baldwin, S. L., & Lister, G. S. (1998). Thermochronology of the South Cyclades Shear Zone, Ios, Greece: Effects of ductile shear in the argon partial retention zone. *Journal of Geophysical Research*, *103*(B4), 7315. https://doi.org/10.1029/97JB03106

Baldwin, S. L., Lister, G. S., Hill, E. J., Foster, D. A., & McDougall, I. (1993). Thermochronologic constraints on the tectonic evolution of active metamorphic core complexes, D'entrecasteaux Islands, Papua New Guinea. *Tectonics*, *12*(3), 611–628. https://doi.org/10.1029/93TC00235

Berger, A., Schneider, D. A., Grasemann, B., & Stockli, D. (2013). Footwall mineralization during Late Miocene extension along the West Cycladic Detachment System, Lavrion, Greece. *Terra Nova*, *25*(3), 181–191. https://doi.org/10.1111/ ter.12016

Blake, M. C., Bonneau, M., Geyssant, J., Kienast, J. R., Lepvrier, C., Maluski, H., & Papanikolaou, D. (1981). A geologic reconnaissance of the Cycladic blueschist belt, Greece. *Geological Society of America Bulletin*, *92*(5), 247–254. https://doi.org/10.1130/0016-7606(1981)92<247:AGROTC>2.0.CO;2

Bohnhoff, M., Rische, M., Meier, T., Becker, D., Stavrakakis, G., & Harjes, H.-P. (2006). Microseismic activity in the Hellenic Volcanic Arc, Greece, with emphasis on the seismotectonic setting of the Santorini–Amorgos zone. *Tectonophysics*, *423*(1–4), 17–33. https://doi.org/10.1016/j.tecto.2006.03.024

Bohnhoff, M., Rische, M., Meier, T., Endrun, B., Becker, D., Harjes, H.-P., & Stavrakakis, G. (2004). CYC-NET: A Temporary Seismic Network on the Cyclades (Aegean Sea, Greece). *Seismological Research Letters*, *75*(3), 352–359. https://doi.org/10.1785/gssrl.75.3.352

Bolhar, R., Ring, U., & Allen, C. M. (2010). An integrated zircon geochronological and geochemical investigation into the Miocene plutonic evolution of the Cyclades, Aegean Sea, Greece: Part 1: Geochronology. *Contributions to Mineralogy and Petrology*, *160*(5), 719–742. https://doi.org/10.1007/s00410-010-0504-4

Bolhar, R., Ring, U., Kemp, A. I. S., Whitehouse, M. J., Weaver, S. D., Woodhead, J. D., … Turnbull, R. (2012). An integrated zircon geochronological and geochemical investigation into the Miocene plutonic evolution of the Cyclades, Aegean Sea, Greece: part 2: geochemistry. *Contributions to Mineralogy and Petrology*, *164*(6), 915–933. https://doi.org/10.1007/s00410-012-0759-z

Bonini, M., Sokoutis, D., Mulugeta, G., Boccaletti, M., Corti, G., Innocenti, F., … Mazzarini, F. (2001). Dynamics of magma emplacement in centrifuge models of continental extension with implications for flank volcanism. *Tectonics*, *20*(6), 1053–1065. https://doi.org/10.1029/2001TC900017

Bonneau, M. (1984). Correlation of the Hellenide nappes in the south-east Aegean and their tectonic reconstruction. *Geological Society, London, Special Publications*, *17*(1), 517–527. https://doi.org/10.1144/GSL.SP.1984.017.01.38

Bozkurt, E., & Park, L. R. G. (1994). Southern Menderes Massif: an incipient metamorphic core complex in western Anatolia, Turkey. *Journal of the Geological Society*, *151*(2), 213–216. https://doi.org/10.1144/gsjgs.151.2.0213

Brichau, S., Ring, U., Ketcham, R. A., Carter, A., Stockli, D., & Brunel, M. (2006). Constraining the long-term evolution of the slip rate for a major extensional fault system in the central Aegean, Greece, using thermochronology. *Earth and Planetary Science Letters*, *241*(1–2), 293–306. https://doi.org/10.1016/j.epsl.2005.09.065

Brichau, S., Ring, U., Carter, A., Monié, P., Bolhar, R., Stockli, D., & Brunel, M. (2007). Extensional faulting on Tinos Island, Aegean Sea, Greece: How many detachments? *Tectonics*, *26*(4), 1–19. https://doi.org/10.1029/2006TC001969

Brichau, S., Ring, U., Carter, A., Bolhar, R., Monie, P., Stockli, D., & Brunel, M. (2008). Timing, slip rate, displacement and cooling history of the Mykonos detachment footwall, Cyclades, Greece, and implications for the opening of the Aegean Sea basin. *Journal of the Geological Society*, *165*(1), 263–277. https://doi.org/10.1144/0016-76492006-145

Bröcker, M., & Franz, L. (1994). The contact aureole on Tinos (Cyclades, Greece). Part I: field relationships, petrography and P-T conditions. *Chemie Der Erde-Geochemistry*, *54*(4), 262–280.

Bröcker, M., Kreuzer, H., Matthews, A., & Okrusch, M. (1993). ^{40}Ar/ ^{39}Ar and oxygen isotope studies of polymetamorphism from Tinos Island, Cycladic blueschist belt, Greece. *Journal of Metamorphic Geology*, *11*(2), 223–240. https://doi.org/10.1111/j.1525-1314.1993.tb00144.x

Brown, M., & Dallmeyer, R. D. (1996). Rapid Variscan exhumation and the role of magma in core complex formation: southern Brittany metamorphic belt, France. *Journal of Metamorphic Geology*, *14*(3), 361–379. https://doi.org/10.1111/j.1525-1314.1996.00361.x

Brun, J.-P., Sokoutis, D., Tirel, C., Gueydan, F., Van Den Driessche, J., & Beslier, M.-O. (2017). Crustal versus mantle core complexes. *Tectonophysics*. https://doi.org/10.1016/j.tecto.2017.09.017

Brun, J.-P., & Faccenna, C. (2008). Exhumation of high-pressure rocks driven by slab rollback. *Earth and Planetary Science Letters*, *272*(1–2), 1–7. https://doi.org/10.1016/j.epsl.2008.02.038

Brun, J.-P., Sokoutis, D., & Van Den Driessche, J. (1994). Analogue modeling of detachment fault systems and core complexes. *Geology*, *22*(4), 319–322. https://doi.org/10.1130/0091-7613(1994)022<0319:AMODFS>2.3.CO;2

Buck, W. R. (1988). flexural rotation of normal faults. *Tectonics*, *7*(5), 959–973. https://doi.org/10.1029/TC007i005p00959

Campbell-Stone, E., John, B. E., Foster, D. A., Geissman, J. W., & Livaccari, R. F. (2000). Mechanisms for accommodation of Miocene extension: Low-angle normal faulting, magmatism, and secondary breakaway faulting in the southern Sacramento Mountains, southeastern California. *Tectonics*, *19*(3), 566–587. https://doi.org/10.1029/1999TC001133

Cao, S., Neubauer, F., Bernroider, M., Genser, J., Liu, J., & Friedl, G. (2017). Low-grade retrogression of a high-temperature metamorphic core complex: Naxos, Cyclades, Greece. *Geological Society of America Bulletin*, *129*(1–2), 93–117. https://doi.org/10.1130/B31502.1

Caricchi, L., Burlini, L., Ulmer, P., Gerya, T., Vassalli, M., & Papale, P. (2007). Non-Newtonian rheology of crystal-bearing magmas and implications for magma ascent dynamics. *Earth and Planetary Science Letters*, *264*(3–4), 402–419. https://doi.org/10.1016/j.epsl.2007.09.032

Carr, S. D. (1992). Tectonic setting and U-Pb geochronology of the Early Tertiary Ladybird Leucogranite Suite, Thor-Odin - Pinnacles Area, Southern Omineca Belt, British Columbia. *Tectonics*, *11*(2), 258–278. https://doi.org/10.1029/91TC01644

Champallier, R., Bystricky, M., & Arbaret, L. (2008). Experimental investigation of magma rheology at 300 MPa: From pure hydrous melt to 76 vol.% of crystals. *Earth and Planetary Science Letters*, *267*(3–4), 571–583. https://doi.org/10.1016/j.epsl.2007.11.065

Charles, N., Gumiaux, C., Augier, R., Chen, Y., Zhu, R., & Lin, W. (2011). Metamorphic Core Complexes vs. synkinematic plutons in continental extension setting: Insights from key structures (Shandong Province, eastern China). *Journal of Asian Earth Sciences*, *40*(1), 261–278. https://doi.org/10.1016/j.jseaes.2010.07.006

Charles, N., Augier, R., Gumiaux, C., Monié, P., Chen, Y., Faure, M., & Zhu, R. (2013). Timing, duration and role of magmatism in wide rift systems: Insights from the Jiaodong Peninsula (China, East Asia). *Gondwana Research*, *24*(1), 412–428. https://doi.org/10.1016/j.gr.2012.10.011

Christiansen, P. P., & Pollard, D. D. (1997). Nucleation, growth and structural development of mylonitic shear zones in granitic rock. *Journal of Structural Geology*, *19*(9), 1159–1172. https://doi.org/10.1016/S0191-8141(97)00025-4

Cimarelli, C., Costa, A., Mueller, S., & Mader, H. M. (2011). Rheology of magmas with bimodal crystal size and shape distributions: Insights from analog experiments: RHEOLOGY OF PORPHYRITIC MAGMAS. *Geochemistry, Geophysics, Geosystems*, *12*(7), n/a-n/a. https://doi.org/10.1029/2011GC003606

Coney, P. J., & Harms, T. A. (1984). Cordilleran metamorphic core complexes: Cenozoic extensional relics of Mesozoic compression. *Geology*, *12*(9), 550–554. https://doi.org/10.1130/0091-7613(1984)12<550:CMCCCE>2.0.CO;2

Cordonnier, B., Caricchi, L., Pistone, M., Castro, J., Hess, K.-U., Gottschaller, S., … Burlini, L. (2012). The viscous-brittle transition of crystal-bearing silicic melt: Direct observation of magma rupture and healing. *Geology*, *40*(7), 611–614. https://doi.org/10.1130/G3914.1

Crittenden, M. D., Coney, P. J., & Davis, G. H. (Eds.). (1980). *Cordilleran metamorphic core complexes*. Boulder, Colorado: Geological Society of America.

Dallmeyer, R. D., Snoke, A. W., & McKee, E. H. (1986). The Mesozoic-Cenozoic tectonothermal evolution of the Ruby Mountains, East Humboldt Range, Nevada: A Cordilleran Metamorphic Core Complex. *Tectonics*, *5*(6), 931–954. https://doi.org/10.1029/TC005i006p00931

Daniel, J.-M., & Jolivet, L. (1995). Detachment faults and pluton emplacement; Elba Island (Tyrrhenian Sea). *Bulletin de La Societe Geologique de France*, *166*(4), 341–354.

Davis, G. A., Fowler, T. K., Bishop, K. M., Brudos, T. C., Friedmann, S. J., Burbank, D. W., … Burchfiel, B. C. (1993). Pluton pinning of an active Miocene detachment fault system, eastern Mojave Desert, California. *Geology*, *21*(7), 627–630. https://doi.org/10.1130/0091-7613(1993)021<0627:PPOAAM>2.3.CO;2

Davis, G. A., Qian, X., Zheng, Y., Yu, H., Wang, C., Mao, T. H., … Fryxell, J. E. (1996). Mesozoic deformation and plutonism in the Yunmeng Shan: a Chinese metamorphic core complex north of Beijing, China. In *The tectonic evolution of Asia* (pp. 253–280). Cambridge: Cambridge Univ. Press.

Davis, G. H., & Coney, P. J. (1979). Geologic development of the Cordilleran metamorphic core complexes. *Geology*, *7*(3), 120–124. https://doi.org/10.1130/0091-7613(1979)7<120:GDOTCM>2.0.CO;2

Denèle, Y., Lecomte, E., Jolivet, L., Lacombe, O., Labrousse, L., Huet, B., & Le Pourhiet, L. (2011). Granite intrusion in a metamorphic core complex: The example of the Mykonos laccolith (Cyclades, Greece). *Tectonophysics*, *501*(1–4), 52–70. https://doi.org/10.1016/j.tecto.2011.01.013

Dimitriadis, I., Karagianni, E., Panagiotopoulos, D., Papazachos, C., Hatzidimitriou, P., Bohnhoff, M., … Meier, T. (2009). Seismicity and active tectonics at Coloumbo Reef (Aegean Sea, Greece): Monitoring an active volcano at Santorini Volcanic Center using a temporary seismic network. *Tectonophysics*, *465*(1–4), 136–149. https://doi.org/10.1016/j.tecto.2008.11.005

Dinter, D. A., & Royden, L. (1993). Late Cenozoic extension in northeastern Greece: Strymon Valley detachment system and Rhodope metamorphic core complex. *Geology*, *21*(1), 45–48. https://doi.org/10.1130/0091-7613(1993)021<0045:LCEING>2.3.CO;2

Duretz, T., Petri, B., Mohn, G., Schmalholz, S. M., Schenker, F. L., & Müntener, O. (2016). The importance of structural softening for the evolution and architecture of passive margins. *Scientific Reports*, *6*(1). https://doi.org/10.1038/srep38704

Dürr, S., Altherr, R., Keller, J., Okrusch, M., & Seidel, E. (1978). The median Aegean crystalline belt: stratigraphy, structure, metamorphism, magmatism. *Alps, Apennines, Hellenides*, *38*, 455–476.

Ersoy, E. Y., & Palmer, M. R. (2013). Eocene-Quaternary magmatic activity in the Aegean: Implications for mantle

metasomatism and magma genesis in an evolving orogeny. *Lithos*, *180–181*, 5–24. https://doi.org/10.1016/j.lithos.2013.06.007

Faure, M., Sun, Y., Shu, L., Monié, P., & Charvet, J. (1996). Extensional tectonics within a subduction-type orogen. The case study of the Wugongshan dome (Jiangxi Province, southeastern China). *Tectonophysics*, *263*(1–4), 77–106. https://doi.org/10.1016/S0040-1951(97)81487-4

Faure, M., Bonneau, M., & Pons, J. (1991). Ductile deformation and syntectonic granite emplacement during the late Miocene extension of the Aegea (Greece). *Bulletin de La Societe Geologique de France*, *162*, 3–11.

Fletcher, J. M., Bartley, J. M., Martin, M. W., Glazner, A. F., & Walker, J. D. (1995). Large-magnitude continental extension: An example from the central Mojave metamorphic core complex. *Geological Society of America Bulletin*, *107*(12), 1468–1483. https://doi.org/10.1130/0016-7606(1995)107<1468:LMCEAE>2.3.CO;2

Forien, M., Arbaret, L., Burgisser, A., & Champallier, R. (2011). Experimental constrains on shear-induced crystal breakage in magmas. *Journal of Geophysical Research*, *116*(B8). https://doi.org/10.1029/2010JB008026

Forster, M., & Lister, G. (2009). Core-complex-related extension of the Aegean lithosphere initiated at the Eocene-Oligocene transition. *Journal of Geophysical Research*, *114*(B2), 1–36. https://doi.org/10.1029/2007JB005382

Gans, P. B. (1987). An open-system, two-layer crustal stretching model for the Eastern Great Basin. *Tectonics*, *6*(1), 1–12. https://doi.org/10.1029/TC006i001p00001

Gautier, P., & Brun, J.-P. (1994a). Crustal-scale geometry and kinematics of late-orogenic extension in the central Aegean (Cyclades and Ewia Island). *Tectonophysics*, *238*(1–4), 399–424. https://doi.org/10.1016/0040-1951(94)90066-3

Gautier, P., & Brun, J.-P. (1994b). Ductile crust exhumation and extensional detachments in the central Aegean (Cyclades and Evvia islands). *Geodinamica Acta*, *7*(2), 57–85.

Gautier, P., Brun, J.-P., & Jolivet, L. (1993). Structure and kinematics of Upper Cenozoic extensional detachment on Naxos and Paros (Cyclades Islands, Greece). *Tectonics*, *12*(5), 1180–1194. https://doi.org/10.1029/93TC01131

Gautier, P., Brun, J.-P., Moriceau, R., Sokoutis, D., Martinod, J., & Jolivet, L. (1999). Timing, kinematics and cause of Aegean extension: a scenario based on a comparison with simple analogue experiments. *Tectonophysics*, *315*(1–4), 31–72. https://doi.org/10.1016/S0040-1951(99)00281-4

Gibson, G. M. (1990). Uplift and exhumation of middle and lower crustal rocks in an extensional tectonic setting, Fiordland, New Zealand. In *Exposed cross-sections of the continental crust* (pp. 71–101). Springer Netherlands.

Goldsworthy, M., Jackson, J., & Haines, J. (2002). The continuity of active fault systems in Greece. *Geophysical Journal International*, *148*(3), 596–618. https://doi.org/10.1046/j.1365-246X.2002.01609.x

Grasemann, B., Schneider, D. A., Stockli, D. F., & Iglseder, C. (2012). Miocene bivergent crustal extension in the Aegean: Evidence from the western Cyclades (Greece). *Lithosphere*, *4*(1), 23–39. https://doi.org/10.1130/L164.1

Grasemann, B., & Petrakakis, K. (2007). Evolution of the Serifos metamorphic core complex. *Journal of the Virtual Explorer*, *27*, 1–18.

Groppo, C., Forster, M., Lister, G., & Compagnoni, R. (2009). Glaucophane schists and associated rocks from Sifnos (Cyclades, Greece): New constraints on the P–T evolution from oxidized systems. *Lithos*, *109*(3–4), 254–273. https://doi.org/10.1016/j.lithos.2008.10.005

Hatzfeld, D., Karakostas, V., Ziazia, M., Kassaras, I., Papadimitriou, E., Makropoulos, K., … Papaioannou, C. (2000). Microseismicity and faulting geometry in the Gulf of Corinth (Greece). *Geophysical Journal International*, *141*(2), 438–456. https://doi.org/10.1046/j.1365-246x.2000.00092.x

Henjes-Kunst, F., & Kreuzer, H. (1982). Isotopic dating of pre-Alpidic rocks from the island of Ios (Cyclades, Greece). *Contributions to Mineralogy and Petrology*, *80*(3), 245–253. https://doi.org/10.1007/BF00371354

Hetzel, R., Ring, U., Akal, C., & Troesch, M. (1995). Miocene NNE-directed extensional unroofing in the Menderes Massif, southwestern Turkey. *Journal of the Geological Society*, *152*(4), 639–654. https://doi.org/10.1144/gsjgs.152.4.0639

Hill, E. J. (1987). Active extension in the D'Entrecasteaux Islands, Papua New Guinea. *Bureau of Mineral Resources Research Symposium 87*, *87*, 51–57.

Hill, E. J. (1991). *Metamorphic core complexes in the D'Entrecasteaux Islands, Papua New Guinea* (Ph.D thesis). Monash University, Melbourne, Australia.

Hill, E. J., Baldwin, S. L., & Lister, G. S. (1995). Magmatism as an essential driving force for formation of active metamorphic core complexes in eastern Papua New Guinea. *Journal of Geophysical Research*, *100*(B6), 10441–10451. https://doi.org/10.1029/94JB03329

van Hinsbergen, D. J. J., Hafkenscheid, E., Spakman, W., Meulenkamp, J. E., & Wortel, R. (2005). Nappe stacking resulting from subduction of oceanic and continental lithosphere below Greece. *Geology*, *33*(4), 325–328. https://doi.org/10.1130/G20878.1

Huet, B., Labrousse, L., & Jolivet, L. (2009). Thrust or detachment? Exhumation processes in the Aegean: Insight from a field study on Ios (Cyclades, Greece). *Tectonics*, *28*(3), 1–27. https://doi.org/10.1029/2008TC002397

Huet, B., Le Pourhiet, L., Labrousse, L., Burov, E. B., & Jolivet, L. (2011a). Formation of metamorphic core complex in inherited wedges: A thermomechanical modelling study. *Earth and Planetary Science Letters*, *309*(3–4), 249–257. https://doi.org/10.1016/j.epsl.2011.07.004

Huet, B., Le Pourhiet, L., Labrousse, L., Burov, E., & Jolivet, L. (2011b). Post-orogenic extension and metamorphic core complexes in a heterogeneous crust: the role of crustal layering inherited from collision. Application to the Cyclades (Aegean domain): Core complexes in a heterogeneous crust. *Geophysical Journal International*, *184*(2), 611–625. https://doi.org/10.1111/j.1365-246X.2010.04849.x

Huet, B., Labrousse, L., Monié, P., Malvoisin, B., & Jolivet, L. (2015). Coupled phengite ^{40}Ar/^{39}Ar geochronology and thermobarometry: P-T-t evolution of Andros Island (Cyclades, Greece). *Geological Magazine*, *152*(4), 711–727. https://doi.org/10.1017/S0016756814000661

Hyndman, D. W. (1980). Bitterroot dome-Sapphire tectonic block, an example of a plutonic-core gneiss-dome complex with its detached suprastructure. In *Geological Society of America Memoirs* (Vol. 153, pp. 427–444). Geological Society of America.

Iglseder, C., Grasemann, B., Schneider, D. A., Petrakakis, K., Miller, C., Klötzli, U. S., … Rambousek, C. (2009). I and S-type plutonism on Serifos (W-Cyclades, Greece). *Tectonophysics*, *473*(1–2), 69–83. https://doi.org/10.1016/j.tecto.2008.09.021

Iglseder, C., Grasemann, B., Rice, A. H. N., Petrakakis, K., & Schneider, D. A. (2011). Miocene south directed low-angle normal fault evolution on Kea Island (West Cycladic Detachment System, Greece). *Tectonics*, *30*(4), 1–31. https://doi.org/10.1029/2010TC002802

Jackson, J. (1994). Active Tectonics of the Aegean Region. *Annual Review of Earth and Planetary Sciences*, *22*(1), 239–271. https://doi.org/10.1146/annurev.earth.22.1.239

Jacobshagen, V., Dürr, S., Kockel, F., Kopp, K. O., Kowalczyk, G., Berckhemer, H., & Büttner, D. (1978). Structure and geodynamic evolution of the Aegean region. *Alps, Apennines, Hellenides*, 537–564.

Jolivet, L. (2003). Subduction tectonics and exhumation of high-pressure metamorphic rocks in the Mediterranean orogens. *American Journal of Science*, *303*(5), 353–409. https://doi.org/10.2475/ajs.303.5.353

Jolivet, L., & Brun, J.-P. (2010). Cenozoic geodynamic evolution of the Aegean. *International Journal of Earth Sciences*, *99*(1), 109–138. https://doi.org/10.1007/s00531-008-0366-4

Jolivet, L., Rimmelé, G., Oberhänsli, R., Goffé, B., & Candan, O. (2004). Correlation of syn-orogenic tectonic and metamorphic events in the Cyclades, the Lycian nappes and the Menderes massif. Geodynamic implications. *Bulletin de La Societe Geologique de France*, *175*(3), 217–238. https://doi.org/10.2113/175.3.217

Jolivet, L., Faccenna, C., Huet, B., Labrousse, L., Le Pourhiet, L., Lacombe, O., … Driussi, O. (2013). Aegean tectonics: Strain localisation, slab tearing and trench retreat. *Tectonophysics*, *597–598*, 1–33. https://doi.org/10.1016/j.tecto.2012.06.011

Jolivet, L., & Faccenna, C. (2000). Mediterranean extension and the Africa-Eurasia collision. *Tectonics*, *19*(6), 1095–1106. https://doi.org/10.1029/2000TC900018

Jolivet, L., Daniel, J. M., Truffert, C., & Goffé, B. (1994). Exhumation of deep crustal metamorphic rocks and crustal extension in arc and back-arc regions. *Lithos*, *33*(1–3), 3–30. https://doi.org/10.1016/0024-4937(94)90051-5

Jolivet, L., Menant, A., Sternai, P., Rabillard, A., Arbaret, L., Augier, R., … Le Pourhiet, L. (2015). The geological signature of a slab tear below the Aegean. *Tectonophysics*, *659*, 166–182. https://doi.org/10.1016/j.tecto.2015.08.004

Jolivet, L., Lecomte, E., Huet, B., Denèle, Y., Lacombe, O., Labrousse, L., … Mehl, C. (2010). The North Cycladic Detachment System. *Earth and Planetary Science Letters*, *289*(1–2), 87–104. https://doi.org/10.1016/j.epsl.2009.10.032

Jolivet, L., Faccenna, C., Goffé, B., Mattei, M., Rossetti, F., Brunet, C., … Parra, T. (1998). Midcrustal shear zones in postorogenic extension: Example from the northern Tyrrhenian Sea. *Journal of Geophysical Research*, *103*(B6), 12123–12160. https://doi.org/10.1029/97JB03616

Jolivet, L., Famin, V., Mehl, C., Parra, T., Aubourg, C., Hébert, R., & Philippot, P. (2004). Strain localization during crustal-scale boudinage to form extensional metamorphic domes in the Aegean Sea. In *Gneiss Domes in Orogeny* (Vol. 380, pp. 185–210). Boulder, Colorado: Geological Society of America. Retrieved from http://specialpapers.gsapubs.org/cgi/doi/10.1130/0-8137-2380-9.185

Katzir, Y., Matthews, A. L. A. N., Garfunkel, Z., Schliestedt, M., & Avigad, D. (1996). The tectono-metamorphic evolution of a dismembered ophiolite (Tinos, Cyclades, Greece). *Geological Magazine*, *133*(3), 237–254.

Keay, S. (1998). *The geological evolution of the Cyclades, Greece, constraints from SHRIMP U/Pb geochronology* (Ph.D thesis). Research School of Earth Sciences, Australian National University, Cambera, Australia.

Keay, S., Lister, G., & Buick, I. (2001). The timing of partial melting, Barrovian metamorphism and granite intrusion in the Naxos metamorphic core complex, Cyclades, Aegean Sea, Greece. *Tectonophysics*, *342*(3–4), 275–312. https://doi.org/10.1016/S0040-1951(01)00168-8

Keay, S., & Lister, G. (2002). African provenance for the metasediments and metaigneous rocks of the Cyclades, Aegean Sea, Greece. *Geology*, *30*(3), 235–238. https://doi.org/10.1130/0091-7613(2002)030<0235:APFTMA>2.0.CO;2

Keiter, M., Piepjohn, K., Ballhaus, C., Lagos, M., & Bode, M. (2004). Structural development of high-pressure metamorphic rocks on Syros island (Cyclades, Greece). *Journal of Structural Geology*, *26*(8), 1433–1445. https://doi.org/10.1016/j.jsg.2003.11.027

Koukouvelas, I. K., & Kokkalas, S. (2003). Emplacement of the Miocene west Naxos pluton (Aegean Sea, Greece): a structural study. *Geological Magazine*, *140*(1), 45–61. https://doi.org/10.1017/S0016756802007094

Krohe, A., Mposkos, E., Diamantopoulos, A., & Kaouras, G. (2010). Formation of basins and mountain ranges in Attica (Greece): The role of Miocene to Recent low-angle normal detachment faults. *Earth-Science Reviews*, *98*(1–2), 81–104. https://doi.org/10.1016/j.earscirev.2009.10.005

Kuhlemann, J., Frisch, W., Dunkl, I., Kázmér, M., & Schmiedl, G. (2004). Miocene siliciclastic deposits of Naxos Island: Geodynamic and environmental implications for the evolution of the southern Aegean Sea (Greece). In *Special Paper 378: Detrital thermochronology - Provenance analysis, exhumation, and landscape evolution of mountain belts* (Vol. 378, pp. 51–65). Geological Society of America. Retrieved from http://specialpapers.gsapubs.org/cgi/doi/10.1130/0-8137-2378-7.51

Labrousse, L., Huet, B., Le Pourhiet, L., Jolivet, L., & Burov, E. (2016). Rheological implications of extensional detachments: Mediterranean and numerical insights. *Earth-Science Reviews*, *161*, 233–258. https://doi.org/10.1016/j.earscirev.2016.09.003

Laumonier, M., Arbaret, L., Burgisser, A., & Champallier, R. (2011). Porosity redistribution enhanced by strain localization in crystal-rich magmas. *Geology*, *39*(8), 715–718. https://doi.org/10.1130/G31803.1

Lavier, L. L., Roger Buck, W., & Poliakov, A. N. B. (1999). Self-consistent rolling-hinge model for the evolution of large-offset low-angle normal faults. *Geology*, *27*(12), 1127. https://doi.org/10.1130/0091-7613(1999)027<1127:SCRHMF>2.3.CO;2

Le Pichon, X., & Angelier, J. (1981). The Aegean Sea. *Philosophical Transactions of the Royal Society A: Mathematical, Physical and Engineering Sciences*, *300*(1454), 357–372.

Le Pourhiet, L., Burov, E., & Moretti, I. (2004). Rifting through a stack of inhomogeneous thrusts (the dipping pie concept). *Tectonics*, *23*(4),. https://doi.org/10.1029/2003TC001584

Lecomte, E., Jolivet, L., Lacombe, O., Denèle, Y., Labrousse, L., & Le Pourhiet, L. (2010). Geometry and kinematics of Mykonos detachment, Cyclades, Greece: Evidence for slip at shallow dip. *Tectonics*, *29*(5), 1–22. https://doi.org/10.1029/2009TC002564

Lee Armstrong, R., & Ward, P. (1991). Evolving geographic patterns of Cenozoic magmatism in the North American Cordillera: The temporal and spatial association of magmatism and metamorphic core complexes. *Journal of Geophysical Research*, *96*(B8), 13201–13224. https://doi.org/10.1029/91JB00412

Lee, J., & Lister, G. S. (1992). Late Miocene ductile extension and detachment faulting, Mykonos, Greece. *Geology*, *20*(2), 121–124. https://doi.org/10.1130/0091-7613(1992)020<0121:LMDEAD>2.3.CO;2

Lejeune, A.-M., & Richet, P. (1995). Rheology of crystal-bearing silicate melts: An experimental study at high viscosities. *Journal of Geophysical Research: Solid Earth*, *100*(B3), 4215–4229. https://doi.org/10.1029/94JB02985

Lin, W., Faure, M., Monié, P., Schärer, U., & Panis, D. (2008). Mesozoic Extensional Tectonics in Eastern Asia: The South Liaodong Peninsula Metamorphic Core Complex (NE China). *The Journal of Geology*, *116*(2), 134–154. https://doi.org/10.1086/527456

Lin, W., & Wang, Q. (2006). Late Mesozoic extensional tectonics in the North China

block: a crustal response to subcontinental mantle removal? *Bulletin de La Societe Geologique de France*, *177*(6), 287–297. https://doi.org/10.2113/gssgfbull.177.6.287

Lister, G. S., & Baldwin, S. L. (1993). Plutonism and the origin of metamorphic core complexes. *Geology*, *21*(7), 607–610. https://doi.org/10.1130/0091-7613(1993)021<0607:PATOOM>2.3.CO;2

Lister, G. S., & Davis, G. A. (1989). The origin of metamorphic core complexes and detachment faults formed during Tertiary continental extension in the northern Colorado River region, U.S.A. *Journal of Structural Geology*, *11*(1–2), 65–94. https://doi.org/10.1016/0191-8141(89)90036-9

Lister, G. S., Banga, G., & Feenstra, A. (1984). Metamorphic core complexes of Cordilleran type in the Cyclades, Aegean Sea, Greece. *Geology*, *12*(4), 221–225. https://doi.org/10.1130/0091-7613(1984)12<221:MCCOCT>2.0.CO;2

Lucas, I. (1999). *Le pluton de Mykonos-Delos-Rhenee (Cyclades, Grèce): un exemple de mise en place synchrone de l'extension crustale* (Ph.D thesis). University of Orléans, Orléans, France.

Lynch, H. D., & Morgan, P. (1987). The tensile strength of the lithosphere and the localization of extension. *Geological Society, London, Special Publications*, *28*(1), 53–65. https://doi.org/10.1144/GSL.SP.1987.028.01.05

MacCready, T., Snoke, A. W., Wright, J. E., & Howard, K. A. (1997). Mid-crustal flow during Tertiary extension in the Ruby Mountains core complex, Nevada. *Geological Society of America Bulletin*, *109*(12), 1576–1594. https://doi.org/10.1130/0016-7606(1997)109<1576:MCFDTE>2.3.CO;2

Maluski, H., Bonneau, M., & Kienast, J. R. (1987). Dating the metamorphic events in the Cycladic area; 39 Ar/40 Ar data from metamorphic rocks of the Island of Syros (Greece). *Bulletin de La Société Géologique de France*, *3*(5), 833–842.

Mancktelow, N. S., & Pennacchioni, G. (2013). Late magmatic healed fractures in granitoids and their influence on subsequent solid-state deformation. *Journal of Structural Geology*, *57*, 81–96. https://doi.org/10.1016/j.jsg.2013.09.006

Martha, S. O., Dörr, W., Gerdes, A., Petschick, R., Schastok, J., Xypolias, P., & Zulauf, G. (2016). New structural and U–Pb zircon data from Anafi crystalline basement (Cyclades, Greece): constraints on the evolution of a Late Cretaceous magmatic arc in the Internal Hellenides. *International Journal of Earth Sciences*, *105*(7), 2031–2060. https://doi.org/10.1007/s00531-016-1346-8

Menant, A., Sternai, P., Jolivet, L., Guillou-Frottier, L., & Gerya, T. (2016). 3D numerical modeling of mantle flow, crustal dynamics and magma genesis associated with slab roll-back and tearing: The eastern Mediterranean case. *Earth and Planetary Science Letters*, *442*, 93–107. https://doi.org/10.1016/j.epsl.2016.03.002

Menant, A., Jolivet, L., & Vrielynck, B. (2016). Kinematic reconstructions and magmatic evolution illuminating crustal and mantle dynamics of the eastern Mediterranean region since the late Cretaceous. *Tectonophysics*, *675*, 103–140. https://doi.org/10.1016/j.tecto.2016.03.007

Miller, E. L., Gans, P. B., & Garing, J. (1983). The Snake Range Décollement: An exhumed Mid-Tertiary ductile-brittle transition. *Tectonics*, *2*(3), 239–263. https://doi.org/10.1029/TC002i003p00239

Moitra, P., & Gonnermann, H. M. (2015). Effects of crystal shape- and size-modality on magma rheology. *Geochemistry, Geophysics, Geosystems*, *16*(1), 1–26. https://doi.org/10.1002/2014GC005554

Mueller, S., Llewellin, E. W., & Mader, H. M. (2010). The rheology of suspensions of solid particles. *Proceedings of the Royal Society A: Mathematical, Physical and Engineering Sciences*, *466*(2116), 1201–1228. https://doi.org/10.1098/rspa.2009.0445

Okumura, S., Kushnir, A. R. L., Martel, C., Champallier, R., Thibault, Q., & Takeuchi, S. (2016). Rheology of crystal-bearing natural magmas: Torsional deformation experiments at 800°C and 100MPa. *Journal of Volcanology and Geothermal Research*, *328*, 237–246. https://doi.org/10.1016/j.jvolgeores.2016.11.009

Papanikolaou, D. (2009). Timing of tectonic emplacement of the ophiolites and terrane paleogeography in the Hellenides. *Lithos*, *108*(1–4), 262–280. https://doi.org/10.1016/j.lithos.2008.08.003

Parra, T., Vidal, O., & Jolivet, L. (2002). Relation between the intensity of deformation and retrogression in blueschist metapelites of Tinos Island (Greece) evidenced by chlorite–mica local equilibria. *Lithos*, *63*(1–2), 41–66. https://doi.org/10.1016/S0024-4937(02)00115-9

Patzak, M., Okrusch, M., & Kreuzer, H. (1994). The Akrotiri Unit on the island of Tinos, Cyclades, Greece: Witness to a lost terrane of Late Cretaceous age. *Neues Jahrbuch Fur Geologie Und Palaontologie-Abhandlungen*, *194*, 211–252.

Pavlis, T. L. (1996). Fabric development in syn-tectonic intrusive sheets as a consequence of melt-dominated flow and thermal softening of the crust. *Tectonophysics*, *253*(1–2), 1–31. https://doi.org/10.1016/0040-1951(95)00049-6

Pennacchioni, G. (2005). Control of the geometry of precursor brittle structures on the type of ductile shear zone in the Adamello tonalites, Southern Alps (Italy). *Journal of Structural Geology*, *27*(4), 627–644. https://doi.org/10.1016/j.jsg.2004.11.008

Pennacchioni, G., & Mancktelow, N. S. (2007). Nucleation and initial growth of a shear zone network within compositionally and structurally heterogeneous granitoids under amphibolite facies conditions. *Journal of Structural Geology*, *29*(11), 1757–1780. https://doi.org/10.1016/j.jsg.2007.06.002

Pe-Piper, G. (2000). Origin of S-type granites coeval with I-type granites in the Hellenic subduction system, Miocene of Naxos, Greece. *European Journal of Mineralogy*, *12*(4), 859–875. https://doi.org/10.1127/ejm/12/4/0859

Pe-Piper, G., & Piper, D. J. W. (2006). Unique features of the Cenozoic igneous rocks of Greece. In *Special Paper 409: Postcollisional Tectonics and Magmatism in the Mediterranean Region and Asia* (Vol. 409, pp. 259–282). Geological Society of America. Retrieved from http://specialpapers.gsapubs.org/cgi/doi/10.1130/2006.2409(14)

Pe-Piper, G., Kotopouli, C. N., & Piper, D. J. W. (1997). Granitoid rocks of Naxos, Greece: regional geology and petrology. *Geological Journal*, *32*(2), 153–171. https://doi.org/10.1002/(SICI)1099-1034(199706)32:2<153::AID-GJ737>3.0.CO;2-1

Picard, D. (2009). *Déformation HP-HT des magmas siliceux: contraintes expérimentales sur l'évolution structurale et les transitions rhéologiques aux moyennes et fortes cristallinités* (Ph.D thesis). Univ. Orléans, Orléans, France.

Picard, D., Arbaret, L., Pichavant, M., Champallier, R., & Launeau, P. (2011). Rheology and microstructure of experimentally deformed plagioclase suspensions. *Geology*, *39*(8), 747–750. https://doi.org/10.1130/G32217.1

Picard, D., Arbaret, L., Pichavant, M., Champallier, R., & Launeau, P. (2013). The rheological transition in plagioclase-bearing magmas. *Journal of Geophysical Research: Solid Earth*, *118*(4), 1363–1377. https://doi.org/10.1002/jgrb.50091

Reinecke, T., Altherr, R., Hartung, B., Hatzipanagiotou, K., Kreuzer, H., Harre, W., … Boger, H. (1982). Remnants of a Late Cretaceous high temperature belt on the island of Anafi (Cyclades, Greece), *145*, 157–182.

Rice, A. H. N., Iglseder, C., Grasemann, B., Zamoly, A., Nikolakopoulos, K. G., Mitropoulos, D., … Tsombos, P. (2012). A new geological map of the crustal-scale detachment on Kea (Western Cyclades,

Greece). *Australian Journal of Earth Sciences*, *105*(3), 108–124.

Ring, U., Will, T., Glodny, J., Kumerics, C., Gessner, K., Thomson, S., … Drüppel, K. (2007). Early exhumation of high-pressure rocks in extrusion wedges: Cycladic blueschist unit in the eastern Aegean, Greece, and Turkey. *Tectonics*, *26*(2), 1–23. https://doi.org/10.1029/2005TC001872

Ring, U., Gessner, K., Gungor, T., & Passchier, C. W. (1999). The Menderes Massif of western Turkey and the Cycladic Massif in the Aegean--do they really correlate? *Journal of the Geological Society*, *156*(1), 3–6. https://doi.org/10.1144/gsjgs.156.1.0003

Ring, U., Glodny, J., Will, T., & Thomson, S. (2007). An Oligocene extrusion wedge of blueschist-facies nappes on Evia, Aegean Sea, Greece: implications for the early exhumation of high-pressure rocks. *Journal of the Geological Society*, *164*(3), 637–652. https://doi.org/10.1144/0016-76492006-041

Ring, U., Glodny, J., Will, T., & Thomson, S. (2010). The Hellenic Subduction System: High-Pressure Metamorphism, Exhumation, Normal Faulting, and Large-Scale Extension. *Annual Review of Earth and Planetary Sciences*, *38*(1), 45–76. https://doi.org/10.1146/annurev.earth.050708.170910

Ring, U., Glodny, J., Will, T. M., & Thomson, S. (2011). Normal faulting on Sifnos and the South Cycladic Detachment System, Aegean Sea, Greece. *Journal of the Geological Society*, *168*(3), 751–768. https://doi.org/10.1144/0016-76492010-064

Roche, V., Laurent, V., Cardello, G. L., Jolivet, L., & Scaillet, S. (2016). Anatomy of the Cycladic Blueschist Unit on Sifnos Island (Cyclades, Greece). *Journal of Geodynamics*, *97*, 62–87. https://doi.org/10.1016/j.jog.2016.03.008

Rossetti, F., Faccenna, C., Jolivet, L., Funiciello, R., Tecce, F., & Brunet, C. (1999). Syn- versus post-orogenic extension: the case study of Giglio Island (Northern Tyrrhenian Sea, Italy). *Tectonophysics*, *304*(1–2), 71–93. https://doi.org/10.1016/S0040-1951(98)00304-7

Royden, L. H., & Papanikolaou, D. J. (2011). Slab segmentation and late Cenozoic disruption of the Hellenic arc. *Geochemistry, Geophysics, Geosystems*, *12*(3), 1–24. https://doi.org/10.1029/2010GC003280

Sanchez-Gomez, M., Avigad, D., & Heimann, A. (2002). Geochronology of clasts in allochthonous Miocene sedimentary sequences on Mykonos and Paros Islands: implications for back-arc extension in the Aegean Sea. *Journal of the Geological Society*, *159*(1), 45–60. https://doi.org/10.1144/0016-764901031

Shu, L., Sun, Y., Wang, D., Faure, M., Monie, P., & Charvet, J. (1998). Mesozoic doming extensional tectonics of Wugongshan, South China. *Science in China Series D: Earth Sciences*, *41*(6), 601–608. https://doi.org/10.1007/BF02878742

Skarpelis, N. (2007). The Lavrion deposit (SE Attica, Greece): geology, mineralogy and minor elements chemistry. *Neues Jahrbuch Für Mineralogie - Abhandlungen*, *183*(3), 227–249. https://doi.org/10.1127/0077-7757/2007/0067

Spencer, J. E. (1984). Role of tectonic denudation in warping and uplift of low-angle normal faults. *Geology*, *12*(2), 95–98. https://doi.org/10.1130/0091-7613(1984)12<95:ROTDIW>2.0.CO;2

St. Seymour, K., Zouzias, D., Tombros, S., & Kolaiti, E. (2009). Geochemistry of the Serifos pluton (Cycladic islands) and associated iron oxide and sulfide ores: Skarn or metamorphosed exhalite deposits? *Neues Jahrbuch Für Mineralogie - Abhandlungen*, *186*(3), 249–270. https://doi.org/10.1127/0077-7757/2009/0143

Stouraiti, C., Mitropoulos, P., Tarney, J., Barreiro, B., McGrath, A. M., & Baltatzis, E. (2010). Geochemistry and petrogenesis of late Miocene granitoids, Cyclades, southern Aegean: Nature of source components. *Lithos*, *114*(3–4), 337–352. https://doi.org/10.1016/j.lithos.2009.09.010

Teyssier, C., Ferré, E. C., Whitney, D. L., Norlander, B., Vanderhaeghe, O., & Parkinson, D. (2005). Flow of partially molten crust and origin of detachments during collapse of the Cordilleran Orogen. *Geological Society, London, Special Publications*, *245*(1), 39–64. https://doi.org/10.1144/GSL.SP.2005.245.01.03

Teyssier, C., & Whitney, D. L. (2002). Gneiss domes and orogeny. *Geology*, *30*(12), 1139–1142. https://doi.org/10.1130/0091-7613(2002)030<1139:GDAO>2.0.CO;2

Tikoff, B., & Teyssier, C. (1994). Strain and fabric analyses based on porphyroclast interaction. *Journal of Structural Geology*, *16*(4), 477–491. https://doi.org/10.1016/0191-8141(94)90092-2

Tirel, C., Brun, J.-P., & Burov, E. (2004). Thermomechanical modeling of extensional gneiss domes. In *Special Paper 380: Gneiss Domes in Orogeny* (Vol. 380, pp. 67–78). Geological Society of America. Retrieved from http://specialpapers.gsapubs.org/cgi/doi/10.1130/0-8137-2380-9.67

Tirel, C., Brun, J.-P., & Burov, E. (2008). Dynamics and structural development of metamorphic core complexes. *Journal of Geophysical Research*, *113*(B4). https://doi.org/10.1029/2005JB003694

Trotet, F., Vidal, O., & Jolivet, L. (2001). Exhumation of Syros and Sifnos metamorphic rocks (Cyclades, Greece). New constraints on the P-T paths. *European Journal of Mineralogy*, *13*(5), 901–920. https://doi.org/10.1127/0935-1221/2001/0013/0901

Van Den Driessche, J., & Brun, J.-P. (1992). Tectonic evolution of the Montagne Noire (french Massif Central): a model of extensional gneiss dome. *Geodinamica Acta*, *5*(1–2), 85–97. https://doi.org/10.1080/09853111.1992.11105221

Vandenberg, L. C., & Lister, G. S. (1996). Structural analysis of basement tectonites from the Aegean metamorphic core complex of Ios, Cyclades, Greece. *Journal of Structural Geology*, *18*(12), 1437–1454. https://doi.org/10.1016/S0191-8141(96)00068-5

Vanderhaeghe, O. (1999). Pervasive melt migration from migmatites to leucogranite in the Shuswap metamorphic core complex, Canada: control of regional deformation. *Tectonophysics*, *312*(1), 35–55. https://doi.org/10.1016/S0040-1951(99)00171-7

Vanderhaeghe, O. (2004). Structural development of the Naxos migmatite dome. In *Gneiss Domes in Orogeny* (Vol. 380, pp. 211–227). Boulder, Colorado: Geological Society of America. Retrieved from http://specialpapers.gsapubs.org/cgi/doi/10.1130/0-8137-2380-9.211

Vanderhaeghe, O. (2012). The thermal–mechanical evolution of crustal orogenic belts at convergent plate boundaries: A reappraisal of the orogenic cycle. *Journal of Geodynamics*, *56–57*, 124–145. https://doi.org/10.1016/j.jog.2011.10.004

Vanderhaeghe, O., & Teyssier, C. (1997). Formation of the Shuswap metamorphic core complex during late-orogenic collapse of the Canadian Cordillera: Role of ductile thinning and partial melting of the mid-to lower crust. *Geodinamica Acta*, *10*(2), 41–58. https://doi.org/10.1080/09853111.1997.11105292

Vanderhaeghe, O., & Teyssier, C. (2001). Partial melting and flow of orogens. *Tectonophysics*, *342*(3–4), 451–472. https://doi.org/10.1016/S0040-1951(01)00175-5

Vigneresse, J. L., Barbey, P., & Cuney, M. (1996). Rheological Transitions During Partial Melting and Crystallization with Application to Felsic Magma Segregation and Transfer. *Journal of Petrology*, *37*(6), 1579–1600. https://doi.org/10.1093/petrology/37.6.1579

Webb, L. E., Graham, S. A., Johnson, C. L., Badarch, G., & Hendrix, M. S. (1999). Occurrence, age, and implications of the Yagan–Onch Hayrhan metamorphic core complex, southern Mongolia. *Geology*, *27*(2), 143–146. https://doi.org/10.1130/0091-7613(1999)027<0143:OAAIOT>2.3.CO;2

Whitney, D. L., Teyssier, C., Rey, P., & Buck, W. R. (2013). Continental and oceanic core complexes. *Geological Society of America Bulletin*, *125*(3–4), 273–298. https://doi.org/0.1130/B30754.1

Whitney, D. L., & Dilek, Y. (1997). Core complex development in central Anatolia, Turkey. *Geology*, *25*(11), 1023–1026. https://doi.org/10.1130/0091-7613(1997)025<1023:CCDICA>2.3.CO;2

Whitney, D. L., Teyssier, C., & Fayon, A. K. (2004). Isothermal decompression, partial melting and exhumation of deep continental crust. *Geological Society, London, Special Publications*, *227*(1), 313–326. https://doi.org/10.1144/GSL.SP.2004.227.01.16

Wijbrans, J. R., & McDougall, I. (1986). ^{40}Ar/^{39} dating of white micas from an Alpine high-pressure metamorphic belt on Naxos (Greece): the resetting of the argon isotopic system. *Contributions to Mineralogy and Petrology*, *93*(2), 187–194. https://doi.org/10.1007/BF00371320

Wijbrans, J. R., & McDougall, I. (1988). Metamorphic evolution of the Attic Cycladic Metamorphic Belt on Naxos (Cyclades, Greece) utilizing ^{40}Ar/^{39} age spectrum measurements. *Journal of Metamorphic Geology*, *6*(5), 571–594. https://doi.org/10.1111/j.1525-1314.1988.tb00441.x

Wu, G., & Lavier, L. L. (2016). The effects of lower crustal strength and preexisting midcrustal shear zones on the formation of continental core complexes and low-angle normal faults: Core Complex and Low-Angle Normal Fault. *Tectonics*, *35*(9), 2195–2214. https://doi.org/10.1002/2016TC004245

Chapitre II

Structuration d'un granitoïde sous un détachement d'échelle crustale : le dôme métamorphique de Naxos (Cyclades, Grèce)

Sommaire

Résumé étendu

Problématique et démarche

Située au cœur des Cyclades, l'île de Naxos forme un dôme métamorphique extensif (MCC) de haute température (Figure II-0), dont l'exhumation au cours de l'extension Miocène fut accompagnée par l'intrusion d'un corps magmatique monzogranitique (13-11 Ma ; [*Keay et al.*, 2001; *Bolhar et al.*, 2010]) et le développement d'un système de deux détachements aux cinématiques comparables (i.e, les détachements top-N de Naxos et Moutsouna). Si dans l'état actuel des connaissances l'architecture globale du dôme métamorphique et les modalités de déformation aux abords des détachements sont relativement bien contraints, il n'en va pas de même concernant la structure du corps intrusif placé sous le détachement supérieur de Moutsouna au nord-ouest de l'île. Dans la perspective d'une étude plus vaste sur les interactions entre magmatisme et dynamique des MCCs (cf. chapitre IV), ce second chapitre se limite à obtenir **des contraintes sur la distribution et l'évolution de la déformation au sein du corps magmatique syn-extensif**. Ce travail compile ainsi données structurales, observations microstructurales, analyses tomographiques par absorption de rayon X et enfin mesures 3-D d'orientations préférentielles d'axes cristallographiques du quartz par EBSD (en anglais *Electron BackScattered Diffraction)*. Les résultats obtenus sont rédigés sous la forme d'un article soumis au journal *Tectonics*.

Résultats majeurs

Les observations de terrain, combinées aux mesures systématiques de la cinématique, ont tout d'abord permis d'élaborer une carte d'intensité de la déformation. Dans l'ensemble, le corps intrusif offre à l'affleurement un vaste spectre de structures et fabriques acquises dans l'état magmatique, ductile ou bien cassante. Les textures magmatiques primaires se situent dans la partie interne du corps intrusif, loin du plan de détachement de Moutsouna. Vers les zones marginales, les fabriques syn-magmatiques sont progressivement effacées par un cisaillement ductile top-N. A l'échelle du corps intrusif, l'attitude globale des foliations tectoniques soutient une structure en forme de dôme à travers laquelle l'intensité de la déformation finie augmente progressivement en direction de la carapace. Cependant, la zone la plus fortement déformée se concentre essentiellement au nord, à proximité du détachement de Moutsouna. Le long d'une section de 300-500 m d'épaisseur, nous avons ainsi mis en évidence un gradient d'intensité du cisaillement vers le nord, allant d'une monzogranite faiblement déformée jusqu' à des mylonites associées à de nombreuses bandes d'ultramylonites anastomosées, reprises ensuite par une déformation cataclastique juste au-dessous du plan de détachement.

D'autre part, l'analyse d'images de terrain par tomographie à rayon X et les mesures EBSD ont permis respectivement de (1) quantifier l'intensité de la fabrique de forme minéralogique en 2- et 3-D le long du gradient de déformation, et (2) remonter aux mécanismes de déformation syn-cinématique. Les variations de forme des ellipsoïdes de déformation

corroborent les observations de terrain, suggérant ainsi une bonne corrélation entre études qualitatives et quantitatives. Les mesures EBSD du quartz indiquent quant à elles que la déformation ductile le long du gradient fut principalement dominé par le mécanisme de type fluage-dislocation depuis une température minimum de 500°C jusqu'à ~350°C, (transition ductile-cassant). Cependant, les mesures EBSD le long de bandes de cisaillement montrent également une contribution significative du mécanisme de déformation de type glissement aux joints de grain, en combinaison avec le fluage dislocation.

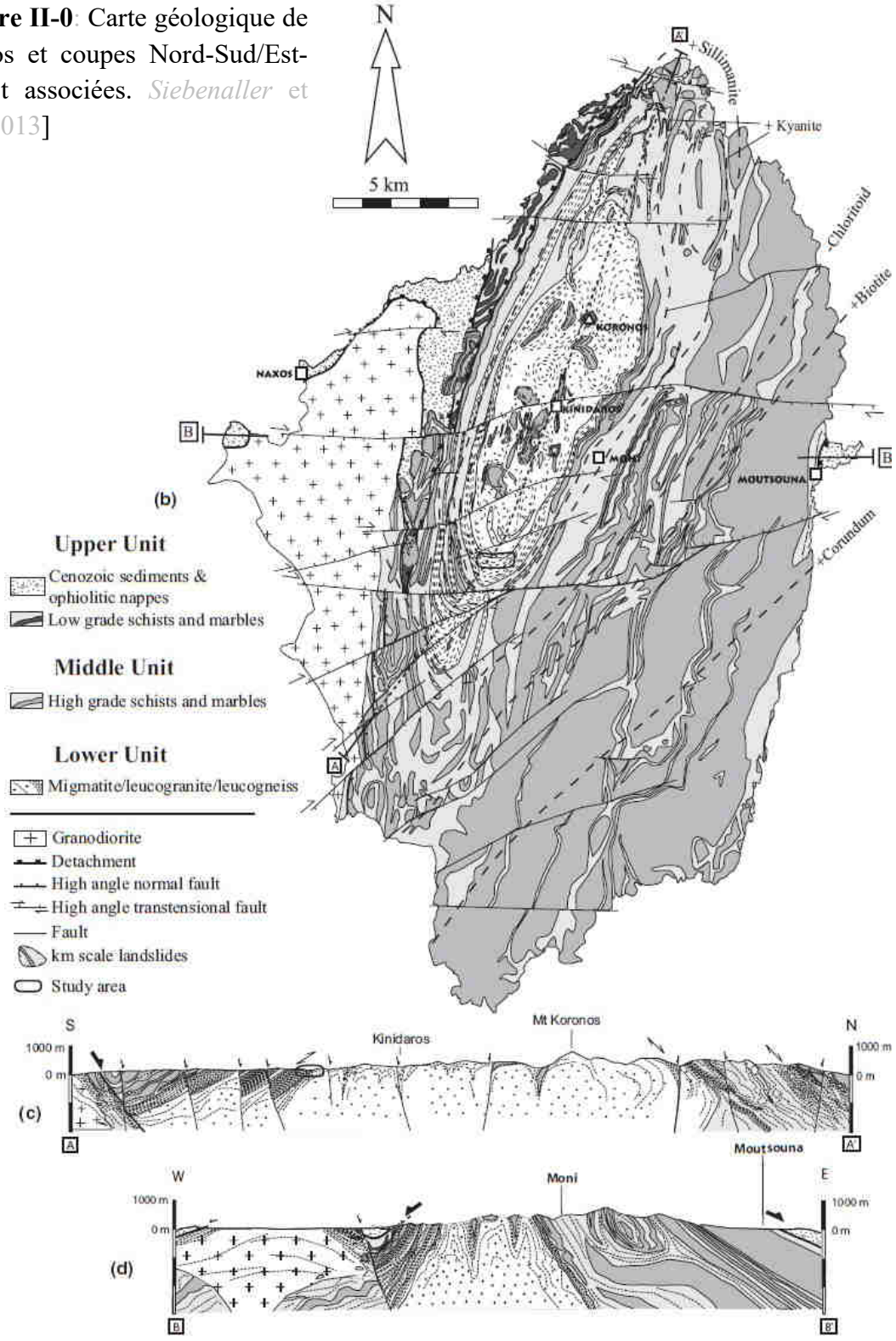

Figure II-0: Carte géologique de Naxos et coupes Nord-Sud/Est-Ouest associées. *Siebenaller* et al. [2013]

Article: Strain localization within a syn-tectonic intrusion in a back-arc extensional context, the Naxos monzogranite (Greece)

Soumis dans la revue *Tectonics*

Eloïse Bessière[1,2,3], **Aurélien Rabillard**[1,2,3], Jacques Précigout[1,2,3], Laurent Arbaret[1,2,3], Laurent Jolivet[1,2,3], Romain Augier[1,2,3], Armel Menant[1,2,3,4], Nicolas Mansard[1,2,3]

(1) Université d'Orléans, ISTO, UMR 7327, 45071, Orléans, France
(2) CNRS/INSU, ISTO, UMR 7327, 45071 Orléans, France
(3) BRGM, ISTO, UMR 7327, BP 36009, 45060 Orléans, France
(4) Now at Institut de Physique du Globe de Paris, Paris Sorbonne Cité, Univ. Diderot, UMR 7154-CNRS, Tectonique et Mécanique de la Lithosphère, Paris, France

Abstract

Although fundamental to understanding crustal dynamics in extensional setting, the relationships between the emplacement of granitic plutons and activity of their overlying detachments still remain very elusive. Through a multi-scale approach, we here document a continuous deformation history between the monzogranitic pluton of Naxos and the Naxos-Paros Detachment System (Cyclades, Greece). Field observations first show an early magmatic deformation followed by solid-state, ductile-then-brittle deformation when approaching the detachment zone, such as highlighted by a thick cataclastic zone and abundant pseudotachylite veins. From these observations, we define six strain facies that characterize a positive strain gradient from core to rim of the Naxos monzogranite. Based on field pictures, X-ray tomography and Electron BackScatter Diffraction (EBSD) analyses along the strain gradient, we then quantify the intensity of mineralogical fabrics in 2D and 3D and better characterize the deformation mechanisms. Our measured shape variations of the strain ellipsoid corroborate the large-scale strain gradient, showing a good correlation between qualitative and quantitative studies. In addition, EBSD data indicate that dislocation creep was predominant from more than 500°C to temperature conditions of the ductile-to-brittle transition. However, 1) a weakening of quartz lattice preferred orientation with increasing strain and 2) evidence of numerous four-grain junctions in high-strain shear bands also indicate that grain boundary sliding significantly contributed to the deformation. Although the source of grain boundary sliding remains to be constrained, it provides a consistent approach to account for strain localization in Naxos.

Keywords: Strain localization, magmatic emplacement, extensional context, detachment, 3D shape fabric, X-ray tomography, EBSD, Naxos Island.

1. Introduction

During the last thirty years, several studies have been devoted to the strain localization problematic linked with the interactions between plutonic activity and shear zones development in extensional [e.g., *Baldwin et al.*, 1993], transtensional [e.g., *Hutton*, 1982] or transpressional tectonic settings [e.g., *McCaffrey*, 1992]. In extensional continental regions, especially where "Metamorphic Core Complexes" (MCCs) form, the nucleation and ensuing development of shear zones within the continental crust are often coeval with the crystallization of granitoid intrusions. MCCs are crustal-scale structures that develop during the thinning of a previously thickened crust in an extensional post-orogenic context [*Coney & Harms*, 1984; *Lister & Davis*, 1989]. MCCs are inherently characterized by a low-angle normal fault or detachment, separating an upper unit, slightly or non-metamorphosed, from a lower unit with a higher metamorphic grade, frequently but not systematically associated with partial melting (see recent review of *Platt et al.* [2015]). Field-based and thermo-chronological studies have identified close spatio-temporal relationships between plutonic activity and MCCs development, as in the Basin & Range [*Crittenden et al.*, 1980; *Wernicke et al.*, 1987; *Gans et al.*, 1989; *Davis et al.*, 1993], the Mediterranean region [*Daniel & Jolivet*, 1995; *Jolivet et al.*, 1998; *Acocella & Rossetti*, 2002; *Smith et al.*, 2011] and more recently in East Asia [*Charles et al.*, 2011]. Such correlations have been especially documented in the Cyclades (Aegean Sea, Greece) [*Faure et al.*, 1991; *Lee & Lister*, 1992; *Koukouvelas & Kokkalas*, 2003; *Kumerics et al.*, 2005; *Brichau et al.*, 2007; *Tschegg & Grasemann*, 2009; *Denèle et al.*, 2011; *Kokkalas & Aydin*, 2013; *Laurent et al.*, 2015; *Rabillard et al.*, 2015].

Two opposing models were used to explain these spatio-temporal interactions. On the one hand, it was often suggested that active or pre-existing shear zones serve as upward drains for magma transfer as well as mechanical boundaries for magma storage [*D'Lemos et al.*, 1992; *Tikoff & Teyssier*, 1992; *Brown*, 1994; *Vigneresse*, 1995]. On the other hand, partially crystallized magmatic bodies are likely to produce strong rheological contrasts along which deformation can be efficiently accumulate and localized into shear zones [*Lister & Baldwin*, 1993; *Davidson et al.*, 1994; *Tommasi et al.*, 1994].

To better constrain the interactions between strain localization processes and plutonic activity during MCCs development, detailed structural field studies are required. The Cyclades appears as an ideal natural laboratory as major extensional shear zones (i.e. the detachments), metamorphic domes and plutonic intrusions were described as contemporaneous. Recent such surveys have been already conducted in this area, in Serifos, Mykonos and Ikaria islands [*Denèle et al.*, 2011; *Laurent et al.*, 2015; *Rabillard et al.*, 2015]. Study of syn-tectonic granitoids have thus shown progressive ductile-then-brittle strain localization starting with shear zones nucleation during their cooling and followed by the development of large-scale strain gradient after complete crystallization toward the upper tectonic contact between the pluton and enclosing rocks. These observations combined with the overall asymmetrical architecture of the intrusions thus suggest that their emplacement was entirely controlled by active detachments. In recent studies, it have been also demonstrated a control of the intrusions on the detachment activity, gradually inactivating preexisting detachments, and forcing their migration structurally upward in the crust [*Laurent et al.*, 2015; *Rabillard et al.*, 2015].

Although the Naxos metamorphic dome was the first MCC described in the Cyclades [*Lister et al.*, 1984], there is no detailed study on the strain localization within the intrusion associated and lately emplaced within this MCC. To achieve this goal, this paper presents two approaches, one qualitative, with field observations over the whole pluton together with a mapping of the intensity of the shearing deformation, and one involving quantification of strain with a 3D study of the rock shape fabrics by means of image analysis, X-ray tomography and EBSD (Electron BackScatter Diffraction) measurements.

2. Geological and geodynamic setting

2.1. Geological evolution of the Aegean region

The present-day architecture of the Aegean region (Figure II-1a), corresponding to the collapsed central part of the Hellenides-Tauride chain, results from a complex tectonic history which can be summarized as a two-stepped evolution: (1) an episode of crustal thickening resulting from the successive subduction of the Tethyan oceanic and Apulian continental lithospheres beneath the Eurasian plate during the Eocene [*Bonneau & Kienast*, 1982; *van Hinsbergen et al.*, 2005], followed by (2) a post-orogenic collapse of the chain, forming a back-arc basin as a result of the retreat of the African slab operating since the end of the Eocene with an acceleration after 35 Ma [*Jolivet & Faccenna*, 2000; *Jolivet & Brun*, 2010] or later (23-19 Ma) according to *Ring et al.* [2010].

Located in the central part of the Aegean region, the Cyclades consists in series of MCCs where the deepest parts of the Hellenides-Taurides chain were exhumed owing to post-orogenic extension. Classically, three main units are distinguished in the Cyclades [*Bonneau*, 1984; *Jolivet et al.*, 2004; *van Hinsbergen et al.*, 2005]: (1) The Cycladic Continental Basement (CCB) composed of orthogneisses, paragneisses and micaschists of Paleozoic age [*Henjes-Kunst & Kreuzer*, 1982; *Andriessen et al.*, 1987; *Keay & Lister*, 2002]. It crops out on Naxos, Paros, Ikaria, Ios, Serifos or Sikinos islands [*Andriessen et al.*, 1987; *Grasemann & Petrakakis*, 2007; *Huet et al.*, 2009; *Augier et al.*, 2015; *Beaudoin et al.*, 2015]. (2) The Cycladic Blueschists Unit (CBU) is characterized by a sequence of metapelites, marbles, quartzites and mafic rocks (meta-gabbro and meta-basalts) and equilibrated in the eclogites or blueschists facies conditions during subduction [*Blake et al.*, 1981, 1984; *Bonneau & Kienast*, 1982; *Reinecke et al.*, 1982; *Avigad & Garfunkel*, 1989; *Keiter et al.*, 2004]. (3) The Upper Cycladic Unit (UCU) is a complex assemblage of low-metamorphic grade tectonic units resting at the top of the nappe stack from the northern Cyclades all the way to Crete (Asteroussia Nappe). This unit contains pieces of the Pelagonian basement and its non-metamorphic cover, ophiolitic units related either to a Jurassic or a Cretaceous obduction event [e.g., *Maluski et al.*, 1987; *Patzak et al.*, 1994; *Katzir et al.*, 1996; *Papanikolaou*, 2009; *Martha et al.*, 2016], Late Jurassic Blueschists and Miocene sediments deposited during the activity of the Aegean detachments [*Sanchez-Gomez et al.*, 2002; *Kuhlemann et al.*, 2004].

The tectonic history of the Cyclades spans the whole Cenozoic. Age of the high pressure-low temperature (H*P*-L*T*) metamorphism is well documented in the CBU, and

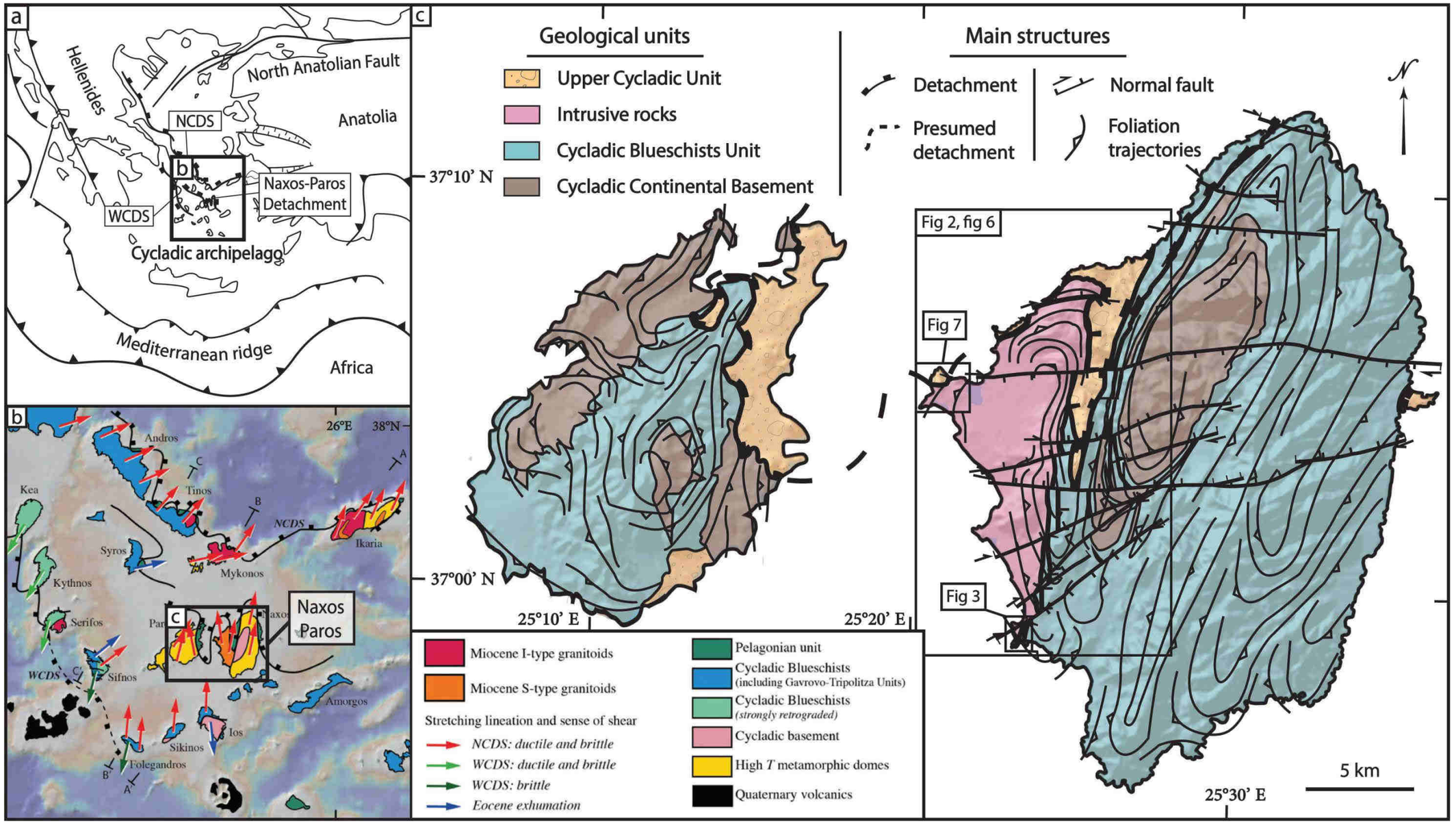

Figure II-1: *tectonic and geological maps and location of the studied area. (a) Simplified tectonic map of the Aegean region showing the main structures: the North Cycladic Detachment System (NCDS), the West Cycladic Detachment System (WCDS), and the location of Cyclades archipelago. (b) Tectonic map of the Cyclades archipelago showing the main structures, the main metamorphic core complexes and plutons, as well as kinematic indicators with the location of Naxos-Paros Islands, modified after Jolivet et al. [2015]. (c) Geological map of Naxos and Paros islands, modified after Gauthier et al. [1993] and Siebenaller [2008].*

radiometric ages associated with the H*P*-L*T* metamorphism range between 70 and 35 Ma with the majority of ages grouped in the middle Eocene (50-40 Ma) [e.g., *Altherr et al.*, 1979; *Maluski et al.*, 1987; *Wijbrans et al.*, 1990; *Bröcker & Enders*, 1999]. This H*P*-L*T* episode corresponds to the burial and the syn-orogenic exhumation of the CBU and CCB within the Hellenic subduction channel [*Jolivet et al.*, 2003; *Brun & Faccenna*, 2008; *Jolivet & Brun*, 2010; *Ring et al.*, 2010]. A second episode is associated with medium pressure-medium to high temperature (M*P*-M*T*/H*T*) metamorphism in the conditions of the greenschist and more locally of the amphibolite facies, affecting the two lowest units of the Cyclades in the Oligo-Miocene [*Altherr et al.*, 1982]. During the lithospheric thinning of the Aegean area, post-orogenic extension led to the reworking of the nappe stack by low-angle normal faults and the exhumation of MCCs under crustal-scale detachment systems [e.g., *Lister et al.*, 1984; *Urai et al.*, 1990; *Faure et al.*, 1991; *Buick*, 1991a, 1991b; *Gautier et al.*, 1993; *Gautier & Brun*, 1994a, 1994b] including the North Cycladic Detachment System (NCDS) [*Jolivet et al.*, 2010; *Lecomte et al.*, 2010; *Menant et al.*, 2013], the Naxos-Paros Detachment System [*Gautier et al.*, 1993; *Brichau et al.*, 2006; *Bargnesi et al.*, 2013] and the West Cycladic Detachment System (WCDS) [*Grasemann & Petrakakis*, 2007; *Iglseder et al.*, 2011; *Grasemann et al.*, 2012] (Figures II-1a and -1b). Coevally with the activity of these detachments systems, S- and I-type granitoids intruded in the Aegean crust between 15 and 9 Ma [*Keay*, 1998; *Keay et al.*, 2001; *Brichau et al.*, 2007, 2008; *Iglseder et al.*, 2009; *Bolhar et al.*, 2010], such as on the islands of Tinos, Mykonos-Delos-Rhenia, Serifos, Ikaria and Naxos. These magmatic bodies are temporally and spatially emplaced in close interaction with Miocene MCCs and their associated detachments [*Faure et al.*, 1991; *Lee & Lister*, 1992; *Brichau et al.*, 2007, 2008, 2010; *Grasemann & Petrakakis*, 2007; *Denèle et al.*, 2011; *Laurent et al.*, 2015; *Rabillard et al.*, 2015].

2.2. Geology of Naxos

Naxos is the largest island of the Cyclades, located in the center of the archipelago (Figure II-1b). The main part of the island is a N-S elongated gneiss dome cored with migmatites (Figure II-1c) [*Jansen*, 1973; *Urai et al.*, 1990; *Buick*, 1991a; *Vanderhaeghe*, 2004]. Numerous studies have been devoted to the structure of the metamorphic dome [*Andriessen et al.*, 1979; *Wijbrans & McDougall*, 1988; *Urai et al.*, 1990; *Gautier et al.*, 1993; *Keay et al.*, 2001; *Koukouvelas & Kokkalas*, 2003; *Kuhlemann et al.*, 2004; *Duchêne et al.*, 2006; *Seward et al.*, 2009; *Kruckenberg et al.*, 2011] and the overlying UCU that consists in Miocene sandstones, conglomerates and remnants of ophiolitic rocks [*Bögek*, 1983; *Kuhlemann et al.*, 2004; *Seward et al.*, 2009]. Metamorphic units in the dome of Naxos Island are classically attributed either to the CBU or the CCB. They consist in an alternation of metapelitic rocks, metavolcanics and abundant marbles locally associated with metabauxites [*Feenstra*, 1985]. The metasediments making the cover of the migmatites contain very little metabasites and they resemble the cover of the Menderes Massif rather than the CBU consisting in an alternation of metabasites, marbles and metapelites. We thus consider the core of the Naxos metamorphic dome as part of the CCB as in *Jolivet et al.* [2004] or the Basal Unit of *Ring & Layer* [2003]. Local remnants of blueschist parageneses from the earlier

Eocene subduction-related H*P*-L*T* episode [*Wijbrans & McDougall*, 1988] are preserved in the southern part of the dome [*Jansen*, 1977; *Avigad*, 1998] despite the overprint of the high-temperature Oligo-Miocene event. Later, during the formation of the Aegean Sea in back-arc context, the dome underwent a M*P*-M*T*/H*T* event, dated between 20.7 and 16.8 Ma by SHRIMP U-Pb on zircons [*Keay et al*., 2001], resulting in a retrograde metamorphism under greenschist- to amphibolite-facies conditions with a gradient of peak-temperature toward the core of the dome where partial melting has been described [*Jansen*, 1977; *Vanderhaeghe*, 2004; *Duchêne et al*., 2006]. Final exhumation of all of these units was achieved by the activity of the crustal-scale Naxos-Paros Detachment System (Figure II-1c) [*Buick*, 1991a, 1991b; *Gautier et al*., 1993; *Siebenaller*, 2008].

Intrusive bodies cropping out on Naxos can be compositionally separated into S- and I-type granitoids. S-type granitoids are typified by numerous yet small peraluminous leucogranite intrusions with a variable composition in terms of chemistry and mineralogy, involving different protoliths [*Pe-Piper et al*., 1997]. The western I-type granitoid consists in a voluminous composite intrusion characterized by a hornblende-biotite monzogranite (two feldspars, quartz, biotite, amphibole, titanite and oxides) in the inner part and a subordinate peripheral granodiorite [*Jansen*, 1973; *Altherr et al*., 1982; *Wijbrans & McDougall*, 1988; *Pe-Piper et al*., 1997; *Pe-Piper*, 2000; *Keay et al*., 2001; *Altherr & Siebel*, 2002]. Al-in-hornblende barometer indicates crystallization pressures ranging from 200 and 300 MPa [*Jansen & Schuiling*, 1976; *Cao et al*., 2017]. The emplacement of this monzogranitic intrusion was dated at ca. 15-14 Ma by U/Pb analyses on zircon. Subsequent cooling occurred quite fast between ~13.6 and ~11 Ma as constrained by K-Ar and Ar-Ar on hornblende [*Henjes-Kunst et al*., 1988; *Wijbrans & McDougall*, 1988; *Keay et al*., 2001; *Altherr & Siebel*, 2002]. These results are consistent with those obtained for the M*P*-H*T* retrograde metamorphism [*Gautier et al*., 1993] and trace elements content, especially Y, Nb, Rb and Ba, fit a gneissic source for this monzogranite [*Pe-Piper et al*., 1997]. All these data indicate a post-orogenic intrusion with a dominant crustal contribution emplaced in an extensional context [*Pe-Piper et al*., 1997]. The monzogranite is intersected by a late leucogranite that is a late differentiation of the same hornblende-biotite-bearing magma [*Pe-Piper et al*., 1997]. These observations support a syn-extensional emplacement of the intrusion associated to the Naxos-Paros Detachment System characterized by three major structures according to *Siebenaller* [2008]: (1) a "décollement" operating at the boundary between the amphibolite and greenschist-facies metamorphic rocks, (2) a "décollement" operating within the greenschist-facies metamorphic rocks and (3) an upper brittle detachment separating the greenschist-facies rocks and the UCU.

3. Large-scale geometry and internal architecture of the intrusion

3.1. Finite strain markers

Only few field studies focused in the geometry of the monzogranite intrusion of Naxos [*Gautier et al*., 1993]. To document the overall geometry of the intrusion and then to study the internal distribution of strain, we first complemented the geological map of Naxos [*Jansen*, 1973; *Siebenaller*, 2008] and described finite strain markers over the whole intrusion. The

resulting new structural map of the intrusion is proposed on Figure II-2. Results from the measurements of finite strain markers are gathered in two synthetic maps showing either the foliation (Figure II-2a) or the lineation and associated sense of shear (Figure II-2b).

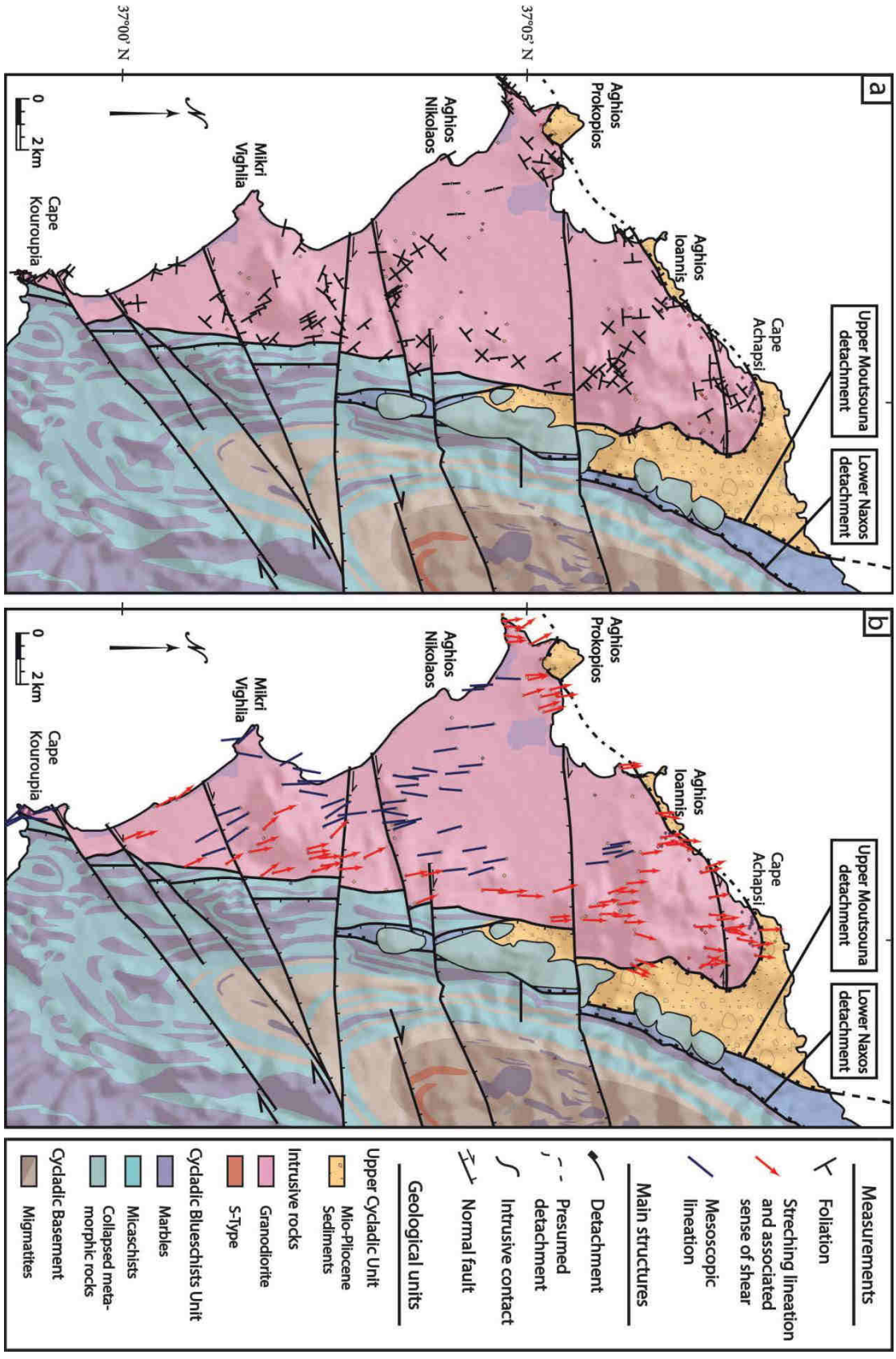

Figure II-2: *geological map of the western part of Naxos with the main tectonic structures, including the (a) foliations and (b) the stretching lineations with associated sense of shear.*

Foliation is heterogeneously developed within the Naxos intrusion. The dip of the foliation displays a large range of variation from 0° to 90° while most of dips are comprised between ca. 25° to 50°. Sub-vertical and steeply dipping foliation planes appear restricted to the center of the intrusion, near Aghios Nikolaos (Figure II-2). At the first glance, the foliation planes commonly dip away from the center of the intrusion and the attitude of foliation traces shows a dome-shaped pattern marked by a NE long axis (Figure II-2a). This curved pattern is best expressed in the northern part of the intrusion where the foliation planes rapidly turns from a N60° preferred orientation along the NW coast to more N90° to N120° along the NE contact.

Stretching lineation is a common feature of the intrusion. It is mostly outlined by the elongation of primary magmatic minerals (K-feldspar) and by the orientation of phyllosilicate aggregates. Orientation of the stretching lineation shows a very little dispersion. Trends are comprised between N010° and N340°, with an average value close to N0° (Figure II-2b) while plunges are consistently oriented toward the north. When the sense of shear (top-to-the-north) can be deduced, the stretching lineation is overall plunging to the north, with variations from top-to-the-NNW to top-to-the-NNE (Figure II-2b). Rocks in the vicinity of the UCU and locally the Naxos MCC exhibit an intense top-to-the-N shearing deformation (Figure II-2b). There, kinematic indicators (asymmetric boudinage, rotations, large-scale sigmoïds, or micas with fish-type geometries into the XZ plane) are restricted to a dense array of top-to-the-N shear bands. Conversely, less deformed areas present a less non-coaxial deformation and numerous outcrops only display a clear N-S stretching or mineral lineation (Figure II-2b).

3.2. Description of the first order geometry

From south to north, different types of contact of the monzogranitic intrusion with host-rocks can be observed with a high variability in terms of deformation intensity. At Cape Kouroupia, in the southern part of the intrusion, field observations show a folded intrusive contact between the monzogranite intrusion and enclosing gneisses and marbles (Figures II-3a and -3b). Numerous gneissic septa are present into the intrusive body and the metamorphic host-rocks are injected by an important dike array (Figures II-3c and -3d). A gradual transition from the metamorphic host-rocks to the monzogranite is observed with the appearance of granodioritic veins in gneisses, then gneissic fragments embedded in the monzogranite, ending with the complete disappearance of the metamorphic unit (Figure II-3b). Finally, foliations measured in the monzogranite near the intrusive contact are generally steeply dipping (average value of orientations N147° with a dip of 60° to the NE), while they are moderately dipping in the gneiss (orientation mean N154° and a dip of 40° to the NE) (Figure II-3a). In addition, tension gashes filled with tourmaline are observed in the intrusive veins, mostly oriented NW-SE, and compatible with a dextral component of deformation (Figure II-3d). In parallel, numerous elongated mafic enclaves are present, with sharp or diffuse margins, sometimes cut by late leucocratic dikes (aplite). More or less extensive schlierens zones, sometimes folded, are also noticed (Figure II-3e), as well as the occurrence of folded injection veins (Figure II-3f). Late-magmatic deformation is highlighted by N45°E-trending fractures filled with tourmaline, in the K-feldspar phenocrysts. Similarly, these K-feldspars can be affected by N40°E-oriented fractures with quartz filling. Locally, skarns are observed either in marble

oralong the contact between the monzogranite and the gneisses (Figure II-3g). Finally, the marbles are affected by significant fracturing linked to the strike-slip faulting (Figure II-3a).

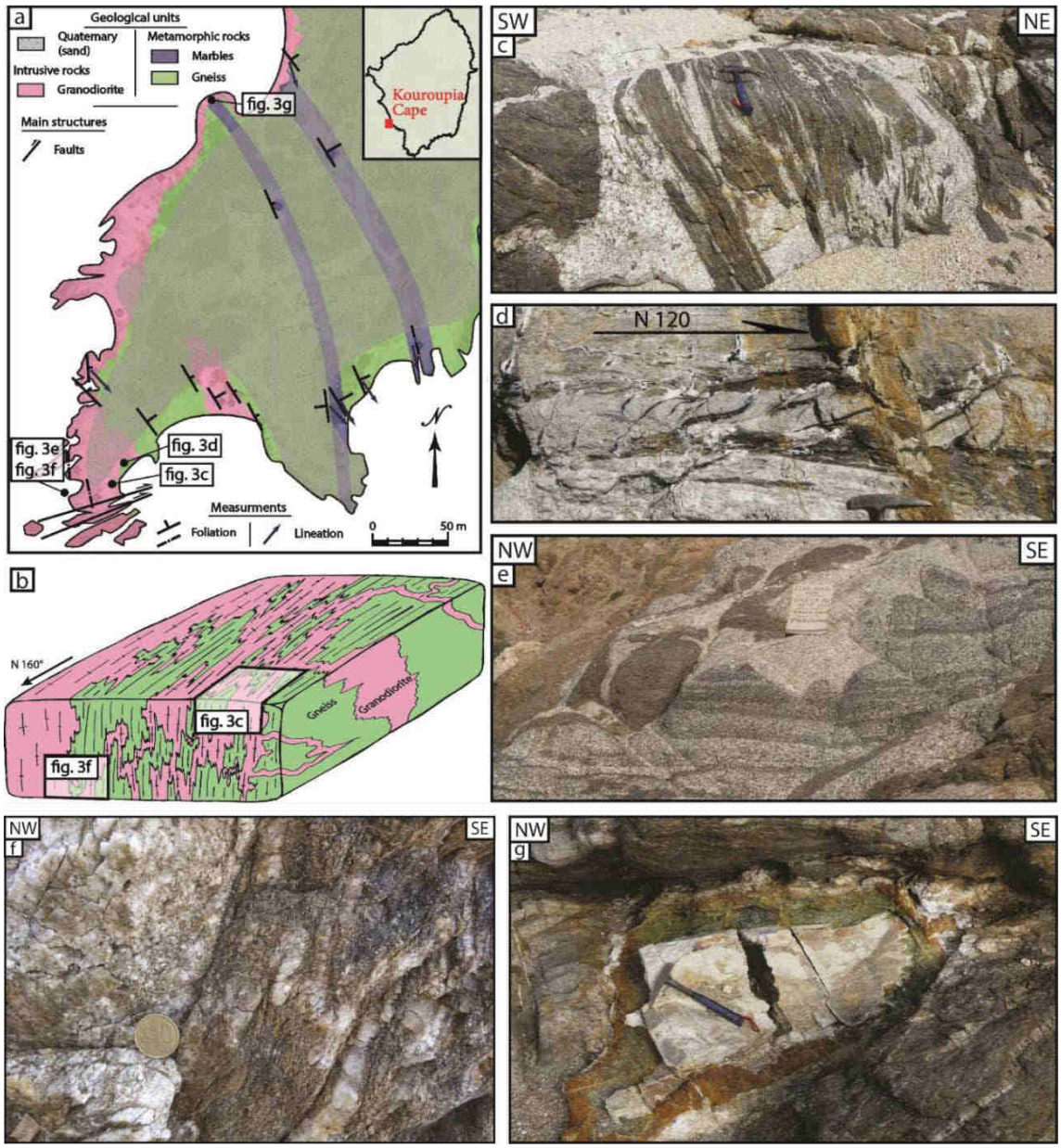

Figure II-3: overview of the *Cape Kouroupia contact in the southern part of the Naxos intrusion. (a) Geological map of the area with measured foliations and the lineations. See the inset at upper left for the exact location. (b) Synthetic 3D diagram summarizing the structuration and the main features observed along the Cape Kouroupia contact. Outcrop pictures of (c) gneiss septas within the monzogranitic intrusion, (d) leucogranitic intrusive vein sheared with tourmaline-filled sheared tension gashes, (e) schlieren zone within the monzogranitic intrusion, (f) deformed and folded intrusive vein, (g) skarn localized at the contact between gneiss and the monzogranitic intrusion.*

In the northern part of the intrusion, the Cape Achapsi area is characterized by a well-marked tectonic contact between the monzogranite and Miocene conglomerates (Figure II-4a). This contact is marked by a clear-cut detachment plane dipping 20° to the north on top of a massive 50m-thick cataclasite consisting in a fine-grained greenish matrix with clasts smaller

than one centimeter and numerous inframillimetric pyrites, along joints (Figure II-4b). The detachment plane is marked by large-scale corrugations oriented N10°E. Conglomerates in the hanging wall are affected by brittle deformation, marked by fracturing of pebbles indicating a NW-SE extension. Below this major tectonic contact, a strain gradient both in the ductile and brittle regimes is observed in the monzogranite in all the area of Cape Achapsi, not yet described precisely.

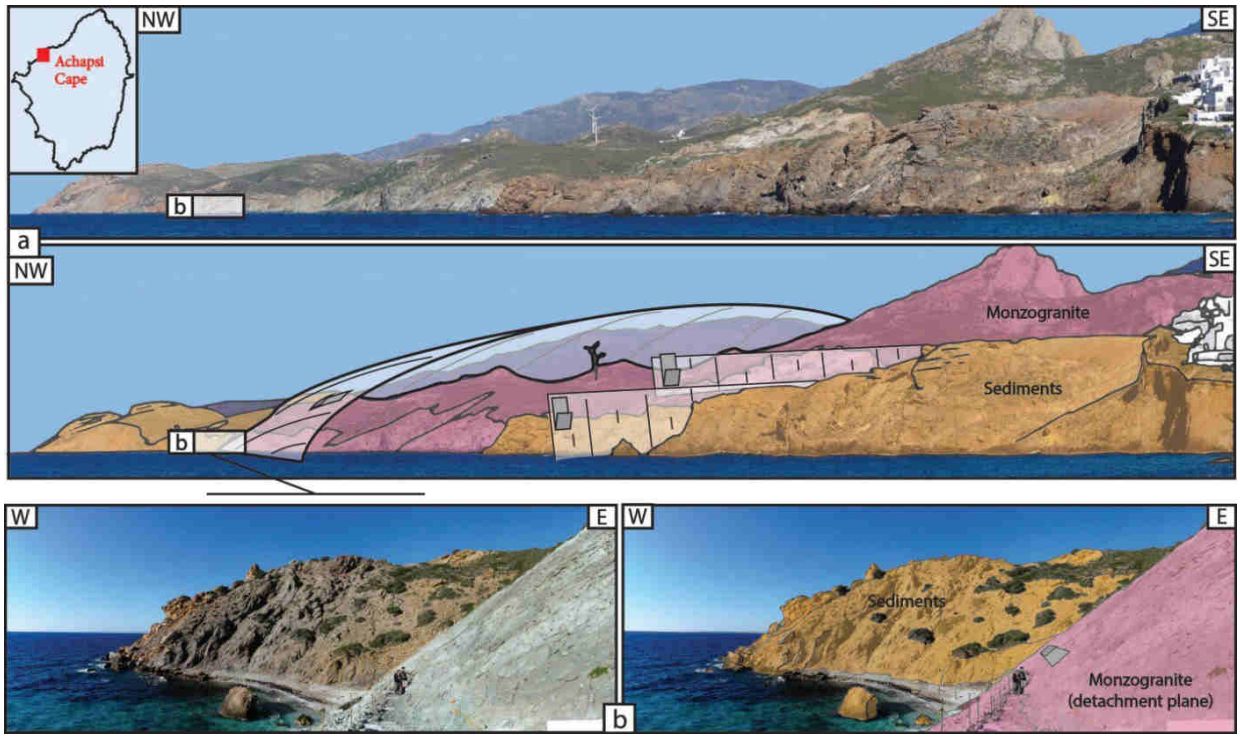

Figure II-4: *overview of the Cape Achapsi contactin the northern part of the Naxos intrusion. (a) Panorama view of the Cape Achapsi from the Naxos port. The tectonic contact, with top-to-the-north kinematic, between Miocene sediments and the Naxos monzogranite is segmented by late normal faults. (b) Detailed picture of the detachment plane showing the Miocene sediments overlying the monzogranite. Corrugations, oriented N10°, indicate top-to-the-north kinematics.*

3.3. Mapping the strain gradient within the intrusion

In order to map the strain distribution within the Naxos intrusion, a deformation scale was constructed based on macro-structural criteria observed in the field [*Agard et al.*, 2011], consistent with microstructural observations. This approach is similar, on the principle, to that conducted in recent studies [*Huet et al.*, 2009; *Charles et al.*, 2011; *Laurent et al.*, 2015].

3.3.1. Scale of deformation intensity

The gradual evolution of deformation intensity from magmatic to sub-solidus conditions has been separated in six strain grades based on structural and textural field observations. This scale starts from the magmatic stage with grade 0 and ends in the ductile then brittle conditions with grade 5 as follows:

Grade 0 corresponds to an isotropic magmatic fabric (Figure II-5a). The term "magmatic fabric" is used in the mechanical sense, when there is no direct interaction (contact) in the magma between crystals [*Vernon*, 2000]. A magmatic preferred orientation, mainly corresponding to the alignment of K-feldspar phenocrystals, starts to develop with a low shape fabric intensity. In the field, the monzogranite shows neither clear planar nor linear shape fabrics, and minerals are not deformed.

Grade 1 corresponds to a clear anisotropic magmatic fabric (Figure II-5b). Minerals are not deformed but an incipient foliation and/or lineation can be observed, especially with the preferred alignment of biotite and amphibole. Phenocrysts of feldspar are still visible and mafic enclaves display a profiled and oriented shape.

Grade 2 can no longer be considered as a pure magmatic fabric (Figure II-5c). Feldspar megacrysts start to be deformed, suggesting contact interactions between crystals in a solid network within the magma. Some feldspar phenocrysts are not deformed while others are stretched, boudinaged and sheared. Additionally, mafic enclaves are now clearly deformed with slender shapes and smaller dimensions. Elongated clusters of biotite mark the stretching lineation.

Grade 3 is marked by the appearance of a weak tectonic foliation, a clear stretching lineation, a few penetrative shear bands that affect large volume of rocks, grain-size reduction and clear quartz ribbons (Figure II-5d). This shape fabric can be qualified as protomylonitic.

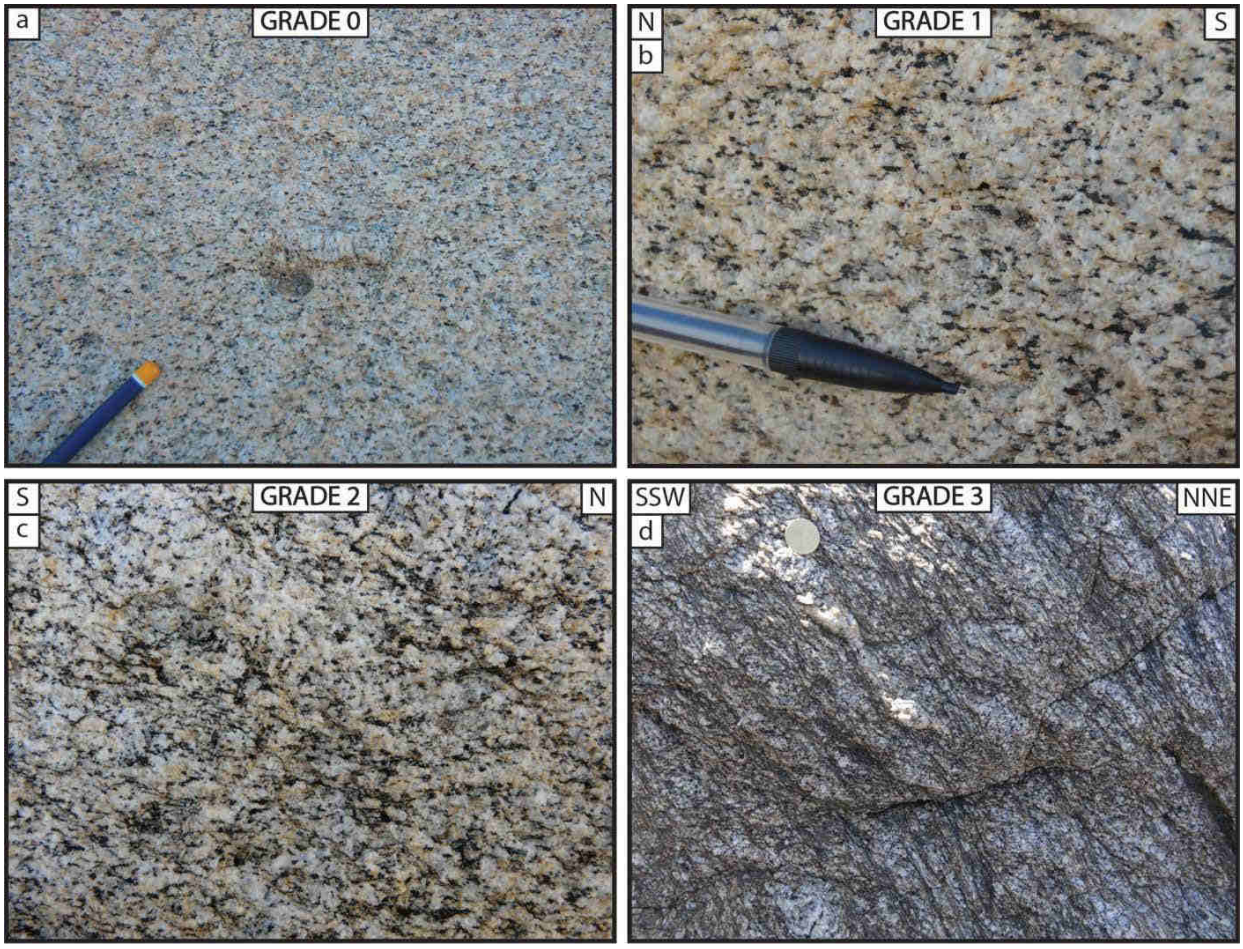

(continued)

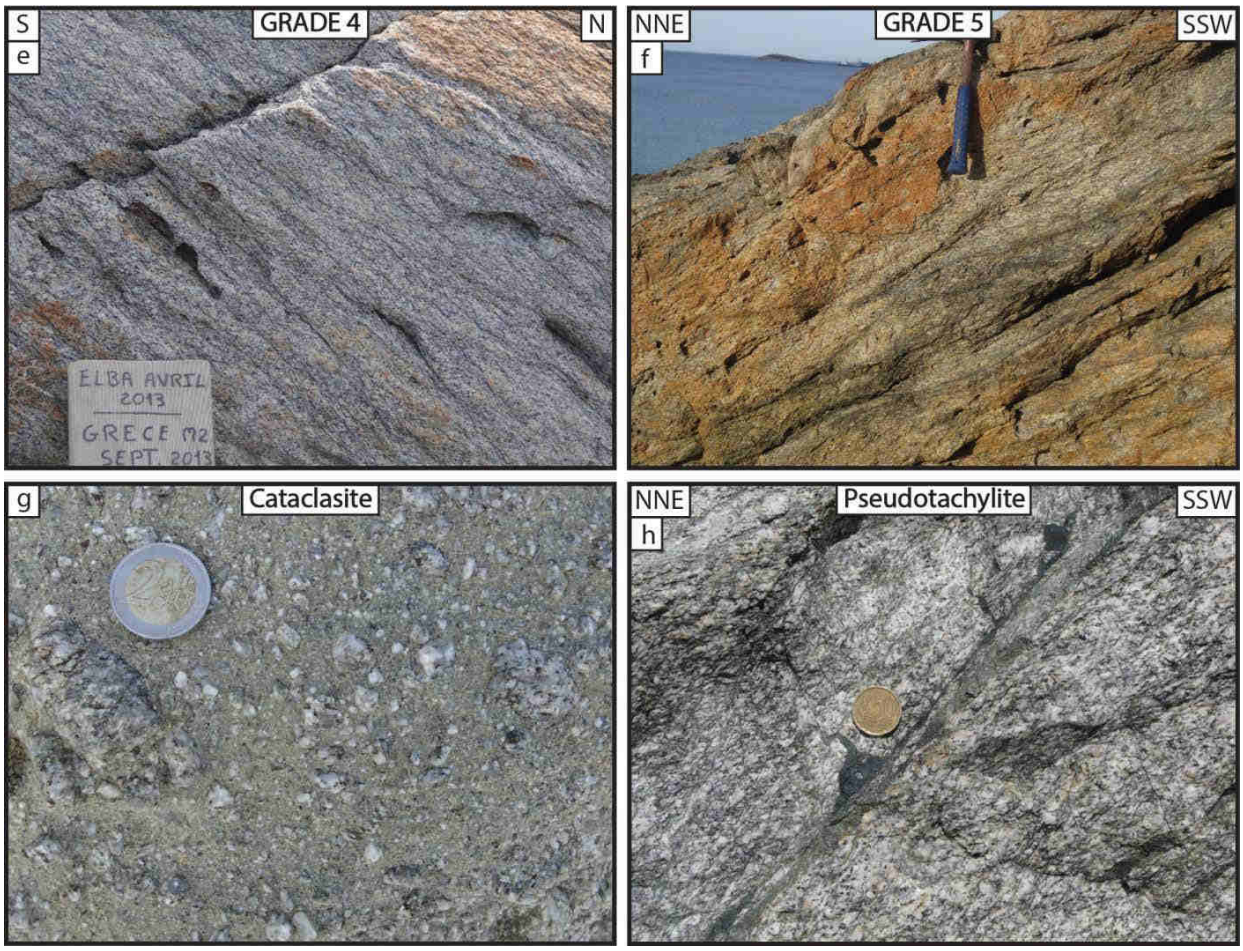

Figure II-5: *presentation of the deformation intensity scale with field pictures. (a) Grade 0: isotropic magmatic fabric. (b) Grade 1: anisotropic magmatic deformation. (c) Grade 2: first strain localization with ductile deformation. (d) Grade 3: first shear bands. (e) Grade 4: first ultramylonitic bands. (f) Grade 5: intensification and development of ultramylonitic bands. (g) Cataclasite. (h) Pseudotachylyte veins.*

Grade 4 is characterized by a strong foliation and lineation with increasing number and thickness of shear bands associated with stretched biotite and quartz ribbons (Figure II-5e). This shape fabric can be qualified as mylonitic.

Grade 5 show both a thickening and an interconnection of mylonitic shear bands, up to grow locally into darkish, anastomosing ultramylonitic shear bands (Figure II-5f). These cm- to dm-wide ultramylonite bands are defined by an intense grain-size reduction resulting in phase mixing, and mesoscopically, do not exhibit visible grains or only a few feldspar remnant clasts.

In addition to this scale of ductile deformation intensity, brittle/cataclastic features were recognized and mapped separately. The uppermost level of mylonites (ca. 50-100m) was indeed reworked by a cataclastic deformation, ranging from protocataclasites in which angular clasts from mylonitized rocks (from grade 3 to 5) have been preserved (Figure II-5g), to cohesively foliated ultracataclasites. Some pseudotachylyte veins also occur and have been

more precisely observed within the grade 5 along ultramylonite bands (Figure II-5h). Clear stretching-perpendicular, 1- to 5-mm-thick injection veins are discernible.

3.3.2. Strain distribution at the scale of the Naxos intrusion

This scale of finite deformation was used to map the strain distribution within the Naxos intrusion. 245 outcrops were visited (colored points on Figure II-6). Results show a gradual increase in strain intensity from internal parts of the intrusion to the contact with the surrounding wall-rocks (Figure II-6). The still-undamaged magmatic rocks (grades 0 and 1) are found from the southwest coast between the Aghios Nikolaos and Mikri Vighlia villages (Figures II-6). Strain grades arranged as concentric zones draw quite continuous strain gradients approaching the contact zone with the upper unit where strongly deformed rocks occur. Internal architecture of this strain gradient which is spectacularly exposed along the coast at the Aghios Prokopios can be studied as a representative example (see location on Figures II-6). There, deformation intensity increases significantly from south to north over an approximately 1 km thick strain gradient, from the first evidence of strain localization (grade 2) to ultramylonitic facies (grade 5) (Figures II-7a and -7b). 3D sketches illustrate the different key-outcrops as well as the evolution of deformation intensity of the peninsula (Figures II-7c to 7f).

To the south, the Aghios Nikolaos area is only characterized by a weak magmatic fabric or even isotropic magmatic fabrics (Figure II-6). Deformation incipiently localizes around the K-feldspar phenocrysts with the alignment of biotite flakes. Mineral orientation is then increasingly pronounced, particularly for biotite grains (Figure II-7c). Then, K-feldspar phenocrysts are boudinaged, associated with the appearance of sigmoidal foliation, shear bands and mica fish. Foliation shows a regular dip of 35° to the NW, with a northwest-trending stretching lineation (Figure II-7a). The associated sense of shear is also consistent, always top-to-the-NNW. This is accompanied by a significant reduction of grain-size (quartz and feldspars) and the disappearance of feldspar phenocrysts (Figure II-7d). From 600m below the contact, shear bands become gradually thicker and denser with locally occurrences of cm-wide ultramylonite bands. K-feldspars are often affected by antithetic shears. It is also worthy to note the pronounced shape fabric of quartz grains in the sigmoidal foliation between shear bands (Figure II-7e). From ca. 150-250m below the contact, ultramylonite bands are widespread and display an overall strike N50° with a dip of N50° to the northwest, while shear planes show strikes around N72° and a dip of 38° to the northwest. The sense of shear remains top-to-the-NNW. In the vicinity of the contact, ultramylonite bands anastomose. However, the ductile fabric is locally strongly reworked by brittle features such as a 60-100 meter-thick cataclasite body and localized pseudotachylyte veins. Pseudotachylyte veins that occur as a dense array are either parallel to the ultramylonitic bands or perpendicular to them, filling extensional veins perpendicular to the stretching direction (Figure II-7f). Cataclasites occur as a massive and chloritized cataclastic body characterized by a heterogeneous grain-size with elements reaching cm-scale wrapped into a fine-grained matrix. The upper contact of the intrusion is characterized by a thick fault gouge that marks the contact with diabase belonging to the UCU, itself unconformably overlain by Miocene sandstone.

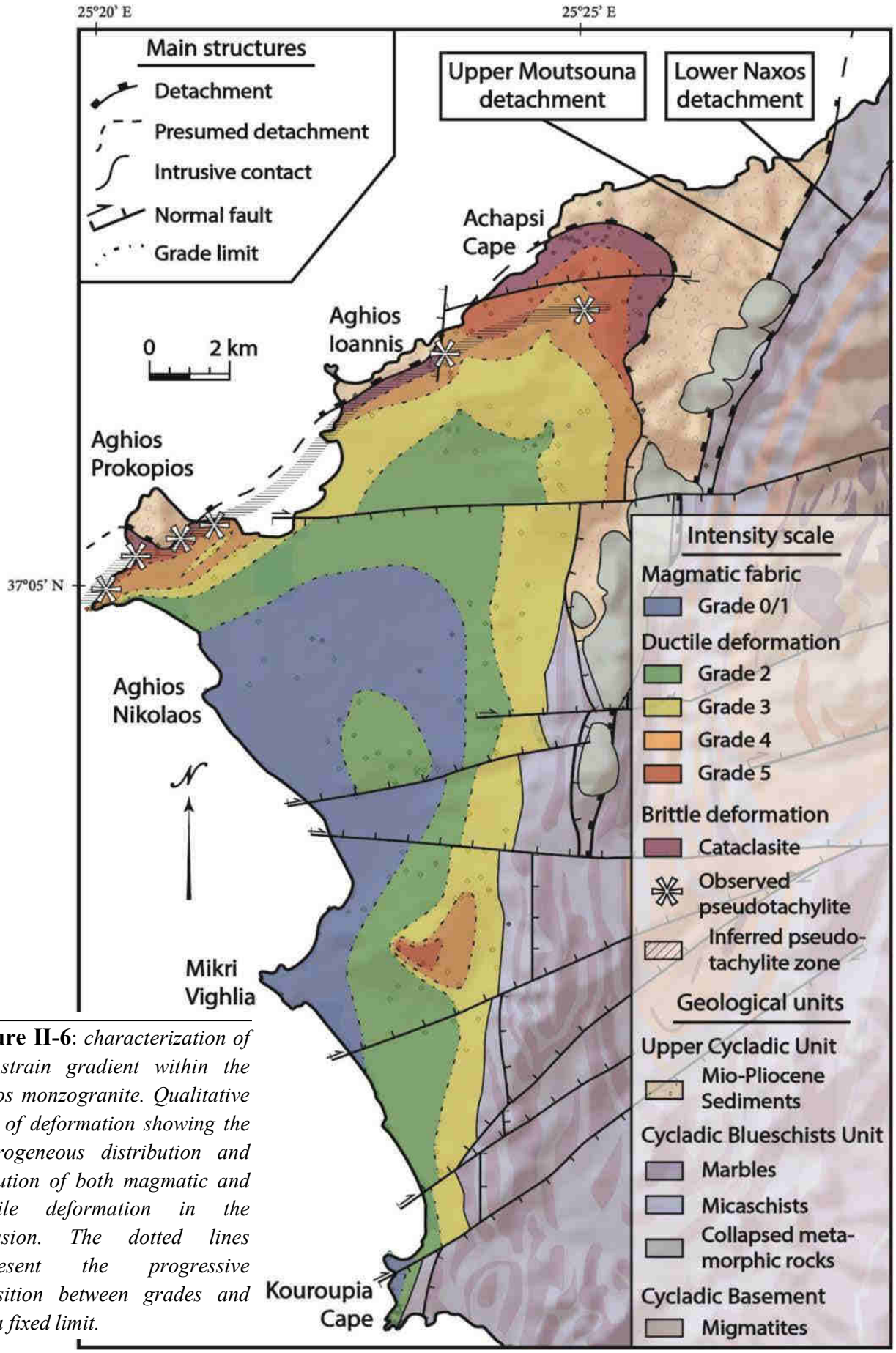

Figure II-6: *characterization of the strain gradient within the Naxos monzogranite. Qualitative map of deformation showing the heterogeneous distribution and evolution of both magmatic and ductile deformation in the intrusion. The dotted lines represent the progressive transition between grades and not a fixed limit.*

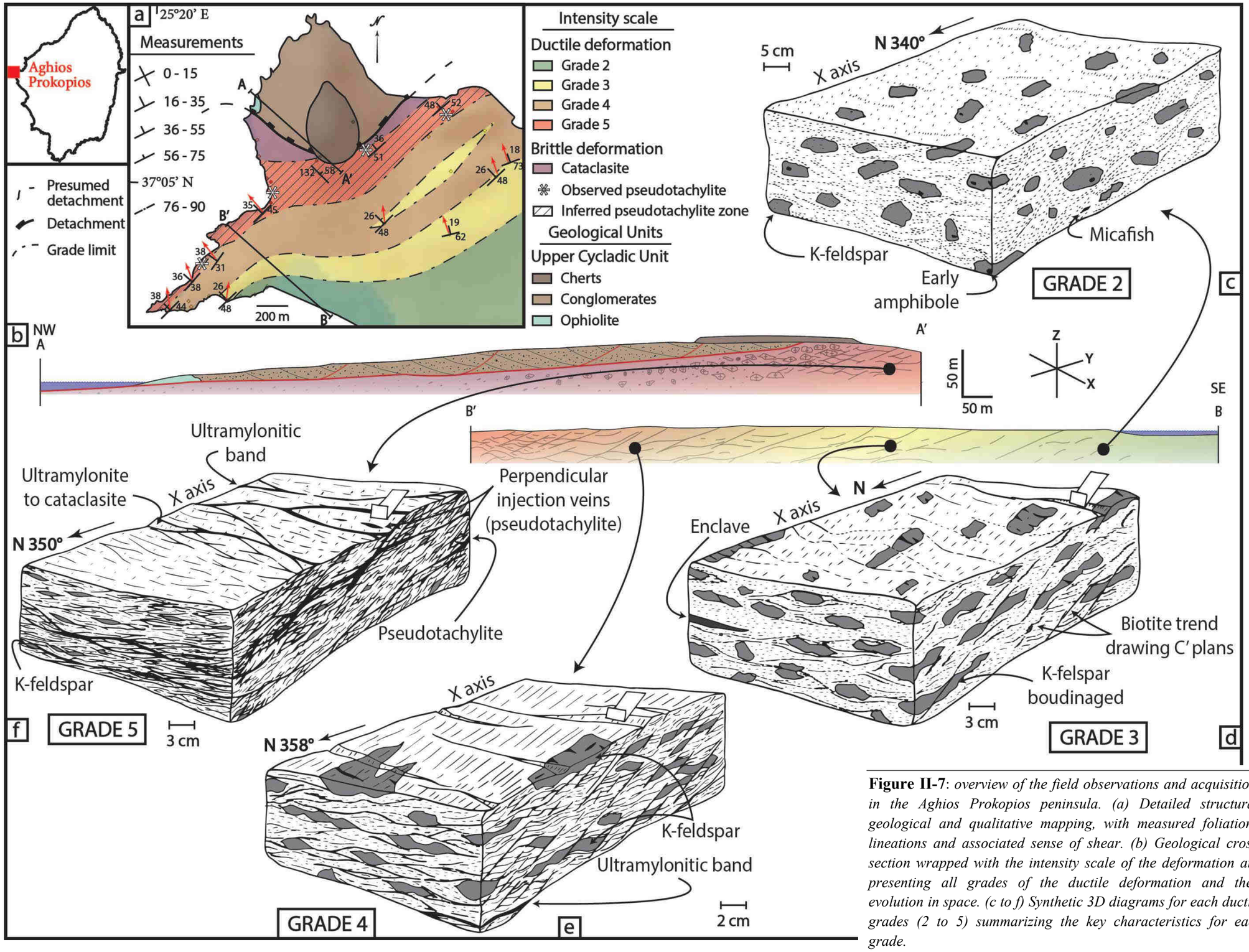

Figure II-7: *overview of the field observations and acquisitions in the Aghios Prokopios peninsula. (a) Detailed structural, geological and qualitative mapping, with measured foliations, lineations and associated sense of shear. (b) Geological cross-section wrapped with the intensity scale of the deformation and presenting all grades of the ductile deformation and their evolution in space. (c to f) Synthetic 3D diagrams for each ductile grades (2 to 5) summarizing the key characteristics for each grade.*

4. Microscopic observations

Grades 0 and 1, representative of an isotropic and anisotropic magmatic fabric, are characterized by very few deformed minerals, but also by monzonitic textures defined by the growth of large euhedral K-feldspars including smaller ones (Figure II-8a). In addition, observations at microscopic scale show fractures mainly affecting K-feldspars (Figure II-8b). Moreover, it is interesting to note that these micro-fractures tend to disappear gradually as the ductile deformation takes place and becomes more intense.

Grade 2 is characterized by an incipient preferential orientation of minerals, especially quartz with a grain-size reduction resulting from dynamic recrystallization. Biotite presents the first traces of strain, marking planar or linear alignment and wrap around K-feldspars (Figure II-8c).

Grade 3 is marked by the development of shear bands, with a clear alignment of biotite and the appearance of mica fish. However, only slightly deformed biotite clusters are still widely observed. In addition, the boudinage of K-feldspars and hornblendes is now clearly visible and they are affected by the localization of shear bands (Figure II-8d).

Grade 4 is characterized by an intensification of finite deformation, especially in K-feldspars that underwent a partial or even total recrystallization. Boudinage is also more

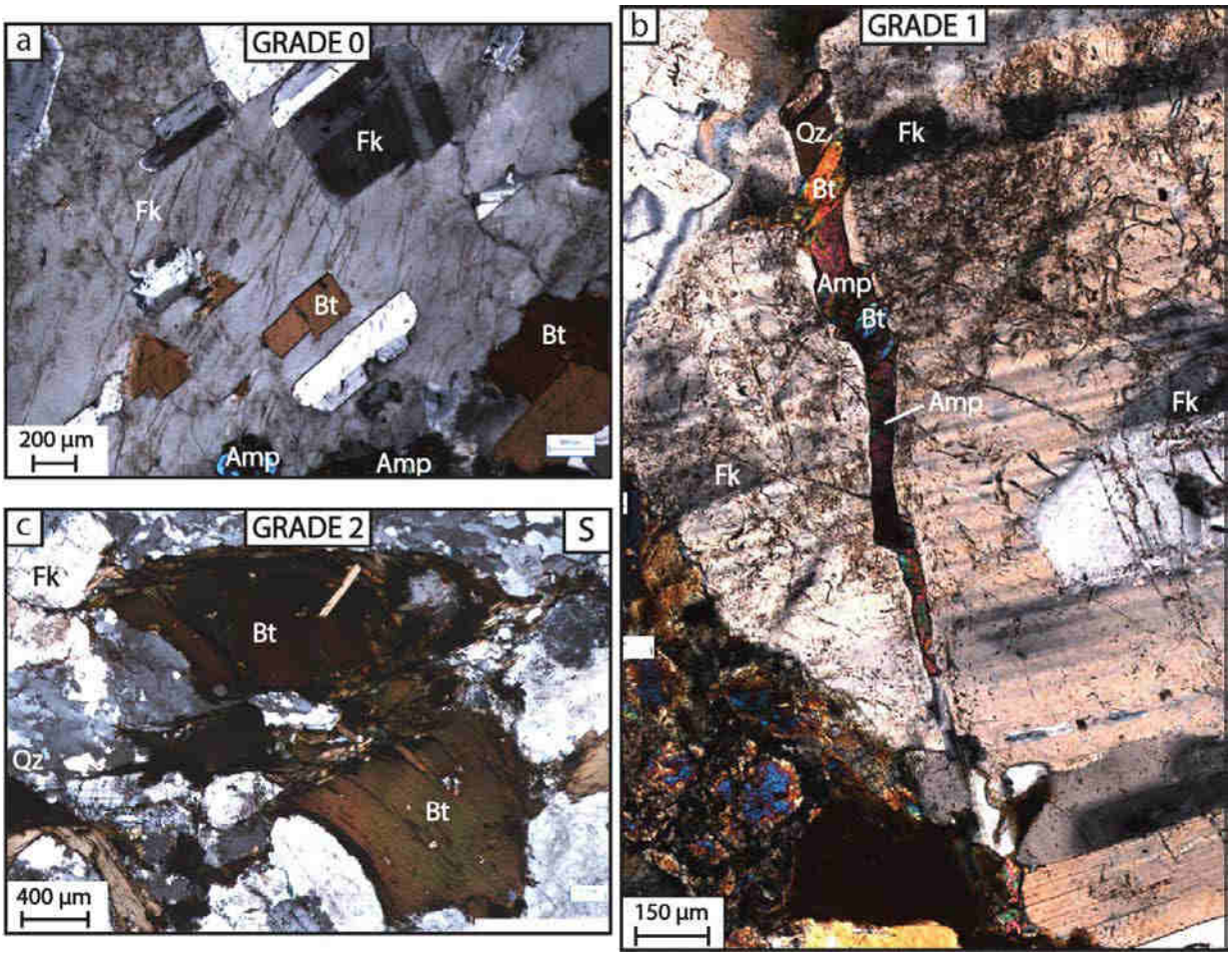

(continued)

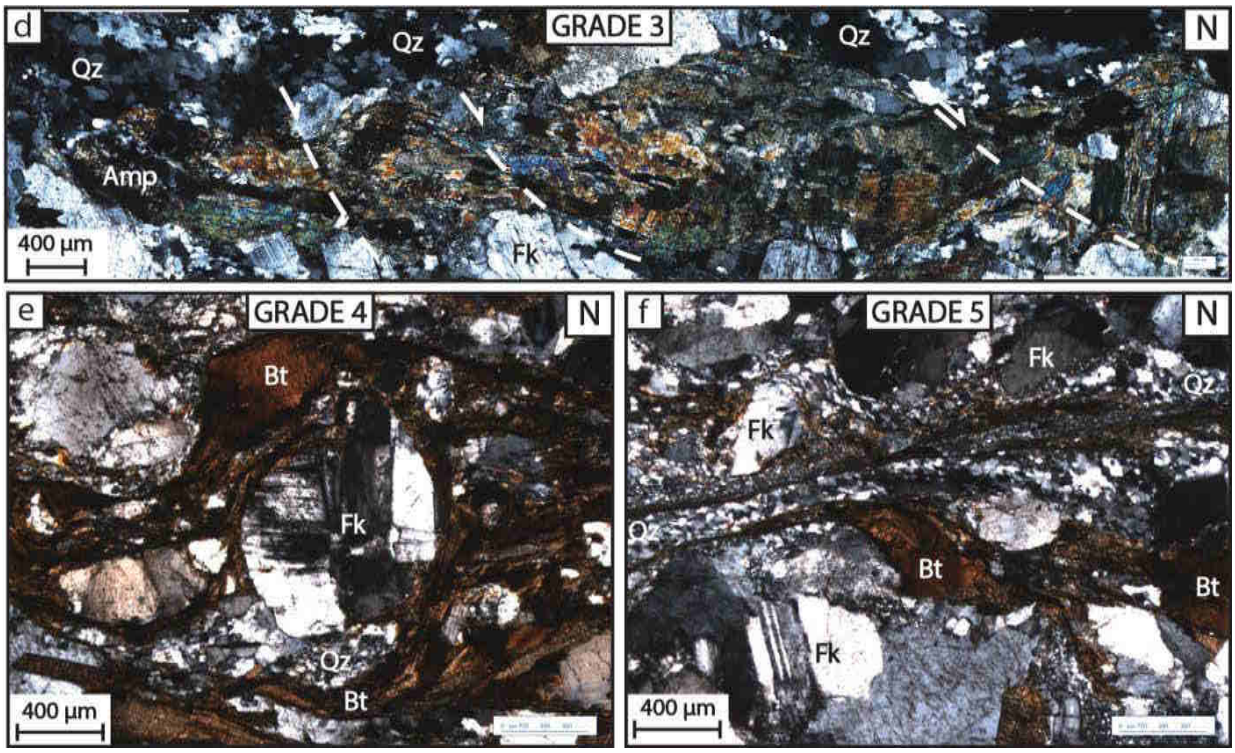

Figure II-8: *microscopic observations for each grade of deformation in the XZ plane. Amp: Amphibole, Bt: Biotite, Fk: K feldspar, Qz: Quartz. (a) Grade 0: monzonitic texture. (b) Grade 1: syn-magmatic fracture inside a feldspar crystal with a QZ-Bt-Amp filling. (c) Grade 2: first step of biotite deformation. (d) Grade 3: boudinaged and sheared amphibole. (e) Grade 4: first anastomosed micro-shear bands and antithetic shearing. (f) Grade 5: intense deformation with re-oriented and very fine-grained quartz, stretched biotites and anastomosed shear bands.*

intense, as well as shearing. It is interesting to note that the shear bands affecting feldspars are antithetic, as observed in the field. In the most deformed bands wrapping around the K-feldspar boudins, quartz shows a significant grain-size reduction (Figure II-8e).

Grade 5 is characterized by a strong increase of K-feldspar boudinage (Figure II-8f). In addition, the texture of quartz aggregates shows two successive stages of strain accommodation. The first stage shows grain-size reduction associated with a shape preferred orientation of grains parallel to newly formed quartz ribbon planes. The second stage, locally overprinting the primary texture, is characterized by an additional strong grain-size reduction of quartz located in shear bands. The transition between the two quartz textures is clearly visible in the shear band boundaries (Figure II-8f). Other shear bands initiate along biotite grains that show mica fish morphology. Lengthwise propagation of these bands and their connection with shear bands mainly composed of small new quartz aggregates allow the development of a connected anastomosed network (Figure II-8f). Ultimately, an ultramylonitic texture, possibly with some cataclastic flow, is locally evidenced in some shear bands thanks to the presence of angular K-feldspar clasts included in a very fine matrix whose composition remains undeterminable at the scale of observation.

5. Strain quantification

In order to put quantitative constraints on the qualitative distribution of strain deduced from the field approach, a quantitative study of the intensity of the shape fabric is performed by determining the shape preferred orientation (SPO) of magmatic minerals. The SPO of minerals can be induced by syn-magmatic and/or subsequent later tectonic deformation. Syn-magmatic deformation is linked with the magma dynamics during emplacement of the intrusion and has mainly an impact on the orientation of crystals. Conversely, tectonic deformation appears at any deformation stage and has consequences on the both SPO and the mineral deformation. Determining these parameters allows evaluating and precisely quantifying the deformation history and its intensity. For each grade of the deformation scale, we thus collect oriented samples from the same cross-section (see location in Figures II-6 and -7), from the south (Aghios Nikolaos) to the north (Aghios Prokopios). We then perform the strain quantification by analyzing pictures of the three orthogonal planes: (1) the XZ plane, perpendicular to foliation and parallel to lineation, (2) the YZ plane, perpendicular to lineation and (3) the XY plane, parallel to foliation plane. Several methods were then used: (i) X-ray computed tomography is helpful to image cores and produce 3D views and orthogonal planes, then (ii) analyses of these orthogonal pictures were performed with softwares SPO2003 and Intercept 2003, finally (iii) we completed this analysis by an EBSD study.

5.1. Imaging and analytical methods

5.1.1. X-ray Tomography

X-ray computed tomography (XCT) is a non-destructive technique that allows the discrimination in a solid volume, mineral on the basis of their bulk densities [*Ketcham & Carlson*, 2001; *Mees et al.*, 2003; *Ketcham*, 2005; *Gualda & Rivers*, 2006; *Baker et al.*, 2012]. Data were obtained following three steps: (1) the acquisition of many views by turning the sample from 0° to 360°, the distance between the X-ray source and the sample determines the final resolution, (2) the reconstruction that consists of determining the attenuation coefficients for each line of pixels in each view using the Beer's law [*Baker et al.,* 2012; *Ketcham & Carlson,* 2001]. This stage also includes artifact correction that comprise beam hardening, ring artifacts and misalignments [*Ketcham & Carlson,* 2001]. (3) The stack of slices consists in assembling all 2D sections of the sample to form the 3D image of the cores. Data are acquired with a Phoenix Nanotom system with a resolution smaller than 5 microns per unit of volume (voxels) while the segmentation of mineral phases were realized by using ImageJ and VG-Studio Max softwares.

5.1.2. Estimation of the shape preferred orientation (SPO)

A 2.5cm diameter-core from each strain grade was analyzed by X-ray tomography. Cores were virtually cut according to XZ, YZ and XY planes. Due to the poor differentiation between K-feldspars and quartz on pictures, and a good discrimination betweenbiotite/amphibole and feldspar/quartz groups, we choose a simple segmentation of

dark minerals/clear minerals. Images treatment and phase's segmentation have been done by using both Photoshop and GIMP2 softwares. The filtering and segmentation protocol being identical for all samples, only the grey level values chosen during the final segmentation procedure were different, depending to the grey level histogram specific to each picture. More than 30 pictures (2D images) were extracted for each plane of each sample, giving a total of 570 pictures treated and then analyzed.

Firstly, the SPO analysis of the dark phase composed of biotite and amphibole grains was performed with two different softwares: SPO2003 and Intercepts2003 [*Launeau & Robin*, 1996, 2005; *Launeau et al*., 2010]. SPO2003 software allows determining the eccentricity *R* and the long axis orientation α of the inertia tensor calculated for each element of the black phase. An element either corresponds to an individual mineral grain or a clustering of mineral grains. The average shape fabric of the black phase corresponds to the tensorial mean of the tensors calculated for each element. This method is used when each element is isolated and allows the statistical analysis of the SPO of the whole population. When clusters of elements cannot be separated, Intercepts2003 software was used. The principle of this software is based on the intercepts method, which analyses the boundaries of the black phase over the entire image as a population of lines. The method involves a Fourier series decomposition of the polar plot of intercepts and yields a rose of directions [*Saltykov*, 1958; *Launeau & Robin*, 1996]. As for the inertia tensor method, an eccentricity *R* and a long axis orientation α can then be calculated for the whole population.

Secondly, the 3D fabric ellipsoid was calculated by using the 2D analyzes performed on the three orthogonal faces of our samples [*Launeau et al*., 2010]. The reconstruction of this ellipsoid allowed calculating the degree of anisotropy (P') and the shape parameter (T) of the biotite/amphibole fabric for each association of images (8 associations for each grade) [*Jelinek*, 1981; *Launeau & Robin*, 2005]. P' refers to the eccentricity of the 3D fabric ellipsoid and can be correlated with the intensity of the biotite/amphibole preferred orientation. T refers to the symmetry of the 3D fabric ellipsoid and varies from -1 (perfectly linear fabric) to +1 (perfectly planar fabric) passing through 0 (plano-linear fabric); see equations in *Borradaile & Werner* [1994]). We consider thereafter that values lower than -0.2 involve prolate shapes whereas those higher than 0.2 form oblate shapes.

5.1.3. Quartz lattice preferred orientation

During ductile flow, rock-forming minerals are subjected to plastic deformation that may give rise to some lattice preferred orientation (LPO) depending on the dominant deformation mechanism, like grain-size-insentive (GSI) dislocation creep or grain-size-sensitive (GSS) creep [*Otani & Wallis*, 2006; *Kilian et al*., 2011]. For crustal rocks, the pattern of quartz LPO also provide crucial information on temperature conditions, finite strain and kinematics during deformation [*Stipp et al*., 2002; *Heilbronner & Tullis*, 2006]. To better characterize the temperature conditions involved during strain localization within the Naxos monzogranite, we thus documented the quartz LPO through electron backscatter diffraction (EBSD) analyzes. EBSD data were collected using a scanning electron microscope coupled

with an EDAX Pegasus system at ISTO/BRGM (Orléans, France). Analytical conditions involved a working distance of 15 mm, an acceleration voltage of 20 kV and a probe current of ~6nA on polished thin sections (diamond paste of 0.25 µm followed by colloidal silica). In order to avoid indexing errors, equal-area lower-hemisphere pole figures have been constructed using one measurement per grain collected manually through a whole thin section. For EBSD maps, we considered the mean orientations of each grain that compose the whole map or a selected area. The iso-contours and grey shadings on pole figures were plotted using the Unicef careware software package (Mainprice; www.gm.univ-montp2.fr/PERSO/mainprice/W_data/CareWare_Unicef_Programs). To plot EBSD maps and to calculate the texture (J) and misorientation (M) indices, that both give the degree of mineral alignment between J = 1/M = 0 for a random orientation and J = ∞/M = 1 for a crystal-like alignment, we used the OIM software (EDAX) and the open-source matlab-based MTEX toolbox [*Bachmann et al.*, 2010; *Mainprice et al.*, 2015]. Each map has been cleaned considering a minimum of 5 neighbour-based pixels on several raws. Using MTEX, we also merged dauphine-type twin boundaries with parent grains and we chose to define the size of recrystallized grains by selecting grains with a maximum intragranular misorientation angle of 10° (the misorientation is calculated for each grain with respect to their respective mean orientation). Both poles figures and J_{index} were calculated using a Gaussian half-width angle of 10°.

5.2. Results

5.2.1. X-ray Tomography

X-ray tomography imaging allows us vizualizing samples in 3D. It is also possible to make segregation of the phases based on their response to radiation and thus access to a 3D view of mineral shape fabric inside the core (Figure II-9).

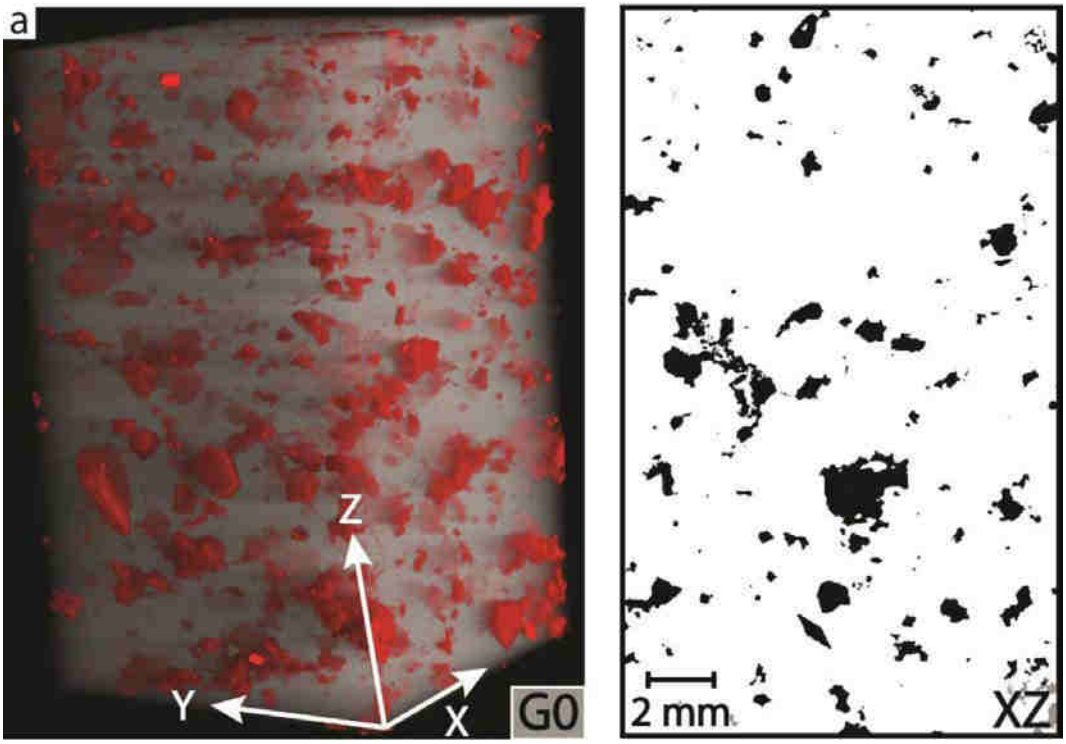

(continued)

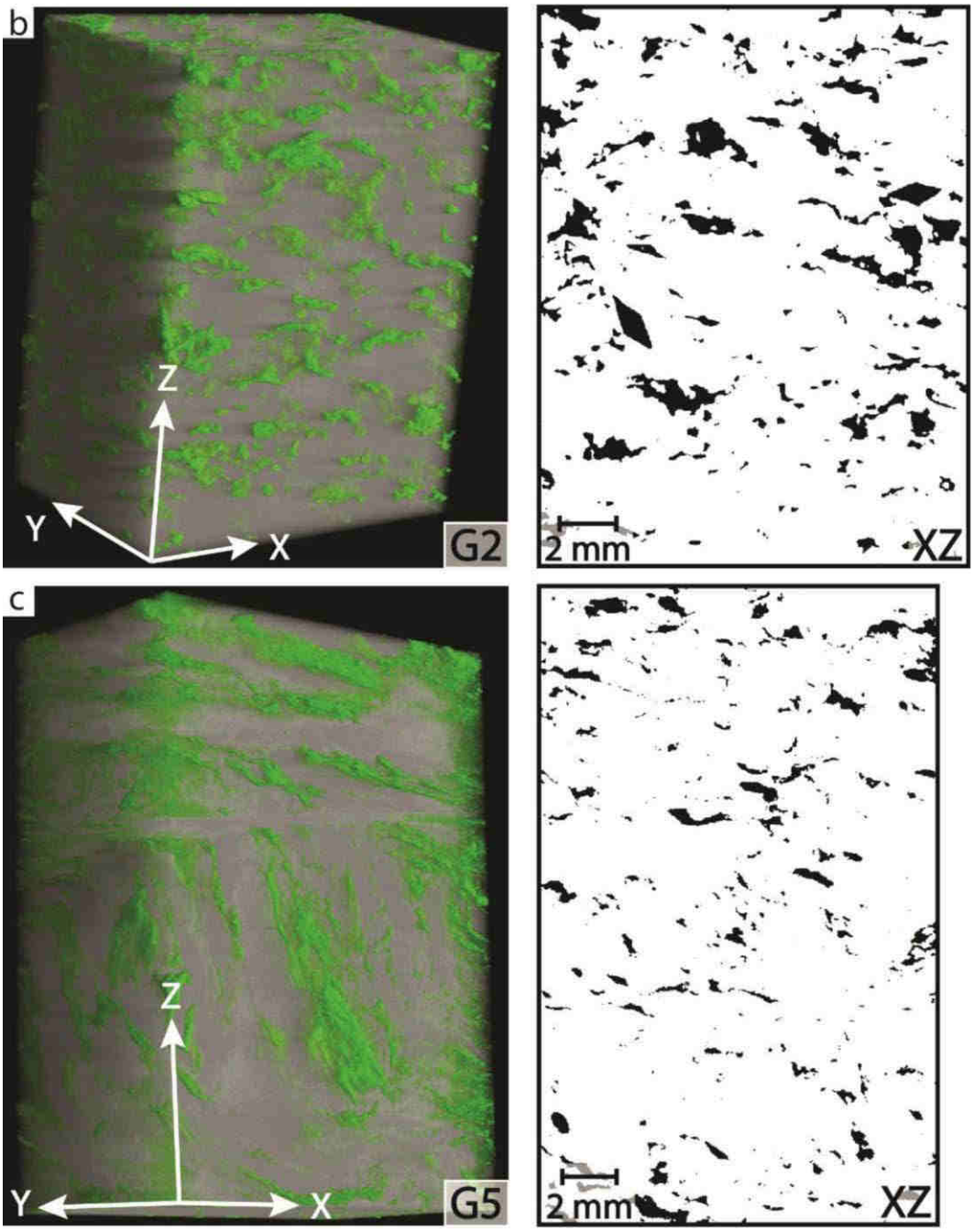

Figure II-9: *3D views of imaged cores by X-ray tomography method and the associated 2D pictures (XZ plane) extracted from the 3D views. (a) Grade 0. (b) Grade 2. (c) Grade 5.*

We can thus visualize in 3D the main grades of our deformation intensity scale by evidencing an evolution of the internal structure of the sample according to the deformation intensity that is very similar to the previous macroscopic and microscopic descriptions. Indeed, grade 0 is characterized by an isotropic magmatic fabric (Figure II-9a) that evolves toward a localization of deformation with a preferred orientation of the dark minerals (biotite and amphibole; Figure II-9b), finally reaching grade 5 where deformation is marked by pervasive structures and the development of ultramylonite shear bands (Figure II-9c).

5.2.2. Shape Preferred Orientation

The P' and T fabric parameters for the 6 grades are shown on Figure II-10. The P'= f(T) diagram clearly shows an evolution of the shape parameter (T) and the degree of anisotropy (P'). Results highlight a good correlation between P' and the qualitative scale based on field observations. Indeed, the first grade (grade 0) is characterized by the lowest anisotropy degree, with P' ~1.11, while grade 5 presents the highest values with P' ~1.58. In the same way, an evolution of T (shape parameter) is observed with the degree of anisotropy P'. Thus, the ellipsoid in the lowest grade is characterized by a prolate shape and evolves progressively toward a nearly perfect oblate shape with respect to the increasing anisotropy degree.

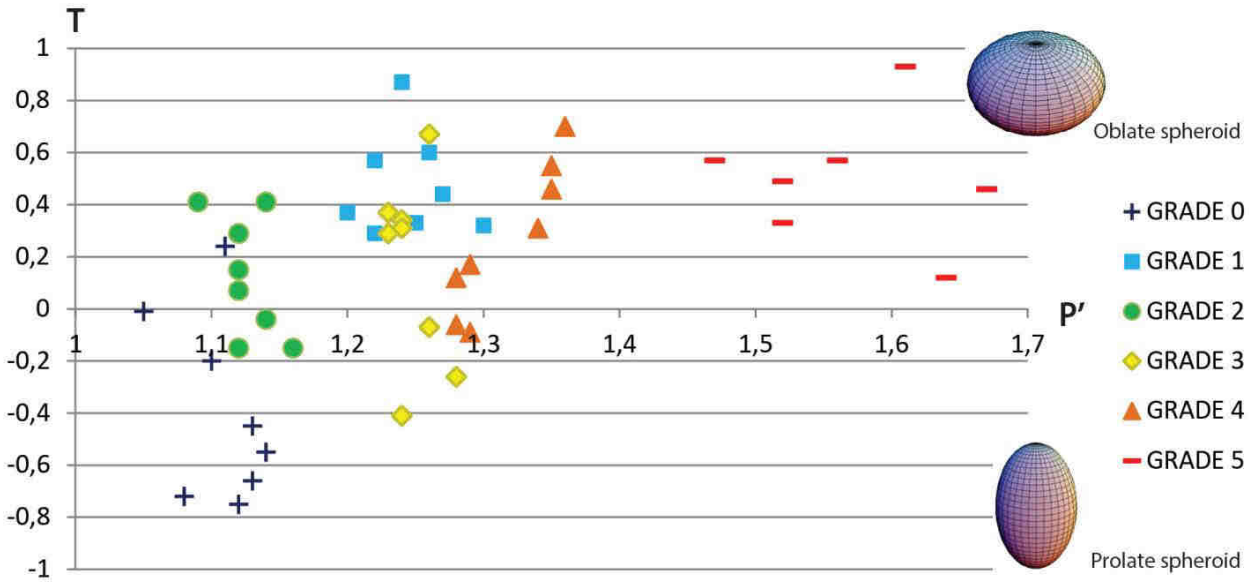

Figure II-10: *Shape parameter (T) vs. anisotropic degree (P') diagram characterizing the shape preferred orientation (SPO) of magmatic minerals (biotites and amphiboles) with increasing strain, i.e., from grade 0 to 5.*

5.2.3. Quartz lattice preferred orientation

In Figure II-11, we show the quartz LPO for each grade of the monzogranite intrusion. LPOs are shown with respect to the foliation and lineation, such as observed on the field or defined by tomographic images (for grades 0 and 1, Figure II-11a). From grades 0 to 5, i.e. with increasing strain and decreasing grain-size, we document a similar pattern of quartz LPO, which involves the [c] ([0001]) axes normal to the lineation within the foliation plane. Accordingly, the <a> (<11-20>) axes distribute within a solid angle of 90° around the [c] axis maximum with six maxima located at 60° from each other, such as expected for the crystal system of quartz (trigonal 32). This type of LPO is typical of prism <a> slip LPO [*Stipp et al.*, 2002; *Muto et al.*, 2011], but the [c] axis also tends to form a girdle around the X-axis in high-strain grades (3-5), suggesting a weak activation of other slip-systems. Furthermore, the strength of quartz LPO first increases from grade 0 (J = 4.35; M = 0.07) to grade 2 (J = 7.55; M = 0.36), and then decreases up to grades 4 (J = 3.36; M = 0.19), before slightly increasing again to grade 5 (J = 3.57; M = 0.24) (Figure II-11b). The strength drop is correlated with weakening

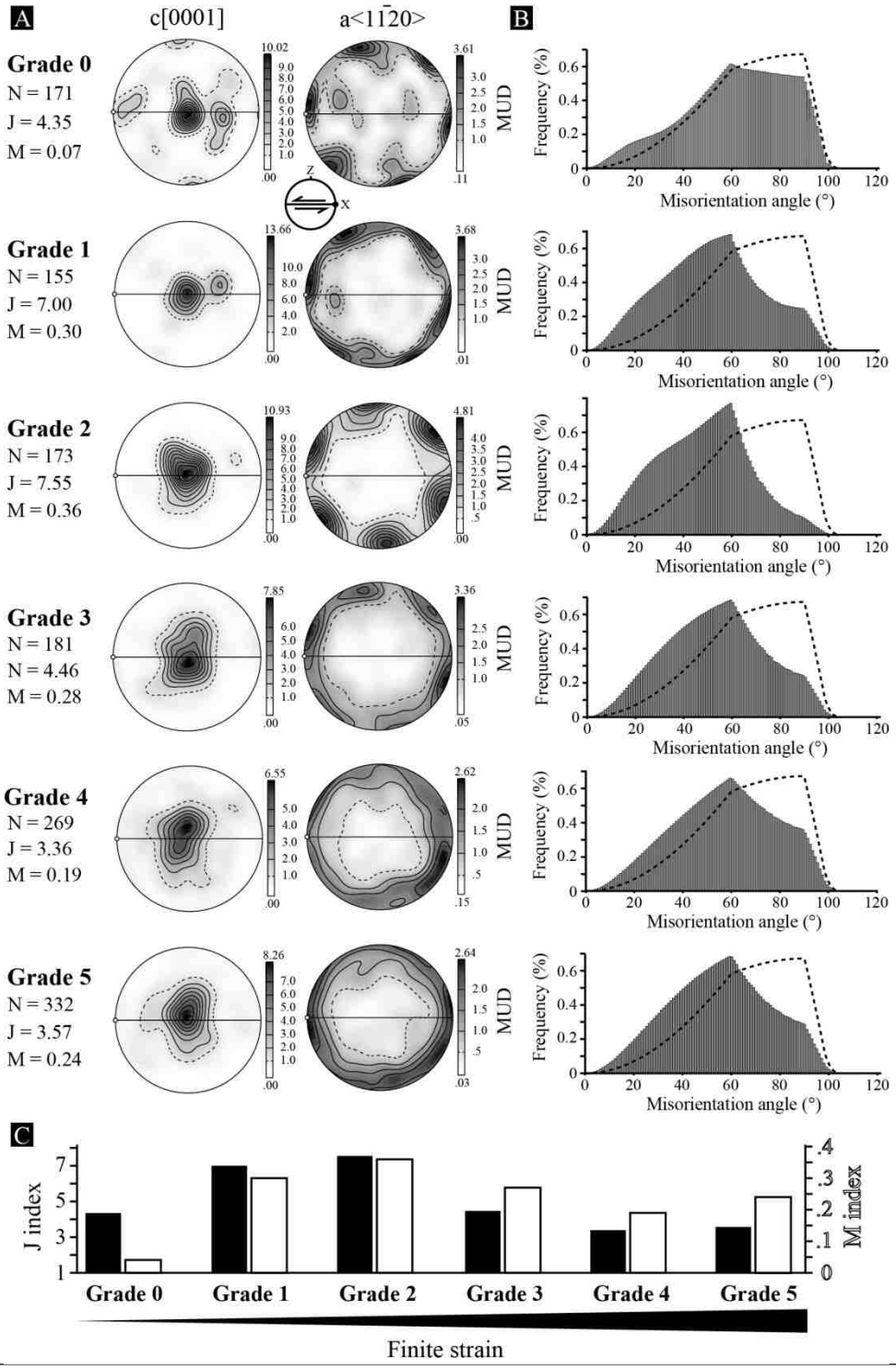

Figure II-11: *quartz lattice preferred orientation (LPO) across the Naxos intrusion. (a) Equal-area lower-hemisphere pole figures of the c[0001] and a<11-20> axes for trigonal quartz with increasing strain, i.e., from grade 0 to 5. Pole figures are shown with respect to the foliation (horizontal line) and lineation (white dot) in the XZ plane. The EBSD data have been collected through a whole thin section considering one measurement per grain. The iso-contours are multiples of uniform distribution using a linear distribution with a kernel gaussian half-width angle of 10°. N = number of grains; J = texture index [Bunge, 1982]; M = misorientation index [Skemer et al., 2005]. (b) Distribution of uncorrelated misorientation angles of the respective quartz LPO shown in Figure II-11a. The M_{index} is calculated from this distribution with respect to the theoretical distribution of a random LPO [dotted line; Skemer et al., 2005]. (c) Distribution of J (solid bars) and M (empty bars) indices across the strain gradient.*

of the [c] axis around Y and smearing out of the <a> axes maxima in the X-Z plane. These features are further supported by the distribution of uncorrelated misorientation angles (Figure II-11c), which starts from a close to random distribution (dotted line in Figure II-11c) in grade 0, progressively shifts towards low values up to grade 2, and then shift back to higher values for grades 4 and 5. At a first order, we document therefore a moderate fabric strength that first strengthens, and then weakens with increasing strain and decreasing grain-size.

To better document the quartz preferred orientation of high-strain samples, we then performed high-resolution (< 1 µm step size) EBSD maps within quartz-rich shear bands (Figure II-12). We chose to focus on grade 4 where shear bands are easy to isolate from each other. These maps document monomineralic quartz aggregates with a mean grain-size of ~30 µm and a unimodal log-normal distribution, suggesting a high degree of dynamic recrystallization (Figures II-12a, -12b and -12c). No change occurs in the LPO pattern (prism <a> slip LPO) and we document a moderate mineral alignment strength with J = 3.86 and M = 0.29, such as revealed by the c[0001] axis pole figure (Figure II-12d) and inverse pole figure combined with the EBSD map (Figure II-12a). Despite large finite strain, the mineral alignment strength in shear bands thus remains very similar to the overall shape fabric of grade 4 (Figure II-11). However, while some areas show quartz grains that have a strong alignment strength – the stronger one with have documented so far (J = 7.47; M = 0.42; Figure II-12E$_1$) -, some others show a weak alignment, weaker than ever documented across the whole shear zone (J = 2.7; M = 0.18; Figure II-12E$_2$). The mean grain size slightly decreases between the high-strength area (31.5 µm) and low-strength area (29.6 µm). Accordingly, the distribution of uncorrelated misorientation angles significantly shifts towards low values for the high-strength area and tends to the uniform distribution for the low-strength area (Figures II-12E$_1$ and -E$_2$). The mineral alignment strength therefore does not distribute homogeneously across the high-strain shear bands.

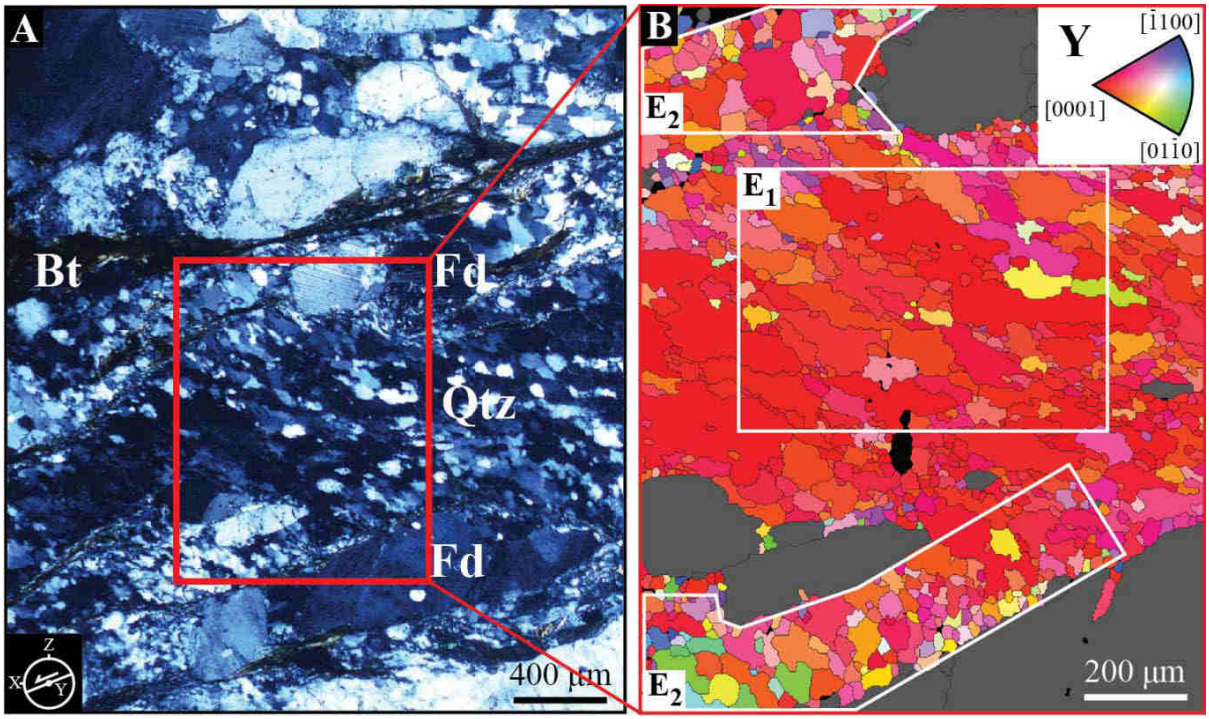

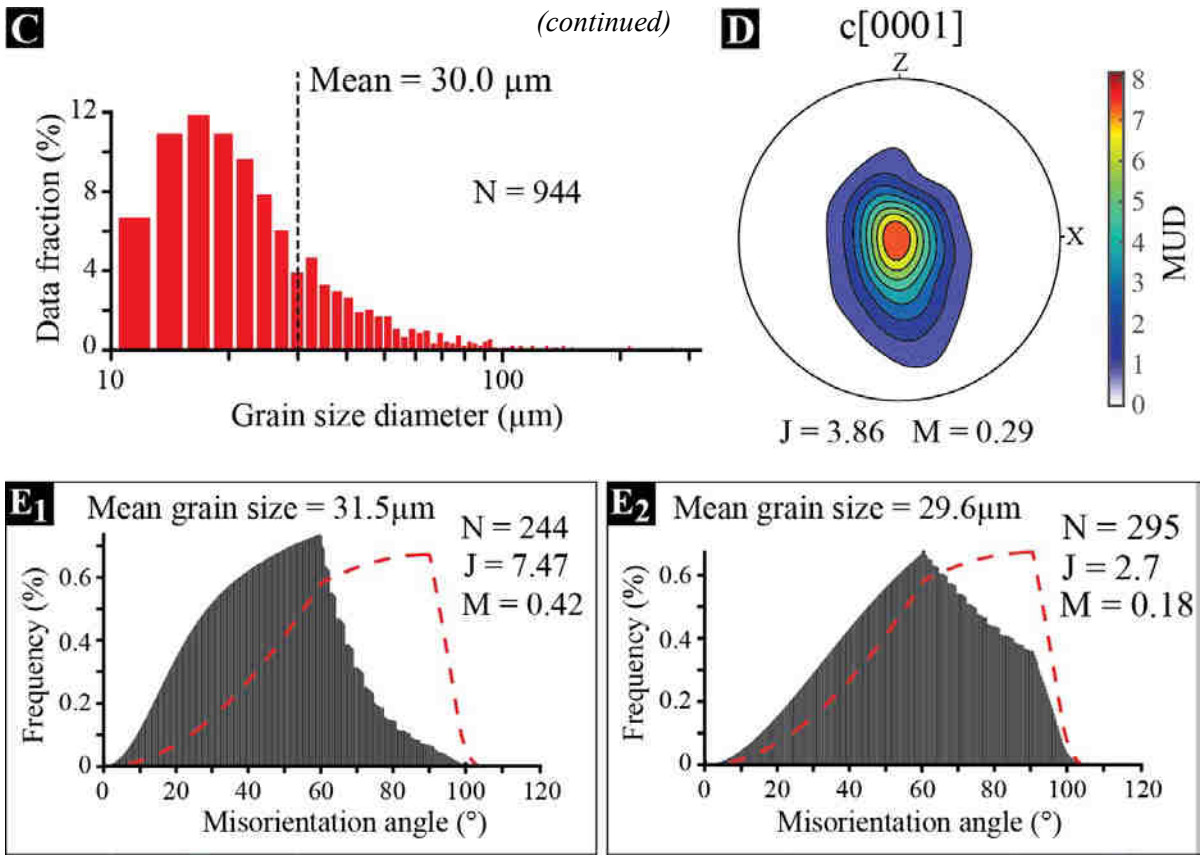

Figure II-12: *quartz-related microstructures in high-strain shear bands. (a) Thin section (polarized light) of a shear band in the XZ plane (in grade 4). Fd = Feldspar; Qz = quartz; Bt = Biotite. (b) EBSD map combined with inverse pole figure (IPF map) with respect to the Y axis (top right inset), i.e., the deformation axis normal to the lineation in the foliation plane (location in Figure II-12a). The color coding refers to the angle of one given axis with respect to Y. While the grey areas correspond to feldspar grains, the black areas give areas of non-indexed points. (c) Bar graph of the grain size distribution for quartz, highlighting a lognormal distribution with a mean grain size of 30 µm. N = number of grains. (d) LPO of the quartz [c] axis considering one point per grain (mean orientation). The iso-contours and color coding are multiples of a uniform distribution. J = texture index; M = misorientation index. (e) Bar graphs of uncorrelated misorientation angle distribution for two specific areas located in Figure II-12b. While the grain size slightly decreases from area E1 (31.5 µm) to area E2 (29.6 µm), the mineral alignment strength (J and M indices) significantly drops and the angle distribution gets close to the uniform distribution (dotted red line). N = number of grains.*

In addition, we used EBSD maps to document the distribution of sub-grain boundaries (i.e., correlated misorientation angles between 2 and 10°) in quartz-rich shear bands and tails of recrystallized grains (Figure II-13). In shear bands, we highlight numerous four-grain junctions and a significant amount of sub-grain boundaries with rotation angles that distribute around the c[0001] axis (Figure II-13a), which is consistent with dominant tilt boundaries induced by dislocation glide on the {m}<a> slip system, in agreement with prism <a> slip LPO [*Lloyd, 2004*] (Figures II-13a and -13b). We also identify a significant amount of recrystallized grains between 10 and 100 µm with a mean grain size and mode (following a lognormal distribution) of 26.2 µm and ~19 µm, respectively (Figure II-13c). In contrast, we document large grains with lobate boundaries and a few sub-grain boundaries in recrystallized tails of quartz

porphyroclasts, most of these latter standing by the fine-grained shear band (Figure II-13d). Yet, we document a clear c[0001] axis maxima that stands parallel to Y, such as observed in the whole intrusion (Figure II-13e). Quartz porphyroclasts also contain plenty of healed cracks with fluid inclusions (Figure II-13d).

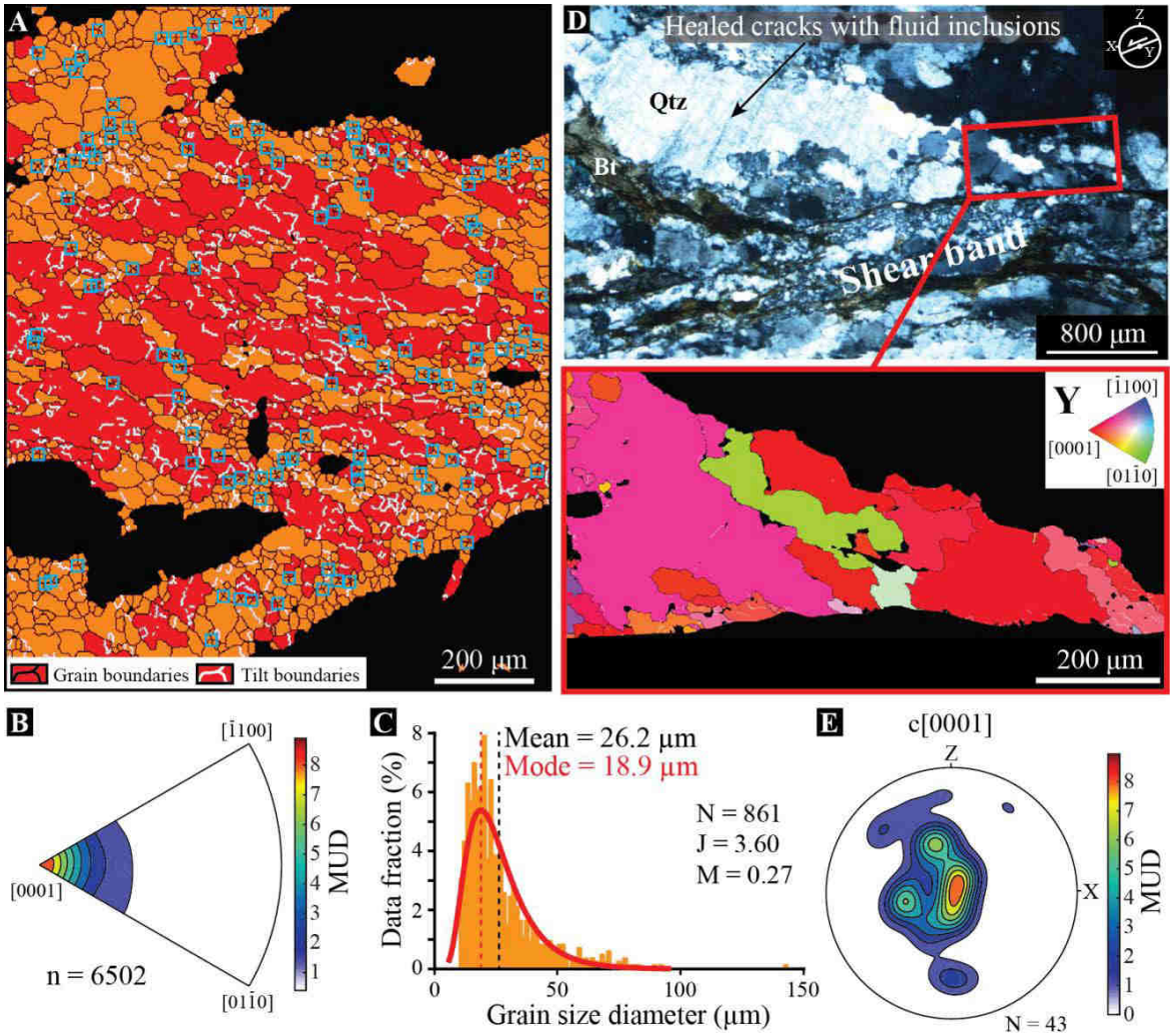

Figure II-13: *grain boundaries and tilt boundaries of quartz aggregates in shear bands and recrystallized tails. (a) Phase map of the high-strain shear band shown in Figure II-12, including quartz porphyroclasts (red) and recrystallized grains (orange). While grain boundaries (black lines) are defined by correlated misorientation angles higher than 10°, the tilt boundaries (white lines) refer to correlated misorientation angles between 2 and 10°. The blue empty squares highlight four-grain junctions (121). Black areas correspond to other phases and non-indexed points. (b) Inverse pole figure showing the distribution of rotation axes related to tilt boundaries in quartz aggregates. The concentration of misorientation axes around the c[0001] axis indicates that sub-grain boundaries are tilt boundaries that results from dislocation glide on the {m}<a> slip system [Lloyd, 2004], coherent with prism <a> slip LPO. (c) Grain size distribution of recrystallized grains. While the mean grain size (26.6 µm) is calculated using the bar graph distribution, we applied a lognormal distribution to calculate the mode (18.9 µm). (d) Thin section (polarized light) and EBSD map (IPF map) of quartz grains and tilt boundaries through a recrystallized tail by a high-strain shear band. Unlike to quartz-rich shear bands, we document lobate boundaries and a few tilt boundaries (see text). (e) Quartz c[0001] axis pole figure for the map in Figure II-13d. The iso-contours and color-coding are multiples of uniform distribution (MUD). N = number of grains; J = texture index; M = misorientation index.*

6. Discussion

6.1. Evolution of the shape fabrics along the strain gradient

A schematic evolution of the P'-T parameters characterizing the shape fabric ellipsoid with increasing deformation is represented in Figure II-14 by using the means and associated standard deviation of each grade. On the basis of our field observations and the shape fabric analyses, we propose to divide the evolution of the shape fabric in four successive stages (colored arrows, Figure II-14).

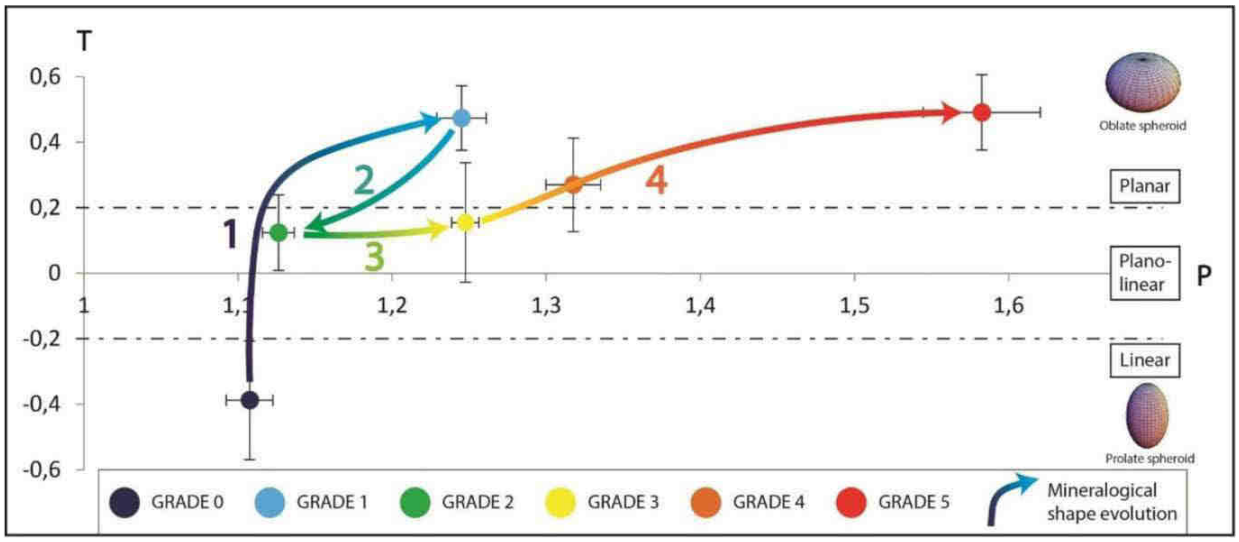

Figure II-14: *interpreted shape parameter (T) vs. anisotropic degree (P') diagram of the strain pattern evolution in the Naxos monzogranite. Colored dots correspond to the arithmetic average and associated standard deviation for each grade. Colored arrows symbolize the different stages of the deformation path discussed in the text.*

The stage 1 is related to the progressive evolution from a prolate magmatic fabric with low eccentricity (P'~1.11) toward a clear oblate fabric with a moderate eccentricity in grade 1. The prolate fabric in grade 0 is due to the shape preferred orientation of amphiboles, while biotite flakes do not show any clear preferred orientation (Figure II-8a). The grade 1 already shows a clear evolution of the degree of anisotropy, from 11% to about 25%, together with a flattening of the ellipsoid, which becomes strongly oblate (T=0.47). This evolution is correlated with the marked organization of the biotite developing a flatten shape preferred orientation. This transition from a prolate to an oblate magmatic fabric can be viewed as an evolution from a purely constrictional magmatic flow to a syn-magmatic deformation (weakly oblate fabric), tectonically driven by the N-directed regional extension.

The stage 2 corresponds to an evolution from an oblate to a plano-linear shape fabric associated with a decrease in eccentricity between the grades 1 and 2. Grade 2 shows scattered T values (-0.15 to 0.41) showing the progressive strain localization by the localized re-orientation of biotite grains (Figure II-8c). This evolution in shape fabric properties of the

ferromagnesian phases exemplify a local superimposition of the stage 1 syn-magmatic pervasive fabric by an incipient localized shearing marked by proto-shear bands and related onset of ferromagnesian minerals concentrations.

The stage 3 is marked by an increasing anisotropy, from a P'~1.13 to P'~1.25, while the shape parameter (T) remains plano-linear. This is correlated with a generalized nucleation of shear bands associated with the mineral re-orientation of amphibole and biotite and quartz ribbons development wrapping around feldspar clasts with rare cataclasites (Figure II-8d).

The stage 4 is characterized by a shape fabric eccentricity P' that evolves from 1.25 (stage 3) to 1.58 and a T parameter that express a strong oblate shape. This final stage is characterized by the densification of shear bands that often become tickers compared to those observed in the stage 3. In those bands, the mylonitic fabric is generalized with local cataclase of quartz ribbons (Figures II-8e and -8f). At this stage, there is no evidence of locally preserved initial, magmatic to late-magmatic, fabrics developed during the 2 first stages.

To summarize this analysis, step 1 corresponds to a syn-magmatic fabric development while step 2 can be assimilated to the onset of strain localization under very late magmatic to solid-state ductile conditions. Step 3 corresponds to the development of a more pervasive network of cm-scale anastomosed shear bands in ductile conditions. Stage 4 represents the generalization of a pervasive mylonitic shearing with local ultramylonitic to brittle/cataclastic fabrics. A similar gradient was observed by [*Laurent et al.*, 2015] by using similar field and analytical approaches in the Ikaria syn-tectonic intrusion. The authors showed the same evolution from a linear magmatic fabric with a very low degree of anisotropy, about 10%, toward mylonitic facies characterized by a very high degree of anisotropy.

6.2. A continuum of deformation

The four stages previously proposed to describe the evolution of the mineral fabrics and the development of discrete structures is based on local analyses and sampling along the gradient zone. Over the Naxos intrusion, field-based observations of the finite deformation from syn-magmatic conditions to solid state ductile, locally brittle, reveals a continuum through the strain gradient zone (Figures II-6 and -7). The Naxos intrusion recorded a strong gradient of deformation that progressively localize along the corrugated N-dipping detachment, thereby preserving a magmatic fabric in the southern part of the intrusion body. The succession of events is further consistent with kinematics recorded within the metamorphic dome. This demonstrates that the MCC, together with the intrusion and associated detachments developed coevally and represent different sequential events in the same extensional event.

The preserved magmatic foliations from the center areas of the intrusion are sub-verticals (Figure II-2a). They tend to become horizontal in zones where grade 2 of the strain gradient is preserved. The map of stretching lineations (Figure II-2b) shows a progressive rotation from N10°-trending lineations to N340°-trending ones in the northern part of the intrusion, suggesting that mineral and stretching lineations in the south are, at least partly, due to shearing related to regional extension.

An evolution from a linear to a planar shape fabric characterizes grade 1 of deformation (Figures II-10 and -14) and is interpreted as the switch between a more pronounced SPO of amphibole and biotite grains. Grade 1 is also marked by the presence of fractures in stretched K-feldspars (Figure II-8b). This type of structures usually results from a sub-solidus state deformation and requires a sufficiently high shearing stress applied on a cooling magma comprising 10 to 30 % of residual liquid [*Paterson et al*., 1989; *Bouchez et al*., 1992]. Quartz, biotite and hornblende that crystalized in fractures affecting the feldspar megacrysts are the expression of this residual liquid. *Bouchez et al.* [1992] set prerequisites to consider such structures as late-magmatic micro-fractures. First, each micro-fracture should affect only one crystal and never overlap more. Then, mineral phases filling the fracture are crystallographically continuous and do not appear to change in their chemical composition. Finally, we observe that the filling phases are quartz, biotite and hornblende (Figure II-8b), which correspond to the magmatic parageneses of the intrusion. Moreover, they tend to gradually disappear as the later solid-state deformation becomes more intense and superimposes this sub-magmatic deformation. All of these elements show that the Naxos monzogranite is a syn-tectonic intrusion.

Then, the intensity of finite deformation drastically increases approaching the northern contact and the detachment (Figures II-6 and -7). Indeed, at Aghios Prokopios peninsula, the transition from proto-mylonitic to mylonitic and even ultramylonitic fabric is achieved within only 500m with a clear evolution of the degree of anisotropy but also a change from a plano-linear to a strongly planar fabric (Figures II-7, -10 and -14). Furthermore, measured orientation of the shear planes appear to be parallel to the main detachment plane. Stretching lineations always oriented north-south, and the overall top-to-the-north sense of shear are comparable with those measured in the dome.

The last increments of deformation in the Naxos monzogranite comprise brittle deformation with ultracataclasites, pseudotachylytes or late steeply-dipping normal faults. Cataclasites structurally occur within the highest grade of ductile deformation with an unclear transition as shown above (Figures II-6 and -7) and they are topped by the detachment. They are characterized by a large thickness around several tens of meters, up to 50 meters at Cape Achapsi where they are strongly chloritized and where two facies can be distinguished, a coarse-grained and fine-grained one. Finally, pseudotachylytes veins develop along small-scale ultra-mylonitic shear planes near the detachment, reflecting a sudden and rapid acceleration of the local strain rate. The timing of pseudotachylyte development remains unclear as they could represent either a logical continuation of the same deformation in the brittle field or be part of a more recent deformation episode.

All of these deformation stages show a progressive evolution from magmatic to submagmatic, ductile and then brittle deformation. This evolution demonstrates that the Naxos pluton emplaced during top-to-the north shearing, and started to be deformed while it remained about 10 to 30% of residual magmatic liquids in the crystallizing magma below a top-to-the north shallow-dipping shear zone.

6.3. Deformation mechanisms

The development of shear zone typically arises from strain localization during ductile deformation. In this regime, strain is accommodated by plastic processes that involve several competing deformation mechanisms, the dominant conditions of which depend on temperature, strain rate, stress and grain-size (Figure II-15). For quartz in fully plastic conditions, two deformation mechanisms have been mainly considered so far: dislocation creep and diffusion creep [*Gleason & Tullis*, 1995; *Hirth et al.*, 2001; *Bürgmann & Dresen*, 2008]. While dislocation creep refers to plastic flow achieved by lattice-controlled migration of intra-granular line defects (dislocations), diffusion creep involves the diffusion of vacancies through the crystal lattice. These two mechanisms may also combine with grain boundary sliding depending on the deformation conditions [*Boullier & Gueguen*, 1975; *Stünitz & Fitz Gerald*, 1993; *Kruse & Stünitz*, 1999; *Mehl & Hirth*, 2008; *Kilian et al.*, 2011; *Rahl & Skemer*, 2016]. Unlike dislocation creep, both diffusion creep and grain boundary sliding are dependent on grain-size, which may promote a drop of viscosity during grain-size reduction, giving rise to a rheological weakening and possibly strain localization [*De Bresser et al.*, 2001; *Platt & Behr*, 2011].

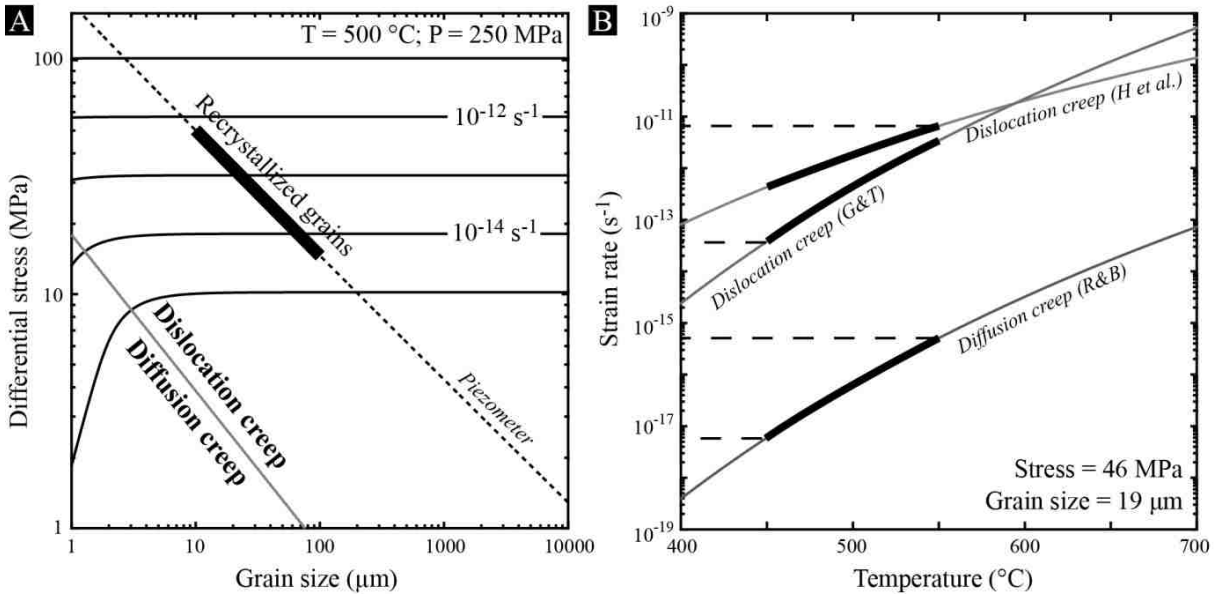

Figure II-15: *deformation mechanism maps for wet quartz at 500°C and 250 MPa. The flow laws for dislocation creep and diffusion creep are from Gleason & Tullis [1995] and Rutter & Brodie [2004], respectively. Based on the quartz piezometer (Stipp & Tullis [2003] corrected by Holyoke & Kronenberg [2010]) and using the size of recrystallized grains in high-strain shear bands (10-100 µm), we predict predominant dislocation creep for high-strain shear bands of grade 4. (b) Predicted strain rates (black thick lines) of quartz aggregates as a function of temperature considering either dislocation creep (including the flow law from Hirth et al. [2001]) or diffusion creep. For calculations, we used the mode of recrystallized grains (~19 µm) and a stress of 46 MPa, such as predicted by the piezometer. For the flow law of Hirth et al. [2001], we applied a water fugacity of 87 MPa using the equation of state from Pitzer & Sterner [1994] at 500°C and 250 MPa. Considering temperatures between 450 and 550 °C, as deduced from quartz mineral alignment in high-strain shear bands, we only predict realistic strain rates (4.10^{-14}-7.10^{-12} s^{-1}) for dislocation creep, excluding diffusion creep as a source for grain boundary sliding (see text).*

When diffusion creep is dominant, it commonly relates to a weak or absent LPO. In contrast, a dominant dislocation creep produces a strong LPO [*Baker & Wenk*, 1972], a strong SPO [*Stipp et al*., 2002] and new recrystallized grains whose the size mostly depends on stress conditions [*Stipp & Tullis*, 2003; *Austin & Evans*, 2007]. Natural observations and experimental investigations have also shown that both the process of dynamic recrystallization and pattern of recrystallized quartz LPO directly depend on strain rate, finite strain and temperature during dislocation creep [*Hirth & Tullis*, 1992; *Stipp et al*., 2002]. With increasing temperature (or decreasing strain rate), the type of recrystallization changes from bulging recrystallization to sub-grain rotation, and then to a combination of both mechanisms due to efficient grain boundary migration, which becomes dominant above 500 °C [*Hirth & Tullis,* 1992]. In relation to this, the pattern of recrystallized quartz LPO switches from dominant basal <a> slip LPO at low temperature – in combination with other slip systems (basal, rhomb and prism) – to dominant prism <a> slip LPO at high temperature. The transition has been estimated around 500°C, but this value may also change depending on the finite strain involved [*Stipp et al*., 2002].

In Naxos, the presence of an SPO and a moderate to strong prism <a> slip LPO combined with microstructural evidence of sub-grain boundaries and recrystallized tails of quartz supports dominant dislocation creep through the whole studied intrusion. It further indicates high-temperature deformation of more than 500°C, but the evolution towards multiple slip-systems with increasing strain, as shown by girdle development, and the occurrence of brittle deformation in grade 5 suggest that deformation also occurred down to ~350°C in high-strain grades. The occurrence of lobate grain boundaries is also indicative of significant grain boundary migration during deformation [*Hirth & Tullis*, 1992; *Heilbronner & Tullis*, 2006], and probably in presence of fluids, such as deduced from the presence of strain-related fluid inclusions. However, although quartz LPO never fully randomizes, we document a drop of overall mineral alignment strength with increasing strain (Figure II-11). This feature contradicts lab-based experiments that always documented an increasing LPO with increasing strain when dislocation creep is dominant [*Heilbronner & Tullis*, 2006; *Hansen et al*., 2014; *Mainprice et al*., 2015]. As one possibility, such a drop could be an effect of dynamic recrystallization [*Hirth & Tullis*, 1992], but recent deformation experiments of poly-crystal quartzite have shown that quartz LPO significantly strengthens with increasing degree of dynamic recrystallization [*Heilbronner & Tullis*, 2006]. Another possibility implies the overprinting of a previous mineral alignment by a new one, such as highlighted by our SPO dataset. In this case, the grade 0 may have been affected by grades 1 and 2 during a former stage of deformation, and then grades 3 to 5 may result from latter stages of strain localization, but with different orientations of the deformation axes. Nonetheless, although we do not exclude this effect, our dataset does not show any combined patterns of quartz LPO, and it does not account for the drop of mineral alignment strength between grades 3 and 4.

Alternatively, the large amount of four-grain junctions indicates that grain boundary sliding has significantly contributed to the deformation [*Ree*, 1994]. Previous documentations of quartz-rich mylonite have shown indeed that grain-size-sensitive creep, including grain boundary sliding, may occur during dynamic recrystallization in presence of fluids [*Halfpenny*

et al., 2006; *Rahl & Skemer*, 2016]. This would account for the progressive drop of overall mineral alignment strength with increasing strain, i.e., with increasing degree of recrystallization and related grain size reduction. The quartz LPO might also locally weaken depending on the degree of dynamic recrystallization or local amount of fluid at grain boundaries, such as expected in high-strain shear bands. We would finally expect a strengthening of quartz LPO in grade 5 if we consider that most of the rock has achieved 100% of recrystallization. Our LPO features indicate therefore that grain boundary sliding probably occurred in combination with dislocation creep during deformation of the Naxos shear zone. Together with grain size reduction, this provides a consistent approach to account for the occurrence of weakening and subsequent strain localization across the intrusion.

Nevertheless, the source of grain boundary sliding in Naxos remains a fundamental issue. Based on available flow laws [*Gleason & Tullis*, 1995; *Hirth et al*., 2001; *Rutter & Brodie*, 2004] and using the mode of recrystallized grain size (~19 μm) to estimate the differential stress [*Stipp & Tullis*, 2003 corrected by *Holyoke & Kronenberg*, 2010], we predict dislocation creep as dominating the rheology of the high-strain shear bands, and by deduction, the rheology of the host rock, which necessarily stands above the piezometer (Figure II-15a). We used the mode rather than the mean grain size to minimize the effect of porphyroclasts. Furthermore, while dominant dislocation creep implies realistic strain rates between 4.10^{-14} and 7.10^{-12} s^{-1} for a temperature ranging from 450 to 550 °C, dominant diffusion creep involves much slower and unrealistic strain rates (5.10^{-18}–5.10^{-16} s^{-1}) in the same temperature conditions (Figure II-15b). This definitely excludes diffusion creep as a source for grain boundary sliding, requiring an alternative mechanism.

On this base, we may envisage two possibilities that imply either dislocation-accommodated grain boundary sliding (disGBS) or pressure-solution creep [*Hirth & Kohlstedt*, 2003; *Gratier et al*., 2013]. These two mechanisms are indeed grain size dependent and they involve, or combine with, grain boundary sliding. However, although disGBS has been only highlighted and quantified for olivine aggregates [*Hirth & Kohlstedt*, 2003], 1) it never arises in presence of fluids, 2) it results in a strong crystal preferred orientation, the strength of which increases with increasing strain [*Hansen et al*., 2012], and 3) its grain size dependency is not sufficient to promote strain localization [*Gueydan & Précigout*, 2014]. DisGBS does not seem therefore to be the best candidate to account for the microstructural features and strain localization in Naxos. In contrast, the highly grain-size-sensitive pressure-solution creep, which is conditional upon the presence of fluids, would represent an appropriate candidate. But here, more data and evidence of dissolution-precipitation are needed to go further in the discussion.

Conclusion

This study gives information on the emplacement mechanisms and subsequent retrograde deformation about the Naxos pluton. Using field structural data associated with EBSD, 2D and 3D textural and structural analyses, we document a rapid evolution of the deformation gradient approaching the major detachment along the northern border of the intrusion. At both macroscopic and microscopic scales, stress related to the emplacement of the intrusion first guides the development of a magmatic shape fabric of amphibole and biotite grains. During the detachment activity, the preexisting localization of the deformation linked with the intrusion emplacement played also an important role in the localization of the deformation and the development of the shearing structures.

The continuum of deformation into solid-state ductile-then-brittle conditions is characterized by a persistent stretching direction and the development of an anastomosed network of discrete shear bands that evolves to a penetrative mylonitic texture approaching the detachment fault. All together, these features indicate that the Naxos pluton recorded a strong gradient of deformation that progressively localized along the north-dipping detachment. This accounts for the preservation of a magmatic fabric in the core of the intrusion. The succession of events is also consistent with the top-to-the-N kinematics within the neighboring Naxos metamorphic dome. This clearly demonstrates that the MCC together with the intrusion and associated detachments developed coevally, recording different sequential steps within a single crustal-scale extensional event.

Furthermore, microstructural features indicate that plastic flow of the whole intrusion has been dominated by dislocation creep from more than 500°C to ~350°C (ductile-to-brittle transition). However, numerous four-grain junctions also indicate a significant contribution of grain boundary sliding, in combination with dislocation creep. Together with grain size reduction induced by dynamic recrystallization, this grain size sensitive mechanism provides a good candidate to account for strain localization in Naxos. Nevertheless, the source of grain boundary sliding remains to be better constrained.

Acknowledgments

Acknowledgments: this study is a contribution of the ERC REOLITH Project (ERC Advanced Grant n°290864. Dataset is available, in open access, at https://zenodo.org/record/88718. We gratefully acknowledge the reviewer, Andrew Cross, for his constructive and insightful comments and suggestions that contributed to improve the quality of the manuscript. Our gratitude is also extended to Editor, Claudio Faccenna and the Associate Editor who provided additional helpful comments.

Références bibliographiques

Acocella, V., & **Rossetti, F.** (2002). The role of extensional tectonics at different crustal levels on granite ascent and emplacement: an example from Tuscany (Italy). *Tectonophysics*, *354*(1–2), 71–83. https://doi.org/10.1016/S0040-1951(02)00290-1

Agard, P., Omrani, J., Jolivet, L., Whitechurch, H., Vrielynck, B., Spakman, W., … Wortel, R. (2011). Zagros orogeny: a subduction-dominated process. *Geological Magazine*, *148*(5–6), 692–725. https://doi.org/10.1017/S001675681100046X

Altherr, R., Kreuzer, H., Wendt, I., Lenz, H., Wagner, G. A., Keller, J., … Höhndorf, A. (1982). A late Oligocene/early Miocene high temperature belt in the Attic-Cycladic crystalline complex (SE Pelagonian, Greece). *Geologisches Jahrbuch*, *E23*, 97–164.

Altherr, R., & **Siebel, W.** (2002). I-type plutonism in a continental back-arc setting: Miocene granitoids and monzonites from the central Aegean Sea, Greece. *Contributions to Mineralogy and Petrology*, *143*(4), 397–415. https://doi.org/10.1007/s00410-002-0352-y

Altherr, R., Schliestedt, M., Okrusch, M., Seidel, E., Kreuzer, H., Harre, W., … Wagner, G. A. (1979). Geochronology of high-pressure rocks on Sifnos (Cyclades, Greece). *Contributions to Mineralogy and Petrology*, *70*(3), 245–255. https://doi.org/10.1007/BF00375354

Andriessen, P. A. M., Banga, G., & Hebeda, E. H. (1987). Isotopic age study of pre-Alpine rocks in the basal units on Naxos, Sikinos and Ios, Greek Cyclades., *66*, 3–14.

Andriessen, P. A. M., Boelrijk, N. A. I. M., Hebeda, E. H., Priem, H. N. A., Verdurnen, E. A. T., & Verschure, R. H. (1979). Dating the events of metamorphism and granitic magmatism in the Alpine orogen of Naxos (Cyclades, Greece). *Contributions to Mineralogy and Petrology*, *69*(3), 215–225. https://doi.org/10.1007/BF00372323

Augier, R., Jolivet, L., Gadenne, L., Lahfid, A., & Driussi, O. (2015). Exhumation kinematics of the Cycladic Blueschists unit and back-arc extension, insight from the Southern Cyclades (Sikinos and Folegandros Islands, Greece). *Tectonics*, *34*(1), 152–185. https://doi.org/10.1002/2014TC003664

Austin, N. J., & **Evans, B.** (2007). Paleowattmeters: A scaling relation for dynamically recrystallized grain size. *Geology*, *35*(4), 343–346. https://doi.org/10.1130/G23 244A.

Avigad, D. (1998). High-pressure metamorphism and cooling on SE Naxos (Cyclades, Greece). *European Journal of Mineralogy*, *10*(6), 1309–1319.

Avigad, D., & **Garfunkel, Z.** (1989). Low-angle faults above and below a blueschist belt - Tinos Island, Cyclades, Greece. *Terra Nova*, *1*(2), 182–187. https://doi.org/10.1111/j.1365-3121.1989.tb00350.x

Bachmann, F., Hielscher, R., & Schaeben, H. (2010). Texture Analysis with MTEX – free and Open Source Software Toolbox. *Solid State Phenomena*, *160*, 63–68. https://doi.org/10.4028/www.scientific.net/SSP.160.63

Baker, D. R., Mancini, L., Polacci, M., Higgins, M. D., Gualda, G. A. R., Hill, R. J., & Rivers, M. L. (2012). An introduction to the application of X-ray microtomography to the three-dimensional study of igneous rocks. *Lithos*, *148*, 262–276. https://doi.org/10.1016/j.lithos.2012.06.008

Baker, D. W., & **Wenk, H.-R.** (1972). Preferred orientation in a low-symmetry quartz mylonite. *The Journal of Geology*, *80*(1), 81–105. https://doi.org/10.1086/627714

Baldwin, S. L., Lister, G. S., Hill, E. J., Foster, D. A., & McDougall, I. (1993). Thermochronologic constraints on the tectonic evolution of active metamorphic core complexes, D'entrecasteaux Islands, Papua New Guinea. *Tectonics*, *12*(3), 611–628. https://doi.org/10.1029/93TC00235

Bargnesi, E. A., Stockli, D. F., Mancktelow, N., & Soukis, K. (2013). Miocene core complex development and coeval supradetachment basin evolution of Paros, Greece, insights from (U–Th)/He thermochronometry. *Tectonophysics*, *595–596*, 165–182. https://doi.org/10.1016/j.tecto.2012.07.015

Blake, M. C., Bonneau, M., Geyssant, J., Kienast, J. R., Lepvrier, C., Maluski, H., & Papanikolaou, D. (1981). A geologic reconnaissance of the Cycladic blueschist belt, Greece. *Geological Society of America Bulletin*, *92*(5), 247–254. https://doi.org/10.1130/0016-7606(1981)92<247:AGROTC>2.0.CO;2

Blake, M. C., Bonneau, M., Geyssant, J., Kienast, J. R., Lepvrier, C., Maluski, H., & Papanikolaou, D. (1984). A geologic reconnaissance of the Cycladic blueschist belt, Greece: Discussion and reply. *Geological Society of America Bulletin*, *95*(1), 119. https://doi.org/10.1130/0016-7606(1984)95<119:AGROTC>2.0.CO;2

Bögek, H. (1983). Stratigraphische und tektonische Verknüpfungen kontinentaler Sedimente des Neogens im Ägäis-Raum. *Geologische Rundschau*, *72*(3), 771–813. https://doi.org/10.1007/BF01848344

Bolhar, R., Ring, U., & Allen, C. M. (2010). An integrated zircon geochronological and geochemical investigation into the Miocene plutonic evolution of the Cyclades, Aegean Sea, Greece: Part 1: Geochronology. *Contributions to Mineralogy and Petrology*, *160*(5), 719–742. https://doi.org/10.1007/s00410-010-0504-4

Bonneau, M. (1984). Correlation of the Hellenide nappes in the south-east Aegean and their tectonic reconstruction. *Geological Society, London, Special Publications*, *17*(1), 517–527. https://doi.org/10.1144/GSL.SP.1984.017.01.38

Bonneau, M., & **Kienast, J.** (1982). Subduction, collision et schistes bleus : exemple de l'Egée. *Bulletin de La Société Géologique de France*, *24*, 781–791.

Borradaile, G. J., & **Werner, T.** (1994). Magnetic anisotropy of some phyllosilicates. *Tectonophysics*, *235*(3), 223–248. https://doi.org/10.1016/0040-1951(94)90196-1

Bouchez, J. L., Delas, C., Gleizes, G., Nédélec, A., & Cuney, M. (1992). Submagmatic microfractures in granites. *Geology*, *20*(1), 35–38. https://doi.org/10.1130/0091-7613(1992)020<0035:SMIG>2.3.CO;2

Boullier, A. M., & **Gueguen, Y.** (1975). SP-Mylonites: Origin of some mylonites by superplastic flow. *Contributions to Mineralogy and Petrology*, *50*(2), 93–104. https://doi.org/10.1007/BF00373329

Brichau, S., Ring, U., Ketcham, R. A., Carter, A., Stockli, D., & Brunel, M. (2006). Constraining the long-term evolution of the slip rate for a major extensional fault system in the central Aegean, Greece, using thermochronology. *Earth and Planetary Science Letters*, *241*(1–2), 293–306. https://doi.org/10.1016/j.epsl.2005.09.065

Brichau, S., Ring, U., Carter, A., Monié, P., Bolhar, R., Stockli, D., & Brunel, M. (2007). Extensional faulting on Tinos Island, Aegean Sea, Greece: How many detachments? *Tectonics*, *26*(4), 1–19. https://doi.org/10.1029/2006TC001969

Brichau, S., Ring, U., Carter, A., Bolhar, R., Monie, P., Stockli, D., & Brunel, M. (2008). Timing, slip rate, displacement and cooling history of the Mykonos detachment footwall, Cyclades, Greece, and implications for the opening of the Aegean Sea basin. *Journal of the Geological Society*, *165*(1), 263–277. https://doi.org/10.1144/0016-76492006-145

Brichau, S., Thomson, S., & Ring, U. (2010). Thermochronometric constraints on the tectonic evolution of the Serifos detachment, Aegean Sea, Greece. *International Journal of Earth Sciences*, *99*(2), 379–393. https://doi.org/10.1007/s00531-008-0386-0

Bröcker, M., & **Enders, M.** (1999). U–Pb zircon geochronology of unusual eclogite-facies rocks from Syros and Tinos (Cyclades, Greece). *Geological Magazine*, *136*(2), 111–118.

Brown, M. (1994). The generation, segregation, ascent and emplacement of granite magma: the migmatite-to-crustally-derived granite connection in thickened orogens. *Earth-Science Reviews*, *36*(1–2), 83–130. https://doi.org/10.1016/0012-8252(94)90009-4

Brun, J.-P., & **Faccenna, C.** (2008). Exhumation of high-pressure rocks driven by slab rollback. *Earth and Planetary Science Letters*, *272*(1–2), 1–7. https://doi.org/10.1016/j.epsl.2008.02.038

Buick, I. S. (1991a). Mylonite fabric development on Naxos, Greece. *Journal of Structural Geology*, *13*(6), 643–655. https://doi.org/10.1016/0191-8141(91)90027-G

Buick, I. S. (1991b). The late Alpine evolution of an extensional shear zone, Naxos, Greece. *Journal of the Geological Society*, *148*(1), 93–103. https://doi.org/10.1144/gsjgs.148.1.0093

Bunge, H. J. (1982). Inhomogeneous textures. *Zeitschrift Fur Metallkunde*, *73*(8), 483–488.

Bürgmann, R., & **Dresen, G.** (2008). Rheology of the lower crust and upper mantle: Evidence from rock mechanics, geodesy, and field observations. *Annual Review of Earth and Planetary Sciences*, *36*(1), 531–567. https://doi.org/10.1146/annurev.earth.36.031207.124326

Cao, S., Neubauer, F., Bernroider, M., Genser, J., Liu, J., & Friedl, G. (2017). Low-grade retrogression of a high-temperature metamorphic core complex: Naxos, Cyclades, Greece. *Geological Society of America Bulletin*, *129*(1–2), 93–117. https://doi.org/10.1130/B31502.1

Charles, N., Gumiaux, C., Augier, R., Chen, Y., Zhu, R., & Lin, W. (2011). Metamorphic Core Complexes vs. synkinematic plutons in continental extension setting: Insights from key structures (Shandong Province, eastern China). *Journal of Asian Earth Sciences*, *40*(1), 261–278. https://doi.org/10.1016/j.jseaes.2010.07.006

Coney, P. J., & **Harms, T. A.** (1984). Cordilleran metamorphic core complexes: Cenozoic extensional relics of Mesozoic compression. *Geology*, *12*(9), 550–554. https://doi.org/10.1130/0091-7613(1984)12<550:CMCCCE>2.0.CO;2

Crittenden, M. D., Coney, P. J., & Davis, G. H. (Eds.). (1980). *Cordilleran metamorphic core complexes*. Boulder, Colorado: Geological Society of America.

Daniel, J.-M., & **Jolivet, L.** (1995). Detachment faults and pluton emplacement; Elba Island (Tyrrhenian Sea). *Bulletin de La Societe Geologique de France*, *166*(4), 341–354.

Davidson, C., Schmid, S. M., & Hollister, L. S. (1994). Role of melt during deformation in the deep crust. *Terra Nova*, *6*(2), 133–142. https://doi.org/10.1111/j.1365-3121.1994.tb00646.x

Davis, G. A., Fowler, T. K., Bishop, K. M., Brudos, T. C., Friedmann, S. J., Burbank, D. W., … Burchfiel, B. C. (1993). Pluton pinning of an active Miocene detachment fault system, eastern Mojave Desert, California. *Geology*, *21*(7), 627–630. https://doi.org/10.1130/0091-7613(1993)021<0627:PPOAAM>2.3.CO;2

De Bresser, J., Ter Heege, J., & Spiers, C. (2001). Grain size reduction by dynamic recrystallization: can it result in major rheological weakening? *International Journal of Earth Sciences*, *90*(1), 28–45. https://doi.org/10.1007/s005310000149

Denèle, Y., Lecomte, E., Jolivet, L., Lacombe, O., Labrousse, L., Huet, B., & Le Pourhiet, L. (2011). Granite intrusion in a metamorphic core complex: The example of the Mykonos laccolith (Cyclades, Greece). *Tectonophysics*, *501*(1–4), 52–70. https://doi.org/10.1016/j.tecto.2011.01.013

D'Lemos, R. S., Brown, M., & Strachan, R. A. (1992). Granite magma generation, ascent and emplacement within a transpressional orogen. *Journal of the Geological Society*, *149*(4), 487–490. https://doi.org/10.1144/gsjgs.149.4.0487

Duchêne, S., Aïssa, R., & Vanderhaeghe, O. (2006). Pressure-Temperature-time Evolution of Metamorphic Rocks from Naxos (Cyclades, Greece): Constraints from Thermobarometry and Rb/Sr dating. *Geodinamica Acta*, *19*(5), 301–321. https://doi.org/10.3166/ga.19.301-321

Faure, M., Bonneau, M., & Pons, J. (1991). Ductile deformation and syntectonic granite emplacement during the late Miocene extension of the Aegea (Greece). *Bulletin de La Societe Geologique de France*, *162*, 3–11.

Feenstra, A. (1985). *Metamorphism of bauxites on Naxos, Greece* (Ph.D thesis). Instituut voor Aardwetenschappen, Utrecht University Repository, Netherlands.

Gans, P. B., Mahood, G. A., & Schermer, E. (1989). Synextensional magmatism in the Basin and Range Province; A case study from the eastern Great Basin. In *Geological Society of America Special Papers* (Vol. 233, pp. 1–53). Geological Society of America. Retrieved from http://specialpapers.gsapubs.org/lookup/doi/10.1130/SPE233-p1

Gautier, P., & **Brun, J.-P.** (1994a). Crustal-scale geometry and kinematics of late-orogenic extension in the central Aegean (Cyclades and Ewia Island). *Tectonophysics*, *238*(1–4), 399–424. https://doi.org/10.1016/0040-1951(94)90066-3

Gautier, P., & **Brun, J.-P.** (1994b). Ductile crust exhumation and extensional detachments in the central Aegean (Cyclades and Evvia islands). *Geodinamica Acta*, *7*(2), 57–85.

Gautier, P., Brun, J.-P., & Jolivet, L. (1993). Structure and kinematics of Upper Cenozoic extensional detachment on Naxos and Paros (Cyclades Islands, Greece). *Tectonics*, *12*(5), 1180–1194. https://doi.org/10.1029/93TC01131

Gleason, G. C., & **Tullis, J.** (1995). A flow law for dislocation creep of quartz aggregates determined with the molten salt cell. *Tectonophysics*, *247*(1–4), 1–23. https://doi.org/10.1016/0040-1951(95)00011-B

Grasemann, B., Schneider, D. A., Stockli, D. F., & Iglseder, C. (2012). Miocene bivergent crustal extension in the Aegean: Evidence from the western Cyclades (Greece). *Lithosphere*, *4*(1), 23–39. https://doi.org/10.1130/L164.1

Grasemann, B., & **Petrakakis, K.** (2007). Evolution of the Serifos metamorphic core complex. *Journal of the Virtual Explorer*, *27*, 1–18.

Gratier, J.-P., Dysthe, D. K., & Renard, F. (2013). The Role of Pressure Solution Creep in the Ductility of the Earth's Upper Crust. In *Advances in Geophysics* (Vol. 54, pp. 47–179). Elsevier. https://doi.org/10.1016/B978-0-12-380940-7.00002-0

Gualda, G. A. R., & **Rivers, M.** (2006). Quantitative 3D petrography using x-ray tomography: Application to Bishop Tuff pumice clasts. *Journal of Volcanology and Geothermal Research*, *154*(1–2), 48–62. https://doi.org/10.1016/j.jvolgeores.2005.09.019

Gueydan, F., & **Précigout, J.** (2014). Modes of continental rifting as a function of ductile strain localization in the lithospheric mantle. *Tectonophysics*, *612–613*, 18–25. https://doi. org/10.1016/j.tecto.2013.11.029

Halfpenny, A., Prior, D. J., & Wheeler, J. (2006). Analysis of dynamic recrystallization and nucleation in a quartzite mylonite. *Tectonophysics*, *427*(1–4), 3–14. https://doi.org/10.1016/j.tecto.2006.05.016

Hansen, L. N., Zimmerman, M. E., & Kohlstedt, D. L. (2012). The influence of microstructure on deformation of olivine in the grain-boundary sliding regime. *Journal of Geophysical Research: Solid Earth*, *117*(B9), 1–17. https://doi.org/10.1029/2012JB009305

Hansen, L. N., Zhao, Y.-H., Zimmerman, M. E., & Kohlstedt, D. L. (2014). Protracted fabric evolution in olivine: Implications for the relationship among strain, crystallographic fabric, and seismic anisotropy. *Earth and Planetary Science Letters*, *387*, 157–168. https://doi.org/10.101

6/j.epsl.2013.11.009

Heilbronner, R., & **Tullis, J.** (2006). Evolution of c axis pole figures and grain size during dynamic recrystallization: Results from experimentally sheared quartzite. *Journal of Geophysical Research*, *111*(B10), 1–19. https://doi.org/10.1029/2005JB004194

Henjes-Kunst, F., Altherr, R., Kreuzer, H., & Hansen, B. T. (1988). Disturbed U-Th-Pb systematics of young zircons and uranothorites: The case of the Miocene Aegean Granitoids (Greece). *Chemical Geology: Isotope Geoscience Section*, *73*(2), 125–145. https://doi.org/10.1016/0168-9622(88)90011-5

Henjes-Kunst, F., & **Kreuzer, H.** (1982). Isotopic dating of pre-Alpidic rocks from the island of Ios (Cyclades, Greece). *Contributions to Mineralogy and Petrology*, *80*(3), 245–253. https://doi.org/10.1007/BF00371354

van Hinsbergen, D. J. J., Hafkenscheid, E., Spakman, W., Meulenkamp, J. E., & Wortel, R. (2005). Nappe stacking resulting from subduction of oceanic and continental lithosphere below Greece. *Geology*, *33*(4), 325–328. https://doi.org/10.1130/G20878.1

Hirth, G., Teyssier, C., & Dunlap, J. W. (2001). An evaluation of quartzite flow laws based on comparisons between experimentally and naturally deformed rocks. *International Journal of Earth Sciences*, *90*(1), 77–87. https://doi.org/10.1007/s005310000152

Hirth, G., & **Kohlstedt, D.** (2003). Rheology of the upper mantle and the mantle wedge: A view from the experimentalists. In J. Eiler (Ed.), *Geophysical Monograph Series* (Vol. 138, pp. 83–105). Washington, D. C.: American Geophysical Union. https://doi.org /10.1029/138GM06

Hirth, G., & **Tullis, J.** (1992). Dislocation creep regimes in quartz aggregates. *Journal of Structural Geology*, *14*(2), 145–159. https://doi.org/10.1016/0191-8141(92)90053-Y

Holyoke, C. W., & **Kronenberg, A. K.** (2010). Accurate differential stress measurement using the molten salt cell and solid salt assemblies in the Griggs apparatus with applications to strength, piezometers and rheology. *Tectonophysics*, *494*(1–2), 17–31. https://doi.org/10.1016/j.tecto.2010.08.001

Huet, B., Labrousse, L., & Jolivet, L. (2009). Thrust or detachment? Exhumation processes in the Aegean: Insight from a field study on Ios (Cyclades, Greece). *Tectonics*, *28*(3), 1–27. https://doi.org/10.1029/2008TC002397

Hutton, D. H. W. (1982). A tectonic model for the emplacement of the Main Donegal Granite, NW Ireland. *Journal of the Geological Society*, *139*(5), 615–631. https://doi.org/10.1144/gsjgs.139.5.0615

Iglseder, C., Grasemann, B., Schneider, D. A., Petrakakis, K., Miller, C., Klötzli, U. S., … Rambousek, C. (2009). I and S-type plutonism on Serifos (W-Cyclades, Greece). *Tectonophysics*, *473*(1–2), 69–83. https://doi.org/10.1016/j.tecto.2008.09.021

Iglseder, C., Grasemann, B., Rice, A. H. N., Petrakakis, K., & Schneider, D. A. (2011). Miocene south directed low-angle normal fault evolution on Kea Island (West Cycladic Detachment System, Greece). *Tectonics*, *30*(4), 1–31. https://doi.org/10.1029/2010TC002802

Jansen, J. B. H. (1973). Geological map of Greece, Island of Naxos (1/50 000), Nation. Inst. Geol. Mining Res., Athens. Greece.

Jansen, J. B. H. (1977). *Metamorphism on Naxos, Greece* (PhD thesis). Univ. of Utrecht, Utrecht, Netherlands.

Jansen, J. B. H., & **Schuiling, R. D.** (1976). Metamorphism on Naxos; petrology and geothermal gradients. *American Journal of Science*, *276*(10), 1225–1253. https://doi.org /10.2475/ajs.276.10.1225

Jelinek, V. (1981). Characterization of the magnetic fabric of rocks. *Tectonophysics*, *79*(3–4), T63–T67. https://doi.org/10.1016/0040-1951(81)90110-4

Jolivet, L. (2003). Subduction tectonics and exhumation of high-pressure metamorphic rocks in the Mediterranean orogens. *American Journal of Science*, *303*(5), 353–409. https://doi.org/10.2475/ajs.303.5.353

Jolivet, L., & **Brun, J.-P.** (2010). Cenozoic geodynamic evolution of the Aegean. *International Journal of Earth Sciences*, *99*(1), 109–138. https://doi.org/10.1007/s00531-008-0366-4

Jolivet, L., Rimmelé, G., Oberhänsli, R., Goffé, B., & Candan, O. (2004). Correlation of syn-orogenic tectonic and metamorphic events in the Cyclades, the Lycian nappes and the Menderes massif. Geodynamic implications. *Bulletin de La Societe Geologique de France*, *175*(3), 217–238. https://doi.org/10.2113/175.3.217

Jolivet, L., & **Faccenna, C.** (2000). Mediterranean extension and the Africa-Eurasia collision. *Tectonics*, *19*(6), 1095–1106. https://doi.org/10.1029/2000TC900018

Jolivet, L., Menant, A., Sternai, P., Rabillard, A., Arbaret, L., Augier, R., … Le Pourhiet, L. (2015). The geological signature of a slab tear below the Aegean. *Tectonophysics*, *659*, 166–182. https://doi.org/10.1016/j.tecto.2015.08.004

Jolivet, L., Lecomte, E., Huet, B., Denèle, Y., Lacombe, O., Labrousse, L., … Mehl, C. (2010). The North Cycladic Detachment System. *Earth and Planetary Science Letters*, *289*(1–2), 87–104. https://doi.org/10.1016/j.epsl.2009.10.032

Jolivet, L., Faccenna, C., Goffé, B., Mattei, M., Rossetti, F., Brunet, C., … Parra, T. (1998). Midcrustal shear zones in postorogenic extension: Example from the northern Tyrrhenian Sea. *Journal of Geophysical Research*, *103*(B6), 12123–12160. https://doi.org/10.1029/97JB03616

Katzir, Y., Matthews, A. L. A. N., Garfunkel, Z., Schliestedt, M., & Avigad, D. (1996). The tectono-metamorphic evolution of a dismembered ophiolite (Tinos, Cyclades, Greece). *Geological Magazine*, *133*(3), 237–254.

Keay, S. (1998). *The geological evolution of the Cyclades, Greece, constraints from SHRIMP U/Pb geochronology* (Ph.D thesis). Research School of Earth Sciences, Australian National University, Cambera, Australia.

Keay, S., Lister, G., & Buick, I. (2001). The timing of partial melting, Barrovian metamorphism and granite intrusion in the Naxos metamorphic core complex, Cyclades, Aegean Sea, Greece. *Tectonophysics*, *342*(3–4), 275–312. https://doi.org/10.1016/S0040-1951(01)00168-8

Keay, S., & Lister, G. (2002). African provenance for the metasediments and metaigneous rocks of the Cyclades, Aegean Sea, Greece. *Geology*, *30*(3), 235–238. https://doi.org/10.1130/0091-7613(2002)030<0235:APFTMA>2.0.CO;2

Keiter, M., Piepjohn, K., Ballhaus, C., Lagos, M., & Bode, M. (2004). Structural development of high-pressure metamorphic rocks on Syros island (Cyclades, Greece). *Journal of Structural Geology*, *26*(8), 1433–1445. https://doi.org/10.1016/j.jsg.2003.11.027

Ketcham, R. A. (2005). Three-dimensional grain fabric measurements using high-resolution X-ray computed tomography. *Journal of Structural Geology*, *27*(7), 1217–1228. https://doi.org/10.1016/j.jsg.2005.02.006

Ketcham, R. A., & **Carlson, W. D.** (2001). Acquisition, optimization and interpretation of X-ray computed tomographic imagery: applications to the geosciences. *Computers & Geosciences*, *27*(4), 381–400. https://doi.org/10.1016/S0098-3004(00)00116-3

Kilian, R., Heilbronner, R., & Stünitz, H. (2011). Quartz grain size reduction in a granitoid rock and the transition from dislocation to diffusion creep. *Journal of Structural Geology*, *33*(8), 1265–1284. https://doi.org/10.1016/j.jsg.2011.05.004

Kokkalas, S., & **Aydin, A.** (2013). Is there a link between faulting and magmatism in the

south-central Aegean Sea? *Geological Magazine*, *150*(02), 193–224. https://doi.org/10.1017/S0016756812000453

Koukouvelas, I. K., & **Kokkalas, S.** (2003). Emplacement of the Miocene west Naxos pluton (Aegean Sea, Greece): a structural study. *Geological Magazine*, *140*(1), 45–61. https://doi.org/10.1017/S0016756802007094

Kruckenberg, S. C., Vanderhaeghe, O., Ferré, E. C., Teyssier, C., & Whitney, D. L. (2011). Flow of partially molten crust and the internal dynamics of a migmatite dome, Naxos, Greece. *Tectonics*, *30*(3), 1–24. https://doi.org/10.1029/2010TC002751

Kruse, R., & **Stünitz, H.** (1999). Deformation mechanisms and phase distribution in mafic high-temperature mylonites from the Jotun Nappe, southern Norway. *Tectonophysics*, *303*(1–4), 223–249. https://doi.org/10.1016/S0040-1951(98)00255-8

Kuhlemann, J., Frisch, W., Dunkl, I., Kázmér, M., & Schmiedl, G. (2004). Miocene siliciclastic deposits of Naxos Island: Geodynamic and environmental implications for the evolution of the southern Aegean Sea (Greece). In *Special Paper 378: Detrital thermochronology - Provenance analysis, exhumation, and landscape evolution of mountain belts* (Vol. 378, pp. 51–65). Geological Society of America. Retrieved from http://specialpapers.gsapubs.org/cgi/doi/10.1130/0-8137-2378-7.51

Kumerics, C., Ring, U., Brichau, S., Glodny, J., & Monie, P. (2005). The extensional Messaria shear zone and associated brittle detachment faults, Aegean Sea, Greece. *Journal of the Geological Society*, *162*(4), 701–721. https://doi.org/10.1144/0016-764904-041

Launeau, P., Archanjo, C. J., Picard, D., Arbaret, L., & Robin, P.-Y. (2010). Two- and three-dimensional shape fabric analysis by the intercept method in grey levels. *Tectonophysics*, *492*(1–4), 230–239. https://doi.org/10.1016/j.tecto.2010.06.005

Launeau, P., & **Robin, P.-Y. F.** (1996). Fabric analysis using the intercept method. *Tectonophysics*, *267*(1–4), 91–119. https://doi.org/10.1016/S0040-1951(96)00091-1

Launeau, P., & **Robin, P.-Y. F.** (2005). Determination of fabric and strain ellipsoids from measured sectional ellipses—implementation and applications. *Journal of Structural Geology*, *27*(12), 2223–2233. https://doi.org/10.1016/j.jsg.2005.08.003

Laurent, V., Beaudoin, A., Jolivet, L., Arbaret, L., Augier, R., Rabillard, A., & Menant, A. (2015). Interrelations between extensional shear zones and synkinematic intrusions: The example of Ikaria Island (NE Cyclades, Greece). *Tectonophysics*, *651–652*, 152–171. https://doi.org/10.1016/j.tecto.2015.03.020

Lecomte, E., Jolivet, L., Lacombe, O., Denèle, Y., Labrousse, L., & Le Pourhiet, L. (2010). Geometry and kinematics of Mykonos detachment, Cyclades, Greece: Evidence for slip at shallow dip. *Tectonics*, *29*(5), 1–22. https://doi.org/10.1029/2009TC002564

Lee, J., & **Lister, G. S**. (1992). Late Miocene ductile extension and detachment faulting, Mykonos, Greece. *Geology*, *20*(2), 121–124. https://doi.org/10.1130/0091-7613(1992)020<0121:LMDEAD>2.3.CO;2

Lister, G. S., & **Baldwin, S. L.** (1993). Plutonism and the origin of metamorphic core complexes. *Geology*, *21*(7), 607–610. https://doi.org/10.1130/0091-7613(1993)021<0607:PATOOM>2.3.CO;2

Lister, G. S., & **Davis, G. A.** (1989). The origin of metamorphic core complexes and detachment faults formed during Tertiary continental extension in the northern Colorado River region, U.S.A. *Journal of Structural Geology*, *11*(1–2), 65–94. https://doi.org/10.1016/0191-8141(89)90036-9

Lister, G. S., Banga, G., & Feenstra, A. (1984). Metamorphic core complexes of Cordilleran type in the Cyclades, Aegean Sea, Greece. *Geology*, *12*(4), 221–225. https://doi.org/10.1130/0091-7613(1984)12<221:MCCOCT>2.0.CO;2

Lloyd, G. E. (2004). Microstructural evolution in a mylonitic quartz simple shear zone: the significant roles of dauphine twinning and misorientation. *Geological Society, London, Special Publications*, *224*(1), 39–61. https://doi.org/10.1144/GSL.SP.2004.224.01.04

Mainprice, D., Bachmann, F., Hielscher, R., & Schaeben, H. (2015). Descriptive tools for the analysis of texture projects with large datasets using MTEX : strength, symmetry and components. *Geological Society, London, Special Publications*, *409*(1), 251–271. https://doi.org/10.1144/SP409.8

Maluski, H., Bonneau, M., & Kienast, J. R. (1987). Dating the metamorphic events in the Cycladic area; 39 Ar/40 Ar data from metamorphic rocks of the Island of Syros (Greece). *Bulletin de La Société Géologique de France*, *3*(5), 833–842.

Martha, S. O., Dörr, W., Gerdes, A., Petschick, R., Schastok, J., Xypolias, P., & Zulauf, G. (2016). New structural and U–Pb zircon data from Anafi crystalline basement (Cyclades, Greece): constraints on the evolution of a Late Cretaceous magmatic arc in the Internal Hellenides. *International Journal of Earth Sciences*, *105*(7), 2031–2060. https://doi.org/10.1007/s00531-016-1346-8

McCaffrey, K. J. W. (1992). Igneous emplacement in a transpressive shear zone: Ox Mountains igneous complex. *Journal of the Geological Society*, *149*(2), 221–235. https://doi.org/10.1144/gsjgs.149.2.0221

Mees, F., Swennen, R., Geet, M. V., & Jacobs, P. (2003). Applications of X-ray computed tomography in the geosciences. *Geological Society, London, Special Publications*, *215*(1), 1–6. https://doi.org/10.1144/GSL.SP.2003.215.01.01

Mehl, L., & **Hirth, G.** (2008). Plagioclase preferred orientation in layered mylonites: Evaluation of flow laws for the lower crust. *Journal of Geophysical Research*, *113*(B5), 1–19. https://doi.org/10.1029/2007JB005075

Menant, A., Jolivet, L., Augier, R., & Skarpelis, N. (2013). The North Cycladic Detachment System and associated mineralization, Mykonos, Greece: Insights on the evolution of the Aegean domain. *Tectonics*, *32*(3), 433–452. https://doi.org/10.1002/tect.20037

Muto, J., Hirth, G., Heilbronner, R., & Tullis, J. (2011). Plastic anisotropy and fabric evolution in sheared and recrystallized quartz single crystals. *Journal of Geophysical Research*, *116*(B2), 1–18. https://doi.org/10.1029/2010JB007891

Otani, M., & **Wallis, S.** (2006). Quartz lattice preferred orientation patterns and static recrystallization: Natural examples from the Ryoke belt, Japan. *Geology*, *34*(7), 561–564. https://doi.org/10.1130/G22430.1

Papanikolaou, D. (2009). Timing of tectonic emplacement of the ophiolites and terrane paleogeography in the Hellenides. *Lithos*, *108*(1–4), 262–280. https://doi.org/10.1016/j.lithos.2008.08.003

Paterson, S. R., Vernon, R. H., & Tobisch, O. T. (1989). A review of criteria for the identification of magmatic and tectonic foliations in granitoids. *Journal of Structural Geology*, *11*(3), 349–363. https://doi.org/10.1016/0191-8141(89)90074-6

Patzak, M., Okrusch, M., & Kreuzer, H. (1994). The Akrotiri Unit on the island of Tinos, Cyclades, Greece: Witness to a lost terrane of Late Cretaceous age. *Neues Jahrbuch Fur Geologie Und Palaontologie-Abhandlungen*, *194*, 211–252.

Pe-Piper, G. (2000). Origin of S-type granites coeval with I-type granites in the Hellenic subduction system, Miocene of Naxos, Greece. *European Journal of Mineralogy*, *12*(4), 859–875. https://doi.org/10.1127/ejm/12/4/0859

Pe-Piper, G., Kotopouli, C. N., & Piper, D. J. W. (1997). Granitoid rocks of Naxos, Greece: regional geology and petrology. *Geological Journal*, *32*(2), 153–171. https://doi.org/10.1002/(SICI)1099-1034(199706)32:2<153::AID-GJ737>3.0.CO;2-1

Pitzer, K. S., & **Sterner, S. M.** (1994). Equations of state valid continuously from zero to extreme pressures for H_2O and CO_2. *The Journal of Chemical Physics*, *101*(4), 3111–3116. https://doi.org/10.1063/1.467624

Platt, J. P., & **Behr, W. M.** (2011). Lithospheric shear zones as constant stress experiments. *Geology*, *39*(2), 127–130. https://doi.org/10.1130/G31561.1

Platt, J. P., Behr, W. M., & Cooper, F. J. (2015). Metamorphic core complexes: windows into the mechanics and rheology of the crust. *Journal of the Geological Society*, *172*(1), 9–27. https://doi.org/10.1144/jgs2014-036

Rabillard, A., Arbaret, L., Jolivet, L., Le Breton, N., Gumiaux, C., Augier, R., & Grasemann, B. (2015). Interactions between plutonism and detachments during metamorphic core complex formation, Serifos Island (Cyclades, Greece). *Tectonics*, *34*(6), 1080–1106. https://doi.org/10.1002/2014TC 003650

Rahl, J. M., & **Skemer, P.** (2016). Microstructural evolution and rheology of quartz in a mid-crustal shear zone. *Tectonophysics*, *680*, 129–139. https://doi.org/10.1016/j.tecto.2016.05.022

Ree, J.-H. (1994). Grain boundary sliding and development of grain boundary openings in experimentally deformed octachloropropane. *Journal of Structural Geology*, *16*(3), 403–418. https://doi.org/10.1016/0191-8141(94)90044-2

Reinecke, T., Altherr, R., Hartung, B., Hatzipanagiotou, K., Kreuzer, H., Harre, W., … Boger, H. (1982). Remnants of a Late Cretaceous high temperature belt on the island of Anafi (Cyclades, Greece), *145*, 157–182.

Ring, U., & **Layer, P. W.** (2003). High-pressure metamorphism in the Aegean, eastern Mediterranean: Underplating and exhumation from the Late Cretaceous until the Miocene to Recent above the retreating Hellenic subduction zone. *Tectonics*, *22*(3), 1–6. https://doi.org/10.1029/2001TC001350

Ring, U., Glodny, J., Will, T., & Thomson, S. (2010). The Hellenic Subduction System: High-Pressure Metamorphism, Exhumation, Normal Faulting, and Large-Scale Extension. *Annual Review of Earth and Planetary Sciences*, *38*(1), 45–76. https://doi.org/10.1146/annurev.earth.050708.170910

Rutter, E. ., & **Brodie, K.** . (2004). Experimental intracrystalline plastic flow in hot-pressed synthetic quartzite prepared from Brazilian quartz crystals. *Journal of Structural Geology*, *26*(2), 259–270. https://doi.org/10.1016/S0191-8141 (03)00096-8

Saltykov, S. A. (1958). *Stereometric Metallography* (2nd ed.). Moscou, Russia: Metallurgizdat.

Sanchez-Gomez, M., Avigad, D., & Heimann, A. (2002). Geochronology of clasts in allochthonous Miocene sedimentary sequences on Mykonos and Paros Islands: implications for back-arc extension in the Aegean Sea. *Journal of the Geological Society*, *159*(1), 45–60. https://doi.org/10.1144/0016-764901031

Seward, D., Vanderhaeghe, O., Siebenaller, L., Thomson, S., Hibsch, C., Zingg, A., … Duchene, S. (2009). Cenozoic tectonic evolution of Naxos Island through a multi-faceted approach of fission-track analysis. *Geological Society, London, Special Publications*, *321*(1), 179–196. https://doi.org/10.1144/SP321.9

Siebenaller, L. (2008). *Circulations fluides au cours de l'effondrement d'un prisme d'accrétion crustal: L'exemple du "Metamorphic Core Complex" de l'Île de Naxos (Cyclades, Grèce)* (Ph.D thesis). Univ. Henri Poincaré, Nancy, France.

Skemer, P., Katayama, I., Jiang, Z., & Karato, S. (2005). The misorientation index: Development of a new method for calculating the strength of lattice-preferred orientation. *Tectonophysics*, *411*(1–4), 157–167. https://doi.org/10.1016/j.tecto.2005.08.023

Smith, S. A. F., Holdsworth, R. E., & Collettini, C. (2011). Interactions between low-angle normal faults and plutonism in the upper crust: Insights from the Island of Elba, Italy. *Geological Society of America Bulletin*, *123*(1–2), 329–346. https://doi.org/10.1130/B30200.1

Stipp, M., Stünitz, H., Heilbronner, R., & Schmid, S. M. (2002). The eastern Tonale fault zone: a 'natural laboratory' for crystal plastic deformation of quartz over a temperature range from 250 to 700°C. *Journal of Structural Geology*, *24*(12), 1861–1884. https://doi.org/10.1016/S0191-8141(02)00035-4

Stipp, M., & **Tullis, J.** (2003). The recrystallized grain size piezometer for quartz. *Geophysical Research Letters*, *30*(21), 1–5. https://doi.org/10.1029/2003GL018444

Stünitz, H., & **Fitz Gerald, J. D.** (1993). Deformation of granitoids at low metamorphic grade. II: Granular flow in albite-rich mylonites. *Tectonophysics*, *221*(3–4), 299–324. https://doi.org/10.1016/0040-1951(93)90164-F

Tikoff, B., & **Teyssier, C.** (1992). Crustal-scale, en echelon "P-shear" tensional bridges: A possible solution to the batholithic room problem. *Geology*, *20*(10), 927–930. https://doi.org/10.1130/0091-7613(1992)020<0927:CSEEPS>2.3.CO;2

Tommasi, A., Vauchez, A., Femandes, L. A. D., & Porcher, C. C. (1994). Magma-assisted strain localization in an orogen-parallel transcurrent shear zone of southern Brazil. *Tectonics*, *13*(2), 421–437. https://doi.org/10.1029/93TC03319

Tschegg, C., & **Grasemann, B.** (2009). Deformation and alteration of a granodiorite during low-angle normal faulting (Serifos, Greece). *Lithosphere*, *1*(3), 139–154. https://doi.org/10.1130/L33.1

Urai, J. L., Schuiling, R. D., & Jansen, J. B. H. (1990). Alpine deformation on Naxos (Greece). *Geological Society, London, Special Publications*, *54*(1), 509–522. https://doi.org/10.1144/GSL.SP.1990.054.01

Vanderhaeghe, O. (2004). Structural development of the Naxos migmatite dome. In *Gneiss Domes in Orogeny* (Vol. 380, pp. 211–227). Boulder, Colorado: Geological Society of America. Retrieved from http://specialpapers.gsapubs.org/cgi/doi/10.1130/0-8137-2380-9.211

Vernon, R. H. (2000). Review of Microstructural Evidence of Magmatic and Solid-State Flow. *Visual Geosciences*, *5*(2), 1–23. https://doi.org/10.1007/s10069-000-0002-3

Vigneresse, J. L. (1995). Crustal regime of deformation and ascent of granitic magma. *Tectonophysics*, *249*(3–4), 187–202. https://doi.org/10.1016/0040-1951(95)00005-8

Wernicke, B. P., England, P. C., Sonder, L. J., & Christiansen, R. L. (1987). Tectonomagmatic evolution of Cenozoic extension in the North American Cordillera. *Geological Society, London, Special Publications*, *28*(1), 203–221. https://doi.org/10.1144/GSL.SP.1987.028.01.15

Wijbrans, J. R., & **McDougall, I.** (1988). Metamorphic evolution of the Attic Cycladic Metamorphic Belt on Naxos (Cyclades, Greece) utilizing $^{40}Ar/^{39}$ age spectrum measurements. *Journal of Metamorphic Geology*, *6*(5), 571–594. https://doi.org/10.1111/j.1525-1314.1988.tb00441.x

Wijbrans, J. R., Schliestedt, M., & York, D. (1990). Single grain argon laser probe dating of phengites from the blueschist to greenschist transition on Sifnos (Cyclades, Greece). *Contributions to Mineralogy and Petrology*, *104*(5), 582–593. https://doi.org/10.1007/ BF00306666

Chapitre III

Interactions entre magmatisme et un système de détachements : le dôme métamorphqiue de Serifos (Cyclades, Grèce)

Sommaire

Résumé étendu

Problématique et démarche

Ce présent chapitre vise à **décrypter le ou les processus(s) à l'origine de l'association étroite entre activité magmatique et phénomène de localisation de la déformation le long de détachements à l'échelle du dôme métamorphique extensif (MCC) de Serifos**. Située dans la partie occidentale de l'archipel des Cyclades (Grèce), Serifos appartient à un chapelet d'îles (Kea, Kythnos) où affleure désormais une série de dômes métamorphiques aux histoires d'exhumation comparables. Dans ce secteur des Cyclades, la tectonique extensive Miocène fut tout particulièrement marquée par le développement d'une déformation ductile à cinématique vers le sud-ouest et la localisation de multiples détachements crustaux responsables de l'exhumation des dômes [e.g., *Iglseder et al.*, 2011; *Grasemann et al.*, 2012; *Rice et al.*, 2012]. Ces détachements, par leur cinématique commune, ont été récemment regroupés sous le nom de *West Cycladic Detachement System* (WCDS) [*Grasemann et al.*, 2012]. Parmi les dômes métamorphiques de l'ouest des Cyclades, celui de Serifos présente l'originalité de voir son cœur dominé par un corps intrusif syn-extensif (11-9 Ma ; âge de l'intrusion granodioritique par analyse (U-Th/Pb) sur zircons, *Iglseder et al.* [2009]) et son architecture globale façonnée par trois branches appartenant au *WCDS* (détachements de Meghàlo Livadhi, Kàvos Kiklopas et Aghios Sostis, Figure III-1). Si la cinématique et les modalités de déformation le long de ces détachements ont été largement abordées par un certain nombre d'études [e.g., *Grasemann & Petrakakis*, 2007; *Tschegg & Grasemann*, 2009; *Grasemann & Tschegg*, 2012; *Grasemann et al.*, 2012], aucune d'entre elles ne s'est en revanche réellement attachée à décrire (1) la distribution et l'évolution de la déformation dans l'ensemble de la

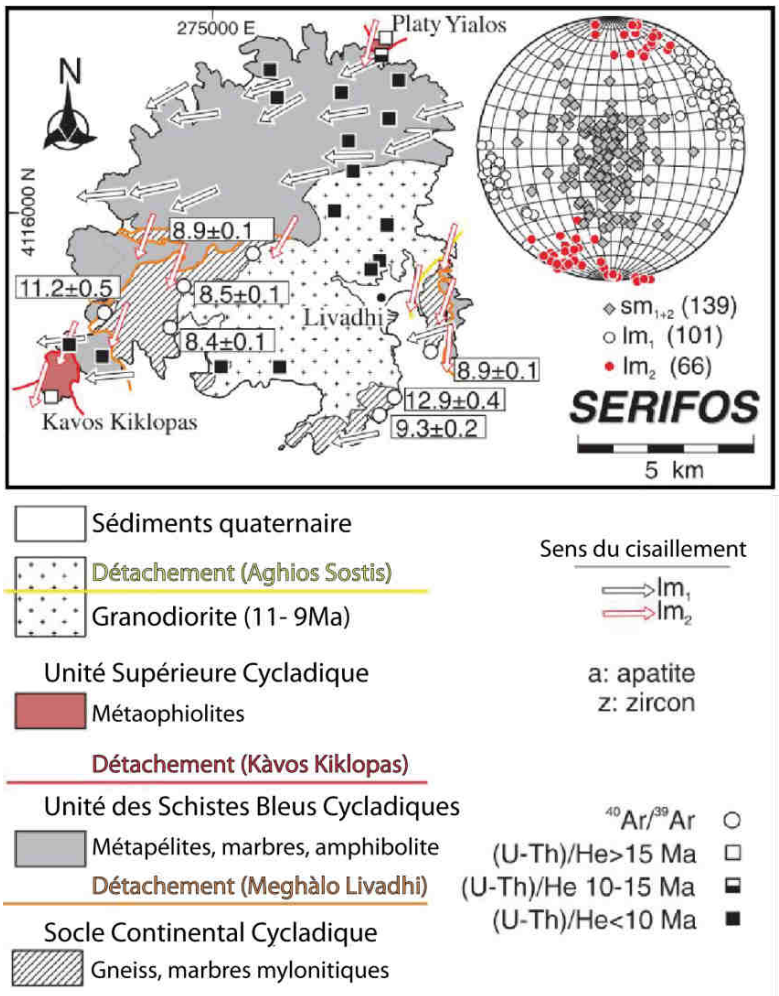

Figure III-1: *carte géologique et tectonique simplifiée du dôme métamorphique extensif (MCC) de Serifos et son système de détachements associé. Modifié d'après Grasemann et al. [2012].*

granodiorite et (2) les relations géométriques entre ce corps magmatique, les séries encaissantes et les détachements crustaux. Ce manque de données et observations, notamment structurales, soulève ainsi deux questions majeures. Le magmatisme syn-extensif a-t-il joué un rôle précurseur dans l'initiation de zones de détachements ou a-t-il été totalement passif vis-à-vis de la tectonique extensive ? Les divers détachements observés se sont-ils développés de manière séquentielle ou simultanée? Afin de discuter de ces quelques points, l'étude présentée ci-après, et valorisée dans la revue *Tectonics*, s'est essentiellement basée sur une approche naturelle (observation de terrain et microstructurale). En complément des mesures structurales, l'acquisition de données d'anisotropie de susceptibilité magnétique (ASM) ont été aussi nécessaires.

Résultats majeurs

Les observations sur la structure du dôme métamorphique et du corps intrusif ont permis de reconstituer l'architecture globale de l'île, d'en soustraire une coupe originale et de discuter des processus d'évolution sous forme d'un modèle d'interaction entre les détachements et la granodiorite. Au travers de la collecte de données structurales et d'ASM, il apparaît ainsi que la granodiorite adopte une géométrie asymétrique claire en lien avec le développement d'une déformation ductile cisaillante vers le sud-ouest et la localisation de zones de cisaillement à grande échelle (Vaghia, Aghios Sostis). Cette asymétrie induite par ces zones de cisaillement se reflète dans la granodiorite par (1) une préservation de fabriques magmatiques au nord où le contact intrusif recoupe le détachement inférieur de Meghàlo Livadhi, et (2) un fort gradient dans l'intensité de la déformation au niveau de la bordure sud.

L'assimilation de ces nouvelles observations structurales aux données de la littérature nous a finalement menés à émettre un scénario tectonique dans lequel le magmatisme endosse un rôle majeur dans les processus de redistribution et de localisation de la déformation dans l'histoire d'exhumation tardive du dôme métamorphique de Serifos. Nous suggérons ainsi une première phase durant laquelle l'accommodation de l'extension NE-SO et l'exhumation du dôme s'effectuent à la faveur du seul détachement de Meghàlo Livadhi en régime ductile puis cassant. Dans ce schéma évolutif, la venue tardive du magmatisme le long de ce détachement préexistant perturbe à la fois la structure thermique et le régime de déformation régnant dans le système environnant. Le pluton, traversant le détachement de Meghàlo Livadhi, est alors à l'origine d'une migration spatiale de la déformation extensive non loin de son contact supérieur où la nucléation et le développement ultérieurs de détachements (Aghios Sostis/ Vaghia et Kàvos Kiklopas) se réalisent là aussi en domaine ductile, puis cassant.

Données complémentaires : géométrie et cinématique du détachement d'Aghios Sostis

Le détachement d'Aghios Sostis, affleurant au sein même de la granodiorite (Sud-Est du corps magmatique, Figure III-2), fut la cible principale d'une étude structurale, pétrologique et géochimique de *Tschegg & Grasemann* [2009]. C'est pourquoi dans le manuscrit présenté

ci-dessous les détails concernant la géométrie du plan de faille, les critères cinématiques et le style de déformation à l'approche de ce détachement n'ont été que très succintement décrits. De manière à ce que la compréhension de l'article soit améliorée, nous relayons ici quelques illustrations et éléments structuraux complémentaires.

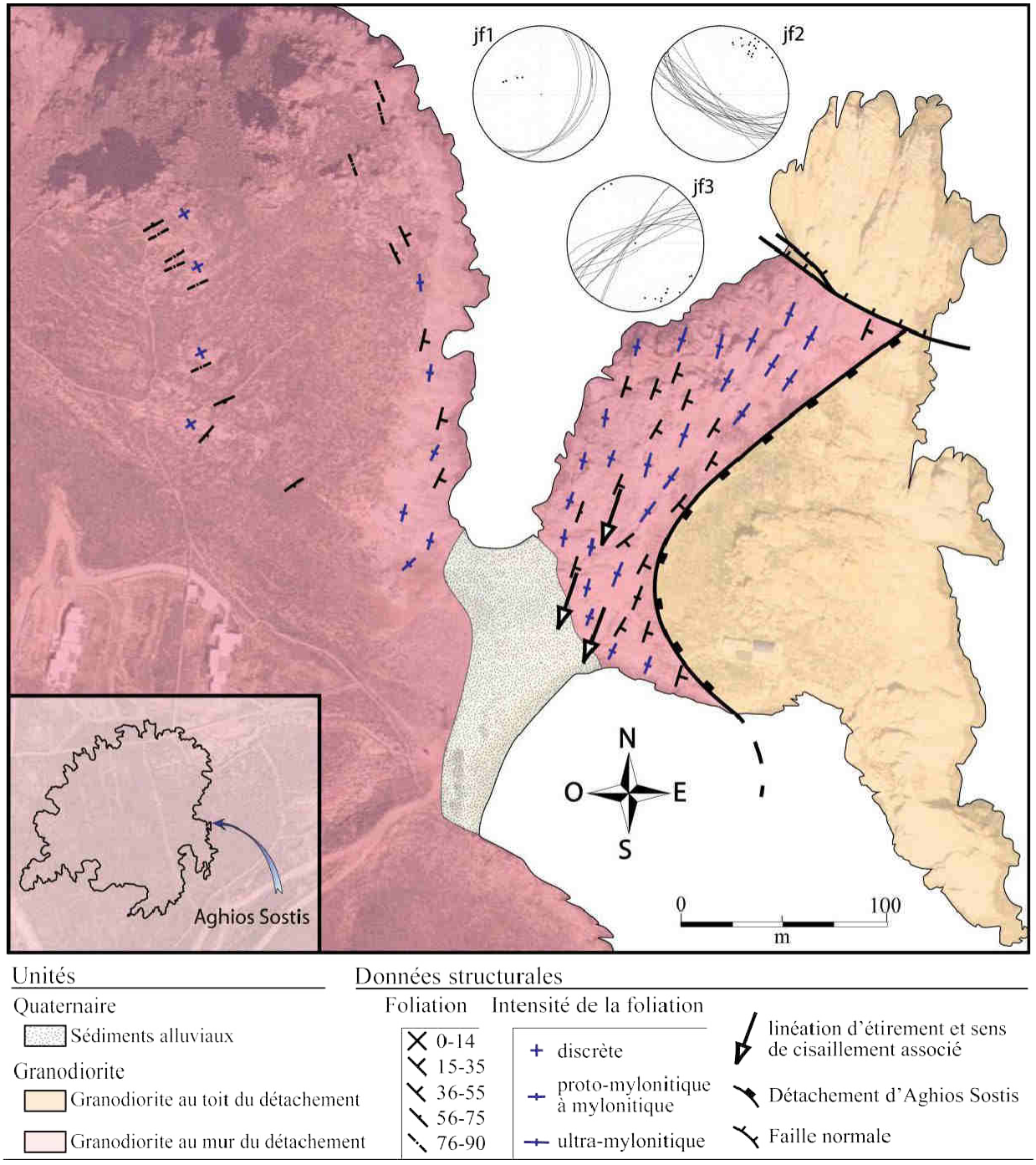

Figure III-2: *carte tectonique de la péninsule d'Aghios Sostis sur laquelle est indiquée la trajectoire du plan de détachement, les marqueurs de la déformation finie (foliation, linéation), l'intensité de la déformation et l'orientation de fractures (jf1, jf2, jf3).*

Suivant les travaux de *Tschegg & Grasemann* [2009] et nos propres observations, le détachement d'Aghios Sostis représente l'état fini du développement d'un cisaillement ductile extrêmement localisé évoluant par la suite vers une attitude plus cassante au travers d'une faille normale à faible angle. A l'affleurement, le plan de détachement arbore un pendage moyen de 30-40° vers le sud-est et juxtapose une granodiorite faiblement déformée et lessivée au sommet d'une bande ultra-mylonitique de quelques mètres d'épaisseur ; l'ensemble étant repris par un jeu de failles à fort pendage (Figures III-3a et -3b). Comme le dévoile la carte de répartition de l'intensité de la déformation (Figure III-2), les roches ultramylonitiques appartiennent structuralement au niveau supérieur d'un gradient de déformation. L'intensité de déformation décroît ensuite fortement sur une épaisseur de plusieurs dizaines de mètres, passant ainsi d'une (ultra)mylonite à une granodiorite n'exprimant qu'une déformation ductile discrète, jusqu'à l'entière conservation d'une fabrique magmatique vers le cœur du corps intrusif. Au travers de ce gradient de déformation, un changement graduel des foliations tectoniques peut être remarqué.

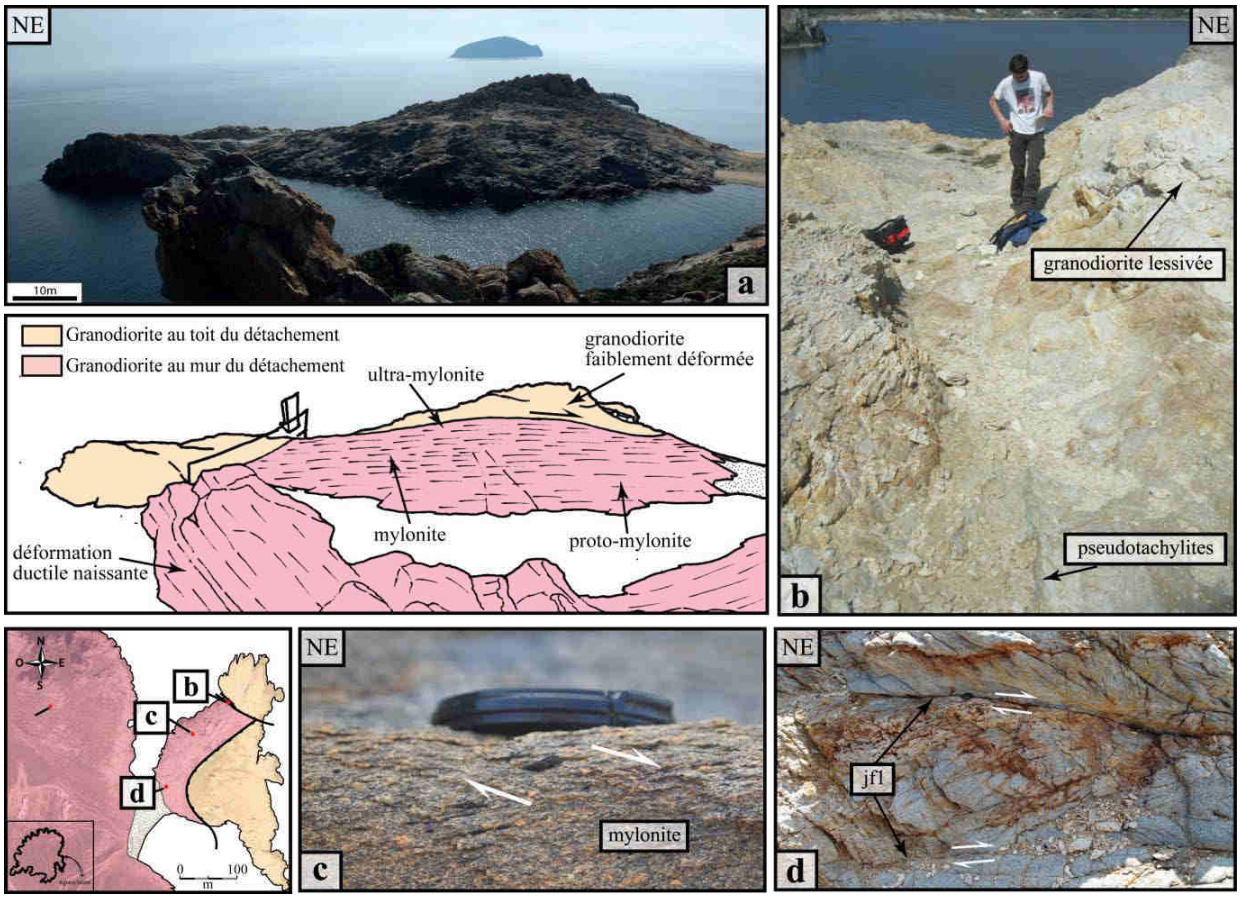

Figure III-3: *(a) panorama de la zone de détachement d'Aghios Sostis et son dessein interprétatif. (b) Vue d'un système de failles à fort pendage. (c) Granodiorite mylonitisée et critère de cisaillement associé (top vers le sud-ouest). (d) Nucléation de zones de cisaillement ductile le long de plans de fracture préexistants et dont l'orientation est parallèle au système de fractures (jf1).*

Sur la carte (Figure III-2), la trace des foliations évolue en effet depuis une direction NE sous le plan de détachement à une direction plutôt N-S à NNO-SSE dans les niveaux où

une déformation proto-mylonitique prédomine. Les foliations minérales mesurées dans la zone où la déformation semble la plus discrète se distinguent en revanche par des trajectoires ENE à NE et des pendages sub-verticaux, témoignant possiblement d'une fabrique magmatique partiellement préservée. Bien que les foliations tectoniques montrent une trajectoire courbe, les linéations minérales ou d'étirement plongent constamment selon une direction NE-SO et les marqueurs cinématiques associés à la déformation ductile révèlent un cisaillement vers le sud-ouest.

Les critères cinématiques sont visibles dans tous les grades de déformation, depuis le simple tuilage d'agrégats de biotite (déformation discrète) jusqu'à la présence pervasive de bandes de cisaillement (grade mylonitique, Figure III-3c), en passant par le développement de zones de cisaillement isolées ou anastomosées (Figure III-3d) dans le grade proto-mylonitique. Les zones de cisaillement localisées, d'une puissance pluri-centimétrique, ont la particularité de s'être nucléés le long de fractures préexistantes ; fractures ayant la même orientation que l'une des familles de fractures mesurées au sein de la granodiorite non ou peu déformée (jf1, Figure III-2). Ce comportement transitionnel d'une déformation cassante à ductile peut être expliquée et induite par une augmentation transitoire de la température, un saut dans les conditions de pression fluide et/ou de confinement ou encore un changement dans les vitesses de déformation [*Tullis & Yund*, 1977; *Kolb et al.*, 2004].

Article: Interactions between plutonism and detachments during metamorphic core complex formation, Serifos Island (Cyclades, Greece)

Publié dans la revue *Tectonics*, Avril 2015

doi: 10.1002/2014TC003650

Aurélien Rabillard [1,2,3], Laurent Arbaret[1,2,3], Laurent Jolivet[1,2,3], Nicole Le Breton[1,2,3], Charles Gumiaux[1,2,3], Romain Augier[1,2,3], Bernhard Grasemann[4]

(1) Université d'Orléans, ISTO, UMR 7327, 45071, Orléans, France
(2) CNRS/INSU, ISTO, UMR 7327, 45071 Orléans, France
(3) BRGM, ISTO, UMR 7327, BP 36009, 45060 Orléans, France
(4) Department for Geodynamics and Sedimentology, University of Vienna, Althanstrasse 14, 1090 Vienna, Austria

Abstract

In order to better understand the interactions between plutonic activity and strain localization during metamorphic core complexes formation the Miocene granodioritic pluton of Serifos (Cyclades, Greece) is studied. This pluton (11.6-9.5 Ma) intruded the Cycladic Blueschists during thinning of the Aegean domain along a system of low-angle normal faults belonging to the south-dipping West Cycladic Detachment System (WCDS). Based on structural fieldwork, together with microstructural observations and anisotropy of magnetic susceptibility (AMS), we recognize a continuum of deformation from magmatic to brittle conditions within the magmatic body. This succession of deformation events is kinematically compatible with the development of the WCDS. The architecture of the pluton shows a marked asymmetry resulting from its interaction with the detachments. We propose a tectonic scenario for the emplacement of Serifos pluton and its subsequent cooling during the Aegean extension. (1) A first stage corresponds to the metamorphic core complex initiation and associated southwestward shearing along the Meghàlo Livadhi detachment. (2) In a second stage the Serifos pluton has intruded the dome at shallow crustal level, piercing through the ductile/brittle Meghàlo Livadhi detachment. Southwest-directed extensional deformation was contemporaneously transferred upward in the crust along the more localized Kàvos Kiklopas detachment. (3) A third stage was marked by syn-magmatic extensional deformation and strain localization at the contact between the pluton and the host rocks resulting in narrow shear zones nucleation which (4) continued to develop after the pluton solidification.

Key words: plutonism; syntectonic; detachment; extension; Aegean; Serifos

1. Introduction

Over the past 30 years, intense research has been devoted to interrelations of plutonic activity and shear zone formation in various tectonic settings, from extensional [*Baldwin et al.*, 1993; *Neves et al.*, 1996; *Turrillot et al.*, 2011], transtensional [*Hutton*, 1982], to transpressional [*McCaffrey*, 1992]. Within deforming continental regions, especially regions where metamorphic core complexes (MCCs) developed, plutonism interacts with processes of strain localization in the crust, and shear zone nucleation and its subsequent development is often coeval with magma crystallization. Precise fieldworks and thermochronological studies have confirmed the spatiotemporal relation between MCC formation and plutonic activity as documented in the Basin and Range Province [e.g., *Crittenden et al.*, 1980; *Wernicke et al.*, 1987; *Gans et al.*, 1989; *Davis et al.*, 1993], the Mediterranean Region [e.g., *Daniel & Jolivet*, 1995; *Jolivet et al.*, 1998; *Acocella & Rossetti*, 2002; *Smith et al.*, 2011], and more recently in East Asia [*Charles et al.*, 2011]. Correlations, in a broad sense, have been particularly documented in the Cycladic islands in the Aegean Sea [*Faure et al.*, 1991; *Lee & Lister*, 1992; *Koukouvelas & Kokkalas*, 2003; *Kumerics et al.*, 2005; *Brichau et al.*, 2007; *Tschegg & Grasemann*, 2009; *Denèle et al.*, 2011; *Kokkalas & Aydin*, 2013; *Laurent et al.*, 2015].

Different causes were inferred to explain these spatial and temporal interactions. It was often suggested that shear zones can create space for magma ascent, while the site of pluton emplacement is controlled by preexisting or active shear zones [e.g., *D'Lemos et al.*, 1992; *Tikoff & Teyssier*, 1992; *Brown*, 1994; *Vigneresse*, 1995a]. An alternative view is that partially crystallized magmatic bodies represent rheologically weak heterogeneities in the crust that may trigger strain localization and shear zone nucleation [e.g., *Lister & Baldwin*, 1993; *Davidson et al.*, 1994; *Tommasi et al.*, 1994]. At the scale of a single magmatic body, how pluton interacts with extensional shear zones is still an open question.

To better understand the feedback relations between processes of shear localization and pluton emplacement that operate during MCC formation, it is necessary to document areas where development of crustal-scale shear zones, metamorphism, and plutonism are shown to be synchronous. The Miocene granodioritic pluton of Serifos [*Altherr et al.*, 1982; *Iglseder et al.*, 2009; *Brichau et al.*, 2010], in the Cyclades (Greece), offers an example of an intrusion contemporaneous with the activity of a detachment system, namely, the West Cycladic Detachment System (WCDS) [*Iglseder et al.*, 2011; *Grasemann et al.*, 2012]. On the basis of a structural fieldwork, together with microstructural and anisotropy of magnetic susceptibility (AMS) data, we describe a strongly asymmetric structure at the pluton scale and a progressive evolution from magmatic to brittle deformation within the magmatic body, kinematically consistent with the dome development and associated detachments. We evaluate (1) the geometrical relations between the Serifos pluton, host rocks, and large-scale detachments and build an original cross section; (2) the distribution of kinematic indicators inside and outside the pluton; and (3) the distribution and evolution of deformation within the pluton during its cooling. This approach leads us to propose a new model of pluton emplacement during crustal extension in interaction with extensional shear zones.

2. Geological and geodynamic setting

2.1. Geology and geodynamic evolution of the Aegean region

The convergence between Africa and the Aegean region is accommodated in the Hellenic subduction zone where the Mediterranean Ridge accretionary complex has developed. Back-arc active extension is restricted to the periphery of the Aegean domain with two regions of fast N-S extension, the Corinth rift and the western part of Turkey [*Eyidoğan & Jackson*, 1985; *Armijo et al.*, 1996; *Hatzfeld et al.*, 2000; *Bozkurt & Sözbilir*, 2004; *Rohais et al.*, 2007; *Aktug et al.*, 2009; *Le Pichon & Kreemer*, 2010]. Slower E-W extension is recorded in the Hellenic arc, southern Peloponnese, and Crete [*Armijo et al.*, 1992; *Jackson*, 1994; *Goldsworthy et al.*, 2002]. In addition to this extension, GPS measurements also record a rigid body motion of the Anatolian Plate, guided by the North Anatolian Fault, which has propagated since 5Ma from the Marmara Sea to the Aegean Sea [*Armijo et al.*, 1999; *McClusky et al.*, 2000; *Reilinger et al.*, 2010; *Pérouse et al.*, 2012].

The current deformation pattern reworks a protracted tectonic history of crustal thickening followed by extensional collapse in the back-arc region of the north dipping Hellenic subduction (see syntheses by *Jolivet & Brun* [2010], *Jolivet et al.* [2013], and references therein). The Cycladic archipelago (i.e., the Cyclades, thereafter), in the central part of the Aegean Sea (Figure III-4a), forms one of the most deeply exhumed parts of the Hellenic belt. Classically, three main units are distinguished in the Cyclades [*Bonneau*, 1984; *Jolivet et al.*, 2004; *van Hinsbergen et al.*, 2005]. From structurally lowest to highest, these units are the following: (1) The Cycladic Basement Unit (CBU) crops out on several Cycladic islands (Naxos, Paros, Ios, Sikinos, and Serifos) [*Andriessen et al.*, 1987; *Grasemann & Petrakakis*, 2007; *Huet et al.*, 2009]. It consists of medium to high-grade rocks (paragneiss and orthogneiss) equilibrated in the amphibolite facies conditions of Variscan or even pre-Variscan age [*Henjes-Kunst & Kreuzer*, 1982; *Andriessen et al.*, 1987; *Keay & Lister*, 2002]. (2) The Cycladic Blueschists, a metasedimentary unit predominantly made up of metapelites and marbles with locally intercalated metabasic rocks. While these rocks preserve a conspicuous high-pressure (H*P*) imprint (i.e., eclogites and blueschists), the overlying (3) Upper Cycladic Unit comprises a continental basement (amphibolites, gneisses) that preserves Late Cretaceous H*T* metamorphic age, topped by ophiolitic material (i.e., serpentinites, gabbros, and basalts) that obducted in the Late Jurassic [*Maluski et al.*, 1987; *Katzir et al.*, 1996].

Two major tectonometamorphic episodes have been recognized in the Cyclades corresponding to two clusters of metamorphic ages [*Altherr et al.*, 1979, 1982; *Wijbrans & McDougall*, 1988; *Bröcker et al.*, 1993; *Ring et al.*, 2010]. A first Eocene episode of crustal thickening was followed by an Oligo-Miocene post-orogenic extension driven by the southward retreat of the African slab from approximately 35 Ma to the present according to *Jolivet & Faccenna* [2000] and *Jolivet & Brun* [2010] or slightly younger (23-19 Ma) following *Ring et al.* [2010]. An earlier extension is also recognized farther north in the Rhodope Massif since 45 Ma [*Brun & Sokoutis*, 2010].

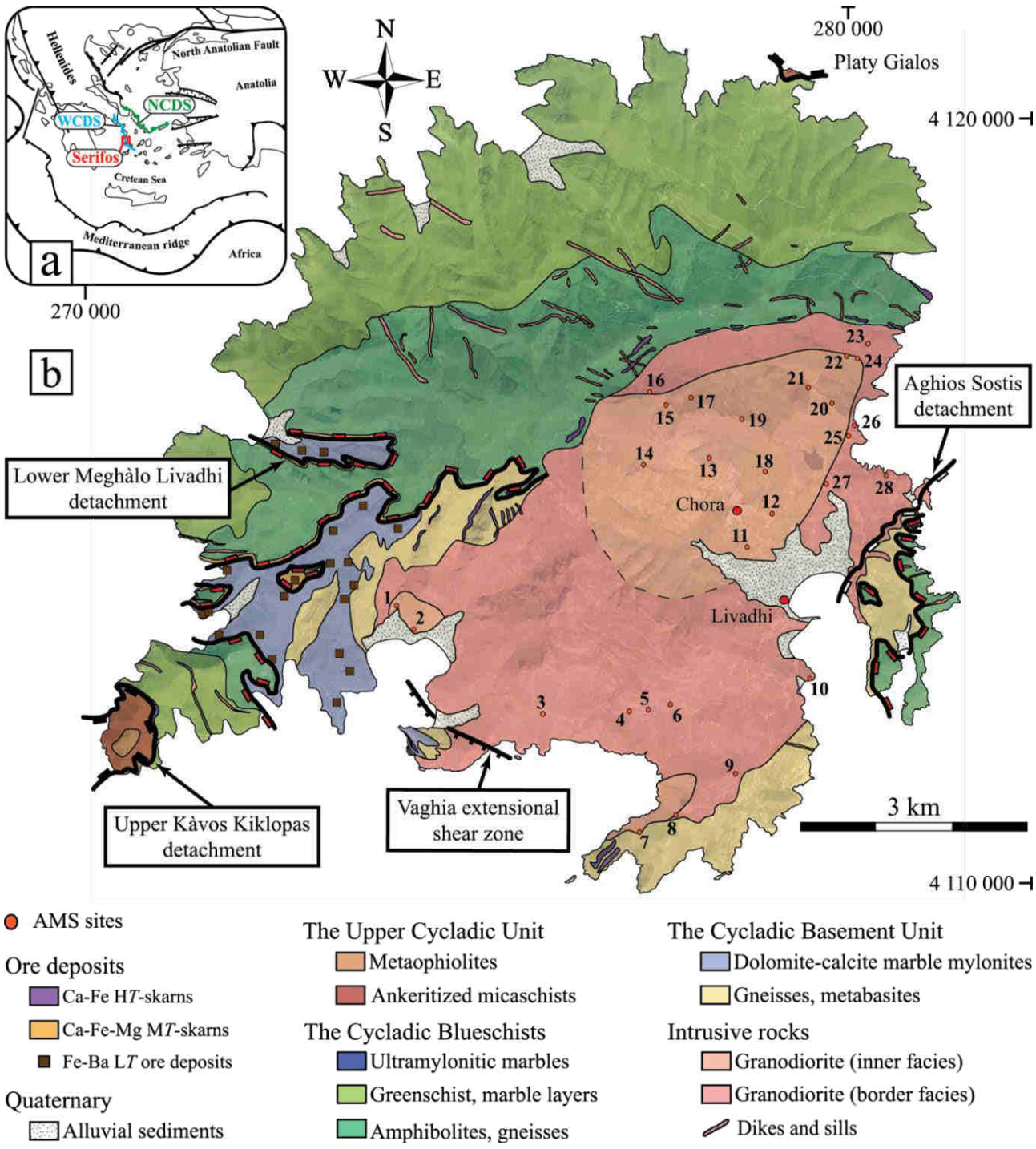

Figure III-4: *(a) tectonic map of the Aegean region showing the main structures, the North Cycladic Detachment System (NCDS), the West Cycladic Detachment System (WCDS), and the location of Serifos Island. (b) Geological map of the studied area (modified after Salemink [1985], Grasemann & Petrakakis [2007], and Petrakakis et al. [2010]) and location of the AMS sites. Coordinates on map are given in UTM zone 35°N, WGS 1984.*

The first episode is associated with high-pressure–low-temperature (H*P*-L*T*) metamorphism under eclogite and blueschist facies conditions [*Trotet et al.*, 2001a, 2001b; *Groppo et al.*, 2009; *Augier et al.*, 2015]. It is largely documented in the Cycladic Blueschists

but poorly recorded in the CBU. Radiometric ages range from 70 to 35 Ma [*Altherr et al.*, 1979; *Maluski et al.*, 1987; *Wijbrans et al.*, 1990; *Bröcker & Enders*, 1999], but most of them cluster between 50 and 40 Ma, in the middle Eocene. This H*P*-L*T* episode has been linked to the burial and the exhumation in the Hellenic subduction zone of the Cycladic Blueschists and the CBU.

The second extensional episode is related to low-pressure–high-temperature (L*P*-H*T*) gradient that affected the two lower Cycladic units. During thinning of the Aegean domain, the Eocene nappe stack was disrupted and MCCs were exhumed below crustal-scale detachments [*Lister et al.*, 1984; *Gautier & Brun*, 1994a, 1994b; *Jolivet et al.*, 1994a; *Gautier et al.*, 1999]. Extension along the north dipping North Cycladic Detachment System (NCDS) [*Jolivet et al.*, 2010; *Lecomte et al.*, 2010] and the south dipping West Cycladic Detachment System (WCDS) [*Iglseder et al.*, 2011; *Grasemann et al.*, 2012] has led to the exhumation of the northern and western parts of the Cyclades, respectively (Figure III-4a). While extension and exhumation were accommodated by detachment systems, I-type granitoids intruded the Aegean crust over few million years (17–9 Ma) [*Altherr et al.*, 1982; *Keay et al.*, 2001; *Bolhar et al.*, 2010]. The Cycladic granitoids crop out on Tinos, Mykonos-Delos, Naxos, Ikaria, as well as on Serifos Island [*Altherr et al.*, 1982, 1988; *Lee & Lister*, 1992]. They were temporally and spatially emplaced in close interaction with Miocene metamorphic domes and associated crustal-scale detachments [*Faure et al.*, 1991; *Lister & Baldwin*, 1993; *Koukouvelas & Kokkalas*, 2003; *Brichau et al.*, 2007, 2008, 2010; *Grasemann & Petrakakis*, 2007; *Denèle et al.*, 2011; *Laurent et al.*, 2015].

2.2. Geology of Serifos Island

Architecture of Serifos Island is described as a MCC [*Grasemann & Petrakakis*, 2007; *Grasemann et al.*, 2012] intruded by an I-type granodiorite that was emplaced above the brittle-ductile transition zone [*Marinos*, 1951; *Altherr & Siebel*, 2002; *Iglseder et al.*, 2009; *Stouraiti et al.*, 2010]. Two main petrographic facies have been recognized within the kilometer-scale Serifos granodiorite (Figure III-4b). The inner facies is described as a fine-grained and equigranular, non-foliated granodiorite, while the border facies is foliated, coarse-grained, and locally contains enclaves [*Salemink*, 1985]. Geobarometry using the total aluminum content of amphiboles from the Serifos pluton suggests emplacement and cooling at shallow crustal levels, around 8–12 km [*Stouraiti & Mitropoulos*, 1999; *St. Seymour et al.*, 2009]. Emplacement age of the main pluton and the associated dikes span over 2 Ma between 11.6 ± 0.1Ma and 9.5 ± 0.1 Ma (U/Pb zircon ages, *Iglseder et al.* [2009]). Cooling ages (K-Ar hornblende age of 9.5 ± 0.3 Ma and K-Ar and Rb-Sr biotite ages of 8.6 ± 0.2 Ma) indicate a rather fast cooling after emplacement [*Altherr et al.*, 1982]. Additionally, *Iglseder et al.* [2009] reported Rb-Sr biotite ages between 8.5 Ma and 7.7 Ma. Furthermore, both zircon and apatite (U-Th)/He ages from the Serifos granodiorite and its host rocks plot between 8 Ma and 5 Ma [*Altherr et al.*, 1982; *Hejl et al.*, 2002; *Grasemann et al.*, 2012], indicating a common cooling history within the brittle crust. *Brichau et al.* [2010] reported slightly older apatite and zircon fission track ages ranging from 13 Ma to 6 Ma.

The late Miocene Serifos pluton has intruded into a sequence of metamorphic rocks that can be subdivided in three distinct units (Figure III-4b). From bottom to top of the tectonic stack, *Grasemann & Petrakakis* [2007] described (1) gneisses and dolomite-calcite marble mylonites of the CBU; metabasite intercalations within gneisses are also identified by *Salemink* [1985]; (2) amphibolites intercalated with gneisses, as well as greenschists intercalated with marbles belonging to the Cycladic Blueschists; and (3) marbles dominated cataclastic lithologies, metabasites, and serpentinites of the Upper Cycladic Unit. These units are separated by two branches of low-angle normal faults belonging to the WCDS [*Grasemann et al.*, 2012]. They show similar NE-SW oriented stretching lineation with top-to-the-SW shear sense [*Grasemann & Petrakakis*, 2007; *Petrakakis et al.*, 2010; *Grasemann et al.*, 2012]. The lower detachment, called Meghàlo Livadhi detachment hereafter, separates the CBU from the Cycladic Blueschists, while the upper one, named Kàvos Kiklopas detachment hereafter, separates the Cycladic Blueschists from the Upper Cycladic Unit. On the basis of thermochronological data, cooling ages obtained on both the Cycladic Blueschists and the CBU range from 15 to 6 Ma (Rb/Sr muscovite ages [*Iglseder et al.*, 2009], $^{40}Ar/^{39}Ar$ ages on muscovite [*Grasemann et al.*, 2012], and zircon and apatite (U-Th)/He ages [*Brichau et al.*, 2010]). Besides, approximately 15–11 Ma ages are ascribed to mylonitization over the Meghàlo Livadhi detachment. Along its western margin, the magmatic body pierces the Meghàlo Livadhi detachment. Furthermore, the eastern margin of the granodiorite is deformed by an additional detachment (Aghios Sostis detachment hereafter) that shows an evolution from ductile to brittle conditions during cooling and exhumation [*Tschegg & Grasemann*, 2009]. While the stretching lineation trends NE-SW with a clear top-to-the-southwest sense of shear along the two detachments, a well-preserved E-W to ENE-WSW oriented stretching lineation with top-to-the west shear sense can be found throughout the CBU and the Cycladic Blueschists. Previous $^{40}Ar/^{39}Ar$ analyses on white micas of the Cycladic Blueschists preserve ages of 38–35 Ma [*Schneider et al.*, 2011], suggesting that the E-W to ENE-WSW trending lineations were the result of an earlier phase of deformation within the western Cyclades, predating the NE-SW directed extension [*Grasemann et al.*, 2012].

3. Large-scale structures in metamorphic host rocks

3.1. Meghàlo Livadhi detachment

3.1.1. Southwestern part of Serifos Island

Meghàlo Livadhi Bay marks the location of the lowermost low-angle normal fault that separates the CBU and the Cycladic Blueschists (Figures III-5a, -6a and -6b). The west dipping detachment evolved from ductile to brittle conditions. At deeper structural levels, dolomite-calcite mylonitic marbles and gneisses belonging to the CBU display an E-W to ENE-WSW trending stretching lineation with consistent top-to-the-W kinematic indicators such as sigma and delta feldspar porphyroclasts [*Grasemann & Petrakakis*, 2007; *Grasemann et al.*, 2012].

About 30m below the Meghàlo Livadhi detachment, a conspicuous top-to-the-SW shearing overprints the earlier top-to-the-W ductile deformation. An overall southwestward and

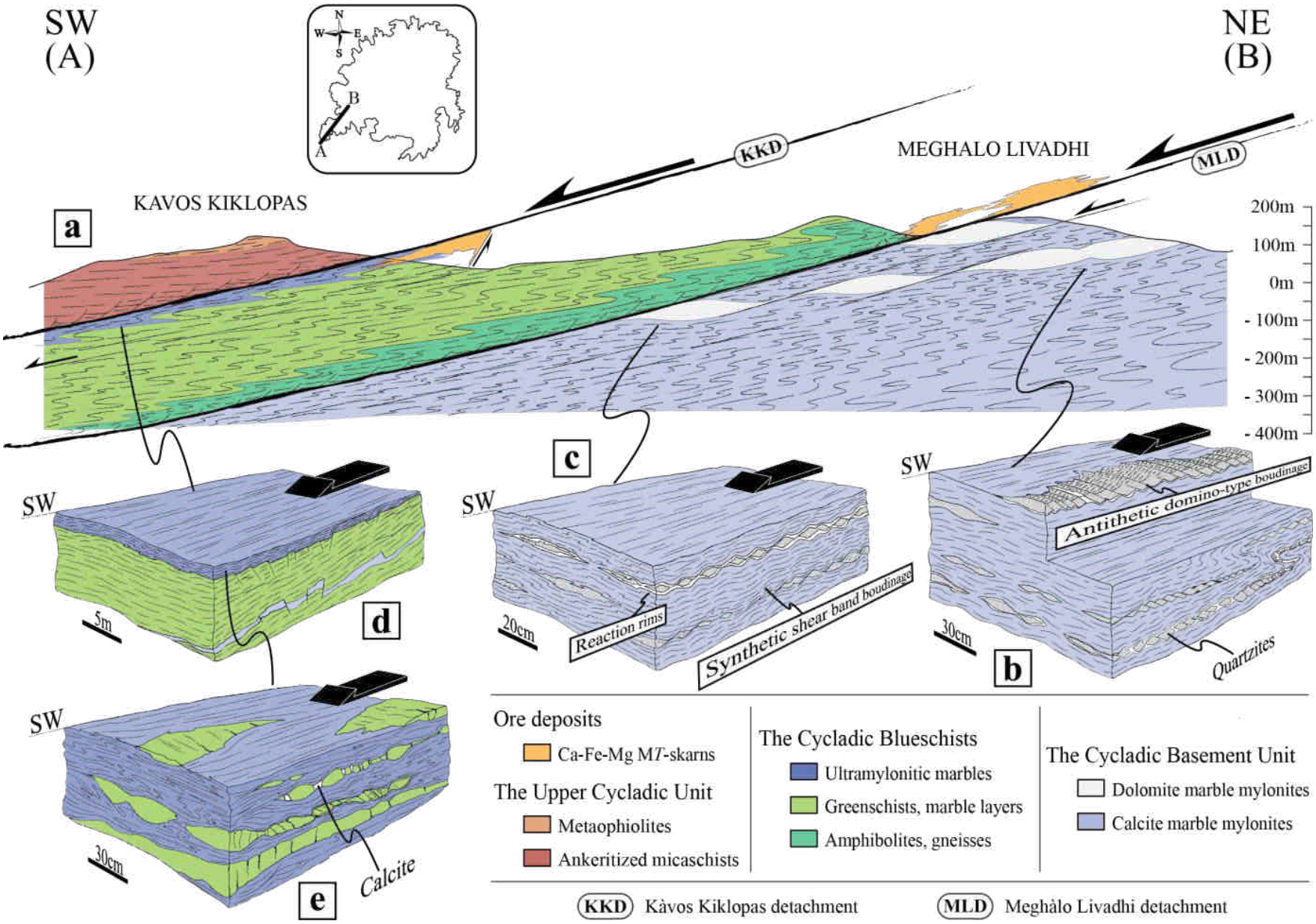
SW
(A)
NE
(B)
N
W
E
S
A
B
KAVOS KIKLOPAS
KKD
MEGHALO LIVADHI
MLD
a
200m
100m
0m
- 100m
- 200m
- 300m
- 400m
c
SW
SW
5m
d
SW
20cm
Reaction rims
Synthetic shear band boudinage
SW
Antithetic domino-type boudinage
30cm
b
Quartzites
30cm
Calcite
e
Ore deposits
Ca-Fe-Mg MT-skarns
The Upper Cycladic Unit
Metaophiolites
Ankeritized micaschists
The Cycladic Blueschists
Ultramylonitic marbles
Greenschists, marble layers
Amphibolites, gneisses
The Cycladic Basement Unit
Dolomite marble mylonites
Calcite marble mylonites
KKD Kàvos Kiklopas detachment
MLD Meghàlo Livadhi detachment

Figure III-5: *(a) structural cross section of the southwestern part of Serifos Island oriented parallel to the stretching direction (A-B, location in the map inset at upper left). This cross section shows the Meghàlo Livadhi detachment and the Kàvos Kiklopas detachment that separate the Cycladic Basement Unit from the Cycladic Blueschists and the Cycladic Blueschists from the Upper Cycladic Unit, respectively. They display similar NE-SW oriented stretching lineation and SW directed shear sense. Extensional shearing is associated with Ca-Fe-Mg MT skarns that involve hydrothermal circulation of fluids during intrusion and cooling of the granodiorite. (b–e) The 3-D block diagrams illustrating field structures related to the stable top-to-the-SW shearing below each detachment (see text for further explanations).*

upward strain gradient can be observed, suggesting the presence of a SW directed crustal-scale shear zone as described by *Grasemann & Petrakakis* [2007] and *Grasemann & Tschegg* [2012]. Quartzites intercalated with dolomite-calcite marble mylonites show an intense boudinage developed under a southwest directed shearing (see 3-D block diagrams in Figures III-5b and -5c), revealed by asymmetric shapes of boudins evolving from antithetic domino-type to synthetic shear band boudinage, and ultimately complete dismembering (classification and terminology after *Goscombe et al.* [2004]). The earlier W to WSW oriented mylonitic lineation can still be recognized directly on the foliation surface of boudins [*Grasemann & Tschegg*, 2012]. The boudinage of quartzite layers is often associated with reaction rims and the growth of talc-tremolite and calcite. These reaction rims thicken in the vicinity of the detachment [*Grasemann & Tschegg*, 2012], suggesting fluid circulations. This hydrothermal activity is also recognized by Fe-Ba L*T* massive and veins deposits, within or perpendicular to the mylonitic foliation.

Toward Cape Psari Myti (4112049°N, 274095°E; the GPS coordinates are given in universal time meridian (UTM) zone 35°N, World Geodetic System (WGS) 1984) and Cape Platini (4111487°N, 274363°E), the CBU crops out; it consists of gneisses with mylonitic marble intercalations and metabasites dipping gently to the SW. A clear stretching lineation trends southwestward with macroscale evidence for top-to-the-SW sense of shear. Sheath folds with NE-SW axes are preserved within mylonitic marbles (Figure III-6c). Metabasites with gneissic intercalations retrogressed under greenschist conditions reveal grains of biotite with fish-like geometries suggesting a consistent top-to-the-SW sense of shear.

The hanging wall of the Meghàlo Livadhi detachment, consisting of amphibolites, shows an extensional deformation that is recognized as a thick zone of cataclastic deformation and high-angle normal faults, indicating a NE-SW direction of extension (Figure III-6d), consistent with shearing of the footwall. Cataclastic amphibolites belonging to the Cycladic Blueschists have also been affected by an intense fluid circulation evidenced by 30m thick zone of breccia-hosted ore deposits composed mainly of hedenbergite, ilvaite, calcite, and quartz (Figures III-6a and -6b). These Ca-Fe-Mg M*T*-exoskarns correspond to a regional level associated to the Meghàlo Livadhi detachment. Interestingly, several mafic and granodioritic sills crop out throughout the southwestern part of Serifos Island (Figure III-6a), especially in the hanging wall of the Meghàlo Livadhi detachment.

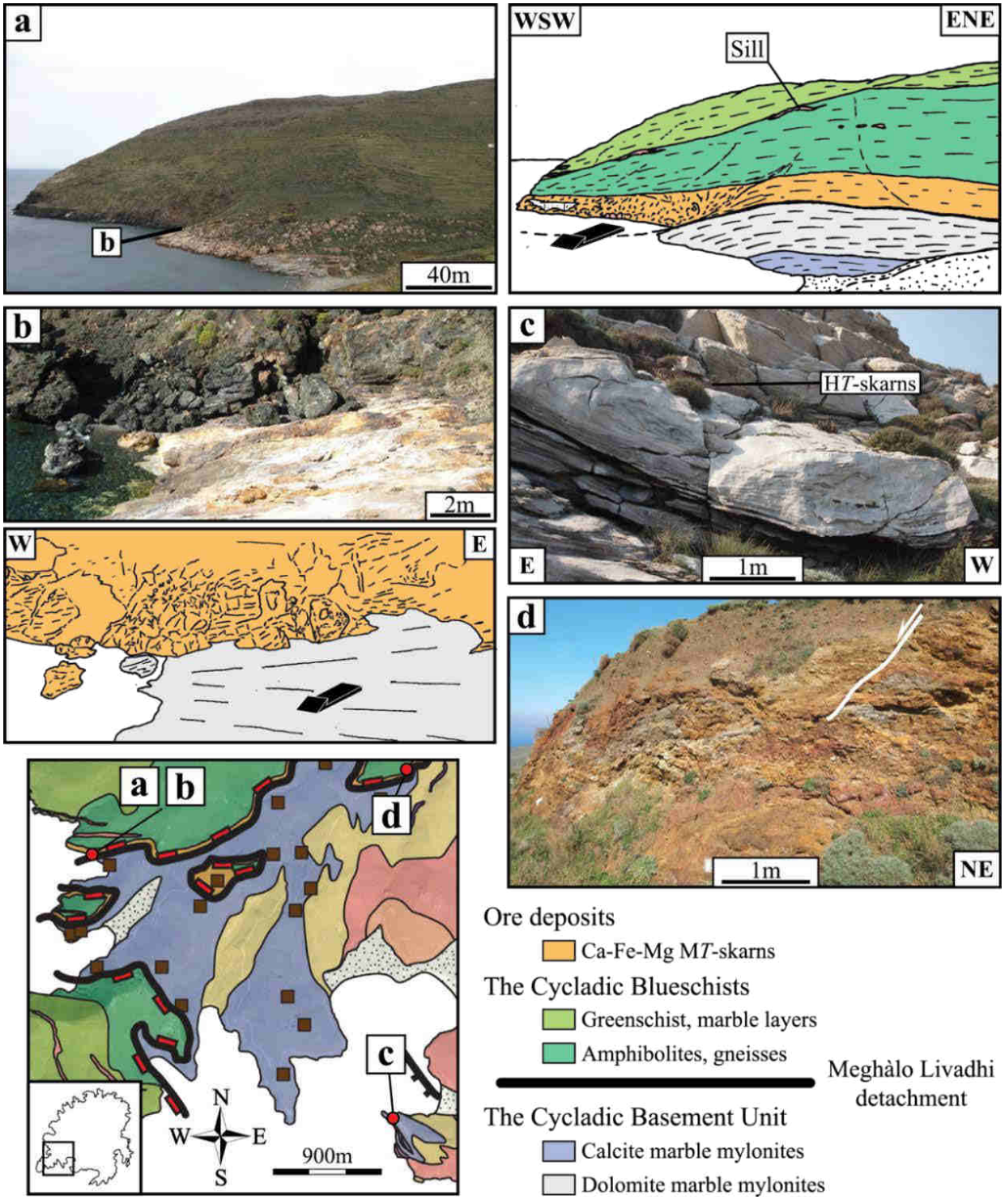

Figure III-6: *photographs related to the lowermost Meghàlo Livadhi detachment in southwestern Serifos (locations in the map inset at lower left). (a) View of the west dipping detachment that separates greenschists and amphibolites in the hanging wall from marble mylonites in the footwall. Amphibolites have been affected by fluid circulation evidenced by 30m thick zone of Ca-Fe-Mg MT skarns. Mafic and granodioritic sills outcrop in the hanging wall of the Meghàlo Livadhi detachment. (b) View of the Meghàlo Livadhi detachment plane. (c) Sheath folds with NE-SW axe within mylonitic marbles near Cape Psari Myti. (d) Cataclastic deformation and high-angle normal faults indicating a NE-SW direction of extension.*

3.1.2. Kéntarchos and Panagia areas

The basal amphibolites-gneisses sequence belonging to the Cycladic Blueschists locally recorded a continuum of deformation from ductile to brittle conditions (Figure III-7a). The succession of deformation events was kinematically compatible with the development of the Meghàlo Livadhi detachment. Near Kéntarchos village (4118317°N, 279447°E), one can indeed recognize intense folding defined by NW-SE fold axes (Figure III-7b), overprinted by gently NE dipping ductile/brittle shear zones. Kinematic indicators indicate a top-to-the-SW shear sense. Continuum of deformation finally evolved to a brittle regime evidenced by a system of conjugate high-angle normal faults, consistent with NE-SW oriented extension.

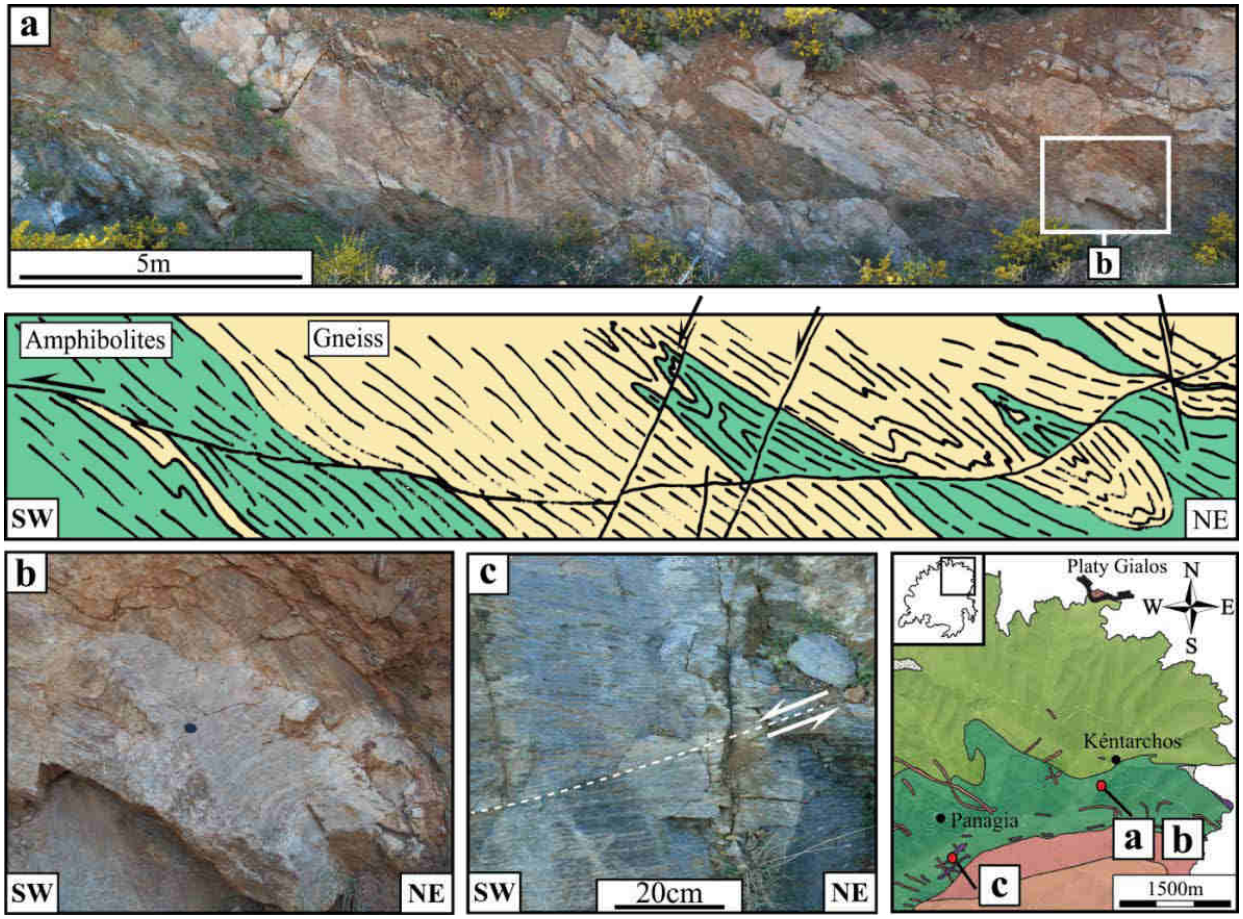

Figure III-7: *photographs of deformation and associated kinematic indicators in the basal amphibolites-gneisses sequence belonging to the Cycladic Blueschists (locations in the map inset at lower right). (a) NE-SW deformation events with a continuum from ductile to brittle conditions. (b) Folding of gneisses defined by NW-SE fold axes. (c) Shear band with a top-to-the-SW sense of shear.*

At deeper structural level, toward the contact with the pluton (Panagia area, 4117548°N, 277015°E), well-preserved ductile deformation has been observed. Gneissic intercalations with amphibolites were intensely deformed with a coaxial component. Mylonitic foliation dips gently northward and carries a NE-SW stretching lineation. Meter-scale shear bands reveal a top-to-the-SW sense of shear (Figure III-7c).

3.2. Kàvos Kiklopas detachment

3.2.1. Southwestern part of Serifos Island

The uppermost branch of the low-angle normal fault system crops out around Kàvos Kiklopas Peninsula (Figures III-4b and -5a). The Kàvos Kiklopas detachment dips 10° westward and separates marbles and micaschists in the footwall from cataclastic ankeritized micaschists in the hanging wall (Figure III-8a). A few meter thick mylonitized marbles belonging to the Cycladic Blueschists crop out directly below the low-angle normal fault and record an intense top-to-the-SW shearing, consistent with the kinematics of Meghàlo Livadhi detachment (see 3-D block diagrams in Figures III-5d and -5e). The greenschists alternating with ultramylonitic marbles were folded, boudinaged, and truncated into isolated fragments (Figure III-5b and 3-D block diagram in Figure III-5e). Brittle fracturing, only observed in the greenschists, provides evidence of rheological contrast between micaschists and alternating marbles, which are more ductile. Metapelites with marble intercalations occur structurally below the ultramylonitic marbles (Figure III-8a). Metamorphic rocks underwent retrograde metamorphism under greenschist-facies conditions and record a top-to-the-WSW shear sense as revealed by shear bands. Locally, the footwall was reworked by brittle high-angle normal faults indicating a late brittle increment of extensional deformation (Figures III-8a and -8b).

Extension in the footwall was thereby accommodated by a localized ductile/brittle deformation supported by few meters thick ultramylonitic marbles associated with top-to-the-SW shear sense, whereas rocks of the hanging wall accommodated extension along high-angle normal faults. Near the southernmost tip of Kàvos Kiklopas Peninsula, a decametric thick zone of ultracataclasites and protocataclasites has developed directly above the detachment (Figure III-5c). Brittle deformation affected ankeritized micaschists belonging to the Upper Cycladic Unit showing a NE-SW extension and a SW directed displacement, compatible with brittle/ductile deformation in the footwall. The ankeritized micaschists are overlain by altered serpentinites and talc-schists that dip gently 10°–15°.

3.2.2. Northeastern part of Serifos Island

The Kàvos Kiklopas detachment between the Cycladic Blueschists and the Upper Cycladic Unit crops out around Platy Gialos Peninsula in the northeasternmost part of Serifos, showing a well-exposed section of this brittle-ductile low-angle normal fault dipping 12°–15° northeastward (Figure III-9).

The footwall consists mainly of greenschists/calcschists with metaconglomerate intercalations and ultramylonitic marbles at the top of the unit, similar to the southern outcrops. The whole sequence records a gradient in shearing as well as a progressive rotation of the stretching direction when approaching the detachment. At deeper structural level, carbonate stretched pebbles in a metaconglomerate show a prolate shape with an E-W long axis, evolving toward a conspicuous ENE-WSW trending lineation and a subsequent striation toward the brittle detachment plane. Kinematic indicators show a top-to-the-WSW shear sense (Figure III-9a).

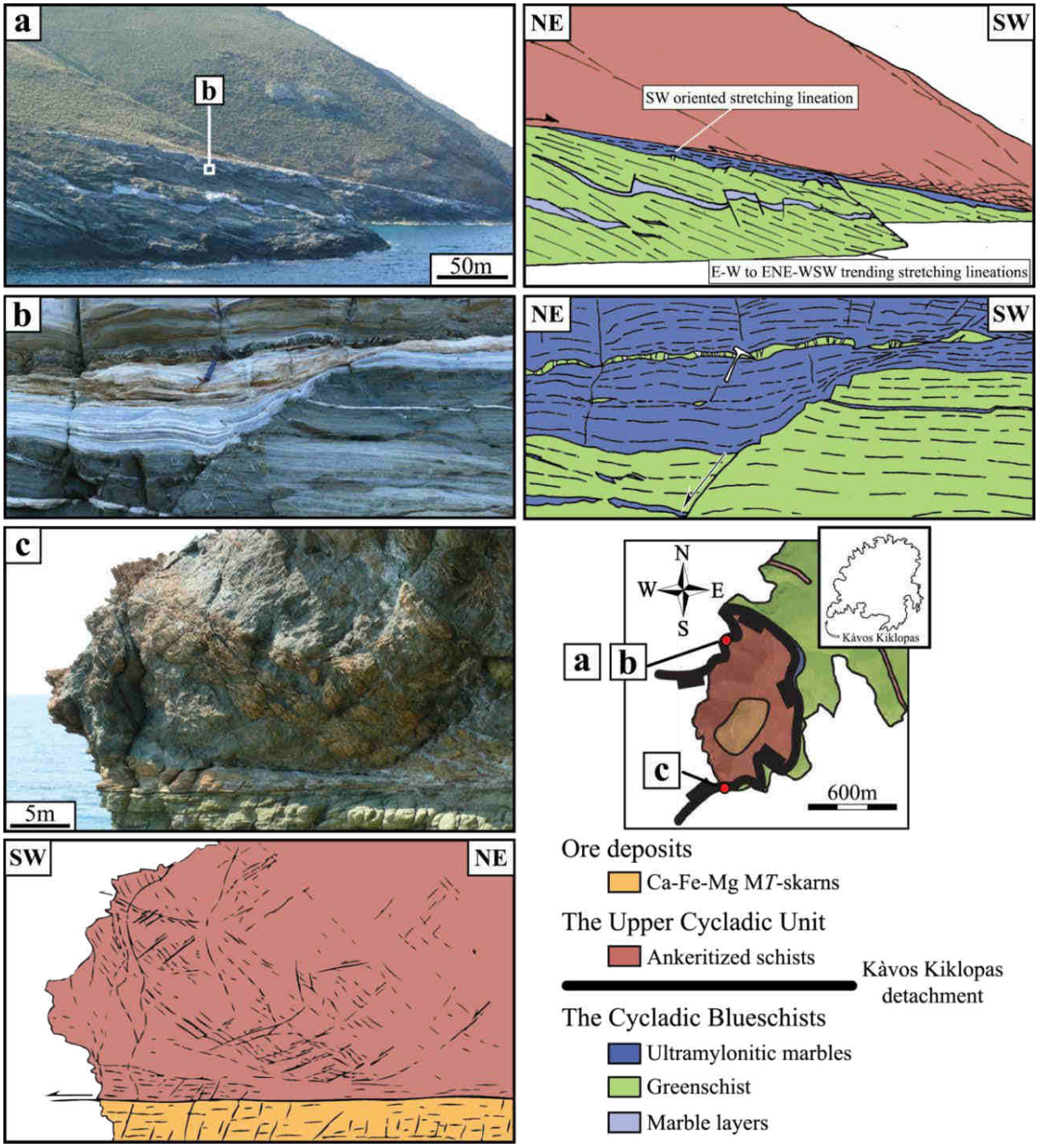

Figure III-8: *photographs of the uppermost Kàvos Kiklopas detachment in southwestern Serifos (locations in the map inset at lower right). (a) View of the west dipping detachment that separates marbles and micaschists in the footwall from cataclastic ankeritized schists in the hanging wall. (b) Greenschists with mylonitized marbles just below the Kàvos Kiklopas detachment. (c) View of the Kàvos Kiklopas detachment. Brittle deformation affects ankeritized micaschists belonging to the hanging wall (the Upper Cycladic Unit) with NE-SW extension and a southwest directed displacement.*

Directly below the detachment plane, a few meters thick ultramylonitic marbles are observed (Figures III-9b and -9c); they show intense intrafolial folding and a SW-NE oriented stretching lineation. These ultramylonitic marbles are separated from a thick zone of cataclasites by a low-angle normal fault (Figures III-9b and -9c). Outcrops of the detachment

plane show an intense striation parallel to the stretching lineation in the underlying ultramylonitic marbles (Figure III-9c). The detachment plane is overlain by a centimeter thick of detachment gouge and ultracataclasites of graphitic schists, marbles, and calcschists (Figure III-9b). The whole sequence belonging to the Upper Cycladic Unit records brittle extensional structures with SW directed displacement, consistent with the brittle-ductile deformation of the ultramylonitic marbles. Furthermore, both hanging wall and footwall record a component of subhorizontal shortening, perpendicular to the shearing direction, resulting in box-shaped folding of the penetrative fabric (Figure III-9c).

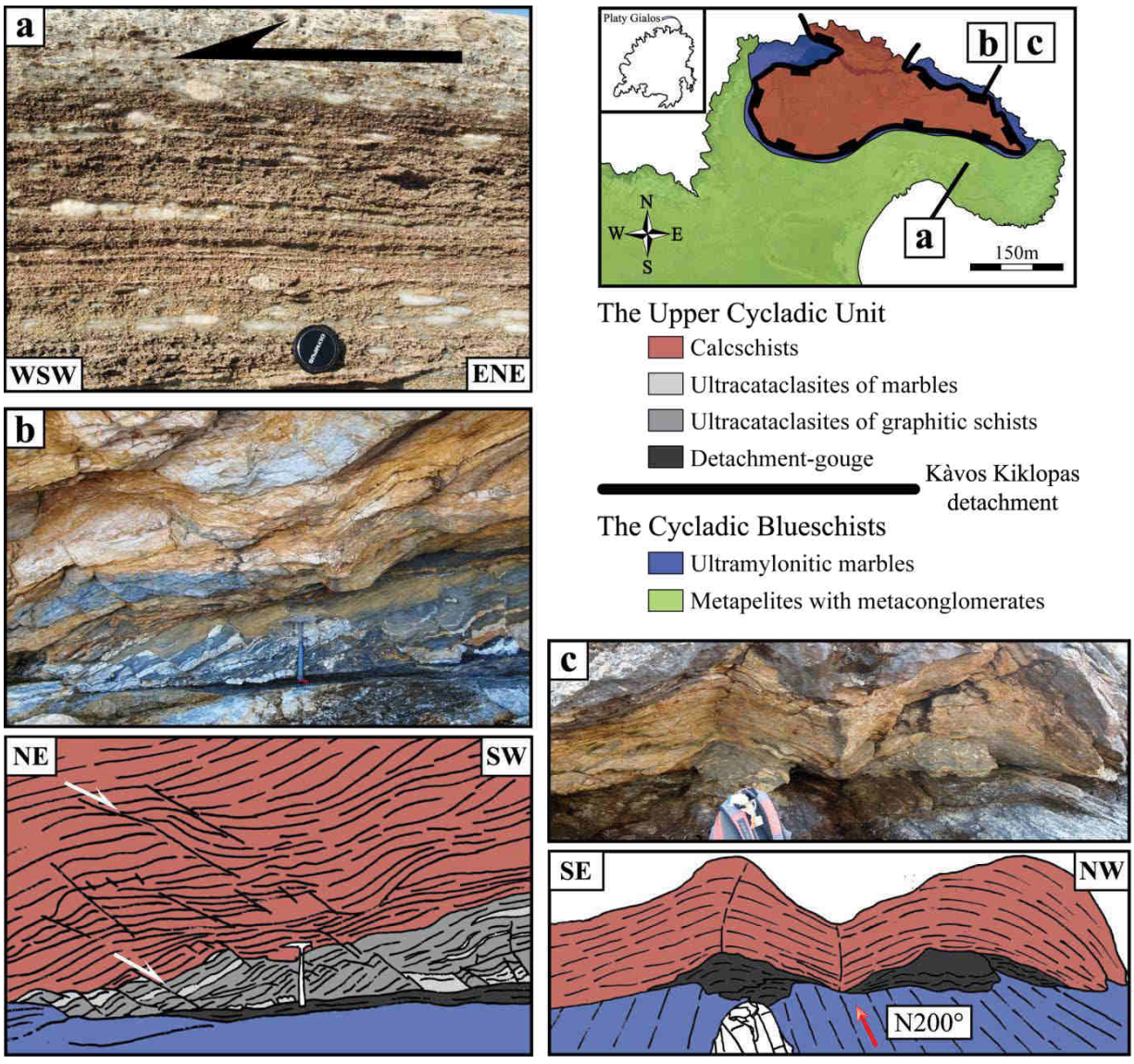

Figure III-9: *Kàvos Kiklopas detachment in northeastern Serifos (Platy Gialos peninsula; location in the map inset at upper right). The footwall consists of metapelites with metaconglomerate intercalations and ultramylonitic marbles at the top of the unit (the Cycladic Blueschists). The hanging wall consists of calcschists belonging to the Upper Cycladic Unit. (a) Carbonate stretched pebbles in a metaconglomerate showing a top-to-the-WSW shear sense. (b) Thick zone of cataclasites in the hanging wall with SW directed displacement. (c) View of the Kàvos Kiklopas detachment plane showing a NE-SW striation parallel to the stretching lineation in the underlying ultramylonitic marbles.*

4. Field observations in the Serifos granodiorite

4.1. Mesoscopic fabrics and field structures

In order to characterize the mesoscopic fabric pattern of the Serifos granodiorite and the kinematic of its deformation, we performed a detailed structural fieldwork. Fabric is usually well developed in the southwestern and eastern border facies, whereas the northern border facies and the inner facies reveal either a weak or indiscernible mesoscopic fabric. Importantly, transitions between these facies are gradational, and no sharp contact was observed. Foliation is defined by the shape-preferred orientation of biotite flakes. Orientation of the lineation trajectories is based on the measurements of elongation of amphibole grains. Our own measurements of foliation and associated lineations are presented in Figures III-10a and -10b.

4.1.1. Southern margin

The border facies outcropping in the southern contact of the intrusive body reveals a strongly prolate fabric. Even if foliation is difficult to discern macroscopically, biotite flakes dip very gently 10°–15° southeastward and strike NE-SW, roughly parallel to the pluton margin (Figure III-10a).

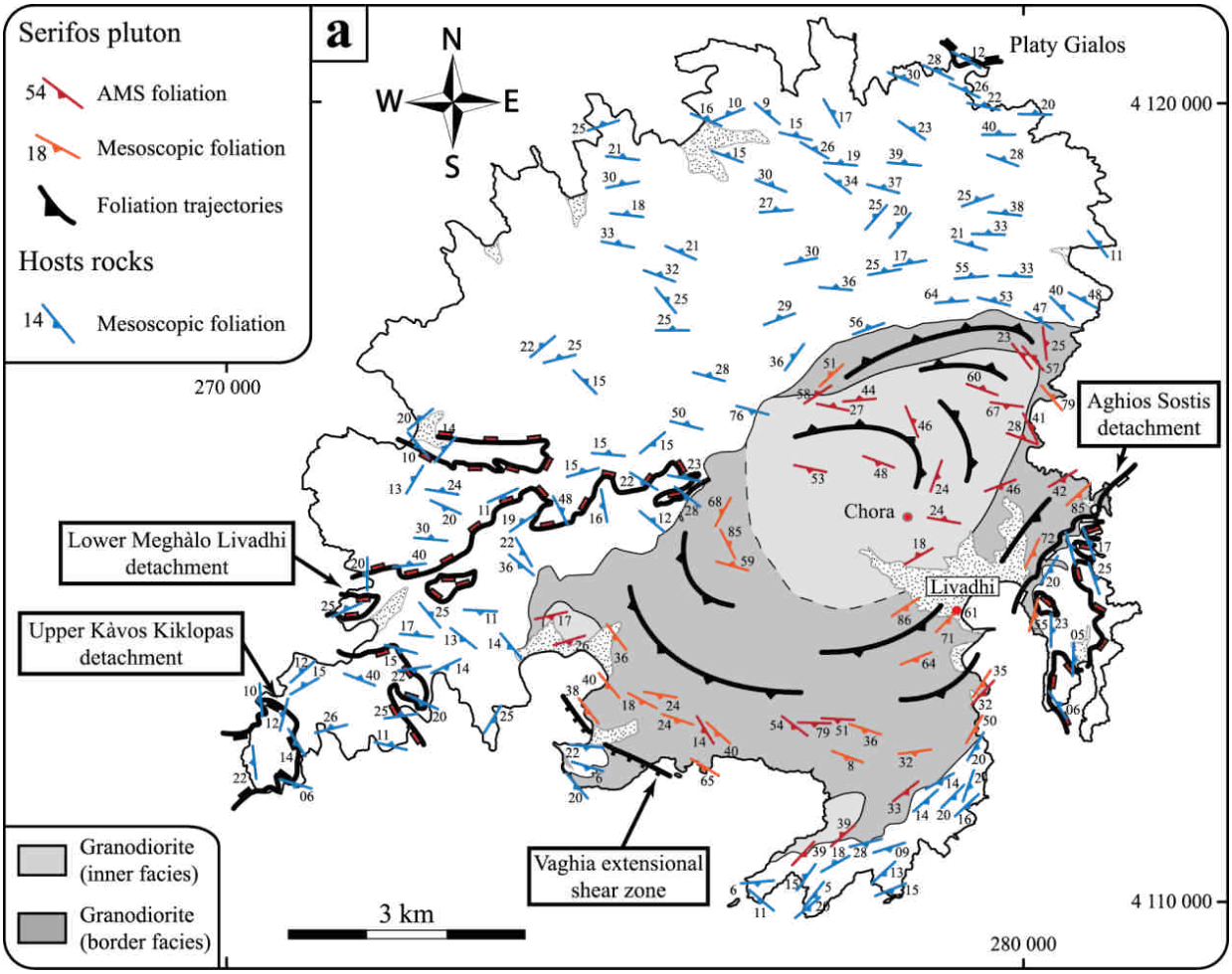

(continued)

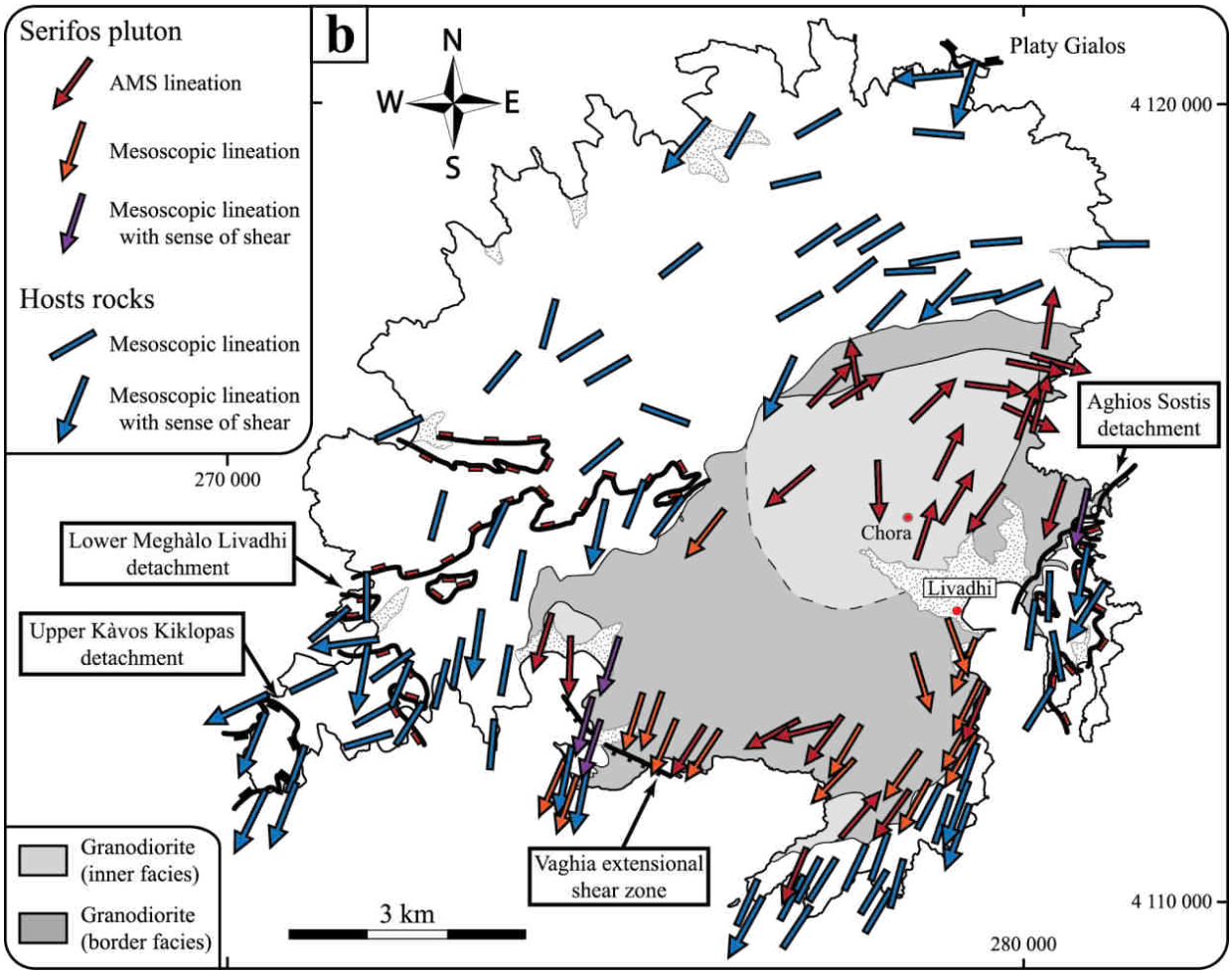

Figure III-10: *structure and finite strain maps of the studied area. (a) AMS foliations and mesoscopic foliations. (b) AMS lineations and mesoscopic lineations.*

When amphibole can be distinguished, the lineation is marked by the direction of its [c] axis, and it trends southwest-northeast (Figure III-10b). Interestingly, the fabric becomes steeper northward (60° to 85°) with subvertical lineations, especially in the sector of Chora/Livadhi (Figures III-10a and -10b).

4.1.2. Southwestern margin

In Koutalas-Vaghia Bay (Figures III-4b and -10), the border facies exhibits an apparent stronger fabric than the southern margin of the pluton. As described in the southern margin, the border facies displays an oblate fabric (Figures III-10a and -10b). While foliation is more easily discernible and dips 20°–40° southwestward, lineation outlined by amphibole grains plunges systematically 20°–30° southwestward. Close to the contact with host rocks, the border facies was affected by the development of an extensional shear zone that partially overprinted the earlier SL fabric. Field observations show a widespread consistent NE-SW direction of stretching. Evidence of ductile deformation and top-to-the-southwest shearing is especially

provided by the development of mica fish (classification and terminology after *Lister & Snoke* [1984], *ten Grotenhuis et al.* [2003] and *Mukherjee* [2010]) (Figure III-11a; 4112280.66°N, 274603.87°E). Furthermore, the south-western pluton was affected by a network of ductile/brittle high-angle normal faults showing NE-SW oriented extension (Figure III-11b; 4113557.64 °N, 274771.51°E).

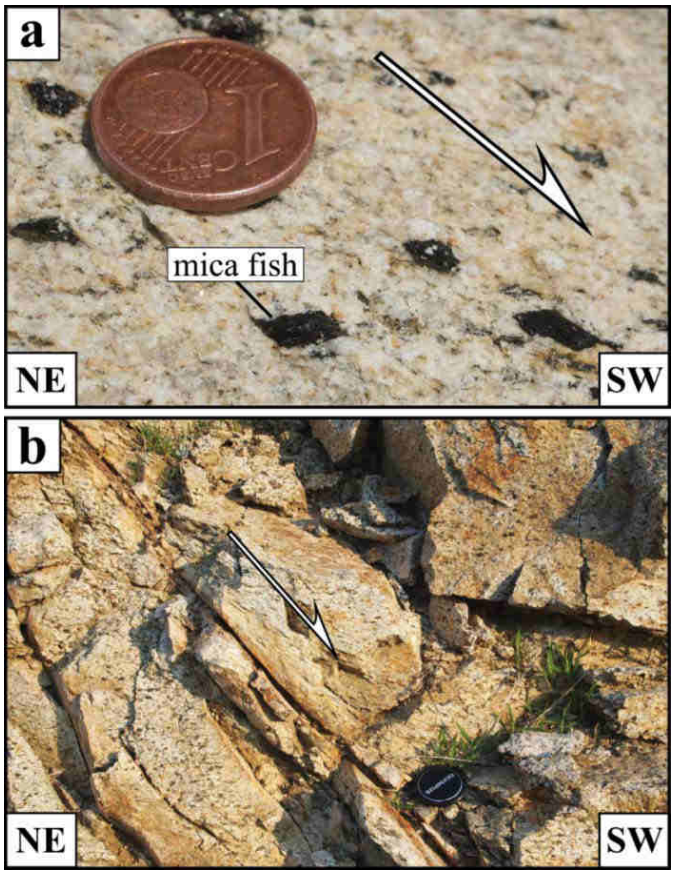

Figure III-11: *photographs showing structural observations in the southwestern margin of Serifos pluton (border facies). (a) Development of mica fish with top-to-the-SW shearing (4112280.66°N, 274603.87°E). (b) Ductile/brittle high-angle normal fault (4113557.64°N, 274771.51°E).*

4.1.3. Eastern margin

The apparent strongest deformation was recorded at the eastern margin of the Serifos pluton, toward Aghios Sostis Peninsula (Figures III-4b, -10a and -10b). This zone corresponds to the development of a SE dipping low-angle normal fault that separates ultramylonitic granodiorite in the footwall from strongly bleached granodiorite in the hanging wall, as described by *Grasemann & Petrakakis* [2007] and *Tschegg & Grasemann* [2009].

The footwall records a southeastward and upward gradient of shearing, suggesting the presence of a ductile shear zone. Particularly, mesoscopic observations show a progressive transition from weakly deformed granodiorite at deeper structural level to an ultramylonitic fabric in the vicinity of the detachment. A conspicuous stretching lineation trends to the southwest in the whole sequence. SC′ fabric, mica fish clasts, and "tiling" of biotite flakes indicate homogeneously a top-to-the-SW sense of shear. Furthermore, up to decimeter thick synthetic and antithetic shear bands separating ultramylonitic granodiorite from less strongly deformed granodiorite can be also observed. This anastomosing network of ductile shear bands nucleated along brittle precursor joints indicates a top-to-the-SW sense of shear [*Tschegg & Grasemann*, 2009]. Structural field observations provide a gradual change of foliation directions within structurally deeper granodiorite. Approaching the detachment, the SL fabric evolves from steeply W dipping foliation to gently SE dipping foliation, which is consistent with a top-to-the-SW sense of shear. However, at the deepest structural level, the shape-preferred orientation of biotite defines a weak foliation steeply dipping to the SSE, suggesting an S fabric apparently incompatible with the top-to-the SW shear sense. This fabric could thus correspond to an earlier fabric, partially preserved since shear zone nucleation.

The hanging wall granodiorite above the detachment recorded completely different metamorphic, structural, and geochemical evolution (for more details, see *Tschegg & Grasemann* [2009]). This granodiorite recorded a weak deformation under greenschist facies and was strongly bleached reflecting metasomatic-hydrothermal activity. The Aghios Sostis Peninsula was then crosscut by a NW-SE striking, high-angle normal fault, indicating ongoing NE-SW oriented extension.

4.2. Enclaves and syn-plutonic dikes

The Serifos granodiorite, especially the border facies, contains abundant enclaves and synplutonic dikes. On the basis of field observations, one can distinguish isolated enclaves, monogenic/polygenic swarms of enclaves, dike-like monogenic swarms, and undisturbed or partially disaggregated dikes. Isolated enclaves will not be described in this study.

4.2.1. Swarms of enclaves

Monogenic swarms are mainly disseminated throughout the southern margin of the Serifos pluton. The term "swarm" is used to describe areas in the intrusion where enclaves are most abundant and are separated by the minimal amount of host material. In the field, variable sizes of enclaves occur, cropping out from decimeter size to decameter size. Their shapes display a wide range of morphologies, most frequently tapered but sometimes angular. Contacts with the host granodiorite are commonly lobate (Figure III-12a), suggesting a relatively low viscosity contrast among the involved magmas [e.g., *Sparks & Marshall*, 1986; *Vernon et al.*, 1988; *Tobisch et al.*, 1997; *Paterson et al.*, 2004; *Barbarin*, 2005]. Moreover, mineral fabric of enclaves appears systematically sub-parallel to principal fabric within the granodiorite, trending N20° to N30° (Figure III-12a). At some localities, polygenic swarms of enclaves are exposed. The best representative example is located at Koutalas-Vaghia Bay, where the footwall of a sill intruding the host mylonitic marble contains a polygenic swarm (4111848.86°N, 274196.41°E). Enclaves mostly have diffuse contacts and consist of dioritic enclaves and melanocratic to mesocratic enclaves. They have either ellipsoidal or random shapes and are often elongated parallel to the NE-SW stretching direction observed in the granodiorite.

4.2.2. Syn-plutonic dikes

Synplutonic dikes have been especially observed at the pluton rim where all the intermediate stages between undisturbed dikes and dike-like monogenic swarms are found. The southernmost granodiorite was abundantly intruded by undisturbed mafic/felsic dikes, particularly extensive sets of leucocratic/dioritic dikes crosscutting swarms of enclaves (Figure III-12a). Contacts between these dikes and the enclosing granodiorite remain sharp and straight. Toward Koutalas-Vaghia Bay, where an extensional shear zone has developed, NW-SE to WNW-ESE trending dioritic/aplitic dikes are sometimes affected by antithetic top-

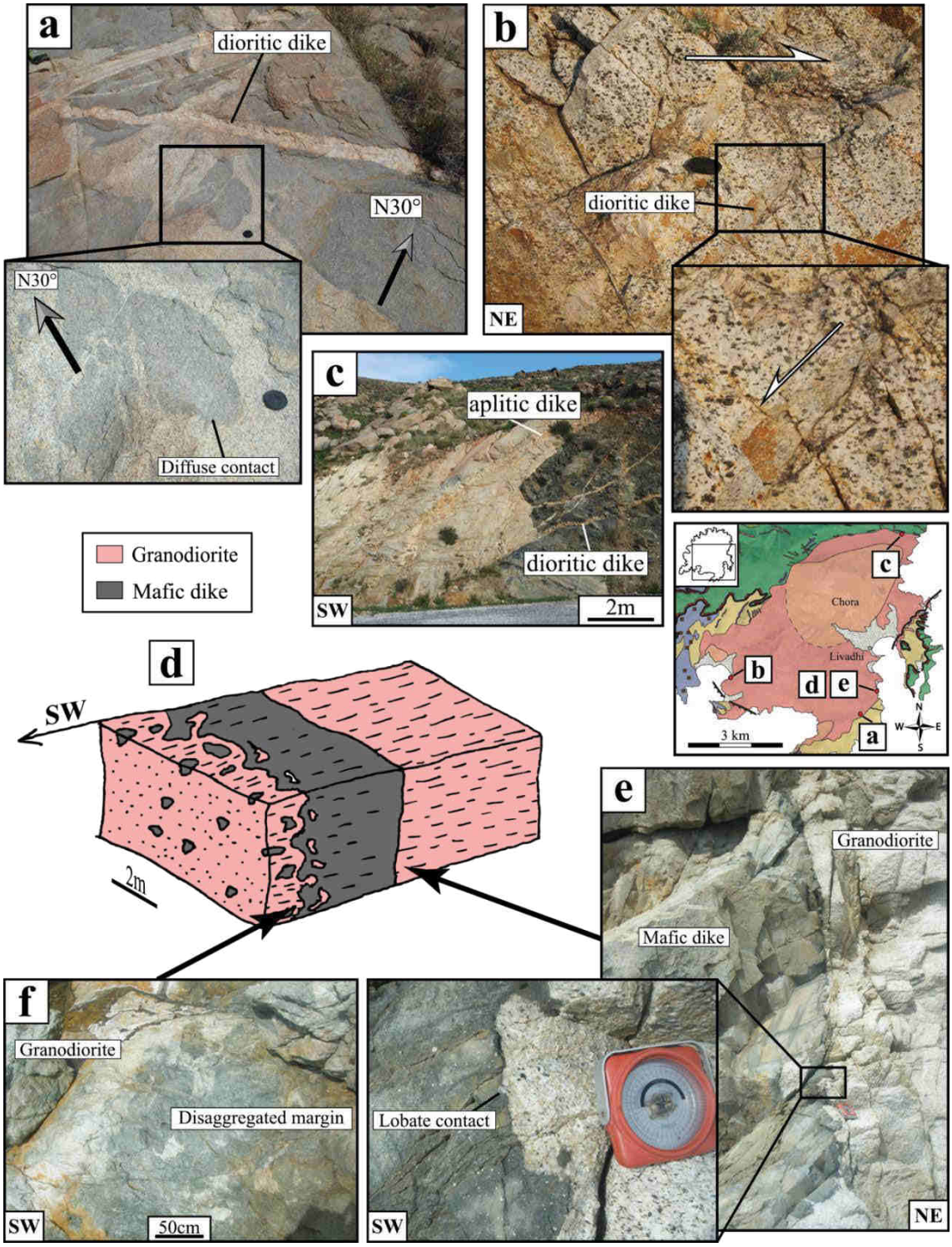

Figure III-12: *Photographs and 3-D block diagram of swarms of enclaves and synplutonic dikes. (a) Example of Monogenic swarm located at the southern rim. Note that mineral fabrics of enclaves are subparallel to the host granodiorite fabric. Dioritic dikes crosscutting swarm can also be observed. (b) NW-SE striking dioritic dike affected by an antithetic top-to-the-SW shearing (4113360.04°N, 274884.10°E). (c) Intrusive contact with host rocks at the northeastern part. Note that dioritic/ aplitic dikes have the same orientation as NW-SE striking brittle high-angle normal faults. (d) The 3-D block diagram showing a vertical partially disaggregated mafic dike; its margins are submitted to heterogeneous mingling. (e) Northeastern margin of the partially disaggregated mafic dike. (f) Southwestern margin of the partially disaggregated mafic dike.*

to-the-SW shearing (Figure III-12b; 4113360.04°N, 274884.10°E). On the other hand, in the northern pluton margin, some dioritic/aplitic dikes crosscut the marginal coarse-grained facies that follow roughly NW-SE striking brittle high-angle normal faults (Figure III-12c).

Dike-like monogenic swarms of enclaves crop out near Vaghia Bay (4112308.43°N, 274586.41°E). This sector shows swarms that resemble disaggregated mafic dikes within partially crystallized host magma. The dike-like monogenic swarms are a few tens of meters wide with commonly rectilinear borders.

Among synplutonic dikes, some of them have locally fine-grained disaggregated margins where thermal contrasts between the two magmas appear relatively weak. An outcrop to the east of Rammos village reflects an interesting example of a partially disaggregated synplutonic dike. This NW-SE striking mafic dike, a few meters wide, has intruded vertically the granodioritic host rock (Figure III-12d). Its margins show heterogeneous mingling. Its northeastern margin display lobate contacts with the enclosing host granodiorite (Figure III-12e), whereas its southwestern margin is disaggregated in enclaves formed by synmagmatic mingling (Figure III-12f).

4.3. Late brittle structures

Structural fieldwork allowed us to identify the geometry of the fault network and associated kinematics. Measurements of small-scale fault planes and their kinematic indicators were carried out at several sites of the granodiorite (Figure III-13a). At map scale, this study indicates that Serifos granodiorite is predominantly dominated by sets of WNW-ESE striking conjugate high-angle normal faults. Measured striae indicate a NE-SW component of extension.

Furthermore, the Serifos granodiorite is crosscut by a network of fractures, previously well documented by *Lambrakis et al.* [2000]. At map scale, two sets of fractures can be distinguished (Figure III-13a). NW striking fractures mostly crosscut the northeastern part (Figure III-13b), whereas the southwestern part of Serifos granodiorite is mainly affected by NE-SW and E-W striking fractures (Figure III-13c). These two sets of fractures are spatially divided by a major kilometer-scale length brittle structure which trends NW-SE. In detail, this major brittle structure contains a considerable amount of spaced joint systems along which the granodiorite was completely bleached by fluid circulation.

Along the northern margin, several centimeter- to decimeter-sized fracture systems crosscut the undeformed border facies of the granodiorite. Figure III-13d includes a cross section of typical fracture systems observed in this sector. Four kinds of fractures can thus be distinguished corresponding to either spaced joints or conjugate normal faults to dextral strike-slip faults along which fluids have bleached the magmatic rock in a zone of up to several centimeters wide. They are usually filled with chlorite, epidote, and carbonates. Even if some of them are steeply dipping and others are shallow dipping, their slickensides trend approximately NW-SE with NNE-SSW trending extensional component (Figure III-13d).

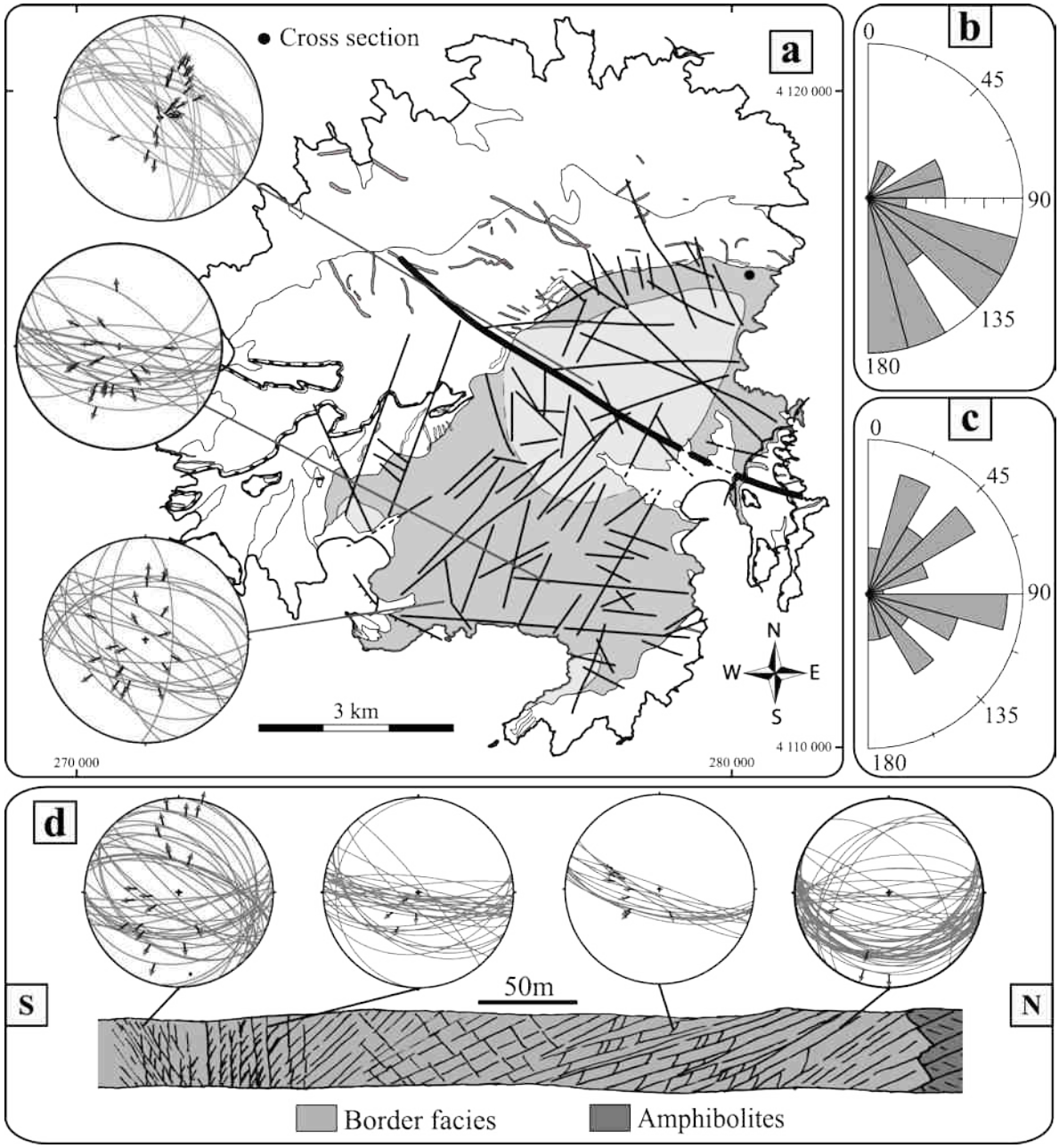

Figure III-13: *brittle structures in Serifos pluton. (a) Tectonic map showing steep fractures (modified after Lambrakis et al. [2000]) with stereonets of macroscale fault planes and their kinematic indicators. (b and c) Stereonets showing two sets of fractures. (d) Cross section in northeastern Serifos margin showing typical fracture systems observed in this sector.*

5. Microstructure and anisotropy of magnetic anisotropy in the Serifos granodiorite

5.1. Microstructural observations

Microstructural investigations within syntectonic plutons provide insights about the history of a continuous deformation developed during pluton cooling and its subsequent

unroofing [*Paterson et al.*, 1989]. This method also gives useful information as to how both mesoscopic and magnetic fabrics should be interpreted (see section 5.2 for AMS measurements). In this sense, a microstructural analysis was performed in some key outcrops of the Serifos granodiorite except along the Aghios Sostis detachment where a detailed microstructural study was already performed by *Tschegg & Grasemann* [2009]. Microstructural features of typical investigated samples are summarized in Figure III-14.

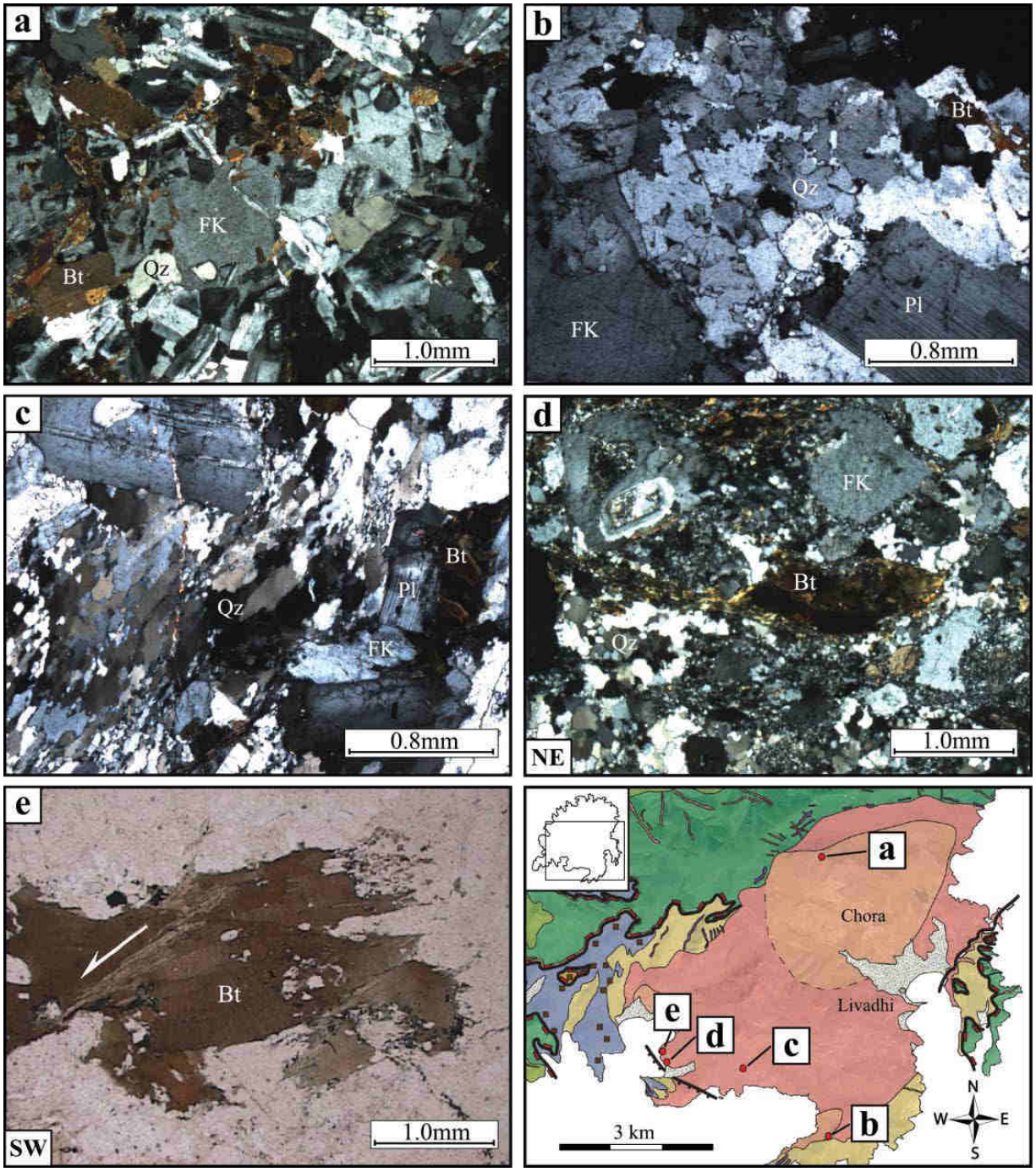

Figure III-14: *microstructural features of typical investigated samples within the Serifos pluton (sample locations in the map inset at lower right), see explanation in the text for more details. Bt = biotite, Kf = K-feldspar, Pl = Plagioclase, Qz = quartz.*

In the northern and central parts of the Serifos pluton, both fine-grained and coarse-grained facies display magmatic microstructures without any significant solid-state overprint (Figure III-14a). Mineral phases are usually uniformly dispersed, and some weak undulatory extinction in anhedral, interstitial quartz grains is quite common. Late brittle fracturing can be also observed, as in the whole pluton. At the southern margin of the plutonic body, a moderate-preferred orientation of biotite is observed. In thin sections, some biotite flakes appear to be undeformed, whereas others are slightly bent and/or locally kinked. Amphibole grains show scarce evidence of deformation, having sharp or slight undulose extinction. Quartz with undulatory extinction and irregular grain boundaries are commonly found, together with smaller independent new grains (Figure III-14b).

Approaching the southwestern margin, where an extensional shear zone has developed, microfabric intensity significantly increases. Bending, strong kinking, and recrystallization are particularly common in biotite flakes. Polycrystalline quartz aggregates with irregular grain boundaries recorded a widespread recrystallization by subgrain rotation or grain boundary migration (Figure III-14c). K-feldspar and plagioclase grains locally display narrow recrystallized mantle. K-feldspar can also exhibit marginal replacement by myrmekite [*Simpson & Wintsch*, 1989; *Vernon*, 1991]. Toward Koutalas-Vaghia Bay, thin sections reveal a significant grain size reduction of all mineral phases (Figure III-14d). Biotite is subjected to large ductile deformation and partial to complete transformation to aggregates. Mica fish are common and record consistently a top-to-the-SW sense of shear (Figure III-14e). Nucleation and growth of new quartz and feldspar grains occur widely, visible in thin section, e.g., by the development of new fine-grained feldspar around cores of old grains (Figure III-14d).

5.2. Anisotropy of magnetic susceptibility

5.2.1. Methodology: sampling and measurements

Anisotropy of magnetic susceptibility (AMS) describes parameters of the magnetic susceptibility ellipsoid. Magnetic fabrics are then often used to complement structural data recorded in the field in weakly deformed rocks and in localities where no mesoscopic features are observed [e.g., *Bouchez et al.*, 1990; *Archanjo et al.*, 1994; *Benn et al.*, 2001]. As the mesoscopic fabric is generally cryptic within the inner facies, we use AMS (for reviews and basic principles of the method, see, e.g., *Borradaile & Henry* [1997], *Bouchez* [2000], *Borradaile & Jackson* [2010]) to reveal faint anisotropies in granodiorite subjected to imperceptible tectonic imprints. We also use AMS to compare with field data within the border facies.

A total of 28 sampling sites were drilled in the Serifos granodiorite: 15 sample sites in the inner facies and 13 in the border facies (see Figure III-4b for locations). At each site, 3 to 14 samples (cylinder-shaped cores) were analyzed. Anisotropy of magnetic susceptibility was measured with a kappabridge susceptometer [*Jelínek & Pokorný*, 1997] at Institut des Sciences de la Terre d'Orléans (ISTO). A statistical analysis of the AMS data was carried out using the ANISOFT package of programs [*Jelínek & Kropáček*, 1978; *Hrouda et al.*, 1990].

Furthermore, in order to understand the geological significance of these measured magnetic fabrics, the identification of the main carriers that contribute to the magnetic signal was undertaken. The magnetic mineralogy was investigated with the following methods: (1) the mean magnetic susceptibility (K_m), (2) thermomagnetic measurements (K(T) curves), and (3) hysteresis loops. Thermal magnetic experiments were performed at Institut des Sciences de la Terre d'Orléans (ISTO, France) using a kappabridge susceptometer coupled to a CS3 furnace and a pump-assisted cooling system. Samples were heated from room temperature to 700°C and subsequently cooled down to 40°C. Resulting K(T) curves were treated with Cureval 8 software (AGICO). Magnetic hysteresis loops were obtained with a homemade magnetic inductometer at Institut de Physique du Globe de Paris (Saint-Maur, France).

5.2.2. Magnetic mineralogy

Figure III-15a shows the distribution of the mean magnetic susceptibility (K_m expressed in μSI) deduced from the laboratory measurements of the 28 sampling sites. K_m displays a rather large range of values, from 203 μSI to 21,200 μSI. At first glance, a broad correlation between petrographic facies type and K_m variations can be observed, with higher Km values from the granodioritic border facies (5690 μSI to 21,200 μSI) than those to the inner facies (230 μSI to 8240 μSI). Interestingly, all measurements within the border facies exhibit Km values larger than 5000 μSI, a threshold beyond which the effect of paramagnetic contribution can be considered insignificant in granitic rocks [e.g., *Hrouda & Kahan*, 1991]. This implies a ferromagnetic behavior with the presence of magnetite-type minerals as main carriers of AMS. In contrast, K_m measurements from the inner facies define a more complex distribution: (1) 20% of sampling sites reveal a K_m less than 500 μSI, usually attributed to the paramagnetic contribution such as Fe-bearing silicates [e.g., *Rochette et al.*, 1992; *Bouchez*, 2000]; (2) 20% with a ferromagnetic contribution (K_m>5000 μSI); and (3) 60 % of these sites fall in the K_m range of 500–5000 μSI, suggesting a combined effect of both ferromagnetic and paramagnetic minerals.

In addition, thermomagnetic measurements widely reflect multimineral contributions. The resulting K(T) curves can be ranked in three different groups according to the heating curve geometry. From the higher to the lower Km value, one can recognize (1) heating curves with a sharp drop of the magnetic susceptibility from 550°C to 580°C (Figure III-15b), consistent with the Curie point (T_c) of magnetite at 580°C [e.g., *Dunlop & Özdemir*, 1997]. A subsidiary decrease of the magnetic susceptibility from 600°C to 700°C can also be observed, indicating a minor contribution of maghemite, an oxidized magnetite (T_c = 590–675°C, *Dunlop & Özdemir* [1997]). (2) Ferromagnetic curves with an abrupt decrease in magnetic susceptibility from 350 to 420°C (Figure III-15c) probably due to the Curie point of Ti-poor titanomagnetite (or titanomaghemite) [e.g., *Keefer & Shive*, 1981], followed by a sudden drop at 580°C (Tc magnetite), and (3) heating curves with a hyperbolic geometry suggesting that the magnetic signal is controlled by paramagnetic mineral phases [*Hrouda*, 1994]. In some case, this regular decay is concealed above 400–500°C by a weak peak in magnetic susceptibility (Figure III-15d) caused by either a progressive unblocking of single-domain ferromagnetic

grains before the Curie point or a neoformation of magnetite from the iron existing in paramagnetic mineral phases [*Dunlop & Özdemir*, 1997].

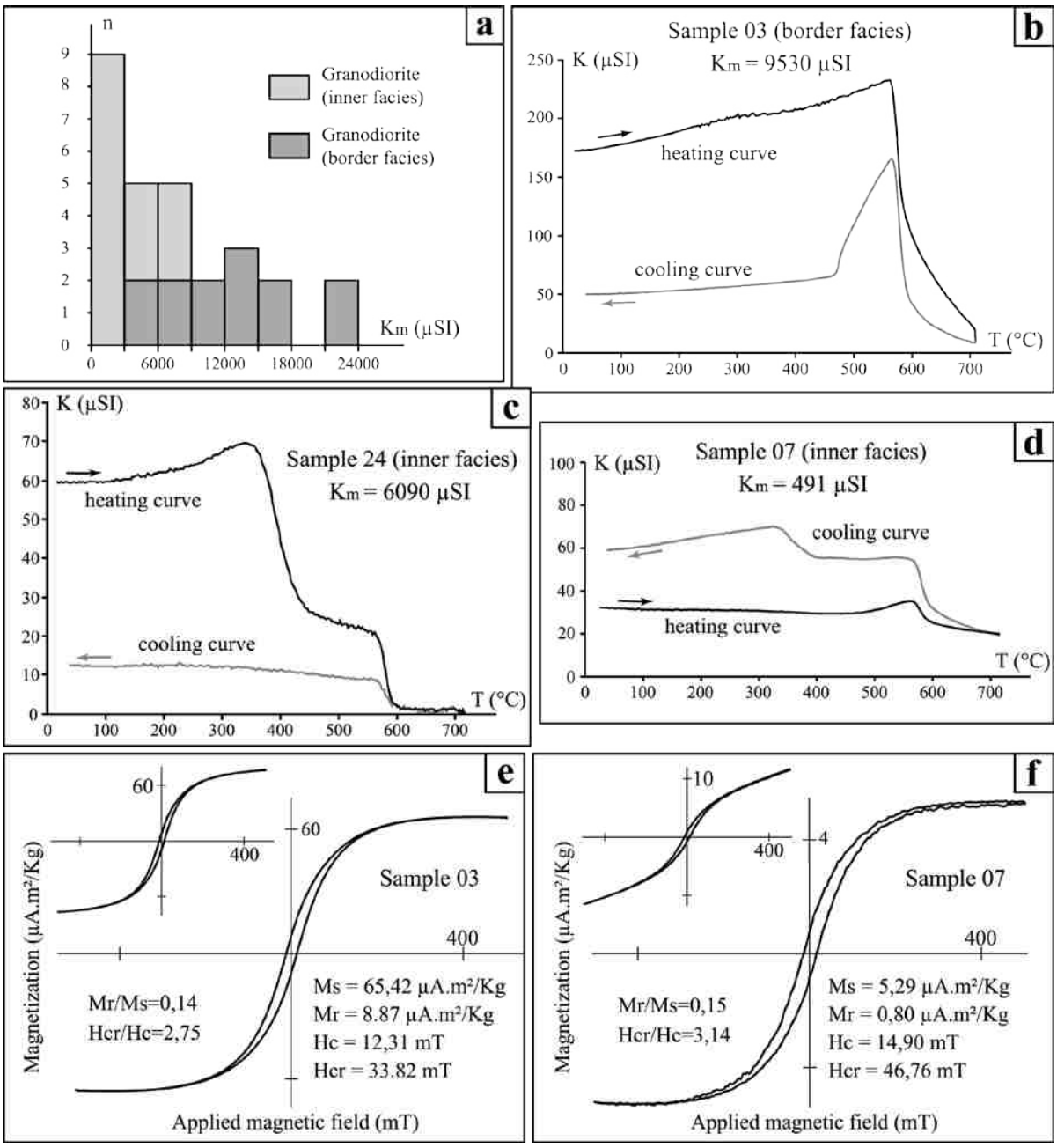

Figure III-15: *Magnetic mineralogy. (a) Histogram of the mean magnetic susceptibility values (K_m). (b–d) Examples of thermomagnetic curves (see text for explanations). (e and f) Representative hysteresis loops showing the typical shape for the ferromagnetic minerals. Paramagnetic corrections have been applied to the loops, but the uncorrected loops are also shown in the inset. Hysteresis parameter values are also indicated with Mrs = saturation remanence, Ms = saturation magnetization, Hcr = remanent coercivity, and Hc = coercivity of mineral. Hysteresis ratios (Mr/Ms and Hcr/Hc) are characteristic of pseudosingle domain magnetite grains.*

Figures III-15e and -15f exhibit hysteresis loops of two representative samples, one from the border facies (Sample 03; K_m = 9530 µSI) and one from the inner facies with low Km

value (Sample 07; K_m = 491 µSI). A paramagnetic correction was applied to the linear part of original loops (see upper left insets). The induced magnetic moment varies from the order of 10^{-1} to 10^{1} µAm^2/kg, which indicates a relatively weak content of magnetic minerals within the granodiorite. Furthermore, the narrow-waisted loops and the low-coercivity values for both specimens indicate that the ferromagnetic contribution is predominantly carried by the magnetite. Ratios of hysteresis parameters M_r/M_s and H_{cr}/H_c also reveal a mean magnetic grain size within the pseudosingle domain (PSD) range [*Day et al.*, 1977; *Dunlop*, 2002a, 2002b].

To summarize, thermomagnetic measurements and hysteresis loops show that magnetic susceptibility vary according to petrofacies type and the relative contents of ferromagnetic minerals (magnetite, maghemite, and titanomagnetite) and paramagnetic mafic silicates (e.g., biotite and hornblende). In this study, *P* and *T* parameters, usually used to describe the degree of AMS and the shape of the AMS ellipsoid, respectively [*Nagata*, 1961; *Jelinek*, 1981], cannot constrain strain pattern because of mixed paramagnetic and ferromagnetic mineralogy. As shown in Figure III-16, a close correlation between *P* and K_m can be observed, with lower degrees of anisotropy within paramagnetic samples than those to the ferromagnetic samples.

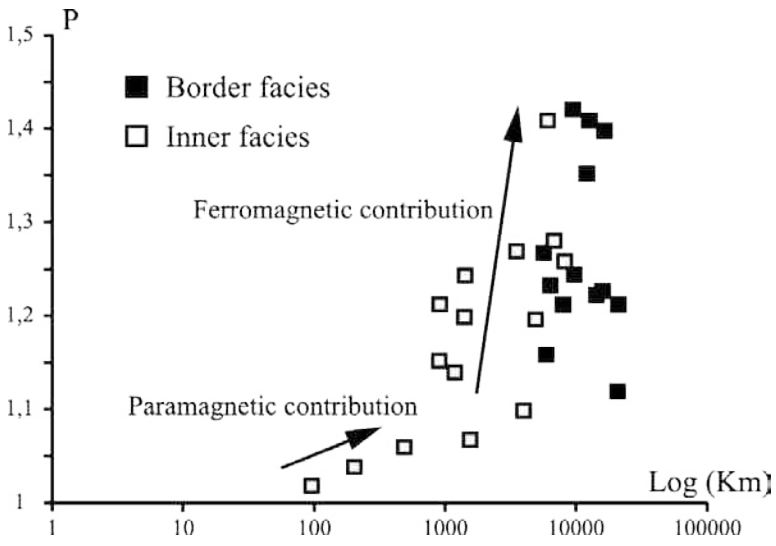

Figure III-16: *P(Km) diagram showing a broad correlation between P (degree of anisotropy) and Km values due to the iron content of ferromagnetic minerals and paramagnetic mafic silicates.*

5.2.3. Map-scale pattern of magnetic fabric and comparison with mesoscopic fabric

Orientations of the magnetic foliation (defined as the plane normal to K_3) and magnetic lineations (parallel to K_1) are illustrated as locality mean values on the maps (Figures III-10a and -10b). In areas where both magnetic and mesoscopic fabrics have been measured, orientations of magnetic foliation and magnetic lineation are broadly consistent with structural field observations. We consequently assume that the following map-scale pattern can be presented and subsequently discussed.

At map scale, magnetic foliations together with mesoscopic foliations display an elliptic configuration with NE-SW directed long axis (Figure III-10a). Note that these foliations throughout the pluton are fairly parallel to the petrographic contacts. Importantly, along NE-SW cross section, the magnetic foliation dips moderately to the NE close to the northeastern

margin, becomes steeper in the core, and dips gently to the SW in the southwestern margin of the pluton.

At map scale, magnetic lineations are homogeneously oriented with mesoscopic lineations and concordant with the southwest directed stretching lineation measured along the Vaghia shear zone and the Aghios Sostis detachment (Figure III-10b). Toward the pluton core, lineations trend to the south with subvertical plunges that become gentler at the southern and southwestern margins of the pluton where the trend is constantly NE-SW. In contrast, lineations at the northeastern margin define a complex pattern. Two sets of lineation trends have been recognized: (1) an abundant NE-SW family representing the continuity of the lineations found in the whole granodiorite; (2) locally, an E-W family is observed near the petrographic contact between the inner and border facies.

6. Discussion

6.1. Evidence for a continuum of deformation in Serifos pluton from magmatic to ductile/brittle solid-state conditions

Our new field investigations, together with microstructural and AMS data, allow us to recognize a continuum of deformation from magmatic to brittle conditions within the Serifos pluton. This succession of deformation events, entirely kinematically compatible with the top-to-the-SW shearing in host rocks, undoubtedly shows the contemporaneity between the development of the WCDS and pluton emplacement. Moreover, following the distribution of both microstructures and mesoscopic fabrics, it should be noted that the Serifos pluton has undergone a localized southwestward gradient of shearing, leaving preserved magmatic fabrics in the northern and central parts.

In the northern and central parts of the Serifos pluton, both the coarse-grained and fine-grained facies display a weak or indiscernible mesoscopic fabrics, and they show magmatic textures without any significant solid-state overprint. Consequently, we consider that the obtained magnetic fabric reflects probably a magmatic fabric developed close to magma solidus [*Vernon*, 2000]. Both mesoscopic and magnetic foliations display a well-defined elliptic pattern carrying a NE-SW oriented long axis. These foliations, fairly parallel to the wall-rock contact, may represent relics of emplacement-related fabric. More specifically, the magmatic lineations measured in the central part are constantly oriented to the southwest and concordant to stretching lineations observed in the host metamorphic rocks along the WCDS. This observation leads us to interpret this fabric orientation as recording a synmagmatic flow, tectonically driven by the NE-SW regional extension. Conversely, E-W to NW-SE trending magnetic lineations have been locally detected by AMS in the northeastern part of the pluton. The interpretation of such magnetic lineations is not straightforward. In our case, this could be due to either physical or geological reasons: the former being (1) the predominance of pseudosingle domain (PSD) magnetite grains that control AMS signal could produce an abnormal fabric [*Rochette et al.*, 1999]; (2) anisotropic distribution of ferromagnetic particles [*Hargraves et al.*, 1991]; (3) lack of mineral preferred orientation at some sample sites, the

latter being (4) emplacement-related magma flow along E-W to NW-SE oriented tensional zones whose direction of opening could be consistent with the NE-SW directed regional extension.

Overprinting of a constrictional deformation on the previous northeastern synmagmatic fabric can be observed along the southern rim where the border facies displays a strongly prolate fabric, NE-SW subhorizontal lineations, and locally L*T* solid-state microstructures. We further contend that the measured constrictional fabric in this area could reflect a southwestward synmagmatic flow which could be incompletely overprinted by regional strain and tectonically driven by vertical shortening associated to the NE-SW regional extension. As revealed by both field and microstructural observations, the prolate fabric was subsequently overprinted by a top-to-the-SW ductile shearing according to an upward and southwestward gradient of shearing. The granodioritic fabric progressively evolves from weakly oblate to strongly oblate, resulting into mylonites close to the SW directed Koutalas-Vaghia shear zone.

Along its eastern margin (Aghios Sostis Peninsula), the roof was affected by a low-angle normal fault consistently compatible with a southwest directed extension. Structural observations show a diffuse strain gradient in the footwall from undeformed granodiorite to L*T* ultramylonites below the detachment. *Tschegg & Grasemann* [2009] had especially described dislocation climb in K-feldspar as well as isochemical nucleation and growth of new grains of K-feldspar in ultramylonites, suggesting deformation temperatures above 450–500°C at relevant strain rates (*Passchier & Trouw* [2005], and references therein). According to these results, since the pluton intruded the Cycladic Blueschists piercing the Meghàlo Livadhi detachment whose shear deformation is well constrained to 300°C [*Grasemann & Tschegg*, 2012; *Dabrowski & Grasemann*, 2014], the Aghios Sostis shear zone should have nucleated during the cooling of the pluton and continued to develop afterward.

Finally, ductile/brittle to brittle, WNW-ESE striking, conjugate high-angle normal faults crosscut the whole Serifos Island, including the granodiorite and the metamorphic host rocks. These faults suggest ongoing NE-SW extension after ductile exhumation of the dome.

6.2. Building of detailed cross-section of Serifos Island

On the basis of our own field study, we propose a detailed NE-SW cross section of Serifos Island, in which geometrical relations between the pluton, host rocks, and major structures are highlighted (Figure III-17).

The metamorphic dome and the granodiorite were exhumed below two branches of a crustal-scale low-angle normal fault system. The detachment system is arched with northeast dipping planes at Platy Gialos to the north and southwest dipping planes at Meghàlo Livadhi and Kàvos Kiklopas. It provides evidence that the granodioritic intrusion was coeval with an overall updoming of the surrounding host rocks before it perforated the lower Meghàlo Livadhi detachment. A continuum from ductile to brittle conditions and a stable top-to-the-SW shearing shows the progressive exhumation of the dome below the WCDS. The Kàvos

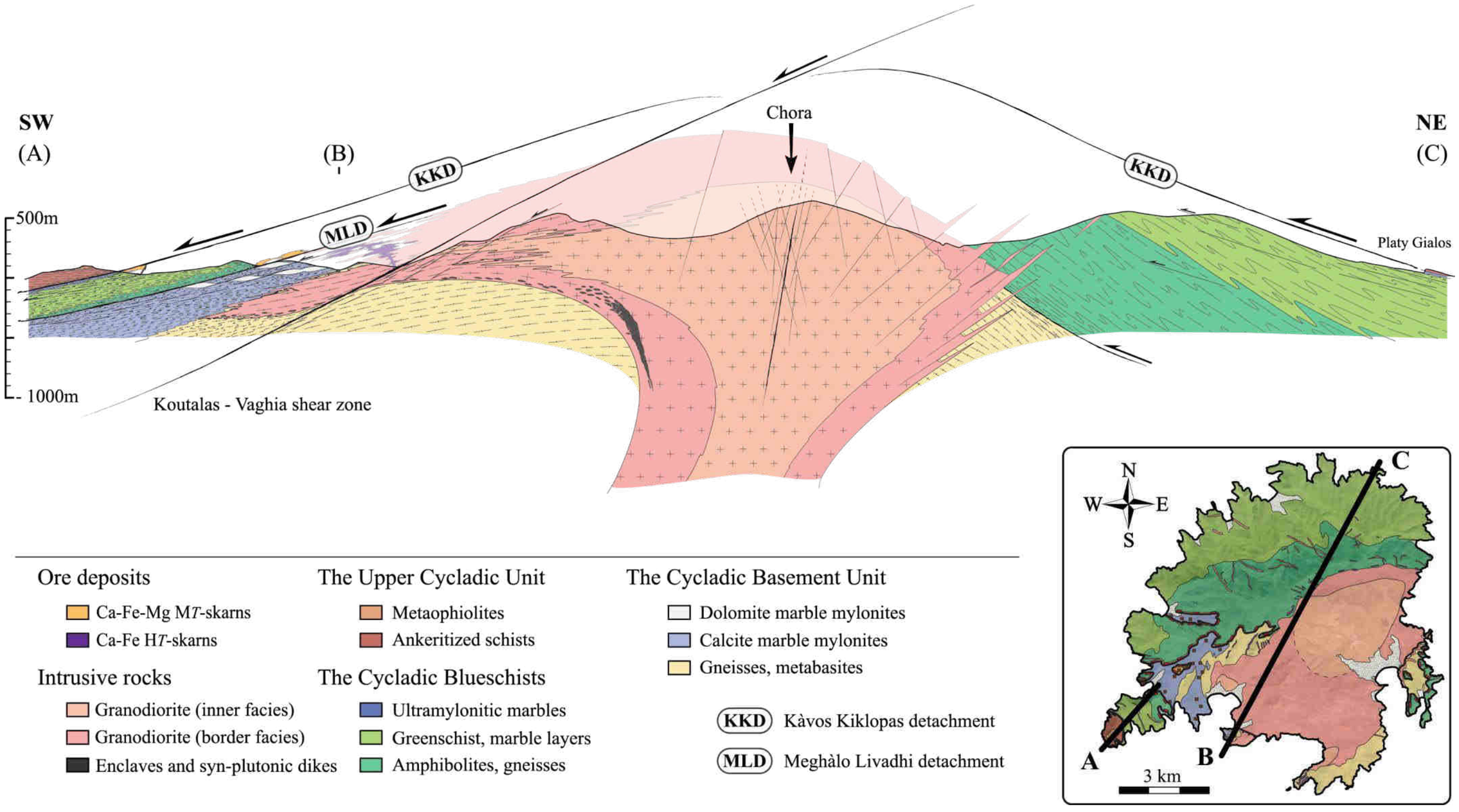

Figure III-17: *Cross section of Serifos Island (A-B, B-C; location in the map inset at lower right) showing relations between the Serifos granodiorite, the host rocks, and large-scale detachments belonging to the WCDS (the lowermost Meghàlo Livadhi detachment and the uppermost Kàvos Kiklopas detachment). Importantly, this cross section shows that the Serifos pluton has intruded the MCC up to piercing the brittle/ductile Meghàlo Livadhi detachment.*

Kiklopas detachment was formed above the Meghàlo Livadhi detachment, and it was more localized. Extensional shearing was also associated with exoskarn and endoskarn mineralizations showing hydrothermal circulations of fluids during intrusion and cooling of the pluton.

The NE-SW cross section thereby shows a complete section of the pluton with superficial parts of the intrusion to the north and deeper ones to the south. The northern part shows a sharp intrusive contact with preserved magmatic fabric, while the pluton was progressively affected by a top-to-the-SW ductile shearing to the southwest rim, gradually transformed into mylonites or even ultramylonites at its eastern margin. The marginal coarse-grained facies of the granodiorite was thus dissected by a series of ductile extensional shear zones, kinematically and temporally consistent with the development of the WCDS. These shear zones have been arched upward during later doming, but they also cut the intrusion down-section toward the southwest. The deepest parts of the intrusion are also rich in swarms of enclaves, dike-like monogenic swarms, and partially disaggregated synplutonic dikes. They have been formed by magmatic mingling processes involving mafic magma intrusion within partially crystallized host granodioritic magma. Field observations further show that their morphologies and their mesoscopic fabrics are compatible with the fabric of both the host granodiorite and the metamorphic host rocks. The asymmetric disaggregation of NW-SE striking subvertical synplutonic dikes could be explained by the pulling force to the southwest of these synplutonic dikes during their injection within a general top-to-the SW noncoaxial flow.

In areas where magmatic fabric is preserved without any ductile shearing overprint, especially west of Chora and Livadhi villages, the coarse-grained facies shows steeply dipping foliations and N-S to NE-SW subvertical lineations. The SL fabric could then represent in this case a subvertical magmatic flow coming out of the feeding zone. In the absence of direct information on the deep structure that gravimetry or drilling could provide, we tentatively suggest that the Serifos pluton is an asymmetrical intrusion with a root zone offset toward the north (Chora village). The deepest parts of the intrusion with magmatic inclusions have been dragged southwestward along southwest dipping shear zones, while the magma was still unconsolidated and ultimately sheared below the WCDS. A similar geometry was inferred for other plutons emplaced into zones affected by noncoaxial shearing [*Bouillin et al.*, 1993; *Acocella & Rossetti*, 2002; *Kratinová et al.*, 2007; *Denèle et al.*, 2011; *Lehmann et al.*, 2013; *Laurent et al.*, 2015] and also modeled by *Schulmann & Ježek* [2012].

6.3. Tectonic scenario for the Serifos pluton emplacement and cooling

Intrusion, cooling, and internal deformation of the Serifos granodiorite were synchronous with southwestward shearing along crustal-scale low-angle normal faults that evolved during the Miocene. Integrating existing data and our new observations, we propose the following tectonic scenario of Serifos Island, which can be isolated into four main stages from MCC development to granodiorite unroofing during crustal extension (Figure III-18).

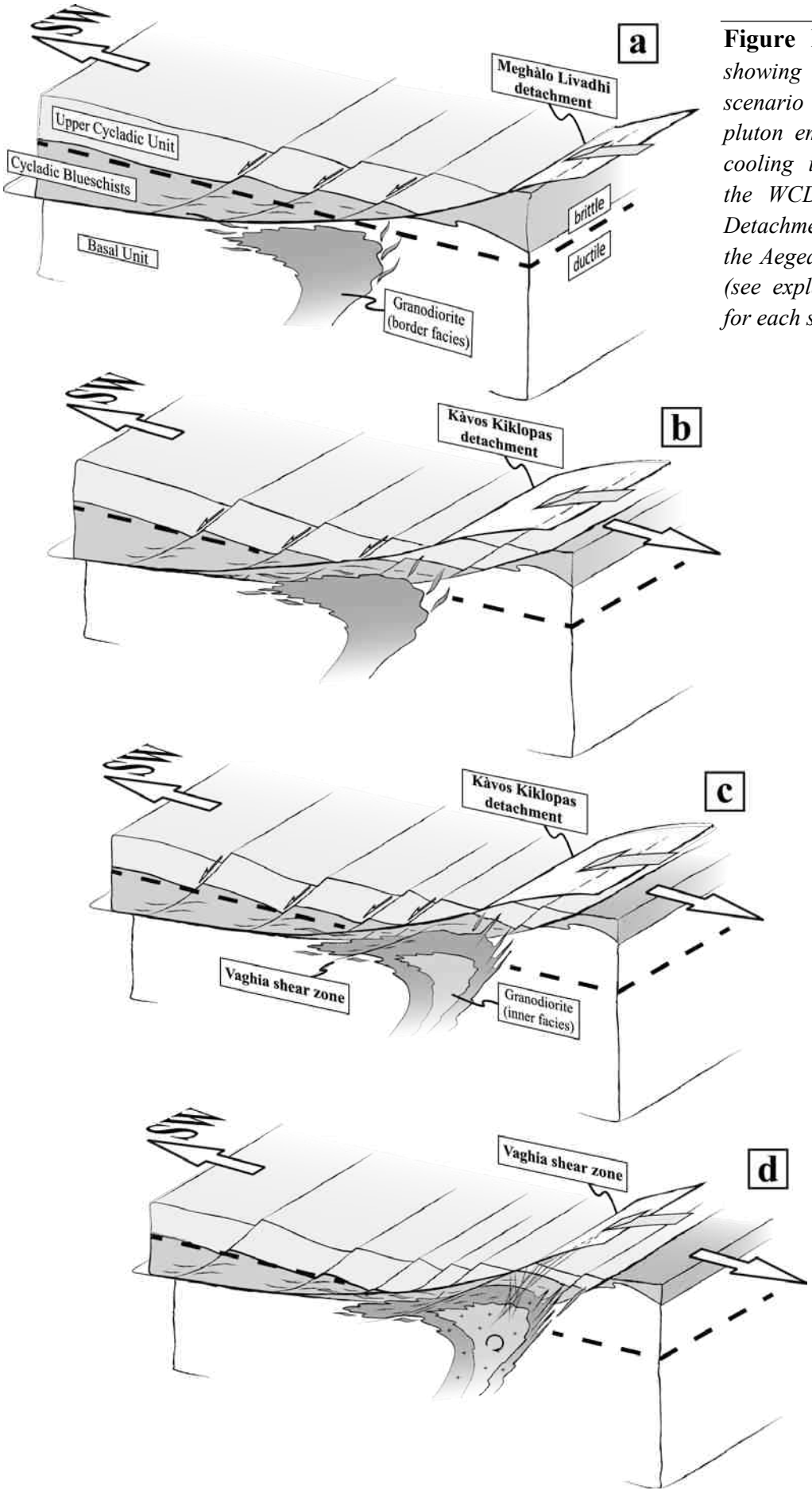

Figure III-18: *3-D views showing the tectonic scenario for the Serifos pluton emplacement and its cooling in interaction with the WCDS (West Cycladic Detachment System) during the Aegean crustal extension (see explanation in the text for each stage).*

(1) The first stage is related to greenschist retrogression that affected the two lower Cycladic units outcropping on Serifos Island. In the Cyclades, L*P*-H*T* metamorphism has been interpreted as the result of Oligocene- Miocene crustal-scale extension controlled by the southward fast retreat of the African slab from approximately 35–30 Ma [*Jolivet & Faccenna*, 2000; *Jolivet & Brun*, 2010; *Ring et al.*, 2010]. During this episode, the change of stress regime is accompanied by a strong heating that led to partial melting of the lower extending crust [*Jolivet & Brun*, 2010; *Jolivet et al.*, 2010, 2013]; migmatite domes thus developed in the central parts of the Aegean domain [*Vanderhaeghe*, 2004]. The upper crust recorded bivergent crustal-scale boudinage leading to development of the Cycladic MCCs and associated northern and western detachment systems [*Lister et al.*, 1984; *Gautier & Brun*, 1994a; *Jolivet et al.*, 2010; *Grasemann et al.*, 2012].

On Serifos Island, extension and exhumation were accommodated by the upper Kàvos Kiklopas branch and the lower Meghàlo Livadhi branch of the WCDS [*Grasemann & Petrakakis*, 2007; *Grasemann et al.*, 2012] with similar NE-SW oriented stretching lineation and southwest directed shear sense. Observations of preserved earlier ENE-WSW oriented stretching lineation in a large part of the island testify for a strongly localized deformation along these crustal-scale detachments, more localized than along the NCDS or farther west along the WCDS. The earlier ENE-WSW directed stretching lineation is indeed strongly overprinted by southwest directed shearing on Kea and well preserved on Kythnos where the WCDS crops out [*Iglseder et al.*, 2011; *Grasemann et al.*, 2012]. On Serifos, thermochronological data suggest that the overall cooling of the Cycladic Blueschists and the Cycladic Basement Unit below approximately 450 ± 50°C [*Villa*, 1998] occured at approximately 15 Ma (Rb/Sr muscovite ages [*Iglseder et al.*, 2009] and $^{40}Ar/^{3}9Ar$ ages muscovite [*Grasemann et al.*, 2012]). However, the exact onset of ductile shearing along each detachment is unclear. On Kea and Kythnos Islands, cooling ages suggest that ductile shearing along the WCDS was active between 21 and 13 Ma and between 26 and 20 Ma, respectively [*Schliestedt et al.*, 1994; *Iglseder et al.*, 2011; *Grasemann et al.*, 2012].

Taking into account structural observations, we assume that the MCC initiation and associated top-to-the- SW shearing are due to a single detachment that migrated upward with time. This tectonic evolution can be interpreted as the result of the interrelations between regional tectonics and the more local plutonic intrusion. Southwest directed extensional shearing was first localized along the lowermost Meghàlo Livadhi detachment, leading to the Cycladic Basement Unit exhumation (Figure III-18a). Furthermore, the observation that a continuum of deformation from ductile to brittle conditions was recorded along the Meghàlo Livadhi detachment shows that the whole system had already crossed the brittle-ductile transition zone before it was perforated by the intrusion.

(2) The second stage is marked by the Serifos pluton emplacement and associated dikes at shallow crustal level above the brittle-ductile transition zone (approximately 8–12 km depth [*Stouraiti & Mitropoulos*, 1999; *St. Seymour et al.*, 2009]). Between 11.6 Ma and 9.5 Ma (U/Pb zircon ages [*Iglseder et al.*, 2009]), the Serifos pluton has intruded the MCC up to piercing the brittle/ductile Meghàlo Livadhi detachment (Figure III-18b). The plutonic body

and associated dikes clearly crosscut both the Meghàlo Livadhi detachment and the regional preexisting metamorphic fabric. Most of the dikes are parallel with/or follow the NW-SE striking, brittle high-angle normal faults, attesting for pluton emplacement at upper crustal depth. Contemporaneously, the granodioritic intrusion radically altered the local temperature, reheating host rocks and inducing some ductile deformation. Southwest directed extensional shearing was thereby transferred upward in the crust along the more localized Kàvos Kiklopas detachment, where high-strain was mainly accommodated by few meter thick ultramylonitic marbles. The upward migration of the detachment due to intrusions is similarly recorded along the NCDS in the islands of Tinos and Mykonos [*Jolivet & Patriat*, 1999; *Jolivet et al.*, 2010]

(3) Subsequently, pluton emplacement was followed by a rather fast cooling [*Altherr et al.*, 1982; *Iglseder et al.*, 2009]. During the magmatic crystallization, both the coarse-grained (i.e., border facies) and fine-grained (i.e., inner facies) granitoids were affected in a short time by a synmagmatic extensional deformation below the Kàvos Kiklopas detachment (Figure III-18c). The large-scale structure of the pluton, especially its overall asymmetry, was entirely controlled by the top-to-the-southwest shearing associated with the WCDS, while noncoaxial deformation localized, leading to the nucleation of narrow shear zones during pluton cooling.

(4) After the complete crystallization of the pluton, the top-to-the-SW extensional deformation continued to affect both the pluton and the metamorphic dome. Ductile shearing was increasingly localized with time at the southwestern and eastern margins where the Vaghia and the Aghios Sostis shear zones developed, leaving preserved magmatic fabrics at northern and central parts of the pluton. During the final exhumation stage, series of ductile extensional shear zones that dissected both the pluton and the metamorphic dome evolved through time into brittle detachments (Figure III-18d). Afterward, NW-SE striking, conjugate high-angle normal faults crosscut the whole Serifos Island. These structures suggest ongoing NE-SW extension after ductile/brittle exhumation of the Serifos MCC. In this scenario, we assume that the end of exhumation to the surface has been achieved by this set of steep normal faults and/or other unroofing mechanism such as erosion.

Conclusion

Serifos Island forms a well-suited example to study the interrelations between plutonic activity and localizing events in the crust during MCC formation. Serifos Island, located in the western Cyclades (Greece), is described as a MCC intruded by an I-type granodiorite at shallow crustal levels. This Miocene pluton had intruded during the thinning of the Aegean Sea, and it was spatially connected to the activity of the WCDS. Based on a structural fieldwork, together with microstructural and AMS data, we have recognized a continuum of deformation from magmatic to brittle conditions in the Serifos pluton during its cooling and subsequent unroofing, consistent with the top-to-the-southwest shearing recorded within host rocks. Serifos pluton thereby shows a strong asymmetric architecture with preserved magmatic fabrics northeastward and a southwestern margin sheared toward the south along the WCDS.

The existing data and our new observations made on Serifos Island thus lead to propose a tectonic scenario for the Miocene pluton emplacement in extending crust, along the WCDS: (1) a first stage corresponding to the MCC initiation and associated ductile shearing along the lowermost Meghàlo Livadhi detachment; (2) a second stage related to the Serifos pluton emplacement above the brittle-ductile transition, piercing through the ductile/brittle Meghàlo Livadhi detachment. Intrusion inactivated the deeper branch, and the southwest oriented extensional deformation migrated upward in the crust along the more localized Kàvos Kiklopas detachment. (3) After pluton emplacement, the Serifos pluton recorded in short time span strain localization resulting in shear zones nucleation during its cooling, and (4) their subsequent development after the complete crystallization of the pluton. Continuum of deformation finally evolved to a brittle regime during the later exhumation stage.

Acknowledgments

Data sets are available upon request from the first author. This work was funded by the European Research Council (ERC) under the 7th Framework Programme of the European Union (ERC Advanced Grant, grant agreement No 290864, RHEOLITH) with a contribution from the Laboratoire d'Excellence (LABEX) VOLTAIRE (Convention n°ANR-10-LABEX-100-01) of the University of Orléans. The authors wish to express their thanks to Jiří Žák and anonymous reviewers for their useful comments.

Références bibliographiques

Acocella, V., and F. Rossetti (2002), The role of extensional tectonics at different crustal levels on granite ascent and emplacement: an example from Tuscany (Italy), *Tectonophysics*, *354*(1–2), 71–83, doi:10.1016/S0040-1951(02)00290-1.

Aktug, B. et al. (2009), Deformation of western Turkey from a combination of permanent and campaign GPS data: Limits to block-like behavior, *Journal of Geophysical Research*, *114*(B10), 1–22, doi:10.1029/2008JB006000.

Altherr, R., and W. Siebel (2002), I-type plutonism in a continental back-arc setting: Miocene granitoids and monzonites from the central Aegean Sea, Greece, *Contributions to Mineralogy and Petrology*, *143*(4), 397–415, doi:10.1007/s00410-002-0352-y.

Altherr, R., M. Schliestedt, M. Okrusch, E. Seidel, H. Kreuzer, W. Harre, H. Lenz, I. Wendt, and G. A. Wagner (1979), Geochronology of high-pressure rocks on Sifnos (Cyclades, Greece), *Contributions to Mineralogy and Petrology*, *70*(3), 245–255, doi:10.1007/BF00375354.

Altherr, R., H. Kreuzer, I. Wendt, H. Lenz, G. A. Wagner, J. Keller, W. Harre, and A. Höhndorf (1982), A late Oligocene/early Miocene high temperature belt in the Attic-Cycladic crystalline complex (SE Pelagonian, Greece), *Geologisches Jahrbuch*, *E23*, 97–164.

Altherr, R., F. Henjes-Kunst, A. Matthews, H. Friedrichsen, and B. T. Hansen (1988), O-Sr isotopic variations in Miocene granitoids from the Aegean: evidence for an origin by combined assimilation and fractional crystallization, *Contributions to Mineralogy and Petrology*, *100*(4), 528–541, doi:10.1007/BF00371381.

Andriessen, P. A. M., G. Banga, and E. H. Hebeda (1987), Isotopic age study of pre-Alpine rocks in the basal units on Naxos, Sikinos and Ios, Greek Cyclades, *Geol. Mijnbouw*, *66*, 3–14.

Archanjo, C. J., P. Launeau, and J. L. Bouchez (1994), Magnetic fabric vs. magnetite and biotite shape fabrics of the magnetite-bearing granite pluton of Gameleiras (Northeast Brazil), *Physics of the Earth and Planetary Interiors*, *89*(1–2), 63–75, doi:10.1016/0031-9201(94)02997-P.

Armijo, R., H. Lyon-Caen, and D. Papanastassiou (1992), East-west extension and Holocene normal-fault scarps in the Hellenic arc, *Geology*, *20*(6), 491–494, doi:10.1130/0091-7613(1992)020<0491:EWEAHN>2.3.CO;2.

Armijo, R., B. Meyer, G. C. P. King, A. Rigo, and D. Papanastassiou (1996), Quaternary evolution of the Corinth Rift and its implications for the Late Cenozoic evolution of the Aegean, *Geophysical Journal International*, *126*(1), 11–53, doi:10.1111/j.1365-246X.1996.tb05264.x.

Armijo, R., B. Meyer, A. Hubert, and A. Barka (1999), Westward propagation of the North Anatolian fault into the northern Aegean: Timing and kinematics, *Geology*, *27*(3), 267–270, doi:10.1130/0091-7613(1999)027<0267:WPOTNA>2.3.CO;2.

Augier, R., L. Jolivet, L. Gadenne, A. Lahfid, and O. Driussi (2015), Exhumation kinematics of the Cycladic Blueschists unit and back-arc extension, insight from the Southern Cyclades (Sikinos and Folegandros Islands, Greece), *Tectonics*, *34*(1), 152–185, doi:10.1002/2014TC003664.

Baldwin, S. L., G. S. Lister, E. J. Hill, D. A. Foster, and I. McDougall (1993), Thermochronologic constraints on the tectonic evolution of active metamorphic core complexes, D'entrecasteaux Islands, Papua New Guinea, *Tectonics*, *12*(3), 611–628, doi:10.1029/93TC00235.

Barbarin, B. (2005), Mafic magmatic enclaves and mafic rocks associated with some granitoids of the central Sierra Nevada batholith, California: nature, origin, and relations with the hosts, *Lithos*, *80*(1–4), 155–177, doi:10.1016/j.lithos.2004.05.010.

Benn, K., S. R. Paterson, S. P. Lund, G. S. Pignotta, and S. Kruse (2001), Magmatic fabrics in batholiths as markers of regional strains and plate kinematics: example of the Cretaceous Mt. Stuart batholith, *Physics and Chemistry of the Earth, Part A: Solid Earth and Geodesy*, *26*(4–5), 343–354, doi:10.1016/S1464-1895(01)00064-3.

Bolhar, R., U. Ring, and C. M. Allen (2010), An integrated zircon geochronological and geochemical investigation into the Miocene plutonic evolution of the Cyclades, Aegean Sea, Greece: Part 1: Geochronology, *Contributions to Mineralogy and Petrology*, *160*(5), 719–742, doi:10.1007/s00410-010-0504-4.

Bonneau, M. (1984), Correlation of the Hellenide nappes in the south-east Aegean and their tectonic reconstruction, *Geological Society, London, Special Publications*, *17*(1), 517–527, doi:10.1144/GSL.SP.1984.017.01.38.

Borradaile, G. J., and B. Henry (1997), Tectonic applications of magnetic susceptibility and its anisotropy, *Earth-Science Reviews*, *42*(1–2), 49–93, doi:10.1016/S0012-8252(96)00044-X.

Borradaile, G. J., and M. Jackson (2010), Structural geology, petrofabrics and magnetic fabrics (AMS, AARM, AIRM), *Journal of Structural Geology*, *32*(10), 1519–1551, doi:10.1016/j.jsg.2009.09.006.

Bouchez, J. L., G. Gleizes, T. Djouadi, and P. Rochette (1990), Microstructure and magnetic susceptibility applied to emplacement kinematics of granites: the example of the foix pluton (French pyrenees), *Tectonophysics*, *184*(2), 157–171, doi:10.1016/0040-1951(90)90051-9.

Bouchez, J.-L. (2000), Anisotropie de susceptibilité magnétique et fabrique des granites, *Comptes Rendus de l'Académie des Sciences - Series IIA - Earth and Planetary Science*, *330*(1), 1–14, doi:10.1016/S1251-8050(00)00120-8.

Bouillin, J.-P., J.-L. Bouchez, P. Lespinasse, and A. Peˆcher (1993), Granite emplacement in an extensional setting: an AMS study of the magmatic structures of Monte Capanne (Elba, Italy), *Earth and Planetary Science Letters*, *118*(1–4), 263–279, doi:10.1016/0012-821X(93)90172-6.

Bozkurt, E., and H. Sözbilir (2004), Tectonic evolution of the Gediz Graben: field evidence for an episodic, two-stage extension in western Turkey, *Geological Magazine*, *141*(1), 63–79, doi:10.1017/S0016756803008379.

Brichau, S., U. Ring, A. Carter, P. Monié, R. Bolhar, D. Stockli, and M. Brunel (2007), Extensional faulting on Tinos Island, Aegean Sea, Greece: How many detachments?, *Tectonics*, *26*(4), 1–19, doi:10.1029/2006TC001969.

Brichau, S., U. Ring, A. Carter, R. Bolhar, P. Monie, D. Stockli, and M. Brunel (2008), Timing, slip rate, displacement and cooling history of the Mykonos detachment footwall, Cyclades, Greece, and implications for the opening of the Aegean Sea basin, *Journal of the Geological Society*, *165*(1), 263–277, doi:10.1144/0016-76492006-145.

Brichau, S., S. Thomson, and U. Ring (2010), Thermochronometric constraints on the tectonic evolution of the Serifos detachment, Aegean Sea, Greece, *International Journal of Earth Sciences*, *99*(2), 379–393, doi:10.1007/s00531-008-0386-0.

Bröcker, M., and M. Enders (1999), U–Pb zircon geochronology of unusual eclogite-facies rocks from Syros and Tinos (Cyclades, Greece), *Geological Magazine*, *136*(2), 111–118, doi:10.1017/S0016756899002320.

Bröcker, M., H. Kreuzer, A. Matthews, and M. Okrusch (1993), $^{40}Ar/^{39}Ar$ and oxygen isotope studies of polymetamorphism from Tinos Island, Cycladic blueschist belt, Greece, *Journal of Metamorphic Geology*, *11*(2), 223–240, doi:10.1111/j.1525-1314.1993.tb00144.x.

Brown, M. (1994), The generation, segregation, ascent and emplacement of granite magma: the migmatite-to-crustally-derived granite connection in thickened orogens, *Earth-Science Reviews*, *36*(1–2),

83–130, doi:10.1016/0012-8252(94)90009-4.

Brun, J.-P., and D. Sokoutis (2010), 45 m.y. of Aegean crust and mantle flow driven by trench retreat, *Geology*, *38*(9), 815–818, doi:10.1130/G30950.1.

Charles, N., C. Gumiaux, R. Augier, Y. Chen, R. Zhu, and W. Lin (2011), Metamorphic Core Complexes vs. synkinematic plutons in continental extension setting: Insights from key structures (Shandong Province, eastern China), *Journal of Asian Earth Sciences*, *40*(1), 261–278, doi:10.1016/j.jseaes.2010.07.006.

Crittenden, M. D., P. J. Coney, and G. H. Davis (Eds.) (1980), *Cordilleran metamorphic core complexes*, Memoir - The Geological Society of America 153, Geological Society of America, Boulder, Colorado.

Dabrowski, M., and B. Grasemann (2014), Domino boudinage under layer-parallel simple shear, *Journal of Structural Geology*, *68*, 58–65, doi:10.1016/j.jsg.2014.09.006.

Daniel, J.-M., and L. Jolivet (1995), Detachment faults and pluton emplacement; Elba Island (Tyrrhenian Sea), *Bulletin de la Societe Geologique de France*, *166*(4), 341–354.

Davidson, C., S. M. Schmid, and L. S. Hollister (1994), Role of melt during deformation in the deep crust, *Terra Nova*, *6*(2), 133–142, doi:10.1111/j.1365-3121.1994.tb00646.x.

Davis, G. A., T. K. Fowler, K. M. Bishop, T. C. Brudos, S. J. Friedmann, D. W. Burbank, M. A. Parke, and B. C. Burchfiel (1993), Pluton pinning of an active Miocene detachment fault system, eastern Mojave Desert, California, *Geology*, *21*(7), 627–630, doi:10.1130/0091-7613(1993)021<0627:PPOAAM>2.3.CO;2.

Day, R., M. Fuller, and V. A. Schmidt (1977), Hysteresis properties of titanomagnetites: Grain-size and compositional dependence, *Physics of the Earth and Planetary Interiors*, *13*(4), 260–267, doi:10.1016/0031-9201(77)90108-X.

Denèle, Y., E. Lecomte, L. Jolivet, O. Lacombe, L. Labrousse, B. Huet, and L. Le Pourhiet (2011), Granite intrusion in a metamorphic core complex: The example of the Mykonos laccolith (Cyclades, Greece), *Tectonophysics*, *501*(1–4), 52–70, doi:10.1016/j.tecto.2011.01.013.

D'Lemos, R. S., M. Brown, and R. A. Strachan (1992), Granite magma generation, ascent and emplacement within a transpressional orogen, *Journal of the Geological Society*, *149*(4), 487–490, doi:10.1144/gsjgs.149.4.0487.

Dunlop, D. J. (2002a), Theory and application of the Day plot (Mrs/Ms versus Hcr/Hc) 1. Theoretical curves and tests using titanomagnetite data, *Journal of Geophysical Research*, *107*(B3), doi:10.1029/2001JB000486.

Dunlop, D. J. (2002b), Theory and application of the Day plot (Mrs/Ms versus Hcr/Hc) 2. Application to data for rocks, sediments, and soils, *Journal of Geophysical Research*, *107*(B3), doi:10.1029/2001JB000487.

Dunlop, D. J., and Ö. Özdemir (1997), *Rock magnetism fundamentals and frontiers*, Cambridge University Press, Cambridge; New York.

Eyidoğan, H., and J. Jackson (1985), A seismological study of normal faulting in the Demirci, Ala ehir and Gediz earthquakes of 1969-70 in western Turkey: implications for the nature and geometry of deformation in the continental crust, *Geophysical Journal International*, *81*(3), 569–607, doi:10.1111/j.1365-246X.1985.tb06423.x.

Faure, M., M. Bonneau, and J. Pons (1991), Ductile deformation and syntectonic granite emplacement during the late Miocene extension of the Aegea (Greece), *Bulletin de la Societe Geologique de France*, *162*, 3–11.

Foster, D. A., C. Schafer, C. M. Fanning, and D. W. Hyndman (2001), Relationships between crustal partial melting, plutonism, orogeny, and exhumation: Idaho?Bitterroot batholith, *Tectonophysics*, *342*(3–4), 313–350, doi:10.1016/S0040-1951(01)00169-X.

Gautier, P., and J.-P. Brun (1994a), Crustal-scale geometry and kinematics of late-orogenic extension in the central Aegean (Cyclades and Ewia Island), *Tectonophysics*, *238*(1–4), 399–424, doi:10.1016/0040-1951(94)90066-3.

Gautier, P., and J.-P. Brun (1994b), Ductile crust exhumation and extensional detachments in the central Aegean (Cyclades and Evvia islands), *Geodinamica Acta*, *7*(2), 57–85.

Gautier, P., J.-P. Brun, R. Moriceau, D. Sokoutis, J. Martinod, and L. Jolivet (1999), Timing, kinematics and cause of Aegean extension: a scenario based on a comparison with simple analogue experiments, *Tectonophysics*, *315*(1–4), 31–72, doi:10.1016/S0040-1951(99)00281-4.

Goldsworthy, M., J. Jackson, and J. Haines (2002), The continuity of active fault systems in Greece: Fault continuity in Greece, *Geophysical Journal International*, *148*(3), 596–618, doi:10.1046/j.1365-246X.2002.01609.x.

Goscombe, B. D., C. W. Passchier, and M. Hand (2004), Boudinage classification: end-member boudin types and modified boudin structures, *Journal of Structural Geology*, *26*(4), 739–763, doi:10.1016/j.jsg.2003.08.015.

Grasemann, B., and K. Petrakakis (2007), Evolution of the Serifos metamorphic core complex, *Journal of the Virtual Explorer*, *27*, 1–18.

Grasemann, B., and C. Tschegg (2012), Localization of deformation triggered by chemo-mechanical feedback processes, *Geological Society of America Bulletin*, *124*(5–6), 737–745, doi:10.1130/B30504.1.

Grasemann, B., D. A. Schneider, D. F. Stockli, and C. Iglseder (2012), Miocene bivergent crustal extension in the Aegean: Evidence from the western Cyclades (Greece), *Lithosphere*, *4*(1), 23–39, doi:10.1130/L164.1.

Groppo, C., M. Forster, G. Lister, and R. Compagnoni (2009), Glaucophane schists and associated rocks from Sifnos (Cyclades, Greece): New constraints on the P–T evolution from oxidized systems, *Lithos*, *109*(3–4), 254–273, doi:10.1016/j.lithos.2008.10.005.

ten Grotenhuis, S. M., R. A. J. Trouw, and C. W. Passchier (2003), Evolution of mica fish in mylonitic rocks, *Tectonophysics*, *372*(1–2), 1–21, doi:10.1016/S0040-1951(03)00231-2.

Hargraves, R. B., D. Johnson, and C. Y. Chan (1991), Distribution anisotropy: The cause of AMS in igneous rocks?, *Geophysical Research Letters*, *18*(12), 2193–2196, doi:10.1029/91GL01777.

Hatzfeld, D., V. Karakostas, M. Ziazia, I. Kassaras, E. Papadimitriou, K. Makropoulos, N. Voulgaris, and C. Papaioannou (2000), Microseismicity and faulting geometry in the Gulf of Corinth (Greece), *Geophysical Journal International*, *141*(2), 438–456, doi:10.1046/j.1365-246x.2000.00092.x.

Hejl, E., H. Riedl, and H. Weingartner (2002), Post-plutonic unroofing and morphogenesis of the Attic–Cycladic complex (Aegea, Greece), *Tectonophysics*, *349*(1–4), 37–56, doi:10.1016/S0040-1951(02)00045-8.

Henjes-Kunst, F., and H. Kreuzer (1982), Isotopic dating of pre-Alpidic rocks from the island of Ios (Cyclades, Greece), *Contributions to Mineralogy and Petrology*, *80*(3), 245–253, doi:10.1007/BF00371354.

van Hinsbergen, D. J. J., E. Hafkenscheid, W. Spakman, J. E. Meulenkamp, and R. Wortel (2005), Nappe stacking resulting from subduction of oceanic and continental lithosphere below Greece, *Geology*, *33*(4), 325–328, doi:10.1130/G20878.1.

Hrouda, F. (1994), A technique for the measurement of thermal changes of magnetic susceptibility of weakly magnetic rocks by the CS-2 apparatus and KLY-2 Kappabridge, *Geophysical Journal International*, *118*(3), 604–612, doi:10.1111/j.1365-246X.1994.tb03987.x.

Hrouda, F., and štefan Kahan (1991), The

magnetic fabric relationship between sedimentary and basement nappes in the High Tatra Mountains, N. Slovakia, *Journal of Structural Geology*, *13*(4), 431–442, doi:10.1016/0191-8141(91)90016-C.

Hrouda, F., V. Jelinek, and L. Hruskova (1990), A package of programs for statistical evaluation of magnetic data using IBM-PC computers, vol. 71, p. 1289, San Fransisco.

Huet, B., L. Labrousse, and L. Jolivet (2009), Thrust or detachment? Exhumation processes in the Aegean: Insight from a field study on Ios (Cyclades, Greece), *Tectonics*, *28*(3), 1–27, doi:10.1029/2008TC002397.

Hutton, D. H. W. (1982), A tectonic model for the emplacement of the Main Donegal Granite, NW Ireland, *Journal of the Geological Society*, *139*(5), 615–631, doi:10.1144/gsjgs.139.5.0615.

Iglseder, C., B. Grasemann, D. A. Schneider, K. Petrakakis, C. Miller, U. S. Klötzli, M. Thöni, A. Zámolyi, and C. Rambousek (2009), I and S-type plutonism on Serifos (W-Cyclades, Greece), *Tectonophysics*, *473*(1–2), 69–83, doi:10.1016/j.tecto .2008.09.021.

Iglseder, C., B. Grasemann, A. H. N. Rice, K. Petrakakis, and D. A. Schneider (2011), Miocene south directed low-angle normal fault evolution on Kea Island (West Cycladic Detachment System, Greece), *Tectonics*, *30*(4), 1–31, doi:10.1029/201 0TC002802.

Jackson, J. (1994), Active Tectonics of the Aegean Region, *Annual Review of Earth and Planetary Sciences*, *22*(1), 239–271, doi:10.1146/annurev.earth.22.1.239.

Jelinek, V. (1981), Characterization of the magnetic fabric of rocks, *Tectonophysics*, *79*(3–4), T63–T67, doi:10.1016/0040-1951(81)90110-4.

Jelínek, V., and V. Kropáček (1978), Statistical processing of anisotropy of magnetic susceptibility measured on groups of specimens, *Studia Geophysica et Geodaetica*, *22*(1), 50–62, doi:10.1007/ BF01613632.

Jelínek, V., and J. Pokorný (1997), Some new concepts in technology of transformer bridges for measuring susceptibility anisotropy of rocks, *Physics and Chemistry of the Earth*, *22*(1–2), 179–181, doi:10.1016/S0079-1946(97)00099-2.

Jolivet, L., and J.-P. Brun (2010), Cenozoic geodynamic evolution of the Aegean, *International Journal of Earth Sciences*, *99*(1), 109–138, doi:10.1007/s00531-008-0366-4.

Jolivet, L., and C. Faccenna (2000), Mediterranean extension and the Africa-Eurasia collision, *Tectonics*, *19*(6), 1095–1106, doi:10.1029/2000TC900018.

Jolivet, L., and M. Patriat (1999), Ductile extension and the formation of the Aegean Sea, *Geological Society, London, Special Publications*, *156*(1), 427–456, doi:10.114 4/GSL.SP.1999.156.01.20.

Jolivet, L., J.-P. Brun, P. Gautier, S. Lallemant, and M. Patriat (1994), 3D-kinematics of extension in the Aegean region from the early Miocene to the present; insights from the ductile crust, *Bull. Soc. Geol. France*, *165*(3), 195–209.

Jolivet, L. et al. (1998), Midcrustal shear zones in postorogenic extension: Example from the northern Tyrrhenian Sea, *Journal of Geophysical Research: Solid Earth*, *103*(B6), 12123–12160, doi:10.1029/9 7JB03616.

Jolivet, L., G. Rimmelé, R. Oberhänsli, B. Goffé, and O. Candan (2004), Correlation of syn-orogenic tectonic and metamorphic events in the Cyclades, the Lycian nappes and the Menderes massif. Geodynamic implications, *Bulletin de la Societe Geologique de France*, *175*(3), 217–238, doi:10.2113/175.3.217.

Jolivet, L., E. Lecomte, B. Huet, Y. Denèle, O. Lacombe, L. Labrousse, L. Le Pourhiet, and C. Mehl (2010), The North Cycladic Detachment System, *Earth and Planetary Science Letters*, *289*(1–2), 87–104, doi:10.1016/j.epsl.2009.10.032.

Jolivet, L. et al. (2013), Aegean tectonics:

Strain localisation, slab tearing and trench retreat, *Tectonophysics*, *597–598*, 1–33, doi:10.1016/j.tecto.2012.06.011.

Katzir, Y., A. L. A. N. Matthews, Z. Garfunkel, M. Schliestedt, and D. Avigad (1996), The tectono-metamorphic evolution of a dismembered ophiolite (Tinos, Cyclades, Greece), *Geological Magazine*, *133*(3), 237–254.

Keay, S., and G. Lister (2002), African provenance for the metasediments and metaigneous rocks of the Cyclades, Aegean Sea, Greece, *Geology*, *30*(3), 235–238, doi:10.1130/0091-7613(2002)030<0235:APFTMA>2.0.CO;2.

Keay, S., G. Lister, and I. Buick (2001), The timing of partial melting, Barrovian metamorphism and granite intrusion in the Naxos metamorphic core complex, Cyclades, Aegean Sea, Greece, *Tectonophysics*, *342*(3–4), 275–312, doi:10.1016/S0040-1951(01)00168-8.

Keefer, C. M., and P. N. Shive (1981), Curie temperature and lattice constant reference contours for synthetic titanomaghemites, *Journal of Geophysical Research: Solid Earth*, *86*(B2), 987–998, doi:10.1029/JB086iB02p00987.

Kokkalas, S., and A. Aydin (2013), Is there a link between faulting and magmatism in the south-central Aegean Sea?, *Geological Magazine*, *150*(02), 193–224, doi:10.1017/S0016756812000453.

Kolb, J., A. Rogers, F. M. Meyer, and T. W. Vennemann (2004), Development of fluid conduits in the auriferous shear zones of the Hutti Gold Mine, India: evidence for spatially and temporally heterogeneous fluid flow, *Tectonophysics*, *378*(1–2), 65–84, doi:10.1016/j.tecto.2003.10.009.

Koukouvelas, I. K., and S. Kokkalas (2003), Emplacement of the Miocene west Naxos pluton (Aegean Sea, Greece): a structural study, *Geological Magazine*, *140*(1), 45–61, doi:10.1017/S0016756802007094.

Kratinová, Z., K. Schulmann, J.-B. Edel, J. Ježek, and U. Schaltegger (2007), Model of successive granite sheet emplacement in transtensional setting: Integrated microstructural and anisotropy of magnetic susceptibility study, *Tectonics*, *26*(6), 1–26, doi:10.1029/2006TC002035.

Kumerics, C., U. Ring, S. Brichau, J. Glodny, and P. Monie (2005), The extensional Messaria shear zone and associated brittle detachment faults, Aegean Sea, Greece, *Journal of the Geological Society*, *162*(4), 701–721, doi:10.1144/0016-764904-041.

Lambrakis, N., L. Tiniakos, K. Voudouris, and G. Kallergis (2000), Hydrogeologische Untersuchungen auf der Insel Serifos: Beschaffenheit der granodioritischen Wasser Steir, *Beitrage zur Hydrogeologie*, (51), 95–110.

Laurent, V., A. Beaudoin, L. Jolivet, L. Arbaret, R. Augier, A. Rabillard, and A. Menant (2015), Interrelations between extensional shear zones and synkinematic intrusions: The example of Ikaria Island (NE Cyclades, Greece), *Tectonophysics*, *651–652*, 152–171, doi:10.1016/j.tecto.2015.03.020.

Le Pichon, X., and C. Kreemer (2010), The Miocene-to-Present Kinematic Evolution of the Eastern Mediterranean and Middle East and Its Implications for Dynamics, *Annual Review of Earth and Planetary Sciences*, *38*(1), 323–351, doi:10.1146/annurev-earth-040809-152419.

Lecomte, E., L. Jolivet, O. Lacombe, Y. Den?le, L. Labrousse, and L. Le Pourhiet (2010), Geometry and kinematics of Mykonos detachment, Cyclades, Greece: Evidence for slip at shallow dip, *Tectonics*, *29*(5), 1–22, doi:10.1029/2009TC002564.

Lee, J., and G. S. Lister (1992), Late Miocene ductile extension and detachment faulting, Mykonos, Greece, *Geology*, *20*(2), 121–124, doi:10.1130/0091-7613(1992)020<0121:LMDEAD>2.3.CO;2.

Lehmann, J., K. Schulmann, J.-B. Edel, J. Ježek, F. Hrouda, O. Lexa, and F. Chopin (2013), Structural and anisotropy of magnetic susceptibility records of granitoid sheets emplacement during growth of a

continental gneiss dome (Central Sudetes, European Variscan Belt), *Tectonics*, *32*(3), 797–820, doi:10.1002/tect.20028.

Lister, G. S., and S. L. Baldwin (1993), Plutonism and the origin of metamorphic core complexes, *Geology*, *21*(7), 607–610, doi:10.1130/0091-7613(1993)021<0607:PATOOM>2.3.CO;2.

Lister, G. S., and A. W. Snoke (1984), S-C Mylonites, *Journal of Structural Geology*, *6*(6), 617–638, doi:10.1016/0191-8141(84)90001-4.

Lister, G. S., G. Banga, and A. Feenstra (1984), Metamorphic core complexes of Cordilleran type in the Cyclades, Aegean Sea, Greece, *Geology*, *12*(4), 221–225, doi:10.1130/0091-7613(1984)12<221:MCCOCT>2.0.CO;2.

Maluski, H., M. Bonneau, and J. R. Kienast (1987), Dating the metamorphic events in the Cycladic area; $^{39}Ar/^{40}Ar$ data from metamorphic rocks of the Island of Syros (Greece), *Bull. Soc. Geol. France*, *3*(5), 833–842.

Marinos, G. (1951), Geology and metallogeny of Serifos island, *Geological and Geophysical Research*, *1*, 95–127.

Mccaffrey, K. J. W. (1992), Igneous emplacement in a transpressive shear zone: Ox Mountains igneous complex, *Journal of the Geological Society*, *149*(2), 221–235, doi:10.1144/gsjgs.149.2.0221.

McClusky, S. et al. (2000), Global Positioning System constraints on plate kinematics and dynamics in the eastern Mediterranean and Caucasus, *Journal of Geophysical Research: Solid Earth*, *105*(B3), 5695–5719, doi:10.1029/1999JB900351.

Mukherjee, S. (2010), Mineral fish: their morphological classification, usefulness as shear sense indicators and genesis, *International Journal of Earth Sciences*, *100*(6), 1303–1314, doi:10.1007/s00531-010-0535-0.

Nagata, T. (1961), *Rock Magnetism*, Maruzen Co., Tokyo.

Neves, S. P., A. Vauchez, and C. J. Archanjo (1996), Shear zone-controlled magma emplacement or magma-assisted nucleation of shear zones? Insights from northeast Brazil, *Tectonophysics*, *262*(1–4), 349–364, doi:10.1016/0040-1951(96)00007-8.

Passchier, C. W., and R. A. J. Trouw (2005), *Microtectonics*, Springer, Berlin; New York.

Paterson, S. R., R. H. Vernon, and O. T. Tobisch (1989), A review of criteria for the identification of magmatic and tectonic foliations in granitoids, *Journal of Structural Geology*, *11*(3), 349–363, doi:10.1016/0191-8141(89)90074-6.

Paterson, S. R., G. S. Pignotta, and R. H. Vernon (2004), The significance of microgranitoid enclave shapes and orientations, *Journal of Structural Geology*, *26*(8), 1465–1481, doi:10.1016/j.jsg.2003.08.013.

Pérouse, E., N. Chamot-Rooke, A. Rabaute, P. Briole, F. Jouanne, I. Georgiev, and D. Dimitrov (2012), Bridging onshore and offshore present-day kinematics of central and eastern Mediterranean: Implications for crustal dynamics and mantle flow, *Geochemistry, Geophysics, Geosystems*, *13*(9), doi:10.1029/2012GC004289.

Petrakakis, K., C. Iglseder, A. Zámolyi, C. Rambousek, B. Grasemann, E. Draganitis, A. Kurka, and A. Photiades (2010), Geological Map of Greece, Serifos Island, Institute of Geology and Mineral Exploration (IGME), Athens.

Reilinger, R., S. McClusky, D. Paradissis, S. Ergintav, and P. Vernant (2010), Geodetic constraints on the tectonic evolution of the Aegean region and strain accumulation along the Hellenic subduction zone, *Tectonophysics*, *488*(1–4), 22–30, doi:10.1016/j.tecto.2009.05.027.

Rice, A. H. N. et al. (2012), A new geological map of the crustal-scale detachment on Kea (Western Cyclades, Greece), *Australian Journal of Earth Sciences*, *105*(3), 108–124.

Ring, U., J. Glodny, T. Will, and S. Thomson (2010), The Hellenic Subduction System:

High-Pressure Metamorphism, Exhumation, Normal Faulting, and Large-Scale Extension, *Annual Review of Earth and Planetary Sciences*, *38*(1), 45–76, doi:10.1146/annurev.earth.050708.170910.

Rochette, P., M. Jackson, and C. Aubourg (1992), Rock magnetism and the interpretation of anisotropy of magnetic susceptibility, *Reviews of Geophysics*, *30*(3), 209, doi:10.1029/92RG00733.

Rochette, P., C. Aubourg, and M. Perrin (1999), Is this magnetic fabric normal? A review and case studies in volcanic formations, *Tectonophysics*, *307*(1–2), 219–234, doi:10.1016/S0040-1951(99)00127-4.

Rohais, S., R. Eschard, M. Ford, F. Guillocheau, and I. Moretti (2007), Stratigraphic architecture of the Plio-Pleistocene infill of the Corinth Rift: Implications for its structural evolution, *Tectonophysics*, *440*(1–4), 5–28, doi:10.1016/j.tecto.2006.11.006.

Salemink, J. (1985), Skarn and ore formation at Serifos, Greece, as a consequence of granodiorite intrusion, Ph.D thesis, University of Utrecht, Netherlands.

Schliestedt, M., V. Bartsch, M. Carl, A. Matthews, and F. Henjes-Kunst (1994), The P-T path of Greenschist-facies rocks from the island of Kithnos (Cyclades, Greece), *Chemie der Erde*, *54*, 281–296.

Schneider, D. A., C. Senkowski, H. Vogel, B. Grasemann, C. Iglseder, and A. K. Schmitt (2011), Eocene tectonometamorphism on Serifos (western Cyclades) deduced from zircon depth-profiling geochronology and mica thermochronology, *Lithos*, *125*(1–2), 151–172, doi:10.1016/j.lithos.2011.02.005.

Schulmann, K., and J. Ježek (2012), Some remarks on fabric overprints and constrictional AMS fabrics in igneous rocks, *International Journal of Earth Sciences*, *101*(3), 705–714, doi:10.1007/s00531-011-0681-z.

Simpson, C., and R. P. Wintsch (1989), Evidence for deformation-induced K-feldspar replacement by myrmekite, *Journal of Metamorphic Geology*, *7*(2), 261–275, doi:10.1111/j.1525-1314.1989.tb00588.x.

Smith, S. A. F., R. E. Holdsworth, and C. Collettini (2011), Interactions between low-angle normal faults and plutonism in the upper crust: Insights from the Island of Elba, Italy, *Geological Society of America Bulletin*, *123*(1–2), 329–346, doi:10.1130/B30200.1.

Sparks, R. S. J., and L. A. Marshall (1986), Thermal and mechanical constraints on mixing between mafic and silicic magmas, *Journal of Volcanology and Geothermal Research*, *29*(1–4), 99–124, doi:10.1016/0377-0273(86)90041-7.

St. Seymour, K., D. Zouzias, S. Tombros, and E. Kolaiti (2009), Geochemistry of the Serifos pluton (Cycladic islands) and associated iron oxide and sulfide ores: Skarn or metamorphosed exhalite deposits?, *Neues Jahrbuch für Mineralogie - Abhandlungen*, *186*(3), 249–270, doi:10.1127/0077-7757/2009/0143.

Stouraiti, C., and P. Mitropoulos (1999), Variation in amphibole composition from the Serifos intrusive complex (Greece), under magmatic and hydrothermal alteration conditions: An application of hornblende geobarometry, *Bulletin of the Geological Society of Greece*, *33*, 39–50.

Stouraiti, C., P. Mitropoulos, J. Tarney, B. Barreiro, A. M. McGrath, and E. Baltatzis (2010), Geochemistry and petrogenesis of late Miocene granitoids, Cyclades, southern Aegean: Nature of source components, *Lithos*, *114*(3–4), 337–352, doi:10.1016/j.lithos.2009.09.010.

Tikoff, B., and C. Teyssier (1992), Crustal-scale, en echelon "P-shear" tensional bridges: A possible solution to the batholithic room problem, *Geology*, *20*(10), 927–930, doi:10.1130/0091-7613(1992)020<0927:CSEEPS>2.3.CO;2.

Tobisch, O. T., B. A. McNulty, and R. H. Vernon (1997), Microgranitoid enclave swarms in granitic plutons, central Sierra Nevada, California, *Lithos*, *40*(2–4), 321–339, doi:10.1016/S0024-4937(97)00004-2.

Tommasi, A., A. Vauchez, L. A. D. Femandes, and C. C. Porcher (1994), Magma-assisted strain localization in an orogen-parallel transcurrent shear zone of southern Brazil, *Tectonics*, *13*(2), 421–437, doi:10.1029/93 TC03319.

Trotet, F., O. Vidal, and L. Jolivet (2001a), Exhumation of Syros and Sifnos metamorphic rocks (Cyclades, Greece). New constraints on the P-T paths, *European Journal of Mineralogy*, *13*(5), 901–920, doi:10.1127/0935-1221/2001/0013/0901.

Trotet, F., L. Jolivet, and O. Vidal (2001b), Tectono-metamorphic evolution of Syros and Sifnos islands (Cyclades, Greece), *Tectonophysics*, *338*(2), 179–206, doi:10.1016/S0040-1951(01)00138-X.

Tschegg, C., and B. Grasemann (2009), Deformation and alteration of a granodiorite during low-angle normal faulting (Serifos, Greece), *Lithosphere*, *1*(3), 139–154, doi:10.1130/L33.1.

Tullis, J., and R. A. Yund (1977), Experimental deformation of dry westerly granite, *Journal of Geophysical Research*, *82*(36), 5705–5718, doi:10.1029/JB082i036p05705.

Turrillot, P., M. Faure, G. Martelet, Y. Chen, and R. Augier (2011), Pluton-dyke relationships in a Variscan granitic complex from AMS and gravity modelling. Inception of the extensional tectonics in the South Armorican Domain (France), *Journal of Structural Geology*, *33*(11), 1681–1698, doi:10.1016/j.jsg.2011.08.004.

Vanderhaeghe, O. (2004), Structural development of the Naxos migmatite dome, in *Gneiss Domes in Orogeny*, vol. 380, pp. 211–227, Geological Society of America, Boulder, Colorado.

Vernon, R. H. (1991), Questions about myrmekite in deformed rocks, *Journal of Structural Geology*, *13*(9), 979–985, doi:10.1016/0191-8141(91)90050-S.

Vernon, R. H. (2000), Review of Microstructural Evidence of Magmatic and Solid-State Flow, *Visual Geosciences*, *5*(2), 1–23, doi:10.1007/s10069-000-0002-3.

Vernon, R. H., M. A. Etheridge, and V. J. Wall (1988), Shape and microstructure of microgranitoid enclaves: Indicators of magma mingling and flow, *Lithos*, *22*(1), 1–11, doi:10.1016/0024-4937(88)90024-2.

Vigneresse, J. L. (1995), Control of granite emplacement by regional deformation, *Tectonophysics*, *249*(3–4), 173–186, doi:10.1016/0040-1951(95)00004-7.

Villa (1998), Isotopic closure, *Terra Nova*, *10*(1), 42–47, doi:10.1046/j.1365-3121.19 98.00156.x.

Wernicke, B. P., P. C. England, L. J. Sonder, and R. L. Christiansen (1987), Tectonomagmatic evolution of Cenozoic extension in the North American Cordillera, *Geological Society, London, Special Publications*, *28*(1), 203–221, doi:10.1144 /GSL.SP.1987.028.01.15.

Wijbrans, J. R., and I. McDougall (1988), Metamorphic evolution of the Attic Cycladic Metamorphic Belt on Naxos (Cyclades, Greece) utilizing $^{40}Ar/^{39}Ar$ age spectrum measurements, *Journal of Metamorphic Geology*, *6*(5), 571–594, doi:10.1111/j.1525-1314.1988.tb00441.x.

Wijbrans, J. R., M. Schliestedt, and D. York (1990), Single grain argon laser probe dating of phengites from the blueschist to greenschist transition on Sifnos (Cyclades, Greece), *Contributions to Mineralogy and Petrology*, *104*(5), 582–593, doi:10.1007 /BF00306666

Chapitre IV

Comment le magmatisme syn-extensif a-t-il impacté l'évolution tardive des dômes métamorphiques cycladiques

Sommaire

Résumé étendu

Problématique et démarche

En intégrant les observations terrain, analyses et discussions des précédents chapitres ainsi qu'un certain nombre d'éléments clés de la littérature accumulés ces dernières décennies, ce quatrième chapitre se propose **d'évaluer à l'échelle de l'ensemble du domaine des Cyclades l'impact du magmatisme intrusif sur la dynamique des dômes métamorphiques extensifs (MCCs)**. Ce chapitre, rédigé sous la forme d'un article de synthèse, englobe une étude comparative des cinq dômes métamorphiques extensifs où les complexes plutoniques affleurent à proximité de détachements (Tinos, Mykonos-Delos-Rhenia, Ikaria, Naxos et Serifos). Afin de dissocier autant que possible les données bibliographiques de celles acquises au cours de nos différentes campagnes de terrain, le manuscrit s'est organisé selon deux grands axes.

La première partie recense tout un arsenal d'âges radiométriques et de caractéristiques tectono-métamorphiques en lien avec le développement de ces MCCs et leurs détachements associés. Une attention particulière est également portée sur la relation temporelle entre les intrusions et le métamorphisme rétrograde lié à l'exhumation des dômes. La seconde partie, quant à elle, comprend à la fois un bref aperçu des types de roche ignée exposés au cœur des dômes métamorphiques ainsi qu'une description plus exhaustive consacrée à l'état de déformation finie fossilisé à l'intérieur de chaque corps intrusif. Avec l'objectif d'illustrer des gradients de déformation latéraux, il est établi des cartes d'intensité de la déformation découlant soit de nos propres investigations (Naxos, chapitre II ; Serifos, chapitre III ; Ikaria, voir les deux publications associées en annexe A [*Laurent et al.*, 2015] et en annexe B [*Beaudoin et al.*, 2015]), soit d'observations structurales déjà publiées (Tinos, Mykonos).

Résultats majeurs

Il en ressort au travers de cette compilation de données une ressemblance frappante quant à l'évolution et l'architecture globale de ces différents MCCs. D'une part, il apparaît que les histoires d'exhumation des dômes métamorphiques se soient systématiquement accomplies le long de multiples détachements formés de manière séquentielle; les détachements superficiels disséquant les plus profonds. D'autre part, la venue d'intrusions magmatiques au sein de la croûte moyenne/supérieure égéenne semble s'être limitée dans un intervalle de 15 à 9 Ma, soit plusieurs millions d'années après le début de l'extension arrière-arc et les premières étapes d'exhumation des dômes métamorphiques. Ce déphasage temporel confirme dès lors que le magmatisme ne peut être un réel candidat pour la genèse des MCCs, mais serait au contraire le produit d'un environnement thermique plus chaud au cours de l'amincissement lithosphérique. Dans ce sens, il est possible d'imaginer que la migration des produits magmatiques syn-extensifs générés au sein de la lithosphère profonde aurait été en partie

guidée par les gradients de pressions engendrés par l'extension et les zones d'intense déformation, jusqu'à atteindre le cœur des MCCs déjà formés. Cette affirmation reste cependant totalement spéculative et repose uniquement sur des modèles pré-existants, dans la mesure où aucune observation de terrain ne permet de mesurer l'influence des zones de déformation localisée sur le transport de magmas à travers la croûte continentale.

Pour autant, les observations structurales et relations géométriques attestent d'une interaction étroite entre intrusions et développement de détachements. Tous ces complexes magmatiques, placés structuralement sous les détachements les plus superficiels, arborent en effet divers niveaux d'intensité de la déformation depuis les prémices d'une structuration syn-magmatique jusqu'à la mylonitisation à l'approche des détachements, voire même une déformation cassante-cataclastique le long de ces discontinuités. Ces continuums témoigneraient ainsi d'une localisation progressive de la déformation extensive le long de leur marge intrusive. En conséquence, nous proposons dans ce papier un schéma généralisable à l'ensemble de ces MCCs, dans lequel le développement séquentiel de détachements résulte de l'interaction locale et transitoire avec une intrusion magmatique. Nous soutenons que ces intrusions auraient inhibé l'activité de détachements précoces en les perforant et modifiant ainsi la position des plus forts contrastes rhéologiques. La déformation extensive, redistribuée le long des marges intrusives, se localiserait avec le temps au travers de détachements nouvellement formés, achevant l'exhumation des dômes métamorphiques. Ainsi, ce scénario dans lequel le magmatisme impacte dynamiquement l'évolution tardive des dômes métamorphiques implique que les corps magmatiques, considérés comme des instabilités thermo-mécaniques ponctuelles, sont capables d'introduire des contrastes rhéologiques drastiques de courte durée et provoquer localement des cycles d'affaiblissement-durcissement mécaniques de roches crustales.

Article: How synextensional magmatism dynamically impacted late-stage evolutions of Cycladic metamorphic core complexes (Aegean Sea, Greece)

Soumis dans la revue *Tectonics*

Aurélien Rabillard [1,2,3], Laurent Jolivet [1,2,3], Laurent Arbaret [1,2,3], Eloïse Bessière [1,2,3], Valentin Laurent [1,2,3], Armel Menant [1,2,3,4], Romain Augier [1,2,3] and Alexandre Beaudoin [1,2,3]

(1) Université d'Orléans, ISTO, UMR 7327, 45071, Orléans, France
(2) CNRS/INSU, ISTO, UMR 7327, 45071 Orléans, France
(3) BRGM, ISTO, UMR 7327, BP 36009, 45060 Orléans, France
(4) Now at Institut de Physique du Globe de Paris, Paris Sorbonne Cité, Univ. Diderot, UMR 7154-CNRS, Tectonique et Mécanique de la Lithosphère, Paris, France

Abstract

Within deforming continental regions where metamorphic core complexes (MCCs) and synextensional granitoids are closely associated, deciphering the causal link between detachment faulting and magmatism often remains complex as (1) the rheological weakness of magma may stimulate mechanisms of strain localization, and conversely (2) tectonic processes may open/close drains where magmas can intrude. Here, we tackle this issue by focusing on the Cyclades with the comparison of five granitoid-cored MCCs (Tinos, Mykonos, Ikaria, Naxos and Serifos) and their flanking detachment systems. In this region, granitoids were emplaced into the middle/upper crust over a relatively short time period (15-9 Ma) while metamorphic domes were largely exhumed after more than 10 Myrs of extension. None of those intrusions thereby proves to be a real candidate for the genesis of MCCs but would rather be a consequence of a warmer regime during lithospheric thinning. However, all collected structural and kinematic data converge toward a regional scheme in which magmatic activity played a more pivotal role than previously postulated. Indeed, late evolution stages of MCCs were dynamically impacted by intrusions along which a local and transient heterogeneity of the mechanical strength occurred, resulting in the sequential development of detachments. During their tectonically controlled ascent, magmatic products intruded already-formed detachments at depth, inhibited their activities and finally induced a contemporaneous upward migration of extensional deformation that tended to localize through time within intrusion roofs. The newly-formed detachments are expressed within granitoids through a continuum of deformation from co-magmatic to ductile conditions, followed by cataclasis along detachments.

Key words: synkinematic intrusions; metamorphic core complexes; detachment systems; extension; strain localization; Cyclades

1. Introduction

Within highly extended continental domains, the development of Metamorphic Core Complexes (MCCs) represents one of the most effective mechanisms for rapid exhumation of deep-seated materials toward upper crustal levels. Historically described in the North American Cordillera [*Davis & Coney*, 1979; *Crittenden et al.*, 1980], and then evidenced in the Mediterranean Region [*Lister et al.*, 1984; *Avigad & Garfunkel*, 1989] or even in East Asia [*Davis et al.*, 1996; *Faure et al.*, 1996], MCCs are classically regarded as dome-like structures roofed by a single detachment or, in more complex ways, by multiple and closely spaced detachments [*Spencer*, 1984; *Lister & Davis*, 1989]. Usually associated with normal sense displacements of several tens of kilometers, MCC-bounding detachments typically nucleate within the deep crust as thick ductile shear zones that evolve into brittle low-angle normal faults in the upper crust (LANFs, see recent reviews by *Whitney et al.* [2013] or *Platt et al.* [2015]). In addition to an upward mass transfer, lithospheric thinning and formation of MCCs are often coupled with partial melting of the upper mantle and/or the lower crust as well as a heat dissipation toward the Earth's surface, giving rise to recurrent spatiotemporal interrelations between intrusive magmatism and active detachment zones at various crustal levels [e.g., *Vanderhaeghe & Teyssier*, 2001; *Whitney et al.*, 2004a; *Vanderhaeghe*, 2009]. Well documented by field-based contributions worldwide, granitoid-cored MCCs have been for instance widely recognized in the North American Cordillera [e.g., *Davis & Coney*, 1979; *Hyndman*, 1980; *Dallmeyer et al.*, 1986; *Lee Armstrong & Ward*, 1991; *Vanderhaeghe & Teyssier*, 1997; *Campbell-Stone et al.*, 2000], in East Asia [e.g., *Davis et al.*, 1996; *Faure et al.*, 1996; *Shu et al.*, 1998; *Webb et al.*, 1999; *Lin & Wang*, 2006; *Lin et al.*, 2008; *Charles et al.*, 2011, 2013], in the Mediterranean region [e.g., *Dinter & Royden*, 1993; *Bozkurt & Park*, 1994; *Daniel & Jolivet*, 1995; *Hetzel et al.*, 1995; *Whitney & Dilek*, 1997; *Jolivet et al.*, 1998; *Rossetti et al.*, 1999], and particularly in the Aegean Sea (Greece) where several metamorphic domes and their flanking detachment systems developed in close association with plutonic intrusions [*Faure et al.*, 1991; *Lee & Lister*, 1992; *Gautier et al.*, 1993; *Grasemann & Petrakakis*, 2007; *Jolivet et al.*, 2010, 2015; *Denèle et al.*, 2011; *Beaudoin et al.*, 2015; *Laurent et al.*, 2015; *Rabillard et al.*, 2015].

Over the past four decades, studies thus partly focused on assessing geological processes through which MCC-bounding detachments could have been geometrically and kinematically paired with short-lived magmatic episodes during a protracted exhumation history. In particular, the causal link between both phenomena was vigorously discussed and this debate still continues as far as different conceptual models are conceivable depending on whether plutonic activity slightly predates, coincides or postdates the paroxysmal stage of extension. A commonly-held model suggests that pre- to syn-extensional magmatism could embody a prominent catalyst agent for orogenic collapse and a sufficient trigger to form MCCs [e.g., *Carr*, 1992; *Baldwin et al.*, 1993; *Hill et al.*, 1995]. Within the lower and middle crust, the heat flux and accumulation of melting products can indeed transiently introduce a drastic thermal weakening of surrounding rocks promoting a lateral spreading of the orogenic wedge and an upward ductile flow of the dome-shaped partially molten lower crust [e.g., *Armstrong*, 1982; *Coney & Harms*, 1984; *Gans*, 1987; *Brown & Dallmeyer*, 1996; *MacCready et al.*, 1997;

Vanderhaeghe & Teyssier, 2001; *Vanderhaeghe*, 2012; *Augier et al.*, 2015a]. At a more restricted scale, unconsolidated intrusive bodies are capable to generate strong rheological heterogeneities along which the onset of extensional shearing and subsequent mechanisms of strain localization can be efficiently stimulated [e.g., *Lynch & Morgan*, 1987; *Brun et al.*, 1994; *Pavlis*, 1996]. A fast expansion of overpressured magmas may further destabilize over a short time period the ambient stress field by deflecting the maximum principal stress axis away from vertical, thereby favoring a strain accommodation through low-dipping normal faults above intrusive zones [*Parsons & Thompson*, 1993]. Alternatively, when lithospheric thinning appears to be already initiated prior to intrusive magmatism, it was often argued that late- to post-orogenic extensional exhumations below crustal-scale detachments could set off a decompression-driven partial melting of the deep lithosphere and an extraction of magmatic pulses toward shallower crustal levels [e.g., *Teyssier & Whitney*, 2002; *Whitney et al.*, 2004b; *Teyssier et al.*, 2005]. In cooperation with various ascent mechanisms, magma migration through the crust can be partly guided by local pressure gradients induced by high-shear strain zones, as far as reaching major detachment faults acting as mechanical boundaries for magma storage [e.g., *Fletcher et al.*, 1995; *Vanderhaeghe*, 1999; *Bonini et al.*, 2001]. Once accumulated into deforming zones, partially crystallized magmas can in turn temporarily disturb both the thermal structure and the deformational regime prevailing within the surrounding system. As a result, magmas may strongly modify the style and pattern of faulting such as the upward arching of pre-existing detachment surfaces or even the sequential development of localizing events involving a polyphased faulting history [e.g., *Davis et al.*, 1993; *Lister & Baldwin*, 1993; *Daniel & Jolivet*, 1995].

Testing this genetic link at local and regional scales requires a multidisciplinary approach to constrain (1) the relative timing between magmatism, strain localization and related metamorphism, (2) the geometrical relations between granitoids and large-scale tectonic structures, and (3) the distribution and evolution of deformation fossilized inside and outside granitoids. In this perspective, the Cyclades proves to be a valuable natural laboratory since thermochronological investigations have clearly shown that several I- and S-type intrusions were emplaced alongside detachment faults during the late exhumation stage of metamorphic domes [*Keay*, 1998; *Keay et al.*, 2001; *Brichau et al.*, 2007, 2008; *Iglseder et al.*, 2009; *Bolhar et al.*, 2010]. Despite these meaningful progresses on the geological understanding of the Cyclades, no consensus has yet been reached on mechanisms responsible for such association. Indeed, most contributions have concluded that the late plutonic stage neither appears to be a major trigger for the development of MCCs nor a strong helper for strain localization along flanking detachments, and some of them would have merely acted as passive markers of crustal extension [*Brichau et al.*, 2007, 2008; *Bolhar et al.*, 2010]. In this sense, extensional deformation would have rather promoted preferential pathways for magma transport through the crust while the location of pluton emplacement would be controlled by active detachments [*Bolhar et al.*, 2010]. Though acknowledging the logic of this latter proposal some field-based studies have alternatively suggested a more pivotal role of the plutonic activity in redistribution and localization of extensional deformation by promoting the development of new detachment zones [*Jolivet et al.*, 2010; *Denèle et al.*, 2011; *Laurent et al.*, 2015; *Rabillard et al.*, 2015]. Otherwise, a few studies have proposed the preeminent role of transtensional strike-slip faults

for both the emplacement of those granitoids and ensuing deformation [*Boronkay & Doutsos*, 1994; *Koukouvelas & Kokkalas*, 2003; *Kokkalas & Aydin*, 2013].

In the present paper we therefore synthetize key tectonometamorphic and geochronological data related to the development of the Cycladic MCCs where detachment systems were closely associated with granitoids, as well as new structural data we collected from those intrusions. As a result of this review, we propose a regional scheme in which magmatic complexes dynamically impacted the development of MCCs rather than their passive attitude with regard to extensional tectonics.

2. Geodynamic and geological context of the Aegean region with focus on the Cyclades

The Aegean region, i.e. the easternmost Mediterranean back-arc domain, was formed in the overriding plate of the retreating Hellenic subduction zone [*Le Pichon & Angelier*, 1981]. As most extending continental domains, the Aegean region experienced a protracted tectonic history that has produced thermomechanical heterogeneities in the crust, e.g., large thrusts, syn-orogenic detachments, partial-melting zones or even intrusions [*Jolivet & Brun*, 2010; *Royden & Papanikolaou*, 2011; *Jolivet et al.*, 2013]. Driven by the convergence between Africa and Eurasia since the Mesozoic, the Aegean back-arc domain was previously occupied by the Hellenides-Taurides belt, a polygenic orogenic wedge built up by the successive accretion of both oceanic and continental upper crustal units [*Aubouin*, 1958; *Jacobshagen et al.*, 1978; *Bonneau*, 1984; *van Hinsbergen et al.*, 2005; *Ring et al.*, 2010]. The resulting SW- verging nappe stacking have thus triggered successively burial and synorogenic exhumation processes in high-pressure–low-temperature (H*P*-L*T*) metamorphic conditions below crustal- scale thrusts and syn-orogenic detachments respectively [*Jolivet et al.*, 1994, 2003, *Ring et al.*, 2007a, 2007b; *Brun & Faccenna*, 2008; *Huet et al.*, 2009; *Laurent et al.*, 2016]. From the Early Eocene onward (~45 Ma), the Hellenic overthickened crust was first subjected to extensional tectonics by a possible lithospheric delamination while the Hellenic subduction zone remained relatively static or retreated slowly southward, thus allowing the development of the Rhodope MCCs in the northernmost Aegean (see *Burg* [2012] and references therein). In response to a faster backward retreat of the N-dipping Hellenic slab since 35-30 Ma ago, the subduction front was increasingly dragged southward and the Eurasian upper plate underwent extensional collapse in back-arc domain [*Jolivet & Faccenna*, 2000], until reaching the present-day tectonic architecture of the Aegean domain with an arcuate accretionary wedge (i.e. the Mediterranean Ridge, Figure IV-1a). Back-arc active extension is mainly circumscribed around the Aegean Sea, i.e., Western Turkey, the Corinth rift, the southern Peloponnese and Crete [*Jackson*, 1994; *Hatzfeld et al.*, 2000; *Goldsworthy et al.*, 2002]. The almost total lack of seismic activity in the Aegean Sea, only present below the southern Aegean arc volcanoes [*Bohnhoff et al.*, 2004, 2006; *Dimitriadis et al.*, 2009], suggests that this region currently behaves as a rigid block.

In the Cycladic archipelago, located in the central Aegean Sea, back-arc extension was active from the Late Oligocene to the Late Miocene [*Jolivet & Faccenna*, 2000; *Jolivet &*

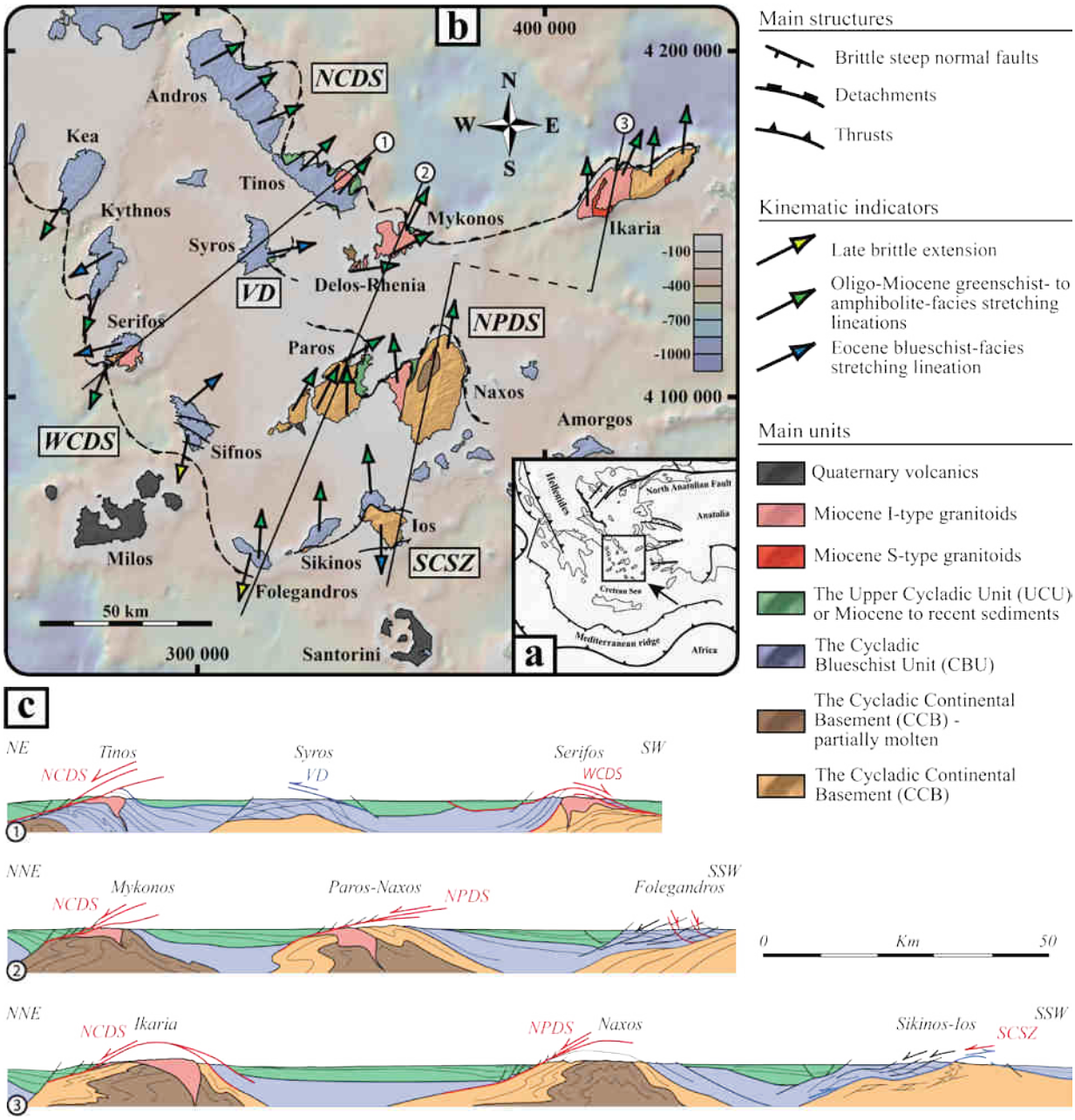

Figure IV-1: *(a) simplified tectonic map of the Aegean domain and location of the studied area. (b) Tectonic map of the Cyclades, modified after Huet et al. [2009], Jolivet et al. [2010, 2015]; Grasemann et al. [2012] and Augier et al. [2015b]. Coordinates on the map, including the following ones, are given in Universal Time Meridian (UTM) zone 35°N, World Geodetic System (WGS) 1984. At regional scale, note the spatial interaction between I-type granitoids (Tinos, Mykonos-Delos-Rhenia, Ikaria, Naxos and Serifos Islands) and metamorphic core complexes together with their flanking detachments. (c) Cross sections through the Cyclades (1-3), modified after Augier et al. [2015b]. Sections are roughly parallel to the tectonic transport and highlight the close interaction between granitoids and detachments. NCDS: North Cycladic Detachment System. NPDS: Naxos–Paros Detachment System. WCDS: West Cycladic Detachment System. SCSZ: South Cyclades Shear Zone. VD: Vari detachment.*

Brun, 2010; Ring et al., 2010]. During this period, slab roll-back and related change of stress regime were presumably accompanied with a lithospheric delamination and a slab tear; all of

that being also coeval with a warmer thermal state in the lithosphere, a partial melting of the extending lower crust and the formation of multiple MCCs [*Lister et al.*, 1984; *Gautier et al.*, 1993; *Gautier & Brun*, 1994a, 1994b; *Keay et al.*, 2001; *Vanderhaeghe*, 2004; *Pe-Piper & Piper*, 2006; *Ersoy & Palmer*, 2013; *Jolivet et al.*, 2013, 2015, *Menant et al.*, 2016a, 2016b]. More specifically, the development of the Cycladic MCCs and their affiliated crustal-scale detachments led to progressive exhumation of the deepest parts of the Hellenic orogenic wedge (i.e. the Cycladic Continental Basement and the Cycladic Blueschist Unit, see thereafter) under greenschist- to amphibolite-facies retrograde metamorphism that partly overprinted a former Eocene subduction-related H*P*-L*T* metamorphism evidenced by relics of eclogite and blueschist parageneses [*Urai et al.*, 1990; *Buick*, 1991b; *Avigad et al.*, 1997; *Jolivet & Patriat*, 1999]. In the northern and central Cyclades, extensional exhumation was respectively achieved below the North Cycladic Detachment System (NCDS, Figures IV-1b and -1c) [*Jolivet et al.*, 2010; *Lecomte et al.*, 2010] and the Naxos–Paros Detachment System (NPDS, Figures IV-1b and -1c) [*Gautier et al.*, 1993; *Brichau et al.*, 2006], two sets of crustal-scale detachments with stable top-to-the-N or -NE kinematics. At the Aegean scale, the NCDS has been tentatively extended over 200 km long from Evia to the northernmost Cycladic Islands (Andros, Tinos and Mykonos), and even farther east on Ikaria Island [*Jolivet et al.*, 2010; *Beaudoin et al.*, 2015]. In the Western Cyclades, a large part of the extensional exhumation was accommodated by the West Cycladic Detachment System (WCDS, Figures IV-1b and -1c), a series of opposite top-to-the-SW detachments that crop out along a discontinuous 100 km long trend from Lavrion (Greece mainland) [*Skarpelis*, 2007; *Krohe et al.*, 2010; *Berger et al.*, 2013] to the westernmost Cycladic Islands (Kythnos, Kea and Serifos) [*Iglseder et al.*, 2011; *Grasemann et al.*, 2012; *Rice et al.*, 2012]. A possible southeastward extension of the WCDS has been proposed offshore south of Sifnos and Folegandros Islands on which S-oriented, late brittle displacements have been described [*Ring et al.*, 2011; *Augier et al.*, 2015b; *Roche et al.*, 2016]. Farther east on Sikinos and Ios Islands, a localized top-to-the-S shearing has been also recognized (Figures IV-1b and -1c), initially interpreted as an extensional shear zone (i.e. the South Cyclades Shear Zone, SCSZ) [*Lister et al.*, 1984; *Vandenberg & Lister*, 1996; *Baldwin & Lister*, 1998; *Forster & Lister*, 2009] but more later viewed as an Eocene H*P*-L*T* event of thrusting, reworked afterward by a top-to-the-N extensional deformation since Oligocene time [*Huet et al.*, 2009; *Augier et al.*, 2015b].

Final exhumation was mainly completed by brittle increments of deformation along detachments, bringing back toward the surface three main units [*Bonneau*, 1984; *Jolivet et al.*, 2004a; *Jolivet & Brun*, 2010; *Ring et al.*, 2010]. From bottom to top of the rearranged Eocene nappe stack, it has been recognized (1) the Cycladic Continental Basement (CCB, thereafter), primarily made up of para- and orthogneissic rocks equilibrated in the amphibolite-facies conditions of Variscan or even pre-Variscan age [*Henjes-Kunst & Kreuzer*, 1982; *Andriessen et al.*, 1987; *Keay & Lister*, 2002]. Well exposed in some tectonic windows (i.e. Naxos, Paros, Ikaria, Ios, Sikinos, Serifos and Mykonos-Delos), the Cycladic basement further contains locally a marble-metapelite cover [*Dürr et al.*, 1978; *Ring et al.*, 1999; *Grasemann & Petrakakis*, 2007; *Beaudoin et al.*, 2015]. The CCB tectonically underlies the (2) Cycladic Blueschist Unit (CBU, thereafter), a metavolcanosedimentary unit dominated by interlayered schists and marbles with embedded metabasite boudins [*Blake et al.*, 1981; *Reinecke et al.*,

1982; *Avigad & Garfunkel*, 1989; *Keiter et al.*, 2004]. While both the CCB and CBU were subjected to a H*P*-L*T* event during the Eocene [*Andriessen et al.*, 1979; *Wijbrans & McDougall*, 1986, 1988; *Maluski et al.*, 1987; *Bröcker et al.*, 1993; *Trotet et al.*, 2001a; *Parra et al.*, 2002; *Groppo et al.*, 2009; *Huet et al.*, 2015; *Laurent et al.*, 2017], the overlying (3) Upper Cycladic Unit (UCU, thereafter) is devoid of synsubduction H*P* imprint, suggesting that it was not buried in the Hellenic subduction zone. Lithologically heterogeneous, the UCU crops out as small klippes. It includes a continental basement (amphibolites, gneisses) that preserves Late Cretaceous H*T* metamorphic ages and a Permian to Mesozoic sedimentary cover topped by ophiolites (i.e. serpentinites, gabbros and basalts) obducted in the Late Jurassic or Late Cretaceous [*Altherr et al.*, 1994; *Patzak et al.*, 1994; *Katzir et al.*, 1996; *Papanikolaou*, 2009; *Martha et al.*, 2016]. This disrupted Eocene nappe stack is frequently bounded by sedimentary basins filled with Miocene to Present detrital shallow marine and continental deposits [*Sanchez-Gomez et al.*, 2002; *Kuhlemann et al.*, 2004]. Clasts from the underlying Cycladic units are commonly observed indicating syntectonic deposition of sediments during footwall denudation [*Kuhlemann et al.*, 2004; *Lecomte et al.*, 2010].

During the extension-related exhumation of the CCB and CBU, several syntectonic granitoids have successively intruded the Cycladic MCCs at middle/upper crustal depths [*Gautier et al.*, 1993; *Bröcker & Franz*, 1994; *Lucas*, 1999; *Pe-Piper*, 2000; *St. Seymour et al.*, 2009; *Laurent et al.*, 2015; *Cao et al.*, 2016]. Precise zircon (U-Th)/Pb ages from those granitoids have thus revealed crystallization histories ranging from 15 to 9 Ma (Figure IV-2) [*Keay*, 1998; *Keay et al.*, 2001; *Brichau et al.*, 2007, 2008; *Iglseder et al.*, 2009; *Bolhar et al.*, 2010], a relatively short time interval during which both I- and S-type intrusions migrated from the north-northeastern Cyclades (Tinos, Mykonos-Delos, Ikaria) to the southwest (Serifos), passing across the central Cyclades (Naxos, Paros). S-type granites were mostly linked to migmatite-cored MCCs and almost systematically older than spatially associated I-type granitoids (Figures IV-2). Voluminous I-type granitoids were especially emplaced alongside crustal-scale detachments and have recorded a similar shearing distribution (Figure IV-1c) [*Faure et al.*, 1991; *Lee & Lister*, 1992; *Denèle et al.*, 2011; *Laurent et al.*, 2015; *Rabillard et al.*, 2015]. I-type granitoids encompass a broad range of modal compositions and some of them constitute composite large-scale intrusions [*Altherr et al.*, 1982; *Pe-Piper et al.*, 1997; *Altherr & Siebel*, 2002; *Iglseder et al.*, 2009; *Denèle et al.*, 2011]. These intrusive bodies typically originated from a mixing between a crustal melting and seemingly mantle-derived magmas in fluctuating proportions, as documented by geochemical studies [*Altherr et al.*, 1988; *Altherr & Siebel*, 2002; *Pe-Piper & Piper*, 2006; *Stouraiti et al.*, 2010; *Bolhar et al.*, 2012]. In the field, remnants of the presumed mantle source and the significant interaction of compositionally heterogeneous magmas during cooling of the intrusions is further supported by common occurrences of mafic enclaves and dikes within more felsic plutonic bodies [e.g., *Avigad et al.*, 1998; *Koukouvelas & Kokkalas*, 2003; *Denèle et al.*, 2011; *Laurent et al.*, 2015; *Rabillard et al.*, 2015]. Accordingly, variation in their petrological and geochemical characteristics led some authors to involve an incremental growing of plutons by multiple and discrete magma pulses, which is supported by high resolution zircon (U-Th)/Pb geochronology reporting complex and multimodal age spectra from those I-type granitoids over few million years [*Bolhar et al.*, 2010, 2012].

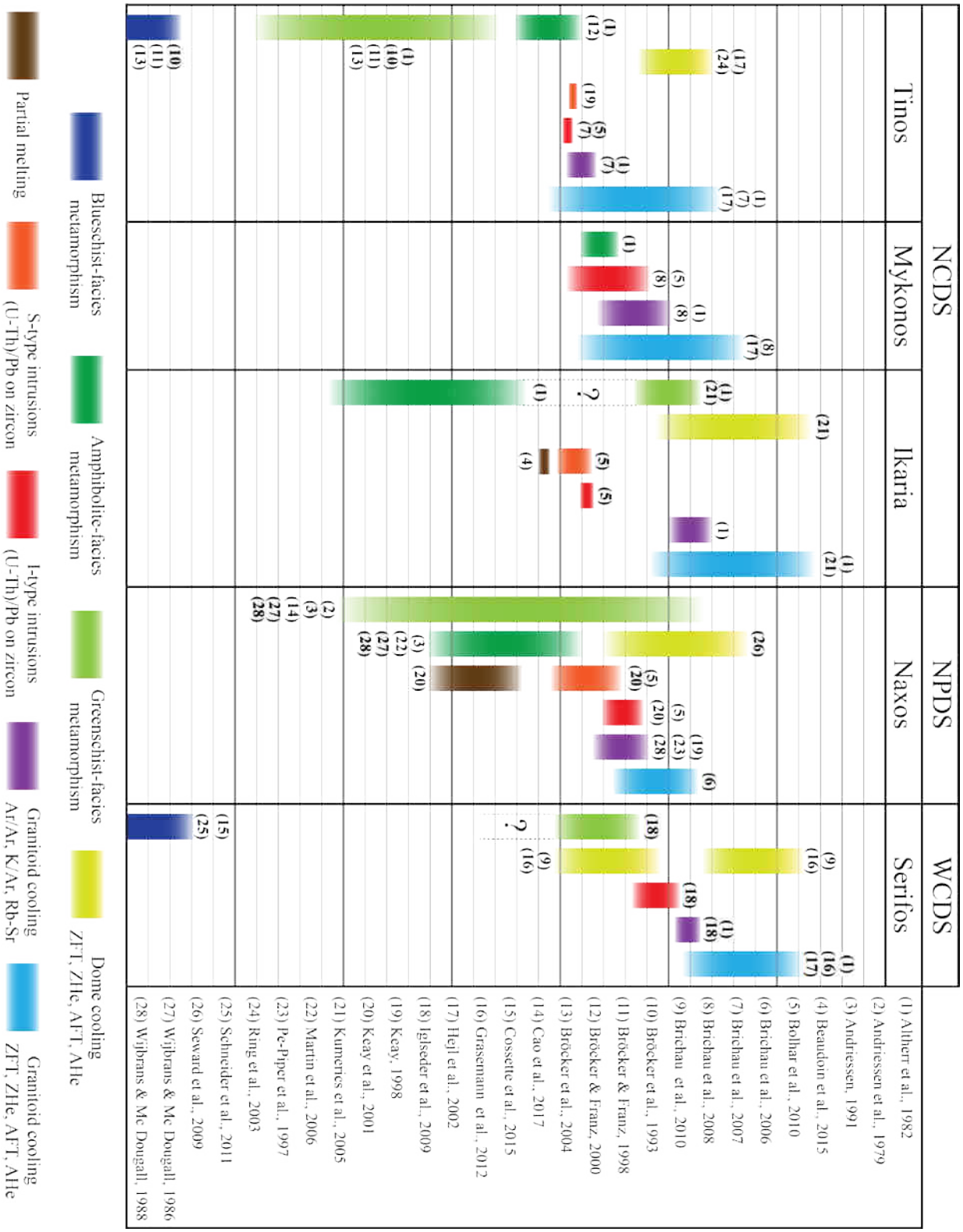

Figure IV-2: *compilation of available radiometric ages from the Cycladic Islands (Tinos, Mykonos-Delos-Rhenia, Ikaria, Naxos and Serifos) where development of metamorphic core complexes and associated detachment systems (i.e., NCDS, NPDS and WCDS) were paired with plutonic activity. Right side of the figure includes all references; see in the text for further information.*

3. Detachment systems and synextensional intrusions within the Cycladic MCCs

In this section, we focus on Cycladic MCCs where crustal-scale detachment systems and I-type granitoids are closely associated (i.e., Tinos, Mykonos-Delos-Rhenia, Ikaria, Naxos and Serifos Islands) and we report the main tectonometamorphic features related to the activity of detachment systems. A special attention is further paid to the spatiotemporal interactions between those detachment systems and plutonism.

3.1. Tinos and Mykonos-Delos-Rhenia Islands

One of the most prominent tectonic responses to the Aegean crustal extension has been particularly recognized over Tinos and Mykonos-Delos-Rhenia Islands since the development of these MCCs has been resolved into a coherent tectonic evolution involving three main branches of the North Cycladic detachment system (NCDS), i.e., the Tinos, Livada and Mykonos detachments [*Jolivet et al.*, 2010]. Associated with a constant NE-directed non-coaxial extensional deformation during the Oligo-Miocene exhumation history, these three detachments accommodated at least 70 km of displacement and reactivated/reworked successively former crustal-scale heterogeneities, suggesting a long-lasting tectonic evolution [*Brichau et al.*, 2008; *Jolivet et al.*, 2010].

The structurally lowermost branch, i.e. the Tinos detachment, can be followed along the northeastern coast of Tinos where it unroofs a metamorphic dome elongated perpendicular to the NE-directed regional extension (Figure IV-3 and in the included map inset at upper right). This sharp, corrugated and shallow NE-dipping normal fault, with dip angles ranging from 15° to 35°, brought in contact the UCU above the CBU (Figure IV-4) [*Avigad & Garfunkel*, 1989; *Jolivet & Patriat*, 1999; *Jolivet et al.*, 2004b]. As well described by previous structural fieldworks, the Tinos detachment acted in the ductile-then-brittle field [*Gautier & Brun*, 1994b; *Jolivet et al.*, 2004b; *Mehl et al.*, 2005]. Below the detachment plane, rocks derived from the underlying CBU were extensively mylonitized under a progressive northeastward and upward strain gradient. Mylonitization was coeval with an intense metamorphic retrogression into the greenschist facies [*Gautier & Brun*, 1994b; *Parra et al.*, 2002] leaving well-preserved Eocene H*P*-L*T* parageneses into the deepest exposed parts of the metamorphic sequence [*Bröcker et al.*, 1993, 2004; *Bröcker & Franz*, 1998; *Parra et al.*, 2002]. Locally, basal rocks of the upper unit recorded a similar top-to-the-NE shearing within a thin zone that never exceeds a few tens of meters [*Zeffren et al.*, 2005]. Close to the detachment plane, ductile shearing was intersected by sets of NW-SE striking, high- and low-angle normal faults and the tectonic contact itself lies beneath a several meter thick level of faulted talc-rich breccias and non-cohesive cataclasites (Figure IV-4) [*Patriat & Jolivet*, 1998; *Mehl et al.*, 2005]. Besides, geochronological analyses ascribed to the greenschist ductile exhumation yielded Oligo-Miocene ages from approximately 29 Ma to 18 Ma (Figure IV-2) [*Altherr et al.*, 1982; *Bröcker et al.*, 1993, 2004; *Bröcker & Franz*, 1998], showing that the Tinos detachment was predominantly active in the ductile field and ended as a brittle detachment before it was pierced

and sealed by the intrusive magmatic complex and associated dike arrays circa 15-14 Ma (Figures IV-2 and -3) [*Keay*, 1998; *Brichau et al.*, 2007; *Bolhar et al.*, 2010]. The Tinos magmatic complex further produced a thermal overprint and consequently a well-developed contact aureole, inducing a partial to complete reset of greenschist-facies recrystallization ages that range from approximately 17 Ma to 14 Ma (Figure IV-2) [*Altherr et al.*, 1982; *Bröcker & Franz*, 1998, 2000].

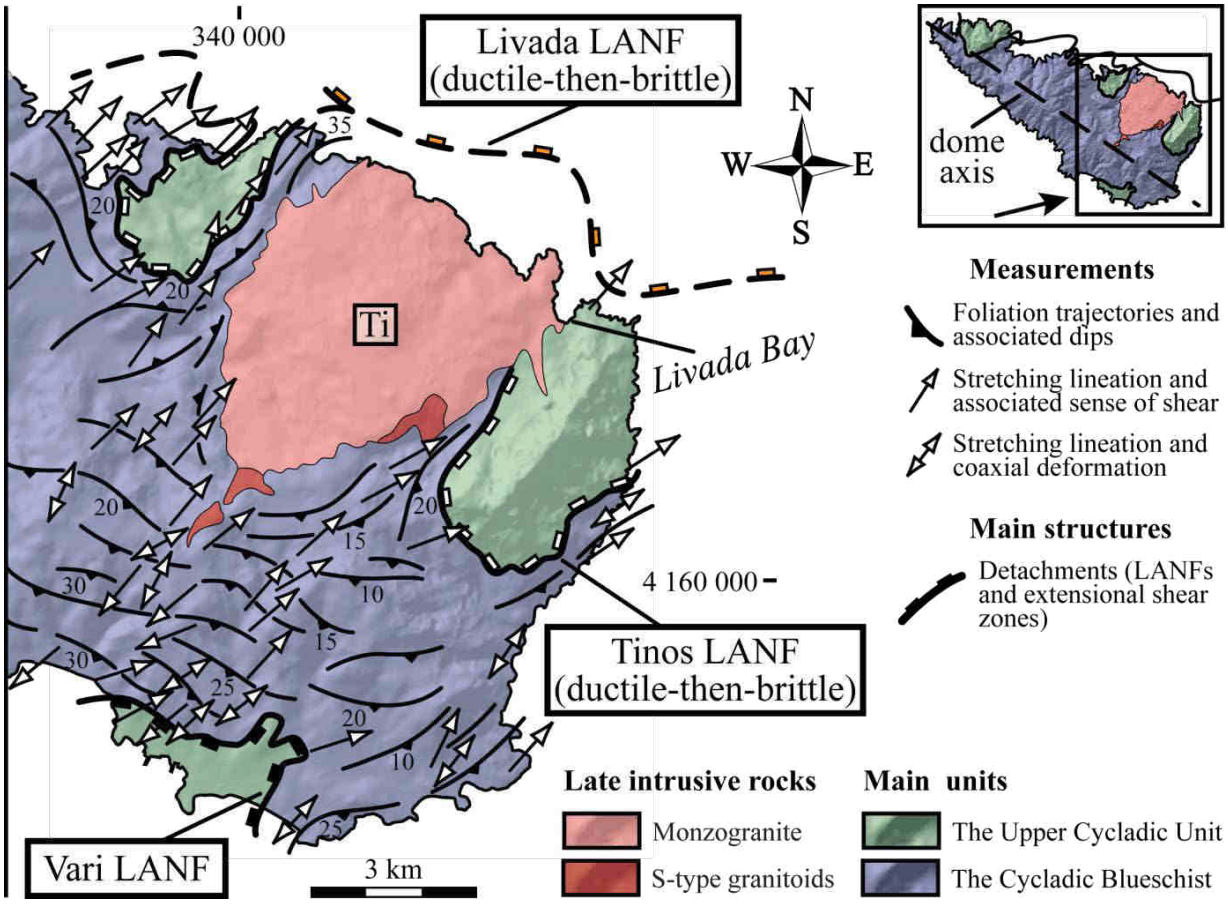

Figure IV-3: *tectonic map of the easternmost side of the Tinos metamorphic core complex and associated flanking detachments (location area in the included map inset at upper right showing the NE-directed elongated metamorphic dome). Field-based measurements of finite strain markers originate from Melidonis & Triantaphyllis [2003], Famin [2003], Mehl et al. [2005] and Jolivet et al. [2010]. Ti: Tinos magmatic complex.*

A tectonic contact between the UCU and CBU is also mapped on the southern tip of Tinos (Figures IV-1b, -1c and -3). At variance with the Tinos detachment, this gently SW-dipping discontinuity immediately occurs on top of blueschists and eclogites with Eocene metamorphic ages [*Bröcker*, 1990; *Bröcker et al.*, 1993; *Bröcker & Franz*, 1998; *Jolivet & Patriat*, 1999; *Parra et al.*, 2002]. On account of these tectonometamorphic features, this crustal-scale structure has been rather considered as an Eocene detachment that led to exhume the CBU in the subduction channel, better known as the Vari detachment [*Jolivet et al.*, 2010]. However, *Ring et al.* [2003] pointed out a strong brittle-cataclastic deformation throughout its

exposure and have suggested its late reactivation in the brittle crust at approximately 11-8 Ma based on zircon and apatite (U-Th)/He low-temperature thermochronology (Figure IV-2).

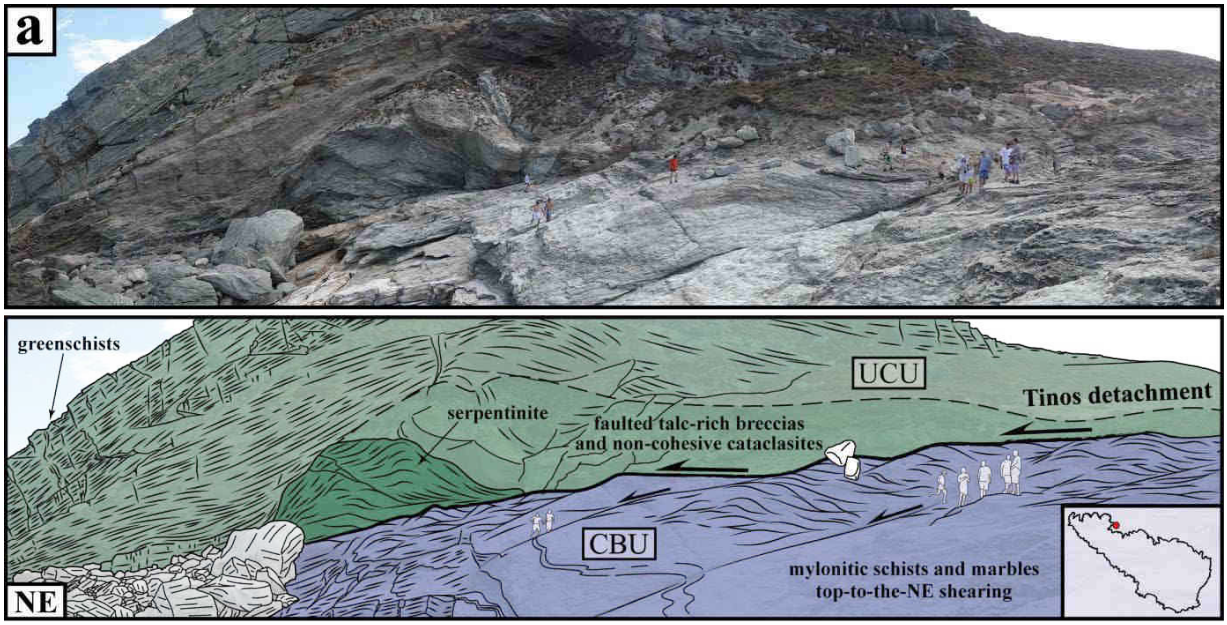

Figure IV-4: *panoramic view and associated interpretive drawing of the North Cycladic Detachment System (NCDS) running across Tinos Island. View of the ductile-to-brittle Tinos detachment on Planitis Peninsula (location in the included map inset at lower right) where it tectonically juxtaposes the Upper Cycladic Unit (UCU) atop the Cycladic Blueschist Unit (CBU).*

At the northeastern tip of Tinos Island where the main intrusion is locally surrounded by the UCU (Livada Bay, location in Figure IV-3), host metamorphic rocks display a well-developed NW-striking tectonic foliation with a conspicuous NE-trending stretching lineation and discrete top-to-the-NE shear bands [*Faure et al.*, 1991; *Brichau et al.*, 2007; *Jolivet et al.*, 2010; *de Saint Blanquat et al.*, 2011]. According to *Jolivet et al.* [2010], this extensional deformation becomes more localized upward and northeastward. Within a thin zone of a few tens of meters, ductile shearing was reworked by a system of NW-striking, ductile/brittle high-angle normal faults that show a consistent NE-SW direction of extension. Even though no detachment plane has been clearly recognized, this succession of deformation events has been structurally and mechanically correlated with the activity of the upper Livada detachment that crops out on the nearby island of Mykonos (Figure IV-5a) [*Jolivet et al.*, 2010; *Lecomte et al.*, 2010; *Menant et al.*, 2013]. There, the ductile-to-brittle Livada detachment contributed in part to the exhumation of a migmatite-cored dome chiefly restricted on Delos-Rhenia Islands, together with a sequence of paragneisses/marbles belonging to the CCB and a 14-11 Ma old magmatic complex slightly younger than the Tinos intrusions (Figures IV-2 and -5a) [*Faure et al.*, 1991; *Lucas*, 1999; *Brichau et al.*, 2008; *Bolhar et al.*, 2010]. This shallow-angle NE-dipping detachment operated under a NE-directed extensional regime at the contact between the Mykonos intrusion and the UCU (Figures IV-5b and -6). Though the apex of the underlying granite was pervasively deformed by a top-to-the-NE simple shear component (for additional information regarding structural records within the Mykonos magmatic complex, see section 4.2), most of the overlying rocks from the UCU do not exhibit any ductile deformation,

except directly above the detachment surface where the same northeastward ductile shearing is locally observed (Cape Haros, Figure IV-5a) [*Lecomte et al.*, 2010; *Menant et al.*, 2013]. Similar to the deformation described in Livada Bay (Tinos Island), a late brittle increment occurred along the detachment zone. With a consistent northeastward slip, the top of the footwall together with the UCU were affected by high- and low-angle, E-dipping normal faults which crosscut or settle onto the detachment surface (Figure IV-6).

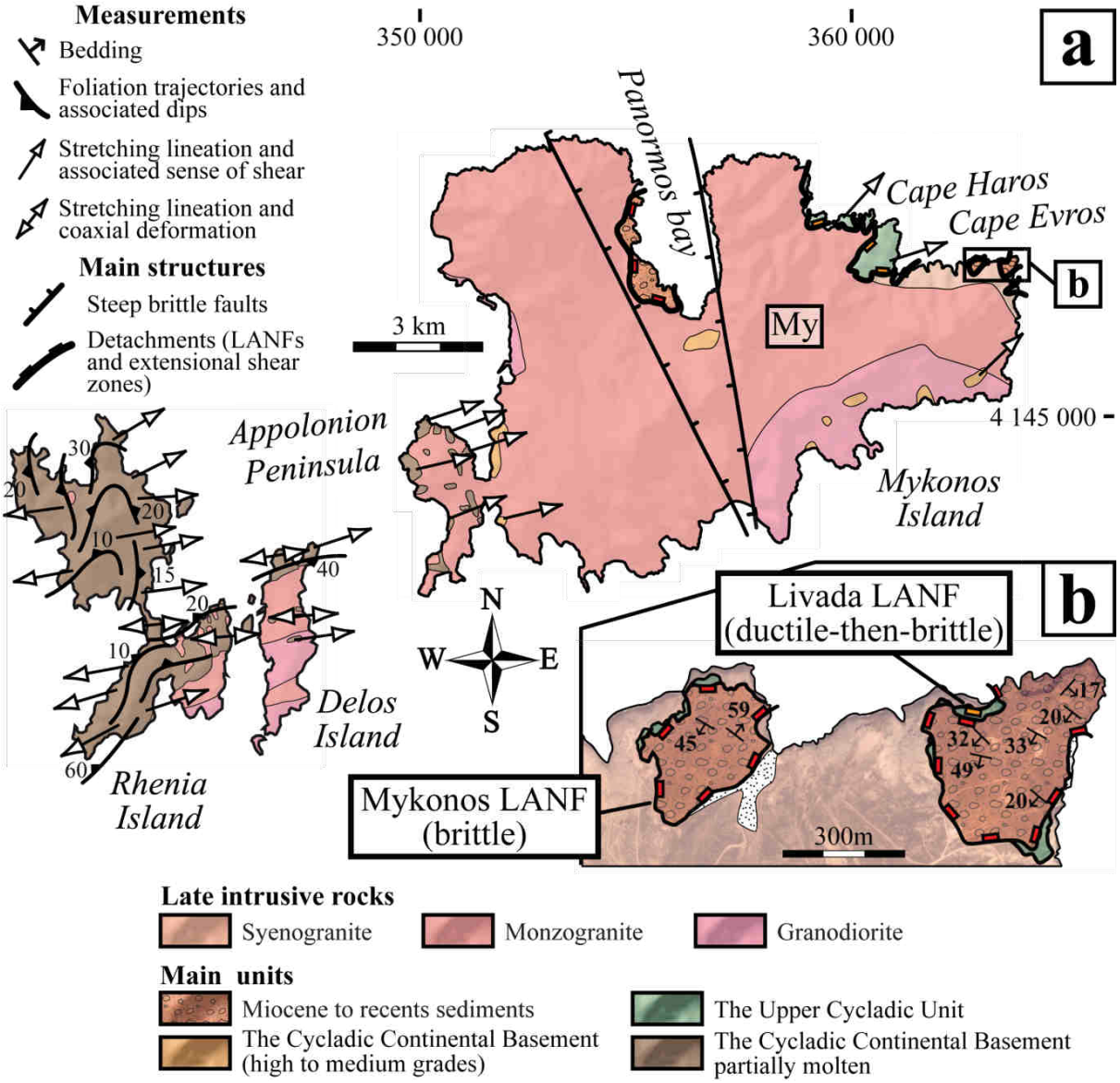

Figure IV-5: *(a) tectonic map of the Mykonos-Delos-Rhenia metamorphic core complex and associated flanking detachments. Field-based measurements of finite strain markers originate from Lucas [1999], Lecomte et al. [2010], Denèle et al. [2011] and Menant et al. [2013]. My: Mykonos magmatic complex. (b) Tectonic map of Cape Evros area showing the tectonic reworking of the Livada detachment by the brittle-cataclastic Mykonos detachment.*

Toward the easternmost side of Mykonos Island (Cape Evros, see map location in the Figure IV-5b), the ductile-to-brittle Livada detachment was dissected by a low-angle

cataclastic-brittle structure, i.e., the Mykonos detachment [*Jolivet et al.*, 2010; *Lecomte et al.*, 2010]. This knife-sharp detachment surface dips 12-15° northeastward and brought in contact Late Miocene synextensional sediments with either the UCU (Cape Evros, Figures IV-5b and -6) or the magmatic complex (Panormos Bay and Cape Evros, see Figures IV-5a and -5b respectively) [*Sanchez-Gomez et al.*, 2002; *Lecomte et al.*, 2010]. In both cases, the damaged zone is marked by 1-5 m thick (ultra)cataclasites in the footwall whereas the basal sedimentary sequence displays silicified breccias of up to 10-20 m thick [*Lecomte et al.*, 2010; *Lacombe et al.*, 2013; *Menant et al.*, 2013]. These brecciated sediments mainly dip toward the southwest and are reworked by numerous high-angle normal faults rooting onto the detachment surface, thereby describing a block-tilted geometry. Where the detachment surface crops out, it further shows NE-oriented striae and corrugations parallel to the measured direction of the stretching lineation in the footwall.

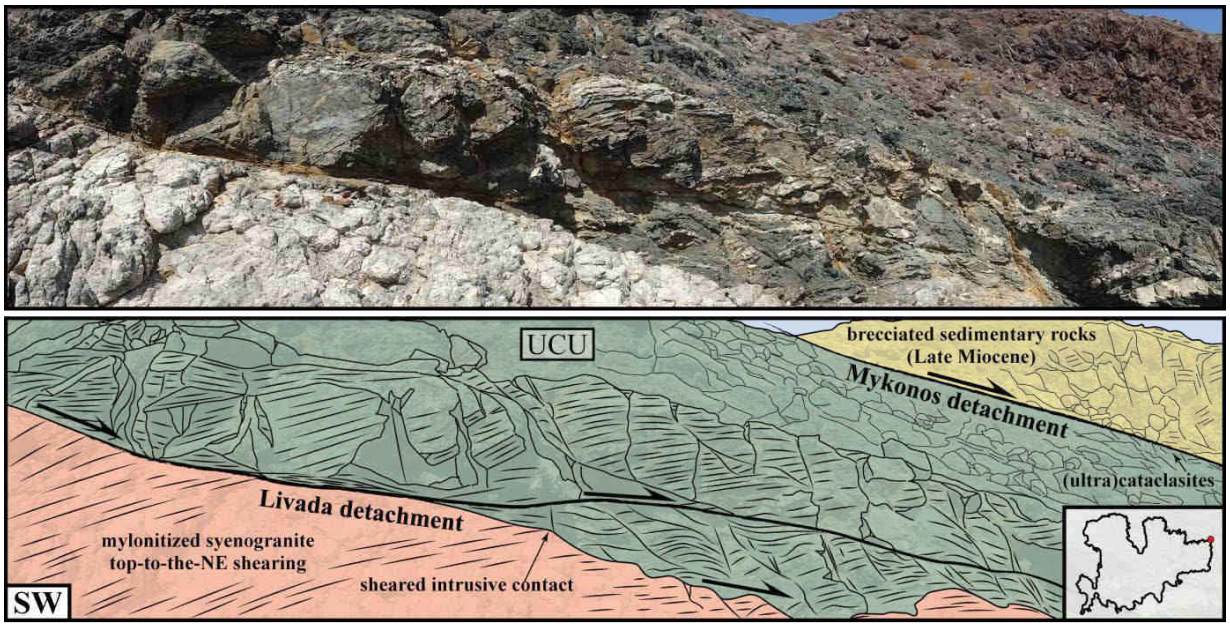

Figure IV-6: *panoramic view and associated interpretive drawing of the two closely spaced branches of the North Cycladic Detachment System on Mykonos Island (eastern side of Cape Evros, location in the included map inset at lower right). Bottom: the ductile-to-brittle Livada detachment reworking the intrusive contact between the syenogranite and the Upper Cycladic Unit (UCU). Top: the brittle-cataclastic Mykonos detachment that separates the UCU in the footwall from brecciated sediments in the hanging wall.*

Consequently, it has been largely assumed that strain accommodations and normal sense of displacements along both the Livada and Mykonos detachments would have tectonically controlled the cooling of the granitoid-cored dome, pointing to a relatively fast cooling and a progressive northeastward unroofing between circa 14 and 7 Ma (Figure IV-2) [*Altherr et al.*, 1982; *Hejl et al.*, 2002; *Brichau et al.*, 2008]. In the same way on Tinos, available low-temperature radiometric ages indicate a nearly concomitant cooling history of the granitoids below the presumed Livada detachment from 15 to 8 Ma [*Altherr et al.*, 1982; *Hejl et al.*, 2002; *Brichau et al.*, 2007].

3.2. Ikaria Island

Located northeast of Mykonos, Ikaria predominantly shows a H*T* metamorphic dome elongated in a NE-SW direction (Figures IV-1b and -7) [*Martin*, 2004; *Photiades*, 2005; *Beaudoin et al.*, 2015]. The exhumation history of the metamorphic dome has been especially linked to the tectonic evolution of the northern Cycladic MCCs since structural and thermochronological contributions have emphasized a dominant top-to-the-N strain component with a progressive strain accommodation through a set of detachments during the Oligo-Miocene [*Kumerics et al.*, 2005; *Ring*, 2007]. Recently, *Laurent et al.* [2015] and *Beaudoin et al.* [2015] have refined the tectonic configuration of the detachment system by bringing additional mesostructural observations together with thermometric constraints using Raman spectrometry of carbonaceous material (RSCM method, [*Beyssac et al.*, 2002]). According to their conjoined interpretation, the final exhumation of the metamorphic dome was controlled by the Agios-Kirykos shear zone and the Fanari-Gialiskari low-angle normal fault (Figure IV-7), two closely spaced high-strain zones that respectively acted through time in ductile and ductile-to-brittle fields.

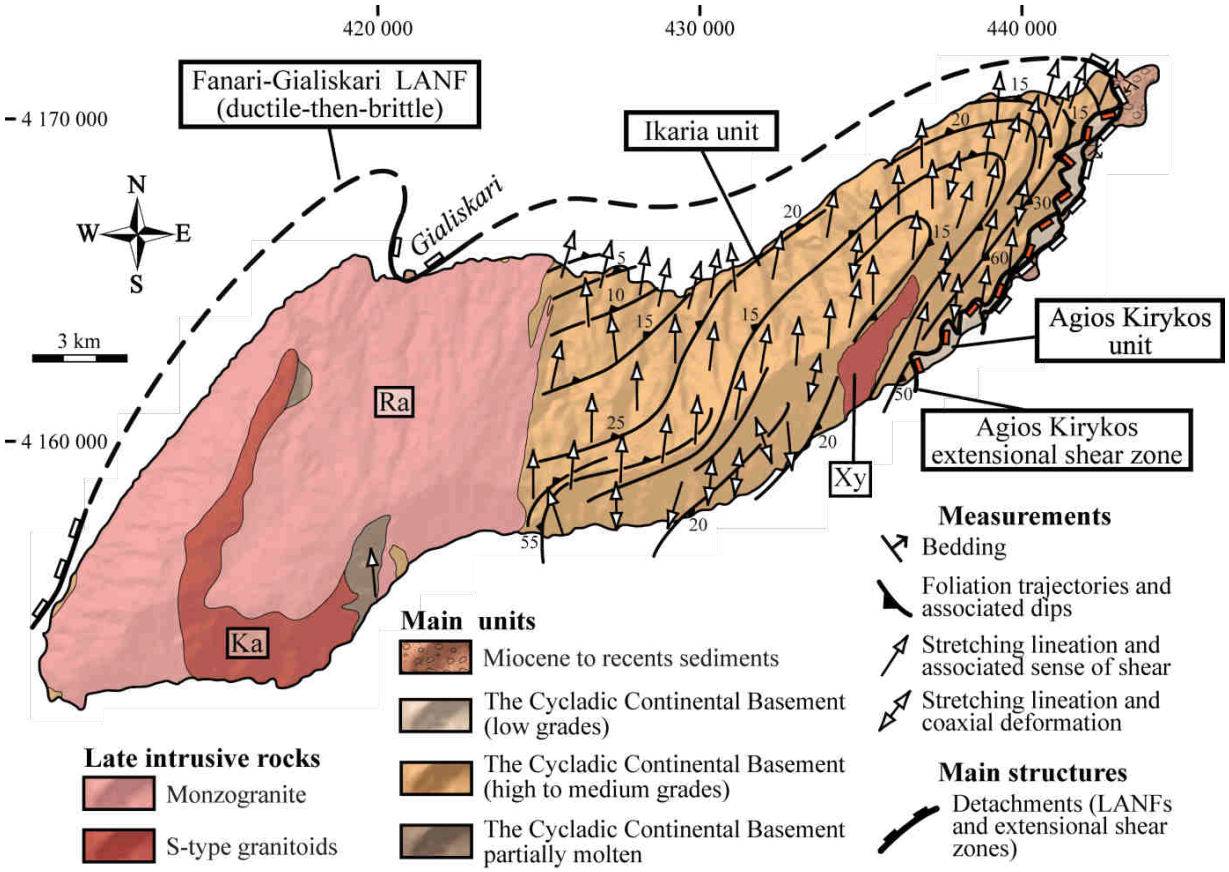

Figure IV-7: *tectonic map of the Ikaria metamorphic core complex and its associated detachment system. Field-based measurements of finite strain markers originate from Photiades [2005], Beaudoin et al. [2015] and Laurent et al. [2015]. Ra: Raches monzogranite. Ka: Karkinagrion S-type bimicaceous leucogranite. Xy: Xylosyrtis S-type bimicaceous leucogranite.*

The Agios-Kirykos shear zone has been mapped on the eastern side of the island where it ductilely affected the metamorphic dome and lastly juxtaposed two subunits supposed to

represent a part of the CCB, i.e., the upper Agios-Kirykos unit and the lower Ikaria unit (Figure IV-7). This SE-dipping shear zone developed initially with a shallow angle with respect to the compositional layering and was subsequently up-domed together with the whole metamorphic sequence [*Beaudoin et al.*, 2015]. Through the distribution of RSCM temperatures acquired over the dome, *Beaudoin et al.* [2015] have further demonstrated that the activity of the Agios-Kirykos shear zone was responsible for a normal sense metamorphic temperature gap. In the field, structural evidences of the shear zone activity are mostly preserved within the underlying Ikaria unit. Over an approximately 500 m-thick zone, footwall rocks underwent a clear upward strain gradient from low-strain protomylonites observed in the most deeply exposed levels of the dome to high-strain mylonites recognized through a band of several tens of meters directly below and above the tectonic contact. The whole strain gradient was also paired with a pervasive top-to-the-N shearing and a synkinematic retrogression into greenschist-facies conditions, while the core of the dome recorded a more coaxial deformation and retained typical amphibolite-facies associations (600-650°C for less 600-800 MPa) [*Martin*, 2004; *Kumerics et al.*, 2005]. High-temperature conditions have also been described in the western part of the island where partially molten gneisses were closely associated with a S-type intrusion (i.e., Karkinagrion granitoid, Figure IV-7) [*Bolhar et al.*, 2010; *Beaudoin et al.*, 2015; *Laurent et al.*, 2015].

Toward the easternmost side of the island, the metamorphic dome is tectonically topped by the Fanari-Gialiskari detachment (Figure IV-7) [*Beaudoin et al.*, 2015; *Laurent et al.*, 2015]. This S- to SE-dipping detachment cuts down through the Agios-Kirykos shear zone and structurally puts in direct contact Late Miocene to Early Pliocene syntectonic sediments on either the Agios-Kirykos unit (Figure IV-8a) or the Ikaria unit. Associated with top-to-the-N or -NE kinematics, extensional shearing in the footwall evolved toward the detachment fault plane from medium-grade mylonites to low-grade ultramylonites. Unlike the Agios-Kirykos shear zone, the Fanari-Gialiskari detachment zone displays evidences of subsequent displacements in the brittle field. The highly sheared rocks were partially reworked by cataclasites and fault-rocks within a thin section of a few meters below the corrugated detachment fault surface, carrying itself large-scale displacement clues in brittle conditions. As suggested by paleostress analyses, development of late brittle structures was persistently controlled by an overall NE-oriented extension [*Kumerics et al.*, 2005; *Beaudoin et al.*, 2015]. On the basis of structural and geometrical similarities, the detachment has been furthermore extended as far as the northeastern part of Ikaria toward the Gialiskari Peninsula (Figure IV-7) where syntectonic sediments rest directly above the I-type Raches intrusion (Figure IV-8b, further details in section 4.3) [*Beaudoin et al.*, 2015; *Laurent et al.*, 2015].

On Ikaria, accurate radiometric time-constraints for the extensional shearing initiation along both detachments and their relative timing are currently poorly known. However, the exhumation history of the metamorphic dome is roughly constrained by the approximately 25-17 Ma ages retrieved from amphibolite-facies sheared rocks [*Altherr et al.*, 1982] and the 11.5-9 Ma ages acquired on fabric-forming micas from the uppermost levels of the dome (Figure IV-2) [*Altherr et al.*, 1982; *Kumerics et al.*, 2005]. Additionally, timing of the H*T* thermal event was constrained by recent (U-Th)/Pb analyses on monazite from the leucosome parts of

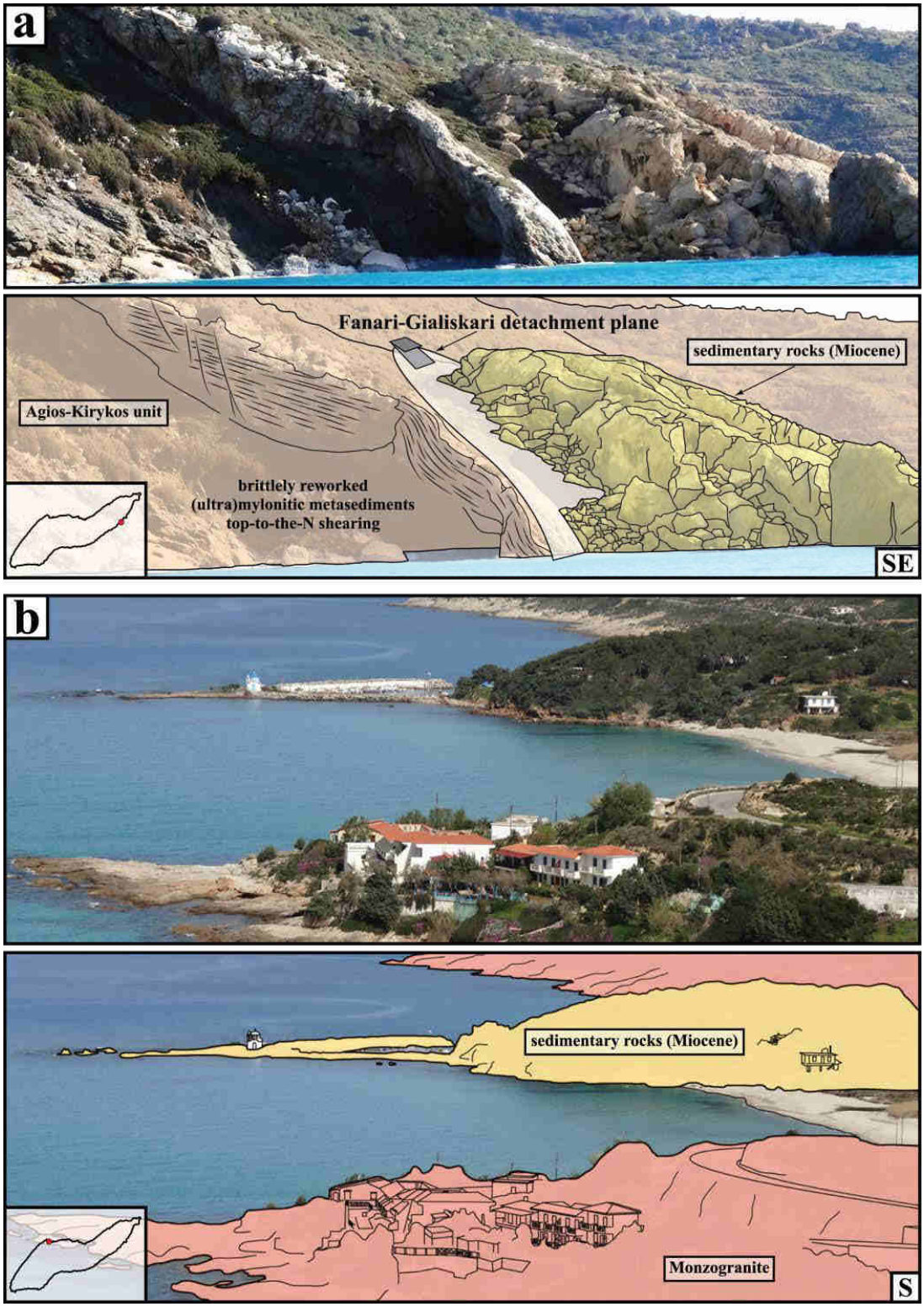

Figure IV-8: *panoramic views and associated interpretive drawings of the ductile-to-brittle Fanari-Gialiskari detachment belonging to the North Cycladic Detachment System (NCDS) on Ikaria Island. (a) View of the S-dipping detachment surface toward the southeastern coast of the Island (location in the included map inset at lower left) where it tectonically separates the underlying Agios-Kirykos unit from brecciated and faulted sedimentary rocks. (b) View of the same detachment at Gialiskari (location in the included map inset at lower left) where it dips to the north and puts in direct contact the syntectonic sedimentary basin on the Raches intrusive body.*

migmatitic gneisses, thus yielding a 15.7 ± 0.2 Ma age (Figure IV-2) [*Beaudoin et al.*, 2015]. *Beaudoin et al.* [2015] tentatively concluded that extensional shearing and strain localization along the Agios-Kirykos shear zone might have started at or even before this H*T* thermal event, later followed by the emplacement of two S-type granitoids between approximately 15 Ma and 14 Ma (i.e., the Xylosyrtis and Karkinagrion intrusions) and the 14 Ma old I-type Raches granitoid (Figure IV-2, *Bolhar et al.* [2010]). On the basis of available low-temperature geochronological data, both the intrusions and the host metamorphic sequence were eventually subjected to a joint cooling episode with reported ages from ~10 Ma to as young as ~4 Ma, together with an apparent northward and upward unroofing in correspondence with the observed top-to-the-N extensional shearing [*Altherr et al.*, 1982; *Kumerics et al.*, 2005].

3.3. Naxos Island

Naxos Island lies within the central part of the Cyclades where the development of large-scale MCCs was governed by an overall N-directed extension and a top-to-the-N shearing through the Naxos-Paros Detachment System (NPDS, Figure IV-1b and -1c) [*Gautier et al.*, 1993; *Brichau et al.*, 2006; *Bargnesi et al.*, 2013]. On Naxos, the late exhumation stage was historically interpreted as stemming from a progressive strain localization along a single crustal-scale detachment (i.e., the Moutsouna detachment, Figure IV-9) [*Lister et al.*, 1984; *Urai et al.*, 1990; *Buick*, 1991]. This localizing event partly brought toward upper crustal levels a H*T* metamorphic dome dominated by a migmatitic gneiss core preserving Variscan protolithic ages of the original CCB [*Andriessen et al.*, 1987; *Jolivet et al.*, 2004a; *Vanderhaeghe*, 2004], and a cover series mostly made of marbles and metapelites that locally retains the former Eocene H*P*-L*T* metamorphic event [*Andriessen et al.*, 1979; *Wijbrans & McDougall*, 1986, 1988; *Avigad*, 1998; *Peillod et al.*, 2017]. More recently, field investigations and resulting tectonic maps have shown a more complex tectonic architecture with two closely spaced branches of the NPDS [*Siebenaller*, 2008; *Kruckenberg*, 2009]. According to the updated geological map (Figure IV-9), the detachment system includes the previously mapped Moutsouna detachment and the Naxos detachment. During their activity, both detachments were associated with similar top-to-the-N displacements and a comparable tectonic evolution from ductile-to-brittle conditions. The detachment system was further folded together with foliations of the migmatitic dome, undulating in large-scale synforms and antiforms whose axes trend parallel to the N-directed stretching lineation (Figure IV-9) [*Avigad et al.*, 2001; *Kruckenberg et al.*, 2011].

Across the entire exposed metamorphic dome, both flanking detachment fault planes discontinuously crop out due to the late brittle reworking of kilometric-scale steep, normal to transtensional faults (Figure IV-9) [*Jansen*, 1973; *Gautier et al.*, 1993; *Vanderhaeghe et al.*, 2007; *Siebenaller*, 2008]. The Naxos detachment fault can only be traced at the northwestern flank of the migmatitic dome where it tectonically dismembered the presumed CCB. Below this steeply NW-dipping detachment, footwall rocks recorded an upward and northwestward non-coaxial shear gradient through a thick section of several hundred meters [*Siebenaller*, 2008]. Coeval with a retrograde metamorphism, mesoscopic and microscopic criteria thus support a spatial evolution of deformation from amphibolite-facies protomylonites and

mylonites surrounding the migmatite-cored dome to greenschist-facies ultramylonites when approaching the detachment surface [*Siebenaller*, 2008; *Kruckenberg et al.*, 2011]. Throughout the detachment zone, late brittle-cataclastic increments have been exclusively observed close to the tectonic contact with several m-thick cataclasites that reworked ultramylonites in the footwall, while low-grade metamorphic rocks from the hanging wall were intensely brecciated over a thin section of a few meters [*Siebenaller*, 2008].

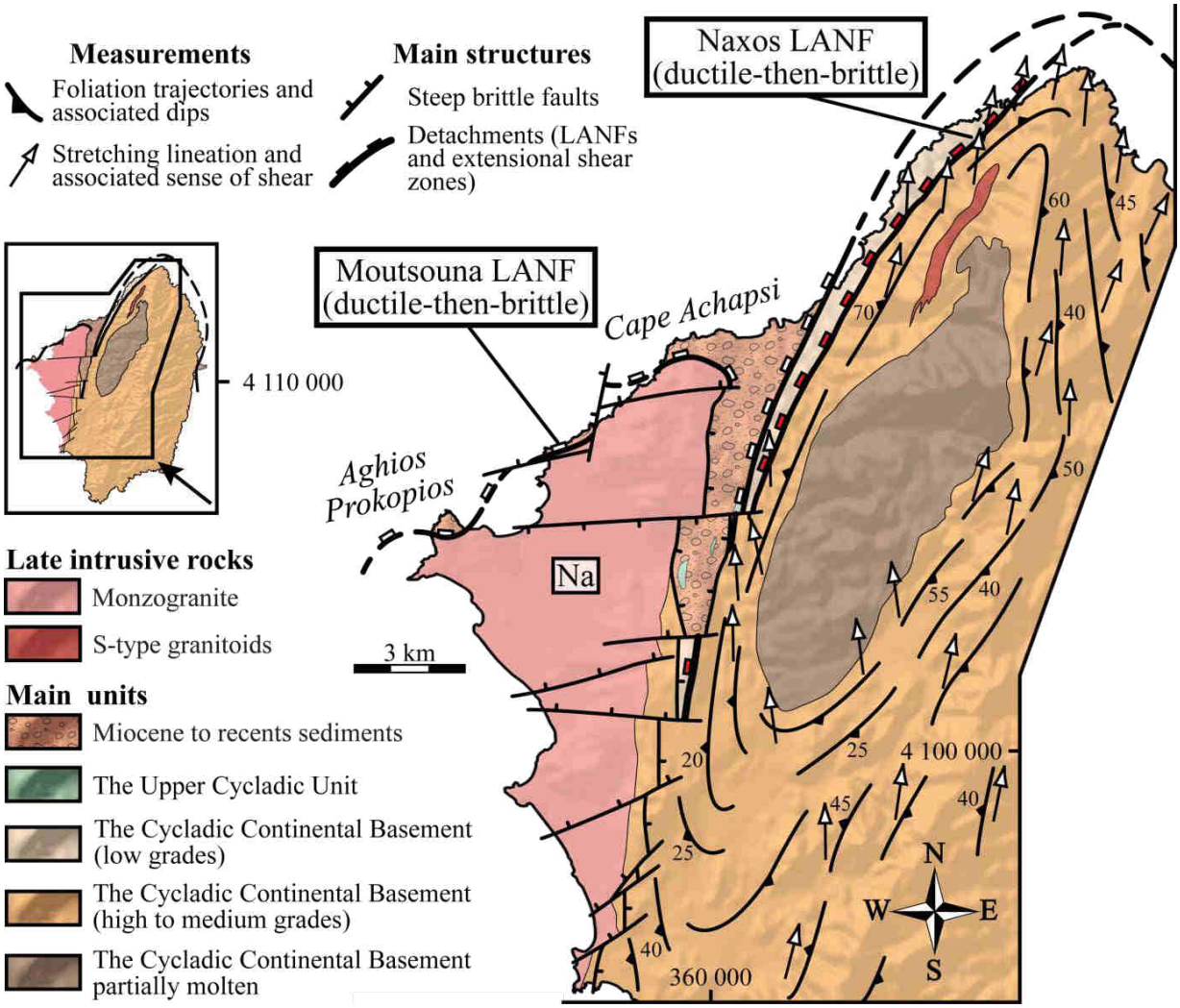

Figure IV-9: *tectonic map of the Naxos metamorphic core complex and its associated detachment system. Field-based measurements of finite strain markers originate from Jansen [1973], Gautier et al. [1993], Siebenaller [2008] and Kruckenberg [2009]. Na: Naxos monzogranite.*

Structurally higher up, the low-grade metamorphic sequence was, in turn, tectonically unroofed by the Moutsouna detachment (Figure IV-9). This detachment displays a sharp fault surface and extension-parallel corrugations with wavelengths ranging from the meter scale to several hundred meters [*Gautier et al.*, 1993], above which lies a syntectonic basin primarily filled with Miocene deposits and containing remnants of ophiolitic rocks issued from the UCU (Figure IV-9) [*Jansen*, 1973; *Angelier et al.*, 1978; *Kuhlemann et al.*, 2004]. The detachment zone has been likewise laterally extended on the eastern flank of the dome where it dips moderately eastward (Figure IV-10a, location in the map inset at lower right).

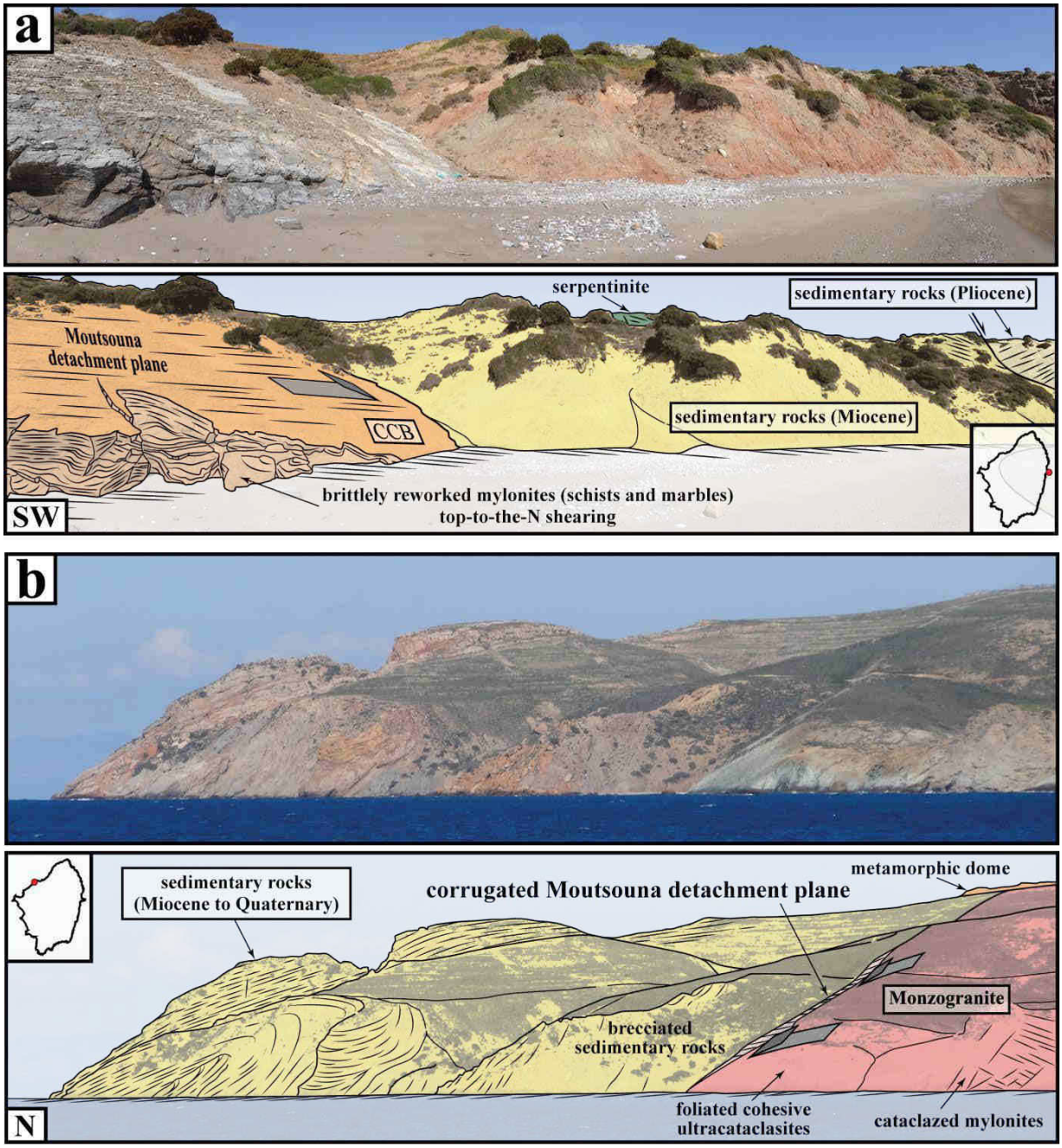

Figure IV-10: ***p****anoramic views and associated interpretive drawings of the ductile-to-brittle Moutsouna detachment belonging to the Naxos-Paros Detachment System (NPDS) on Naxos Island. (a) View of the E-dipping detachment plane toward the easternmost part of the island (Moutsouna peninsula, location in the included map inset at lower right) where brittlely reworked mylonites from the CCB tectonically underlie Miocene sedimentary deposits and relics of ophiolitic rocks (serpentinites) from the UCU. (b) View of the corrugated detachment surface at Cape Achapsi (location in the included map inset at upper left) where the brecciated sedimentary rocks rest directly above the (ultra)cataclazed monzogranite. CCB: Cycladic Continental Basement. UCU: Upper Cycladic Unit.*

There, the activity of the present-day N-striking detachment zone was clearly associated with an intense top-to-the-N mylonitization of footwall rocks depicted by an upward shear strain gradient coupled with a retrograde metamorphism into greenschist-facies conditions

[*Gautier et al.*, 1993; *Vanderhaeghe et al.*, 2007; *Cao et al.*, 2013]. The penetrative amphibolite-facies deformation and related concentric H*T* metamorphic isograds recorded in the lowermost parts of the dome were upwardly intersected and erased by these synkinematic greenschist-facies recrystallizations [*Gautier et al.*, 1993]. Besides, superimposition of ductile structures by brittle ones has been locally observed underneath the fault plane where the strongly sheared rocks were reworked by tectonic microbreccias, a dense network of fractures and variously striking normal faults [*Gautier et al.*, 1993; *John & Howard*, 1995; *Cao et al.*, 2013]. Recurrent high-angle normal faults have also been identified within the sedimentary basin, rooting or cutting through the detachment surface (Figure IV-10a). This ductile-then-brittle event has been approximately recorded through a thick zone of a few hundred meters, suggesting that extension below the Moutsouna detachment was accommodated in more localized horizons than underneath the Naxos detachment. Considering the above tectonometamorphic features, the development of the Moutsouna detachment arguably postdated the activity of the Naxos detachment and ultimately dissected through it, most likely farther offshore north of the island (Figure IV-9).

On Naxos Island, timing for ductile deformation is provided by a large set of thermochronological tools (Figure IV-2) that indicate a ~25-8 Ma old greenschist-facies metamorphism within the lower grade rocks [*Andriessen et al.*, 1979; *Wijbrans & McDougall*, 1986, 1988; *Andriessen*, 1991; *Cao et al.*, 2016] and a peak of H*T* between 21 and 14 Ma within high-grade amphibolite-facies rocks [*Wijbrans & McDougall*, 1986, 1988; *Andriessen*, 1991; *Martin et al.*, 2006a] where the anatectic episode was consistently dated between 21 and 17 Ma [*Keay et al.*, 2001]. Consequently, it was hypothesized that extensional shearing onset and strain localization would have preceded or coincided with the H*T* thermal event [*Buick & Holland*, 1989], but paroxysm of strain accommodation along the detachment system would have been achieved between 17 and 8 Ma [*John & Howard*, 1995; *Brichau et al.*, 2006]. While shear strain was already initiated, both S- and I-type granitoids intruded the metamorphic dome at circa 15-13 Ma and 13-11 Ma respectively (Figure IV-2 and -9) [*Keay et al.*, 2001; *Bolhar et al.*, 2010]. Along with the whole metamorphic pile, the I-type granitoid cooled into the upper crust over a rather short time span of ~4 Ma after its emplacement (Figure IV-2) [*Wijbrans & McDougall*, 1988; *Pe-Piper et al.*, 1997; *Keay*, 1998; *Brichau et al.*, 2006; *Seward et al.*, 2009a]. Low-temperature geochronological investigations performed within this granitoid further yielded an apparent northward rejuvenation of cooling ages, consistent with the top-to-the-N tectonic unroofing thought to be induced by the activity of the Moutsouna detachment exposed at the northern rim of the intrusion (Figures IV-9 and -10b, see section 4.4 for further details) [*Brichau et al.*, 2006; *Seward et al.*, 2009].

3.4. Serifos Island

Serifos Island is part of the western Cyclades where a series of small-scale metamorphic domes were exhumed below the West Cycladic Detachment System (WCDS) under an overall SW-directed extensional regime (Figures IV-1b and -1c) [*Iglseder et al.*, 2011; *Grasemann et al.*, 2012]. Among the western Cycladic domes, Serifos Island offers the most complete structural section with a metamorphic dome incised by the lower Meghàlo

Livadhi detachment and the upper Kàvos Kiklopas detachment, two branches of the WCDS that have tectonically put in direct contact the CBU upon the CCB and the UCU upon the CBU, respectively (Figures IV-11, -12a and -12b) [*Grasemann & Petrakakis*, 2007; *Grasemann et al.*, 2012; *Rabillard et al.*, 2015].

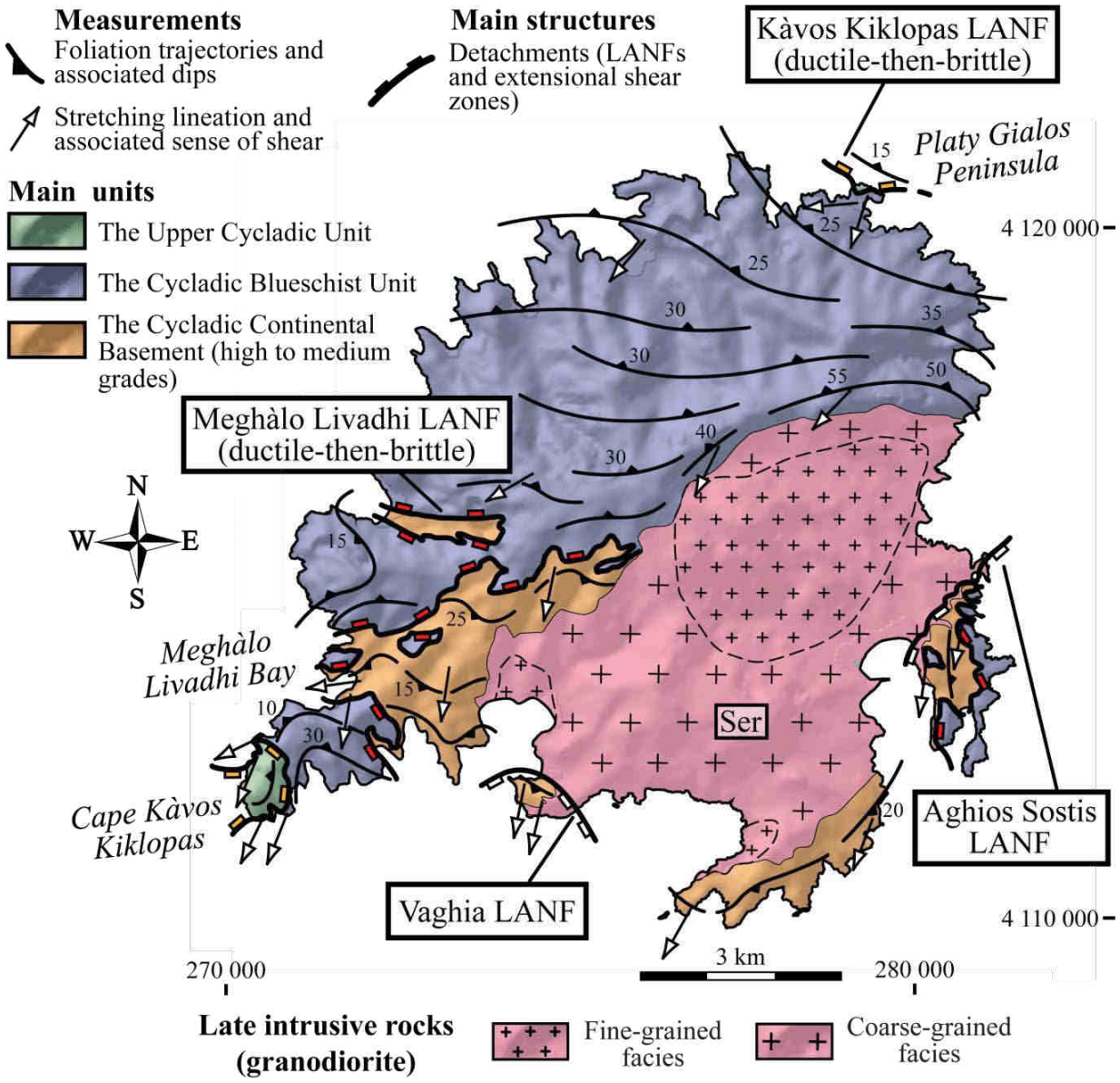

Figure IV-11: *tectonic map of the Serifos metamorphic core complex and its associated detachment system. Field-based measurements of finite strain markers originate from Salemink [1985], Grasemann & Petrakakis [2007], Petrakakis et al. [2010] and Rabillard et al. [2015]. Ser: Serifos granodiorite.*

Along a cross-section parallel to the NE-SW stretching lineation, the detachment system has been arched upward with SW-dipping planes on the southwestern tip (Cape Kàvos Kiklopas and Meghàlo Livadhi Bay) and NE-dipping surfaces in the northeast (Platy Gialos Peninsula). Previous structural field investigations have further shown that both detachments shared a similar tectonic evolution during their development involving a top-to-the-SW, ductile-to-brittle extensional deformation [*Grasemann & Petrakakis*, 2007; *Grasemann & Tschegg*, 2012].

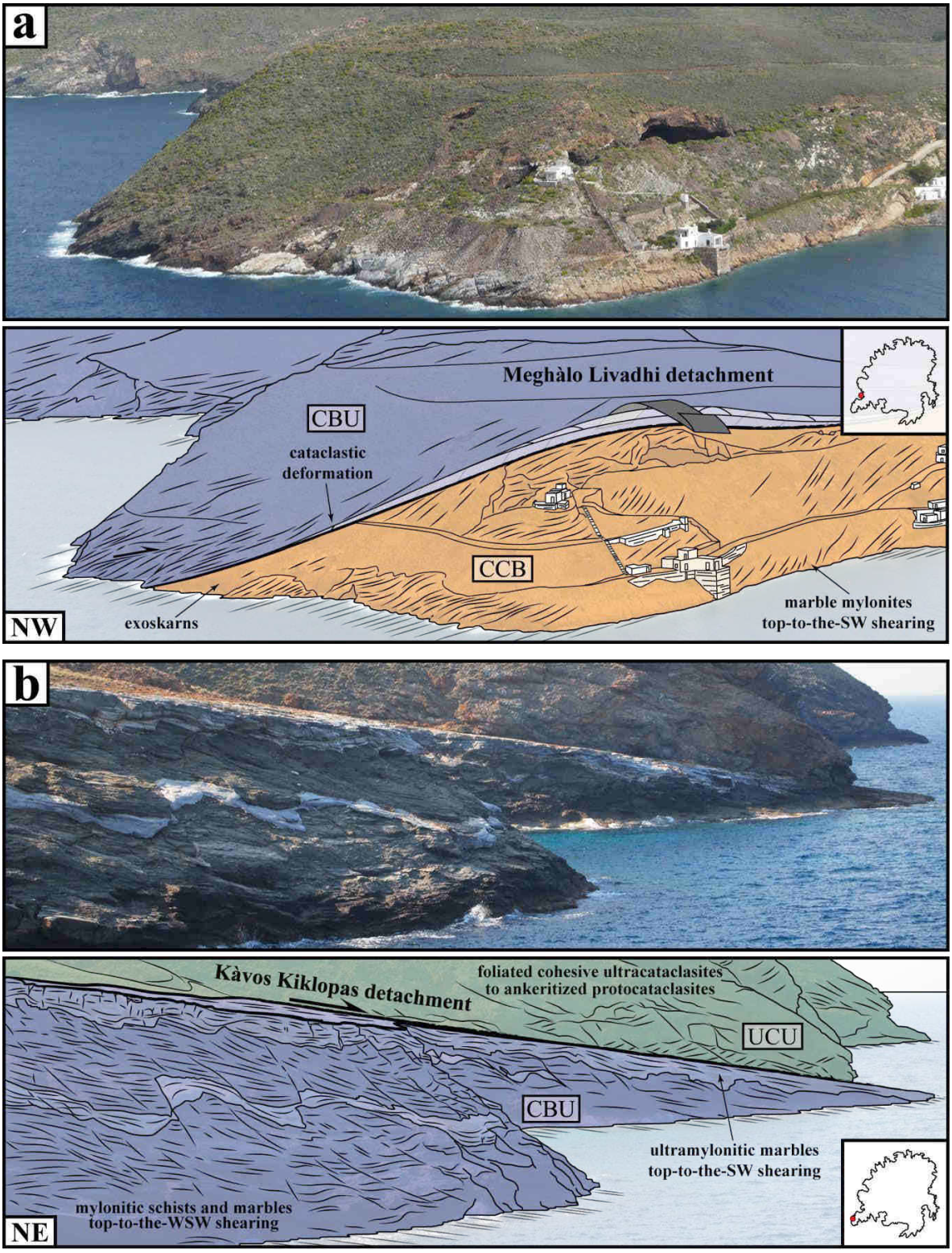

Figure IV-12: *panoramic views and associated interpretive drawings of the West Cycladic Detachment System (WCDS) on Serifos Island. (a) View of the lowermost ductile-to-brittle Meghàlo Livadhi detachment (location in the included map inset at upper right); it separates the CCB (marble mylonites) in the footwall from the CBU (cataclastic greenschists and amphibolites) in the hanging wall. (b) View of the uppermost ductile-to-brittle Kàvos Kiklopas detachment (location in the included map inset at lower right) juxtaposing the UCU above the CBU. CCB: Cycladic Continental Basement. CBU: Cycladic Blueschist Unit. UCU: Upper Cycladic Unit.*

Associated with an exhumation-related retrogressive metamorphism under typical greenschist-facies conditions, the top-to-the-SW ductile deformation was extremely localized in the footwall of both detachment fault planes [*Grasemann & Tschegg*, 2012; *Dabrowski & Grasemann*, 2014], leaving an earlier well-preserved E-W to ENE-WSW trending stretching lineation in large parts of the dome attributed to an Eocene (high pressure?) metamorphic episode (Figure IV-11) [*Schneider et al.*, 2011; *Cossette et al.*, 2015]. Beneath the Meghàlo Livadhi detachment fault surface, extensional shearing was heavily concentrated at the top of the CCB where metamorphic rocks were mylonitized under an upward strain gradient over several tens of meters in thickness and subsequently intersected by sets of high- and low-angle normal faults [*Grasemann & Petrakakis*, 2007; *Grasemann & Tschegg*, 2012]. By contrast, most of the overlying rocks from the CBU were subjected to an intense cataclastic-brittle deformation featured by a level of metasomatized breccias and cataclasites not thicker than a few tens of meters (Figure IV-12a). Although ductile deformation appears indistinguishable at the base of the CBU, top-to-the-SW meter-scale shear bands have been locally described somewhat higher up in the metamorphic pile, showing a probable downward reworking of ductile structures by brittle ones when approaching the detachment surface. Comparatively, the southwestward shearing just below the Kàvos Kiklopas detachment was restricted within a much thinner section of about two meters along which the apical rocks of the CBU were ultramylonitized (Figure IV-12b) [*Grasemann & Petrakakis*, 2007; *Rabillard et al.*, 2015]. Basal rocks of the structurally overlying UCU then recorded a preeminent cataclastic deformation through an apparent thickness of several tens of meters, moving up from a detachment gouge and foliated/folded cohesive ultracataclasites at the base to ankeritized protocataclasites toward upper levels (Figure IV-12b). Where the detachment surface crops out, it clearly bears slickenline lineations compatible with the shear sense deduced from the underlying CBU. Finally, metamorphic rocks from both the CBU and the UCU were cut by well-defined NW-striking, conjugate low- and high-angle normal faults that display consistent SW-oriented offsets.

According to published geochronological data, age-constraints on each detachment activity remain unclear as the retrograde greenschist-facies metamorphic recrystallization was almost completely erased by amphibolite-facies parageneses, plausibly induced by the I-type igneous event that intruded the metamorphic dome (Figure IV-11) or by a regional H*T* event [*Iglseder et al.*, 2009; *Grasemann et al.*, 2012]. However, available thermochronological data yielded syn-greenschist-facies mylonitization ages below the Meghàlo Livadhi detachment between 15 and 11 Ma while the main Serifos granitoid intruded the CBU and pierced the deeper Meghàlo Livadhi detachment between 11.6 Ma and 9.5 Ma (Figure IV-2, *Iglseder et al.* [2009]). Low-temperature ages lastly indicate a fast cooling history of both the metamorphic dome and the intrusion below the Kàvos Kiklopas detachment over a period spanning from ~9 Ma to ~4 Ma [*Altherr et al.*, 1982; *Hejl et al.*, 2002; *Brichau et al.*, 2010; *Grasemann et al.*, 2012].

To sum up a few major points from the above section, it appears that the Oligo-Miocene, extension-related exhumation processes of the targeted Cycladic metamorphic domes occurred consistently below multiple and closely spaced high-strain zones that diversely

evolved under ductile (i.e., the Agios-Kirykos shear zone), ductile-then-brittle (i.e., the Tinos, Livada, Fanari-Gialiskari, Naxos, Moutsouna, Meghàlo Livadhi and Kàvos Kiklopas low-angle normal faults) or purely brittle conditions (i.e., the Mykonos low-angle normal fault). At the scale of a single metamorphic dome, the flanking detachments developed through time with a quite similar sense of shear and/or slip, and, except for Serifos Island where no field-based evidence has been clearly mapped, it appears that the most deeply exposed branches have been cut downward by more surficial ones. In parallel, metamorphic domes were intruded by I- and S-type granitoids while exhumation and corresponding greenschist- to amphibolite-facies retrograde metamorphism seemed to be already initiated (Figure IV-2). First order geometrical aspects further show that (1) some granitoid roofs obviously intruded hanging wall rocks of preexisting detachments (i.e., the Tinos and Serifos intrusions, see tectonic maps in Figures IV-3 and -11), and (2) all of them structurally lie beneath more surficial detachment fault planes.

4. Petrostructural records within the Cycladic granitoids

The present section includes both a brief overview of the igneous rock types exposed in the targeted Cycladic MCCs and a more comprehensive description devoted to the state of finite strain fossilized inside each magmatic complex. With the objective of illustrating lateral shear gradients over both granitoids of Mykonos and Ikaria, *Denèle et al.* [2011] and *Laurent et al.* [2015] respectively elaborated a qualitative scale of strain intensity by defining a succession of deformation grades. By integrating the preexisting data together with our own structural observations, a similar approach with distinctive scales of fabric intensity have been applied across the remaining granitoids of Tinos, Naxos and Serifos. The resulting maps of large-scale patterns of deformation (see Figures IV-13 to -17) are compiled with field-based measurements of finite strain markers and, if appropriate, combined with magnetic fabrics issued from additional laboratory investigations using the anisotropy of magnetic susceptibility (AMS method, for reviews and basic principles see, e.g., *Borradaile & Henry* [1997]; *Borradaile & Jackson* [2010]). Note that though transitions from one grade to another appear gradual in the field, those on the maps have been drawn abruptly for the sake of simplification.

4.1. The Tinos magmatic complex

Intrusive within the northeastern part of the metamorphic dome, the Tinos magmatic complex encompasses an I-type biotite-hornblende monzogranite circumscribed by two smaller S-type garnet-bearing leucogranites (Figure IV-3) [*Altherr et al.*, 1982; *Bröcker & Franz*, 1998; *Altherr & Siebel*, 2002; *Melidonis & Triantaphyllis*, 2003]. Besides the existing broad geochemical and compositional discrepancies between both rock types, the large-scale monzogranite additionally distinguishes itself from leucogranites through its internal petrotextural heterogeneities. By means of meso- and microscopic observations, *Habert* [2004] emphasized within the monzogranite a rather concentric textural zoning with an inward evolution from a fine- to a coarser-grained facies. This texturally zoned body further encloses sporadic petrological heterogeneities exemplified in the field either by disseminated vestiges of non-amalgamated magmatic intrusions, such as isolated microgranitoid enclaves and

synplutonic dikes, or by compositional bandings underlined by biotite-enriched layers [*Altherr & Siebel*, 2002; *Habert*, 2004].

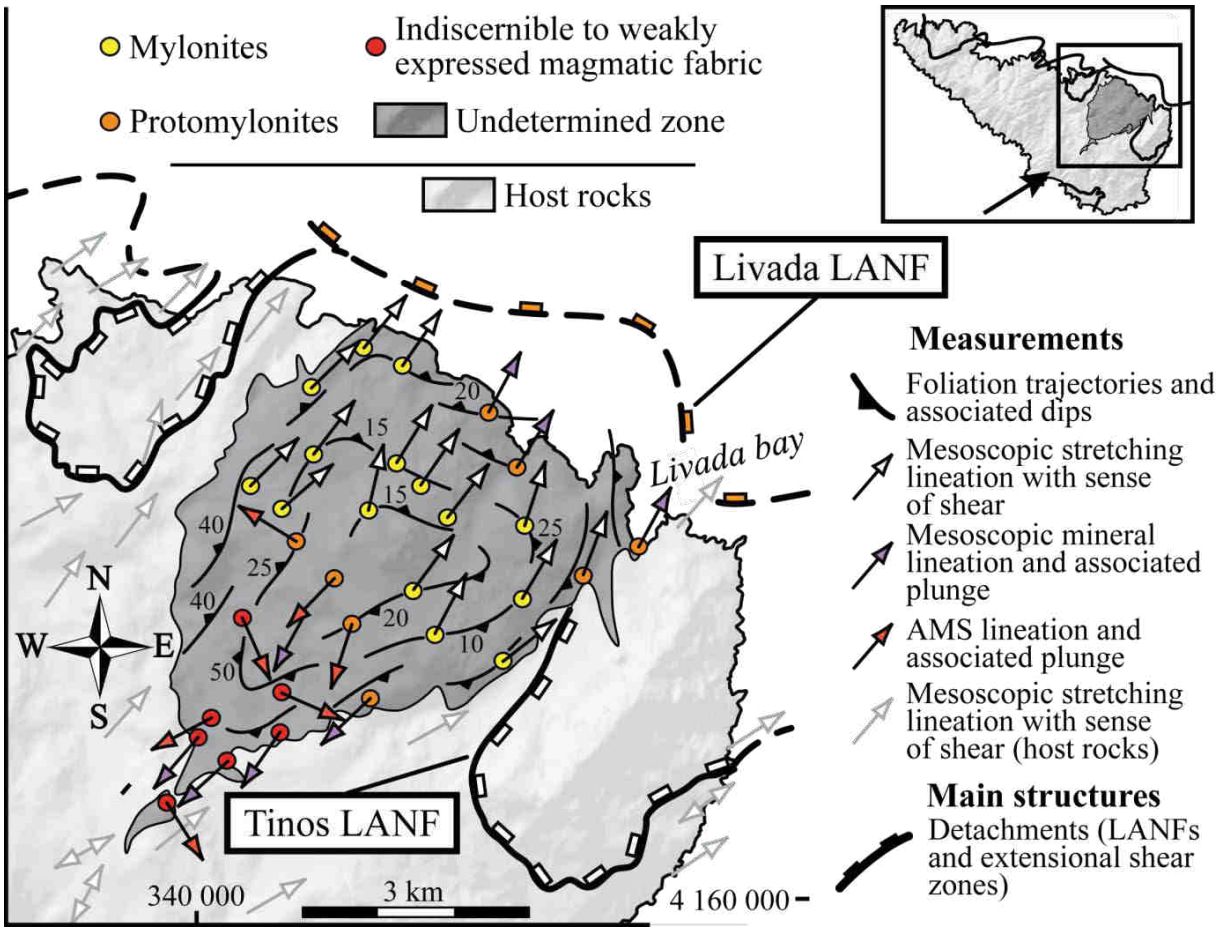

Figure IV-13: *tectonic map of the Tinos magmatic complex incorporating a distribution map of the strain intensity qualitatively built from micro- and macroscopic observations on which it has been superposed finite strain markers (interpolated foliation trajectories, mineral and stretching lineations) collected from field-based and AMS (anisotropy of magnetic susceptibility) measurements. For comparison, stretching lineations recorded over the adjacent metamorphic domes are also redrawn (bleached arrows); data acquired by Habert [2004], Jolivet et al. [2010] and de Saint Blanquat et al. [2011].*

From an architectural point of view, the partially exposed magmatic complex has been defined as a semi-elliptical, pluton-shaped body dominated by a NE-directed long axis (Figure IV-13) [*Habert*, 2004; *Brichau et al.*, 2007; *de Saint Blanquat et al.*, 2011]. Such a 3D finite configuration, inferred from foliation traces, has been regarded as the consequence of a pervasive top-to-the-NE ductile deformation that affected the northeastern two thirds of the monzogranite. Conversely, plutonic rocks from the southwestern edge have preserved magmatic textures with mesoscopically indiscernible or weakly expressed mineral fabrics, devoid of any superposed plastic deformation or recrystallization. Nonetheless, by combining contributions of field measurements and AMS results, it has been evidenced an overall prolate fabric marked by a bimodal direction of mineral and magnetic lineations with a predominant

northeast trend and a subsidiary perpendicular family exclusively detected by AMS signal (Figure IV-13, *Habert* [2004]). These lineations are carried by steeply dipping foliations roughly parallel to those from wall rocks [*Habert*, 2004; *de Saint Blanquat et al.*, 2011].

Farther to the northeast, intrusive rocks were progressively affected by a solid-state shear strain gradient with a northeastward continuum from low-strain protomylonites to high-strain mylonites (Figure IV-13). The protomylonitic grade has been also recognized in the northeastern part of the monzogranite (Livada Bay) where the pluton rim and closely associated synplutonic sills intruding the UCU were ductilely damaged by a non-pervasive top-to-the-NE shearing materialized by discrete NE-dipping shear band surfaces [*Brichau et al.*, 2007; *Jolivet et al.*, 2010; *de Saint Blanquat et al.*, 2011]. In the light of the existing tectonic map, most of intensely sheared rocks have been consequently found in the central and western domains of the monzogranite where the highest topographic zones are tectonically capped by mylonitic rocks. Mylonites bear subhorizontal tectonic foliations, well-grouped NE-trending stretching lineations and unchanging top-to-the-NE kinematics. Locally, the mylonitic fabric was subsequently reworked by breccias, cataclasites or even crosscut by pseudotachylytes [*Brichau et al.*, 2007; *Kokkalas & Aydin*, 2013]. This successive sequence of ductile-then-brittle fabrics imply a proximal influence of a localized major structure at an upper level, supposed to be connected with the activity of the Livada detachment [*Jolivet et al.*, 2010; *de Saint Blanquat et al.*, 2011].

4.2. The Mykonos-Delos-Rhenia magmatic complex

On the Mykonos-Delos-Rhenia archipelago, the Miocene intrusive magmatism stands out from the other Cycladic plutonic events by a greater range of petrological rock types (Figure IV-5). With a gradual trend toward less-differentiated I-type granitoids, it has been precisely mapped (1) a syenogranite localized below the detachment system near Cape Evros (Figure IV-5) where the intrusive contact with the UCU has been locally described (Figure IV-6); (2) a biotite-hornblende monzogranite enclosing rare mafic enclaves but rather rich in xenoliths and septa from the migmatitic dome, and (3) a biotite-hornblende granodiorite with abundant schlierens, isolated enclaves and monogenic/polygenic swarms of enclaves [*Lucas*, 1999; *Pe-Piper et al.*, 2002; *Lecomte et al.*, 2010; *Denèle et al.*, 2011]. These granitoids are primarily delimited by outcrop-scale sharp transitions and form sheet-like intrusions at the scale of the magmatic complex [*Lucas*, 1999; *Denèle et al.*, 2011]. The aforementioned surveys reported NE-SW striking, steeply to moderately dipping magmatic sheets on Delos-Rhenia Islands and gentler NE-dipping petrological contacts over Mykonos Island (Figure IV-14). These observations outline a flat-lying sheeted complex in which the more mafic intrusions constitute the deepest portions.

Via key micro- and macrostructural investigations, a continuous deformation history from magmatic to solid-state ductile/brittle conditions under an overall NE-directed strain component has been identified inside the plurikilometric-scale magmatic complex [*Faure et al.*, 1991; *Lucas*, 1999; *Denèle et al.*, 2011]. The early magmatic or sub-solidus deformational event has been especially preserved on Delos-Rhenia Islands, close to the migmatitic dome and

therefore far away from the detachment system (Figure IV-14). Apart from some near-solidus microstructures revealed by the fracturing of feldspar phenocrysts healed with magmatic minerals (see *Bouchez et al.* [1992] for melt-present fracturing clues), intrusive rocks display typical magmatic microtextures devoid of significant solid-state imprints [*Lucas*, 1999; *Denèle et al.*, 2011]. In the field, previous works further highlighted a mainly prolate magmatic fabric with a steady ENE-trending, shallowly E-plunging mineral lineation carried by weakly expressed NE-striking foliations subparallel to petrological contacts (Figure IV-14) [*Faure et al.*, 1991; *Lucas*, 1999; *Denèle et al.*, 2011]. On Mykonos, even if a broad zone of the magmatic complex recorded a non-coaxial extensional shearing, the synmagmatic deformation can still be discernible in a geographically limited area around the Appolonion Peninsula (Figure IV-14). Thence, the incompletely superimposed magmatic fabric progressively evolves from prolate to weakly oblate. In map view, the above described NE-striking, steeply dipping foliation trajectories drastically deflect and draw a sub-elliptical architecture, elongated parallel to the persistent ENE-trending mineral lineation [*Faure et al.*, 1991; *Lucas*, 1999; *Denèle et al.*, 2011].

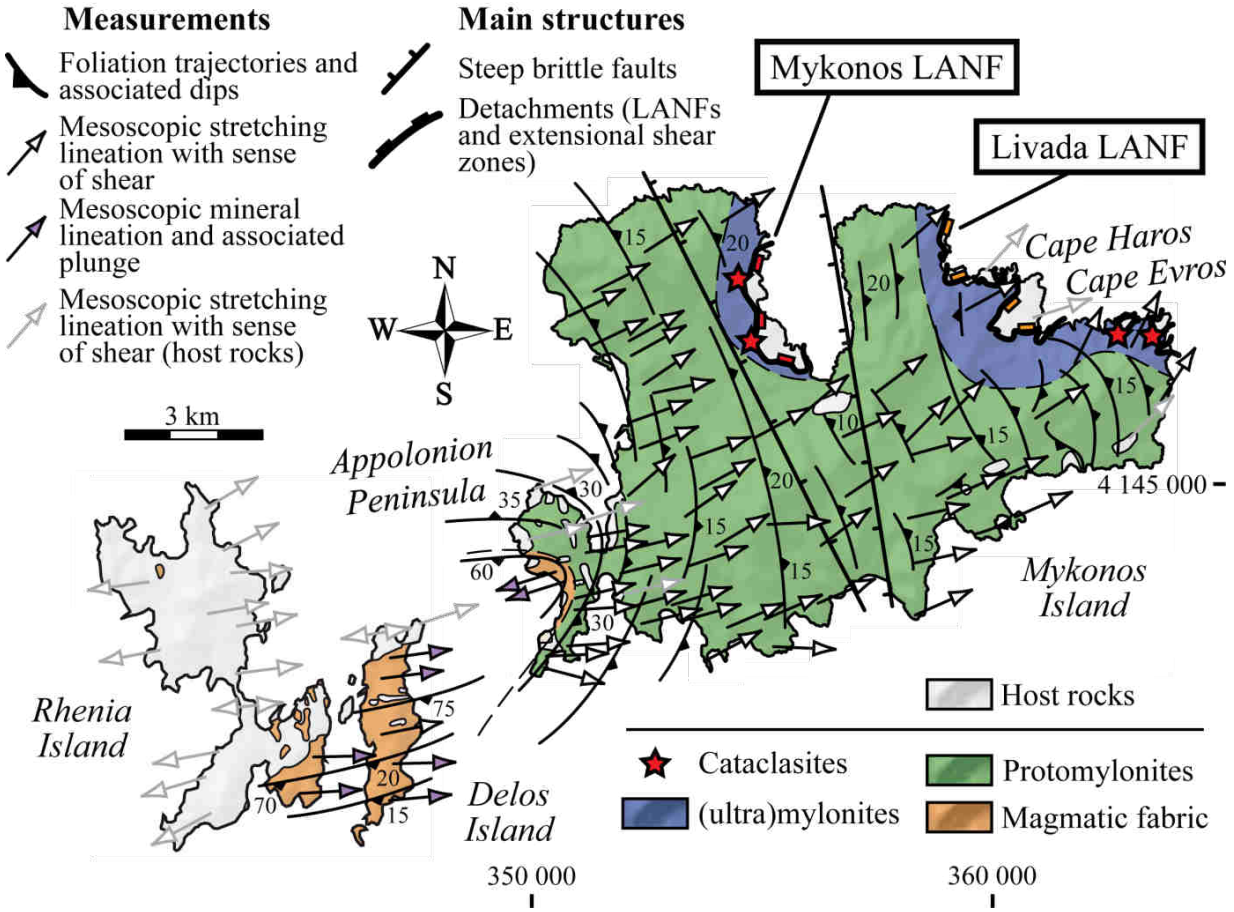

Figure IV-14: *tectonic map of the Mykonos magmatic complex incorporating a distribution map of the strain intensity qualitatively built from micro- and macroscopic observations on which it has been superposed finite strain markers (interpolated foliation trajectories, mineral and stretching lineations) collected from field-based measurements. For comparison, stretching lineations recorded over the adjacent metamorphic domes are also redrawn (bleached arrows); data acquired by Lucas [1999] and Denèle et al. [2011].*

The magmatic complex displays northeastward a diffuse finite ductile strain gradient from protomylonitic to (ultra)mylonitic grades (Figure IV-14). The transition from the magmatic domain to the protomylonitic one has been thereby underlined near the Appolonion Peninsula through relics of high- to medium-temperature solid-state microstructures, as well as incipient shear localization of non-pervasive, gently NE-dipping shear bands that homogeneously indicate a top-to-the-ENE sense of shear [*Lucas*, 1999; *Denèle et al.*, 2011]. These millimeter-wide, normal sense shear bands become increasingly denser and thicker northeastward up to grow into a mylonitic zone just below the detachment system. Here, a several tens of meters thick section displays mylonitized rocks characterized by shallow ne-dipping tectonic foliations, a slightly deviated NE-trending stretching lineation and various kinematic criteria compatible with a top-to-the-NE sense of shear (Figure IV-14) [*Faure et al.*, 1991; *Lee & Lister*, 1992; *Avigad et al.*, 1998; *Lecomte et al.*, 2010; *Denèle et al.*, 2011; *Menant et al.*, 2013].

In line with the upward and northeastward strain gradient, the most intensely deformed rocks have been documented within the uppermost decametric section underneath the detachment surfaces, and especially below the Livada detachment plane where it crops out several centimeter- to meter-wide ultramylonite bands [*Jolivet et al.*, 2010; *Lecomte et al.*, 2010]. These ultramylonitic shear bands, together with the penetrative mylonitic foliation and the locally observed intrusive contact, were asymmetrically folded under a similar NE-directed simple shearing (Figure IV-6). The deformational history ended into semi-brittle to brittle conditions. The last incremental motions can be chiefly sighted through all the northeastern border of the intrusion. The strongly sheared intrusive body, along with its related train of sills and dikes, were reworked by syn- and antithetic Riedel faults or by the above reported massive (ultra)cataclastic deformation linked to the Mykonos detachment activity (see section 3.1) [*Lecomte et al.*, 2010; *Lacombe et al.*, 2013; *Menant et al.*, 2013].

4.3. The Ikaria magmatic complex

On Ikaria, magmatic products were predominantly accumulated into the western half of the dome where the I-type Raches intrusion was spatially emplaced alongside the S-type Karkinagrion intrusion (Figure IV-7), two plurikilometric-scale bodies respectively affiliated to a biotite-hornblende monzogranite [*Altherr et al.*, 1982; *Altherr & Siebel*, 2002] and a two-micas leucogranite [*Ring*, 2007; *Bolhar et al.*, 2010]. These two closely associated granitoids embody together a nested magmatic system wherein the large-scale I-type monzogranite hosts a composite network of synplutonic dikes and exhibits an intrusive character within the S-type leucogranite [*Laurent et al.*, 2015]. Synplutonic dikes have been widely recognized in outer zones of the magmatic system, in particular all the way through the eastern margin where the folded intrusive contact with the metamorphic sequence can be followed over approximately 10 km in a north-south direction [*Beaudoin et al.*, 2015; *Laurent et al.*, 2015]. Farther east, the H*T* metamorphic dome was also intruded by the small-scale Xylosyrtis granitoid (Figure IV-7), another S-type two-micas leucogranite surrounded by a dense array of pegmatitic and aplitic dikes [*Altherr et al.*, 1982; *Kumerics et al.*, 2005; *Photiades*, 2005; *Hezel et al.*, 2011]. Though

it was intrusive within the upper metamorphic pile of the Ikaria unit close to the detachment system, the satellite Xylosyrtis leucogranite appears ductilely undeformed. Only a mineral fabric, probably acquired under a magmatic state, has been distinguished and defined by faintly pronounced SE-dipping foliations and NE-trending lineations (Figure IV-15) [*Kokkalas & Aydin*, 2013].

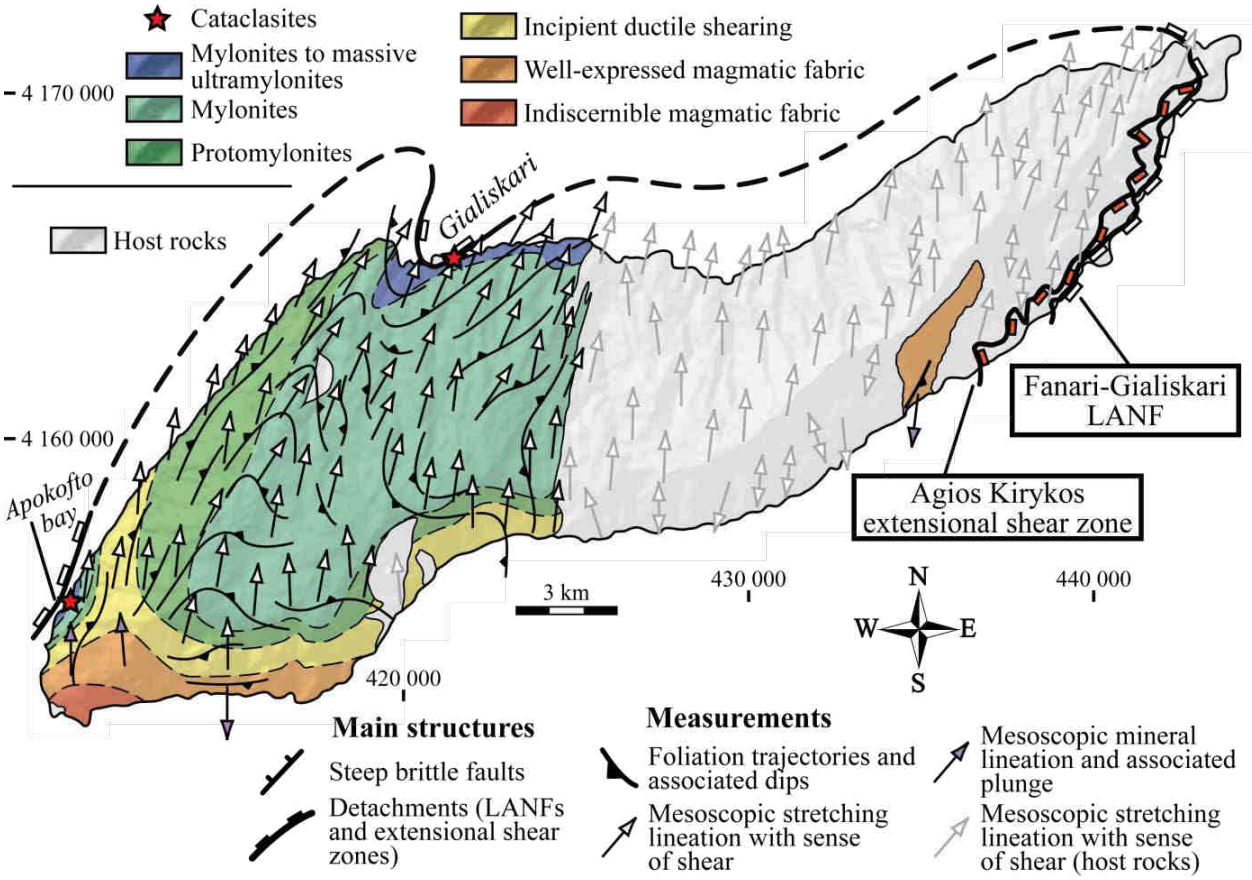

Figure IV-15: *tectonic map of the Ikaria magmatic complex incorporating a distribution map of the strain intensity qualitatively built from micro- and macroscopic observations on which it has been superposed finite strain markers (interpolated foliation trajectories, mineral and stretching lineations) collected from field-based measurements. For comparison, stretching lineations recorded over the adjacent metamorphic domes are also redrawn (bleached arrows); data acquired by Kokkalas & Aydin [2013] and Laurent et al. [2015].*

Conversely, nearly all of the Raches-Karkinagrion magmatic system experienced a significant solid-state deformation under ductile and brittle fields, partially or completely obliterating the primary magmatic texture [*Faure et al.*, 1991; *Boronkay & Doutsos*, 1994; *Kumerics et al.*, 2005; *Ring*, 2007; *Kokkalas & Aydin*, 2013; *Laurent et al.*, 2015]. According to the high-resolution field mapping performed by *Laurent et al.* [2015] (Figure IV-15), the still-undamaged magmatic textures from both magmatic bodies have been solely identified in the southwestern corner of the island. There, aside from the southernmost coastal area where no preferred mineral orientations have been determined, outcropping rocks distinctively show mesoscopic fabrics featured by oblate symmetries, steeply dipping foliations and constant N-

trending mineral lineations. These synmagmatic fabrics are gradually replaced to the north by a post-solidus non-coaxial shearing, asymmetrically distributed throughout the entire ductilely affected domain (Figure IV-15). Overall, the finite strain continuously intensifies when approaching the Fanari-Gialiskari detachment plane (Figure IV-8b). Along a 300-500 m-thick ductile strain gradient, *Laurent et al.* [2015] have indeed divided northward and upward the successive recording of incipiently sheared magmatic rocks, then protomylonites and finally mylonites turned into massive ultramylonites through a thin horizon of a few meters at the vicinity of the Gialiskari-Fanari detachment (Figure IV-15). Within the whole sheared domain, foliation traces dip at gentler angles (< 30°) than those measured in the southern magmatic fabrics and their interpolated trajectories have underscored at map scale a convolute profile carrying NE-directed long axes and typical wavelengths of up to several kilometers. In spite of the change of foliation orientation, stretching lineations keep a stable north-directed trend or slightly deflected toward a northeaster direction into the (ultra)mylonitic rocks. Either way, all assorted kinematic indicators have pointed out an unambiguous top-to-the-N or -NE shear sense.

In addition to the above described knife-sharp fault surface of the Gialiskari-Fanari detachment, evidence of a deformational regime shift toward a more brittle-cataclastic behavior are displayed (1) at various points of the nested magmatic complex where conjugate sets of W-striking, high- to low-angle normal faults have formed in response to an ongoing N- to NE-oriented extension, and (2) immediately underneath the Gialiskari-Fanari detachment with the observation of hydrothermally altered cataclasites [*Laurent et al.*, 2015]. With an apparent thickness reaching approximately 10 meters, these foliated and faulted cataclasites typically contain rock fragments derived from (ultra)mylonites. A comparable evolution of a viscous-to-cataclastic flow has been also emphasized within a thinner section of a few hundred meters toward the western coastal sector (near Apokofto Bay, location in Figure IV-15), sign of a spatial closeness with the sinuous Gialiskari-Fanari detachment most certainly located offshore west of the island.

4.4. The Naxos monzogranite

Like on Tinos and Ikaria islands, Naxos brings together two types of granitoids with (1) a cluster of small-scale, S-type leucogranites intrusive into the northern half of the H*T* dome in close association with the migmatitic core, and (2) a larger I-type intrusion typified by a compositional spectrum ranging from a hornblende-biotite monzogranite in the inner part, to a subordinate peripheral granodiorite invaded by a composite cortege of isolated and swarms of enclaves (for simplification purposes, we consider the I-type body as a monzogranite in Figure IV-9 and in the following text) [*Jansen*, 1973; *Altherr et al.*, 1982; *Wijbrans & McDougall*, 1988; *Pe-Piper et al.*, 1997; *Pe-Piper*, 2000; *Keay et al.*, 2001; *Altherr & Siebel*, 2002]. Magmatic inclusions have been recurrently reported close to the eastern rim where a N-striking, folded intrusive contact extends over ~10 km-long (Figure IV-16). The northern roof of the monzogranite is cut by the corrugated Moutsouna detachment [*Lister et al.*, 1984; *Gautier et al.*, 1993; *John & Howard*, 1995; *Brichau et al.*, 2006].

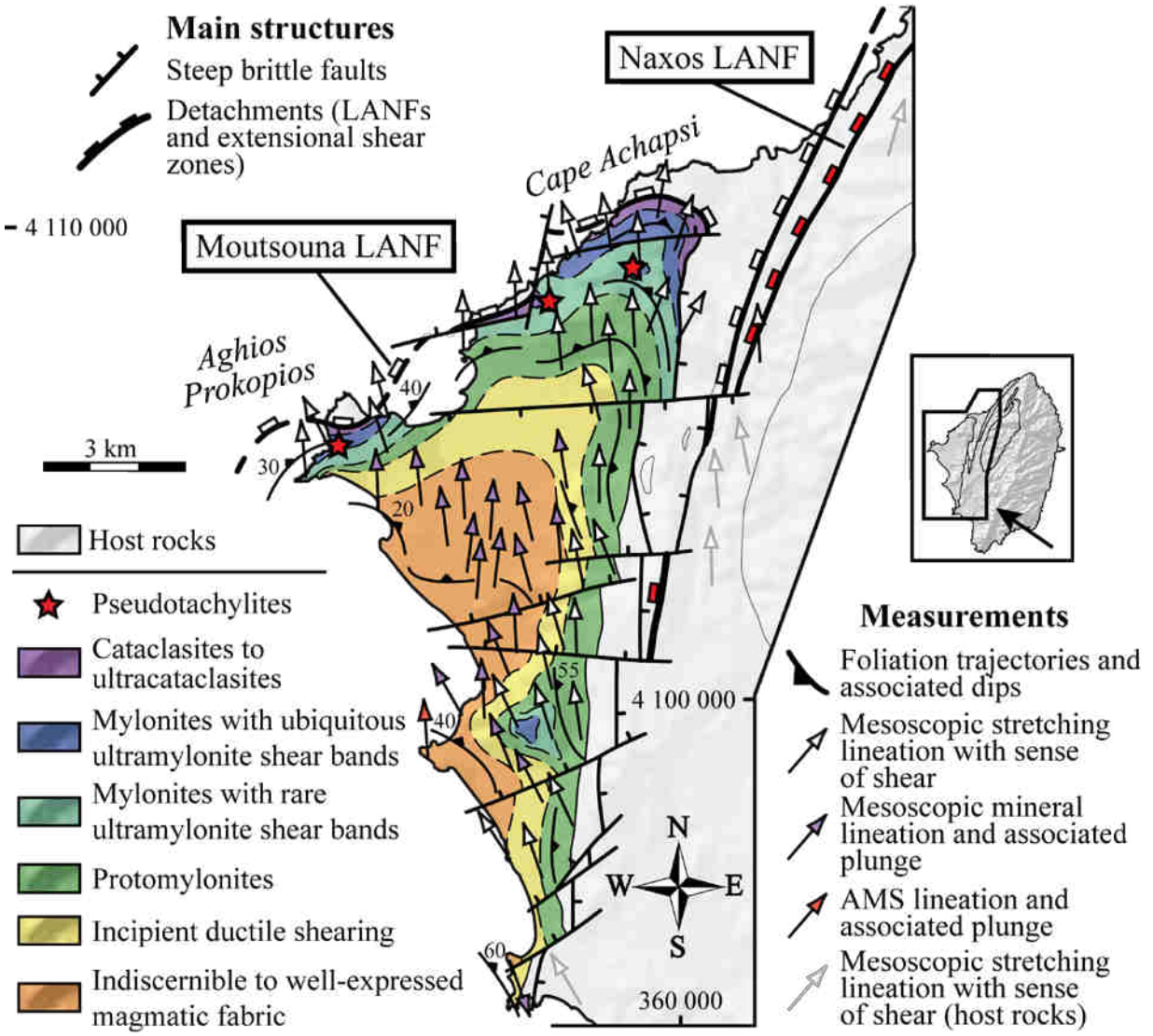

Figure IV-16: *tectonic map of the Naxos monzogranite incorporating a distribution map of the strain intensity qualitatively built from micro- and macroscopic observations on which it has been superposed finite strain markers (interpolated foliation trajectories, mineral and stretching lineations) collected from field-based and AMS (anisotropy of magnetic susceptibility) measurements. For comparison, stretching lineations recorded over the adjacent metamorphic domes are also redrawn (bleached arrows).*

As a whole, the underlying monzogranite offers an extensive array of finite structures and fabrics heterogeneously acquired under magmatic, ductile or brittle conditions depending upon the structural position of intrusive rocks with respect to the Moutsouna detachment (Figure IV-16). The primary magmatic textures are found in the internal portion of the monzogranite, far from the Moutsouna detachment surface. There, a vast majority of outcropping rocks reveals a quite clear mesoscopic fabric marked by N- to NW-trending mineral lineations and relatively low-dipping foliations (<30°) that tend to become steeper (dip angles of about 40-60°) farther southeast. Toward the marginal zones, these synmagmatic fabrics are progressively replaced by a top-to-the-N ductile shearing (Figure IV-16). At the map scale, the overall attitude of tectonic foliations supports a dome-shaped structure through

which the intensity of deformation gradually increases toward the carapace. However, the most intensely deformed zone predominantly concentrates toward the north, in the vicinity of the Moutsouna detachment. Here, an upward and northward gradient of shearing is observed along a 300-500 m-thick section, from a weakly deformed monzogranite up to a mylonitized intrusive rock associated with frequent 1-5 cm-thick anastomosing ultramylonite bands. An equivalent shear strain gradient can be also locally distinguished in the southeastern part of the monzogranite where the highest altitude zone culminates into pervasively foliated mylonites.

Up to approximately several tens of meters underneath the Moutsouna detachment plane, the monzogranite was ultimately reworked by an increasingly intense brittle/cataclastic deformation northward and upward, moving up from fault-rocks and protocataclasites in which fragments from the underlying mylonitized carapace have been preserved, to cohesively foliated ultracataclasites directly beneath the locally observed detachment gouge. When it can be distinguished, the detachment fault surface also bears displacement clues in the brittle field under a coherent NE-oriented extension (e.g., slickenline lineations, corrugations and tension gashes).

4.5. The Serifos granodiorite

The Late Miocene I-type intrusion over Serifos Island has been petrologically ascribed to a biotite-hornblende granodiorite [*Altherr et al.*, 1982; *Altherr & Siebel*, 2002; *Stouraiti et al.*, 2010], a relatively small-scale body defined by a subtle textural zoning wherein an inner fine-grained facies has been differentiated from a marginal coarse-grained facies (Figure IV-11) [*Salemink*, 1985; *Rabillard et al.*, 2015]. Among the Cycladic I-type granitoids, the Serifos granodiorite encloses one of the richest collections in magmatic inclusions with disseminated remnants of monogenic/polygenic swarms of enclaves, dike-like monogenic swarms or compositionally heterogeneous synplutonic dikes [*Iglseder et al.*, 2009; *Rabillard et al.*, 2015]. Most of these composite occurrences crop out in the topographically deeper zones, in particular all along the southern and eastern rims where the granodioritic body was in addition transected by a series of major extensional structures, namely the Vaghia and Aghios Sostis detachments (Figures IV-11 and -17) [*Grasemann & Petrakakis*, 2007; *Tschegg & Grasemann*, 2009; *Rabillard et al.*, 2015].

According to the structural observations from the above referenced fieldworks, both detachments acted over time in similar fashion involving the development of an extremely localized shearing and a subsequent evolution toward a more brittle attitude by way of low-angle normal faulting. As displayed in the distribution map of strain intensity (Figure IV-17), the Vaghia and Aghios Sostis detachments brittlely juxtapose a metasomatized and weakly deformed granodiorite atop a mylonitic band not thicker than a few meters, or even directly against penetratively foliated ultramylonites underneath the Aghios Sostis detachment fault. These intensely sheared rocks structurally belong to the uppermost level of a sharp gradient of shearing, i.e., a narrow domain reaching a few tens to one hundred of meters in thickness through which the intensity of the bulk foliation smoothly decreases toward the inner parts of the granodiorite. With the decreasing magnitude of ductile deformation, it has also been

documented an obvious evolution of the fabric-related symmetry ranging from strongly oblate mylonites to a rather more prolate shape into incipiently sheared intrusive rocks. Despite a fluctuant pattern of foliation trajectories throughout the ductilely deformed part of the intrusion, both the measured stretching and mineral lineations systematically trend toward the southwest and kinematic indicators homogeneously show a top-to-the-SW shearing.

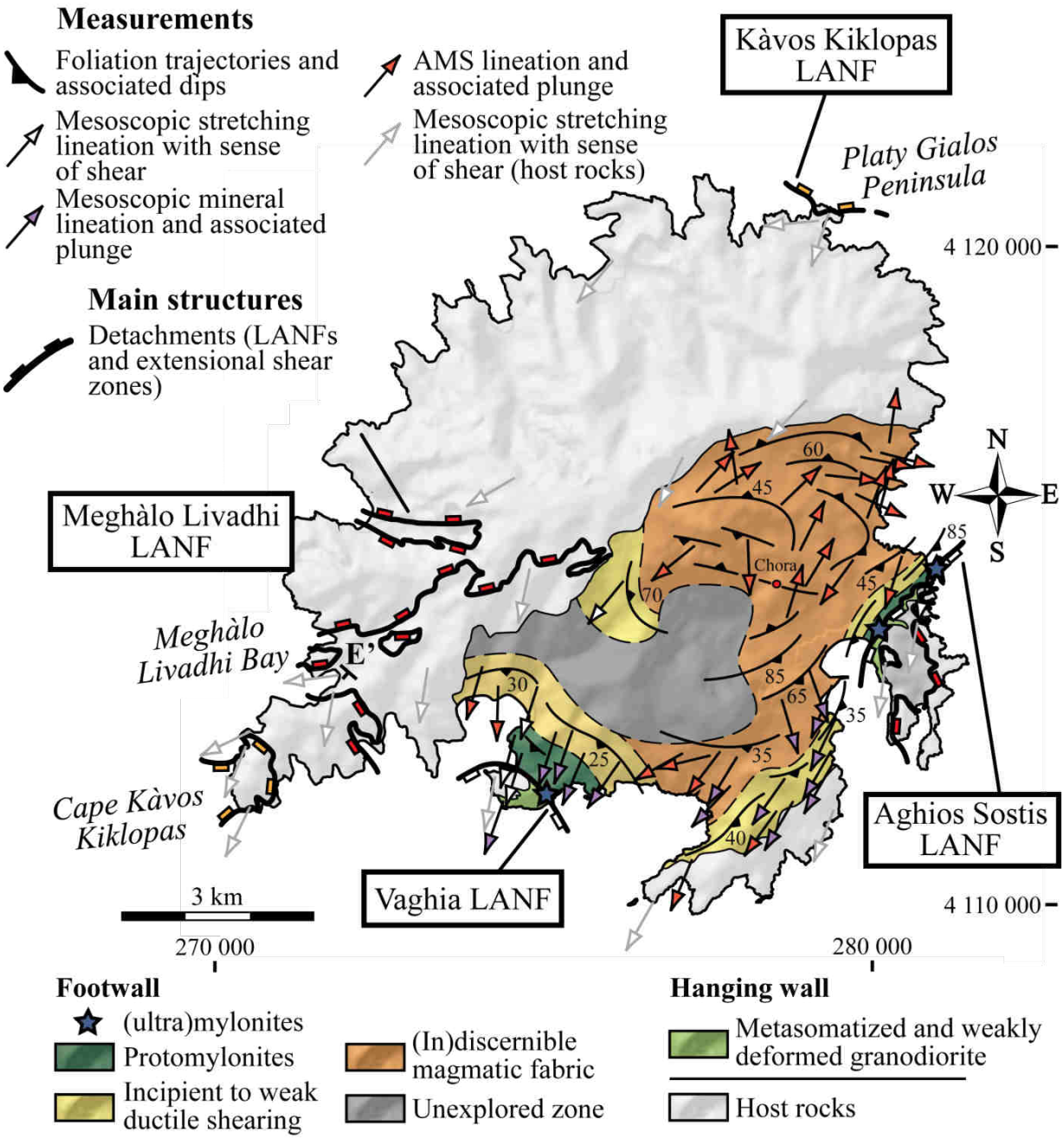

Figure IV-17: *tectonic map of the Serifos granodiorite incorporating a distribution map of the strain intensity qualitatively built from micro- and macroscopic observations on which it has been superposed finite strain markers (interpolated foliation trajectories, mineral and stretching lineations) collected from field-based and AMS (anisotropy of magnetic susceptibility) measurements. For comparison, stretching lineations recorded over the adjacent metamorphic domes are also redrawn (bleached arrows); data acquired by Rabillard et al. [2015].*

As the extensional shearing turns out to be strongly localized, a significant portion of the granodiorite has therefore preserved magmatic textures without any substantial solid-state overprint [*Rabillard et al.*, 2015]. The magmatic domain primarily covers the central part of the intrusive body, as well as its northern edge along which a staircase-shaped intrusive contact cuts across the preexisting regional fabric. In the field, mesoscopic fabrics from both the fine-grained and coarse-grained facies appear indistinguishable or dimly expressed. Combined with an AMS survey [*Rabillard et al.*, 2015], the magnetic and mesoscopic foliations delineate a coherent concentric pattern with a slight shape eccentricity depicted by a SW-directed long axis (Figure IV-17). Conversely, lineations define a more complex pattern, including a preponderant set of south to southwest trends and a second one characterized by perpendicular, E-trending lineations.

5. Discussion

5.1. Finite strain patterns in the Cycladic granitoids: evidences for magma-assisted strain localization along detachments

One barrier in studying the state of finite strain within deformed intrusive bodies is that only the last increments of shearing are mostly discernible and clues for the initial magmatic state are often partially or completely obliterated by a superimposed solid-state deformation. However, the accumulated high-shear strain can be sufficiently localized within a narrow domain so that primary magmatic textures and incipient stages of deformation can be preserved underneath. In particular, magmatic fabrics received increasing attention since they represent a foreground importance for determining fabric-forming processes that operated during the early to sub-solidus states of magma crystallization. According to classical interpretations, magmatic fabrics may originate either from intrinsic (e.g., pressure-driven magmatic flows or emplacement-related conditions) or extrinsic processes (e.g., regional stress regime) [*Paterson et al.*, 1989, 1998; *Vernon*, 2000]. In other words, the synkinematic character of granitoids strongly depends on the degree of coupling between magmatic and host rocks fabrics.

The qualitative field-based mapping of the state of finite strain performed over the five Cycladic magmatic complexes (Tinos, Mykonos-Delos-Rhenia, Ikaria, Naxos and Serifos) yields insight for both the distribution and the evolution of deformation for each case-study. Independently of radiometric time-constraints, the systematic structural mapping through the synextensional intrusions more precisely testifies to their synkinematic nature. The compilation of our structural data with already published ones clearly shows a continuum of deformation from magmatic to solid-state ductile conditions, and finally toward a more brittle/cataclastic behavior (Figures IV-13 to -17). Furthermore, kinematics observed throughout lateral ductile shear gradients are entirely compatible with those recorded within corresponding metamorphic domes and especially on approaching the detachment zones. Although time constants between short-time intrusive events and long-lasting detachment activities are quite different, co-magmatic deformation (or orientation of the flow) and sub-solidus deformation recorded during cooling show a progressive localization toward the detachment planes that cap intrusion roofs. The direction of the magmatic flow (mainly inferred from the direction of the mineral

lineation, e.g., [*Paterson et al.*, 1989]) seems in the great majority of case-studies completely oriented by the regional strain and stress field (i.e., Mykonos, Ikaria, Naxos). A more sophisticated pattern is inferred from the Tinos and Serifos intrusions, especially in magmatic domains where AMS fabrics do not constantly mimic mineral fabrics. The complex trend has been exclusively recorded by AMS signal and was tentatively interpreted as emplacement-related magma infilling along NW-SE oriented tensional zones whose direction of opening could be consistent with the NE-SW directed regional extension [*de Saint Blanquat et al.*, 2011; *Rabillard et al.*, 2015]. For instance, the importance of the coalescence of dikes striking perpendicular to the regional stretching direction to form the intrusive body is well illustrated by the southernmost part of the Tinos intrusion. The exact mechanism that links co-magmatic flow and sub-solidus deformation remains to be ascertained, but the example of Serifos shows that the magma can flow in the direction of shearing. This is indeed suggested by proto-dikes of mafic rocks invading the root zone of the pluton that are dismembered to give mafic enclaves downstream [*Rabillard et al.*, 2015].

Overall, structural investigations both inside and outside synextensional granitoids provide new insights into geological processes through which the Cycladic intrusions have spatially interacted through time with strain localization events. It seems that the bulk architectures and cooling (i.e., the apparent rejuvenation of cooling ages toward detachment planes) of the Cycladic granitoids were tectonically controlled by a contemporaneous non-coaxial shearing that localized over time into detachments through their upper intrusive contacts. This picture thus significantly differs from some previous studies in which the relations between tectonism and magmatism were also investigated at regional scale [*Boronkay & Doutsos*, 1994; *Koukouvelas & Kokkalas*, 2003; *Kokkalas & Aydin*, 2013]. Even if the aforementioned authors recognized that the Cycladic granitoids are spatially associated with low-angle normal faults, they rather concluded that late-stage emplacements and ensuing deformations were primarily controlled by systems of transtensional strike-slip faults. Although strike-slip faults can be recorded over some islands (Naxos, Ikaria, Mykonos), such structures obviously cross cut both across detachments and granitoids and thereby started to localize later than the activity of the detachments and I-type magmatism [e.g., *Siebenaller*, 2008; *Menant et al.*, 2013; *Beaudoin et al.*, 2015].

5.2. Causal links between magmatism, exhumation processes and detachment faulting: toward a coherent regional scheme

In the Cycladic archipelago, one of the most striking features in reviewing the granitoid-cored MCCs is their ubiquitous association with multiple and closely spaced detachments. Such architectural configurations thus raise the question of how these synkinematic granitoids could have been over time geometrically paired with those detachment systems and it brings us back to the causal link between syn-tectonic magmatism, exhumation processes of deep crustal rocks and detachment faulting.

As presented in this synthesis, this issue has been partly resolved via thermochronological investigations acquired in recent years. Through (U-Th)/Pb radiometric

ages reported from the Cycladic granitoids, it seems now well constrained that the magmatic activity took place only in the late exhumation stages of metamorphic domes [*Keay*, 1998; *Keay et al.*, 2001; *Brichau et al.*, 2007, 2008; *Iglseder et al.*, 2009; *Bolhar et al.*, 2010]. The surge of intrusive magmatism, including I- and S-type granitoids, was indeed limited into a relatively short time window (15-9 Ma) while the deeply buried metamorphic rocks from the Hellenic accretionary wedge were already experiencing an overall exhumation-related retrograde metamorphism under greenschist-facies conditions (Figure IV-2). It can thus be concluded that none of those intrusions appears to be a viable candidate for the genesis of MCCs but would rather be a consequence of a warmer geodynamic environment during lithospheric thinning and slab retreat [*Jolivet et al.*, 2015]. In the wake of a faster southward roll-back of the subduction front (since 35-30 Ma ago) and probably a subsequent progressive tearing of the subducting Hellenic slab (between 20 and 16 Ma), the arrival of a hot asthenospheric flow would have therefore progressively replaced the overlying lithosphere, thereby providing a sufficient heat input for a partial melting of the extending lower crust and the metasomatized mantle wedge [*Jolivet et al.*, 2015; *Menant et al.*, 2016a]. With ongoing extension, S- and I-type magmas generated in the deep lithosphere were partly dragged upward through the crust and then accumulated into already-formed MCCs in which detachment faulting was at a mature stage. As a result, some authors tentatively concluded that crustal-scale detachments could behave successively as ready pathways for magma migration through the crust and active mechanical barriers below which composite magmatic bodies were efficiently trapped, stored and quite simply deformed during their subsequent cooling [*Brichau et al.*, 2007, 2008, 2010; *Bolhar et al.*, 2010].

As further shown above, the present-day anatomies of the granitoid-cored metamorphic domes however imply somewhat more complex exhumation histories with the development of multiple detachments. Even if the exact onset of each MCC-bounding detachment remains uncertain through radiometric dating, some key elements reported in this review tend to demonstrate successively active detachments as a result of local and transient interactions with granitoid intrusions, rather than their concomitant existence, as shown on Figure IV-18. All structural, kinematic and geometrical constraints indeed converge upon a coherent model in which the exhumation of the granitoid-cored domes were systematically achieved below a single detachment that was inactivated at the time of intrusion and replaced by a new strain localization zone at the upper intrusive contact of the granitoids.

Such a tectonic scheme has been already proposed for the final exhumation stages of both the Tinos and Mykonos domes along which the sequential generation of three detachments of the NCDS was punctuated by successive and discrete pulses of magma batches [*Jolivet et al.*, 2010]. There, the top-to-the-NE deformation was first progressively localized along the Tinos detachment since ~30 Ma ago (detachment 1 in Figure IV-18). It was essentially active in the ductile field and evolved as a brittle detachment before it was perforated and inhibited by the Tinos magmatic complex at circa 15-14 Ma. The monzogranite intruded the dome at relatively upper crustal depths (related-crystallization pressure estimations: 300-400 MPa, *Bröcker & Franz* [1994]) and concurrently produced a thermal weakening of surrounding rocks as well as a strain reactivation in ductile condition.

Extensional shearing migrated both along the intrusion roof and its upper margin, still under a NE-directed extensional regime. The shear strain was then gradually localized through the Livada detachment along the intrusive contact of the 14-11 Ma old Mykonos sheeted complex, and also likely at the apex of the Tinos monzogranite (detachment 2 in Figure IV-18). Once the granitoids were cold, extensional deformation evolved toward a more brittle-cataclastic behavior and was transferred along the Mykonos detachment at the interface between the MCC and overlying sedimentary basins (detachment 3 in Figure IV-18).

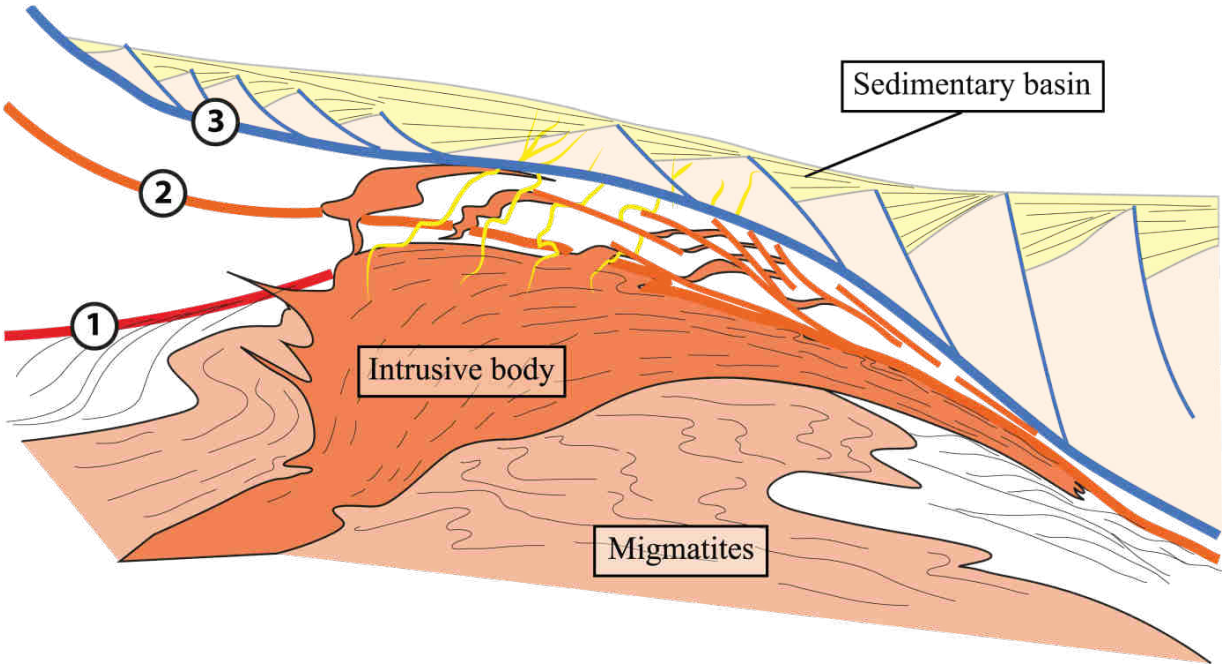

Figure IV-18: *cross section showing the sequentially developed detachment branches as resulting from the local interaction with a granitoid intrusion. This sketch can easily be used for each late exhumation history of metamorphic domes described in this study. The pluton intrudes an already active metamorphic core complex topped with a detachment (1) associated with or without a migmatite dome in its core. The early formed detachment can be the equivalent to the Tinos, Agios-Kirykos, Naxos or Meghàlo Livadhi detachments. The intrusion inactivates the early detachment that is replaced by a new detachment (2) localizing along the upper contact of the pluton, similar to the Livada, Gialiskari-Fanari, Moutsouna or Kàvos Kiklopas detachments. A shear zone develops within the pluton with a continuum of deformation from the co-magmatic flow to sub-solidus colder deformation and mylonitization below the new detachment. Finally, a third detachment may form above, strictly in brittle-cataclastic behavior, and its complete the exhumation of the metamorphic core complex, like the Mykonos detachment.*

This evolution can be seen almost with the same sequence on Ikaria where the magmatic event actively contributed in shaping the present-day architecture of the migmatite-cored MCC [*Beaudoin et al.*, 2015; *Laurent et al.*, 2015]. The final exhumation of the H*T* metamorphic dome was governed by an overall N-directed extension and completed by two anastomosing high-strain zones, i.e. the deeper Agios-Kirykos shear zone and the late and more surficial Gialiskari-Fanari low-angle normal fault. The top-to-the-N strain localization along the Agios-Kirykos shear zone would have started before or simultaneously with the H*T* episode

of partial melting (~16 Ma) and lasted until it was pierced and sealed by early intrusions of the composite magmatic system (15-13 Ma) at mid-crustal level (related-crystallization pressure estimations: 300-500 MPa, *Laurent et al.* [2015]). The extensional deformation then migrated at the top of the Raches monzogranite and lastly localized with time under ductile-to-brittle/cataclastic conditions along the newly-formed Gialiskari-Fanari detachment fault. An analogous tectonic history for the NPDS can also be drawn farther south on Naxos, where the migmatite-cored metamorphic dome was successively exhumed below the ductile-to-brittle Naxos detachment and then below the more localized ductile-to-brittle Moutsouna detachment. Associated with a stable top-to-the-N kinematic, the onset of extensional shearing and subsequent strain localization along the deeper Naxos detachment branch would have preceded and coincided with the peak of H*T* (~21-17 Ma). It predominantly operated in ductile condition and ended as an extensional brittle detachment prior to the 13-11 Ma old I-type intrusion. Magmatic products were emplaced into the hanging wall of the Naxos detachment at upper crustal depths (200-300 MPa, [*Jansen & Schuiling*, 1976; *Gautier et al.*, 1993; *Cao et al.*, 2017]) and had temporarily disturbed both the thermal structure and the deformational regime prevailing within the surrounding system. The resulting ductile shearing was ultimately transferred up-section where the Moutsouna detachment localized along the intrusive margin. In the same way on Serifos, extension-related exhumation of the metamorphic dome was initially accommodated by a single detachment branch of the WCDS that was afterward blocked and substituted by new detachment zones as the result of magmatic activity. From the Middle Miocene onward, the top-to-the-SW shearing was indeed first concentrated along the Meghàlo Livadhi detachment under ductile then brittle conditions before being intruded and sealed by the ~11-9 Ma old granodioritic body at shallow crustal level (approximately 300 MPa, [*St. Seymour et al.*, 2009]). In short time span, the granodioritic intrusion radically altered the local temperature, reheating host rocks and inducing some ductile deformation under an unchanging stress regime. Strain accommodation was thereby achieved higher-up through a set of narrow high-strain zones that tended to localize both at the intrusion roof (i.e., Agios Sostis and Vaghia detachments) and into adjacent host rocks (i.e., Kàvos Kiklopas detachment). Given structural and kinematic similitudes between the newly-formed detachment zones, one can assume that those three branches were contemporaneous and most likely genetically linked as a unique detachment.

Concluding, these similar sequences of events are thus not a local characteristic of the NCDS but it seems to reveal a general behavior of detachments systems interfering with intrusions. Instead of a passive attitude with regard to extensional tectonics, magmatic intrusions have rather dynamically impacted the late evolution stages of the Cycladic MCCs (Figure IV-18). The present scenarii further corroborate the fact that the strength evolution of the crust in MCC-type systems can become non-linear and cyclical with the arrival of episodic and repeated pulses of magma. Partially crystallized plutonic bodies, behaving as transient thermo-mechanical instabilities, may indeed introduce short-lived rheological contrasts and inducing a weakening and then hardening of the upper continental crust.

5.3. Can one expect an analogous tectono-magmatic configuration below the southern Aegean volcanic arc? Some speculations

This analysis of the interactions between the Aegean plutons and contemporaneous detachments shows strong similarities among the different studied examples. The same type of interactions is recognized over the ~5-6 Ma time window during which the Aegean plutons were emplaced. Magmatic activity in the Aegean region has been continuous since the Late Cretaceous when the magmatic arc was located much further north in the Balkans. It then migrated progressively southward with an acceleration some 35 Ma ago following slab retreat. The emplacement of the Aegean granites is partly related to this southward migration and to a slab tearing event that is postulated between 15 and 9 Ma [*Jolivet et al.*, 2015], that is during the same period. The magmatic arc then continued to migrate southward to reach its present position. The question can then be posed of the continuation of the same emplacement dynamics in the recent period, below the active arc, as during the Miocene.

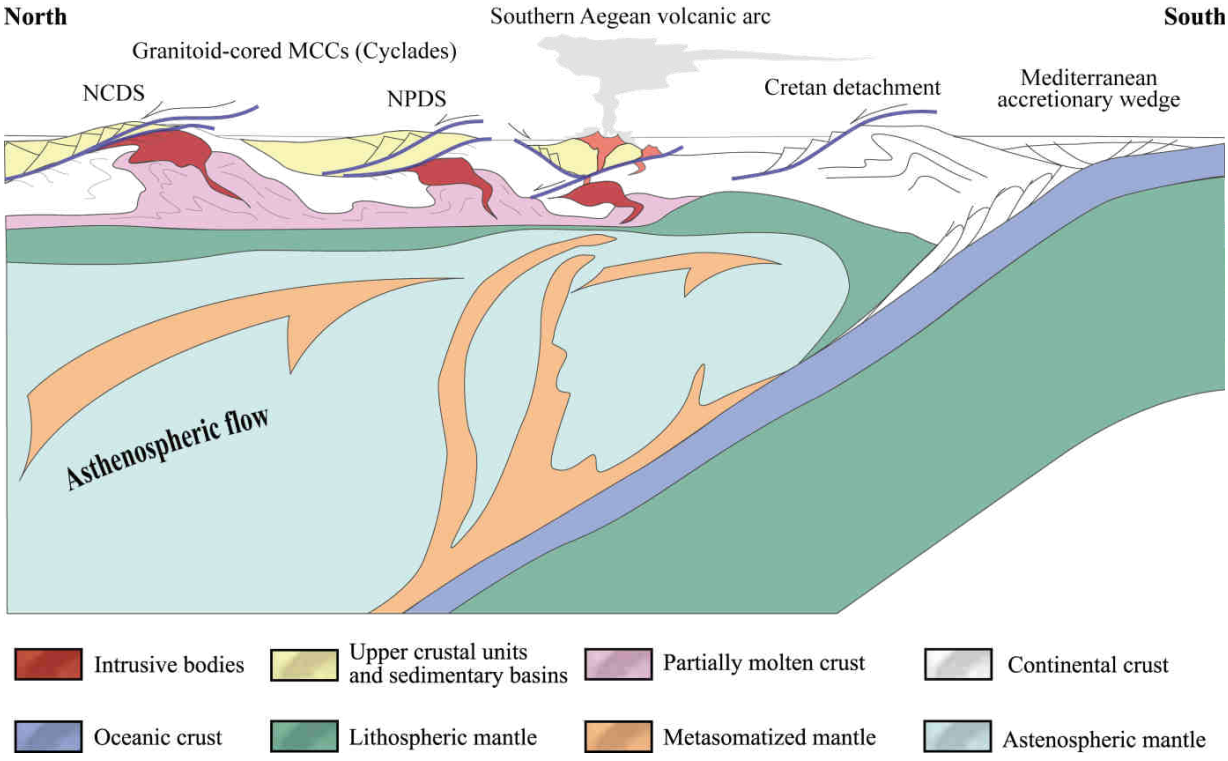

Figure IV-19: *speculative sketch of a retreating subduction zone with back-arc extension and emplacement of plutons below detachments during the retreat and migration of the magmatic arc. We assume that the exhumed structures observed within the exhumed MCC are a good image of the processes active below the Quaternary volcanic arc. NCDS: North Cycladic Detachment System; NPDS: Naxos-Paros Detachment System.*

Figure IV-19 proposes a speculative sketch of a migrating magmatic arc above a retreating subduction. This model is inspired from the interrelations between the Aegean intrusions and the multiple sets of associated detachments described above. It also benefited a lot from numerical modelling of *Menant et al.* [2016a] that shows the dynamics of mantle

flowing between the retreating slab and the upper plate. Leaving aside the 3D complexity of this flow in *Menant et al.* [2016a], we simply retain the geometry of partially molten mantle plume above the subducting slab. The flow induced by slab retreat is southward and the coupling between the flow and the deforming crust above leads to an asymmetrical deformation with N-dipping detachments exhuming crustal boudins and MCCs [*Jolivet et al.*, 2004b, 2009, 2013]. A steady-state slab migration leads to a migration of the volcanic arc at a constant velocity. Our observations on the Serifos pluton suggest that the internal finer-grained facies was emplaced while the magmatic chamber was opened toward the surface, thus calling for the presence of a volcano above. One may then assume the same geometry for the Naxos pluton and all the Aegean plutons. This assumed continuum is reasonable (but not proven) in the light of the comparison between the direction of Miocene shearing direction and active GPS displacements in the Aegean domain [*Jolivet*, 2001]. This is of course highly conjectural as these volcanoes would be preserved in the upper unit, above the detachment, and have thus been displaced by the later motion along the detachment. One may finally postulate that the same geometry and connections between the pluton and the volcano is at work below the present volcanic arc. Some recent seismic tomography model [*Dimitriadis et al.*, 2010] (see their Figure 15) suggests the presence of a high temperature anomaly below Santorini, dipping toward the NE down to 5-8 km. This anomaly could sign the presence of a connected magmatic system down to that depth and its NE-ward dip could be an image of a NE-dipping detachment. If this highly speculative model holds, it means that, during southward slab retreat, the deep parts of similar pluton-volcano systems were progressively exhumed in the back-arc region. The plutonic complexes of Naxos, Serifos, Ikaria, Mykonos and Tinos would then provide images of the plutonic system presently active below Santorini.

Conclusion

The analysis in the field of five Aegean plutons (Tinos, Mykonos, Ikaria, Naxos and Serifos) reveals closely similar evolutions during their emplacement. The interactions between these synkinematic granitoids and the detachments responsible for the exhumation of the metamorphic core complexes, and more generally the H*P* metamorphic rocks in which they intrude show the same sequence of events. These magmatic bodies intrude a MCC that is already forming below a large-scale detachment, either the NCDS, the WCDS or the NPDS. They intrude these MCCs in a quite late stage of their evolution and are thus not the cause for the localization of extension. Granitoids intrude a first generation of detachment that is then inactivated and replaced by a new strain localization zone along the upper contact of the intrusion with its host rock. A ductile shear zone develops within the granitoid with a marked strain gradient toward the new detachment that finally evolves toward a brittle behavior. This detachment may then be in turn replaced by an additional brittle detachment forming higher up in the crust and completing the exhumation of the MCC.

Within the intrusion, a continuum of shearing deformation is observed from the co-magmatic flow to the sub-solidus deformation and the formation of a thick mylonitic zone evolving into cataclasites. The shearing direction at the magmatic stage and during the subsequent colder deformation and mylonitization are parallel showing that the magmatic flow is oriented by the regional deformation pattern in this case. The exact mechanism that controls the flow of magma in such environments remains to be understood.

Finally, we speculate on a possible connection between the present-day Hellenic volcanic arc and potential granitic magmas at depth, assuming that the kinematics of detachments seen for the Miocene record in the Cyclades is still prevailing at depth below Santorini. We further propose that the MCCs exhumed in the Cyclades during slab retreat are a potential equivalent of the active plutons below the present-day volcanic arc.

Acknowledgments: Data sets are available upon request from the first author. This paper is a contribution of the ERC RHEOLITH Project (ERC advanced grant no. 290864) and Labex VOLTAIRE (Convention n°ANR-10-LABEX-100-01). The authors are indebted to IGME and especially to Nikolas Carras and Adonis Photiades for their help.

Références bibliographiques

Altherr, R., and W. Siebel (2002), I-type plutonism in a continental back-arc setting: Miocene granitoids and monzonites from the central Aegean Sea, Greece, *Contributions to Mineralogy and Petrology*, *143*(4), 397–415, doi:10.1007/s00410-002-0352-y.

Altherr, R., H. Kreuzer, I. Wendt, H. Lenz, G. A. Wagner, J. Keller, W. Harre, and A. Höhndorf (1982), A late Oligocene/early Miocene high temperature belt in the Attic-Cycladic crystalline complex (SE Pelagonian, Greece), *Geologisches Jahrbuch*, *E23*, 97–164.

Altherr, R., F. Henjes-Kunst, A. Matthews, H. Friedrichsen, and B. T. Hansen (1988), O-Sr isotopic variations in Miocene granitoids from the Aegean: evidence for an origin by combined assimilation and fractional crystallization, *Contributions to Mineralogy and Petrology*, *100*(4), 528–541, doi:10.1007/BF00371381.

Altherr, R., H. Kreuzer, H. Lenz, I. Wendt, W. Harre, and S. Dürr (1994), Further evidence for a Late Cretaceous low-pressure/high-temperature terrane in the Cyclades, Greece, *Chemie der Erde*, *54*, 319–328.

Andriessen, P. A. M. (1991), K-Ar and Rb-Sr age determinations on micas of impure marbles of Naxos, Greece: the influence of metamorphic fluids and lithology on the blocking temperature, *Schweizerische Petrologie und Mineralogie Mitteilungen*, *71*(8), 89–99.

Andriessen, P. A. M., N. A. I. M. Boelrijk, E. H. Hebeda, H. N. A. Priem, E. A. T. Verdurnen, and R. H. Verschure (1979), Dating the events of metamorphism and granitic magmatism in the Alpine orogen of Naxos (Cyclades, Greece), *Contributions to Mineralogy and Petrology*, *69*(3), 215–225, doi:10.1007/BF00372323.

Andriessen, P. A. M., G. Banga, and E. H. Hebeda (1987), Isotopic age study of pre-Alpine rocks in the basal units on Naxos, Sikinos and Ios, Greek Cyclades, *Geol. Mijnbouw*, *66*, 3–14.

Angelier, J., G. Glaçon, and C. Muller (1978), Sur la présence et la position tectonique du Miocène inférieur marin dans l'archipel de Naxos (Cyclades, Grèce), *CR Acad. Sci. Paris*, *286*, 21–24.

Armstrong, R. L. (1982), Cordilleran Metamorphic Core Complexes - From Arizona to Southern Canada, *Annual Review of Earth and Planetary Sciences*, *10*(1), 129–154, doi:10.1146/annurev.ea.10.050182.001021.

Aubouin, J. (1959), Contribution à l'étude de la Grèce septentrionale; les confins de l'Epire et de la Thessalie, Ph.D thesis, Univ. Paris, France.

Augier, R., F. Choulet, M. Faure, and P. Turrillot (2015a), A turning-point in the evolution of the Variscan orogen: the ca. 325 Ma regional partial-melting event of the coastal South Armorican domain (South Brittany and Vendée, France), *Bulletin de la Société Géologique de France*, *186*(2–3), 63–91, doi:10.2113/gssgfbull.186.2-3.63.

Augier, R., L. Jolivet, L. Gadenne, A. Lahfid, and O. Driussi (2015b), Exhumation kinematics of the Cycladic Blueschists unit and back-arc extension, insight from the Southern Cyclades (Sikinos and Folegandros Islands, Greece), *Tectonics*, *34*(1), 152–185, doi:10.1002/2014TC003664.

Avigad, D. (1998), High-pressure metamorphism and cooling on SE Naxos (Cyclades, Greece), *European Journal of Mineralogy*, *10*(6), 1309–1319.

Avigad, D., and Z. Garfunkel (1989), Low-angle faults above and below a blueschist belt - Tinos Island, Cyclades, Greece, *Terra Nova*, *1*(2), 182–187, doi:10.1111/j.1365-3121.1989.tb00350.x.

Avigad, D., Z. Garfunkel, L. Jolivet, and J. M. Azañón (1997), Back arc extension and denudation of Mediterranean eclogites, *Tectonics*, *16*(6), 924–941, doi:10.1029/97TC02003.

Avigad, D., G. Baer, and A. Heimann (1998), Block rotations and continental extension in the central Aegean Sea: palaeomagnetic and structural evidence from Tinos and Mykonos (Cyclades, Greece), *Earth and Planetary Science Letters*, *157*(1–2), 23–40, doi:10.1016/S0012-821X(98)00024-7.

Avigad, D., A. Ziv, and Z. Garfunkel (2001), Ductile and brittle shortening, extension-parallel folds and maintenance of crustal thickness in the central Aegean (Cyclades, Greece), *Tectonics*, *20*(2), 277–287, doi:10.1029/2000TC001190.

Baldwin, S. L., and G. S. Lister (1998), Thermochronology of the South Cyclades Shear Zone, Ios, Greece: Effects of ductile shear in the argon partial retention zone, *Journal of Geophysical Research: Solid Earth*, *103*(B4), 7315–7336, doi:10.1029/97JB03106.

Baldwin, S. L., G. S. Lister, E. J. Hill, D. A. Foster, and I. McDougall (1993), Thermochronologic constraints on the tectonic evolution of active metamorphic core complexes, D'entrecasteaux Islands, Papua New Guinea, *Tectonics*, *12*(3), 611–628, doi:10.1029/93TC00235.

Bargnesi, E. A., D. F. Stockli, N. Mancktelow, and K. Soukis (2013), Miocene core complex development and coeval supradetachment basin evolution of Paros, Greece, insights from (U–Th)/He thermochronometry, *Tectonophysics*, *595–596*, 165–182, doi:10.1016/j.tecto.2012.07.015.

Beaudoin, A., R. Augier, V. Laurent, L. Jolivet, A. Lahfid, V. Bosse, L. Arbaret, A. Rabillard, and A. Menant (2015), The Ikaria high-temperature Metamorphic Core Complex (Cyclades, Greece): Geometry, kinematics and thermal structure, *Journal of Geodynamics*, *92*, 18–41, doi:10.1016/j.jog.2015.09.004.

Berger, A., D. A. Schneider, B. Grasemann, and D. Stockli (2013), Footwall mineralization during Late Miocene extension along the West Cycladic Detachment System, Lavrion, Greece, *Terra Nova*, *25*(3), 181–191, doi:10.1111/ter.12016.

Beyssac, O., B. Goffé, C. Chopin, and J. N. Rouzaud (2002), Raman spectra of carbonaceous material in metasediments: a new geothermometer, *Journal of Metamorphic Geology*, *20*(9), 859–871, doi:10.1046/j.1525-1314.2002.00408.x.

Blake, M. C., M. Bonneau, J. Geyssant, J. R. Kienast, C. Lepvrier, H. Maluski, and D. Papanikolaou (1981), A geologic reconnaissance of the Cycladic blueschist belt, Greece, *Geological Society of America Bulletin*, *92*(5), 247-254, doi:10.1130/0016-7606(1981)92<247:AGROTC>2.0.CO;2.

Bohnhoff, M., M. Rische, T. Meier, B. Endrun, D. Becker, H.-P. Harjes, and G. Stavrakakis (2004), CYC-NET: A Temporary Seismic Network on the Cyclades (Aegean Sea, Greece), *Seismological Research Letters*, *75*(3), 352–359, doi:10.1785/gssrl.75.3.352.

Bohnhoff, M., M. Rische, T. Meier, D. Becker, G. Stavrakakis, and H.-P. Harjes (2006), Microseismic activity in the Hellenic Volcanic Arc, Greece, with emphasis on the seismotectonic setting of the Santorini–Amorgos zone, *Tectonophysics*, *423*(1–4), 17–33, doi:10.1016/j.tecto.2006.03.024.

Bolhar, R., U. Ring, and C. M. Allen (2010), An integrated zircon geochronological and geochemical investigation into the Miocene plutonic evolution of the Cyclades, Aegean Sea, Greece: Part 1: Geochronology, *Contributions to Mineralogy and Petrology*, *160*(5), 719–742, doi:10.1007/s00410-010-0504-4.

Bolhar, R., U. Ring, A. I. S. Kemp, M. J. Whitehouse, S. D. Weaver, J. D. Woodhead, I. T. Uysal, and R. Turnbull (2012), An integrated zircon geochronological and geochemical investigation into the Miocene plutonic evolution of the Cyclades, Aegean Sea, Greece: Part 2: geochemistry, *Contributions to Mineralogy and Petrology*, *164*(6), 915–933, doi:10.1007/s00410-012-0759-z.

Bonini, M., D. Sokoutis, G. Mulugeta, M. Boccaletti, G. Corti, F. Innocenti, P. Manetti, and F. Mazzarini (2001), Dynamics of magma emplacement in centrifuge models of continental extension with

implications for flank volcanism, *Tectonics*, *20*(6), 1053–1065, doi:10.1029/2001TC900017.

Bonneau, M. (1984), Correlation of the Hellenide nappes in the south-east Aegean and their tectonic reconstruction, *Geological Society, London, Special Publications*, *17*(1), 517–527, doi:10.1144/GSL.SP.1984.017.01.38.

Boronkay, K., and T. Doutsos (1994), Transpression and transtension within different structural levels in the central Aegean region, *Journal of Structural Geology*, *16*(11), 1555–1573, doi:10.1016/0191-8141(94)90033-7.

Borradaile, G. J., and B. Henry (1997), Tectonic applications of magnetic susceptibility and its anisotropy, *Earth-Science Reviews*, *42*(1–2), 49–93, doi:10.1016/S0012-8252(96)00044-X.

Borradaile, G. J., and M. Jackson (2010), Structural geology, petrofabrics and magnetic fabrics (AMS, AARM, AIRM), *Journal of Structural Geology*, *32*(10), 1519–1551, doi:10.1016/j.jsg.2009.09.006.

Bouchez, J. L., C. Delas, G. Gleizes, A. Nédélec, and M. Cuney (1992), Submagmatic microfractures in granites, *Geology*, *20*(1), 35–38, doi:10.1130/0091-7613(1992)020<0035:SMIG>2.3.CO;2.

Bozkurt, E., and L. R. G. Park (1994), Southern Menderes Massif: an incipient metamorphic core complex in western Anatolia, Turkey, *Journal of the Geological Society*, *151*(2), 213–216, doi:10.1144/gsjgs.151.2.0213.

Brichau, S., U. Ring, R. A. Ketcham, A. Carter, D. Stockli, and M. Brunel (2006), Constraining the long-term evolution of the slip rate for a major extensional fault system in the central Aegean, Greece, using thermochronology, *Earth and Planetary Science Letters*, *241*(1–2), 293–306, doi:10.1016/j.epsl.2005.09.065.

Brichau, S., U. Ring, A. Carter, P. Monié, R. Bolhar, D. Stockli, and M. Brunel (2007), Extensional faulting on Tinos Island, Aegean Sea, Greece: How many detachments?, *Tectonics*, *26*(4), 1–19, doi:10.1029/2006TC001969.

Brichau, S., U. Ring, A. Carter, R. Bolhar, P. Monie, D. Stockli, and M. Brunel (2008), Timing, slip rate, displacement and cooling history of the Mykonos detachment footwall, Cyclades, Greece, and implications for the opening of the Aegean Sea basin, *Journal of the Geological Society*, *165*(1), 263–277, doi:10.1144/0016-76492006-145.

Brichau, S., S. Thomson, and U. Ring (2010), Thermochronometric constraints on the tectonic evolution of the Serifos detachment, Aegean Sea, Greece, *International Journal of Earth Sciences*, *99*(2), 379–393, doi:10.1007/s00531-008-0386-0.

Bröcker, M. (1990), Blueschist-to-greenschist transition in metabasites from Tinos Island, Cyclades, Greece: Compositional control or fluid infiltration?, *Lithos*, *25*(1–3), 25–39, doi:10.1016/0024-4937(90)90004-K.

Bröcker, M., and L. Franz (1994), The contact aureole on Tinos (Cyclades, Greece). Part I: field relationships, petrography and P-T conditions, *Chemie Der Erde-Geochemistry*, *54*(4), 262–280.

Bröcker, M., and L. Franz (1998), Rb–Sr isotope studies on Tinos Island (Cyclades, Greece): additional time constraints for metamorphism, extent of infiltration-controlled overprinting and deformational activity, *Geological Magazine*, *135*(3), 369–382, doi:10.1017/S0016756898008681.

Bröcker, M., and L. Franz (2000), The contact aureole on Tinos (Cyclades, Greece): tourmaline-biotite geothermometry and Rb-Sr geochronology, *Mineralogy and Petrology*, *70*(3–4), 257–283, doi:10.1007/s007100070006.

Bröcker, M., H. Kreuzer, A. Matthews, and M. Okrusch (1993), $^{40}Ar/^{39}Ar$ and oxygen isotope studies of polymetamorphism from Tinos Island, Cycladic blueschist belt, Greece, *Journal of Metamorphic Geology*, *11*(2), 223–240, doi:10.1111/j.1525-1314.1993.tb00144.x.

Bröcker, M., D. Bieling, B. Hacker, and P. Gans (2004), High-Si phengite records the time of greenschist facies overprinting: implications for models suggesting mega-detachments in the Aegean Sea, *Journal of Metamorphic Geology*, *22*(5), 427–442, doi:10.1111/j.1525-1314.2004.00524.x.

Brown, M., and R. D. Dallmeyer (1996), Rapid Variscan exhumation and the role of magma in core complex formation: southern Brittany metamorphic belt, France, *Journal of Metamorphic Geology*, *14*(3), 361–379, doi:10.1111/j.1525-1314.1996.00361.x.

Brun, J.-P., and C. Faccenna (2008), Exhumation of high-pressure rocks driven by slab rollback, *Earth and Planetary Science Letters*, *272*(1–2), 1–7, doi:10.1016/j.epsl.2008.02.038.

Brun, J.-P., D. Sokoutis, and J. Van Den Driessche (1994), Analogue modeling of detachment fault systems and core complexes, *Geology*, *22*(4), 319–322, doi:10.1130/0091-7613(1994)022<0319:AMODFS>2.3.CO;2.

Buick, I. S. (1991), The late Alpine evolution of an extensional shear zone, Naxos, Greece, *Journal of the Geological Society*, *148*(1), 93–103, doi:10.1144/gsjgs.148.1.0093.

Buick, I. S., and T. J. B. Holland (1989), The P-T-t path associated with crustal extension, Naxos, Cyclades, Greece, *Geological Society, London, Special Publications*, *43*(1), 365–369, doi:10.1144/GSL.SP.1989.043.01.32.

Burg, J.-P. (2012), Rhodope: From Mesozoic convergence to Cenozoic extension. Review of petro-structural data in the geochronological frame, *Journal of the Virtual Explorer*, *42*(1), doi:10.3809/jvirtex.2011.00270.

Campbell-Stone, E., B. E. John, D. A. Foster, J. W. Geissman, and R. F. Livaccari (2000), Mechanisms for accommodation of Miocene extension: Low-angle normal faulting, magmatism, and secondary breakaway faulting in the southern Sacramento Mountains, southeastern California, *Tectonics*, *19*(3), 566–587, doi:10.1029/1999TC001133.

Cao, S., F. Neubauer, M. Bernroider, and J. Liu (2013), The lateral boundary of a metamorphic core complex: The Moutsounas shear zone on Naxos, Cyclades, Greece, *Journal of Structural Geology*, *54*, 103–128, doi:10.1016/j.jsg.2013.07.002.

Cao, S., F. Neubauer, M. Bernroider, J. Genser, J. Liu, and G. Friedl (2017), Low-grade retrogression of a high-temperature metamorphic core complex: Naxos, Cyclades, Greece, *Geological Society of America Bulletin*, *129*(1–2), 93–117, doi:10.1130/B31502.1.

Carr, S. D. (1992), Tectonic setting and U-Pb geochronology of the Early Tertiary Ladybird Leucogranite Suite, Thor-Odin - Pinnacles Area, Southern Omineca Belt, British Columbia, *Tectonics*, *11*(2), 258–278, doi:10.1029/91TC01644.

Charles, N., C. Gumiaux, R. Augier, Y. Chen, R. Zhu, and W. Lin (2011), Metamorphic Core Complexes vs. synkinematic plutons in continental extension setting: Insights from key structures (Shandong Province, eastern China), *Journal of Asian Earth Sciences*, *40*(1), 261–278, doi:10.1016/j.jseaes.2010.07.006.

Charles, N., R. Augier, C. Gumiaux, P. Monié, Y. Chen, M. Faure, and R. Zhu (2013), Timing, duration and role of magmatism in wide rift systems: Insights from the Jiaodong Peninsula (China, East Asia), *Gondwana Research*, *24*(1), 412–428, doi:10.1016/j.gr.2012.10.011.

Coney, P. J., and T. A. Harms (1984), Cordilleran metamorphic core complexes: Cenozoic extensional relics of Mesozoic compression, *Geology*, *12*(9), 550-554, doi:10.1130/0091-7613(1984)12<550:CMCCCE>2.0.CO;2.

Cossette, é., D. A. Schneider, C. J. Warren, and B. Grasemann (2015), Lithological, rheological, and fluid infiltration control on $^{40}Ar/^{39}Ar$ ages in polydeformed rocks from the West Cycladic detachment system, Greece, *Lithosphere*, *7*(2), 189–205, doi:10.1130/L416.1.

Crittenden, M. D., P. J. Coney, and G. H. Davis (Eds.) (1980), *Cordilleran*

metamorphic core complexes, Memoir - The Geological Society of America, 153, Geological Society of America, Boulder, Colorado.

Dabrowski, M., and B. Grasemann (2014), Domino boudinage under layer-parallel simple shear, *Journal of Structural Geology*, *68*, 58–65, doi:10.1016/j.jsg.2014.09.006.

Dallmeyer, R. D., A. W. Snoke, and E. H. McKee (1986), The Mesozoic-Cenozoic tectonothermal evolution of the Ruby Mountains, East Humboldt Range, Nevada: A Cordilleran Metamorphic Core Complex, *Tectonics*, *5*(6), 931–954, doi:10.1029/TC005i006p00931.

Daniel, J.-M., and L. Jolivet (1995), Detachment faults and pluton emplacement; Elba Island (Tyrrhenian Sea), *Bulletin de la Societe Geologique de France*, *166*(4), 341–354.

Davis, G. A., T. K. Fowler, K. M. Bishop, T. C. Brudos, S. J. Friedmann, D. W. Burbank, M. A. Parke, and B. C. Burchfiel (1993), Pluton pinning of an active Miocene detachment fault system, eastern Mojave Desert, California, *Geology*, *21*(7), 627-630, doi:10.1130/0091-7613(1993)021<0627:PPOAAM>2.3.CO;2.

Davis, G. A., X. Qian, Y. Zheng, H. Yu, C. Wang, T. H. Mao, G. Gehrels, M. Shafiquallah, and J. E. Fryxell (1996), Mesozoic deformation and plutonism in the Yunmeng Shan: a Chinese metamorphic core complex north of Beijing, China, in *The tectonic evolution of Asia*, pp. 253–280, Cambridge Univ. Press, Cambridge.

Davis, G. H., and P. J. Coney (1979), Geologic development of the Cordilleran metamorphic core complexes, *Geology*, *7*(3), 120–124, doi:10.1130/0091-7613(1979)7<120:GDOTCM>2.0.CO;2.

Denèle, Y., E. Lecomte, L. Jolivet, O. Lacombe, L. Labrousse, B. Huet, and L. Le Pourhiet (2011), Granite intrusion in a metamorphic core complex: The example of the Mykonos laccolith (Cyclades, Greece), *Tectonophysics*, *501*(1–4), 52–70, doi:10.1016/j.tecto.2011.01.013.

Dimitriadis, I., E. Karagianni, D. Panagiotopoulos, C. Papazachos, P. Hatzidimitriou, M. Bohnhoff, M. Rische, and T. Meier (2009), Seismicity and active tectonics at Coloumbo Reef (Aegean Sea, Greece): Monitoring an active volcano at Santorini Volcanic Center using a temporary seismic network, *Tectonophysics*, *465*(1–4), 136–149, doi:10.1016/j.tecto.2008.11.005.

Dimitriadis, I., C. Papazachos, D. Panagiotopoulos, P. Hatzidimitriou, M. Bohnhoff, M. Rische, and T. Meier (2010), P and S velocity structures of the Santorini–Coloumbo volcanic system (Aegean Sea, Greece) obtained by non-linear inversion of travel times and its tectonic implications, *Journal of Volcanology and Geothermal Research*, *195*(1), 13–30, doi:10.1016/j.jvolgeores.2010.05.013.

Dinter, D. A., and L. Royden (1993), Late Cenozoic extension in northeastern Greece: Strymon Valley detachment system and Rhodope metamorphic core complex, *Geology*, *21*(1), 45–48, doi:10.1130/0091-7613(1993)021<0045:LCEING>2.3.CO;2.

Dürr, S., R. Altherr, J. Keller, M. Okrusch, and E. Seidel (1978), The median Aegean crystalline belt: stratigraphy, structure, metamorphism, magmatism, *Alps, Apennines, Hellenides*, *38*, 455–476.

Ersoy, E. Y., and M. R. Palmer (2013), Eocene-Quaternary magmatic activity in the Aegean: Implications for mantle metasomatism and magma genesis in an evolving orogeny, *Lithos*, *180*, 5–24, doi:10.1016/j.lithos.2013.06.007.

Famin, V. (2003), Incursion de fluides dans une zone de cisaillement ductile (Tinos, Cyclades, Grèce) : mécanismes d'infiltration et implications tectoniques, Ph.D thesis, Univ. of Pierre et Marie Curie (UPMC), Paris, France.

Faure, M., M. Bonneau, and J. Pons (1991), Ductile deformation and syntectonic granite emplacement during the late Miocene extension of the Aegea (Greece), *Bulletin de la Societe Geologique de France*, *162*, 3–11.

Faure, M., Y. Sun, L. Shu, P. Monié, and J. Charvet (1996), Extensional tectonics within

a subduction-type orogen. The case study of the Wugongshan dome (Jiangxi Province, southeastern China), *Tectonophysics*, *263*(1–4), 77–106, doi:10.1016/S0040-1951(97)81487-4.

Fletcher, J. M., J. M. Bartley, M. W. Martin, A. F. Glazner, and J. D. Walker (1995), Large-magnitude continental extension: An example from the central Mojave metamorphic core complex, *Geological Society of America Bulletin*, *107*(12), 1468–1483, doi:10.1130/0016-7606(1995)107<1468:LMCEAE>2.3.CO;2.

Forster, M., and G. Lister (2009), Core-complex-related extension of the Aegean lithosphere initiated at the Eocene-Oligocene transition, *Journal of Geophysical Research*, *114*(B2), 1–36, doi:10.1029/2007JB005382.

Gans, P. B. (1987), An open-system, two-layer crustal stretching model for the Eastern Great Basin, *Tectonics*, *6*(1), 1–12, doi:10.1029/TC006i001p00001.

Gautier, P., and J.-P. Brun (1994a), Crustal-scale geometry and kinematics of late-orogenic extension in the central Aegean (Cyclades and Ewia Island), *Tectonophysics*, *238*(1–4), 399–424, doi:10.1016/0040-1951(94)90066-3.

Gautier, P., and J.-P. Brun (1994b), Ductile crust exhumation and extensional detachments in the central Aegean (Cyclades and Evvia islands), *Geodinamica Acta*, *7*(2), 57–85.

Gautier, P., J.-P. Brun, and L. Jolivet (1993), Structure and kinematics of Upper Cenozoic extensional detachment on Naxos and Paros (Cyclades Islands, Greece), *Tectonics*, *12*(5), 1180–1194, doi:10.1029/93TC01131.

Goldsworthy, M., J. Jackson, and J. Haines (2002), The continuity of active fault systems in Greece: Fault continuity in Greece, *Geophysical Journal International*, *148*(3), 596–618, doi:10.1046/j.1365-246X.2002.01609.x.

Grasemann, B., and K. Petrakakis (2007), Evolution of the Serifos metamorphic core complex, *Journal of the Virtual Explorer*, *27*, 1–18.

Grasemann, B., and C. Tschegg (2012), Localization of deformation triggered by chemo-mechanical feedback processes, *Geological Society of America Bulletin*, *124*(5–6), 737–745, doi:10.1130/B30504.1.

Grasemann, B., D. A. Schneider, D. F. Stockli, and C. Iglseder (2012), Miocene bivergent crustal extension in the Aegean: Evidence from the western Cyclades (Greece), *Lithosphere*, *4*(1), 23–39, doi:10.1130/L164.1.

Groppo, C., M. Forster, G. Lister, and R. Compagnoni (2009), Glaucophane schists and associated rocks from Sifnos (Cyclades, Greece): New constraints on the P–T evolution from oxidized systems, *Lithos*, *109*(3–4), 254–273, doi:10.1016/j.lithos.2008.10.005.

Habert, G. (2004), Etude des relations entre la structure des granites et le contexte tectonique : exemple des contextes transpressifs, extensifs, et sans tectonique, Ph.D thesis, Univ. Toulouse III - Paul Sabatier, Toulouse, France.

Hatzfeld, D., V. Karakostas, M. Ziazia, I. Kassaras, E. Papadimitriou, K. Makropoulos, N. Voulgaris, and C. Papaioannou (2000), Microseismicity and faulting geometry in the Gulf of Corinth (Greece), *Geophysical Journal International*, *141*(2), 438–456, doi:10.1046/j.1365-246x.2000.00092.x.

Hejl, E., H. Riedl, and H. Weingartner (2002), Post-plutonic unroofing and morphogenesis of the Attic–Cycladic complex (Aegea, Greece), *Tectonophysics*, *349*(1–4), 37–56, doi:10.1016/S0040-1951(02)00045-8.

Henjes-Kunst, F., and H. Kreuzer (1982), Isotopic dating of pre-Alpidic rocks from the island of Ios (Cyclades, Greece), *Contributions to Mineralogy and Petrology*, *80*(3), 245–253, doi:10.1007/BF00371354.

Hetzel, R., U. Ring, C. Akal, and M. Troesch (1995), Miocene NNE-directed extensional unroofing in the Menderes Massif, southwestern Turkey, *Journal of the*

Geological Society, *152*(4), 639–654, doi:10.1144/gsjgs.152.4.0639.

Hezel, D. C., A. Kalt, H. R. Marschall, T. Ludwig, and H.-P. Meyer (2011), Major-element and Li, Be compositional evolution of tourmaline in an S-type granite-pegmatite system and its country rocks: an example from Ikaria, Aegean Sea, Greece, *The Canadian Mineralogist*, *49*(1), 321–340, doi:10.3749/canmin.49.1.321.

Hill, E. J., S. L. Baldwin, and G. S. Lister (1995), Magmatism as an essential driving force for formation of active metamorphic core complexes in eastern Papua New Guinea, *Journal of Geophysical Research: Solid Earth*, *100*(B6), 10441–10451, doi:10.1029/94JB03329.

van Hinsbergen, D. J. J., E. Hafkenscheid, W. Spakman, J. E. Meulenkamp, and R. Wortel (2005), Nappe stacking resulting from subduction of oceanic and continental lithosphere below Greece, *Geology*, *33*(4), 325–328, doi:10.1130/G20878.1.

Huet, B., L. Labrousse, and L. Jolivet (2009), Thrust or detachment? Exhumation processes in the Aegean: Insight from a field study on Ios (Cyclades, Greece), *Tectonics*, *28*(3), 1–27, doi:10.1029/2008TC002397.

Huet, B., L. Labrousse, P. Monié, B. Malvoisin, and L. Jolivet (2015), Coupled phengite $^{40}Ar/^{39}Ar$ geochronology and thermobarometry: P-T-t evolution of Andros Island (Cyclades, Greece), *Geological Magazine*, *152*(04), 711–727, doi:10.1017/S0016756814000661.

Hyndman, D. W. (1980), Bitterroot dome-Sapphire tectonic block, an example of a plutonic-core gneiss-dome complex with its detached suprastructure, in *Geological Society of America Memoirs*, vol. 153, pp. 427–444, Geological Society of America.

Iglseder, C., B. Grasemann, D. A. Schneider, K. Petrakakis, C. Miller, U. S. Klötzli, M. Thöni, A. Zámolyi, and C. Rambousek (2009), I and S-type plutonism on Serifos (W-Cyclades, Greece), *Tectonophysics*, *473*(1–2), 69–83, doi:10.1016/j.tecto.2008.09.021.

Iglseder, C., B. Grasemann, A. H. N. Rice, K. Petrakakis, and D. A. Schneider (2011), Miocene south directed low-angle normal fault evolution on Kea Island (West Cycladic Detachment System, Greece), *Tectonics*, *30*(4), 1–31, doi:10.1029/2010TC002802.

Jackson, J. (1994), Active Tectonics of the Aegean Region, *Annual Review of Earth and Planetary Sciences*, *22*(1), 239–271, doi:10.1146/annurev.earth.22.1.239.

Jacobshagen, V., S. Dürr, F. Kockel, K. O. Kopp, G. Kowalczyk, H. Berckhemer, and D. Büttner (1978), Structure and geodynamic evolution of the Aegean region, *Alps, Apennines, Hellenides*, 537–564.

Jansen, J. B. H. (1973), Geological map of Greece, Island of Naxos (1: 50 000), Nation. Inst. Geol. Mining Res., Athens.

Jansen, J. B. H. (1977), Metamorphism on Naxos, Greece, Ph.D thesis, Univ. of Utrecht, Utrecht, Netherlands.

John, B. E., and K. A. Howard (1995), Rapid extension recorded by cooling-age patterns and brittle deformation, Naxos, Greece, *Journal of Geophysical Research: Solid Earth*, *100*(B6), 9969–9979, doi:10.1029/95JB00665.

Jolivet, L. (2001), A comparison of geodetic and finite strain pattern in the Aegean, geodynamic implications, *Earth and Planetary Science Letters*, *187*(1–2), 95–104, doi:10.1016/S0012-821X(01)00277-1.

Jolivet, L. (2003), Subduction tectonics and exhumation of high-pressure metamorphic rocks in the Mediterranean orogens, *American Journal of Science*, *303*(5), 353–409, doi:10.2475/ajs.303.5.353.

Jolivet, L., and J.-P. Brun (2010), Cenozoic geodynamic evolution of the Aegean, *International Journal of Earth Sciences*, *99*(1), 109–138, doi:10.1007/s00531-008-0366-4.

Jolivet, L., and C. Faccenna (2000), Mediterranean extension and the Africa-Eurasia collision, *Tectonics*, *19*(6), 1095–

1106, doi:10.1029/2000TC900018.

Jolivet, L., and M. Patriat (1999), Ductile extension and the formation of the Aegean Sea, *Geological Society, London, Special Publications*, *156*(1), 427–456, doi:10.1144/GSL.SP.1999.156.01.20.

Jolivet, L., J. M. Daniel, C. Truffert, and B. Goffé (1994), Exhumation of deep crustal metamorphic rocks and crustal extension in arc and back-arc regions, *Lithos*, *33*(1–3), 3–30, doi:10.1016/0024-4937(94)90051-5.

Jolivet, L. et al. (1998), Midcrustal shear zones in postorogenic extension: Example from the northern Tyrrhenian Sea, *Journal of Geophysical Research: Solid Earth*, *103*(B6), 12123–12160, doi:10.1029/97JB03616.

Jolivet, L., G. Rimmelé, R. Oberhänsli, B. Goffé, and O. Candan (2004a), Correlation of syn-orogenic tectonic and metamorphic events in the Cyclades, the Lycian nappes and the Menderes massif. Geodynamic implications, *Bulletin de la Societe Geologique de France*, *175*(3), 217–238, doi:10.2113/175.3.217.

Jolivet, L., V. Famin, C. Mehl, T. Parra, C. Aubourg, R. Hébert, and P. Philippot (2004b), Strain localization during crustal-scale boudinage to form extensional metamorphic domes in the Aegean Sea, in *Gneiss Domes in Orogeny*, vol. 380, pp. 185–210, Geological Society of America, Boulder, Colorado.

Jolivet, L., C. Faccenna, and C. Piromallo (2009), From mantle to crust: Stretching the Mediterranean, *Earth and Planetary Science Letters*, *285*(1–2), 198–209, doi:10.1016/j.epsl.2009.06.017.

Jolivet, L., E. Lecomte, B. Huet, Y. Denèle, O. Lacombe, L. Labrousse, L. Le Pourhiet, and C. Mehl (2010), The North Cycladic Detachment System, *Earth and Planetary Science Letters*, *289*(1–2), 87–104, doi:10.1016/j.epsl.2009.10.032.

Jolivet, L. et al. (2013), Aegean tectonics: Strain localisation, slab tearing and trench retreat, *Tectonophysics*, *597–598*, 1–33, doi:10.1016/j.tecto.2012.06.011.

Jolivet, L. et al. (2015), The geological signature of a slab tear below the Aegean, *Tectonophysics*, *659*, 166–182, doi:10.1016/j.tecto.2015.08.004.

Katzir, Y., A. L. A. N. Matthews, Z. Garfunkel, M. Schliestedt, and D. Avigad (1996), The tectono-metamorphic evolution of a dismembered ophiolite (Tinos, Cyclades, Greece), *Geological Magazine*, *133*(3), 237–254.

Keay, S. (1998), The geological evolution of the Cyclades, Greece, constraints from SHRIMP U/Pb geochronology, Ph.D thesis, Research School of Earth Sciences, Australian National University, Cambera, Australia.

Keay, S., and G. Lister (2002), African provenance for the metasediments and metaigneous rocks of the Cyclades, Aegean Sea, Greece, *Geology*, *30*(3), 235-238, doi:10.1130/0091-7613(2002)030<0235:APFTMA>2.0.CO;2.

Keay, S., G. Lister, and I. Buick (2001), The timing of partial melting, Barrovian metamorphism and granite intrusion in the Naxos metamorphic core complex, Cyclades, Aegean Sea, Greece, *Tectonophysics*, *342*(3–4), 275–312, doi:10.1016/S0040-1951(01)00168-8.

Keiter, M., K. Piepjohn, C. Ballhaus, M. Lagos, and M. Bode (2004), Structural development of high-pressure metamorphic rocks on Syros island (Cyclades, Greece), *Journal of Structural Geology*, *26*(8), 1433–1445, doi:10.1016/j.jsg.2003.11.027.

Kokkalas, S., and A. Aydin (2013), Is there a link between faulting and magmatism in the south-central Aegean Sea?, *Geological Magazine*, *150*(02), 193–224, doi:10.1017/S0016756812000453.

Koukouvelas, I. K., and S. Kokkalas (2003), Emplacement of the Miocene west Naxos pluton (Aegean Sea, Greece): a structural study, *Geological Magazine*, *140*(1), 45–61, doi:10.1017/S0016756802007094.

Krohe, A., E. Mposkos, A. Diamantopoulos, and G. Kaouras (2010), Formation of basins and mountain ranges in Attica (Greece): The role of Miocene to Recent low-angle normal detachment faults, *Earth-Science Reviews*, *98*(1–2), 81–104, doi:10.1016/j.earscirev. 2009.10.005.

Kruckenberg, S. C. (2009), The dynamics of migmatite domes in extending orogens, Ph.D thesis, University of Minnesota, Minneapolis, U.S.A.

Kruckenberg, S. C., O. Vanderhaeghe, E. C. Ferré, C. Teyssier, and D. L. Whitney (2011), Flow of partially molten crust and the internal dynamics of a migmatite dome, Naxos, Greece: internal dynamics of the naxos dome, *Tectonics*, *30*(3), 1–24, doi:10.1029/2010TC002751.

Kuhlemann, J., W. Frisch, I. Dunkl, M. Kázmér, and G. Schmiedl (2004), Miocene siliciclastic deposits of Naxos Island: Geodynamic and environmental implications for the evolution of the southern Aegean Sea (Greece), in *Special Paper 378: Detrital thermochronology - Provenance analysis, exhumation, and landscape evolution of mountain belts*, vol. 378, pp. 51–65, Geological Society of America.

Kumerics, C., U. Ring, S. Brichau, J. Glodny, and P. Monie (2005), The extensional Messaria shear zone and associated brittle detachment faults, Aegean Sea, Greece, *Journal of the Geological Society*, *162*(4), 701–721, doi:10.1144/0016-764904-041.

Lacombe, O., L. Jolivet, L. Le Pourhiet, E. Lecomte, and C. Mehl (2013), Initiation, geometry and mechanics of brittle faulting in exhuming metamorphic rocks: insights from the northern Cycladic islands (Aegean, Greece), *Bulletin de la Societe Geologique de France*, *184*(4–5), 383–403, doi:10.2113/ gs sgfbull.184.4-5.383.

Laurent, V., A. Beaudoin, L. Jolivet, L. Arbaret, R. Augier, A. Rabillard, and A. Menant (2015), Interrelations between extensional shear zones and synkinematic intrusions: The example of Ikaria Island (NE Cyclades, Greece), *Tectonophysics*, *651–652*, 152–171, doi:10.1016/j.tecto.2015 .03.020.

Laurent, V., L. Jolivet, V. Roche, R. Augier, S. Scaillet, and G. L. Cardello (2016), Strain localization in a fossilized subduction channel: Insights from the Cycladic Blueschist Unit (Syros, Greece), *Tectonophysics*, *672–673*, 150–169, doi:10.1016/j.tecto.2016.01.036.

Laurent, V., B. Huet, L. Labrousse, L. Jolivet, P. Monié, and R. Augier (2017), Extraneous argon in high-pressure metamorphic rocks: Distribution, origin and transport in the Cycladic Blueschist Unit (Greece), *Lithos*, *272–273*, 315–335, doi:10.1016/j.lithos .2016.12.013.

Le Pichon, X., and J. Angelier (1981), The Aegean Sea, *Philosophical Transactions of the Royal Society A: Mathematical, Physical and Engineering Sciences*, *300*(1454), 357–372.

Lecomte, E., L. Jolivet, O. Lacombe, Y. Den?le, L. Labrousse, and L. Le Pourhiet (2010), Geometry and kinematics of Mykonos detachment, Cyclades, Greece: Evidence for slip at shallow dip, *Tectonics*, *29*(5), 1–22, doi:10.1029/2009TC002564.

Lee Armstrong, R., and P. Ward (1991), Evolving geographic patterns of Cenozoic magmatism in the North American Cordillera: The temporal and spatial association of magmatism and metamorphic core complexes, *Journal of Geophysical Research: Solid Earth*, *96*(B8), 13201–13224, doi:10.1029/91JB00412.

Lee, J., and G. S. Lister (1992), Late Miocene ductile extension and detachment faulting, Mykonos, Greece, *Geology*, *20*(2), 121–124, doi:10.1130/0091-7613(1992)020<0121:L MDEAD>2.3.CO;2.

Lin, W., and Q. Wang (2006), Late Mesozoic extensional tectonics in the North China block: a crustal response to subcontinental mantle removal?, *Bulletin de la Societe Geologique de France*, *177*(6), 287–297, doi:10.2113/gssgfbull.177.6.287.

Lin, W., M. Faure, P. Monié, U. Schärer, and D. Panis (2008), Mesozoic Extensional

Tectonics in Eastern Asia: The South Liaodong Peninsula Metamorphic Core Complex (NE China), *The Journal of Geology*, *116*(2), 134–154, doi:10.1086/527456.

Lister, G. S., and S. L. Baldwin (1993), Plutonism and the origin of metamorphic core complexes, *Geology*, *21*(7), 607–610, doi:10.1130/0091-7613(1993)021<0607:PATOOM>2.3.CO;2.

Lister, G. S., and G. A. Davis (1989), The origin of metamorphic core complexes and detachment faults formed during Tertiary continental extension in the northern Colorado River region, U.S.A., *Journal of Structural Geology*, *11*(1–2), 65–94, doi:10.1016/0191-8141(89)90036-9.

Lister, G. S., G. Banga, and A. Feenstra (1984), Metamorphic core complexes of Cordilleran type in the Cyclades, Aegean Sea, Greece, *Geology*, *12*(4), 221–225, doi:10.1130/0091-7613(1984)12<221:MCCOCT>2.0.CO;2.

Lucas, I. (1999), Le pluton de Mykonos-Delos-Rhenee (Cyclades, Grèce): un exemple de mise en place synchrone de l'extension crustale, Ph.D thesis, Université d'Orléans, Orléans, France.

Lynch, H. D., and P. Morgan (1987), The tensile strength of the lithosphere and the localization of extension, *Geological Society, London, Special Publications*, *28*(1), 53–65, doi:10.1144/GSL.SP.1987.028.01.05.

MacCready, T., A. W. Snoke, J. E. Wright, and K. A. Howard (1997), Mid-crustal flow during Tertiary extension in the Ruby Mountains core complex, Nevada, *Geological Society of America Bulletin*, *109*(12), 1576–1594, doi:10.1130/0016-7606(1997)109<1576:MCFDTE>2.3.CO;2.

Maluski, H., M. Bonneau, and J. R. Kienast (1987), Dating the metamorphic events in the Cycladic area; $^{39}Ar/^{40}Ar$ data from metamorphic rocks of the Island of Syros (Greece), *Bull. Soc. Geol. France*, *3*(5), 833–842.

Martha, S. O., W. Dörr, A. Gerdes, R. Petschick, J. Schastok, P. Xypolias, and G. Zulauf (2016), New structural and U–Pb zircon data from Anafi crystalline basement (Cyclades, Greece): constraints on the evolution of a Late Cretaceous magmatic arc in the Internal Hellenides, *International Journal of Earth Sciences*, *105*(7), 2031–2060, doi:10.1007/s00531-016-1346-8.

Martin, L. (2004), Signification des âges U–Pb sur zircon dans l'histoire métamorphique de Naxos et Ikaria (Cyclades, Grèce), Ph.D thesis, Univ. Henri Poincaré, Nancy, France.

Martin, L., S. Duchêne, E. Deloule, and O. Vanderhaeghe (2006), The isotopic composition of zircon and garnet: A record of the metamorphic history of Naxos, Greece, *Lithos*, *87*(3–4), 174–192, doi:10.1016/j.lithos.2005.06.016.

Mehl, C., L. Jolivet, and O. Lacombe (2005), From ductile to brittle: Evolution and localization of deformation below a crustal detachment (Tinos, Cyclades, Greece), *Tectonics*, *24*(4), 1–23, doi:10.1029/2004TC001767.

Melidonis, N., and M. Triantaphyllis (2003), Geological map of Greece, Tinos-Yaros Islands (1: 50 000), Institute of Geology and Mineral Exploration (IGME), Athens.

Menant, A., L. Jolivet, R. Augier, and N. Skarpelis (2013), The North Cycladic Detachment System and associated mineralization, Mykonos, Greece: Insights on the evolution of the Aegean domain, *Tectonics*, *32*(3), 433–452, doi:10.1002/tect.20037.

Menant, A., P. Sternai, L. Jolivet, L. Guillou-Frottier, and T. Gerya (2016a), 3D numerical modeling of mantle flow, crustal dynamics and magma genesis associated with slab roll-back and tearing: The eastern Mediterranean case, *Earth and Planetary Science Letters*, *442*, 93–107, doi:10.1016/j.epsl.2016.03.002.

Menant, A., L. Jolivet, and B. Vrielynck (2016b), Kinematic reconstructions and magmatic evolution illuminating crustal and mantle dynamics of the eastern Mediterranean region since the late

Cretaceous, *Tectonophysics*, *675*, 103–140, doi:10.1016/j.tecto.2016.03.007.

Papanikolaou, D. (2009), Timing of tectonic emplacement of the ophiolites and terrane paleogeography in the Hellenides, *Lithos*, *108*(1–4), 262–280, doi:10.1016/j.lithos.2008.08.003.

Parra, T., O. Vidal, and L. Jolivet (2002), Relation between the intensity of deformation and retrogression in blueschist metapelites of Tinos Island (Greece) evidenced by chlorite–mica local equilibria, *Lithos*, *63*(1–2), 41–66, doi:10.1016/S0024-4937(02)00115-9.

Parsons, T., and G. A. Thompson (1993), Does magmatism influence low-angle normal faulting?, *Geology*, *21*(3), 247–250, doi:10.1130/0091-7613(1993)021<0247:DMILAN>2.3.CO;2.

Paterson, S. R., R. H. Vernon, and O. T. Tobisch (1989), A review of criteria for the identification of magmatic and tectonic foliations in granitoids, *Journal of Structural Geology*, *11*(3), 349–363, doi:10.1016/0191-8141(89)90074-6.

Paterson, S. R., T. K. Fowler, K. L. Schmidt, A. S. Yoshinobu, E. S. Yuan, and R. B. Miller (1998), Interpreting magmatic fabric patterns in plutons, *Lithos*, *44*(1–2), 53–82, doi:10.1016/S0024-4937(98)00022-X.

Patriat, M., and L. Jolivet (1998), Post-orogenic extension and shallow-dipping shear zones, study of a brecciated decollement horizon in Tinos (Cyclades, Greece), *Comptes Rendus de l'Académie des Sciences - Series IIA - Earth and Planetary Science*, *326*(5), 355–362, doi:10.1016/S1251-8050(98)80306-6.

Patzak, M., M. Okrusch, and H. Kreuzer (1994), The Akrotiri Unit on the island of Tinos, Cyclades, Greece: Witness to a lost terrane of Late Cretaceous age, *Neues Jahrbuch fur Geologie und Palaontologie-Abhandlungen*, *194*, 211–252.

Pavlis, T. L. (1996), Fabric development in syn-tectonic intrusive sheets as a consequence of melt-dominated flow and thermal softening of the crust, *Tectonophysics*, *253*(1–2), 1–31.

Peillod, A., U. Ring, J. Glodny, and A. Skelton (2017), An Eocene/oligocene blueschist-/greenschist-facies *P-T* loop from the Cycladic blueschist unit on Naxos Island, Greece: Deformation-related reequilibration vs thermal relaxation, *Journal of Metamorphic Geology*, doi:10.1111/jmg.12256.

Pe-Piper, G. (2000), Origin of S-type granites coeval with I-type granites in the Hellenic subduction system, Miocene of Naxos, Greece, *European Journal of Mineralogy*, *12*(4), 859–875, doi:10.1127/ejm/12/4/0859.

Pe-Piper, G., and D. J. W. Piper (2006), Unique features of the Cenozoic igneous rocks of Greece, in *Special Paper 409: Post-collisional Tectonics and Magmatism in the Mediterranean Region and Asia*, vol. 409, 259–282, Geological Society of America.

Pe-Piper, G., C. N. Kotopouli, and D. J. W. Piper (1997), Granitoid rocks of Naxos, Greece: regional geology and petrology, *Geological Journal*, *32*(2), 153–171, doi:10.1002/(SICI)1099-1034(199706)32:2<153::AID-GJ737>3.0.CO;2-1.

Pe-Piper, G., D. J. . Piper, and D. Matarangas (2002), Regional implications of geochemistry and style of emplacement of Miocene I-type diorite and granite, Delos, Cyclades, Greece, *Lithos*, *60*(1–2), 47–66, doi:10.1016/S0024-4937(01)00068-8.

Petrakakis, K., C. Iglseder, A. Zámolyi, C. Rambousek, B. Grasemann, E. Draganitis, A. Kurka, and A. Photiades (2010), Geological Map of Greece, Serifos Island, Institute of Geology and Mineral Exploration (IGME), Athens.

Photiades, A. (2005), Geological map of Greece, Ikaria Island sheet (1: 50 000), Institute of Geology and Mineral Exploration (IGME), Athens.

Platt, J. P., W. M. Behr, and F. J. Cooper (2015), Metamorphic core complexes: windows into the mechanics and rheology of the crust, *Journal of the Geological Society*,

172(1), 9–27, doi:10.1144/jgs2014-036.

Rabillard, A., L. Arbaret, L. Jolivet, N. Le Breton, C. Gumiaux, R. Augier, and B. Grasemann (2015), Interactions between plutonism and detachments during metamorphic core complex formation, Serifos Island (Cyclades, Greece), *Tectonics*, *34*(6), 1080–1106, doi:10.1002/2014TC003650.

Reinecke, T., R. Altherr, B. Hartung, K. Hatzipanagiotou, H. Kreuzer, W. Harre, H. Klein, J. Keller, E. Geenen, and H. Boger (1982), Remnants of a Late Cretaceous high temperature belt on the island of Anafi (Cyclades, Greece), *Neues Jahrb. Mineral. Abh*, *145*, 157–182.

Rice, A. H. N. et al. (2012), A new geological map of the crustal-scale detachment on Kea (Western Cyclades, Greece), *Australian Journal of Earth Sciences*, *105*(3), 108–124.

Ring, U. (2007), The geology of Ikaria Island: The Messaria extensional shear zone, granites and the exotic Ikaria nappe: Inside the Aegean metamorphic core complexes, *Journal of the Virtual Explorer*, *27*(3), 1–32.

Ring, U., K. Gessner, T. Gungor, and C. W. Passchier (1999), The Menderes Massif of western Turkey and the Cycladic Massif in the Aegean--do they really correlate?, *Journal of the Geological Society*, *156*(1), 3–6, doi:10.1144/gsjgs.156.1.0003.

Ring, U., S. N. Thomson, and M. Brcker (2003), Fast extension but little exhumation: the Vari detachment in the Cyclades, Greece, *Geological Magazine*, *140*(3), 245–252, doi:10.1017/S0016756803007799.

Ring, U., J. Glodny, T. Will, and S. Thomson (2007a), An Oligocene extrusion wedge of blueschist-facies nappes on Evia, Aegean Sea, Greece: implications for the early exhumation of high-pressure rocks, *Journal of the Geological Society*, *164*(3), 637–652, doi:10.1144/0016-76492006-041.

Ring, U., T. Will, J. Glodny, C. Kumerics, K. Gessner, S. Thomson, T. Güngör, P. Monié, M. Okrusch, and K. Drüppel (2007b), Early exhumation of high-pressure rocks in extrusion wedges: Cycladic blueschist unit in the eastern Aegean, Greece, and Turkey, *Tectonics*, *26*(2), 1–23, doi:10.1029/2005TC001872.

Ring, U., J. Glodny, T. Will, and S. Thomson (2010), The Hellenic Subduction System: High-Pressure Metamorphism, Exhumation, Normal Faulting, and Large-Scale Extension, *Annual Review of Earth and Planetary Sciences*, *38*(1), 45–76, doi:10.1146/annurev.earth.050708.170910.

Ring, U., J. Glodny, T. M. Will, and S. Thomson (2011), Normal faulting on Sifnos and the South Cycladic Detachment System, Aegean Sea, Greece, *Journal of the Geological Society*, *168*(3), 751–768, doi:10.1144/0016-76492010-064.

Roche, V., V. Laurent, G. L. Cardello, L. Jolivet, and S. Scaillet (2016), Anatomy of the Cycladic Blueschist Unit on Sifnos Island (Cyclades, Greece), *Journal of Geodynamics*, *97*, 62–87, doi:10.1016/j.jog.2016.03.008.

Rossetti, F., C. Faccenna, L. Jolivet, R. Funiciello, F. Tecce, and C. Brunet (1999), Syn- versus post-orogenic extension: the case study of Giglio Island (Northern Tyrrhenian Sea, Italy), *Tectonophysics*, *304*(1–2), 71–93, doi:10.1016/S0040-1951(98)00304-7.

Royden, L. H., and D. J. Papanikolaou (2011), Slab segmentation and late Cenozoic disruption of the Hellenic arc, *Geochemistry, Geophysics, Geosystems*, *12*(3), 1–24, doi:10.1029/2010GC003280.

de Saint Blanquat, M., E. Horsman, G. Habert, S. Morgan, O. Vanderhaeghe, R. Law, and B. Tikoff (2011), Multiscale magmatic cyclicity, duration of pluton construction, and the paradoxical relationship between tectonism and plutonism in continental arcs, *Tectonophysics*, *500*(1–4), 20–33, doi:10.1016/j.tecto.2009.12.009.

Salemink, J. (1985), Skarn and ore formation at Serifos, Greece, as a consequence of granodiorite intrusion, Ph.D thesis, University of Utrecht, Netherlands.

Sanchez-Gomez, M., D. Avigad, and A. Heimann (2002), Geochronology of clasts in allochthonous Miocene sedimentary sequences on Mykonos and Paros Islands: implications for back-arc extension in the Aegean Sea, *Journal of the Geological Society*, *159*(1), 45–60, doi:10.1144/0016-764901031.

Schneider, D. A., C. Senkowski, H. Vogel, B. Grasemann, C. Iglseder, and A. K. Schmitt (2011), Eocene tectonometamorphism on Serifos (western Cyclades) deduced from zircon depth-profiling geochronology and mica thermochronology, *Lithos*, *125*(1–2), 151–172, doi:10.1016/j.lithos.2011.02.005.

Seward, D., O. Vanderhaeghe, L. Siebenaller, S. Thomson, C. Hibsch, A. Zingg, P. Holzner, U. Ring, and S. Duchêne (2009), Cenozoic tectonic evolution of Naxos Island through a multi-faceted approach of fission-track analysis, *Geological Society, London, Special Publications*, *321*(1), 179–196, doi:10.1144/SP321.9.

Shu, L., Y. Sun, D. Wang, M. Faure, P. Monie, and J. Charvet (1998), Mesozoic doming extensional tectonics of Wugongshan, South China, *Science in China Series D: Earth Sciences*, *41*(6), 601–608, doi:10.1007/BF02878742.

Siebenaller, L. (2008), Circulations fluides au cours de l'effondrement d'un prisme d'accrétion crustal: L'exemple du "Metamorphic Core Complex" de l'Île de Naxos (Cyclades, Grèce), Ph.D thesis, Univ. Henri Poincaré, Nancy, France.

Skarpelis, N. (2007), The Lavrion deposit (SE Attica, Greece): geology, mineralogy and minor elements chemistry, *Neues Jahrbuch für Mineralogie - Abhandlungen*, *183*(3), 227–249, doi:10.1127/0077-7757/2007/0067.

Spencer, J. E. (1984), Role of tectonic denudation in warping and uplift of low-angle normal faults, *Geology*, *12*(2), 95–98, doi:10.1130/0091-7613(1984)12<95:ROTDIW>2.0.CO;2.

St. Seymour, K., D. Zouzias, S. Tombros, and E. Kolaiti (2009), Geochemistry of the Serifos pluton (Cycladic islands) and associated iron oxide and sulfide ores: Skarn or metamorphosed exhalite deposits?, *Neues Jahrbuch für Mineralogie - Abhandlungen*, *186*(3), 249–270, doi:10.1127/0077-7757/2009/0143.

Stouraiti, C., P. Mitropoulos, J. Tarney, B. Barreiro, A. M. McGrath, and E. Baltatzis (2010), Geochemistry and petrogenesis of late Miocene granitoids, Cyclades, southern Aegean: Nature of source components, *Lithos*, *114*(3–4), 337–352, doi:10.1016/j.lithos.2009.09.010.

Teyssier, C., and D. L. Whitney (2002), Gneiss domes and orogeny, *Geology*, *30*(12), 1139–1142, doi:10.1130/0091-7613(2002)030<1139:GDAO>2.0.CO;2.

Teyssier, C., E. C. Ferré, D. L. Whitney, B. Norlander, O. Vanderhaeghe, and D. Parkinson (2005), Flow of partially molten crust and origin of detachments during collapse of the Cordilleran Orogen, *Geological Society, London, Special Publications*, *245*(1), 39–64, doi:10.1144/GSL.SP.2005.245.01.03.

Trotet, F., O. Vidal, and L. Jolivet (2001), Exhumation of Syros and Sifnos metamorphic rocks (Cyclades, Greece). New constraints on the P-T paths, *European Journal of Mineralogy*, *13*(5), 901–920, doi:10.1127/0935-1221/2001/0013/0901.

Tschegg, C., and B. Grasemann (2009), Deformation and alteration of a granodiorite during low-angle normal faulting (Serifos, Greece), *Lithosphere*, *1*(3), 139–154, doi:10.1130/L33.1.

Urai, J. L., R. D. Schuiling, and J. B. H. Jansen (1990), Alpine deformation on Naxos (Greece), *Geological Society, London, Special Publications*, *54*(1), 509–522, doi:10.1144/GSL.SP.1990.054.01.47.

Vandenberg, L. C., and G. S. Lister (1996), Structural analysis of basement tectonites from the Aegean metamorphic core complex of Ios, Cyclades, Greece, *Journal of Structural Geology*, *18*(12), 1437–1454, doi:10.1016/S0191-8141(96)00068-5.

Vanderhaeghe, O. (1999), Pervasive melt

migration from migmatites to leucogranite in the Shuswap metamorphic core complex, Canada: control of regional deformation, *Tectonophysics*, *312*(1), 35–55, doi:10.1016/S0040-1951(99)00171-7.

Vanderhaeghe, O. (2004), Structural development of the Naxos migmatite dome, in *Gneiss Domes in Orogeny*, vol. 380, pp. 211–227, Geological Society of America, Boulder, Colorado.

Vanderhaeghe, O. (2009), Migmatites, granites and orogeny: Flow modes of partially-molten rocks and magmas associated with melt/solid segregation in orogenic belts, *Tectonophysics*, *477*(3–4), 119–134, doi:10. 1016/j.tecto.2009.06.021.

Vanderhaeghe, O. (2012), The thermal–mechanical evolution of crustal orogenic belts at convergent plate boundaries: A reappraisal of the orogenic cycle, *Journal of Geodynamics*, *56–57*, 124–145, doi:10.1016/j.jog.2011.10.004.

Vanderhaeghe, O., and C. Teyssier (1997), Formation of the Shuswap metamorphic core complex during late-orogenic collapse of the Canadian Cordillera: Role of ductile thinning and partial melting of the mid-to lower crust, *Geodinamica Acta*, *10*(2), 41–58, doi:10.1080/09853111.1997.11105292.

Vanderhaeghe, O., and C. Teyssier (2001), Partial melting and flow of orogens, *Tectonophysics*, *342*(3–4), 451–472, doi:10.1016/S0040-1951(01)00175-5.

Vanderhaeghe, O., C. Hibsch, L. Siebenaller, S. Duchêne, M. de St Blanquat, S. Kruckenberg, A. Fotiadis, and L. Martin (2007), Penrose Conference - Extending a Continent - Naxos Field Guide, *Journal of the Virtual Explorer*, *27*, 1–23, doi:10.3809/jvirtex.2007.00175.

Vernon, R. H. (2000), Review of Microstructural Evidence of Magmatic and Solid-State Flow, *Visual Geosciences*, *5*(2), 1–23, doi:10.1007/s10069-000-0002-3.

Webb, L. E., S. A. Graham, C. L. Johnson, G. Badarch, and M. S. Hendrix (1999), Occurrence, age, and implications of the Yagan–Onch Hayrhan metamorphic core complex, southern Mongolia, *Geology*, *27*(2), 143–146, doi:10.1130/0091-7613(1999)027<0143:OAAIOT>2.3.CO;2.

Whitney, D. L., and Y. Dilek (1997), Core complex development in central Anatolia, Turkey, *Geology*, *25*(11), 1023–1026, doi:10.1130/0091-7613(1997)025<1023:CCDICA>2.3.CO;2.

Whitney, D. L., C. Teyssier, and O. Vanderhaeghe (2004a), Gneiss domes and crustal flow, in *Special Paper 380: Gneiss Domes in Orogeny*, vol. 380, pp. 15–33, Geological Society of America.

Whitney, D. L., C. Teyssier, and A. K. Fayon (2004b), Isothermal decompression, partial melting and exhumation of deep continental crust, *Geological Society, London, Special Publications*, *227*(1), 313–326, doi:10.1144/GSL.SP.2004.227.01.16.

Whitney, D. L., C. Teyssier, P. Rey, and W. R. Buck (2013), Continental and oceanic core complexes, *Geological Society of America Bulletin*, *125*(3–4), 273–298, doi:10.1130/B30754.1.

Wijbrans, J. R., and I. McDougall (1986), $^{40}Ar/^{39}Ar$ dating of white micas from an Alpine high-pressure metamorphic belt on Naxos (Greece): the resetting of the argon isotopic system, *Contributions to Mineralogy and Petrology*, *93*(2), 187–194, doi:10.1007/BF00371320.

Wijbrans, J. R., and I. McDougall (1988), Metamorphic evolution of the Attic Cycladic Metamorphic Belt on Naxos (Cyclades, Greece) utilizing 40Ar/39Ar age spectrum measurements, *Journal of Metamorphic Geology*, *6*(5), 571–594, doi:10.1111/j.1525-1314.1988.tb00441.x.

Zeffren, S., D. Avigad, A. Heimann, and Z. Gvirtzman (2005), Age resetting of hanging wall rocks above a low-angle detachment fault: Tinos Island (Aegean Sea), *Tectonophysics*, *400*(1–4), 1–25, doi:10.1016/j.tecto.2005.01.003

Chapitre V

Déformation expérimentale de magmas granodioritiques de faible à forte cristallinité

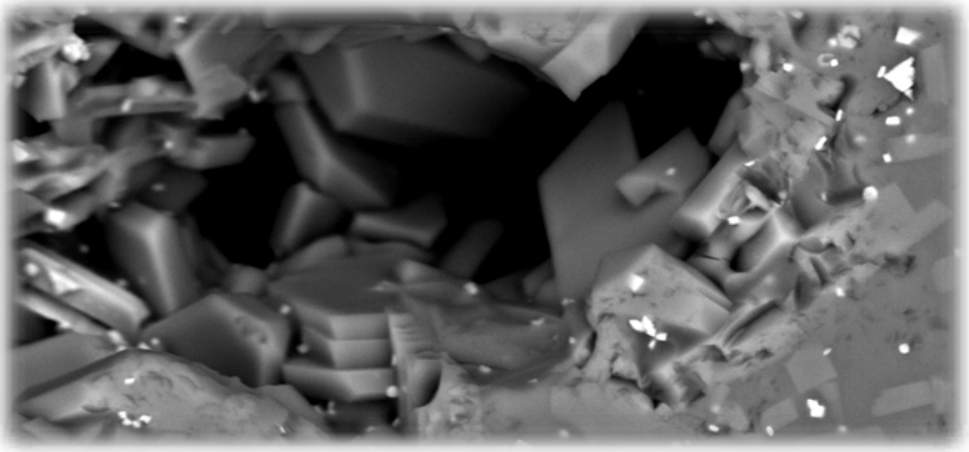

Sommaire

Introduction

À la lumière des observations structurales et éléments bibliographiques fournis dans les précédents chapitres, les complexes magmatiques égéens semblent jouer un rôle majeur dans les processus de redistribution et de localisation de la déformation dans l'histoire d'exhumation des dômes métamorphiques extensifs cycladiques. Quel que soit son origine, le phénomène de localisation de la déformation résulte nécessairement d'une non-linéarité de la résistance mécanique dans le temps et l'espace. Dès lors, face aux contraintes tectoniques, il est communément supposé que les corps magmatiques non consolidés, par leur caractère faiblement visqueux [e.g., *Lejeune & Richet*, 1995], soient capables de générer avec leur encaissant des zones de gradients abrupts de la résistance mécanique le long desquels la localisation de la déformation peut être favorablement stimulée [e.g., *Lynch & Morgan*, 1987; *Brun et al.*, 1994; *Pavlis*, 1996]. Néanmoins, cette hypothèse ne peut être considérée à elle seule comme suffisante pour expliquer l'évolution de la déformation et la manière dont elle se localise au sein même de granitoïdes syn-tectoniques. Dans le cas précis des corps intrusifs cycladiques, le fait d'observer sur de larges portions de plusieurs centaines de mètres d'épaisseur le passage progressif d'une simple structuration syn-magmatique (i.e., fabriques cristallines sans surimposition significative d'une déformation à l'état solide) à une déformation ductile pénétrative implique que la nucléation de zones de détachements crustaux ne relève pas uniquement de contrastes rhéologiques initiaux entre magma et encaissant, mais dépend également de la capacité intrinsèque des corps intrusifs en cours de refroidissement à initier une déformation localisée. Lors de la mise en place et la cristallisation de complexes magmatiques, les variations compositionnelles locales (i.e., filons syn-plutoniques) et la façon dont s'agencent les phases cristallines dans les magmas (i.e., propriétés texturales) peuvent être des hypothèses à l'origine de gradients de résistance interne et ainsi constituer des vecteurs de localisation de la déformation [e.g., *Tikoff & Teyssier*, 1994; *Christiansen & Pollard*, 1997 ; *Pennacchioni & Mancktelow*, 2007]. Alors que les témoins d'une déformation localisée le long d'hétérogénéités compositionnelles sont en général clairement exposés par les observations de terrain, identifier à l'affleurement la sensibilité du phénomène de localisation de la déformation face aux inhomogénéités texturales s'avère bien souvent plus complexe en raison de l'effacement de l'état initial du milieu par les derniers incréments de la déformation.

Avec les approches naturelles (observations de terrain et microstructurales), l'outil expérimental incarne la seule voie susceptible de fournir des contraintes supplémentaires sur la structuration progressive de magmas partiellement cristallisés soumis à un état de contrainte donné et ainsi d'en soustraire les possibles mécanismes précurseurs de localisation de la déformation. Malgré la littérature abondante sur la rhéologie des magmas, peu d'études se sont penchées sur le comportement structural de suspensions magmatiques [*Arbaret et al.*, 2007; *Picard*, 2009; *Forien et al.*, 2011; *Laumonier et al.*, 2011; *Picard et al.*, 2011, 2013; *Cordonnier et al.*, 2012; *Okumura et al.*, 2016]. Les quelques résultats expérimentaux de *Picard et al.* [2011, 2013] ont en particulier montré que le développement de fabriques cristallines et de structures semi-pénétratives à localisées sont intimement liées à la taille et la forme des cristaux, mais également à leur distribution spatiale ainsi que leur interactions

mutuelles au sein d'un liquide silicaté. Toutefois, ces travaux expérimentaux se sont essentiellement focalisés sur des systèmes magmatiques simples, plus ou moins lointains de systèmes magmatiques naturels en termes de textures, d'associations minéralogiques ou encore de chimie. La plupart des systèmes synthétiques, dont la fraction solide est constituée de particules solides dispersés de manière homogène, ne rendent pas forcément compte des possibles agrégats de cristaux qui peuvent se former au cours de la cristallisation en raison de la nucléation hétérogène de nouveaux cristaux sur des sites préexistants (e.g., cristal hôte, bulles, défauts cristallins, impuretés). Pour combler ces quelques lacunes, **ce volet expérimental se propose d'évaluer, sous l'effet d'un cisaillement simple simulé par un mouvement de torsion, le comportement structural de suspensions magmatiques chimiquement et texturalement proches de systèmes naturels, et finalement d'en déduire de possibles mécanismes à l'origine de la localisation de la déformation au sein de magmas ne comportant initialement aucune hétérogénéité forte.** Pour ce faire, nous avons entrepris une série d'expériences en autoclave à chauffage interne afin de synthétiser des magmas granodioritiques hydratés issues de poudres anhydres de la granodiorite de Serifos. Les expériences de synthèse ont ainsi couvert une gamme de cristallinité allant depuis quelques pourcents jusqu'à la quasi-solidification. Ces mêmes produits expérimentaux ont été ensuite déformés au sein d'une presse de type Paterson dans des conditions de pression (300 MPa) et température (800, 750, 700 ou 650°C) identiques à celles imposées durant leur synthèse en autoclave.

1. Méthodes expérimentales & techniques analytiques

1.1. L'autoclave à chauffage interne : synthèse des suspensions magmatiques

1.1.1. Principe de fonctionnement

Les suspensions magmatiques hydratées destinées aux expériences de déformation ont été synthétisées au moyen d'un autoclave vertical à chauffage interne, situé au sein de la plateforme expérimentale du laboratoire d'Orléans. Ce type d'appareillage consiste en une enceinte faite d'acier à l'intérieur de laquelle le four et la charge expérimentale encapsulée (voire plusieurs selon les besoins) sont introduits, puis soumis à une pression gazeuse de confinement contrôlée. L'étanchéité de la cellule sous pression est assurée par deux obturateurs disposés à chaque extrémité de l'enceinte et scellés par deux bouchons (Figure V-1a, schéma d'après *Champallier* [2005]).

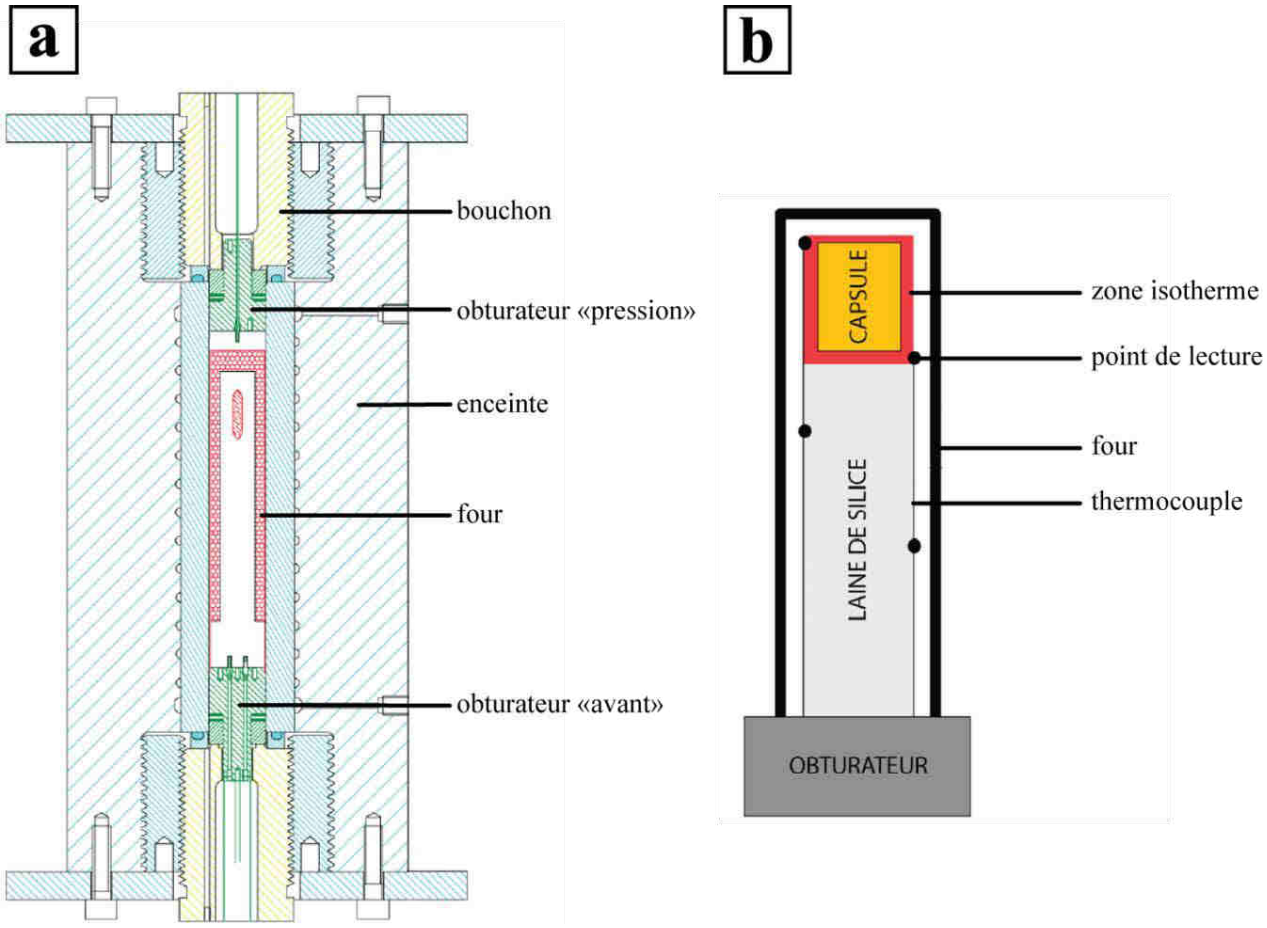

Figure V-1: *(a) coupe longitudinale d'un autoclave à chauffage interne schématisant la disposition du four, des obturateurs et des bouchons associés [Champallier, 2005]. (b) Vue conceptuelle de l'agencement entre thermocouples et capsule au sein d'un four, d'après Picard [2009].*

L'utilisation d'un tel appareillage est optimal pour des expériences allant jusqu'à 1 GPa, soit une pression très largement supérieure aux conditions de pression imposées dans cette étude (300 MPa). Le four, quant à lui, peut induire une température maximale d'environ

1400°C et se compose d'un double enroulement spiralé de câbles en molybdène ou Kanthal, servant de résistances. La puissance apportée à chaque résistance est régulée de manière indépendante et la température régnant au sein de la cellule peut être déchiffrée par deux thermocouples (Figure V-1b). Les deux points de lecture de la température sont généralement espacés de plusieurs centimètres et de préférence placés de part et d'autre de la capsule. Ce dispositif permet ainsi de détecter d'éventuels gradients thermiques, réguler les résistances et finalement maintenir une température homogène sur ~50 mm de hauteur. Compte tenu des dimensions du four et de la zone isotherme, le volume des capsules ne peut généralement dépasser quelques cm^3, soit une dimension maximale de 20x40 mm pour des capsules cylindriques en or, idéales pour la synthèse d'échantillons en vue des expériences de déformation. Les thermocouples et les connexions électriques du système d'alimentation du four sont insérés à travers l'obturateur « avant » via des cônes de passages hermétiques à la pression (Figure V-1a).

1.1.2. Déroulement d'une expérience type

La mise sous pression de la cellule est tout d'abord exercée par l'injection d'un gaz inerte, à savoir de l'argon dans le cas présent, au moyen d'une pompe à air. Au-delà d'une pression de confinement de 50 MPa, l'injection d'argon est bloquée et le gaz est comprimé par un multiplicateur hydraulique jusqu'à 200 MPa, voire par un second multiplicateur pouvant atteindre la limite critique de 1 GPa. Dans le cadre de cette étude, la mise sous pression est interrompue aux alentours de 200 MPa. La montée en température ultérieure permet d'obtenir la pression désirée de 300 MPa par simple expansion thermique du gaz d'argon. Cette montée en température est d'ordinaire exécutée manuellement tandis que le plateau de température est stabilisé à l'aide d'un régulateur, couplé à la façade de contrôle de l'autoclave. Ce régulateur peut être éventuellement utilisé pour programmer des rampes de températures dégressives au cours d'une expérience de synthèse (Figure V-2). La chute progressive de la pression qui en résulte doit alors être compensée en activant les multiplicateurs hydrauliques.

Après une durée déterminée, l'expérience se termine par le refroidissement à pression constante de la suspension magmatique synthétisée, appelé aussi trempe isobare (Figure V-2). La vitesse de la chute de température correspond simplement à celle du four, soit de l'ordre de 80-100°C/min. Ce mode de refroidissement permet de préserver les volatils dissous dans le liquide silicaté et ainsi minimiser la nucléation d'une phase gazeuse (e.g., l'eau) [*Champallier*, 2005]. Des phases de trempe, ou fractions cristallines hors équilibre, peuvent à cette occasion apparaître avant que la température de transition vitreuse (T_g) ne soit franchie. Pour la grande majorité des compositions chimiques de magmas siliceux, la rapidité du refroidissement est cependant suffisante pour qu'aucune phase de trempe ne cristallise [*Champallier*, 2005]. La trempe isobare est systématiquement stoppée à une température légèrement en deçà de la transition vitreuse, puis cette même température est maintenue à un état stationnaire au sein de l'enceinte pendant quelques dizaines d'heures (Figure V-2). Ce procédé favorise la « relaxation » du verre silicaté (diminution de la tension superficielle), empêchant une intense fracturation de la synthèse expérimentale lors de la décompression et la préparation des échantillons pour les expériences en presse Paterson.

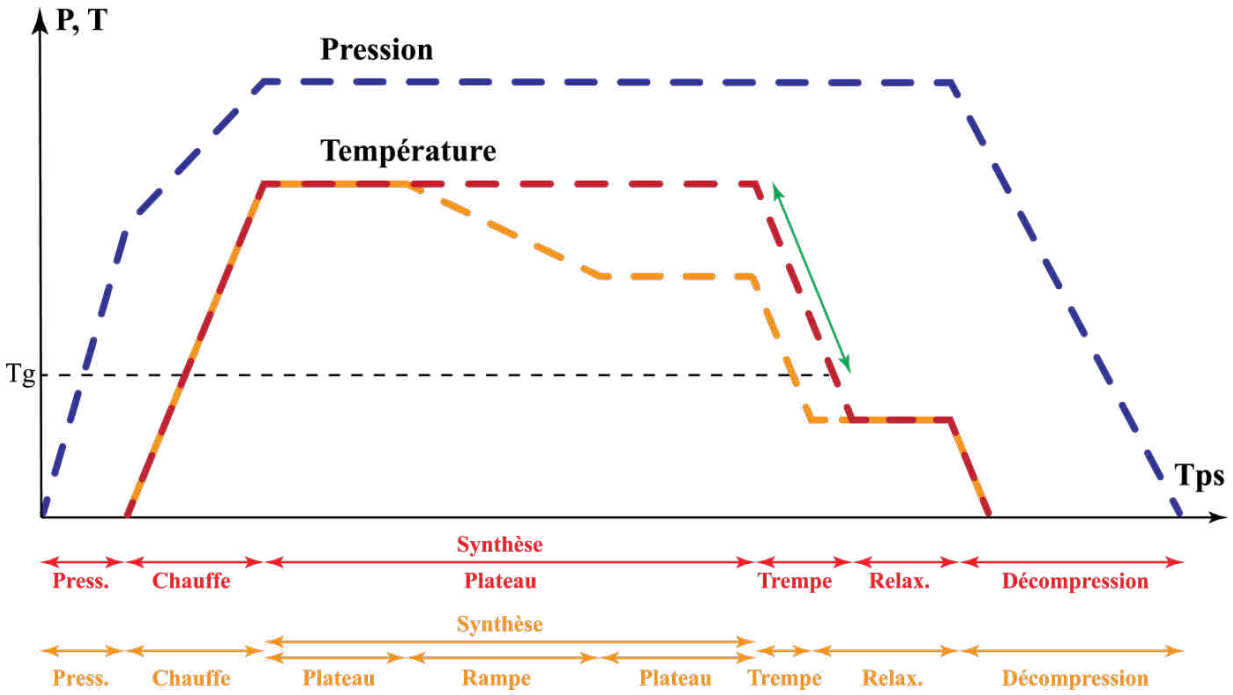

Figure V-2: *chemins pression et température lors d'expériences de synthèse, terminée par le procédé de trempe isobare (modifié de Laumonier [2013]). Selon l'objectif préalablement défini, les expériences de synthèse peuvent être menées (1) en état stationnaire avec des conditions de pression (trajectoire bleue) et de température (trajectoire rouge) constantes, ou (2) en conditions dynamiques avec une chute progressive de la température (trajectoire orange) à pression constante. Tg est la transition vitreuse ayant lieu à une température donnée, dépendante de la vitesse de trempe, de la composition du matériel de départ et de la teneur en eau dissoute dans le verre silicaté. La double flèche verte indique la durée pendant laquelle des phases de trempe peuvent cristalliser. Press. : période de mise en pression avant la montée en température. Relax. : période durant laquelle le verre est « relaxé », après passage de la transition vitreuse.*

1.2. La presse Paterson : déformation des suspensions magmatiques

1.2.1. Principe de fonctionnement

L'appareillage ayant servi aux expériences de déformation de suspensions magmatiques synthétisées est la presse Paterson, de même implantée au sein du laboratoire d'expérimentation de l'ISTO. La presse Paterson se résume en un autoclave à chauffage interne muni de modules de déformation et de cellules de mesures (Figure V-3).

Le principe de fonctionnement de l'autoclave est analogue à celui précédemment détaillé. Il se compose d'un monobloc cylindrique vertical à l'intérieur duquel une pression de confinement est engendrée par l'injection puis la compression d'un gaz, l'argon. La pression maximale exercée par ce système peut théoriquement atteindre 500 MPa. Le four, fixé au sein de l'enceinte haute pression, comprend trois enroulements de molybdène fournissant une température maximale de 1400°C sur une zone isotherme (±2°C) d'environ 20 à 40 mm de hauteur. Au cours de l'expérience, la lecture de la température s'effectue par un seul thermocouple situé à quelques millimètres (~3-5 mm) au-dessus de l'échantillon, séparé par un

disque d'alumine (Figure V-4a). Le four est par conséquent calibré au préalable afin que l'échantillon soit exactement disposé dans la zone isotherme.

L'autoclave est associé à deux modules de déformation, l'un appliquant une déformation coaxiale [*Paterson*, 1990], l'autre simulant un cisaillement simple par torsion [*Paterson & Olgaard*, 2000]. Dans le premier cas, la contrainte appliquée à l'échantillon est

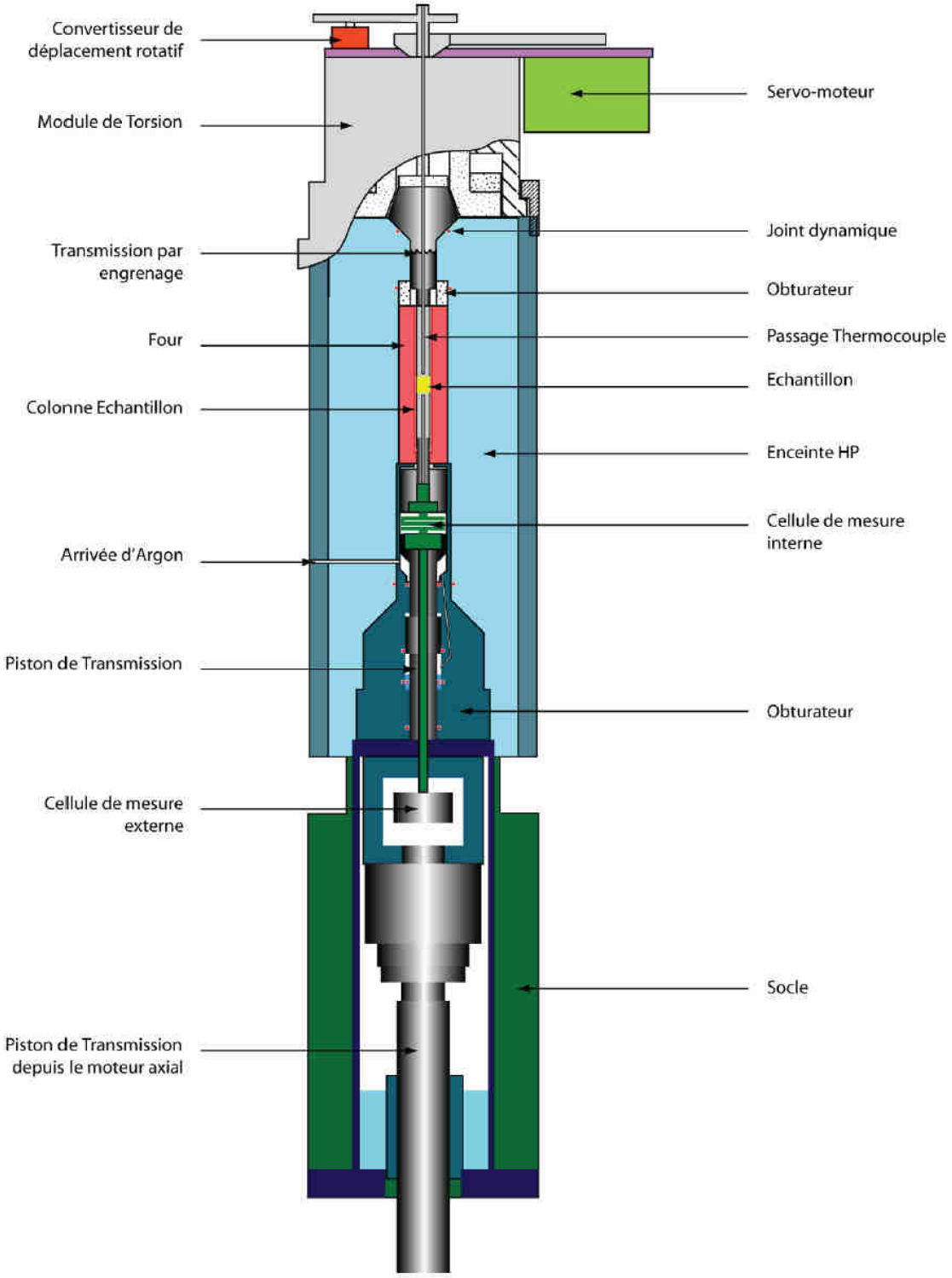

Figure V-3: *schéma d'une presse Paterson dotée du module de torsion, d'après Champallier* [2005].

transmise par un moteur axial placé sous l'autoclave. Dans le cas suivant, un servomoteur est situé au-dessus de l'enceinte haute pression et, par un système d'engrenage, impose une rotation à la moitié haute de la colonne-échantillon tandis que la partie basse reste fixe. (Figure V-3). Deux cellules de mesures (interne et externe à l'autoclave) enregistrent en temps réel la force -déformation coaxiale- ou le moment -déformation en torsion- de résistance de l'échantillon. Dans cette étude, l'ensemble des expériences de déformation ont été réalisées en torsion, et de ce fait, le mode de déformation coaxial ne sera pas détaillé dans ce qui suit.

1.2.2. Préparation & montage de la colonne-échantillon

Pour une expérience de déformation en torsion, la hauteur de la colonne-échantillon doit nécessairement être comprise dans une gamme allant de 176 à 203 millimètres. L'échantillon de synthèse est à cet effet inséré au milieu d'un empilement de disques en alumine et de pistons cylindriques de 14,9 mm de diamètre, composés soit d'alumine, soit de zircone (Figure V-4a). L'assemblage est finalement introduit dans une chemise métallique (Figure V-4b). La chemise endosse le rôle de maintien de la colonne lors de son insertion dans le four puis lors de la phase de déformation de l'échantillon.

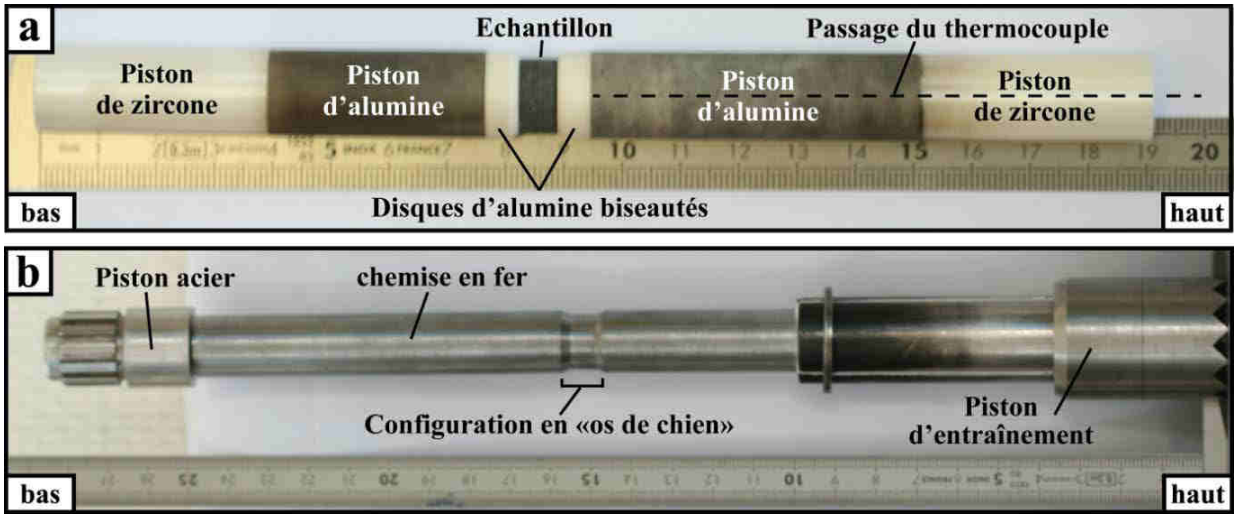

Figure V-4: *(a) photo de la colonne-échantillon sans chemise, constitué d'un assemblage de pistons (alumine, zircone) et de disques d'alumine répartis de part et d'autre de l'échantillon. Les cylindres de la demi-colonne supérieure sont forés en leur centre, laissant un passage pour le thermocouple. (b) Photo de l'assemblage moulé par sa chemise en fer (colonne-échantillon de type « os de chien »).*

Les pistons et disques, plus résistants que des suspensions magmatiques, assurent la transmission des contraintes au travers de l'échantillon sans qu'ils puissent accommoder la déformation. Les pistons de zircone, placés aux extrémités du montage, présentent également la fonction d'isolant thermique pour l'ensemble de la colonne. Lors de l'étape de préparation, la longueur de chaque piston est ajustée en vue de placer exactement l'échantillon au cœur de la zone isotherme du four. Par la suite, les faces basales des différents cylindres et disques sont rectifiées de façon à être rigoureusement planes et orthogonales à l'axe de la colonne, évitant ainsi tout risque de glissement aux interfaces durant la phase de déformation de l'échantillon.

En raison de la géométrie de l'assemblage, les échantillons demandent également d'être usinés de sorte à obtenir une forme cylindrique. Bien que le procédé de « relaxation » du verre silicaté lors des synthèses préalables réduise la probabilité de fracturation des suspensions magmatiques à température ambiante, leur état reste malgré tout fragile et l'étape de préparation d'échantillons cylindriques exige une grande minutie. Pour ce faire, le produit de synthèse, de quelques dizaines de millimètre de hauteur, est soigneusement extrait de sa capsule en or et mis en résine pour être foré. L'échantillon de synthèse est ensuite débité à la micro-scie en plusieurs pastilles de quelques millimètres d'épaisseur (le plus souvent 2 ou 3 par synthèse), puis celles-ci sont rectifiées de manière à ce que leurs faces soient parfaitement parallèles. Les dimensions de l'assemblage pistons-disques et de la chemise métallique qui l'enrobe (Figure V-4b) sont standardisées pour des échantillons de 14,9 mm de diamètre. Hors, la capsule (20x40 mm) et la charge expérimentale, toutes deux portées à haute pression au cours de la phase de synthèse, subissent à chaque expérience une réduction significative de leur volume. Les échantillons conçus durant cette étude n'ont malheureusement pu atteindre ce standard, seules des pastilles de 13 mm de diamètre ont été réalisées. Afin d'assurer un parfait alignement entre échantillons et disques, et par conséquent se préserver d'une possible perte d'étanchéité par la chemise métallique, un montage spécifique en « os de chien » (Figure VI-4b) est classiquement élaboré [*Paterson & Olgaard*, 2000]. Dans ce type de configuration, les faces des disques d'alumine situés de part et d'autre de l'échantillon sont biseautés et leurs diamètres réduits jusqu'à 13 millimètres. La chemise métallique est après quoi montée, moulée à la colonne, et marquée par des gravures rectilignes parallèles à son axe dans le but de mesurer la quantité de déformation finie subie par l'échantillon après expérience. L'étanchéité de la colonne-échantillon est finalement optimisée par deux pistons et joints toriques insérés aux extrémités de la chemise métallique (Figure VI-4b).

Selon les conditions expérimentales appliquées, une chemise de cuivre ou de fer est préconisée [e.g., *Paterson & Olgaard*, 2000; *Arbaret et al.*, 2007; *Champallier et al.*, 2008]. A haute température, le fer constitue un meilleur isolant thermique que le cuivre. Typiquement, au-delà de 700-800°C, une chemise en fer permet de maintenir une zone isotherme plus stable au sein de la colonne. Etant donné les conditions de températures imposées dans cette étude (entre 650-800°C), le choix s'est orienté vers l'usage unique d'une chemise en fer. Toutefois, les liquides silicatés tendent en général à réagir avec le fer en corrodant partiellement la chemise. Pour écarter toute interaction chimique, une fine feuille de platine de 25 µm d'épaisseur est systématiquement intercalée entre la chemise et l'échantillon.

1.2.3. Type d'expériences

Lors d'expériences en presse Paterson, les grandeurs ou paramètres physiques pouvant être directement contraints sont la température, la pression ou encore la quantité et vitesse de déformation. Ces grandeurs et paramètres physiques sont contrôlés et régulés suivant le type d'expérience désiré et la problématique préalablement définie. La mise sous contrainte différentielle de matériaux, en l'occurrence ici de magmas partiellement cristallisés, porte en effet un double intérêt : établir des modèles rhéologiques empiriques par l'apport de données mécaniques (contrainte, viscosité apparente ou relative), et/ou plus simplement caractériser des

fabriques de forme et microstructures se développant au cours d'une cristallisation. Dans l'idéal, déterminer le comportement rhéologique d'un matériel nécessite de multiplier des expériences au travers desquelles diverses vitesses de déformations seraient appliquées dans des conditions de pression et de température fixes [*Paterson & Olgaard*, 2000]. En raison des contraintes de temps et du nombre conséquent d'échantillons que requiert l'acquisition de propriétés rhéologiques, seul le caractère évolutif à la fois des microstructures et des pétrofabriques générées au sein des différentes suspensions magmatiques sont considérées dans ce volet expérimental. Ainsi, le type d'expérience en torsion mené au cours de cette étude est relativement simple : ne jouer que sur la température et implicitement sur la fraction cristalline, tout en appliquant dans la mesure du possible des vitesses de déformation semblables d'une expérience à l'autre. *In fine*, la quantité de déformation dépendra de la durée de l'expérience.

1.2.4. Mécanique de torsion

En mécanique de torsion, la notion de quantité de déformation, notée γ (sans unité), est intimement liée à la géométrie de l'échantillon ainsi qu'au déplacement angulaire $\theta\theta$ (rad) imposé à l'échantillon en un point donné (Figure V-5) [*Paterson & Olgaard*, 2000]. L'angle $\theta\theta$ est donné en temps réel par un convertisseur de déplacement placé au-dessus de l'autoclave. En considérant alors un échantillon de forme cylindrique de longueur l et de rayon R, il est possible de déterminer une quantité de déformation moyenne subie par l'échantillon selon l'équation suivante :

$$\gamma\gamma = \frac{RR \cdot \theta\theta}{ll}$$

La quantité de déformation γ est en ce sens maximale à la périphérie de l'échantillon cylindrique, et nulle en son centre (Figure V-5). La vitesse de déformation $\gamma\dot{\gamma}$ (s^{-1}) peut alors être calculée en déterminant la vitesse de déplacement angulaire $\theta\theta$ ($rad.s^{-1}$) :

$$\gamma\dot{\gamma} = \frac{RR \cdot \theta\theta}{ll}$$

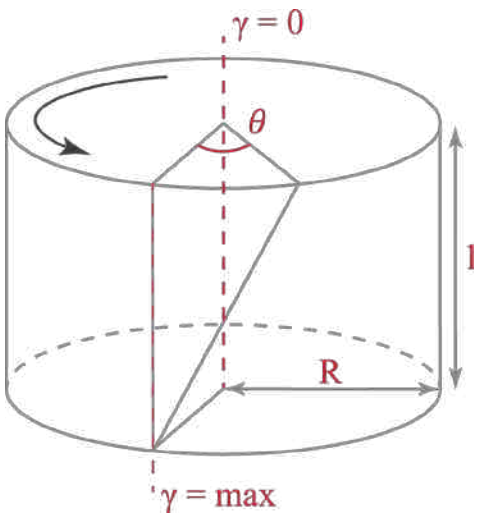

Figure V-5: *schéma d'un échantillon de forme cylindrique (R : rayon ; l : longueur) soumis à une déformation en torsion sous presse Paterson. L'angle* $\boldsymbol{\theta\theta}$ *représente le déplacement angulaire.*

1.2.5. Résultats représentatifs de l'étude

La déformation en torsion peut s'accommoder et se distribuer de diverses façons suivant les conditions expérimentales imposées (température, pression, vitesse de cisaillement), les propriétés intrinsèques des suspensions magmatiques (e.g., taux de cristallinités, homogénéité texturale, quantité de volatils) et par conséquent leur réponse mécanique face aux

contraintes différentielles qui leur sont appliquées. En explorant la structuration de magmas au travers d'une large gamme de cristallinité, plusieurs cas de figure ont été de ce fait rencontrés (Figure V-6).

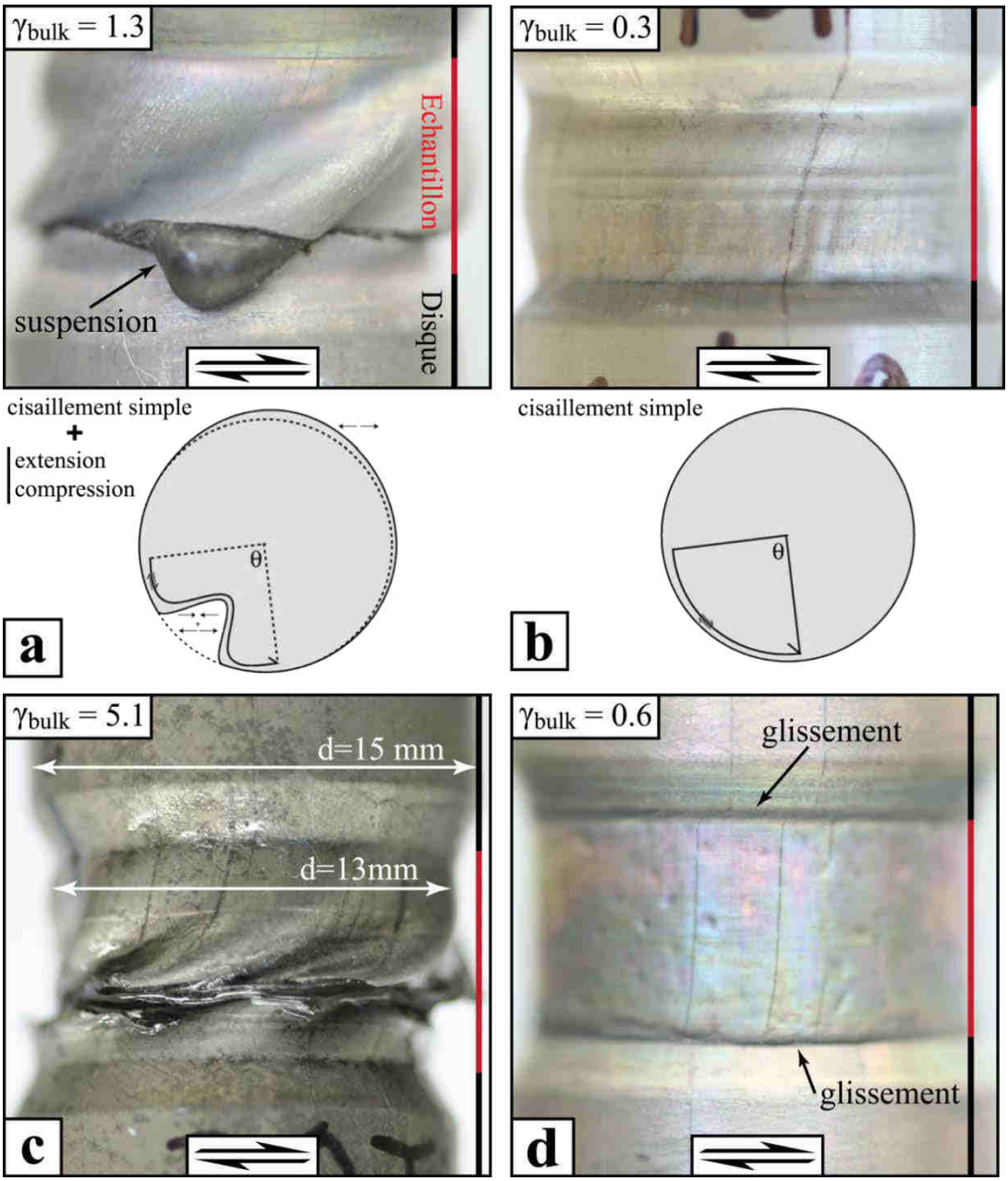

Figure V-6: *clichés de colonnes après expériences en Paterson, montrant divers cas de figure de distribution de la déformation rencontrés dans cette étude. (a) Contribution significative de la chemise en fer sur l'état de déformation finie de l'échantillon, donnant une apparence boursoufflée. La suspension magmatique s'extrude via la zone déchirée de la chemise. Le schéma du dessous présente une section transversale de l'échantillon cylindrique, la déformation se distribue de manière hétérogène et la contrainte cisaillante est associée à une composante en extension et/ou en compression (selon Barnhoorn et al. [2005]). (b) Distribution homogène de la déformation au sein de l'échantillon. (c) Déformation localisée au sein de l'échantillon. En raison d'un déplacement angulaire important et d'une intense concentration de la déformation, la moitié haute de la colonne se désaxe et la chemise se déchire. (d) Glissement aux interfaces lorsque l'échantillon est mécaniquement trop résistant.*

Les suspensions magmatiques de faible à moyenne cristallinité voient généralement leur déformation pour partie contrôlée par la chemise en fer ; celle-ci étant plus résistante aux contraintes appliquées. La faible résistance de ces suspensions magmatiques se matérialise notamment par l'aspect boursouflé de la chemise (Figure V-6a). La contrainte cisaillante est alors localement associée à une composante en extension et/ou en compression [*Barnhoorn et al.*, 2005]. La distribution hétérogène de la déformation peut aboutir dans un cas extrême à une déchirure de la chemise, extravasant une partie de la suspension magmatique (Figure V-6a). Pour minimiser la contribution de la chemise métallique sur la déformation des échantillons, il est en définitive indispensable de modifier la vitesse de cisaillement et indirectement la viscosité du magma. Selon que la suspension soit considérée comme un fluide non-newtonien rhéofluidifiant (la viscosité apparente tend à décroître avec l'augmentation de la vitesse de cisaillement) ou au contraire rhéoépaississant (la viscosité apparente tend à s'accroitre avec l'augmentation de la vitesse de cisaillement), il est respectivement nécessaire de diminuer ou inversement augmenter la vitesse de déformation.

Lorsque la contrainte cisaillante est en grande majorité transmise au travers de l'échantillon, la déformation peut se répartir de manière homogène (Figure V-6b) ou éventuellement se localiser suivant une ou plusieurs bandes de cisaillement (Figure V-6c). En principe, l'emploi du module en torsion permet d'atteindre une quantité de déformation infinie. En pratique, au-delà d'une certaine quantité de déformation accumulée, la colonne-échantillon peut devenir géométriquement instable. A titre d'exemple, la moitié haute de la colonne peut se désaxer par rapport à la moitié basse (Figure V-6c) et la durée de l'expérience s'en retrouve réduite.

Enfin, si la résistance mécanique de l'échantillon face à la contrainte appliquée vient à dépasser celle aux interfaces entre pistons ou entre l'échantillon et les disques d'alumine, il se produit un glissement (Figure V-6d). Ces glissements aux interfaces interviennent régulièrement dans les cas où les suspensions magmatiques comportent une forte proportion cristalline et sont donc caractérisées par une viscosité élevée. Il est parfois possible de diminuer la vitesse de déformation pour que la déformation se concentre de nouveau au sein de l'échantillon.

1.3. Moyens analytiques mis à disposition

1.3.1. Préparation des sections d'étude

Suite aux expériences de synthèse ou de déformation en torsion, un certain nombre de sections polies ont été conçues pour analyse chimique ou observation texturale des suspensions magmatiques. Les sections réalisées au travers d'échantillons cylindriques s'effectuent selon trois plans caractéristiques (Figure V-7a) ; la section [xy] étant un plan transversal à l'échantillon, [xz] un plan longitudinal et tangentiel au cylindre et [yz] un plan orthogonal à la section [xy] passant par l'axe de révolution de l'échantillon. Les analyses chimiques et observations texturales des divers produits synthétisés ont été uniquement réalisées selon une section basale [xy] de sorte qu'un maximum de volume soit préservé pour la préparation d'échantillons en vue des expériences en torsion. A *contrario*, les échantillons déformés sous

presse Paterson ont été majoritairement découpés suivant le plan [xz], orthogonal au plan de cisaillement, où l'état de déformation finie est supposé être maximum. Un exemple de section [xz] est présenté Figure V-7b. Lors de la phase de découpe, les échantillons sont maintenus entre les disques et la chemise en fer afin de garantir son intégrité physique. Les sections d'études sont ensuite mises sous résine, polies et enfin métallisées avant d'être examinées par microscopie et microsonde électroniques.

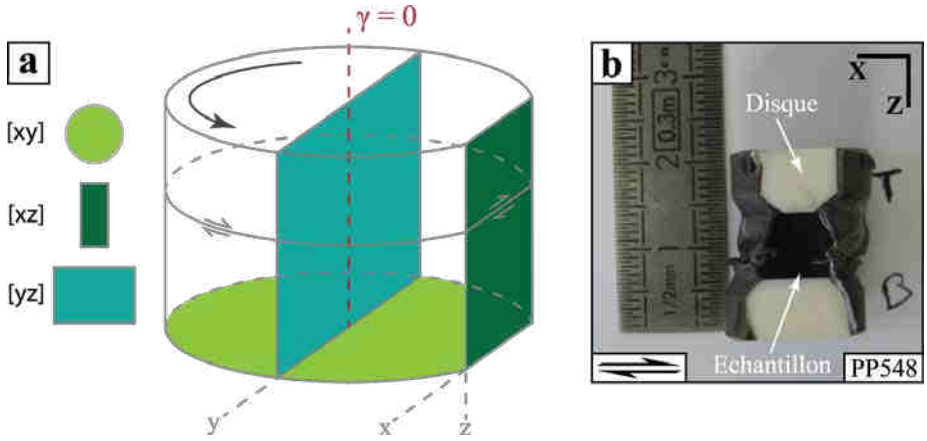

Figure V-7: *sections d'étude pour analyse chimique ou observation texturale/structurale. (a) Schéma représentant les trois sections le plus souvent réalisées au travers des échantillons cylindriques. (b) photo d'un échantillon déformé en torsion et scié avec ses disques et sa chemise selon une section [xz] ; expérience PP548.*

1.3.2. Imagerie par microscopie électronique à balayage (MEB)

Les microtextures, à la fois des synthèses expérimentales et des échantillons déformés, ont été observées au moyen d'un Microscope Electronique à Balayage (MEB). Les images présentées dans cette étude ont été générées par un flux d'électrons rétrodiffusés (ou BSE en anglais, pour Back Scattering Electrons) bombardant la surface des sections d'études. Ces électrons, réémis dans une direction proche de leur direction d'origine, sont particulièrement sensibles au numéro atomique des éléments constituant la phase analysée. En d'autres termes, le nombre d'électrons rétrodiffusés sera d'autant plus grand que le numéro atomique d'un élément sera élevé. Les variations dans l'intensité du flux d'électrons permettent de composer des images en niveaux de gris pour une résolution de l'ordre du micromètre. Dès lors, les tons les plus clairs sur une image MEB correspondent aux phases composées majoritairement d'éléments lourds, tels que les oxydes, tandis que les vésicules apparaîtront noires. L'acquisition de ces images par contraste de phase constitue ainsi une étape exploratrice pour l'analyse chimique ultérieure des phases présentes (minéraux et verres interstitiels) ainsi qu'un support de travail pour caractériser d'éventuelles microstructures et quantifier des fabriques minérales sous logiciels de traitement d'images.

1.3.3. Analyse chimique ponctuelle & « bilan de masse » par microsonde électronique

La base du fonctionnement de la microsonde électronique est sensiblement similaire à celui du MEB. La surface de la section d'étude est bombardée par un faisceau d'électrons

incidents, excitant les atomes constituant les phases de l'échantillon. Les rayonnements résultants de cette sollicitation se propagent dans l'espace selon un angle d'émission propre à chaque élément; on parle alors de raies d'émission. Le spectre est ensuite analysé par un certain nombre de spectromètres disposés tout autour de la plateforme. L'intensité de chaque raie spectrale apporte une information quantitative quant à la composition chimique de chaque phase analysée. Dans le cas des suspensions magmatiques de cette présente étude, quelques 10 oxydes ont été analysés (SiO_2, TiO_2, Al_2O_3, FeO, MnO, MgO, CaO, Na_2O, K_2O et P_2O_5). Les analyses élémentaires des minéraux ont été réalisées par le biais d'un faisceau incident quadrangulaire d'un micron de côté (1x1 µm), tandis que la résolution spatiale du faisceau pour les analyses des verres interstitiels hydratés a été défocalisée selon une zone de 5x5 µm ou 10x10 µm. Cette défocalisation réduit la perte en éléments alcalins (Na, K), qui soumis au flux d'électrons, tendent à migrer hors de la surface d'analyse [*Morgan & London*, 1996].

Outre l'intérêt de déterminer la composition de la séquence cristalline et des verres silicatés, ces analyses chimiques ponctuelles ont eu pour objectif premier d'évaluer le taux de cristallinité des suspensions hydratées par bilan de masse (équilibre entre verre initial et minéraux + verre résiduel). En toute rigueur, cette méthode nécessite au préalable de définir avec exactitude la teneur en eau dissoute au sein des verres silicatés ainsi que celle contenue dans certains minéraux hydratés tels que les micas (biotite) ou les amphiboles. L'hydrogène et l'oxygène, constitutifs de l'eau, sont trop légers pour être analysés par microsonde. Dans ce cas de figure, il est en général réalisé au sein du laboratoire d'Orléans des mesures *in situ* de la concentration en eau par spectroscopie infrarouge (technique non détaillée dans ce mémoire, voir par exemple *Stolper* [1982]). Cette technique d'analyse exige cependant des plages de verre supérieur à 30 µm (limite de la résolution spatiale de l'instrument), ce que les synthèses expérimentales n'ont pu offrir. Il est alors possible d'appliquer une méthode alternative dite de la différence à 100% [*Devine et al.*, 1995]. De cette méthode indirecte, il est approximé que l'écart entre une analyse ponctuelle théorique devant « boucler » à 100% pds d'oxydes et la mesure réelle du poids total d'oxydes correspondrait majoritairement à la teneur en eau contenue dans un minéral ou un liquide silicaté (initial ou résiduel). Les résultats de cette méthode n'ont pas toujours été concluants, et ce, essentiellement en raison de la perte partielle des alcalins, même pour des résolutions focales de 10x10 µm. L'estimation de la fraction cristalline présente au sein de chaque suspension a finalement demandé un appui numérique par traitement d'image de photos MEB.

1.3.4. Analyse de l'Orientation Préférentielle de Forme (OPF) en 2D des phases minérales dans les produits expérimentaux

Méthodologie

L'analyse des fabriques de forme sur des images de terrain, des sections sciées, des images faites au microscope optique ou au MEB peut être abordée par plusieurs méthodes complémentaires dans leur approche et leur domaine de validité. Lorsque les objets constitutifs d'une phase sont initialement isolés, ou l'ont été par traitement d'images, les méthodes des meilleurs axes [*Allard & Benn*, 1989] et la méthode du tenseur d'inertie de forme (normé ou

non à la surface de l'objet, *Launeau & Cruden* [1998]) sont les plus couramment utilisées. Elles permettent de caractériser chaque objet sous la forme simplifiée d'une ellipse, se distinguant par l'orientation de son axe long et son excentricité à la sphéricité ; ce dernier paramètre étant souvent nommé rapport de forme de l'objet moyen. L'analyse statistique permet alors de calculer la modalité de la dite population en termes d'orientation et de degré d'orientation. Les moyennes calculées par analyse tensorielle donnent alors accès à l'orientation de l'axe long et à l'intensité moyenne, c'est-à-dire à l'excentricité du tenseur moyen de la fabrique de la phase considérée.

Lorsque les objets de la phase étudiée ne sont pas - ou ne peuvent pas en pratique être - isolés, il devient alors nécessaire de considérer la phase dans sa globalité. En pratique, cette approche est la plus courante dans l'étude des fabriques minérales. Quelle que soit la méthode d'acquisition employée, il arrive bien souvent que les objets constitutifs d'une même phase soient irrégulièrement distribués et forment des agrégats de tailles variables. La limite entre les objets (les grains d'une espèce minérale en l'occurrence) est alors difficile à détecter par analyse d'images. Dans ce cas, l'utilisation des méthodes par les meilleurs axes ou par le tenseur d'inertie n'est plus du tout pertinente puisqu'un agrégat sera traité comme un objet à part entière. Une méthode maintenant classique permet d'échapper à ce biais : il s'agit de la méthode des intercepts [*Panozzo*, 1987].

La grande majorité de nos produits expérimentaux sont caractérisés par une proportion cristalline relativement forte dans laquelle les phases minérales d'intérêt comme les feldspaths forment des agrégats importants allant jusqu'à une connectivité quasi-totale des objets pour les charges cristallines les plus importantes. C'est pourquoi nous avons quasi-exclusivement utilisé la méthode des intercepts pour distinguer les fabriques minérales obtenues dans nos expériences.

Théorie de la méthode des intercepts

La méthode des intercepts a fait l'objet de nombreux travaux de développement théorique et de programmes informatiques dédiés [*Saltykov*, 1958; *Launeau*, 1990; *Launeau & Robin*, 1996] tels que Intercepts2003 (http://www.sciences.univ-nantes.fr/lpgnantes/index.php?option=com_content&view=article&id=944&lang=en). L'analyse stéréologique théorique détaillée ainsi que son application à la détermination des fabriques de forme bidimensionnelles dans les roches, et plus particulièrement les roches magmatiques, ont été réalisées par *Launeau* [1990], *Launeau & Bouchez* [1992] ou encore par *Launeau & Robin* [2005]. Son application aux roches magmatiques est maintenant classique [*Launeau & Cruden*, 1998; *Archanjo et al.*, 2002; *Arbaret & Burg*, 2003; *Launeau et al.*, 2010]. Plus récemment, elle a été aussi appliquée à l'étude des structures magmatiques engendrées par déformation expérimentale [*Arbaret et al.*, 2007; *Picard et al.*, 2013]. Nous rappelons ici les concepts de base de la méthode paramétrique par comptage des intercepts repris à partir de l'analyse détaillée de *Launeau* [1990] et d'une courte synthèse rédigée par *Arbaret* [1995].

La méthode des intercepts consiste à compter le nombre d'entrées/sorties dans une phase selon une direction donnée (Figure V-8a ; *Launeau & Bouchez* [1992]). L'exploration de

l'image se fait à l'aide d'une trame tournante sur 360°. A chaque pas de rotation angulaire de cette trame, noté Δα, l'image est balayée par un ensemble de droites parallèles (grille de comptage), également espacées d'une distance *i*. L'analyse par comptage des intercepts couvre ainsi une surface d'exploration formant un disque centré sur l'image et d'un diamètre égal au plus petit côté de l'image. La rose des traversées qui en résulte possède une direction d'allongement parallèle à la direction du compte minimum d'intercepts (Figure V-8b). Cette méthode permet d'obtenir la direction moyenne d'orientation préférentielle de la phase et non celle des agrégats (Figure V-9; *Launeau & Cruden* [1998]).

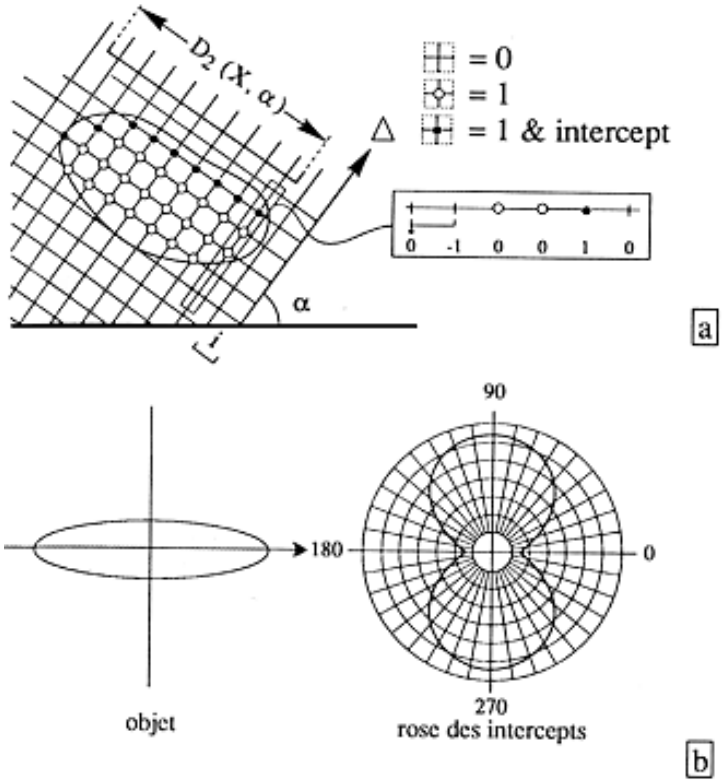

Figure V-8: *construction d'Euler-Poincaré, d'après Coster & Chermant* [1991]. *(a): soit une maille de côté i, constituée de droites d'analyse orthogonales de direction D et d'angle α, un nœud de la maille vaut 1 s'il recouvre la phase X (en gris) et 0 sinon. A(X, α) est le nombre de points comptés valant 1, multiplié par i. En encadré: un intercept est compté sur la direction D si la différence entre un point d'une droite d'analyse et son suivant vaut 1. D (X, α) est la projection de X suivant D: c'est le nombre d'intercepts multiplié par la distance i. (b): la représentation polaire des projections d'un objet suivant toutes les directions du plan donne la rose des intercepts* [*Launeau & Bouchez*, 1992].

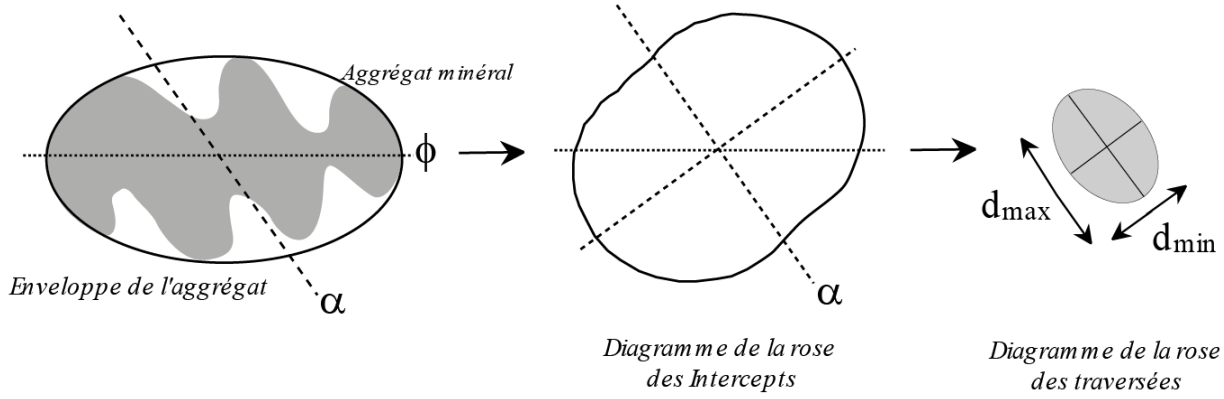

Figure V-9: *relations entre la forme d'un agrégat minéral arbitraire, la rose des intercepts et la rose des traversées produites par la méthode du comptage des intercepts. Notez que cette méthode est sensible à la convexité de l'objet (soit la direction α), alors que d'autres méthodes telles que les tenseurs d'inertie sont sensibles à la forme globale de l'objet (soit la direction ϕ) [Arbaret, 1995].*

La direction moyenne α de l'OPF d'une phase est calculée par la détermination des axes de symétrie donnés par les vecteurs propres de la matrice de dispersion des cosinus directeurs de la rose des intercepts :

$$MM = \begin{pmatrix} \sum \cos^2 & \sum \cos\sin \\ \sum \cos\sin & \sum \sin^2 \end{pmatrix}$$

Où n est le compte total des intercepts et nα est le compte d'intercepts sur la direction α. L'intensité moyenne de l'OPF d'une phase est calculée à partir de l'ellipticité *Ie* de la rose des intercepts tel que :

$$IIII = 1 - \frac{1}{SSRR}$$

Avec SR correspondant à l'intensité de l'anisotropie de la phase (équations et calcul du degré de dispersion angulaire des directions d'allongement des objets d'après *Launeau* [1990]). *Ie* fournit le rapport de forme de l'objet moyen représentatif de la population analysée.

Fabriques de forme 2D locales au sein de suspensions magmatiques

Dans le cadre de nos expériences, la méthode par comptage des intercepts est principalement employée pour déterminer de possibles variations spatiales dans la fabrique minérale bidimensionnelle au travers des sections [xz] d'échantillons déformées en torsion. A l'aide du logiciel Intercepts2003, il est en effet possible de segmenter et analyser des images en niveau de gris pour en quantifier localement les fabriques de forme sur une population d'objets se composant de diverses phases, tels les minéraux ferromagnésiens ou les feldspaths. Pour ce faire, le procédé menant à une représentation cartographique de fabriques minérales locales se décompose en plusieurs étapes successives, résumées sur la Figure V-10.

Les phases dites d'intérêt, mises en évidences sur les clichés MEB bruts (Figure V-10a) ou d'un ensemble de clichés photomontés, sont au préalable isolées en jouant sur le seuillage de couleur ou de contraste via des logiciels d'imagerie numérique (Photoshop™, Image J). Les images qui en résultent (Figure V-10b) sont ensuite virtuellement découpées en plusieurs imagettes sous le logiciel Intercepts2003 ; chaque imagette recouvrant de moitié ses voisines dans les directions X et Z. Pour le comptage des intercepts, le pas angulaire Δα et l'interligne *i* peuvent être prédéfinis par l'utilisateur du logiciel, et donc adaptables à chaque section d'étude. Après calcul, une ellipse tensorielle de la fabrique de forme est attribuée à chaque imagette, représentée en bleu sur la Figure V-10b. Les ellipses locales obtenues, dans ce cas-ci 8x3 ellipses, sont alors caractérisées par leur axe long (en jaune), leur axe court (en violet) et leur excentricité. Dans un souci de clarté, ce type de représentation cartographique ne sera pas adopté. Les directions d'allongement locales de chaque ellipse seront de préférence symbolisées par des doubles flèches blanches et placées au-dessus d'une carte de l'excentricité *Ie* des ellipses tensorielles locales (ou intensité de l'OPF) calculée par krigeage (Figure V-10c), à l'instar de ce qui a été déjà proposé par *Arbaret et al.* [2007].

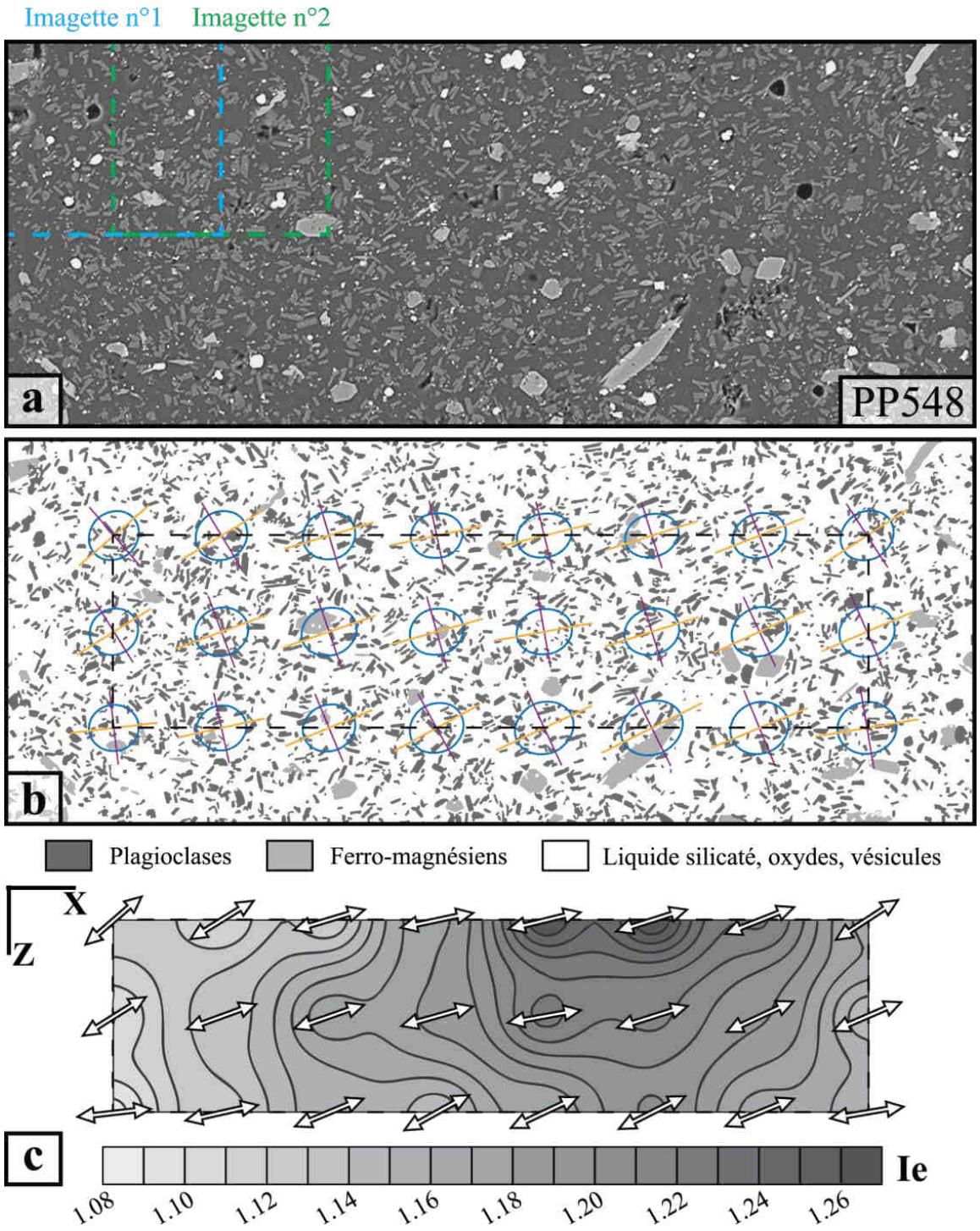

Figure V-10: *(a) cliché MEB d'une section [xz] d'un échantillon déformé (PP548) sur lequel il est affiché la taille d'une imagette définie sous le logiciel Intercepts2003; l'imagette recouvrant de moitié sa voisine. (b) Image MEB seuillée en niveau de gris (chaque niveau de gris représente une phase d'intérêt pour l'étude) sur laquelle les ellipses tensorielles locales (découpage en 8x3 imagettes) sont superposées. Sur cet exemple de comptage d'intercepts, le pas angulaire est Δα=9° et l'interligne i=4 pixels. Le rectangle noir en pointillé délimite la zone utilisée pour la carte (c) de l'intensité moyenne Ie des OPFs locales du groupement d'objets analysés (plagioclases + ferromagnésiens). Cette carte est calculée par méthode de krigeage. Les directions moyennes α des OPFs locales de chaque imagette sont représentées par une double flèche blanche. Représentation cartographique basée sur le travail de Arbaret et al. [2007].*

2. Matériaux de départ & synthèses expérimentales

Afin d'évaluer les vecteurs de localisation de la déformation au sein de magmas silicatés en cours de la cristallisation, nous avons décidé de synthétiser des suspensions magmatiques de diverses fractions cristallines dont les associations minéralogiques sont, autant que possible, proches de systèmes naturels. Pour ce faire, les charges expérimentales ont consisté en une poudre de roche naturelle anhydre et les verres de départ ont été hydratés pour reproduire, à l'image de compositions naturelles, des phases cristallines hydroxylées (par exemple, biotites et amphiboles). Dans ce qui suit, les principales caractéristiques des matériaux de départ (pétrographie et conditions *P-T* de cristallisation) sont dans un premier temps détaillées. Dans un second temps, le protocole de synthèse des suspensions magmatiques sera abordé, depuis la préparation des charges expérimentales jusqu'aux résultats de tests expérimentaux. Les textures et compositions chimiques des produits de synthèse destinés aux expériences de déformation en torsion seront enfin précisées.

2.1. Caractérisation des matériaux de départ

2.1.1. Pétrographie

Les matériaux de départ sont dans leur intégralité issus du corps intrusif de Serifos (Cyclades, Grèce ; Figure V-11). Situé au cœur du dôme métamorphique, ce corps magmatique est pour rappel (cf. chapitre III) apparenté à une granodiorite présentant une paragenèse classique à quartz, feldspaths plagioclase et alcalin, biotite et amphibole principalement (Figure V-12a). Des minéraux accessoires tels que la titanite, l'épidote (allanite) ou encore des oxydes complètent la liste.

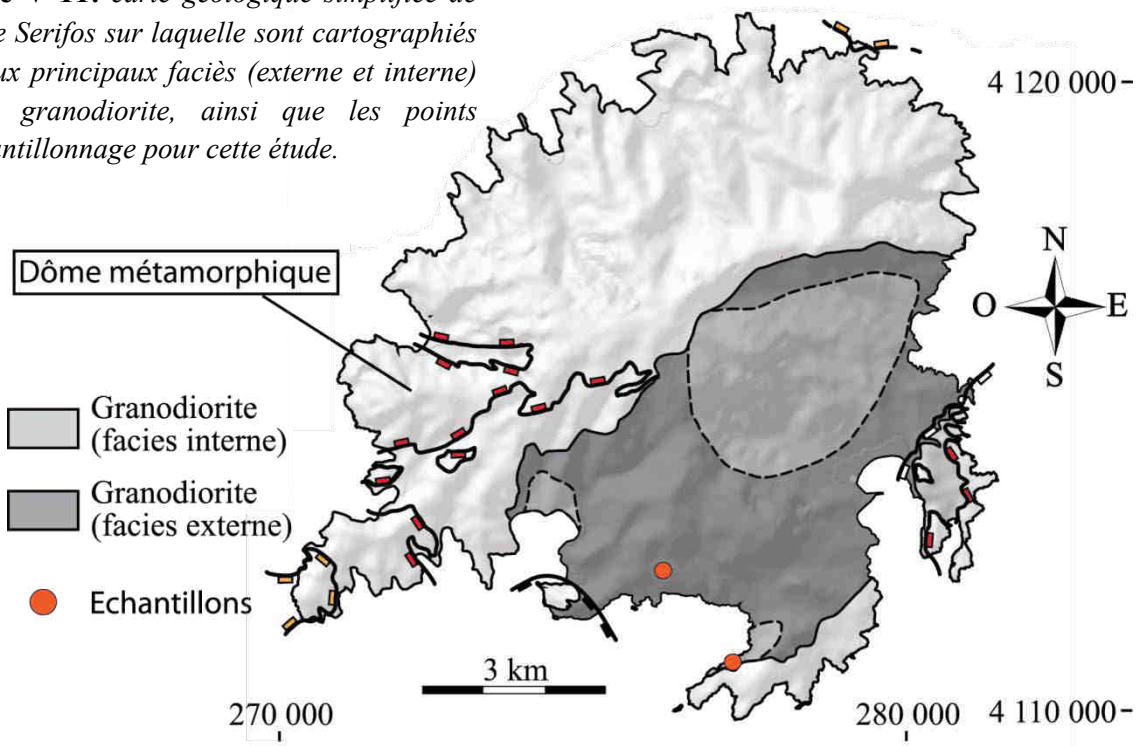

Figure V-11: *carte géologique simplifiée de l'île de Serifos sur laquelle sont cartographiés les deux principaux faciès (externe et interne) de la granodiorite, ainsi que les points d'échantillonnage pour cette étude.*

Cette granodiorite a par ailleurs fait l'objet d'un certain nombre d'investigations pétrographiques [*Altherr et al.*, 1982; *Salemink*, 1985; *Stouraiti & Mitropoulos*, 1999; *Altherr & Siebel*, 2002; *Iglseder et al.*, 2009; *St. Seymour et al.*, 2009; *Bolhar et al.*, 2010; *Stouraiti et al.*, 2010]. Sur la base d'une étude de terrain, *Salemink* [1985] cartographia notamment un corps magmatique texturalement zoné en différenciant ainsi deux principaux faciès, dits externe et interne. Les différentes campagnes de terrain ont permis de collecter un ensemble d'échantillons provenant de ces deux faciès pétrographiques. La Figure V-11 localise les deux échantillons sélectionnés pour la synthèse de suspensions magmatiques (échantillon du faciès externe : 4112235°N, 276058°E ; échantillon du faciès interne : 4110680°N, 277214°E ; les coordonnées GPS sont données en UTM zone 35°N, WGS 1984). Le faciès externe, constituant la majeure partie du corps intrusif, se distingue à l'affleurement par sa teinte leucocrate et sa texture hétérogranulaire, mis en exergue par ses agrégats de biotites de taille plurimillimétrique (> 5mm) au sein d'une matrice à grain relativement moyen (Figure V-12b). Le faciès interne, quant à lui, se démarque macroscopiquement par une teinte mésocrate, une couleur gris-bleu bien reconnaissable et sa texture équigranulaire à grains fins (< 2-3 mm, Figure V-12c).

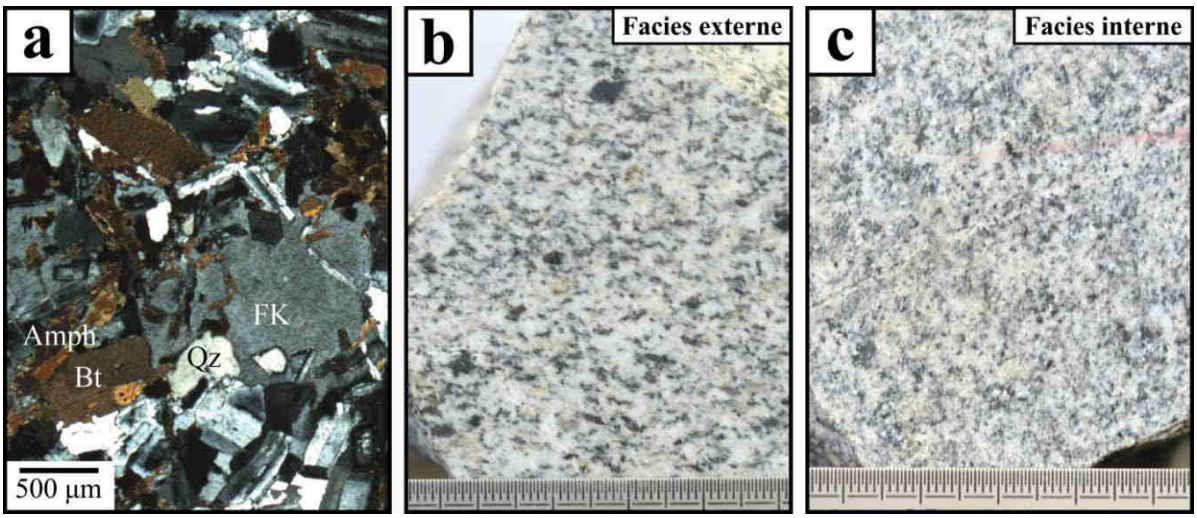

Figure V-12: *(a) vue au microscope de l'association minéralogique de la granodiorite de Serifos (faciès interne). Les clichés (b) et (c) correspondent aux échantillons macroscopiques sélectionnés pour l'étude.*

Outre ces dissemblances texturales, les analyses modales ont également souligné une subtile divergence entre ces deux faciès [*Le Breton & Pons*, non publié]. Les proportions modales des deux faciès sont projetés dans le diagramme QAP (Quartz, feldspaths Alcalins et Plagioclases) de *Streckeisen* [1976] (Figure V-13a). Sept échantillons se rapportent au faciès externe à grain grossier, les dix autres au faciès interne à grain fin. Au-delà de l'homogénéité compositionnelle déjà illustrée par des études antérieures, l'analyse modale de *Le Breton & Pons* soulève le caractère moins felsique du faciès interne, avec pour caractéristique majeure une proportion relative en plagioclase légèrement supérieure. De même, cette bimodalité compositionnelle se retranscrit par les analyses sur roche totale. Deux compositions chimiques représentatives des deux faciès, normalisées à 100% pds d'oxydes, sont données Figure V-13b, montrant entre autre une fraction massique en SiO_2 légèrement inférieure pour le faciès interne.

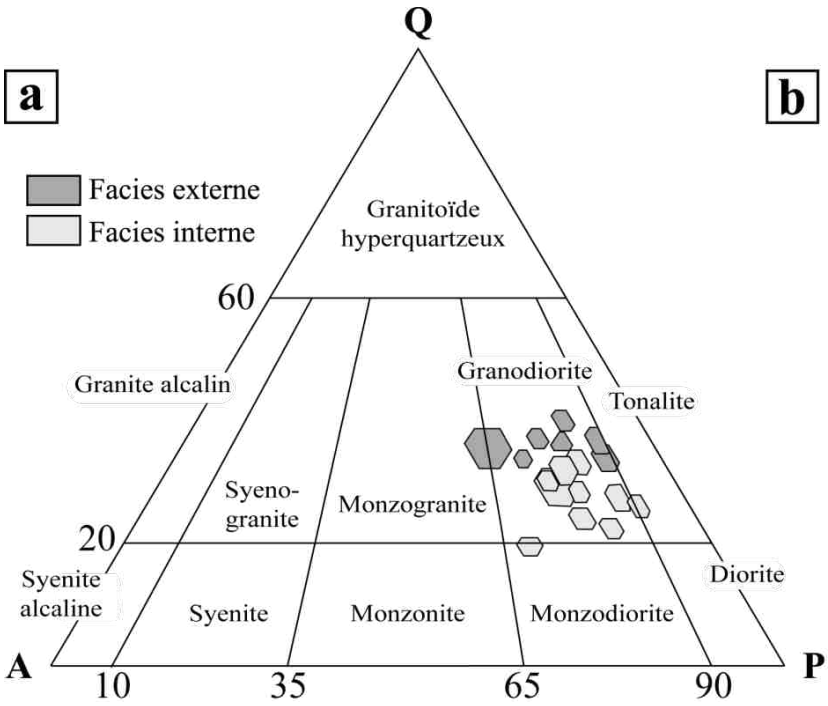

b

Oxyde	FE	FI
SiO2	68,14	65,95
Al2O3	15,48	16,94
FeO tot	3,85	3,48
MnO	0,03	0,05
MgO	1,52	1,88
CaO	4,13	4,12
Na2O	3,46	4,49
K2O	2,71	2,52
TiO2	0,69	0,56
total	100	100
	(% pds)	(% pds)

Figure V-13: *(a) compositions modales des faciès externe et interne de la granodiorite de Serifos, reportées dans le diagramme de Streckeisen (quartz, feldspaths alcalin et plagioclase). (b) compositions chimiques (en % poids d'oxydes) sur roche totale de deux échantillons représentatifs des faciès externe et interne. Abréviations : FE (Faciès externe), FI (Faciès interne).*

2.1.2. Contraintes sur les conditions de mise en place

Quelques précédentes études géobarométriques et thermométriques ont estimé les conditions de mise en place de la granodiorite de Serifos. En appliquant la calibration barométrique Al-in-hornblende de *Schmidt* [1992] et celle thermométrique de *Vyhnal et al.* [1991], *St. Seymour et al.* [2009] ont évalué une cristallisation du cœur d'amphiboles calciques aux alentours de 310 ± 60 MPa pour des températures allant de 748°C et 718°C, respectivement. Une pression de 90 ± 60 MPa a également été calculée pour les bordures de ces mêmes amphiboles, témoignant d'une certaine complexité dans l'histoire de mise en place de ce corps magmatique. Ces dernières valeurs sont en accord avec les estimations de *Stouraiti & Mitropoulos* [1999]. Ces auteurs ont en effet déterminé, à l'aide de la même calibration barométrique, des pressions de cristallisation de bordures d'amphiboles allant de 30 à 170 MPa. Bien que la sensibilité de ce géobaromètre face à la température induise généralement des barres d'erreurs conséquentes, ces conditions de mise en place nous donnent des fenêtres de pression et température dans lesquelles les suspensions magmatiques devront être synthétisées.

2.2. Préparation des charges expérimentales

La synthèse de suspensions magmatiques hydratées nécessite avant tout de maîtriser la concentration en eau introduite dans les charges expérimentales. Il convient à cet effet d'extraire les volatiles contenus dans les phases hydroxylées des roches naturelles en réalisant

une double fusion à pression atmosphérique. Ces fusions successives, portant les matériaux de départ à 1200°C pendant deux heures, ont également l'avantage d'homogénéiser la composition des produits fondus. L'homogénéité des verres anhydres obtenus est généralement vérifiée par analyse chimique ponctuelle à la microsonde électronique. Un broyage automatique et manuel des verres est par la suite réalisé, jusqu'à atteindre une fine poudre dont la granulométrie est inférieure à 50 µm. Cette taille granulométrique maximise la quantité de poudre anhydre pouvant être introduite dans les capsules en or, métal employé dans ce cas présent pour son inertie chimique. Deux types de capsules ont été utilisées: des capsules filiformes pour des synthèses tests (Figure V-14a) et des capsules en « boite de conserve » précédemment évoquées et conditionnées pour les expériences en Paterson (Figure V-14b). Les dimensions des capsules filiformes (2.9 mm de diamètre et 20 mm de longueur) sont ainsi conçues pour être insérées en série dans l'autoclave à chauffage interne. Une unique expérience permettra alors de faire varier un paramètre, telle que la teneur en eau, pour diverses charges expérimentales.

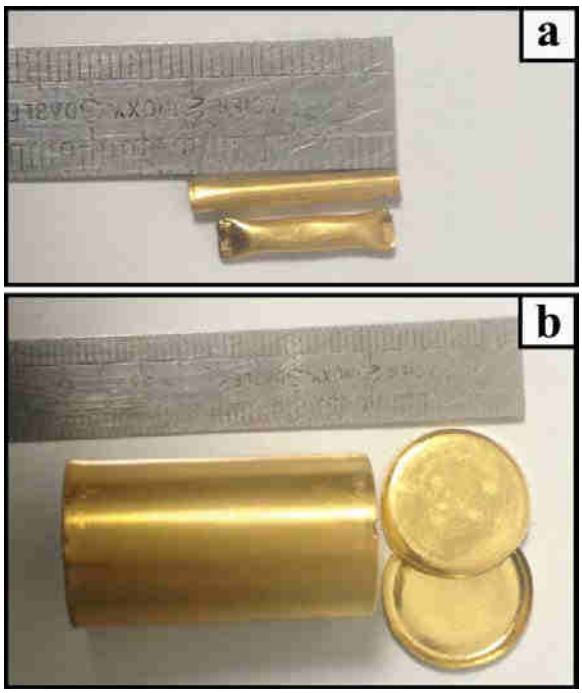

Figure V-14: *capsules (Au) utilisées au cours des expériences de synthèse. (a) Capsules filiformes pour les synthèses tests. (b) Capsule en « boite de conserve » et chapeaux associés pour la synthèse de suspensions magmatiques destinées aux expériences en presse Paterson.*

Quel que soit le type de capsule utilisé, de l'eau déminéralisée est dans un premier temps ajoutée au fond des capsules au moyen d'une micro-seringue. La poudre anhydre n'est qu'ensuite chargée, puis l'ensemble est refermé hermétiquement par soudure au point. Afin de calculer la quantité précise d'eau introduite et éventuellement détecter une perte de masse après soudure, chaque étape de la préparation est soumise à la pesée à l'aide d'une balance de précision. La capsule soudée est enfin placée à l'étuve à 120°C durant plusieurs jours, de sorte à homogénéiser la distribution de l'eau dans la totalité de la charge et s'assurer, par une vérification régulière de la masse, de la bonne étanchéité de la capsule.

2.3. Synthèses de suspensions magmatiques : tests expérimentaux

2.3.1. Stratégie & notions fondamentales

Pour l'étude de déformation de suspensions magmatiques dans la presse Paterson, il convient de disposer de textures initiales propices à l'observation de fabriques de forme et microstructures par images MEB. Une texture adéquate sous-entend principalement d'obtenir des produits de synthèse présentant des tailles de cristaux suffisamment larges (> 5-10 µm). Pour respecter ce dernier point, une série d'expériences tests ont été réalisées; le principal

objectif étant de minimiser sous l'effet d'un certain nombre de paramètres la quantité de germes cristallins (ou nuclei) pour, à l'inverse, induire des taux de croissance élevés. Ces taux de croissance et nucléation dans les magmas siliceux sont grandement influencés par la teneur en eau dissoute, la composition chimique du liquide silicaté, la nature de l'espèce minérale et sa place dans la séquence de cristallisation, ou encore le sous-refroidissement [e.g., *Kirkpatrick*, 1975; *Fenn*, 1977; *Swanson*, 1977]. Le sous-refroidissement ΔT (°C), ou « undercooling » en anglais, n'est autre que l'écart entre la température au liquidus (à savoir, la température minimale à laquelle les cristaux sont absents) et la température d'équilibre à laquelle cristallise une phase minérale. Un exemple de relation entre degré de sous-refroidissement et cinétiques de cristallisation est donné Figure V-15 pour un bain silicaté de composition granodioritique incluant 6.5% pds d'eau en solution [*Swanson*, 1977].

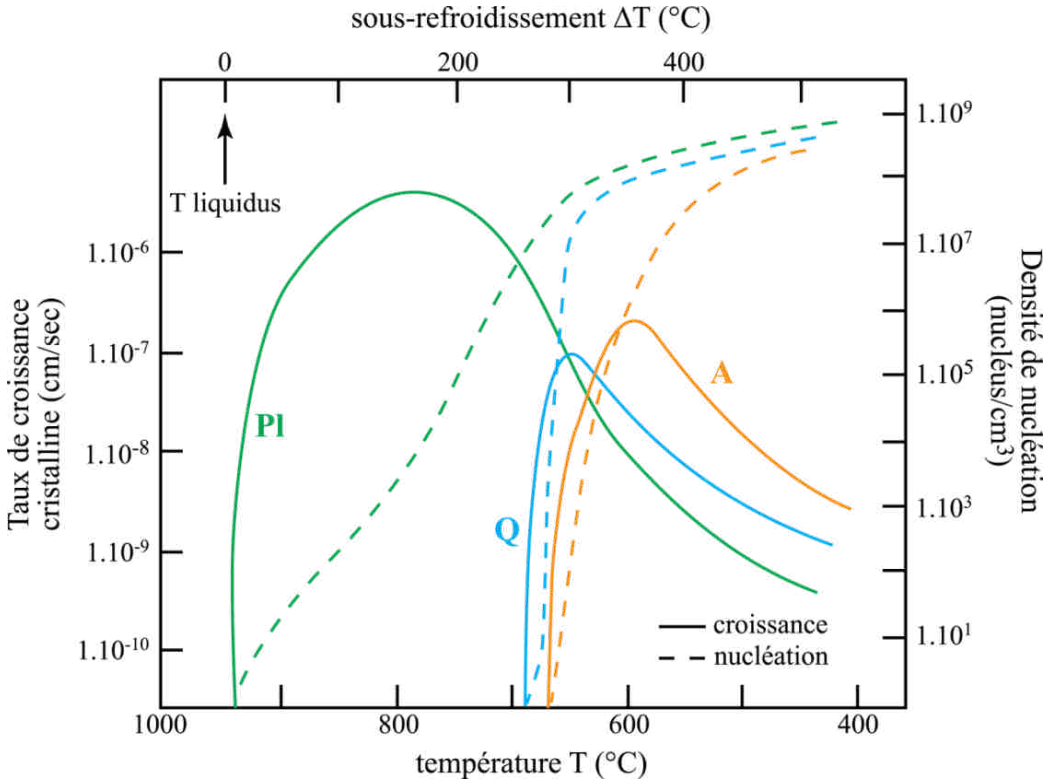

Figure V-15: *évolution du taux de nucléation et croissance de différentes espèces minérales en fonction du sous-refroidissement, pour un liquide silicaté de composition granodioritique (teneur en H_2O = 6,5%), d'après Swanson [1977]. Quelle que soit l'espèce, le pic de nucléation intervient toujours après le pic de croissance. Abréviations : Pl (Plagioclase), Q (Quartz), A (Feldspath alcalin).*

En général, le taux de croissance de cristaux évolue avec le sous-refroidissement selon une courbe en cloche dissymétrique. Pour une espèce minérale donnée, il apparaît ainsi que la vitesse de croissance soit à son pic pour de très faibles sous-refroidissements. Le phénomène de croissance cristalline tendra alors à s'annuler pour un degré de sous-refroidissement important. Avec la diminution de la température au sein du système et par conséquent l'augmentation de la viscosité du liquide silicaté, le transport des atomes est en effet retardé et le taux de croissance s'en retrouve ralentit. En parallèle, la présence de volatils en solution tels que l'eau peut abaisser la viscosité du liquide en endossant le rôle de dépolymérisateur de

réseau [*Dingwell et al.*, 1996; *Hess & Dingwell*, 1996], favorisant une meilleure efficacité dans la diffusion atomique et ainsi une vitesse de croissance plus élevée. A l'inverse, le taux de nucléation atteindra son maximum selon une asymptote à l'approche de l'eutectique. Ce décalage des « pics » de vitesse entre croissance et nucléation cristalline est d'autant plus flagrant pour les espèces minérales se développant précocement dans la séquence de cristallisation, tels les plagioclases dans le cas d'une composition granodioritique (Figure V-15). Il est à noter que ces précédentes considérations s'appliquent dans le cas où la nucléation est homogène, c'est-à-dire que les nuclei apparaissent aléatoirement dans le liquide. La nucléation cristalline est en réalité le plus souvent hétérogène au sein de systèmes magmatiques ouverts et activée préférentiellement au contact de sites préexistants (e.g., cristal hôte, bulles, défauts cristallins, impuretés) [e.g., *Ikeda et al.*, 2002; *Jerram et al.*, 2003; *Špillar & Dolejš*, 2015]. Par ailleurs, dans un contexte de magmatisme intrusif, il est admis que l'effet de la vitesse de refroidissement n'influence généralement que très peu les taux de nucléation et de croissance, dans la mesure où le refroidissement de corps plutoniques s'étend sur une durée beaucoup plus longue que les temps caractéristiques liés aux processus de nucléation et croissance cristalline. Il est évident qu'en pétrologie expérimentale, ces temps caractéristiques ne peuvent être atteints. La vitesse de refroidissement – lorsqu'elle est appliquée à une expérience – joue alors un rôle important dans les cinétiques de cristallisation et la morphologie des phases cristallisées [e.g., *Lofgren*, 1974; *Corrigan*, 1982; *Pupier et al.*, 2008]. En d'autres termes, les taux de nucléation et croissance cristalline dépendront fortement du temps de résidence d'un magma à une température de sous-refroidissement donnée. A titre d'exemple, avec l'effet d'un refroidissement isobarique rapide, les cristaux seront de taille limitée et généralement non automorphes. Dans le cas le plus violent, aucun minéral ne cristallisera, d'où la méthode de trempe rapide ou isobare classiquement adoptée pour la fin d'expériences en autoclave (cf. section 1.1.1.).

En résumé, pour parvenir aux tailles cristallines nécessaires à l'observation de potentielles OPFs et microstructures au sein de suspensions déformées, les effets de la concentration en eau dissoute dans les verres silicatés et d'une rampe de refroidissement ont été testés. Mentionnons qu'à ce stade, seule la caractérisation texturale qualitative semble pertinente. C'est la raison pour laquelle les analyses chimiques quantitatives et les proportions modales des verres silicatés et phases minérales en présence ne seront pas discutées dans cette section. De façon à respecter dans la mesure du possible les conditions dans lesquelles le corps magmatique de Serifos s'est mis en place, une pression de confinement de 300 MPa est appliquée pour l'intégralité des expériences tests, mais aussi pour le reste de l'étude.

2.3.2. Test expérimental n°1 en condition statique : effet de la teneur en eau

Cette première série de synthèse se propose d'étudier l'effet de la concentration en eau sur la croissance cristalline à partir des compositions du faciès interne et externe de la granodiorite. L'expérience a été menée dans des conditions statiques (800°C, 300 MPa) pour une durée totale de 8 jours. Diverses concentrations en eau ont été testées pour chaque composition, allant de 2 à 4% pds. Les textures obtenues pour chaque produit synthétisé sont reportées Figure V-16.

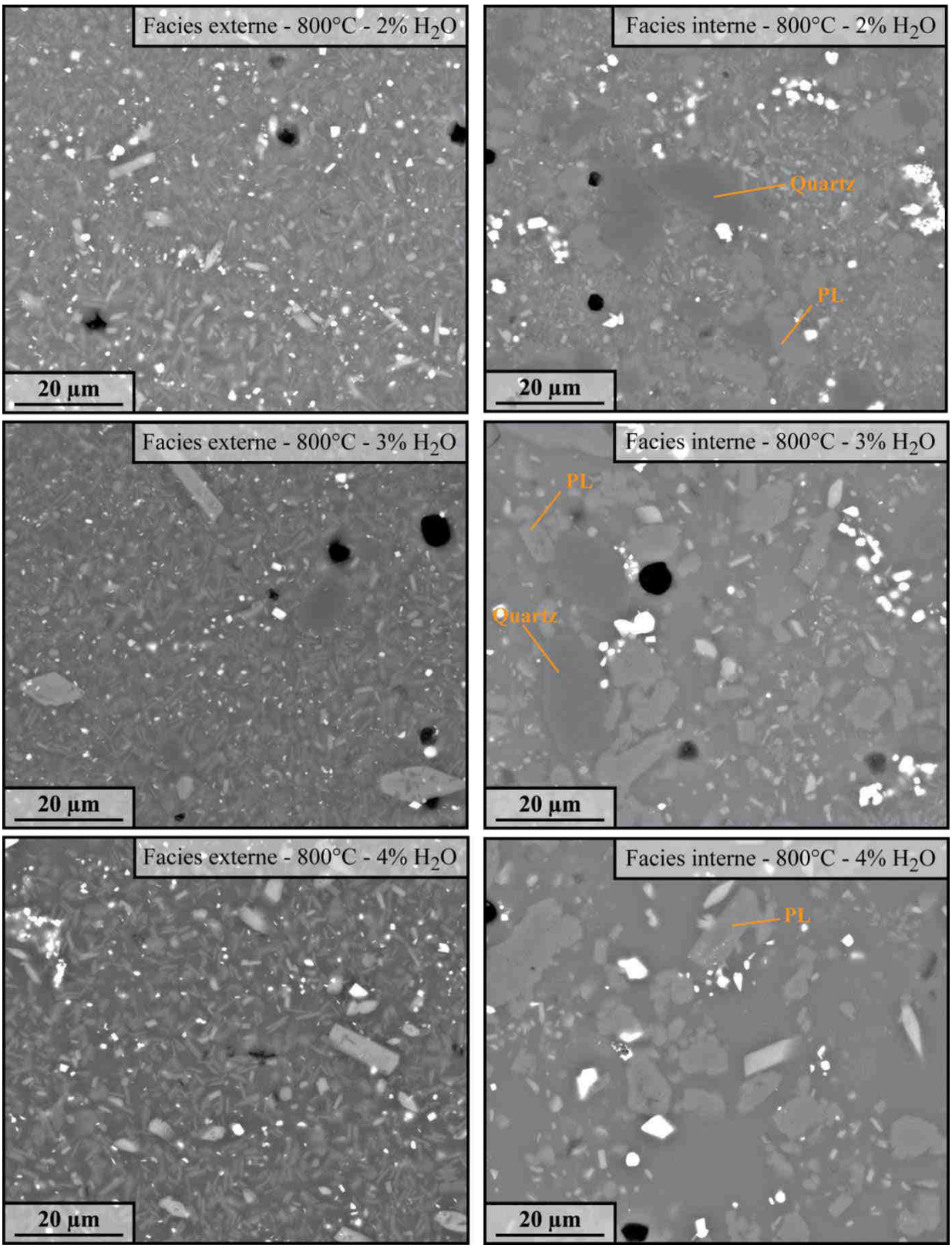

Figure V-16: *clichés MEB des produits de synthèse (faciès interne et externe) de l'expérience test n°1 en condition statique (800°C, 300 MPa), pour différentes concentration en eau (2,3 et 4% pds). La résolution des images est identique pour chaque cliché. PL : feldspath plagioclase.*

L'assemblage minéralogique, déterminée brièvement par analyse semi-quantitative au MEB (méthode *EDS* pour Energy Dispersive Spectroscopy), s'avère être similaire aux deux

compositions de départ. Quelle que soit la quantité d'eau introduite dans les capsules, une association de plagioclases, biotites, amphiboles, pyroxènes et oxydes est principalement retrouvée. Le quartz, reconnaissable par sa teinte de couleur proche du liquide silicaté, n'apparait que dans les produits à 2 et 3% pds H_2O. Par ailleurs, il apparait clairement à travers les clichés pris au MEB que les textures microporphyriques observées pour la composition du faciès interne se singularisent de celles du faciès externe par une distribution de taille des cristaux bien plus hétérogène. Ces tailles varient en effet de quelques micromètres à plusieurs dizaines de micromètres pour la suspension magmatique contenant 4% pds H_2O, dans laquelle la quantité de cristaux micrométriques est significativement réduite. Avec une gamme de taille de cristaux plus restreinte, les suspensions magmatiques du faciès externe ne présentent à l'inverse que très peu d'espèces minérales de taille supérieure à 20 µm. La longueur des axes longs des plagioclases tabulaires sont par exemple très limités, ne dépassant que rarement les 5 µm. D'autre part, l'augmentation de la teneur en eau de 2% pds semble avoir un impact très modeste sur la croissance cristalline. En somme, que ce soit pour les synthèses réalisées à partir du faciès interne ou externe, les textures obtenues en conditions de température constante ne sont pas adaptées pour la déformation de suspensions magmatiques.

2.3.3. Test expérimental n°2 en condition dynamique

Suite à cette première série de synthèses peu concluante, nous avons décidé pour ce second test d'intégrer, en plus de l'impact de la concentration en eau, l'effet d'un refroidissement sur la taille et la morphologie des phases cristallisées. Pour ce faire, l'expérience est segmentée en trois phases principales (cf. Figure V-2, section 1.1.1. pour le principe). Dans un premier temps, les charges expérimentales sont portées à haute température et 300 MPa pendant 24h; le but étant d'amener les produits de départ dans des conditions supra-liquidus. A défaut d'avoir déterminé la température de cristallisation des phases primaires pour chaque verre hydraté, une température de 1000°C a été fixée, soit légèrement en deçà du point de fusion de l'or des capsules (1060°C). Au-delà du temps imparti de 24h, une chute de température est initiée jusqu'à atteindre la température voulue de 800°C, tandis que la pression de confinement de 300 MPa demeure constante. Dans le cadre de cette expérience, une rampe de refroidissement programmée de 0.02°C/min est imposée, soit une durée du second segment de 7 jours environ. Les conditions de pression et température de la dernière phase sont enfin gardées à un état stationnaire sur une durée totale de 8 autres jours.

Seuls les produits de départ à 3 et 4% pds H_2O ont été retenus pour cette série. Les clichés des textures obtenues, à la fois de la composition du faciès externe et interne, sont présentés Figure V-17. En appliquant une baisse progressive de la température, nous pouvons aisément remarquer la nette augmentation de la taille des cristaux, pour un nombre de nuclei très inférieur aux synthèses préalables. Ce constat s'illustre parfaitement par la taille des plagioclases qui, dans le cas des suspensions magmatiques à 3% H_2O, arborent des axes longs moyens de 5-10 µm pour la composition du faciès externe à plusieurs dizaines de micromètres concernant le faciès interne. Les tailles des plagioclases au sein des suspensions contenant en solution 4% pds d'H_2O sont sans doute les plus spectaculaires. Leurs axes longs peuvent en effet atteindre plusieurs centaines de micromètres. Cependant, ces synthèses à 4% H_2O

n'offrent pas de grand intérêt pour la déformation ultérieure de magmas, en raison (1) de la forme aciculaire et squelettique des plagioclases, signe d'une cristallisation en déséquilibre et extrêmement rapide, (2) de la présence d'une orientation préférentielle de forme initiale des cristaux et (3) de la trop forte hétérogénéité dans la distribution de taille des cristaux avec notamment un certain nombre de cristaux inférieur à 10 µm. A *contrario*, les synthèses à 3% H_2O présentent des distributions de taille de cristaux relativement homogènes, tout en proposant des tailles suffisantes pour l'étude des fabriques de forme. Pour une raison arbitraire, uniquement la composition du faciès externe à 3% pds H_2O a été sélectionnée pour les synthèses destinées aux expériences en Paterson.

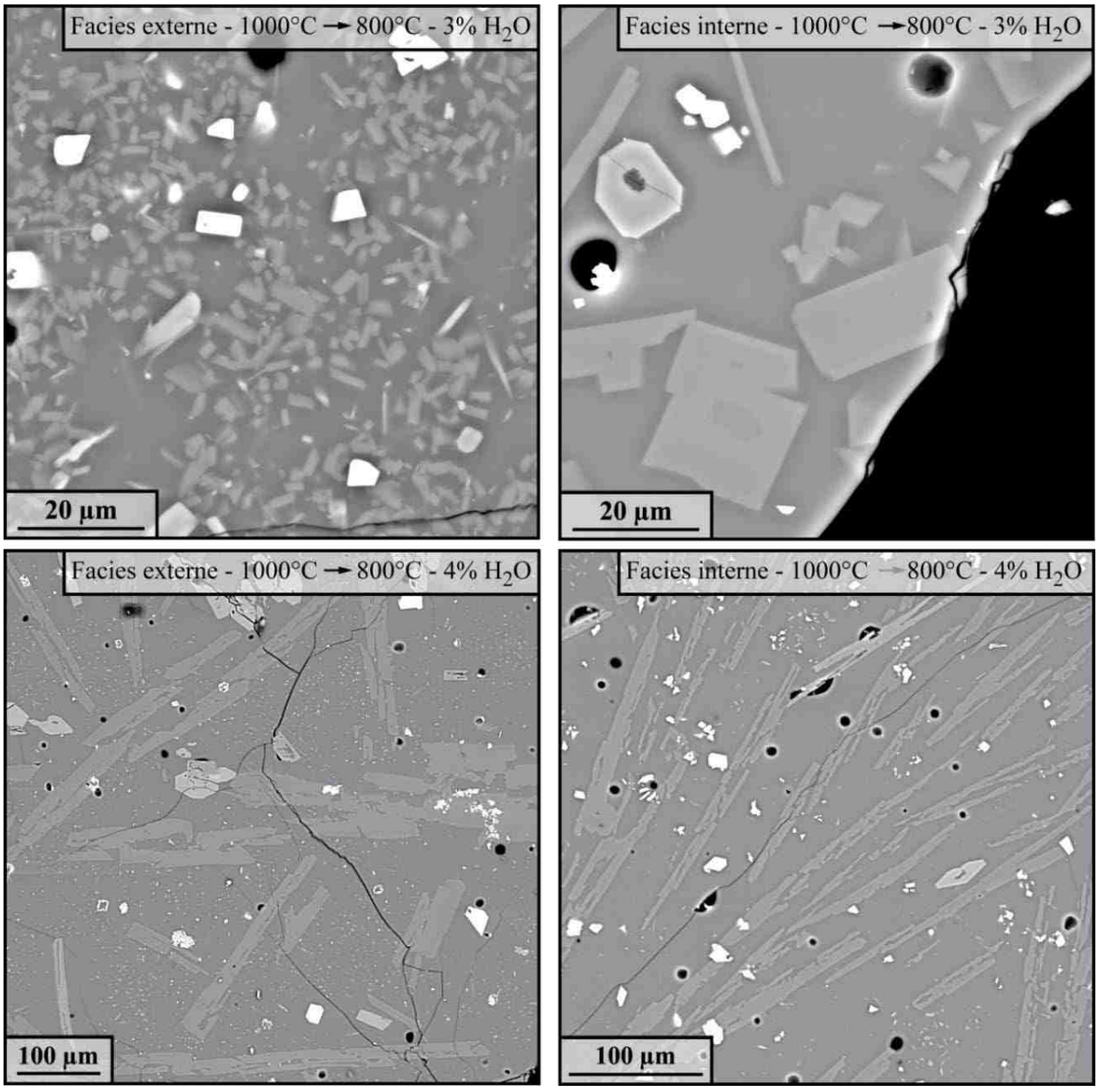

Figure V-17: *Planche photos pris au MEB des produits de synthèse (faciès interne et externe) de l'expérience test n°2 avec chute progressive de la température à pression constante, pour une concentration en eau de 3 et 4% pds. Notez que l'échelle des clichés pour les synthèses à 3% pds H_2O est comparable à celle de la Figure V-16.*

2.4. Textures & chimies des suspensions magmatiques pour la presse Paterson

Sur la base protocolaire du test expérimental n°2, quatre suspensions magmatiques ont été synthétisées à des températures terminales d'expérience de 800, 750, 700 et 650°C, respectivement qualifiées par commodité de langage synthèses #1, #2, #3 et #4. Les conditions expérimentales dans lesquelles les échantillons ont été synthétisés sont résumées dans le Tableau V-1.

Synthèses	H_2O initiale (% pds)	Pression (300 MPa)	Température		
			Plateau 1 (1j)	Rampe de refroidissement (0.02°C/min)	Plateau 2 (8j)
# 1	3	300	1000° C	1000°C → 800°C	800°C
# 2	3	300	1000° C	1000°C → 750°C	750°C
# 3	3	300	1000° C	1000°C → 700°C	700°C
# 4	3	300	1000° C	1000°C → 650°C	650°C

Tableau V-1: *récapitulatif des conditions P, T, t, xH_2O pour les quatre suspensions magmatiques obtenues selon une rampe de refroidissement (0.02°C/min) à pression constante.*

2.4.1. Suspensions magmatiques de faible à moyenne cristallinité

Dans cette section, les principales caractéristiques texturales et compositionnelles des suspensions magmatiques contenant une faible ou moyenne fraction solide sont présentées. Les compositions chimiques du verre de départ anhydre et des verres résiduels hydratés sont reportées sur un diagramme TAS adapté aux roches plutoniques (Total Alkali vs Silica, d'après *Middlemost* [1994], Figure V-18). L'ensemble des analyses chimiques ponctuelles (espèces

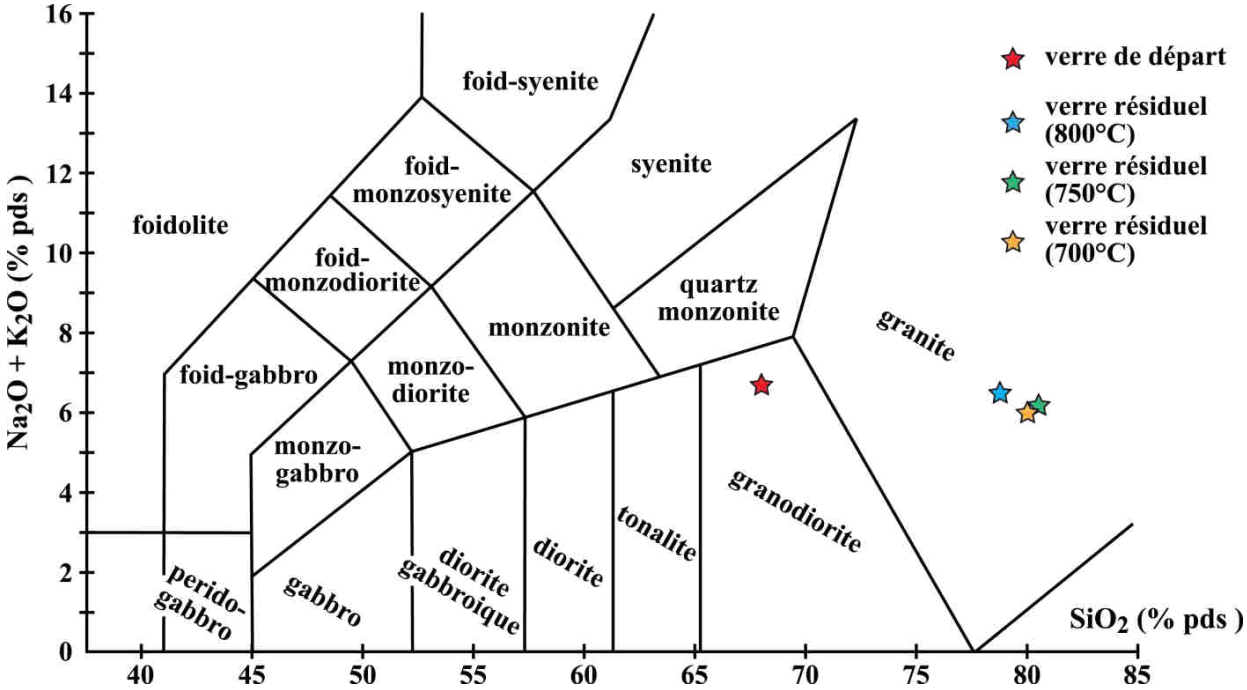

Figure V-18: *classification chimique et nomenclature des roches plutoniques, basées sur le diagramme TAS (Total Alkali vs Silica), d'après Middlemost [1994]. Les compositions du verre de départ anhydre et des verres résiduels y sont reportées.*

minérales + verre silicaté) sont quant à elles récapitulées dans le Tableau V-2. Rappelons aussi que les clichés MEB présentés un peu plus loin ont été pris selon une section basale [xy] d'échantillons cylindriques (cf. Figure V-7, section 1.3.1). C'est pourquoi aucune étude statistique, permettant de détecter d'éventuelles fabriques de forme initiales au sein des diverses suspensions magmatiques, n'a été réalisée. Les dénominations des textures générées sont tirées de *MacKenzie et al.* [1982].

Suspensions magmatiques #1 (800°C ; ϕ_s=0.34)

Les synthèses #1 réalisées à partir de la composition granodioritique du faciès externe (Figure V-18) comportent une paragenèse à plagioclase (labradorite), biotite, amphibole (hornblende magnésienne), pyroxènes (augite-enstatite) et oxydes (Tableau V-2). Le cliché MEB de la synthèse, donné Figure V-19, révèle une texture microporphyrique aphanitique.

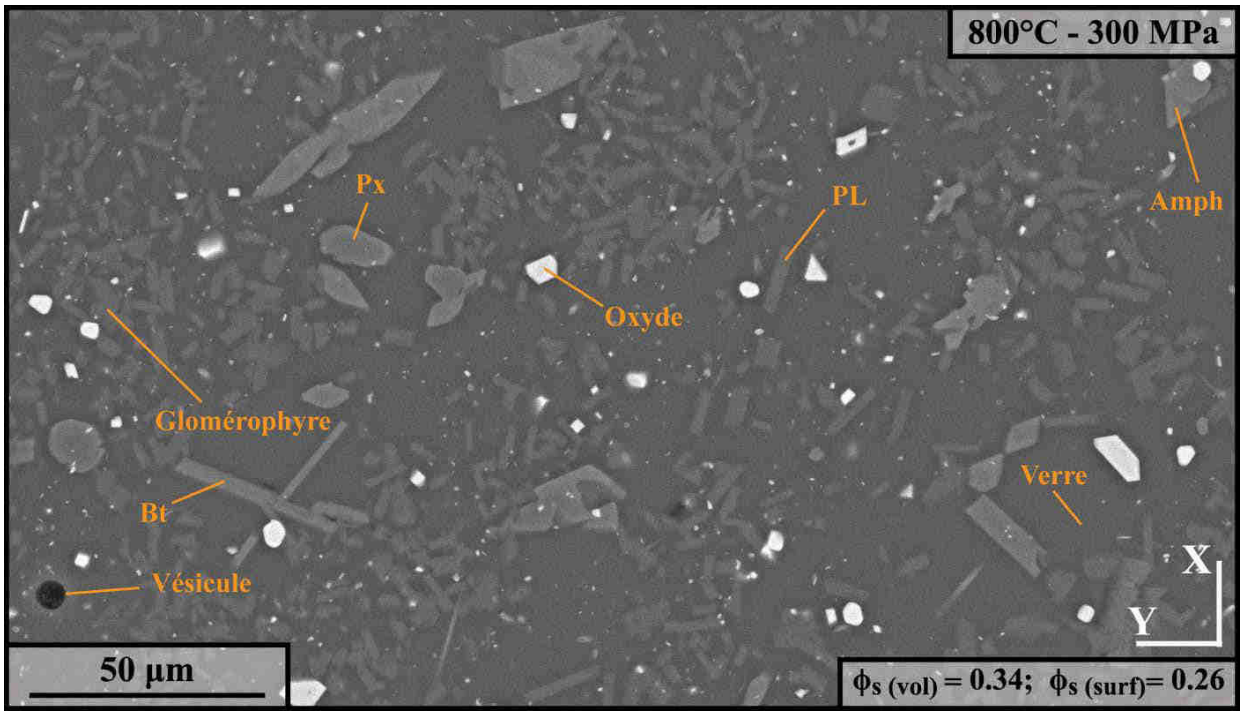

Figure V-19: *cliché MEB de la synthèse #1 réalisée avec une chute de température de 1000 à 800°C. Notez la texture microporphyrique aphanitique présentant localement des glomérophyres plagioclasiques à texture intersertale. Amph : amphibole ; Px : pyroxène ; Bt : biotite ; PL : plagioclase ; ϕ_s(vol) : fraction cristalline volumique. ϕ_s(surf) : fraction cristalline surfacique.*

La taille des cristaux s'échelonne de quelques micromètres (feldspath plagioclase et oxydes) à plusieurs dizaines de micromètres (ferromagnésiens). Le verre interstitiel se caractérise par une composition granitique (SiO_2 = 78.7% pds ± 0.4, Figure V-18 et Tableau V-2) et une teneur en eau dissoute d'environ 3.5 % pds selon la méthode indirecte de la différence à 100%. Par le biais d'un calcul de bilan de masse, il est estimé une proportion volumique en cristaux d'environ 34%. Toutefois, la fraction cristalline surfacique déterminée à partir d'un traitement numérique de la photo MEB avoisine seulement les 26%. Cette disparité dans les estimations du taux de cristallinité peut essentiellement se traduire par (1) une fiabilité

moyenne des analyses chimiques ponctuelles au sein des verres silicatés en raison de la perte en alcalins et/ou (2) une orientation préférentielle de forme développée lors de la synthèse dans la direction de l'allongement de la capsule telle qu'observée dans les synthèses de *Picard* [2009] et/ou (3) une hétérogénéité dans la répartition spatiale des cristaux dans l'ensemble du volume considéré. Au travers de la section [xy] étudiée, la distribution spatiale inhomogène des cristaux se distingue tout particulièrement par la concentration régulière en amas de plagioclases jointifs, constituant ainsi localement des glomérophyres à texture intersertale (Figure V-19). Ne pouvant concrètement déterminer l'origine de cette légère différence de cristallinité entre mesure surfacique et volumique, nous avons opté pour la suite de ce chapitre d'attribuer aux produits expérimentaux #1 la fraction cristalline de 34% vol. obtenue par bilan de masse.

Suspensions magmatiques #2 (750°C ; ϕ_s=0.43)

À l'exception de quartz nouvellement cristallisé, l'association minéralogique des suspensions magmatiques #2 est similaire à celle de la synthèse précédemment décrite (Tableau V-2). Le liquide résiduel, toujours de composition granitique (Figure V-18), voit sa proportion massique en SiO_2 légèrement augmenter (SiO_2 = 80.5% pds ± 0.5), tout comme sa concentration en eau, estimée par différence de masse à ~5.5 % pds. Les suspensions magmatiques #2 se différencient des synthèses #1 par la présence de glomérophyres à texture intergranulaire. Le cliché MEB présenté ci-dessous (Figure V-20) souligne en effet l'apparition d'agglomérats de cristaux cimentés par des feldspaths plagioclase et du quartz.

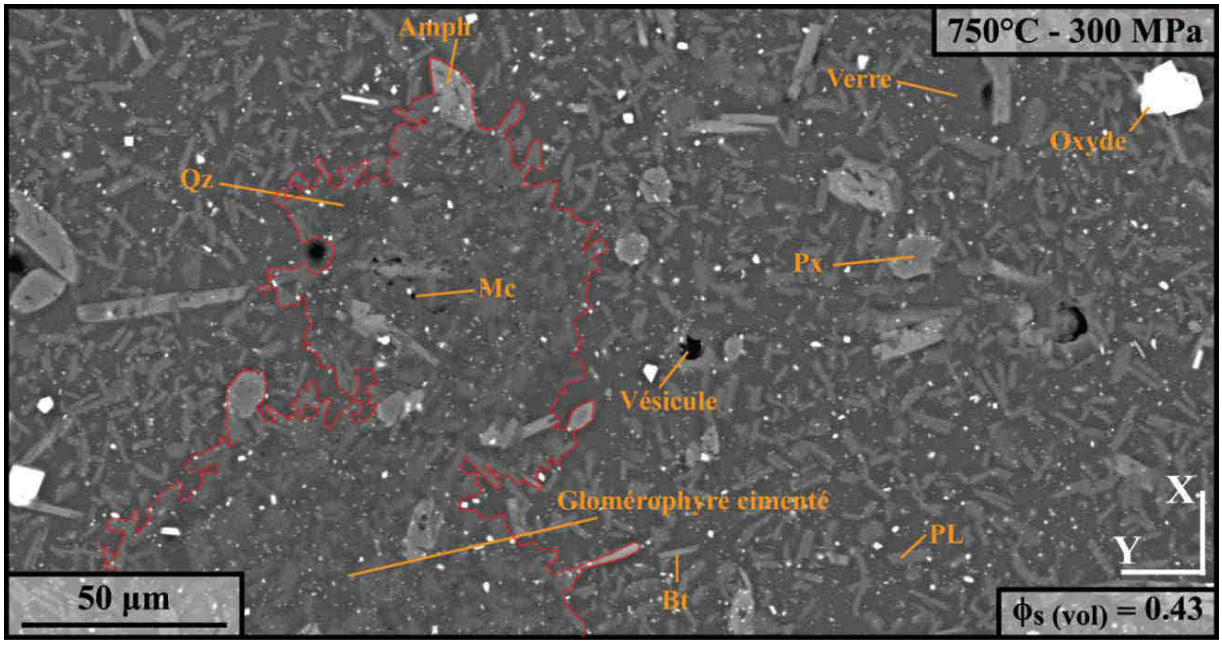

Figure V-20: *cliché MEB de la synthèse #2 réalisée à avec une chute de température de 1000 à 750°C. La suspension magmatique se caractérise par la coexistence de deux textures distinctes : microporphyrique aphanitique et glomérophyrique intergranulaire. La cristallisation de glomérophyres, délimités par un contour rouge, peut aller localement jusqu'à une connectivité cristalline. Px : pyroxène ; Amph : amphibole ; Bt ; biotite ; PL : plagioclase ; Qz : quartz ; Mc : microcavité intercristalline. ϕ_s(vol) : fraction cristalline volumique.*

	SiO_2	σ	TiO_2	σ	Al_2O_3	σ	FeO	σ	MnO	σ	MgO	σ	CaO	σ	Na_2O	σ	K_2O	σ	P_2O_5	σ	Total	H_2O	variété
verre de départ sec	**67,97**	*0,3*	**0,50**	*0,09*	**16,02**	*0,3*	**3,13**	*0,27*	**0,08**	*0,1*	**1,56**	*0,04*	**3,94**	*0,06*	**3,52**	*0,09*	**3,15**	*0,08*	**0,14**	*0,00*	**100**		
Synthèse #1 - 800°C - 300 MPa																							**$\phi_S = 0.34$**
	n	SiO_2	σ	TiO_2	σ	Al_2O_3	σ	FeO	σ	MnO	σ	MgO	σ	CaO	σ	Na_2O	σ	K_2O	σ	P_2O_5	σ	Total	H_2O	variété
Verre	7	**78,71**	*0,44*	**0,20**	*0,16*	**12,24**	*0,18*	**0,94**	*0,24*	**0,01**	*0,02*	**0,18**	*0,01*	**1,01**	*0,06*	**2,19**	*0,13*	**4,30**	*0,14*	**0,21**	*0,13*	**100**	**3,5**	
Plagioclase	8	**54,72**	*0,82*	**0,04**	*0,04*	**27,75**	*0,54*	**0,87**	*0,25*	**0,01**	*0,01*	**0,09**	*0,05*	**11,62**	*0,53*	**4,46**	*0,11*	**0,37**	*0,08*	**0,07**	*0,08*	**100**		**Labradorite**
Biotite	2	**42,78**	*0,31*	**2,51**	*0,19*	**13,42**	*0,01*	**10,45**	*0,21*	**0,14**	*0,06*	**20,87**	*0,38*	**0,15**	*0,17*	**0,58**	*0,06*	**9,05**	*0,18*	**0,05**	*0,06*	**100**	**4,2**	
Amphibole	3	**49,87**	*0,50*	**1,15**	*0,26*	**7,57**	*0,76*	**10,05**	*0,44*	**0,39**	*0,07*	**17,43**	*1,03*	**11,12**	*0,36*	**1,50**	*0,21*	**0,59**	*0,16*	**0,32**	*0,14*	**100**	**2,1**	**Mg-Hornblende**
Pyroxene 1	2	**52,14**	*0,29*	**0,57**	*0,05*	**2,97**	*0,04*	**8,67**	*0,30*	**0,29**	*0,11*	**16,71**	*1,17*	**18,06**	*1,91*	**0,42**	*0,10*	**0,09**	*0,04*	**0,08**	*0,00*	**100**		**Augite**
Pyroxene 2	11	**54,29**	*0,76*	**0,22**	*0,07*	**2,57**	*0,91*	**11,06**	*0,43*	**0,37**	*0,10*	**30,09**	*0,40*	**1,30**	*0,15*	**0,04**	*0,03*	**0,03**	*0,02*	**0,03**	*0,04*	**100**		**Enstatite**
Oxyde 1	4	**0,28**	*0,11*	**3,71**	*0,16*	**1,85**	*0,08*	**91,86**	*0,30*	**0,57**	*0,10*	**1,49**	*0,08*	**0,10**	*0,02*	**0,02**	*0,02*	**0,05**	*0,04*	**0,07**	*0,07*	**100**		**Magnetite**
Oxyde 2	1	**0,32**	*/*	**25,41**	*/*	**0,53**	*/*	**72,21**	*/*	**0,14**	*/*	**1,18**	*/*	**0,17**	*/*	**0,03**	*/*	**0,01**	*/*	**0,00**	*/*	**100**		**Ti-magnetite**
Synthèse #2 - 750°C - 300 MPa																							**$\phi_S = 0.43$**
	n	SiO_2	σ	TiO_2	σ	Al_2O_3	σ	FeO	σ	MnO	σ	MgO	σ	CaO	σ	Na_2O	σ	K_2O	σ	P_2O_5	σ	Total	H_2O	variété
Verre	9	**80,48**	*0,45*	**0,10**	*0,05*	**11,49**	*0,06*	**0,80**	*0,24*	**0,05**	*0,04*	**0,10**	*0,03*	**0,74**	*0,05*	**1,80**	*0,14*	**4,41**	*0,15*	**0,04**	*0,05*	**100**	**5,5**	
Plagioclase	8	**55,42**	*0,87*	**0,07**	*0,05*	**27,18**	*0,54*	**1,03**	*0,12*	**0,00**	*0,01*	**0,06**	*0,02*	**10,80**	*0,50*	**4,97**	*0,16*	**0,43**	*0,11*	**0,04**	*0,07*	**100**		**Labradorite**
Quartz	2	**98,13**	*0,78*	**0,04**	*0,06*	**0,91**	*0,90*	**0,48**	*0,50*	**0,00**	*0,00*	**0,00**	*0,00*	**0,16**	*0,12*	**0,16**	*0,21*	**0,06**	*0,01*	**0,07**	*0,09*	**100**		
Biotite	3	**43,43**	*0,17*	**1,28**	*0,10*	**12,59**	*0,28*	**12,45**	*0,27*	**0,16**	*0,07*	**20,70**	*0,34*	**0,05**	*0,03*	**0,44**	*0,07*	**8,87**	*0,17*	**0,01**	*0,01*	**100**	**4,2**	
Amphibole	4	**50,58**	*0,64*	**0,68**	*0,23*	**6,45**	*0,49*	**12,00**	*0,48*	**0,73**	*0,12*	**16,95**	*0,75*	**10,56**	*0,14*	**1,41**	*0,13*	**0,51**	*0,16*	**0,15**	*0,16*	**100**	**2,1**	**Mg-Hornblende**
Pyroxene 1	2	**51,96**	*2,42*	**0,52**	*0,06*	**4,61**	*0,34*	**7,85**	*0,04*	**0,19**	*0,16*	**14,32**	*1,18*	**19,67**	*1,46*	**0,54**	*0,08*	**0,31**	*0,23*	**0,02**	*0,01*	**100**		**Augite**
Pyroxene 2	8	**54,06**	*0,87*	**0,21**	*0,19*	**2,33**	*0,85*	**10,08**	*0,72*	**0,43**	*0,17*	**31,62**	*0,52*	**1,18**	*0,18*	**0,02**	*0,02*	**0,03**	*0,03*	**0,04**	*0,04*	**100**		**Enstatite**
Oxyde 1	4	**0,18**	*0,06*	**1,85**	*0,16*	**1,28**	*0,11*	**94,99**	*0,24*	**0,70**	*0,07*	**0,80**	*0,06*	**0,09**	*0,02*	**0,01**	*0,01*	**0,09**	*0,02*	**0,02**	*0,01*	**100**		**Magnetite**
Oxyde 2	1	**0,40**	*/*	**18,84**	*/*	**0,41**	*/*	**79,46**	*/*	**0,10**	*/*	**0,49**	*/*	**0,10**	*/*	**0,00**	*/*	**0,20**	*/*	**0,00**	*/*	**100**		**Ti-magnetite**
Synthèse #3 - 700°C - 300 MPa																							**$\phi_S = 0.51$**
	n	SiO_2	σ	TiO_2	σ	Al_2O_3	σ	FeO	σ	MnO	σ	MgO	σ	CaO	σ	Na_2O	σ	K_2O	σ	P_2O_5	σ	Total	H_2O	variété
Verre	7	**79,98**	*0,42*	**0,12**	*0,08*	**12,31**	*0,31*	**0,55**	*0,09*	**0,05**	*0,03*	**0,08**	*0,02*	**0,85**	*0,07*	**1,49**	*0,07*	**4,51**	*0,15*	**0,06**	*0,07*	**100**	**6**	
Plagioclase 1	2	**66,12**	*1,48*	**0,05**	*0,07*	**20,69**	*0,87*	**0,24**	*0,25*	**0,02**	*0,02*	**0,00**	*0,00*	**4,54**	*0,07*	**7,13**	*0,21*	**1,08**	*0,11*	**0,12**	*0,17*	**100**		**Oligoclase**
Plagioclase 2	6	**56,49**	*1,18*	**0,05**	*0,04*	**26,54**	*0,72*	**0,84**	*0,25*	**0,02**	*0,02*	**0,07**	*0,02*	**10,42**	*0,86*	**5,04**	*0,53*	**0,48**	*0,18*	**0,04**	*0,09*	**100**		**Labradorite**
FK	2	**70,43**	*2,72*	**0,03**	*0,04*	**16,04**	*1,50*	**0,25**	*0,01*	**0,01**	*0,01*	**0,01**	*0,01*	**0,38**	*0,01*	**2,52**	*0,10*	**10,33**	*1,12*	**0,00**	*0,01*	**100**		**Sanidine**
Quartz	11	**96,71**	*2,49*	**0,04**	*0,05*	**1,84**	*1,55*	**0,15**	*0,11*	**0,03**	*0,05*	**0,14**	*0,40*	**0,27**	*0,32*	**0,45**	*0,52*	**0,36**	*0,45*	**0,01**	*0,02*	**100**		
Biotite	7	**45,83**	*0,72*	**1,44**	*0,27*	**12,95**	*0,20*	**6,21**	*0,51*	**0,21**	*0,05*	**23,63**	*0,91*	**0,10**	*0,13*	**0,47**	*0,09*	**9,16**	*0,37*	**0,00**	*0,00*	**100**	**4,5**	
Amphibole	10	**50,92**	*1,30*	**0,90**	*0,16*	**7,18**	*0,69*	**6,55**	*0,39*	**0,44**	*0,10*	**20,07**	*0,71*	**11,60**	*0,25*	**1,50**	*0,13*	**0,61**	*0,12*	**0,22**	*0,17*	**100**	**2,1**	**Mg-Hornblende**
Pyroxene	1	**53,33**	*/*	**0,34**	*/*	**4,02**	*/*	**9,52**	*/*	**0,40**	*/*	**29,78**	*/*	**1,00**	*/*	**0,08**	*/*	**1,47**	*/*	**0,05**	*/*	**100**		**Enstatite**
Oxyde	8	**0,29**	*0,11*	**14,00**	*0,88*	**0,65**	*0,07*	**83,60**	*0,82*	**0,31**	*0,05*	**0,88**	*0,14*	**0,14**	*0,03*	**0,02**	*0,02*	**0,06**	*0,04*	**0,06**	*0,09*	**100**		**Ti-magnetite**

Tableau V-2: *résumé des compositions chimiques (cristaux + verre) des suspensions magmatiques de faible à moyenne cristallinité, ainsi que celle du verre de départ anhydre. Les compositions sont indiquées en poids d'oxyde. Le nombre de mesures ponctuelles par espèce est symbolisé par la lettre n. Les écarts types σ sont affichés en italique.*

Ces glomérophyres polyminéraliques, de forme nodulaire, peuvent atteindre plusieurs dizaines de micromètres de diamètre, jusqu'à parfois établir une connectivité cristalline avec d'autres agrégats. Outre la présence de quelques vésicules, des microcavités au sein des glomérophyres peuvent être remarquées. Il est fort probable que ces microcavités intercristallines soient le témoin d'une saturation en volatils au sein du liquide résiduel, volatils sans doute piégés dans le réseau cristallin lors de la cristallisation des phases intergranulaires. Suivant les calculs de bilan de masse, la fraction cristalline pour ces synthèses s'approche de 43% en volume. Du fait des textures générées, la proportion volumique ne peut être réellement comparée et vérifiée par mesure des proportions surfaciques.

Suspensions magmatiques #3 (700°C ; ϕ_s=0.51)

La paragenèse des produits de synthèse #3 se présente comme tel : feldspaths plagioclases (Labradorite-Oligoclase) et potassiques (Sanidine), quartz, biotite, amphibole (Hornblende magnésienne), pyroxène (Enstatite) et oxydes (Tableau V-2). Dans ces suspensions magmatiques, notez que les pyroxènes disparaissent presque entièrement de la séquence cristalline et, ceux encore en présence, montrent des figures de résorption (Figure V-21). La texture de ces suspensions solides est semblable à celle des produits #2. La proportion massique en SiO_2 du liquide granitique interstitiel reste de même inchangée (SiO_2 = 80% pds ± 0.4, Figure V-18) au regard de celle analysée dans le verre de la synthèse #2. La concentration

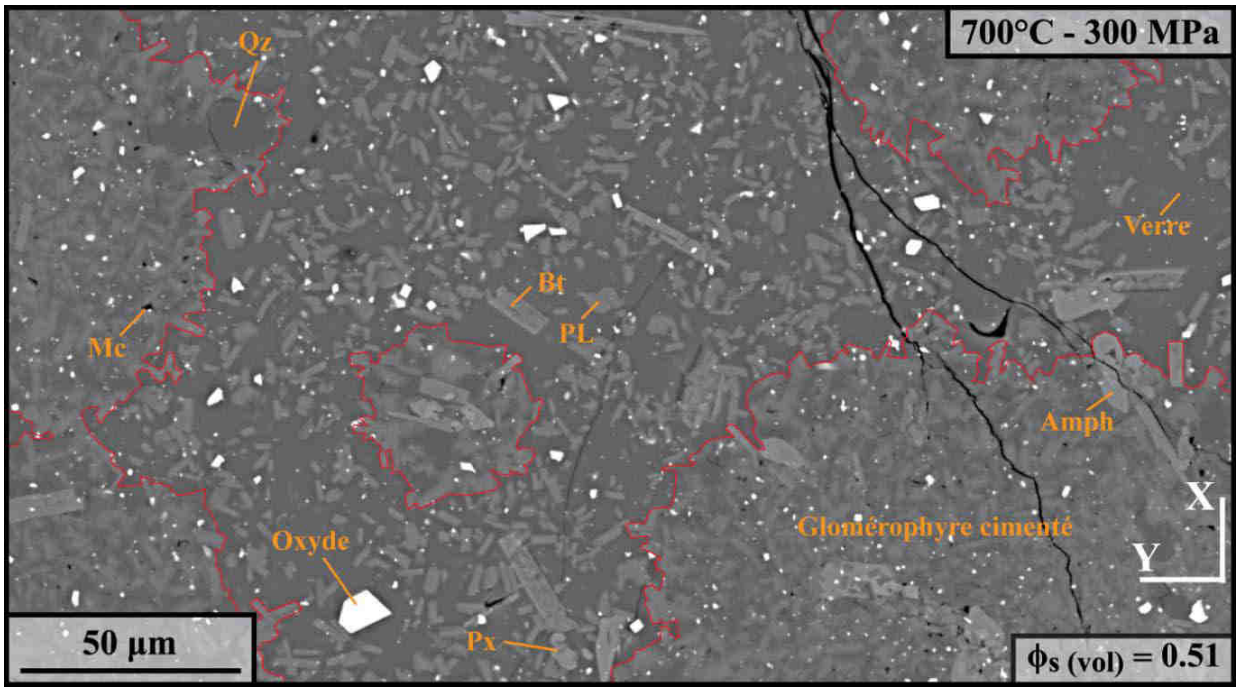

Figure V-21: *cliché MEB de la synthèse #3 réalisée à avec une chute de température de 1000 à 700°C. Tout comme la synthèse #2, cette suspension magmatique se caractérise par une texture microporphyrique aphanitique présentant localement des glomérophyres à texture intergranulaire cimentés par du quartz, des feldspaths plagioclase et potassique. Les glomérophyres, délimités par un contour rouge, peuvent atteindre dans de ce cas présent plusieurs centaines de micromètres de diamètre. Amph : amphibole; Bt : biotite; Px : pyroxène; PL : plagioclase; Qz : quartz; Mc : microcavité intercristalline. ϕ_s(vol) : fraction cristalline volumique.*

en eau semble franchir dans ce cas présent les 6 % pds. Avec l'augmentation de la fraction cristalline, estimée par bilan de masse à 51% vol., la proportion et la taille des glomérophyres polyminéraliques à texture intergranulaire augmentent également (Figure V-21). Certains d'entre eux peuvent ainsi mesurer plusieurs centaines de micromètres de diamètre. Avec les feldspaths plagioclase et le quartz, le feldspath potassique complète la série des espèces minérales cimentant les glomérophyres. La présence de microcavités intercristallines est toujours observée.

2.4.2. Suspensions magmatiques #4 (650°C) à forte fraction cristalline

Comparé aux précédentes suspensions magmatiques synthétisées, les produits expérimentaux #4 présentent la particularité de voir leur texture et leur proportion en verre silicaté évoluer selon une zonation concentrique. L'acquisition d'images MEB au sein d'une même section basale [xy] rend effectivement compte d'une diversité texturale en lien étroit avec une nette augmentation de la fraction en cristaux et cavités depuis le cœur (Figure V-22) vers la bordure (Figure V-23) d'un échantillon.

Le cœur même des synthèses #4 consiste en un produit fortement cristallisé dont la texture glomérophyrique intergranulaire au sein d'une suspension microporphyrique (Figure V-22a) rappelle très exactement celle observée à la fois dans les synthèses #2 et #3. Les glomérophyres sont délimités par un contour rouge sur la Figure V-22a. La nature et la distribution de taille des divers objets cristallins sont également analogues (Figure V-22b). Un exemple de cartographie élémentaire résultant d'une analyse *EDS* est donné Figure V-22c. Le verre interstitiel semble en revanche occuper dans ce cas présent une moindre proportion surfacique et de nombreuses cavités font en parallèle leur apparition. Certaines cavités, de forme irrégulière (vacuoles), peuvent atteindre une centaine de micromètres. Un vaste nombre de microcavités intercristallines sont de même visibles à l'intérieur des glomérophyres. Cet ensemble de cavités serait ainsi le témoignage d'un fluide hydraté coexistant avec le liquide résiduel au cours de la cristallisation. Avec l'existence d'une telle texture, il est manifestement compliqué d'évaluer avec exactitude la proportion de chaque phase en présence (cristaux, liquide) sans l'apport de données quantitatives chimiques et un calcul de bilan de masse. Faute de données quantitatives, seule une estimation surfacique approximative des différentes phases peut être proposée. Suivant le cliché MEB de la Figure V-22a, les cristaux représenteraient au minimum ~67% de la surface analysée, les cavités ~9% et le verre interstitiel environ 24%, soit des proportions respectives entre cristaux et verre de 74% et 26%.

A l'approche de la bordure des échantillons cylindriques, la fraction en verre résiduel diminue drastiquement jusqu'à la disparition totale de cette phase, laissant ainsi place à un système biphasique (cristaux + cavités; Figure V-23a). Cette association de cristaux et cavités se limite en général sur une auréole de plusieurs centaines de micromètres d'épaisseur. Dans cette zone, deux textures indépendantes cohabitent : une texture particulière dite diktytaxitique (Figure V-23b) et une texture microlitique holocristalline (Figure V-23c). Dans la lignée des compositions décrites ci-dessus, l'association minéralogique constitutive de la texture microlitique holocristalline se définit par des feldspaths plagioclase et potassique, du quartz

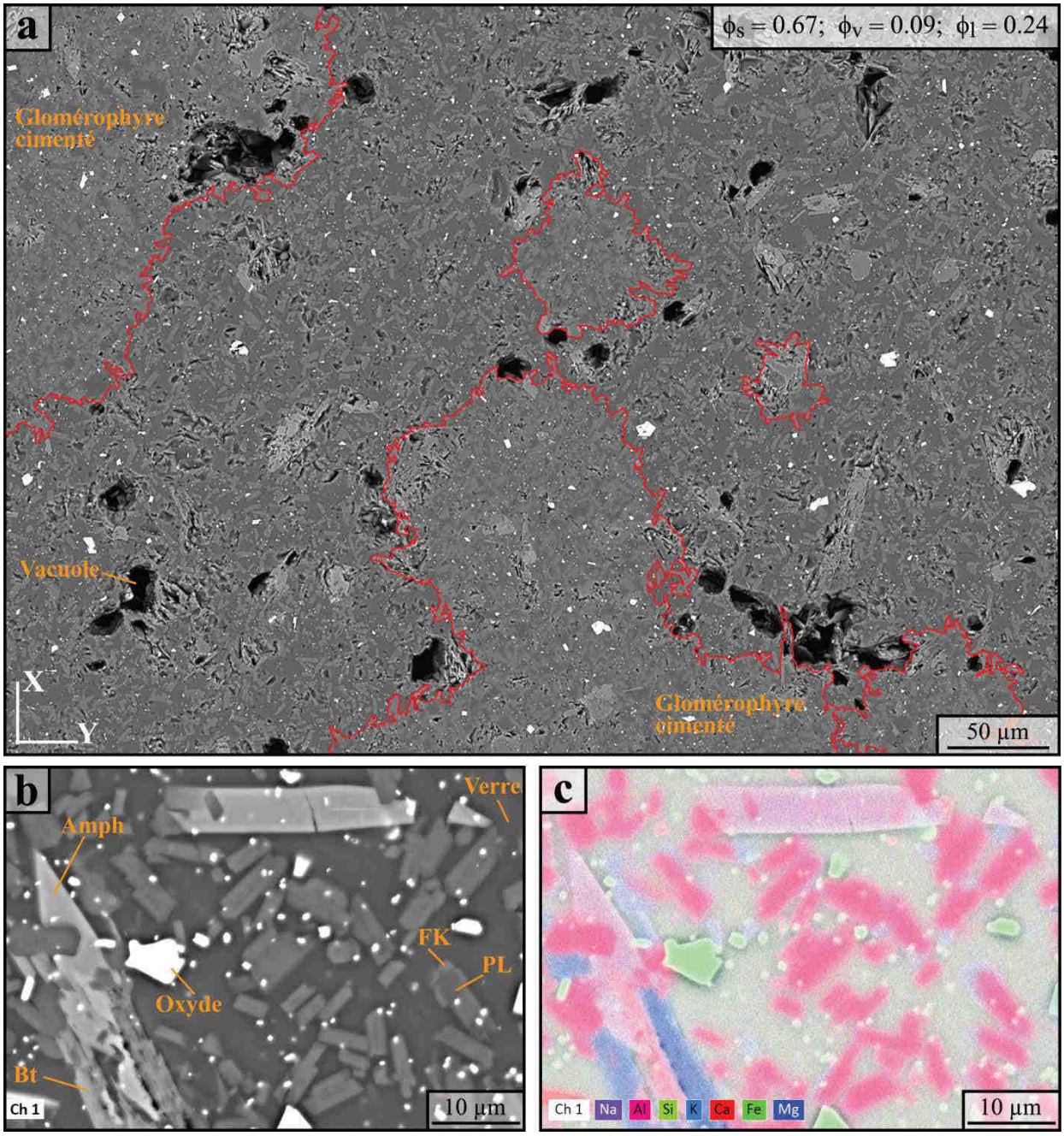

Figure V-22: *cœur partiellement cristallisé de la synthèse #4 réalisée avec une chute de température de 1000 à 650°C. (a) Texture glomérophyrique intergranulaire. ϕ_s: fraction cristalline; ϕ_v: fraction vacuolaire; ϕ_l: fraction du liquide. (b) et (c) correspondent respectivement au cliché MEB et à la cartographie élémentaire associée du cœur de l'échantillon où le liquide subsiste.*

des biotites, des amphiboles et des oxydes (Figure V-23c et 23d). La texture diktytaxitique se réfère quant à elle aux plages de la section d'étude où des vides interstitiels sont associés à un certain nombre d'espèces minérales – le plus souvent représentées par des plagioclases – dont le caractère jointif forme un réseau cristallin plus ou moins dense (Figure V-23b). La fraction surfacique de cette texture est relativement importante mais reste difficile à quantifier avec précision en raison de la distribution irrégulière des vides interstitiels. A titre d'exemple, les

vides à texture diktytaxitique du cliché MEB, présenté Figure V-23a, dépassent en surface la barre des 20% tandis que les cavités constituent environ 11% de la section observée.

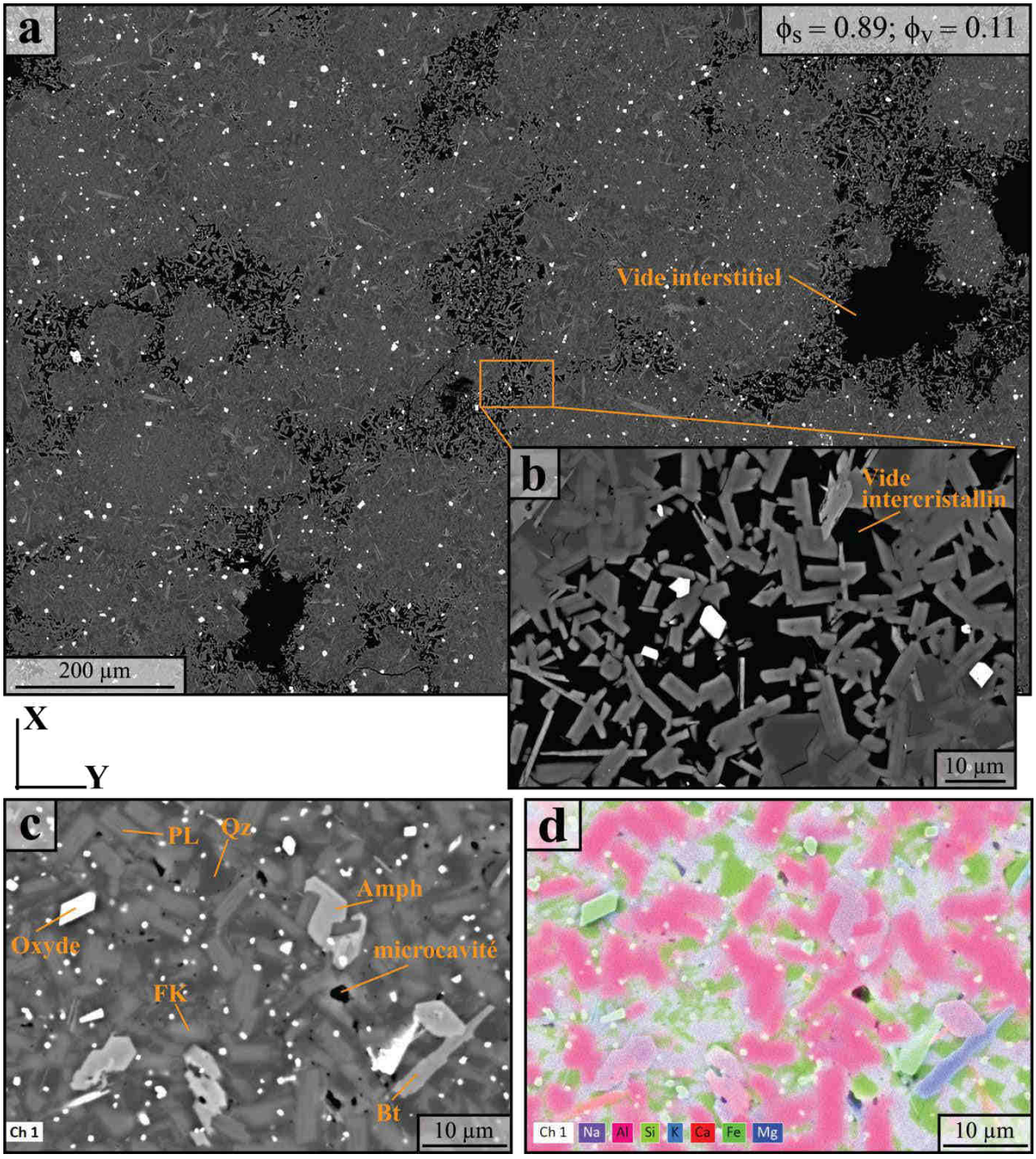

Figure V-23: *bordure du produit expérimental #4, caractérisé par une association de cristaux et cavités. ϕ_s: proportion en cristaux; ϕ_v: proportion en cavités. (b) Vide à texture diktytaxitique. (c) Texture microlithique holocristalline. Amph : amphibole; Bt : biotite; PL : plagioclase; FK : feldspath potassique ; Qz : quartz. (d) analyse cartographique élémentaire par méthode EDS au sein de la texture microlithique holocristalline.*

3. Expériences de déformation en torsion

Dans ce volet de l'étude, quatre expériences de déformation en torsion (PP548, PP554, PP561 et PP565) sont détaillées, à raison d'une expérience représentative par suspension magmatique synthétisée. Les produits expérimentaux ont été déformés dans des conditions de pression (300 MPa) et température (800, 750, 700 ou 650°C) identiques à celles imposées durant leur synthèse en autoclave. Les vitesses de déformation $\dot{\gamma}$ appliquées aux échantillons sont comprises entre $9.3x10^{-6}$ s^{-1} et $4.6x10^{-4}$ s^{-1}, pour des quantités de déformation moyennes γ_{bulk} allant de 0.56 à 5.12. Ces quantités de déformation se rapportent plus exactement aux valeurs maximales qui sont théoriquement atteintes à la périphérie des échantillons cylindriques (cf. Figure V-5, section 1.2.4). Dans le cas de fortes concentrations de la déformation sous la forme de microstructures localisées, une quantité de déformation locale γ_{loc} a pu être déterminée. Les conditions expérimentales, la géométrie des échantillons et les données mécaniques pour chacune des expériences sont résumées dans le Tableau V-3.

Synthèse	ϕs	Expérience Paterson	Température	Echantillon hauteur (mm)	Echantillon rayon (mm)	$\dot{\theta}$ (rad·s^{-1})	$\dot{\gamma}$ (s^{-1})	γ_{bulk}	γ_{loc}
#1	0.34	PP548	800°C	6,93	6,48	$4.9x10^{-4}$	$4.6x10^{-4}$	5.12	/
#2	0.43	PP554	750°C	6,46	6,48	$9.2x10^{-5}$	$9.2x10^{-5}$	0.96	/
#3	0.51	PP561	700°C	7,17	6,48	$9.9x10^{-5}$	$9.0x10^{-5}$	1.14	/
#4	> 0.74	PP565	650°C	6,63	6,48	$9.5x10^{-6}$	$9.3x10^{-6}$	0.56	~2-4

Tableau V-3: *récapitulatif des expériences de déformation en torsion sous presse Paterson. Avec ϕ_s : fraction cristalline ; $\dot{\theta}$: vitesse de déplacement angulaire ; $\dot{\gamma}$: vitesse de déformation ; γ : quantité de déformation et γ_{loc} : quantité de déformation locale.*

3.1. Déformation de magmas granodioritiques de faible et moyenne cristallinité

Dans cette section, sont présentées les diverses observations MEB et analyses quantitatives réalisées à la suite d'expériences de déformation en torsion sur les suspensions magmatiques de faible et moyenne cristallinité (ϕ_s = 0.34, 0.43 et 0.51). Sous l'effet de la contrainte cisaillante, seules des fabriques cristallines se sont développées. L'ensemble des illustrations est compilé dans les Figures V-24 à V-30. Mentionnons que les quantifications des Orientations Préférentielles de Forme (OPFs) locales par comptage des intercepts ont été uniquement menées au travers des faces externes [xz] d'échantillons cylindriques (cf. Figure V-7, section 1.3.1), donnant ainsi au cisaillement un sens apparent dextre. Dans chacune des sections étudiées, quelques zones d'intérêt ont été sélectionnées pour quantifier un peu plus en détail la fabrique développée par la population d'objets analysés (ferromagnésiens + feldspaths, Figures V-25, V-28 et V-30). Les fabriques locales sont illustrées sous la forme d'une carte telle que détaillée en section 2.3.4. Les valeurs des directions d'allongement α et de l'intensité *Ie* des ellipses tensorielles locales sont respectivement données par une rose de fréquence (90° < α < -90° où 0° correspond à la direction de cisaillement <x>) et un histogramme de distribution des fréquences (Figures V-24, V-27 et V-29). Sur ces figures, il

est également associé un diagramme de type Rf/Phi [*Lisle*, 1985] sur lequel les valeurs d'intensité et de direction des fabriques de forme locales sont reportées. Ce type de diagramme donne alors accès à la dispersion des directions d'allongement selon l'évolution de l'intensité des OPFs.

3.1.1. Suspensions magmatiques #1 (expérience PP548; ϕ_s = 0.34 ; 800°C)

Au sein de la suspension magmatique #1 (ϕ_s=0.34), l'état fini des OPFs locales de la fraction cristalline considérée marque une fabrique pénétrative, caractérisée au premier abord par des propriétés directionnelles homogènes sur l'ensemble de la section analysée (Figures V-24 et V-25).

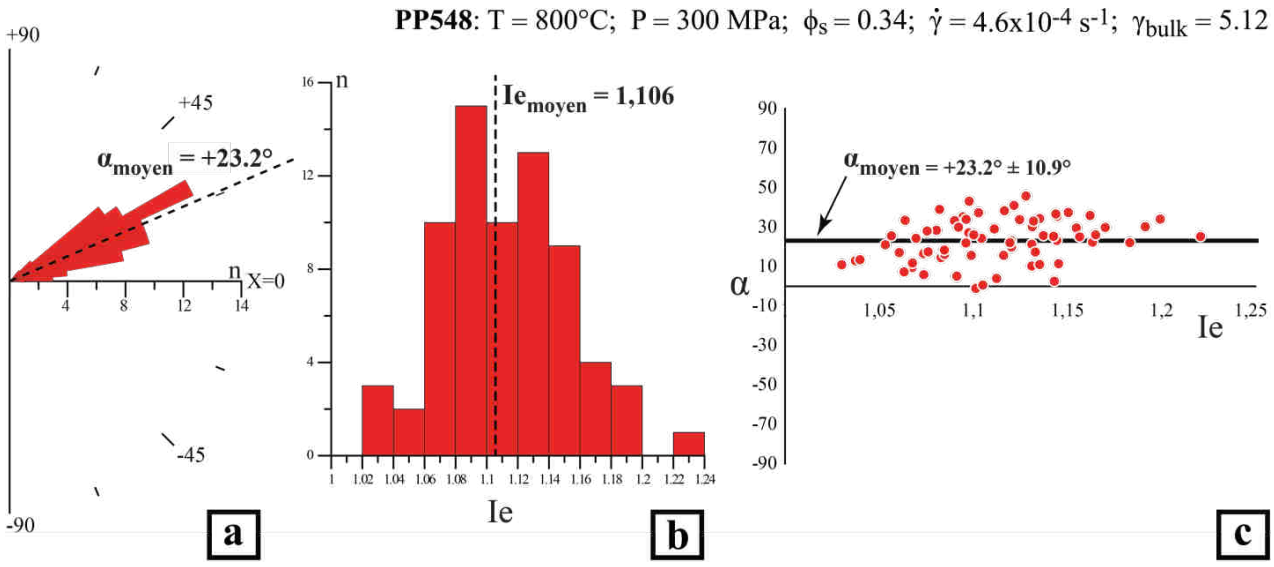

Figure V-24 *: analyses statistiques des OPFs (Orientations Préférentielles de Forme) locales obtenues à partir de la population de cristaux (ferromagnésiens et plagioclases) de la suspension magmatique #1 (fraction cristalline de ϕ_s = 0.34), en réponse à l'expérience de déformation PP548. (a) rose de fréquence pour les directions d'allongement α des ellipses tensorielles locales. (b) distribution des fréquences de l'intensité Ie des OPFs locales. (c) diagramme de type Rf/Phi des OPFs locales illustrant la dispersion des directions α suivant l'évolution de Ie. Les traits en noir et les valeurs associées correspondent aux moyennes arithmétiques de Ie et α.*

Selon l'analyse statistique des ellipses tensorielles obtenues, la direction d'allongement α des fabriques locales ne varie en effet que très peu; celle-ci occupe essentiellement une fenêtre d'angles de 23.2° ± 10.9° par rapport à la direction de cisaillement <x>, avec un maximum de densité compris entre +25° et +30° (Figure V-24a). Les valeurs d'intensité des OPFs associées se distribuent majoritairement dans un intervalle de ~1.05 à ~1.2, pour une moyenne arithmétique estimée à 1.106 (Figure V-24b). Le diagramme de type Rf/Phi révèle quant à lui une corrélation positive, aussi tenue soit elle, entre les propriétés directionnelles et le degré d'intensité des fabriques de forme locales (Figure V-24c). Cette corrélation discrète peut également se visualiser sur la représentation cartographique des intensités et directions d'OPFs (Figure V-25c). Les directions d'allongement (double flèche blanche) avoisinant l'axe

PP548: T = 800°C; P = 300 MPa; $\phi_s = 0.34$; $\dot{\gamma} = 4.6x10^{-4}\ s^{-1}$; $\gamma_{bulk} = 5.12$

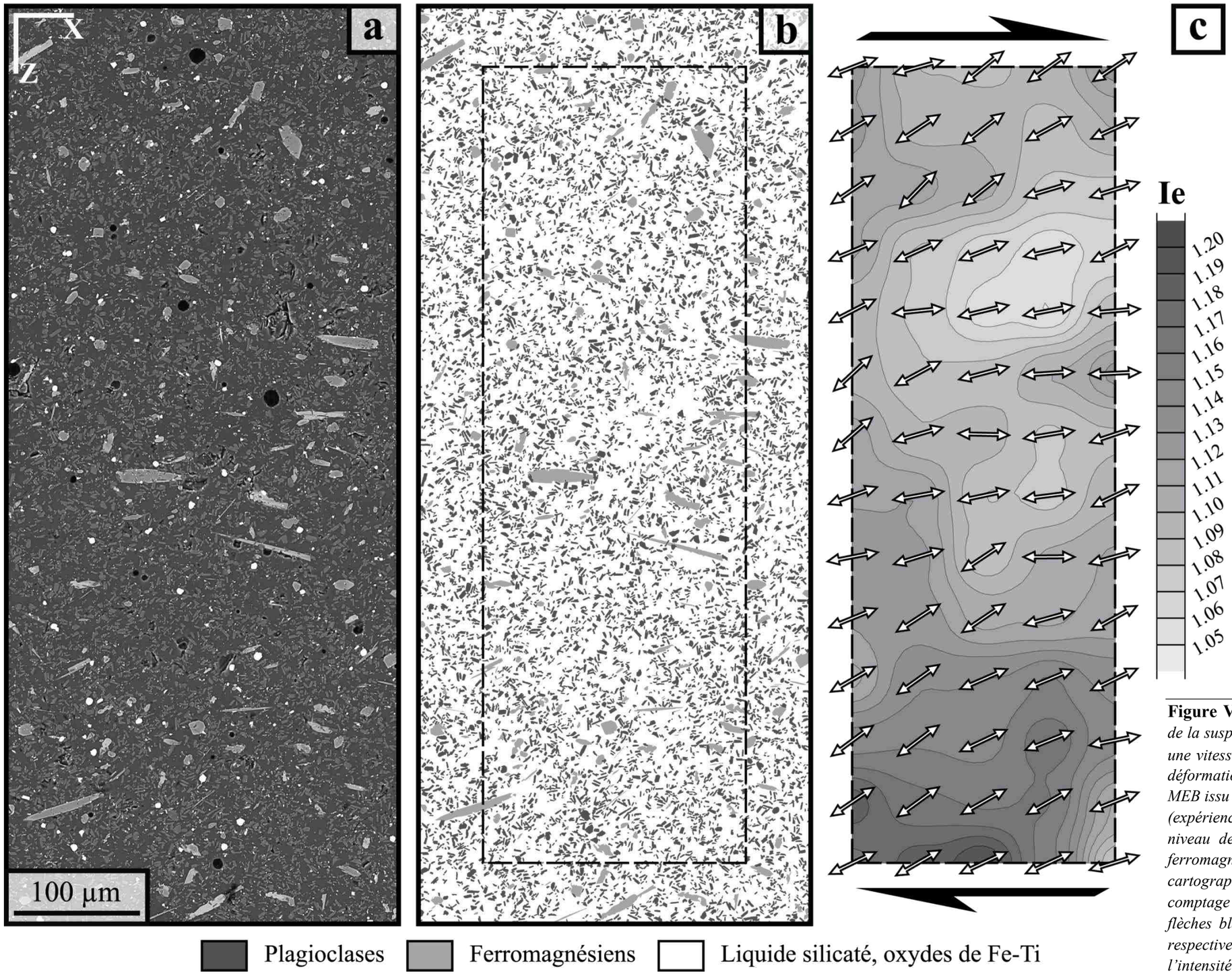

Figure V-25: *étude de la fabrique de forme au sein de la suspension #1 ($\phi_s = 0.34$), déformée en torsion à une vitesse de $\boldsymbol{\gamma\dot{\gamma}} = 4.6x10^{-4}\ s^{-1}$, pour une quantité de déformation totale γ_{bulk} obtenue de 5.12. (a) Cliché MEB issu d'une section [xz] de l'échantillon déformé (expérience PP548). (b) Image MEB seuillée en niveau de gris sur laquelle les plagioclases et les ferromagnésiens sont isolés. (c) Représentation cartographique des OPFs locales calculées par comptage des intercepts ($\Delta\alpha = 9$; $i = 4$). Les doubles flèches blanches et la carte au-dessous représentent respectivement les directions d'allongement α et l'intensité Ie des ellipses tensorielles locales (n=70) de la population d'objets analysés.*

de cisaillement <x> (<10-20°) semblent effectivement en grande partie situées sur une large bande horizontale au centre de l'illustration, le long de laquelle les fabriques de forme perdent légèrement en intensité. Cette perte d'intensité locale peut être mise en relief par l'analyse statistique des orientations préférentielles des axes longs de cristaux ferromagnésiens (pyroxènes, amphiboles), obtenue par un calcul du tenseur d'inertie (Figure V-26). Ainsi, le traitement des grains ferromagnésiens, pris individuellement, montre une orientation de leur axe long majoritairement comprise entre environ +10° et -25° par rapport à l'axe de cisaillement (objets définie par une couleur bleu sur la Figure V-26). Bien qu'il ne soit pas exclu que la relation discrète entre faible degré d'intensité et direction d'allongement sub-horizontale soit tout simplement due à un biais analytique (e.g., effets de la résolution des imagettes ou de la grille de comptage), il semble néanmoins au travers de l'analyse du tenseur d'inertie qu'une sous-fabrique se soit développée sous l'effet de la contrainte différentielle. La présence de cette sous-fabrique, portée par les ferromagnésiens, pourrait ainsi être en partie la cause d'une perte d'intensité des OPFs locales, portées par l'ensemble des objets analysés (feldspaths + ferromagnésiens), et de la faible dispersion des directions d'allongement.

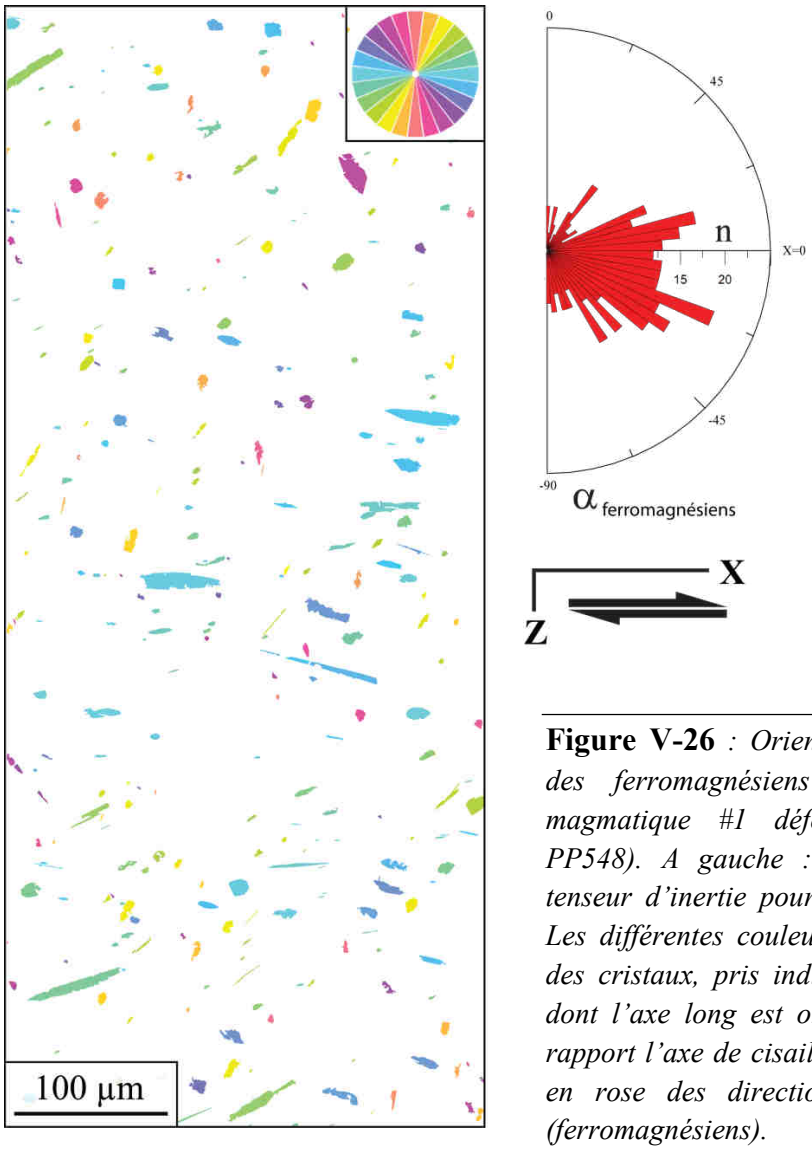

Figure V-26 : *Orientations préférentielles de forme des ferromagnésiens au sein de la suspension magmatique #1 déformée en torsion (expérience PP548). A gauche : image résultant du calcul du tenseur d'inertie pour les cristaux ferromagnésiennes. Les différentes couleurs représentent les orientations des cristaux, pris individuellement; en bleu un objet dont l'axe long est orienté entre +7,5° et -22.5° par rapport l'axe de cisaillement (x). A droite : diagramme en rose des directions d'allongement des cristaux (ferromagnésiens).*

3.1.2. Suspensions magmatiques #2 (expérience PP554; ϕ_s = 0.43 ; 750°C)

Concernant l'expérience de déformation en torsion PP554, l'étude bidimensionnelle des OPFs locales révèle que, sous l'effet d'une contrainte cisaillante, la population d'objets analysés (feldspaths + ferromagnésiens) de la suspension magmatique #2 tend à développer

une fabrique cristalline semi-pénétrative (Figures V-27 et V-28). Le terme semi-pénétratif est dans le cas présent employé pour souligner le fait que seule la fraction cristalline constitutive de la texture microporphyrique aphanitique - donc non cimentée par des feldspaths plagioclase ou du quartz (texture glomérophyrique) - développe une fabrique 2D.

Avec l'augmentation de la proportion cristalline d'environ 10% (ϕ_s=0.43 vol.) et la cristallisation de glomérophyres à texture intergranulaire, les directions d'allongement des ellipses tensorielles locales de la population cristalline analysée ne sont ici plus aussi homogènes que pour celles des suspensions magmatiques #1. Ainsi, il émane de l'étude statistique des OPFs locales une certaine forme de tortuosité à l'égard des directions d'allongement (Figure V-28c). Cette fabrique hétérogène se traduit au travers de la rose des fréquences (Figure V-27a) par des directions α (n=64) se répartissant dans un éventail de 0° à +45° par rapport à l'axe de cisaillement, avec une moyenne arithmétique estimée à +26.2° ± 19.8° (Figure V-27c). Toutefois, une famille comprise entre +20° et +40° compose en très grande majorité les directions d'allongement locales de la fabrique développée ; cette gamme d'orientations étant parallèle à celle mesurée pour l'expérience PP548. Cette direction prédominante s'avère d'ailleurs être corrélée avec un degré d'intensité de l'OPF élevé, comparé aux faibles valeurs d'intensité (<1.1) associées aux directions d'allongement proches de l'axe <x> (Figure V-27c). D'après la représentation cartographique (Figure V-28c), la corrélation entre degrés d'intensité et propriétés directionnelles se matérialise par la présence de bandes parallèles orientées à -20° par rapport à la direction du cisaillement. Notons enfin la relative baisse de la force de fabrique moyenne (Ie_{moyen} = 1.08, Figure V-27b) en comparaison de celle calculée pour l'expérience précédente.

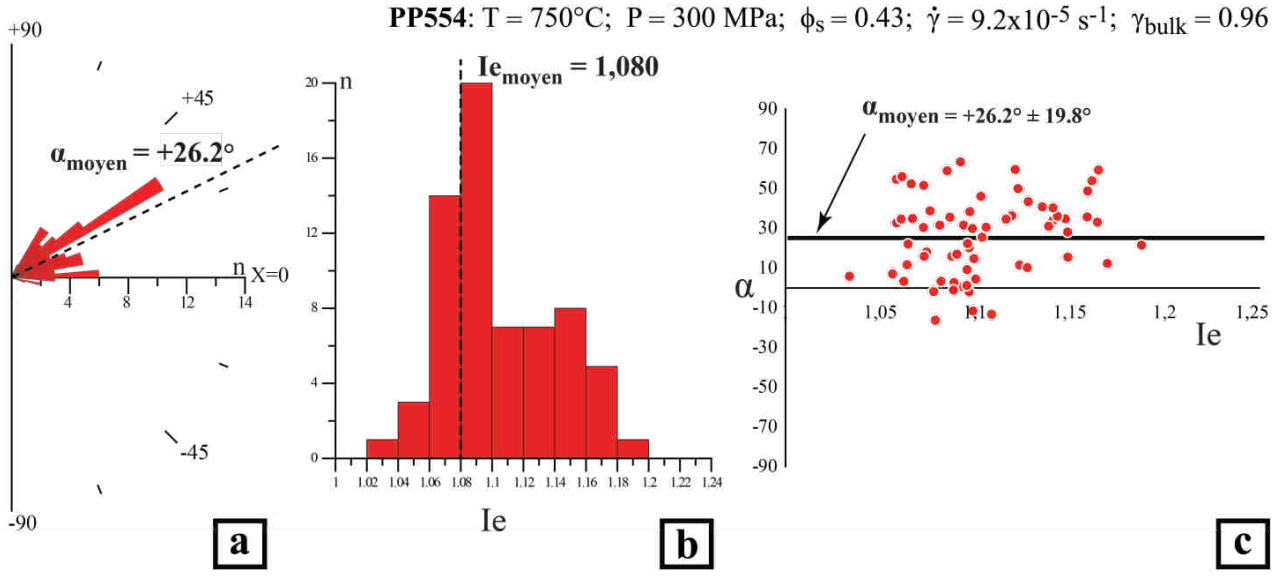

Figure V-12: *analyses statistiques des OPFs (Orientations Préférentielles de Forme) locales obtenues à partir de la population de cristaux (ferromagnésiens et plagioclases) de la suspension magmatique #2 (fraction cristalline de ϕ_s = 0.43), en réponse à l'expérience de déformation PP554. (a) rose de fréquence pour les directions d'allongement α des ellipses tensorielles locales. (b) distribution des fréquences de l'intensité Ie des OPFs locales. (c) diagramme de type Rf/Phi des OPFs locales illustrant la dispersion des directions α suivant l'évolution de Ie. Les traits en noir et les valeurs associées correspondent aux moyennes arithmétiques de Ie et α.*

PP554: T = 750°C; P = 300 MPa; $\phi_s = 0.43$; $\dot{\gamma} = 9.2x10^{-5}\ s^{-1}$; $\gamma_{bulk} = 0.96$

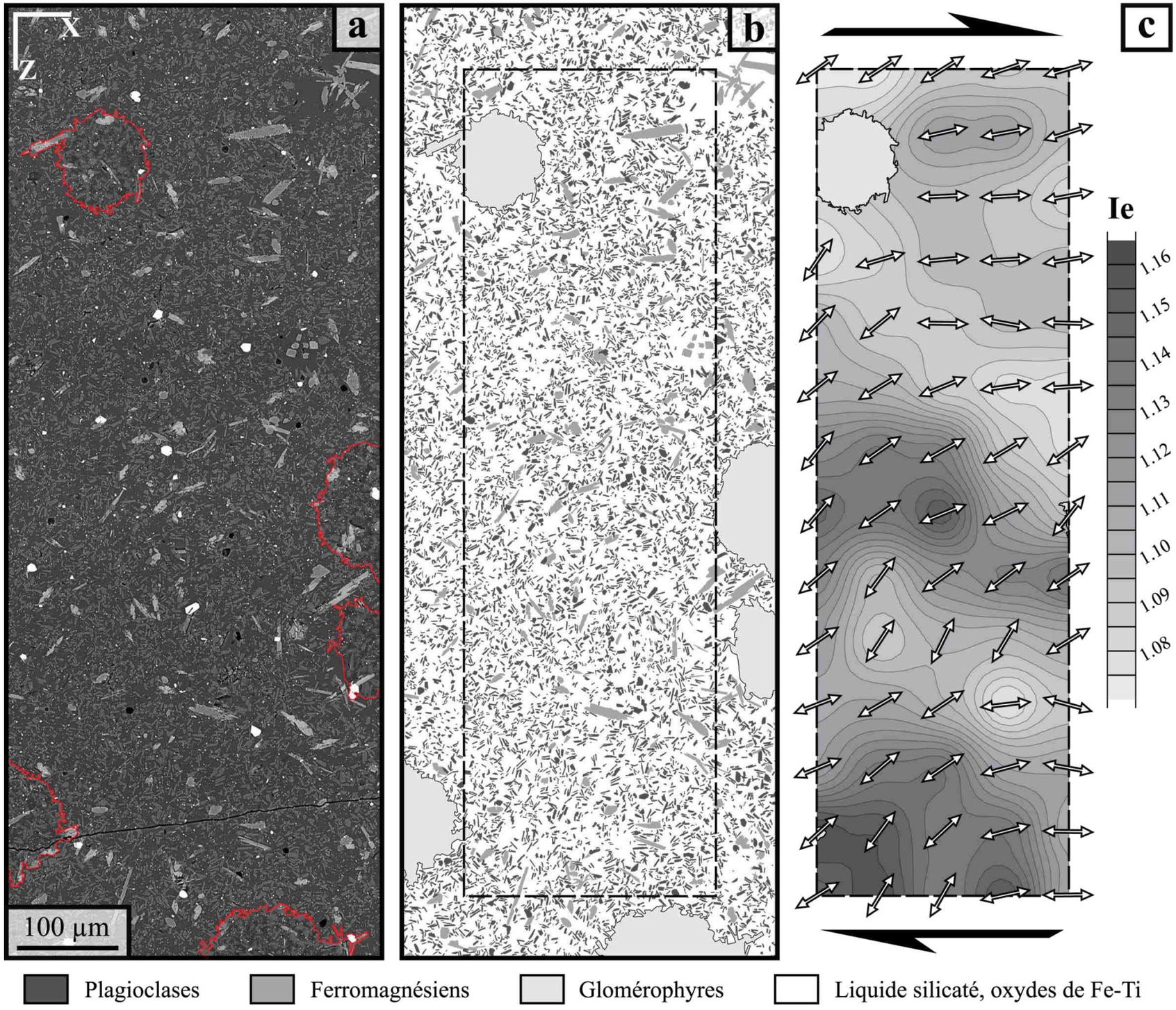

Figure V-28: *étude de la fabrique de forme au sein de la suspension #2 (ϕ_s = 0.43), déformée en torsion à une vitesse de $\dot{\gamma}$= 9.2x10^{-5} s^{-1}, pour une quantité de déformation totale γ_{bulk} obtenue de 0.96. (a) image MEB issue d'une section [xz] de l'échantillon déformé (expérience PP554) sur laquelle les glomérophyres à texture intergranulaire sont entourés par un trait rouge. (b) Image MEB seuillée en niveau de gris sur laquelle les plagioclases, les ferromagnésiens et les glomérophyres sont isolés. (c) Représentation cartographique des OPFs locales calculées par comptage des intercepts (Δα = 6 ; i = 2). Les doubles flèches blanches et la carte au-dessous représentent respectivement les directions d'allongement α et l'intensité Ie des ellipses tensorielles locales (n=64) de la population d'objets analysés.*

3.1.3. Suspensions magmatiques #3 (expérience PP561; ϕ_s = 0.51 ; 700°C)

Suite à l'expérience de déformation en torsion de la suspension magmatique #3, l'organisation spatiale de la fraction cristalline inter-glomérophyrique souligne également une fabrique d'ensemble semi-pénétrative dans laquelle les OPFs locales se distinguent cette fois-ci par des propriétés directionnelles bien plus hétérogènes (Figures V-29 et V-30). Ainsi, deux directions d'allongement α (n=69) ressortent de l'analyse statistique (Figure V-29a). Ces deux directions privilégiées sont symétriques par rapport à la direction de cisaillement <x> et suivent des orientations préférentielles de +25° ± 5° et -25° ± 5°. La moyenne arithmétique des directions d'allongement, estimée à +11.2° ± 35.8°, n'a que peu de valeur dans le cas de directions associées (Figures V-29a et V-29c).

La direction d'allongement orientée globalement à +25° ± 5° représente le maximum de densité (Figure V-29a) et les OPFs de la population cristalline portant cette direction d'allongement majeure semblent être dispersées sur l'ensemble de la section observée (Figure V-30c). À l'inverse, les fabriques de forme locales marquées par la direction d'allongement mineure, orientée à -25° ± 5° ou très proche de l'axe de cisaillement <x>, se concentrent essentiellement le long d'une bande sub-horizontale de plusieurs centaines de micromètres d'épaisseur au centre de la section analysée (Figure V-30c). Cette zone est bordée de part et d'autre par un groupement de glomérophyres, autour desquels la direction des OPFs est sensiblement moins homogène. Aucune de ces directions privilégiées ne s'avère être corrélée avec un degré d'intensité spécifique. Avec une valeur calculée de 1.033 (Figure V-29b), la force de fabrique moyenne *Ie* portée par la phase cristalline s'atténue significativement vis-à-vis des intensités moyennes d'OPF retrouvées pour les précédentes expériences (PP548 et PP554).

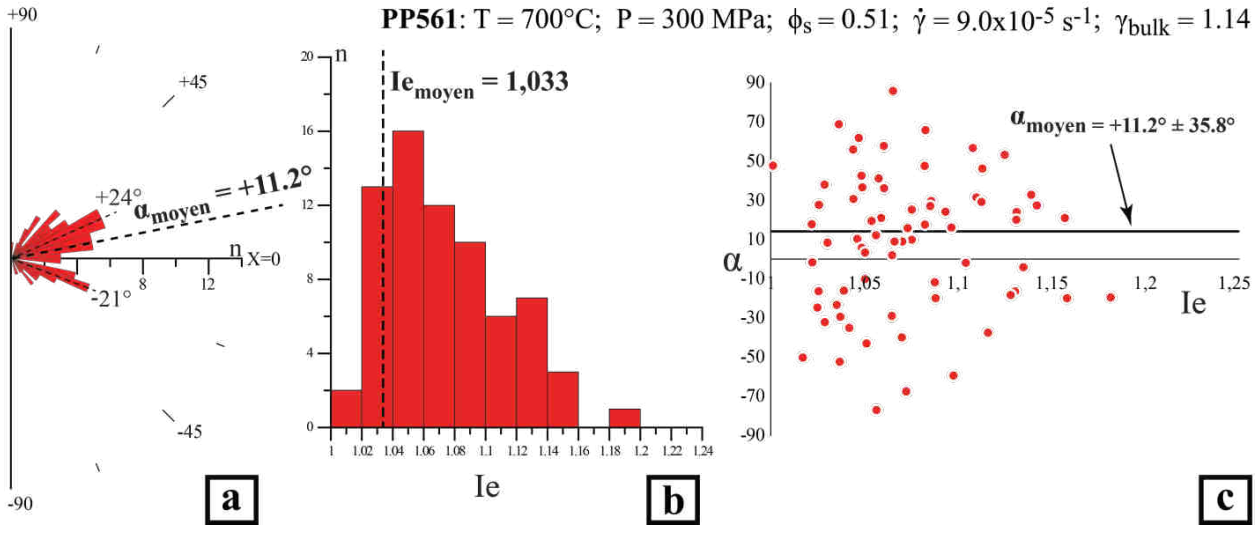

Figure V-29: *analyses statistiques des OPFs (Orientations Préférentielles de Forme) locales obtenues à partir de la population de cristaux (ferromagnésiens et plagioclases) au sein de la suspension magmatique #3 (fraction cristalline de ϕ_s = 0.51), en réponse à l'expérience de déformation PP561. (a) rose de fréquence pour les directions d'allongement α des ellipses tensorielles locales. (b) distribution des fréquences de l'intensité Ie des OPFs locales. (c) diagramme de type Rf/Phi des OPFs locales illustrant la dispersion des directions α suivant l'évolution de Ie. Les traits en noir et les valeurs associées correspondent aux moyennes arithmétiques de Ie et α.*

3.2. Déformation de magmas granodioritiques en conditions tardi-magmatiques (expérience PP565 ; 650°C)

Dans ce volet de l'étude, sont relayées les diverses observations MEB (texturales, microstructurales) et analyses quantitatives (fabriques de forme, propriétés directionnelles) réalisées à la suite de l'expérience de déformation en torsion PP565 sur le produit de synthèse #4. Pour rappel, l'expérience fut menée à une vitesse de déformation $\dot{\gamma}$ de $9.3x10^{-6}$ s^{-1}, soit ~1-2 ordres de grandeur de moins que les vitesses appliquées dans les expériences précédentes (Tableau V-3). Compte tenu du fort taux de cristallinité du produit synthétisé, seule une vitesse de déformation telle qu'imposée ici permet d'assurer la concentration de la déformation au sein même de l'échantillon et ainsi se préserver d'un possible glissement aux interfaces entre ce même échantillon et les disques d'alumine (cf. section 1.2.5.) Le choix stratégique d'appliquer une vitesse de déformation plus lente s'accompagne en contrepartie d'une plus faible quantité de déformation accumulée γ_{bulk} au cours de l'expérience, qui dans le cas présent n'a atteint que 0.56. Plusieurs sections [xz] ont été réalisées au travers de l'échantillon déformé. L'une d'entre elles, présentée Figure V-31a, illustre l'état de déformation finie au sein de la moitié haute de l'échantillon cylindrique et constitue la base de toutes les observations texturales/ microstructurales et études quantitatives 2D présentées par la suite. Notez que ces observations et analyses sont réalisées sur la face externe de la section [xz] du cylindre, attribuant ainsi au cisaillement un sens apparent dextre.

3.2.1. Brève description de l'état de déformation fini au sein de la section [xz]

Contrairement aux suspensions magmatiques de faible et moyenne cristallinité, le produit de synthèse #4 se voit affecté par une déformation localisée (Figure V-31a). Le deuxième cliché MEB de la section considérée (Figure V-31b), sur lequel les diverses textures et microstructures sont annotées ou retracées, témoigne d'une intense concentration de la déformation au niveau de la partie sommitale de l'échantillon. La déformation se concentre plus exactement le long d'une bande sub-horizontale à faiblement inclinée (coloriée en vert sur la figure) dans laquelle il se manifeste (1) un plus large éventail de microstructures que dans le reste de l'échantillon (i.e., micro-fractures, bandes de déformation cataclastique ou bien encore bandes de déformation ductile proto-mylonitique) et (2) des injections magmatiques partiellement cristallisées le long desquelles la déformation ductile se développe. L'épaisseur de cette zone de forte accumulation de la déformation, apparentée à une « zone de cisaillement » dans la suite de l'étude, est variable. La zone de cisaillement s'évase en effet progressivement depuis la droite de l'image MEB vers le disque d'alumine supérieur de la colonne-échantillon, passant ainsi de quelques centaines de microns à plus d'un millimètre d'épaisseur. Suivant cette gamme d'épaisseur, il peut être approximé une quantité de déformation locale de 2 à 4γ (Tableau V-3). Cette estimation omet cependant la quantité de déformation accumulée de part et d'autre de la zone de cisaillement, en particulier celle enregistrée le long du gradient de déformation inférieur de la zone de cisaillement. Cette zone de gradient, subdivisée en 4 sous-zones d'épaisseurs égales (protolithique, distale, centrale et proximale ; Figure V-31b), laisse en effet apparaître un réseau de micro-fractures. Néanmoins, la densité de ces micro-fractures décroît de manière significative depuis la zone du gradient

PP561: T = 700°C; P = 300 MPa; $\phi_s = 0.51$; $\dot{\gamma} = 9.0x10^{-5}\ s^{-1}$; $\gamma_{bulk} = 1.14$

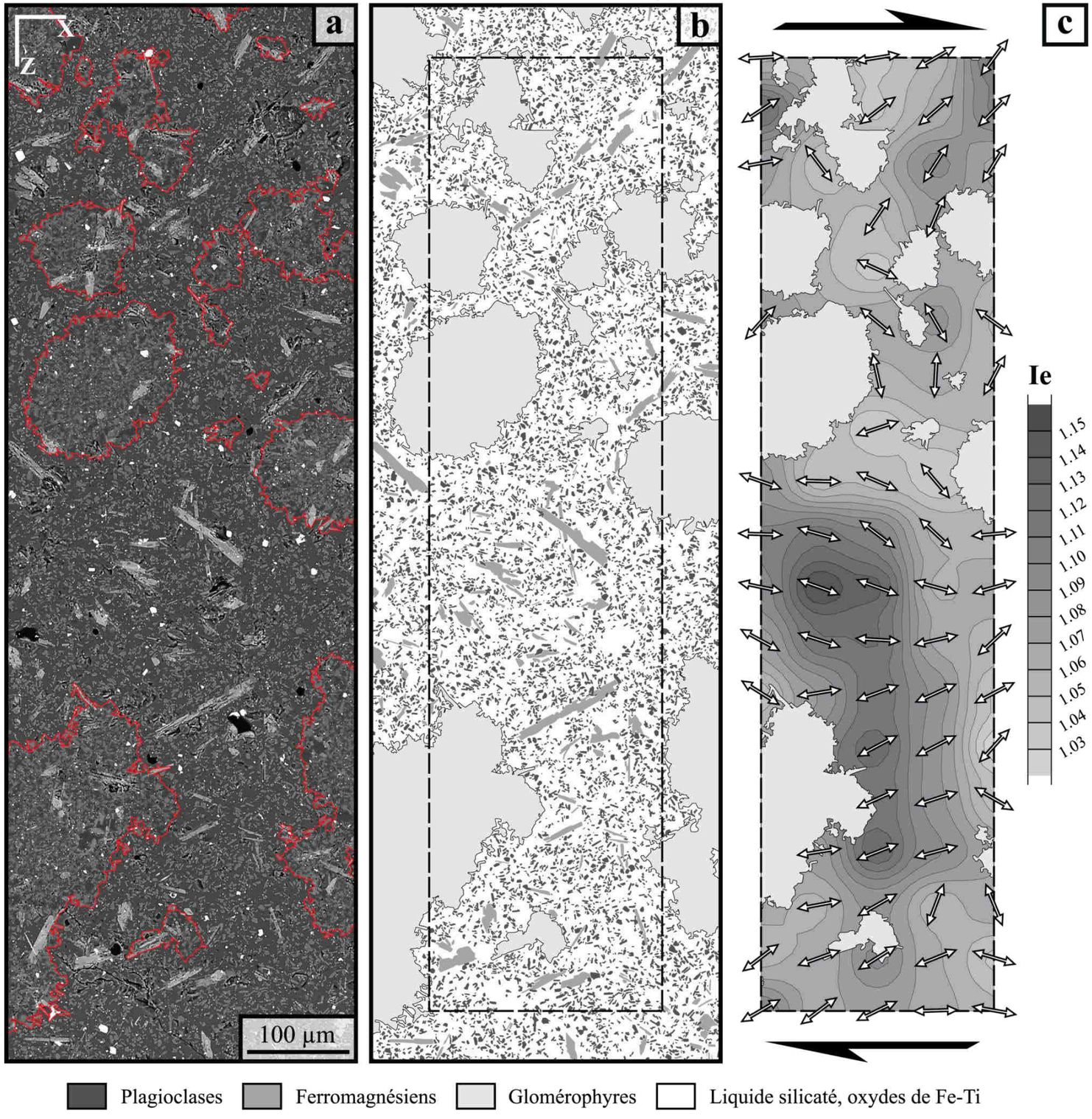

Figure V-30: *étude de la fabrique de forme au sein de la suspension #3 (ϕ_s = 0.51) déformée en torsion à une vitesse de $\dot{\gamma} = 9.0x10^{-5}\ s^{-1}$, pour une quantité de déformation totale γ_{bulk} obtenue de 1.14. (a) cliché MEB issu d'une section [xz] de l'échantillon déformé (expérience PP561) sur laquelle les glomérophyres à texture intergranulaire sont entourés par un trait rouge. (b) Image MEB seuillée en niveau de gris sur laquelle les plagioclases, les ferromagnésiens et les glomérophyres sont isolés. (c) Représentation cartographique des OPFs locales calculées par comptage des intercepts ($\Delta\alpha$ = 4 ; i = 2). Les doubles flèches blanches et la carte au-dessous représentent respectivement les directions d'allongement α et l'intensité Ie des ellipses tensorielles locales (n=69) de la population d'objets analysés.*

PP565: T = 650°C; P = 300 MPa; ϕ_s = ~1.00; $\dot{\gamma}$ = 9.3x10^{-6} s^{-1}; γ_{bulk} = 0.56; γ_{loc} = ~2-4

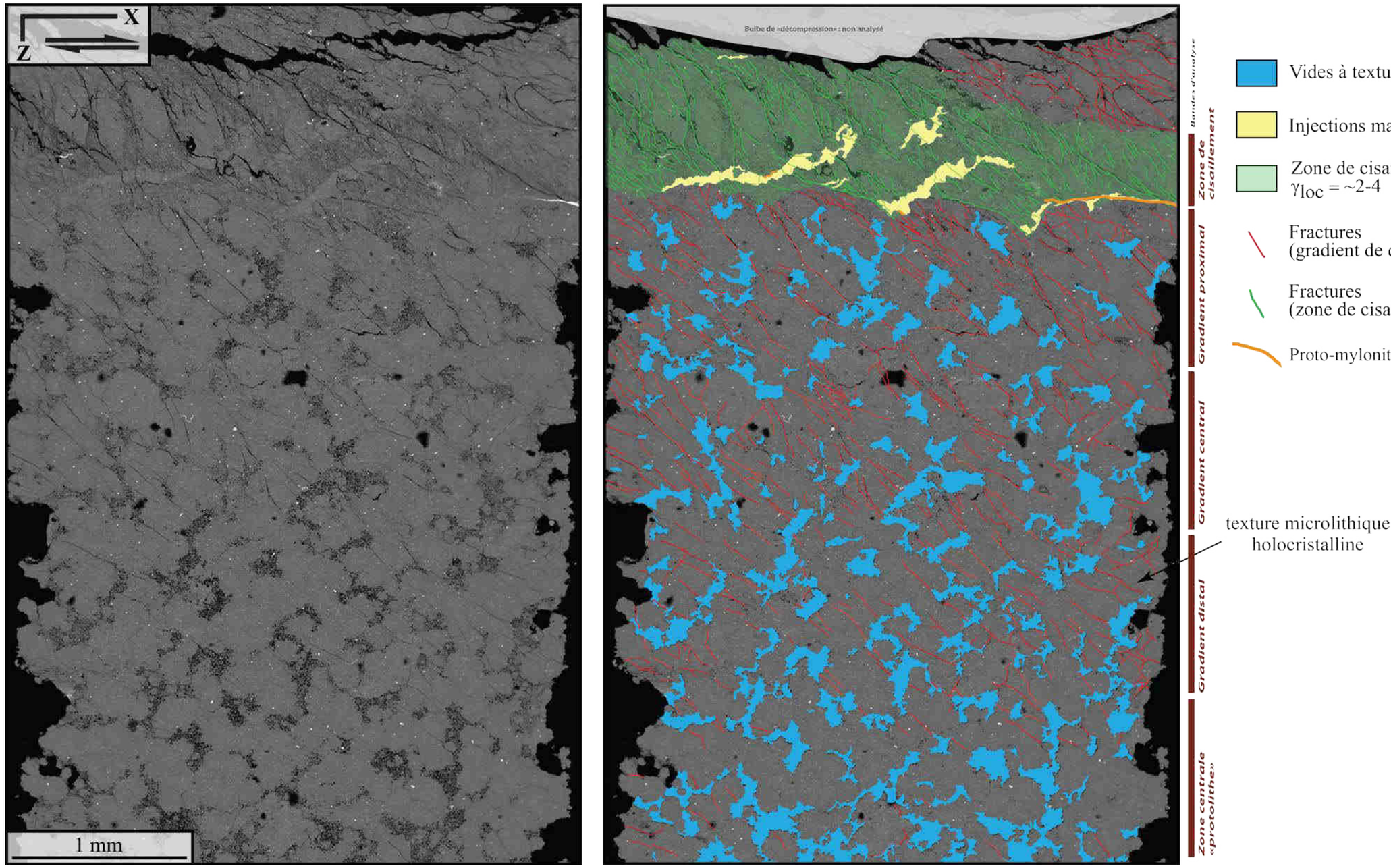

Figure V-31: *section [xz] au travers du produit de synthèse #4 déformé en torsion à une vitesse $\gamma\dot{\gamma}$ de 9.3x10^{-6} s^{-1}, pour une quantité de déformation totale γ_{bulk} obtenue de 0.56 (expérience PP565). À gauche : cliché MEB brut de la partie haute de l'échantillon cylindrique. À droite : même cliché MEB sur lequel sont annotées ou retracées les diverses textures (vides à texture diktytaxitique, injections magmatiques à texture microporphyrique) et microstructures (fractures et zones de déformation mylonitique) observées. Dans cette section [xz], la déformation se concentre essentiellement au niveau de la partie supérieure de l'échantillon sous la forme d'une bande sub-horizontale (coloriée en vert). Avec l'épaisseur variable de cette bande de déformation intense, il est estimé une quantité de déformation locale γ_{bulk} allant de 2 à 4. Notez également la présence d'un gradient de déformation fini sous cette bande de cisaillement. Selon la densité du réseau de micro-fractures, cinq sous-zones peuvent être en définitive délimitées : la zone protolithique, les zones du gradient de déformation (distale, centrale et proximale) et la zone de cisaillement.*

proximale vers la zone du protolithe, dans laquelle les textures anté-déformation (i.e., microlitique holocristalline et diktytaxitique) sont préservées. Puisque la déformation le long de ce gradient se limite au développement d'un réseau peu dense de micro-fractures, les valeurs de 2-4γ semblent à cet effet représenter un ordre de grandeur raisonnable quant à la quantité de déformation locale accumulée le long de la zone de cisaillement. En vue d'évaluer un peu plus en détail la distribution et l'évolution de la déformation à l'approche de la zone de cisaillement et au cœur de celle-ci, la suite de l'étude s'attèle dans un premier temps à mesurer les fabriques de forme et les proportions surfaciques de la texture diktytaxitique. Dans un second temps, les principales caractéristiques de la déformation cassante à cataclastique seront abordées avec notamment une analyse directionnelle des plans de fractures sur l'ensemble de la section d'étude. La géométrie des injections magmatiques et la manière dont se distribue la déformation ductile à cassante aux abords de ces injections seront enfin précisées.

3.2.2. La texture diktytaxitique : proportions surfaciques & fabriques de forme

Les orientations préférentielles de forme (OPFs) des vides à texture diktytaxitique, ainsi que leur proportion surfacique, ont été uniquement déterminées pour la zone protolithique et les zones du gradient de déformation (distal, central et proximal) ; cette texture étant complètement déstructurée au cœur de la zone de cisaillement. À partir du traitement numérique du cliché MEB de la section [xz] présenté précédemment (cf., Figure V-31), il apparaît très clairement une diminution significative de la proportion surfacique des vides à texture diktytaxitique à l'approche de la zone de cisaillement (Figure V-32a). Leur proportion passe ainsi de 21,4% dans la zone protolithique à quelques 10% dans la zone du gradient proximal ; la valeur de 21,4% retrouvée dans la zone protolithique étant d'ailleurs cohérente avec l'estimation réalisée au travers d'une section [xy] du produit de synthèse non déformé (cf., Figure V-23). Afin d'évaluer une possible relation géométrique entre les vides à texture diktytaxitique et les injections magmatiques - objets que nous aborderont un peu plus tard -, une analyse directionnelle de ces cavités a été également effectuée. Ainsi, à chaque zone d'étude, il y est associé une ellipse tensorielle de la fabrique de forme de ladite population (Figure V-32a). Selon ces ellipses, établies par comptage des intercepts, les directions d'allongement α de la fabrique de forme dans la zone protolithique et dans la zone du gradient distal sont relativement proches, avec respectivement des valeurs de +35.1° et +19.5° par rapport à l'axe de cisaillement <x>. Dans les zones du gradient central et proximal, les directions d'allongement de l'OPF des vides à texture diktytaxitique sont quant à elles perpendiculaires à celle mesurée dans la zone du protolithe, estimées respectivement à -39.7° et -34.7°. Néanmoins, compte tenu des faibles valeurs de l'intensité de fabrique Ie, en particulier celles obtenues dans la zone protolithique et dans les zones du gradient distal et central, les directions d'allongement ne peuvent être considérées comme réellement significatives. Dans ces trois zones, les intensités de fabrique s'échelonnent en effet entre 1.048 et 1.063. Le même constat peut être fait concernant les OPFs des phases cristallines (i.e., plagioclases) constitutives de la texture diktytaxitique. Deux exemples sont donnés Figures V-32b et V-32c. Que ce soit dans la zone protolithique ou dans la zone du gradient distal, les analyses par comptage des intercepts sur les plagioclases ne révèlent aucune intensité de fabrique supérieure

à 1.05 (i.e., 1.018 et 1.038). Obtenir de telles forces de fabrique n'est pas étonnant. L'essentiel de la déformation semble en effet être intégrée dans de la zone de cisaillement et par conséquent la réorientation cristalline dans la zone protolithique et les zones du gradient n'est guère envisageable. Ce réarrangement est d'autant plus difficile lorsque les cristaux sont jointifs, tels que constatés pour la texture diktytaxitique.

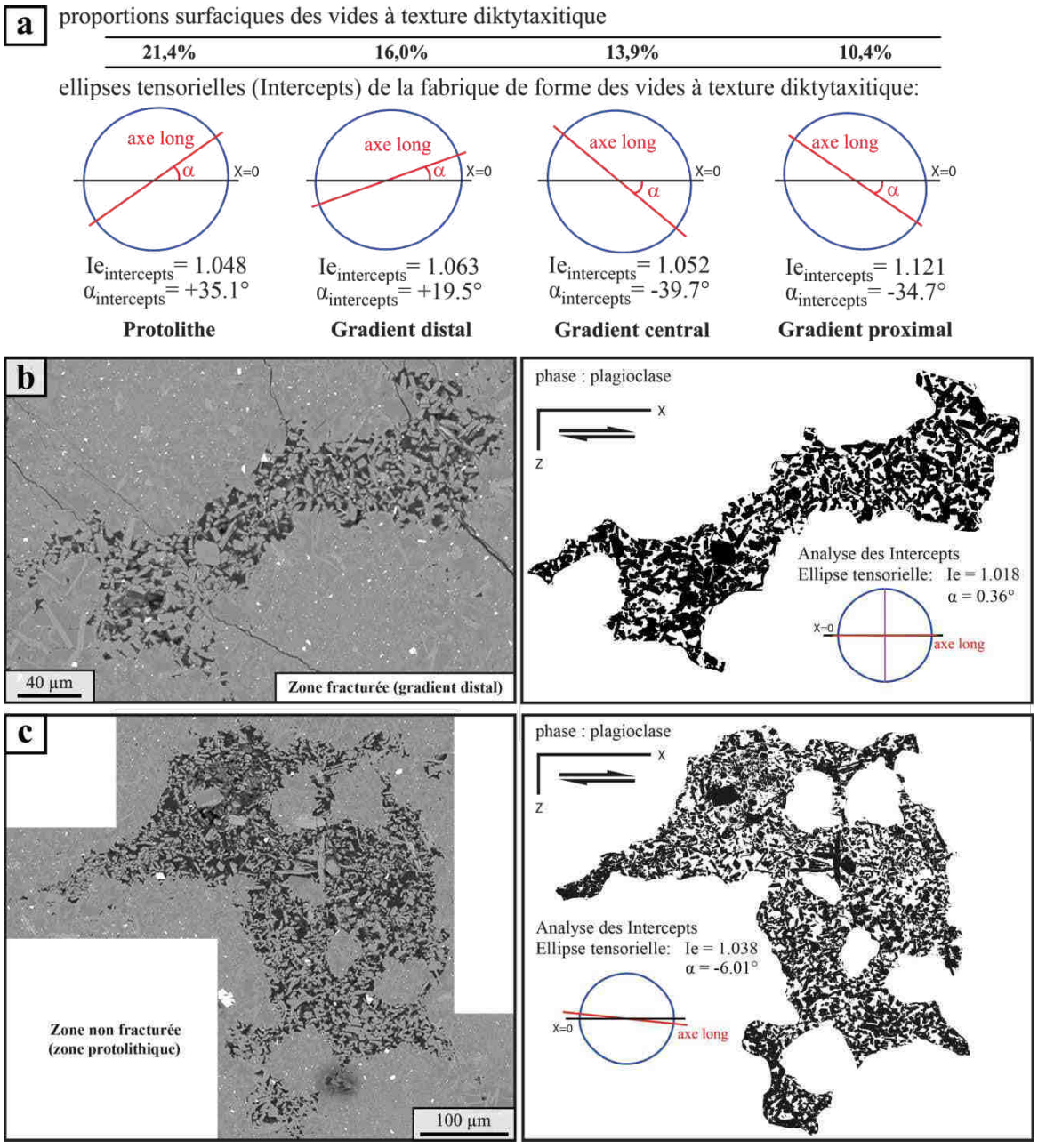

Figure V-32: (a) *proportions surfaciques et analyse statistique des fabriques de forme des vides à texture diktytaxitique dans la zone protolithique et le long du gradient de déformation (distal, central et proximal) au travers de la section [xz] du produit de synthèse déformé #4 (cf. Figure V-31). Les intensités Ie et les directions d'allongement α des ellipses tensorielles ont été estimées par comptage des intercepts. Les illustrations (b) et (c) correspondent quant à elles aux analyses des fabriques de forme (α, Ie) de plagioclases (phases constitutives de la texture diktytaxitique) dans la zone du gradient distal et dans la zone protolithique, respectivement. Les ellipses tensorielles ont été également obtenues par comptage des intercepts.*

3.2.3. Déformation cassante à cataclastique

Bulbes de décompression & micro-fracturation post-expérience

La phase de décompression d'une expérience en autoclave s'accompagne régulièrement d'une micro-fracturation de l'échantillon. Elle se matérialise essentiellement au niveau des parties basales et sommitales de l'échantillon sous la forme d'un bulbe facilement identifiable en section polie (Figure V-31b), zone par conséquent exclue de toute analyse. Quelques micro-fractures post-expérience peuvent également se manifester au cœur même des échantillons. Elles interviennent généralement lors de l'extraction de la colonne-échantillon, en particulier lorsque les suspensions magmatiques contiennent une faible fraction cristalline, sont initialement fragiles ou bien le sont devenues sous l'effet de la contrainte. Dans le cadre de notre expérience PP565, les micro-fractures dites « tardives » sont dans leur grande majorité reconnaissables ; elles se propagent de manière chaotique et sont sécantes aux injections magmatiques. Bien que certaines de ces micro-fractures se soient sûrement glissées dans nos analyses quantitatives, elles ne doivent représenter ici qu'un faible pourcentage des fractures analysées et ne peuvent être considérées comme un biais statistique.

Analyses directionnelles des micro-fractures

Comme il a été suggéré précédemment, seule de la micro-fracturation est perceptible au sein de la zone du protolithe et long du gradient de déformation. Quelle que soit la zone considérée, l'orientation préférentielle des micro-fractures analysées demeure inchangée, et ce, malgré une densification du réseau de fractures à l'approche de la zone de cisaillement (i.e., zone du protolithe, n= 38 ; distale : n= 113 ; centrale : n= 140 ; proximale : n= 155, avec n le nombre d'occurrences, Figure V-33). L'analyse directionnelle des plans de fracture, réalisée

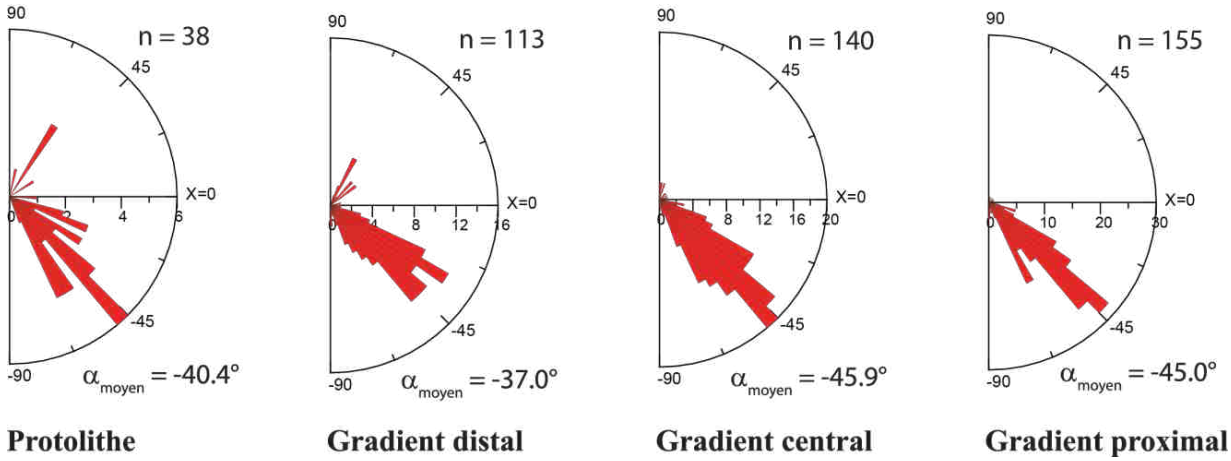

Figure V-33: *analyses directionnelles des micro-fractures dans la zone protolithique et dans les zones du gradient de déformation (distale, centrale et proximale) au sein de la section [xz] du produit expérimental #4 déformé en torsion (expérience PP565 ; cf. Figure V-31); Les directions d'allongement α des ellipses tensorielles des micro-fractures ont été obtenues à l'aide de la méthode du tenseur d'inertie (non normé à la surface) et sont présentées sous la forme d'une rose de fréquence, avec 90° < α < -90° où 0° correspond à la direction de cisaillement <x> ; n : nombre d'occurrences ; α_{moyen} : direction d'allongement de l'ellipse tensorielle moyenne.*

à partir de la méthode du tenseur d'inertie (non normé à la surface, cf. section 2.3.4), ne révèle en effet qu'une unique population de fractures dont l'orientation des lèvres se restreint majoritairement dans une fenêtre de -40° à -50° par rapport à l'axe de cisaillement <x> (Figure V-33). Cette famille d'orientation suggère la présence de micro-fractures tensiles, également appelées fentes de tension T dans le système cassant-cataclastique de Riedel (Figure V-34). Les fentes de tension s'expriment différemment selon leur taille. Les fentes de grande envergure, typiquement au-delà de plusieurs centaines de micromètres, se propagent de cavité en cavité (Figure V-34a), tandis que les plus petites s'organisent davantage en échelon (Figure V-34b). Ces réseaux de fentes sont localement relayés par des micro-fractures sub-horizontales ou faiblement pentées (dans la gamme de -15°/-20°), qui dans ce même système de Riedel, sont respectivement apparentées aux micro-fractures synthétiques de types Y et R (Figure V-34b).

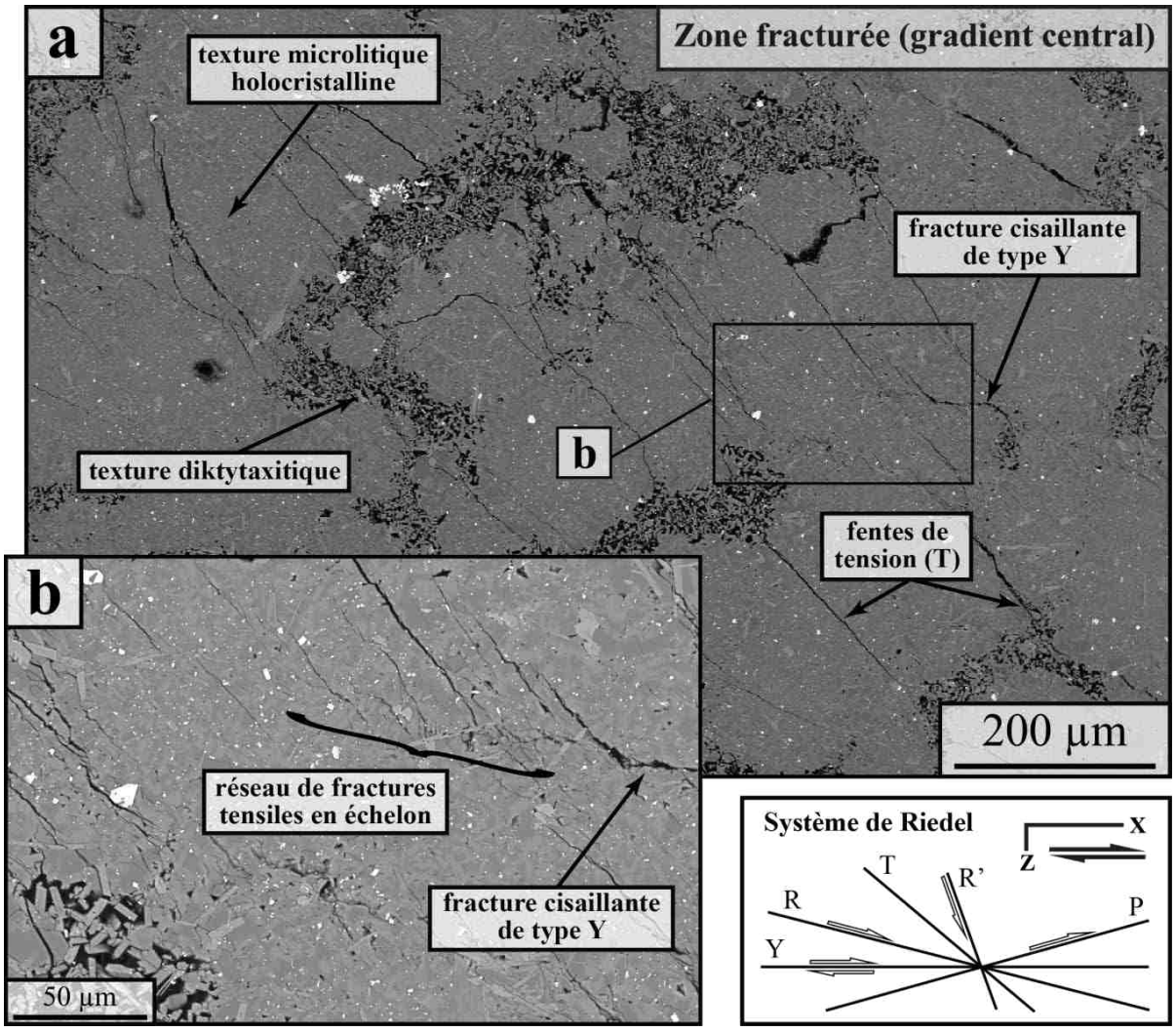

Figure V-34: *micro-fracturation au sein de la section [xz] du produit expérimental #4 déformé en torsion (expérience PP565 ; cf. Figure V-31). (a) cliché MEB de la zone centrale du gradient de déformation montrant la prédominance de fentes de tension T (dénomination basée sur le système de Riedel). Ces fentes de tensions sont également associées à d'autres familles de micro-fractures secondaires (typiquement des micro-fractures synthétiques de type R ou Y). (b) cliché MEB mettant en évidence des réseaux de fentes de tension organisées en échelon et relayés par des micro-fractures synthétiques (de type Y dans le cas présent).*

Si les micro-fractures synthétiques de type R se font plutôt rares dans les zones du gradient de déformation, leur nombre devient sensiblement plus important dans la zone dite de cisaillement. Cette augmentation va néanmoins de pair avec la densification du réseau de micro-fractures (n=340 ; Figure V-35). Leur proportion demeure toujours aussi faible, comme en témoignent les roses de fréquence des orientations préférentielles de micro-fractures analysées (Figure V-35). Suivant ces diagrammes en rose, les micro-fractures dont les lèvres sont orientées autour de -45° par rapport à l'axe <x> prédominent. La déformation en régime cassant le long de la zone de cisaillement se traduit donc préférentiellement par le développement des fentes de tension, en accord avec les résultats obtenus dans les zones du

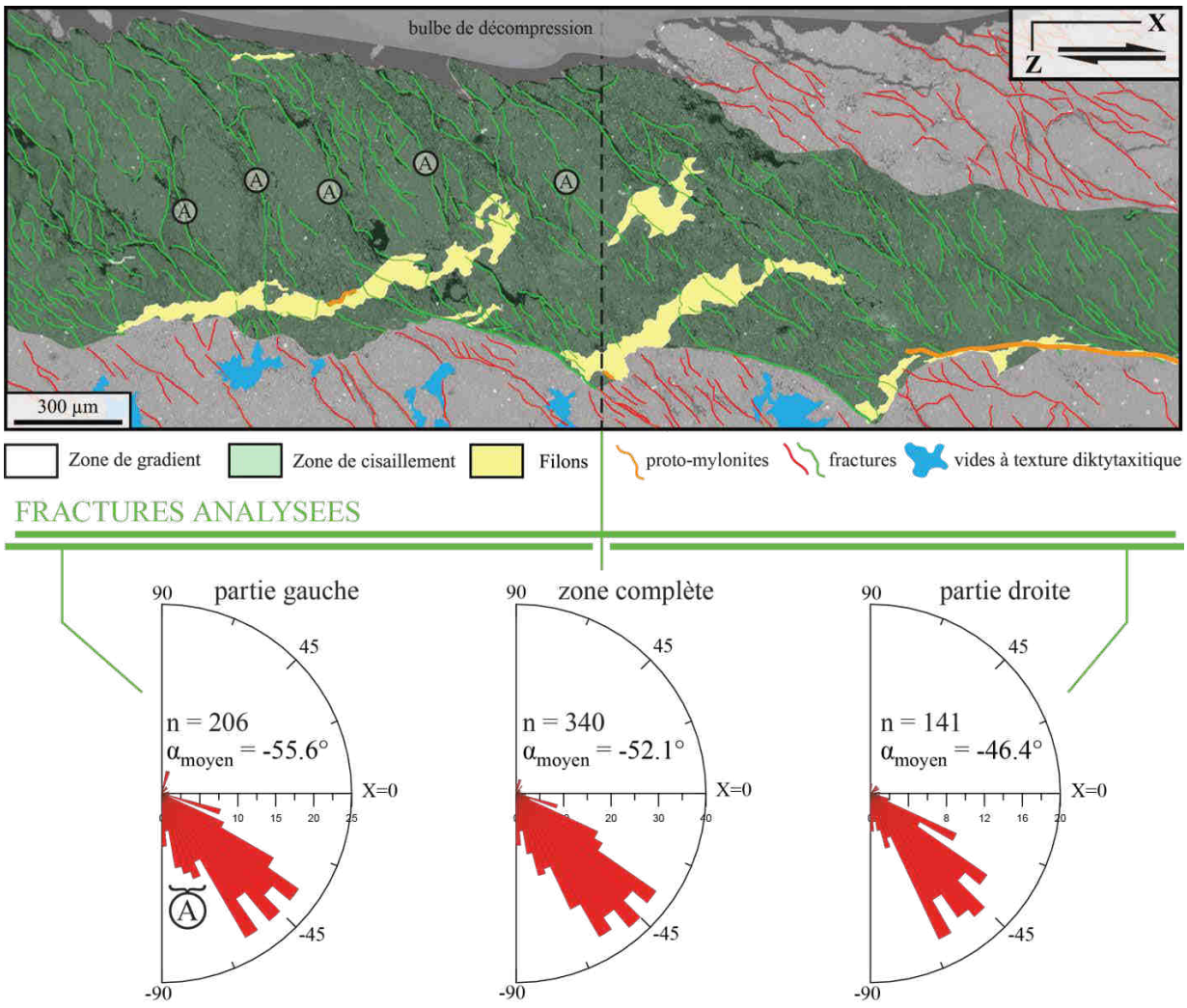

Figure V-35: *analyse directionnelle des micro-fractures (coloriées en vert) dans la zone de cisaillement au sein de la section [xz] du produit expérimental #4 déformé en torsion (expérience PP565 ; cf. Figure V-31); Les directions d'allongement α des ellipses tensorielles des micro-fractures ont été obtenues à l'aide de la méthode du tenseur d'inertie (non normé à la surface) et sont présentées sous la forme de roses de fréquence (zone complète, parties gauche et droite de la zone), avec 90° < α < -90° où 0° correspond à la direction de cisaillement <x>. ; n : nombre d'occurrences ; α_{moyen} : direction d'allongement de l'ellipse tensorielle moyenne. Notez que la direction majeure des plans fractures (environ -45° par rapport à l'axe de cisaillement) est associée localement (partie gauche de la zone de cisaillement) à une seconde famille de fractures orientée cette fois-ci à -70°±10° (indiquée sur le cliché MEB et la rose de fréquence par la lettre A).*

gradient. Toutefois, ladirection d'allongement de l'ellipse tensorielle moyenne de la population de micro-fractures analysées (i.e., α_{moyen}= -52.1°, rose de fréquence de la « zone complète » ; Figure V-35) ne n'entre pas tout à fait dans la gamme de celles mesurées le long du gradient de déformation (i.e., entre -37.0° et -45.9° ; Figure V-33). Cette légère différence angulaire peut se justifier par la distribution plus hétérogène des orientations, mais s'explique surtout par le développement de micro-fractures fortement pentées. La Figure V-35 présente une analyse directionnelle des plans de fractures pour chaque moitié de la zone de cisaillement. L'analyse statistique nous montre que la direction moyenne des micro-fractures dans la moitié droite (i.e., α_{moyen}= -46.4°) est cohérente avec celle obtenue dans la zone du gradient proximal. En revanche, la direction moyenne des micro-fractures dans la moitié gauche est à -55.6° de l'axe de cisaillement <x> et qu'une population de micro-fractures, inclinées à -70° ± 10°, ressort de l'analyse directionnelle. Ces micro-fractures sont annotées par la lettre (A) à la fois sur la rose des fréquences et sur le cliché MEB. Il semble ainsi qu'elles soient localisées aux abords de lentilles non déformées, à savoir le long de zones dans lesquels la texture du protolithe est préservée (Figures V-35 et V-36). Deux hypothèses peuvent être émises pour expliquer le développement de micro-fractures à fort pendage : (1) le simple développement de micro-fractures cisaillantes de type R' (inclinaison de -75° dans le système cassant-cataclastique de Riedel), ou bien (2) le développement de fentes de tension progressivement basculées dans le sens horaire au cours de l'expérience de déformation. Cette seconde hypothèse expliquerait davantage pourquoi les micro-fractures fortement pentées sont spatialement associées aux lentilles non déformées, mais aussi pourquoi il existe un plus large éventail d'orientations de micro-fractures dans la zone de cisaillement (i.e., panel de -45° jusqu'à la quasi-verticalité pour certaines occurrences). En d'autres termes, sous l'effet de la contrainte cisaillante, le basculement horaire et conjoint de quelques micro-fractures synthétiques, de types R ou Y (Figure V-36), et de fentes de tensions serait associé à la rotation de lentilles non déformées.

Fragmentation intra-cristalline et bandes de déformation cataclastique

Lors de l'expérience PP565, la déformation ne s'est pas uniquement manifestée par de la micro-fracturation, mais elle s'est également matérialisée par de la fragmentation intra-cristalline. Excepté l'observation très locale d'une fragmentation intra-cristalline le long de plans de fractures dans les zones du gradient de déformation, seuls des portions de l'échantillon se situant au niveau de la zone cisaillement enregistrent une déformation cataclastique intense. Un exemple de zones endommagées par de la fragmentation est donné Figure V-36a. Sur ce cliché MEB, la déformation dans le régime cataclastique se traduit le long d'une bande faiblement pentée d'environ 70µm d'épaisseur. Cette bande de déformation cataclastique est cernée par deux micro-fractures peu pentées de type R, micro-fractures relayant un réseau de fentes de tension. C'est le long de ces micro-fractures que la déformation est la plus intense. La taille des grains fragmentés, de formes anguleuses, est fortement réduite ; leur taille n'atteint que très rarement les 5µm (Figure V-36b). Il est fort probable que la bande de déformation cataclastique soit le résultat de l'effondrement des cavités et du broyage des phases constitutives de la texture diktytaxitique initialement présente entre les deux micro-fractures. Cette texture est encore observable juste au-dessus de la bande de déformation cataclastique.

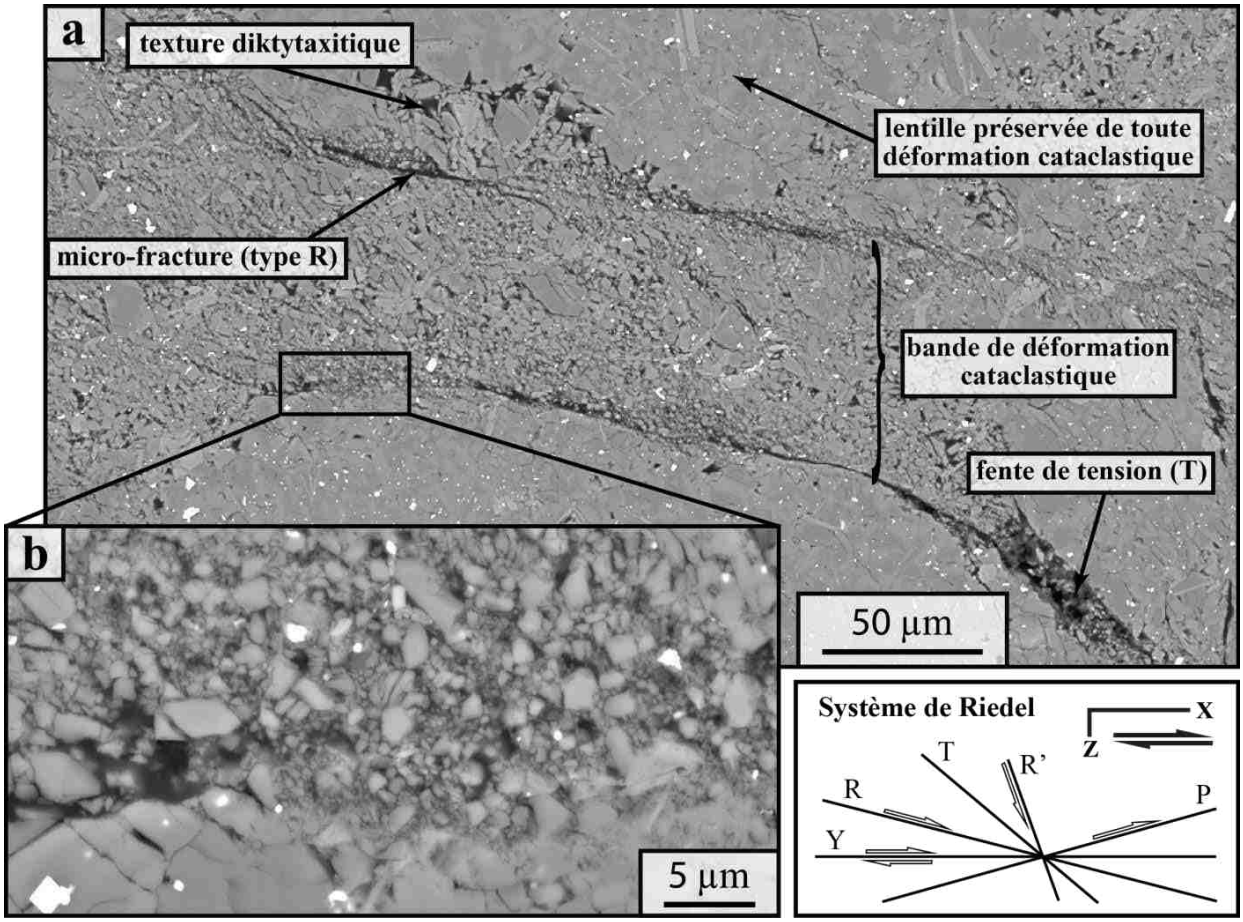

Figure V-36: *clichés MEB pris dans la zone de cisaillement au sein de la section [xz] du produit expérimental #4 déformé en torsion (expérience PP565 ; cf. Figure V-31), illustrant (a) le développement d'une micro-bande de déformation cataclastique faiblement pentée et cernée de part et d'autre par des fractures synthétiques de type R, et (b) la fragmentation intra-cristalline associée.*

3.2.4. Les injections magmatiques

Comme nous l'avons précédemment évoqué, la zone de cisaillement se distingue tout particulièrement du reste de l'échantillon par l'injection de magmas partiellement cristallisés (Figure V-32). Les clichés MEB de ces sept injections magmatiques sont présentées Figure V-37. Mentionnons que les objectifs principaux sont ici (1) de décrire la géométrie globale des injections magmatiques ainsi que d'évaluer par une approche statistique leur orientation préférentielle, (2) quantifier les fabriques de forme des phases cristallines constitutives des injections, et (3) caractériser l'évolution et la distribution de la déformation aux abords des injections magmatiques, en particulier le long de l'injection 34-42 (Figure V-37a).

Morphologies & analyses directionnelles des injections magmatiques

Cette partie de l'étude ne prétend aucunement décrire en détail les caractéristiques morphologiques des injections magmatiques. Néanmoins, quelques points importants doivent être soulignés. Sur ces clichés MEB, vous noterez que la morphologie des injections

magmatiques est plus ou moins complexe selon qu'elles occupent respectivement une forte (i.e., Figures V-37a, V-37b, V-37d et V-37f) ou une faible proportion surfacique (Figures V-37c et V-37e). La géométrie des injections occupant une faible proportion surfacique est simple, à savoir planaire. Pour les injections magmatiques de plus forte proportion surfacique, aux morphologies complexes, vous constaterez le caractère digité des contacts intrusifs. Les magmas empruntent des voies sinueuses, contournant notamment des nodules préservés de toute déformation cassante/cataclastique (Figure V-37b). Leur puissance est variable, dessinant pour certaines de ces injections une succession de poches de magmas interconnectés (Figures V-37a, V-37b et V-37f). Dans cet ensemble d'injections, il est globalement possible de distinguer trois types de géométrie : (1) sigmoïdale, tel qu'observée pour les injections 26-33 et 5-9 (Figures V-37b et V-37d) ; (2) en « marche d'escalier », caractérisant l'injection 12-23 (Figure V-37f) ; et (3) coudée (i.e., virgation de l'une des terminaison de l'injection), tel que constaté pour l'injection 34-42 (Figure V-37a).

Les sept injections magmatiques ont fait l'objet d'une analyse directionnelle, bien qu'une orientation préférentielle soit évidente par la simple observation des clichés MEB. L'analyse statistique, établie par comptage des intercepts, révèle ainsi une direction d'allongement α de l'OPF moyenne des injections de +16.2° par rapport à l'axe de <x>, pour une force de fabrique moyenne Ie de 1.73 (Figure V-37). Prises individuellement, les directions d'allongement des injections magmatiques se distribuent entre +6.9° et +44.8°, soit un écart d'angle relativement fort d'une trentaine de degrés. Néanmoins, la direction d'allongement de +44.8° obtenue pour l'injection 5-9 fait exception (Figure V-37d). En ne considérant que les cinq autres directions, la fenêtre d'angles se réduit alors considérablement, allant de +6.9° à +19.9°.

Fabrique de forme des phases constitutives des injections

La Figure V-38 présente les résultats d'une analyse des OPFs des phases constitutives de l'injection magmatique 26-33. L'étude statistique s'est plus spécifiquement concentrée sur une portion de l'injection 26-33 (cf. Figure V-37b pour la localisation) dont les épontes aux contacts diffus sont orientées à +45° de l'axe de cisaillement <x>, soit perpendiculairement aux fentes de tension (Figures V-38a et V-38b). Cette zone de l'injection magmatique constitue en deux points un site idéal pour l'étude des fabriques de forme développées par les particules en suspensions. D'une part, la puissance de l'injection n'est dans cette zone que très peu changeante, passant d'environ 50µm à 60µm. Les épontes relativement parallèles limitent les variations de fabriques de forme locales en lien avec un changement de la puissance de l'injection et rend ainsi plus lisible les résultats de l'analyse. D'autre part, une injection dont la puissance est de 50-60µm permet d'analyser un nombre d'objets de tailles limitées (i.e., 5-10µm) suffisamment important. Au vu des contacts intrusifs digités et des puissances variables des injections rencontrés au travers de la section [xz], peu de choix s'offraient donc à nous.

Le cœur de l'injection se caractérise plus précisément par une texture microporphyrique aphanitique (Figures V-38a et V-38b). Aucune analyse chimique quantitative ou élémentaire semi-quantitative des phases cristallines n'a été ici réalisée. Il est néanmoins possible de

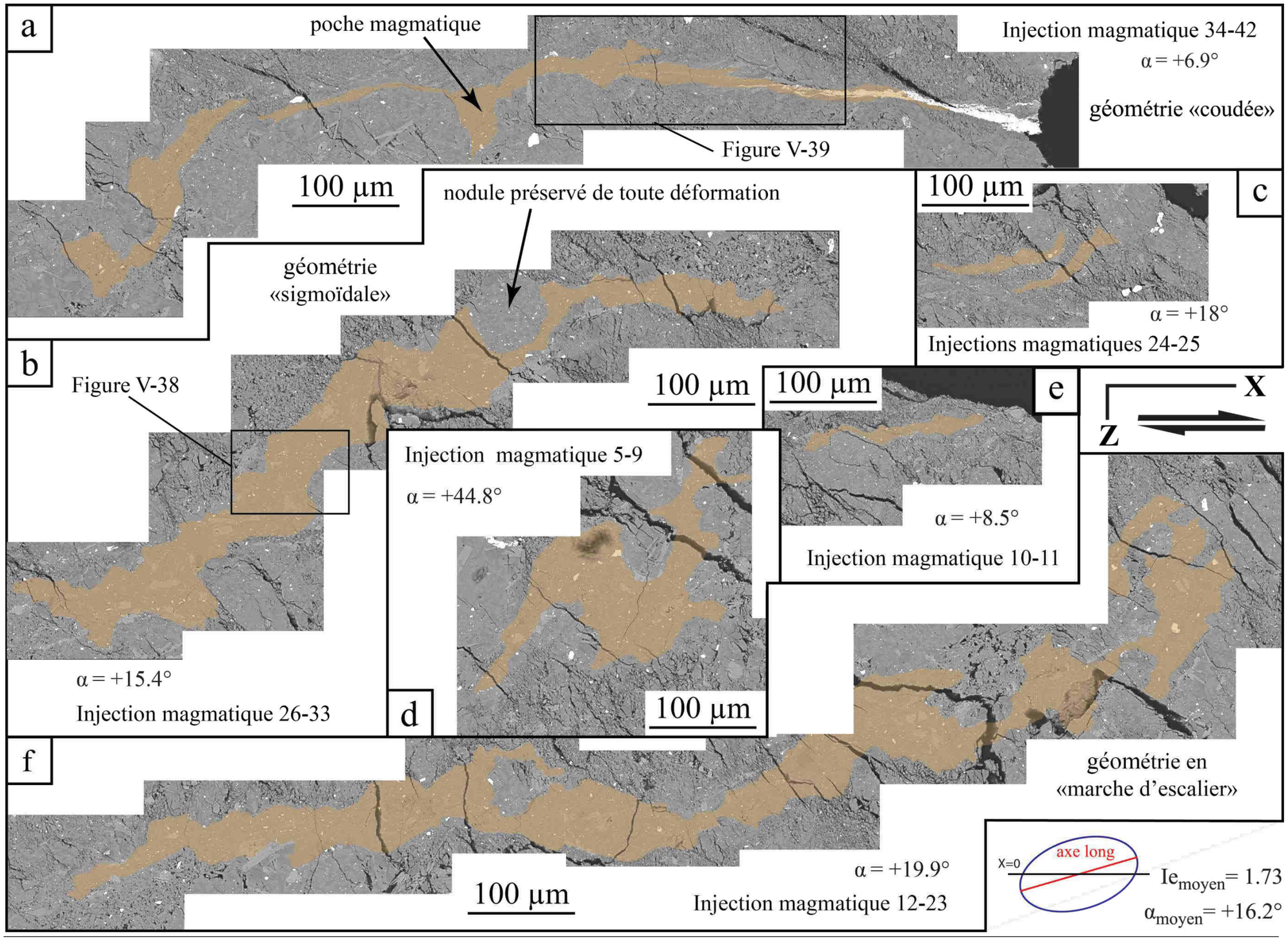

Figure V-37: *clichés MEB pris dans la zone de cisaillement au sein de la section [xz] du produit expérimental #4 déformé en torsion (expérience PP565 ; cf. Figure V-31), répertoriant l'ensemble des injections magmatiques (a-f) observées. Ces injections magmatiques sont coloriées en beige sur les clichés. En bas à droite : ellispse tensorielle moyenne des injections magmatiques, avec α_{moyen} la direction d'allongement moyenne de l'ellipse et Ie_{moyen} la force de fabrique moyenne.*

reconnaître les plagioclases par leur forme tabulaire si particulière. Ces cristaux représentent la grande majorité des phases cristallines baignant dans le liquide silicaté. Leur distribution de taille est assez homogène, bien que quelques grains semblent avoir subi une fragmentation et une réduction de leur taille. Suivant l'analyse statistique, établie par calcul du tenseur d'inertie, la fabrique de forme moyenne portée par ces particules solides se définit par une direction d'allongement α de +38.8° par rapport à l'axe <x>, pour une force de fabrique Ie mesurée de 1.121 (Figures V-38c). La direction α de la fabrique de forme moyenne est pour conclure en totale cohérence avec l'orientation des épontes de l'injection.

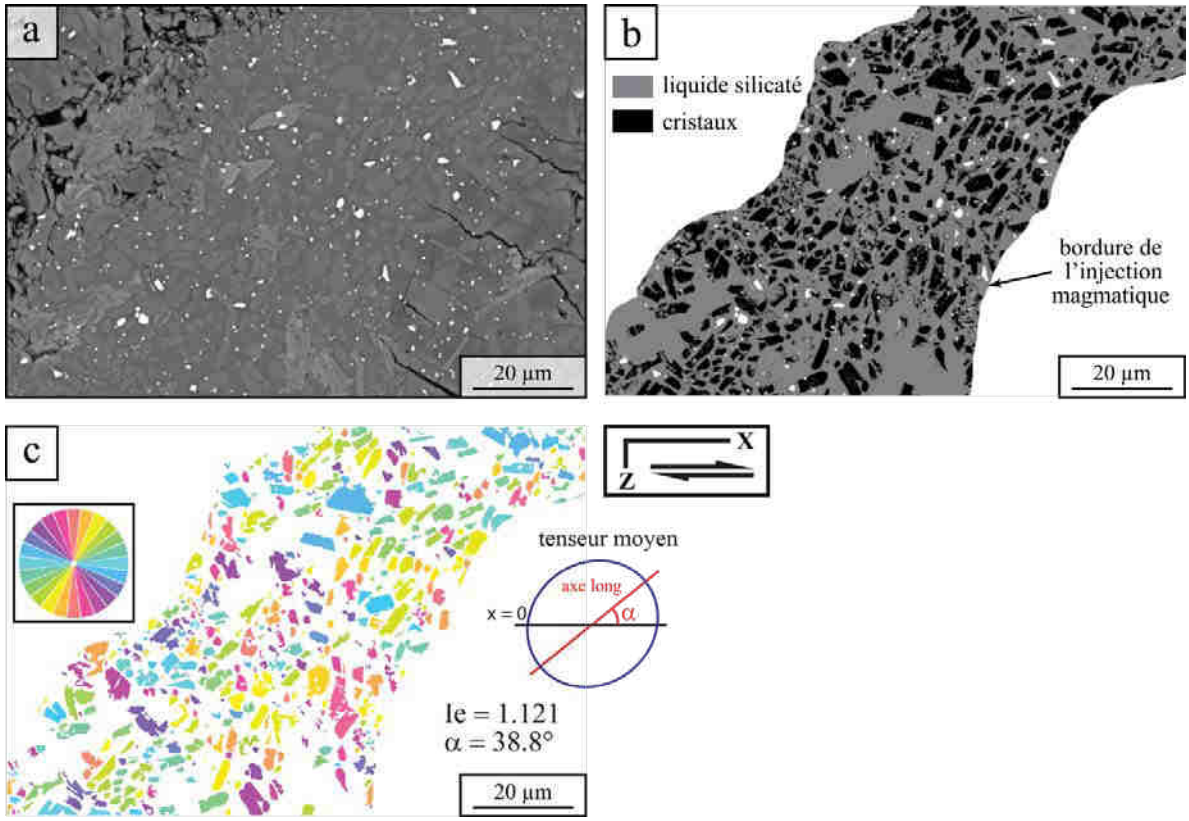

Figure V-38 : *analyse statistique des OPFs (Orientations Préférentielles de Forme) par méthode du tenseur d'inertie de la population de cristaux au sein de l'injection magmatique 26-33 (cf. Figure V-37 pour la localisation). (a) cliché MEB brut à partir duquel les OPFs ont été obtenues. (b) cliché MEB seuillé en niveau de gris sur lequel les cristaux et le liquide silicaté sont isolés. (c) Représentation cartographique des OPFs des cristaux au sein de l'injection magmatique. Les différentes couleurs représentent les orientations des cristaux, pris individuellement. α : direction d'allongement du tenseur moyen de la fabrique ; Ie : intensité de la fabrique de la population cristalline considérée.*

Injections magmatiques & déformation ductile-cataclastique

Dans l'expérience PP565, l'essentiel de la déformation ductile s'est concentré aux abords de l'injection magmatique 34-42 (cf. Figure V-37a pour la localisation). Rappelons tout d'abord que cette injection se définit morphologiquement par une virgation de ses épontes dans la direction du cisaillement <x>, attribuant ainsi à l'injection une forme coudée (Figure V-37a). La Figure V-39a donne une vue d'ensemble de la terminaison droite de l'injection. Les bordures de l'injection sont soulignées par les traits en pointillé rouges. L'injection est ici en

position sub-horizontale à faiblement inclinée par rapport à l'axe <x>. Il est d'ailleurs possible d'observer le coude de l'injection tout à gauche de l'image MEB, tandis que tout à droite du cliché l'injection se termine sous un réseau de micro-fractures cisaillantes : listriques et de type R. Mis à part la présence d'une poche magmatique (Figures V-39a et V-39b), l'injection affiche une faible puissance, d'une vingtaine de microns tout au plus. Les contacts intrusifs supérieurs et inférieurs de l'injection sont tous deux digités. Les doigts sont néanmoins plus marqués au niveau du contact supérieur. Les contacts sont également diffus. Il est parfois difficile de les distinguer distinctement, comme en témoigne la cartographie élémentaire résultant d'une analyse *EDS* au niveau de la poche magmatique (Figure V-39b et V-39c). La composition de l'injection (liquide + cristaux) est en effet très proche de celle de son encaissant et lorsque la suspension magmatique est fortement chargée en cristaux, comme le cas ici, différencier l'injection de son encaissant est quelque peu compliqué. De plus, le liquide silicaté tend à s'immiscer entre les premiers grains au contact de l'injection (Figure V-39b). Vous noterez également qu'il n'existe ni de cristaux de quartz, ni de feldspaths potassiques dans l'injection magmatique (Figure V-39c). Seuls des cristaux ferromagnésiens (amphibole, biotite) et des feldspaths plagioclases constituent la fraction cristalline.

Délimiter le contact intrusif se complique encore davantage lorsque les cristaux de l'encaissant ont subi une fragmentation intense et une forte réduction de leur taille, telles qu'observées sur les clichés MEB des Figures V-39d et V-39e. Dans cette zone, la déformation cataclastique est tout particulièrement associée à de la déformation ductile. Cette association s'observe sur plusieurs dizaines de microns d'épaisseur de part et d'autre de l'injection magmatique (Figure V-3d). Elle résulte sûrement d'une différence de compétence entre cristaux. Au vu des différences de teintes de gris sur les clichés MEB et de l'analyse élémentaire, il semble en effet que les ferromagnésiens soient les seuls cristaux ductilement déformés, tandis que les autres phases sont cataclasées. Les ferromagnésiens sont donc étirés, boudinés et cisaillés, aboutissant notamment à des figures typiques de la déformation ductile que sont les *mica-fish* (Figure V-3e). Ces figures de la déformation ductile sont également observées au niveau de l'éponte inférieure de la poche magmatique (Figure V-3b). Les multiples alignements parallèles de ferromagnésiens déformés dessinent une foliation. Sur les Figures V-3d et V-3e, la trace de la foliation est orientée à 25/30° par rapport à l'axe de cisaillement. Les plans de cisaillement sont quant à eux orientés à 45° de la foliation et leur cinématique indique de manière constante un cisaillement apparent normal dextre. Ce système est plus couramment appelé C'/S avec S la foliation minérale et C' le plan de cisaillement [*Berthé et al.*, 1979]. À plus grande échelle (i.e., Figure 39a), une virgation de la foliation est constatée à l'approche de l'injection. Cette virgation met en évidence un cisaillement apparent dextre généralisé dans un système C/S (avec C l'orientation de l'injection).

La déformation ductile est aussi enregistrée au cœur même de l'injection (Figure V-3d et V-3e). Les cristaux sont dans le cas présent fortement étirés, davantage que dans l'encaissant, et presque méconnaissables. L'étirement des cristaux définit alors une foliation intense des phases constitutives de l'injection s'accompagne également d'un alignement de cristaux cataclasés dont la taille ne dépasse que très rarement les 2µm (Figures V-39d et V-39e).

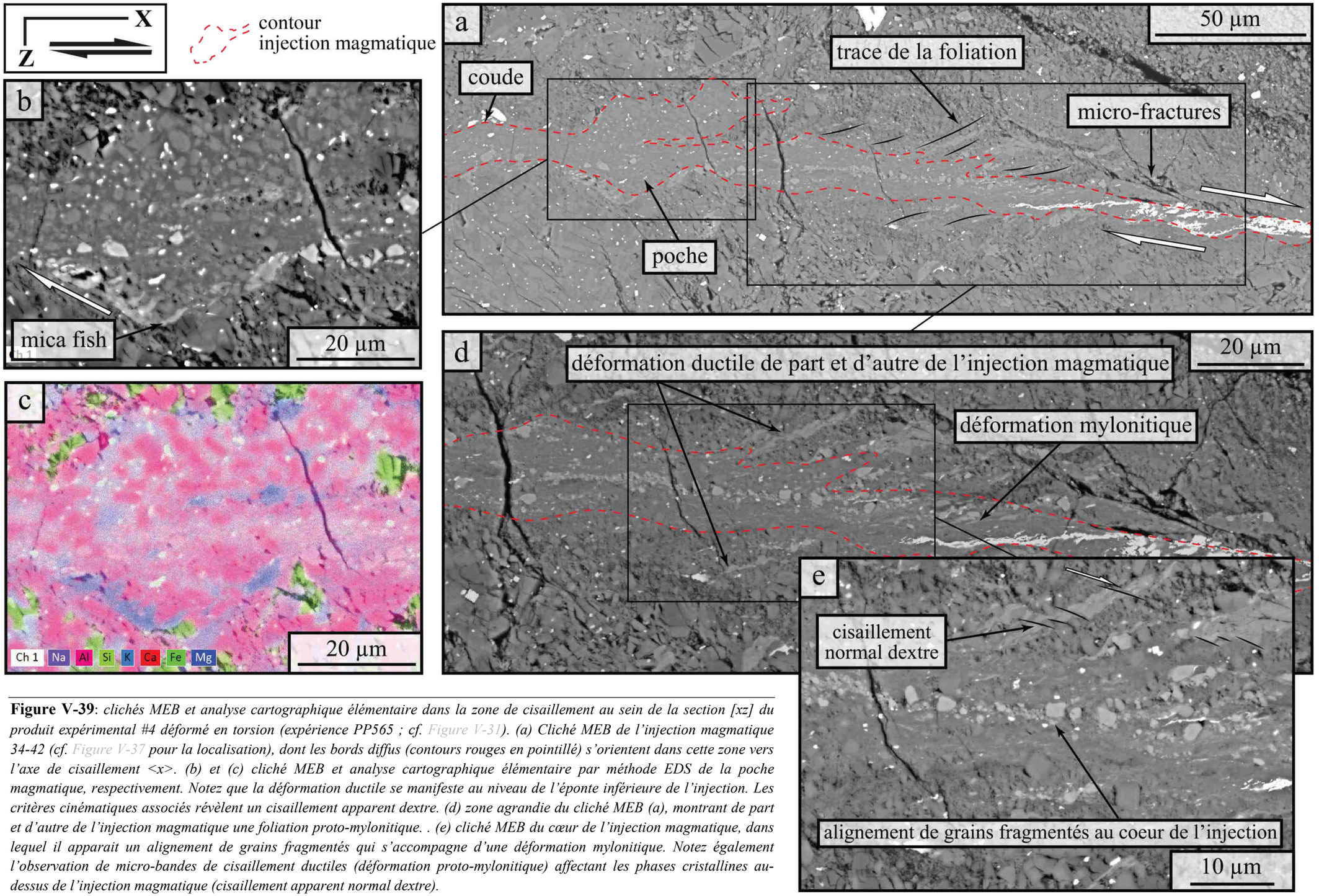

Figure V-39: *clichés MEB et analyse cartographique élémentaire dans la zone de cisaillement au sein de la section [xz] du produit expérimental #4 déformé en torsion (expérience PP565 ; cf. Figure V-31). (a) Cliché MEB de l'injection magmatique 34-42 (cf. Figure V-37 pour la localisation), dont les bords diffus (contours rouges en pointillé) s'orientent dans cette zone vers l'axe de cisaillement <x>. (b) et (c) cliché MEB et analyse cartographique élémentaire par méthode EDS de la poche magmatique, respectivement. Notez que la déformation ductile se manifeste au niveau de l'éponte inférieure de l'injection. Les critères cinématiques associés révèlent un cisaillement apparent dextre. (d) zone agrandie du cliché MEB (a), montrant de part et d'autre de l'injection magmatique une foliation proto-mylonitique. . (e) cliché MEB du cœur de l'injection magmatique, dans lequel il apparait un alignement de grains fragmentés qui s'accompagne d'une déformation mylonitique. Notez également l'observation de micro-bandes de cisaillement ductiles (déformation proto-mylonitique) affectant les phases cristallines au-dessus de l'injection magmatique (cisaillement apparent normal dextre).*

4. Discussion

4.1. Comportements structuraux des magmas granodioritiques de faible & moyenne cristallinité

4.1.1. Magmas de faible cristallinité & fabriques pénétratives (expérience #1)

Dans l'expérience PP548 (800°C, 300MPa), la structuration de la suspension magmatique à texture microporphyrique aphanitique #1 (ϕ_s=0.34) passe par la mise en orientation des phases cristallines suivant une direction majeure proche de l'axe de cisaillement (cf. Figure V-25). Le développement de fabriques pénétratives aux propriétés directionnelles homogènes est classique dans les expériences de déformation de suspensions magmatiques contenant une faible fraction cristalline [*Picard*, 2009; *Picard et al.*, 2013]. Durant les premiers stades de la cristallisation, les suspensions magmatiques se comportent comme un fluide newtonien [e.g., *Lejeune & Richet*, 1995]. Le comportement mécanique de la suspension magmatique est uniquement contrôlé par les propriétés du liquide silicaté et la viscosité dynamique augmente de façon constante avec la fraction cristalline, suivant ainsi le modèle théorique d'Einstein-Roscoe [*Einstein*, 1911; *Roscoe*, 1952]. Sous l'effet d'une contrainte cisaillante, l'écoulement du fluide laminaire s'accompagne de la rotation de cristaux [e.g., *Arbaret et al.*, 1996; *Ildefonse et al.*, 1997]. La vitesse de rotation dépend principalement des angles que font les directions d'allongement α de cristaux par rapport à l'axe de cisaillement (i.e., d'autant plus rapide que l'angle est élevé), mais également de la forme et de la taille des cristaux. La déformation de suspensions magmatiques polyminéraliques, dans lesquelles il existe une vitesse de rotation différentielle en lien avec la nature des cristaux, aboutit en général au développement de sous-fabriques et d'une perte d'intensité des OPFs, tels qu'observés dans cette expérience (cf. Figure V-26).

4.1.2. Magmas de faible à moyenne cristallinité & fabriques semi-pénétratives (expériences #2 et #3)

Dans l'expérience PP554 (750°C, 300MPa, ϕ_s=0.43), la présence en faible proportion de glomérophyres polyminéraliques ne perturbe pas l'OPF moyenne des cristaux libres dans la liquide interstitiel (cf. Figure V-28). Avec l'augmentation de la proportion cristalline d'environ 10% (expérience PP561, 750°C, 300MPa, ϕ_s=0.51), et par conséquent la présence en proportion plus importante de glomérophyres, l'OPF n'est plus homogène (cf. Figure V-30). Autour et entre les glomérophyres, les directions de l'OPF locale varie en tournant autour de ces éléments rigides que forment les glomérophyres. Ce changement dans les fabriques cristallines entre les deux expériences indique des évolutions structurale et mécanique conjointes.

Structuralement, les deux produits utilisés représentent des suspensions solides magmatiques faiblement à moyennement concentrées qui sont caractérisées par une fraction liquide, majoritaire, qui constitue le milieu continu dans lequel les cristaux baignent. Dans ces suspensions soumises à un régime de déformation en cisaillement simple, les expériences analogiques [*Willis,* 1977 ; *Fernandez et al.*, 1983 ; *Arbaret et al.*, 1996] et en expérimentation

H*P*/H*T* [*Arbaret et al*, 2007 ; *Picard et al*, 2011] ont montré que les OPFs cristallines représentent les paléo-lignes d'écoulement du fluide [*Vigneresse et al.*, 2005]. On passe donc d'un régime laminaire homogène pour une fraction cristalline de 0.43 avec peu de glomérophyres à un régime d'écoulement perturbé avec l'apparition d'une tortuosité dans les lignes d'écoulement pour une fraction cristalline de 0.51 caractérisées par une augmentation du nombre de glomérophyres.

Mécaniquement, l'apparition d'une tortuosité d'écoulement dans une suspension solide (i.e., suspension « molle ») caractérise les suspensions congestionnées (i.e., *congested slurries* ; *Petford* [2009]). Cette tortuosité augmente avec la fraction cristalline jusqu'au seuil de fraction cristalline maximum (*maximum packing fraction*, *Vigneresse* [2015] pour une revue) à partir duquel le milieu continu est le solide polycristallin avec un liquide interstitiel, l'ensemble composant une suspension concentrée (i.e., suspension « dure »). L'apparition de la tortuosité d'écoulement du liquide silicaté est souvent invoquée comme étant à l'origine de la transition entre un comportement rhéologique newtonien (comportement linéaire sans seuil de contrainte critique) caractéristique des liquides silicatés purs ou faiblement cristallisées à un comportement rhéologique dit de Bingham (apparition d'un seuil de contrainte critique) communément mesuré dans les suspensions solides moyennement concentrées [*Caricchi et al.*, 2007, *Champallier et al.*, 2008, *Picard et al.*, 2011]. Bien qu'il n'y ait pas été possible de mesurer le comportement mécanique dans les suspensions utilisées pour ce volet expérimental, l'analyse structurale des magmas déformés a montré l'émergence d'une tortuosité d'écoulement significative dès 45 à 50 % de cristallinité en plein accord avec les travaux précédents [*Caricchi et al.*, 2007, *Picard et al.*, 2011].

4.2. Injections magmatiques & localisation de la déformation : cas du produit fortement cristallisé

4.2.1. Processus à l'origine de la texture diktytaxitique

Avant de discuter les résultats de l'expérience de déformation des produits expérimentaux #4 (cf., section 3.2.), il semble nécessaire de revenir sur les possibles processus à l'origine d'une disparité dans le taux de cristallinité entre le cœur et la bordure des échantillons synthétisés. Rappelons donc que les synthèses menées à une température de 650°C ont abouti à la cristallisation de textures particulières avec (1) au cœur des échantillons cylindriques la présence d'un produit fortement cristallisé marqué par la combinaison de textures microporphyriques et glomérophyriques (cf. Figure V-22), et (2) en bordure un produit entièrement cristallisé présentant une texture microlitique et des vides à texture diktytaxitique (cf. Figure V-23).

L'observation de vides à texture diktytaxitique n'est pas rare dans la nature. Ces textures s'avèrent être le plus couramment préservées au sein d'enclaves magmatiques affleurant désormais aux abords de nombreux volcans (e.g., Soufrière Hills, Montserrat [*Edmonds et al.*, 2014; *Murphy et al.*, 2000; *Plail et al.*, 2014]; Mt. Unzen, Japon [*Browne et al.*, 2005]; Santorin et Nisyros, Grèce [*Martin et al.*, 2006; *Zellmer & Turner*, 2007]; Mt.

Pinatubo, Philippines [*Di Muro et al.*, 2008]). La présence d'une telle texture est bien souvent interprétée comme étant le produit d'une décompression isothermie (« first boiling » en anglais) ou de la cristallisation isobarie (« second boilling ») d'un magma, deux processus favorisant la saturation et l'exsolution d'espèces volatiles dans le liquide silicaté [e.g., *Candela*, 1989, 1997; *Sisson & Bacon*, 1999]. Dans le cadre de nos expériences de synthèse, le développement d'une texture diktytaxitique par phénomène de décompression paraît inenvisageable. La cristallisation isobarique semble à l'inverse concevable, mais ne peut expliquer à elle seule le gradient de cristallinité entre le cœur - où le liquide silicaté subsiste - et la bordure - dépourvue de verre interstitiel - de l'échantillon cylindrique. De même, le contrôle d'une température homogène sur toute la hauteur de l'échantillon (±10°C) durant la synthèse exclue toute existence d'une variation latérale de la proportion des diverses phases (cristaux, liquide, vésicules) et d'un changement textural en lien avec un gradient thermique. De manière alternative, il est possible d'envisager un scénario dans lequel la zonation texturale observée découlerait principalement d'une surpression générée par l'exsolution progressive de volatils lors du refroidissement et la cristallisation isobarie du magma. En effet, si le volume d'un magma en cours de cristallisation reste constant, un gradient de pression fluide se développe et la phase volatile, moins « visqueuse » que son milieu, tend à s'individualiser du liquide résiduel et à migrer vers les zones de moindre pression à travers le réseau cristallin [e.g., *Anderson et al.*, 1984; *Sanders*, 1986; *Sisson & Bacon*, 1999]. Dès lors, il est tout à fait vraisemblable que les vésicules produites en conditions de sursaturation eurent la possibilité de migrer massivement vers la bordure de la capsule, au-delà de laquelle la pression de confinement au sein de la cellule de l'autoclave est inférieure. Cette séquence d'exsolution-transfert de volatils pourrait *in fine* influencer le degré de cristallisation du magma. Cette hypothèse n'a cependant jamais été testée en routine par des expériences et demande davantage d'investigations.

4.2.2. Migration du liquide silicaté du cœur vers la bordure de l'échantillon

Dans l'expérience PP565, les observations microstructurales ont été réalisées au travers d'une section [xz] en extrême bordure de l'échantillon cylindrique, zone où en théorie aucune suspension magmatique ne devrait apparaître. Il existe potentiellement deux raisons pour expliquer la présence de liquide silicaté en bordure d'échantillon : (1) la fusion par phénomène de friction (ou « shear heating » en anglais) et (2) la migration de liquide silicaté depuis le cœur vers la bordure de l'échantillon. Une simple observation d'une section [yz] doit pouvoir étayer l'une de ces deux hypothèses. Cependant, aucune section dans ce plan préférentiel n'a été réalisée. La présence de pseudotachylites, produits de la fusion par friction, paraît néanmoins peu probable dans la mesure où les vitesses de déformation nécessaires à leur formation (i.e, 1.10^{-2} à 1 $m.s^{-1}$, *Passchier & Trouw* [2005]) se situent à plusieurs ordres de grandeur d'écart des vitesses appliquées dans le cadre de notre expérience. Il est en ce sens plus raisonnable de penser que la présence d'injections magmatiques soit le fruit d'une migration du liquide silicaté depuis le cœur vers la bordure de l'échantillon déformé. Les cavités initialement présentes en bordure d'échantillon constituent vraisemblablement l'une des voies préférentielles pour le transfert de liquide. Il est en effet plausible que les textures diktytaxitiques, progressivement

réarrangées sous l'effet de la déformation, se soient localement et transitoirement présentées sous la forme d'un réseau de cavités interconnectées, permettant ainsi le transfert du liquide. Un peu à l'image du processus de transfert de volatils lors de l'expérience de synthèse, les cavités situées en extrême bordure de l'échantillon constitueraient des zones de moindre pression (ou pression négative) au sein desquelles le liquide s'accumulerait préférentiellement. L'observation en section [xz] de poches magmatiques au sein des injections peut potentiellement témoigner d'une arrivée puis d'un stockage du liquide au sein des cavités à texture diktytaxitique. Ce scénario implique que la migration du liquide doit nécessairement intervenir précocement dans l'histoire structurale de l'échantillon. Avec la déformation, les cavités s'effondrent progressivement sur elles-mêmes et les phases constitutives de la texture diktytaxitique subissent de la fragmentation, rendant impossible l'arrivée d'un liquide silicaté.

4.2.3. Migration préférentielle des suspensions magmatiques dans le plan [xz]

Ce scenario dans lequel la venue d'un liquide silicaté du cœur vers la bordure de l'échantillon puis de son stockage au sein des cavités ne peut expliquer l'OPF moyenne développée par les injections magmatiques. Deux hypothèses ont été à la base émises pour rendre compte des directions faiblement inclinées des injections magmatiques (i.e., +16.2° ; cf. Figure V-37) : la migration de magmas le long de plans de fractures et/ou l'injection au sein de cavités disposant au préalable une forte excentricité à la sphéricité. Au vu des analyses directionnelles obtenues, aucune corrélation géométrique ne peut être établie entre les structures cassantes développées, les fabriques de forme des textures diktytaxitiques dans la zone du gradient de déformation et les injections magmatiques. Une autre hypothèse peut, de manière alternative, donner sens aux directions préférentielles des injections magmatiques : la migration de magmas partiellement cristallisés dans la direction de la contrainte principale mineure σ3. Trois raisons se conjuguent : (1) les injections connectant les poches magmatiques tendent à s'orienter perpendiculairement aux fentes de tension (i.e., en moyenne à -45° par rapport au plan de cisaillement). Par définition, les lèvres de ces micro-fractures s'ouvrent en tension pure. Il alors possible de remonter aux tenseurs de contrainte locaux de ces micro-fractures, avec les contraintes principales majeure (σ1) et intermédiaire (σ2) contenues dans le plan de fracture, la contrainte principale mineure (σ3) orthogonale à ce plan ; (2) la mise en orientation de phases cristallines non déformées au sein d'injections, dont la direction d'allongement de l'OPF moyenne est parallèle aux épontes d'injection orientées à +45° (cf. Figure V-38). Il est donc possible que le développement de la fabrique cristalline et l'écoulement du liquide silicaté se produisent en réponse aux contraintes appliquées, à 45° du plan de cisaillement.

De cette hypothèse, un scénario complet peut être donné: (1) la migration de magmas depuis le cœur vers la bordure de l'échantillon lié aux gradients de pression engendrés par l'interconnexion de cavités au cours des premiers incréments de la déformation (2) l'accumulation de magmas dans les cavités à texture diktytaxitique, formant ainsi des poches magmatiques; (3) la migration des magmas à 45° du plan de cisaillement en réponse à la contrainte principale majeure (σ1)

4.2.3. Injection magmatique & localisation d'une déformation ductile

Comme nous avons pu le décrire, le produit de synthèse s'est vu affecté par une déformation ductile intense. Cette déformation ductile ne s'est aucunement concentrée le long de fractures préexistantes, mais de part et d'autre d'une injection magmatique ainsi qu'au cœur de celle-ci. Cette relation spatiale entre structures ductiles et injection magmatique confirme expérimentalement que les magmas partiellement cristallisés sont capables de générer une chute soudaine de la résistance mécanique au contact de leur encaissant. Les processus menant à cette localisation de la déformation reste cependant à discuter (e.g., influence de la migration de fluides aqueux de l'injection vers l'encaissant, saut de pression fluide).

Conclusion

Cette étude s'est voulue être la plus complète possible au regard de la caractérisation des fabriques et microstructures en fonction du taux de cristallinité. Ce volet expérimental, bien que ne résolvant pas les lois de la mécanique, a révélé quelques points clés contribuant à la compréhension générale de l'évolution texturale et structurale au sein de magmas partiellement cristallisés face à un état de contrainte donné :

(1) L'impact des inhomogénéités texturales (i.e., glomérophyres) sur le développement de fabriques semi-pénétratives aux propriétés directionnelles inhomogènes et la perturbation de l'écoulement du liquide.
(2) L'impact des injections magmatiques sur la déformation localisée et notamment sur le passage d'une déformation cassante à ductile.

Références bibliographiques

Allard, B., & Benn, K. (1989). Shape preferred-orientation analysis using digitized images on a microcomputer. *Computers & Geosciences*, *15*(3), 441–448. https://doi.org/10.1016/0098-3004(89)90049-6

Altherr, R., Kreuzer, H., Wendt, I., Lenz, H., Wagner, G. A., Keller, J., … Höhndorf, A. (1982). A late Oligocene/early Miocene high temperature belt in the Attic-Cycladic crystalline complex (SE Pelagonian, Greece). *Geologisches Jahrbuch*, *E23*, 97–164.

Altherr, R., & Siebel, W. (2002). I-type plutonism in a continental back-arc setting: Miocene granitoids and monzonites from the central Aegean Sea, Greece. *Contributions to Mineralogy and Petrology*, *143*(4), 397–415. https://doi.org/10.1007/s00410-002-0352-y

Anderson, A. T., Swihart, G. H., Artioli, G., & Geiger, C. A. (1984). Segregation Vesicles, Gas Filter-Pressing, and Igneous Differentiation. *The Journal of Geology*, *92*(1), 55–72. https://doi.org/10.1086/628834

Arbaret, L. (1995). *Orientation Préférentielle de forme dans les magmas: Modélisation analogique 3D en cisaillement simple.* (Ph.D thesis). Univ. Clermont-Ferrand 2, Clermont-Ferrand, France.

Arbaret, L., Diot, H., & Bouchez, J.-L. (1996). Shape fabrics of particles in low concentration suspensions: 2D analogue experiments and application to tiling in magma. *Journal of Structural Geology*, *18*(7), 941–950. https://doi.org/10.1016/0191-8141(96)00011-9

Arbaret, L., & Burg, J.-P. (2003). Complex flow in lowest crustal, anastomosing mylonites: Strain gradients in a Kohistan gabbro, northern Pakistan. *Journal of Geophysical Research: Solid Earth*, *108*(B10), 1–18. https://doi.org/10.1029/2002JB002295

Arbaret, L., Bystricky, M., & Champallier, R. (2007). Microstructures and rheology of hydrous synthetic magmatic suspensions deformed in torsion at high pressure. *Journal of Geophysical Research*, *112*(B10), 1–24. https://doi.org/10.1029/2006JB004856

Arbaret, L., Launeau, P., Diot, H., & Sizaret, S. (2013). Magnetic and shape fabrics of magnetite in simple shear flows. *Journal of Volcanology and Geothermal Research*, *249*, 25–38. https://doi.org/10.1016/j.jvolgeores.2012.09.003

Archanjo, C. J., Araujo, M. G. S., & Launeau, P. (2002). Magnetic fabric patterns of the Mesozoic Rio Ceará-Mirim Dyke swarm (Northeast Brazil) as revealed by anisotropy of magnetic susceptibility and texture analysis. *Journal of Geophysical Research*, *107*, 1–13.

Barnhoorn, A., Bystricky, M., Kunze, K., Burlini, L., & Burg, J. (2005). Strain localisation in bimineralic rocks: Experimental deformation of synthetic calcite–anhydrite aggregates. *Earth and Planetary Science Letters*, *240*(3–4), 748–763. https://doi.org/10.1016/j.epsl.2005.09.014

Berthé, D., Choukroune, P., & Jegouzo, P. (1979). Orthogneiss, mylonite and non coaxial deformation of granites: the example of the South Armorican Shear Zone. *Journal of Structural Geology*, *1*(1), 31–42. https://doi.org/10.1016/0191-8141(79)90019-1

Blumenfeld, P., & Bouchez, J.-L. (1988). Shear criteria in granite and migmatite deformed in the magmatic and solid states. *Journal of Structural Geology*, *10*(4), 361–372. https://doi.org/10.1016/0191-8141(88)90014-4

Bolhar, R., Ring, U., & Allen, C. M. (2010). An integrated zircon geochronological and geochemical investigation into the Miocene plutonic evolution of the Cyclades, Aegean Sea, Greece: Part 1: Geochronology. *Contributions to Mineralogy and Petrology*, *160*(5), 719–742. https://doi.org/10.1007/s00410-010-0504-4

Browne, B. L. (2005). Generation of Porphyritic and Equigranular Mafic Enclaves During Magma Recharge Events at Unzen Volcano, Japan. *Journal of Petrology*, *47*(2), 301–328. https://doi.org/10.1093/petrology/egi076

Brun, J.-P., Sokoutis, D., & Van Den Driessche, J. (1994). Analogue modeling of detachment fault systems and core complexes. *Geology*, *22*(4), 319–322. https://doi.org/10.1130/0091-7613(1994)022<0319:AMODFS>2.3.CO;2

Candela, P. A. (1989). Felsic magmas, volatiles, and metallogenesis. In J. A. Whitney & A. J. Naldrett (Eds.), *Ore deposition associated with magmas* (Vol. 4, pp. 223–233). Society of Economic Geologists, Inc.

Candela, P. A. (1997). A Review of Shallow, Ore-related Granites: Textures, Volatiles, and Ore Metals. *Journal of Petrology*, *38*(12), 1619–1633. https://doi.org/10.1093/petroj/38.12.1619

Caricchi, L., Burlini, L., Ulmer, P., Gerya, T., Vassalli, M., & Papale, P. (2007). Non-Newtonian rheology of crystal-bearing magmas and implications for magma ascent dynamics. *Earth and Planetary Science Letters*, *264*(3–4), 402–419. https://doi.org/10.1016/j.epsl.2007.09.032

Champallier, R. (2005). *Déformation expérimentale à haute température et haute pression de magmas partiellement cristalliséS* (Ph.D thesis). Univ. Orléans, Orléans, France.

Champallier, R., Bystricky, M., & Arbaret, L. (2008). Experimental investigation of magma rheology at 300 MPa: From pure hydrous melt to 76 vol.% of crystals. *Earth and Planetary Science Letters*, *267*(3–4), 571–583. https://doi.org/10.1016/j.epsl.2007.11.065

Christiansen, P. P., & Pollard, D. D. (1997). Nucleation, growth and structural development of mylonitic shear zones in granitic rock. *Journal of Structural Geology*, *19*(9), 1159–1172. https://doi.org/10.1016/S0191-8141(97)00025-4

Cordonnier, B., Caricchi, L., Pistone, M., Castro, J., Hess, K.-U., Gottschaller, S., … Burlini, L. (2012). The viscous-brittle transition of crystal-bearing silicic melt: Direct observation of magma rupture and healing. *Geology*, *40*(7), 611–614. https://doi.org/10.1130/G3914.1

Corrigan, G. M. (1982). The Crystal Morphology of Plagioclase Feldspar Produced During Isothermal Supercooling and Constant Rate Cooling Experiments. *Mineralogical Magazine*, *46*(341), 433–439. https://doi.org/10.1180/minmag.1982.046.341.04

Coster, M., & Chermant, J. L. (1991). *Précis d'analyse d'images*. Paris: Presses du CNRS.

Devine, J. D., Gardner, J. E., Brack, H. P., Layne, G. D., & Rutherford, M. J. (1995). Comparison of microanalytical methods for estimating H_2O contents of silicic volcanic glasses. *American Mineralogist*, *80*(3–4), 319–328. https://doi.org/10.2138/am-1995-3-413

Di Muro, A., Pallister, J., Villemant, B., Newhall, C., Semet, M., Martinez, M., & Mariet, C. (2008). Pre-1991 sulfur transfer between mafic injections and dacite magma in the Mt. Pinatubo reservoir. *Journal of Volcanology and Geothermal Research*, *175*(4), 517–540. https://doi.org/10.1016/j.jvolgeores.2008.02.025

Dingwell, D. B., Romano, C., & Hess, K.-U. (1996). The effect of water on the viscosity of a haplogranitic melt under P-T-X conditions relevant to silicic volcanism. *Contributions to Mineralogy and Petrology*, *124*(1), 19–28. https://doi.org/10.1007/s004100050170

Edmonds, M., Humphreys, M. C. S., Hauri, E. H., Herd, R. A., Wadge, G., Rawson, H., … Guida, R. (2014). Pre-eruptive vapour and its role in controlling eruption style and longevity at Soufriere Hills Volcano. *Geological Society, London, Memoirs*, *39*(1), 291–315. https://doi.org/10.1144/M39.16

Einstein, A. (1911). Berichtigung zu meiner Arbeit: Eine neue Bestimmung der Moleküldimensionen. *Annalen Der Physik*, *339*(3), 391–392.

Fenn, P. M. (1977). The nucleation and growth of alkali feldspars from hydrous melts. *The Canadian Mineralogist*, *15*, 135–161.

Fernandez, A., Feybesse, J.-L., & Mezure, J.-F. (1983). Theoretical and experimental study of fabrics developed by different shaped markers in two-dimensional simple shear. *Bulletin de La Societe Geologique de France*, *S7–XXV*(3), 319–326. https://doi.org/10.2113/gssgfbull.S7-XXV.3.319

Forien, M., Arbaret, L., Burgisser, A., & Champallier, R. (2011). Experimental constrains on shear-induced crystal breakage in magmas. *Journal of Geophysical Research*, *116*(B8). https://doi.org/10.1029/2010JB008026

Hess, K.-U., & Dingwell, D. B. (1996). Viscosities of hydrous leucogranitic melts: A non-Arrhenian model. *American Mineralogist*, *81*(9–10), 1297–1300.

Iglseder, C., Grasemann, B., Schneider, D. A., Petrakakis, K., Miller, C., Klötzli, U. S., … Rambousek, C. (2009). I and S-type plutonism on Serifos (W-Cyclades, Greece). *Tectonophysics*, *473*(1–2), 69–83. https://doi.org/10.1016/j.tecto.2008.09.021

Ikeda, S., Toriumi, M., Yoshida, H., & Shimizu, I. (2002). Experimental study of the textural development of igneous rocks in the late stage of crystallization: the importance of interfacial energies under non-equilibrium conditions. *Contributions to Mineralogy and Petrology*, *142*(4), 397–415. https://doi.org/10.1007/s004100100300

Ildefonse, B., Arbaret, L., & Diot, H. (1997). Rigid Particles in Simple Shear Flow: Is Their Preferred Orientation Periodic or Steady-State ? In J. L. Bouchez, D. H. W. Hutton, & W. E. Stephens (Eds.), *Granite: From Segregation of Melt to Emplacement Fabrics* (Vol. 8, pp. 177–185). Dordrecht: Springer Netherlands. https://doi.org/10.1007/ 978-94-017-1717-5_11

Jeffery, G. B. (1922). The Motion of Ellipsoidal Particles Immersed in a Viscous Fluid. *Proceedings of the Royal Society A: Mathematical, Physical and Engineering Sciences*, *102*(715), 161–179. https://doi.org/10.1098/rspa.1922.0078

Jeffery, G. B. (1922). The motion of ellipsoidal particles immersed in a viscous fluid. *The Royal Society*, *102*(715), 161–179.

Jerram, D. A. (2003). Quantifying the Building Blocks of Igneous Rocks: Are Clustered Crystal Frameworks the Foundation? *Journal of Petrology*, *44*(11), 2033–2051. https://doi.org/10.1093/petrology/egg069

Kirkpatrick, R. J. (1975). Crystal growth from the melt: a review. *American Mineralogist*, *60*, 798–814.

Laumonier, M. (2013). *Mélange de magmas à HP-HT, contraintes expérimentales et application au magmatisme d'arc* (Ph.D thesis). Univ. Orléans, Orléans, France.

Laumonier, M., Arbaret, L., Burgisser, A., & Champallier, R. (2011). Porosity redistribution enhanced by strain localization in crystal-rich magmas. *Geology*, *39*(8), 715–718. https://doi.org/10.1130 /G31803.1

Launeau, P. (1990). *Analyse numérique des images et orientations préférentielles de forme des agrégats polyphasés : application à l'analyse cinématique des granites* (Ph.D thesis). Univ. Toulouse III - Paul Sabatier, Toulouse, France.

Launeau, P., & Bouchez, J.-L. (1992). Mode et orientation preferentielle de formes des granites par analyse d'images numeriques. *Bulletin de La Société Géologique de France*, *163*(6), 721–732.

Launeau, P., & Cruden, A. R. (1998). Magmatic fabric acquisition mechanisms in a syenite: Results of a combined anisotropy of magnetic susceptibility and image analysis study. *Journal of Geophysical Research: Solid Earth*, *103*(B3), 5067–5089. https://doi.org/10.1029/97JB02670

Launeau, P., Archanjo, C. J., Picard, D., Arbaret, L., & Robin, P.-Y. (2010). Two- and three-dimensional shape fabric analysis by the intercept method in grey levels. *Tectonophysics*, *492*(1–4), 230–239. https://doi.org/10.1016/j.tecto.2010.06.005

Launeau, P., & Robin, P.-Y. F. (1996). Fabric analysis using the intercept method. *Tectonophysics*, *267*(1–4), 91–119. https://doi.org/10.1016/S0040-1951(96)00091-1

Launeau, P., & Robin, P.-Y. F. (2005). Determination of fabric and strain ellipsoids from measured sectional ellipses—implementation and applications. *Journal of Structural Geology*, *27*(12), 2223–2233. https://doi.org/10.1016/j.jsg.2005.08.003

Lejeune, A.-M., & Richet, P. (1995). Rheology of crystal-bearing silicate melts: An experimental study at high viscosities. *Journal of Geophysical Research: Solid Earth*, *100*(B3), 4215–4229. https://doi.org/10.1029/94JB02985

Lisle, R. J. (1985). *Geological strain analysis: a manual for the Rf/Ø method* (1st ed). Oxford ; New York: Pergamon Press.

Lofgren, G. (1974). An experimental study of plagioclase crystal morphology; isothermal crystallization. *American Journal of Science*, *274*(3), 243–273. https://doi.org/10.2475/ajs.274.3.243

Lynch, H. D., & Morgan, P. (1987). The tensile strength of the lithosphere and the localization of extension. *Geological Society, London, Special Publications*, *28*(1), 53–65. https://doi.org/10.1144/GSL.SP.1987.028.01.05

MacKenzie, W. S., Donaldson, C. H., & Guilford, C. (1982). *Atlas of igneous rocks and their textures* (1st ed.). Harlow: Longman.

Martin, V. M., Holness, M. B., & Pyle, D. M. (2006). Textural analysis of magmatic enclaves from the Kameni Islands, Santorini, Greece. *Journal of Volcanology and Geothermal Research*, *154*(1–2), 89–102.

Middlemost, E. A. K. (1994). Naming materials in the magma/igneous rock system. *Earth-Science Reviews*, *37*(3–4), 215–224. https://doi.org/10.1016/0012-8252(94)90029-9

Morgan, G. B., & London, D. (1996). Optimizing the electron microprobe analysis of hydrous alkali aluminosilicate glasses. *American Mineralogist*, *81*(9–10), 1176–1185. https://doi.org/10.2138/am-1996-9-1016

Murphy, M. D., Sparks, R. S. J., Barclay, J., Carroll, M. R., & Brewer, T. S. (2000). Remobilization of Andesite Magma by Intrusion of Mafic Magma at the Soufriere Hills Volcano, Montserrat, West Indies. *Journal of Petrology*, *41*(1), 21–42. https://doi.org/10.1093/petrology/41.1.21

Okumura, S., Kushnir, A. R. L., Martel, C., Champallier, R., Thibault, Q., & Takeuchi, S. (2016). Rheology of crystal-bearing natural magmas: Torsional deformation experiments at 800°C and 100MPa. *Journal of Volcanology and Geothermal Research*, *328*, 237–246. https://doi.org/10.1016/j.jvolgeores.2016.11.009

Panozzo, R. (1987). Two-dimensional strain determination by the inverse Surfor wheel. *Journal of Structural Geology*, *9*(1), 115–119. https://doi.org/10.1016/0191-8141(87)90049-6

Passchier, C. W., & Trouw, R. A. J. (2005). *Microtectonics*. Berlin; New York: Springer.

Paterson, M. S. (1990). Rock deformation experimentation. In A. G. Duba, W. B. Durham, J. W. Handin, & H. F. Wang (Eds.), *Geophysical Monograph Series* (Vol. 56, pp. 187–194). Washington, D. C.: American Geophysical Union. https://doi.org/10.1029/GM056p0187

Paterson, M. S., & Olgaard, D. L. (2000). Rock deformation tests to large shear strains in torsion. *Journal of Structural Geology*, *22*(9), 1341–1358. https://doi.org/10.1016/S0191-8141(00)00042-0

Pavlis, T. L. (1996). Fabric development in syn-tectonic intrusive sheets as a

consequence of melt-dominated flow and thermal softening of the crust. *Tectonophysics*, *253*(1–2), 1–31. https://doi.org/10.1016/0040-1951(95)00049-6

Pennacchioni, G., & Mancktelow, N. S. (2007). Nucleation and initial growth of a shear zone network within compositionally and structurally heterogeneous granitoids under amphibolite facies conditions. *Journal of Structural Geology*, *29*(11), 1757–1780. https://doi.org/10.1016/j.jsg.2007.06.002

Petford, N. (2009). Which effective viscosity? *Mineralogical Magazine*, *73*(3), 167–191. https://doi.org/10.1180/minmag.2009.073.2.167

Philpotts, A. R., & Asher, P. M. (1994). Magmatic flow-direction indicators in a giant diabase feeder dike, Connecticut. *Geology*, *22*(4), 363–366. https://doi.org/10.1130/0091-7613(1994)022<0363:MFDIIA>2.3.CO;2

Picard, D. (2009). *Déformation HP-HT des magmas siliceux: contraintes expérimentales sur l'évolution structurale et les transitions rhéologiques aux moyennes et fortes cristallinités* (Ph.D thesis). Univ. Orléans, Orléans, France.

Picard, D., Arbaret, L., Pichavant, M., Champallier, R., & Launeau, P. (2011). Rheology and microstructure of experimentally deformed plagioclase suspensions. *Geology*, *39*(8), 747–750. https://doi.org/10.1130/G32217.1

Picard, D., Arbaret, L., Pichavant, M., Champallier, R., & Launeau, P. (2013). The rheological transition in plagioclase-bearing magmas. *Journal of Geophysical Research: Solid Earth*, *118*(4), 1363–1377. https://doi.org/10.1002/jgrb.50091

Plail, M., Barclay, J., Humphreys, M. C. S., Edmonds, M., Herd, R. A., & Christopher, T. E. (2014). Characterization of mafic enclaves in the erupted products of Soufriere Hills Volcano, Montserrat, 2009 to 2010. *Geological Society, London, Memoirs*, *39*(1), 343–360. https://doi.org/10.1144/M39.18

Pupier, E., Duchene, S., & Toplis, M. J. (2008). Experimental quantification of plagioclase crystal size distribution during cooling of a basaltic liquid. *Contributions to Mineralogy and Petrology*, *155*(5), 555–570. https://doi.org/10.1007/s00410-007-0258-9

Roscoe, R. (1952). The viscosity of suspensions of rigid spheres. *British Journal of Applied Physics*, *3*(8), 267.

Salemink, J. (1985). *Skarn and ore formation at Serifos, Greece, as a consequence of granodiorite intrusion* (PhD thesis). University of Utrecht, Netherlands.

Saltykov, S. A. (1958). *Stereometric Metallography* (2nd ed.). Moscou, Russia: Metallurgizdat.

Sanders, I. S. (1986). Gas filter-pressing origin for segregation vesicles in dykes. *Geological Magazine*, *123*(01), 67. https://doi.org/10.1017/S0016756800026546

Schmidt, M. W. (1992). Amphibole composition in tonalite as a function of pressure: an experimental calibration of the Al-in-hornblende barometer. *Contributions to Mineralogy and Petrology*, *110*(2–3), 304–310. https://doi.org/10.1007/BF00310745

Sisson, T. W., & Bacon, C. R. (1999). Gas-driven filter pressing in magmas. *Geology*, *27*(7), 613–616. https://doi.org/10.1130/0091-7613(1999)027<0613:GDFPIM>2.3.CO;2

Špillar, V., & Dolejš, D. (2015). Heterogeneous nucleation as the predominant mode of crystallization in natural magmas: numerical model and implications for crystal–melt interaction. *Contributions to Mineralogy and Petrology*, *169*(1), 1–16. https://doi.org/10.1007/s00410-014-1103-6

St. Seymour, K., Zouzias, D., Tombros, S., & Kolaiti, E. (2009). Geochemistry of the Serifos pluton (Cycladic islands) and associated iron oxide and sulfide ores: Skarn or metamorphosed exhalite deposits? *Neues*

Jahrbuch Für Mineralogie - Abhandlungen, *186*(3), 249–270. https://doi.org/10.1127/0077-7757/2009/0143

Stolper, E. (1982). Water in silicate glasses: An infrared spectroscopic study. *Contributions to Mineralogy and Petrology*, *81*(1), 1–17. https://doi.org/10.1007/BF00371154

Stouraiti, C., Mitropoulos, P., Tarney, J., Barreiro, B., McGrath, A. M., & Baltatzis, E. (2010). Geochemistry and petrogenesis of late Miocene granitoids, Cyclades, southern Aegean: Nature of source components. *Lithos*, *114*(3–4), 337–352. https://doi.org/10.1016/j.lithos.2009.09.010

Stouraiti, C., & Mitropoulos, P. (1999). Variation in amphibole composition from the Serifos intrusive complex (Greece), under magmatic and hydrothermal alteration conditions: An application of hornblende geobarometry. *Bulletin of the Geological Society of Greece*, *33*, 39–50.

Streckeisen, A. (1976). To each plutonic rock its proper name. *Earth-Science Reviews*, *12*(1), 1–33. https://doi.org/10.1016/0012-8252(76)90052-0

Swanson, S. E. (1977). Relation of nucleation and crystal-growth rate to the development of granitic textures. *American Mineralogist*, *62*, 966–978.

Tikoff, B., & Teyssier, C. (1994). Strain and fabric analyses based on porphyroclast interaction. *Journal of Structural Geology*, *16*(4), 477–491. https://doi.org/10.1016/0191-8141(94)90092-2

Vigneresse, J.-L. (2015). Textures and melt-crystal-gas interactions in granites. *Geoscience Frontiers*, *6*(5), 635–663. https://doi.org/10.1016/j.gsf.2014.12.004

Vyhnal, C. R., McSween, H. Y., & Speer, J. A. (1991). Hornblende chemistry in southern Appalachian granitoids: Implications for aluminum hornblende thermobarometry and magmatic epidote stability. *American Mineralogist*, *76*(1–2), 176–188.

Willis, D. G. (1977). A kinematic model of preferred orientation. *Geological Society of America Bulletin*, *88*(6), 883. https://doi.org/10.1130/0016-7606(1977)88<883:AKMOPO>2.0.CO;2

Zellmer, G. F., & Turner, S. P. (2007). Arc dacite genesis pathways: Evidence from mafic enclaves and their hosts in Aegean lavas. *Lithos*, *95*(3–4), 346–362. https://doi.org/10.1016/j.lithos.2006.08.002

Chapitre VI

Discussion & Perspectives

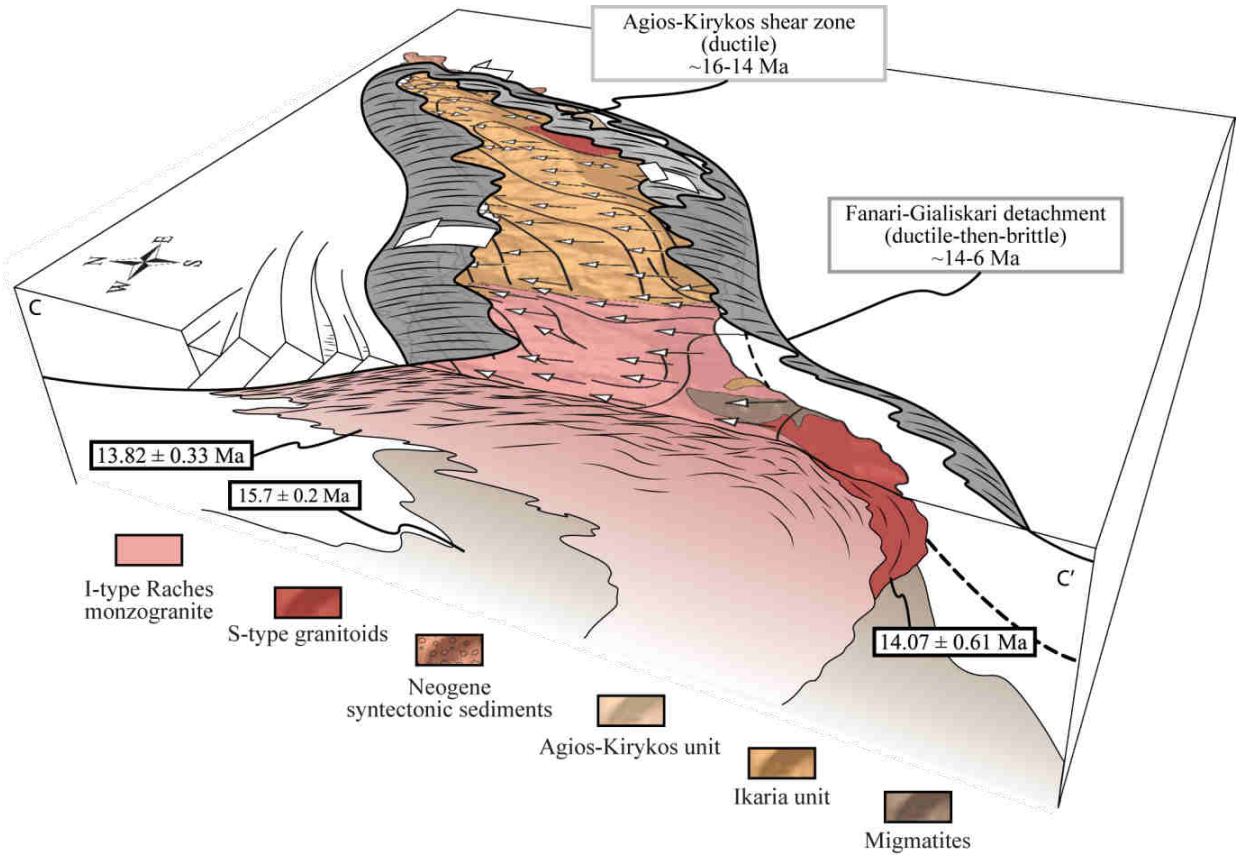

Les objectifs premiers de ce mémoire étaient :

(1) évaluer à l'échelle de l'ensemble du domaine des Cyclades l'impact du magmatisme intrusif sur la dynamique des dômes métamorphiques extensifs (MCCs)

(2) **identifier les possibles mécanismes gouvernant l'initiation d'une déformation localisée au sein de corps magmatiques en cours de cristallisation et estimer leur capacité à localiser la déformation à plus grande échelle**.

Pour ce faire, j'ai combiné avec originalité approche de terrain et étude expérimentale. Les différentes campagnes de terrain (Naxos, chapitre II ; Serifos, chapitre III ; et Ikaria, voir annexe A) ont permis de caractériser l'état de déformation finie au sein des granitoïdes cycladiques syn-extensifs, en utilisant diverses méthodes de quantification de la déformation (tomographiques par absorption de rayon X ; mesures d'orientations préférentielles d'axes cristallographiques de minéraux par EBSD ; analyses de l'anisotropie de susceptibilité magnétique ; méthodes de quantification des fabriques par analyse d'image). L'étude expérimentale a, quant à elle, permit de caractériser le comportement structural de magmas de composition naturelle, depuis de faibles cristallinités jusqu'à la quasi-consolidation.

A : Quel est l'impact du magmatisme dans la dynamique des MCCs ?

Malgré la littérature abondante sur la géologie des Cyclades, aucun consensus n'a encore été établi sur les mécanismes responsables de l'association étroite entre corps magmatiques et les systèmes de détachements exposés à l'affleurement. En combinant les données de terrain et les élèments de la bibliographie, j'ai pu ainsi proposer un modèle d'interaction entre le développement de détachements crustaux et le magmatisme, qui peut être résumé Figure VI-1 (blocs 3-D issus du chapitre III). Selon les données de la littérature, il apparaît dans un premier lieu que l'arrivée de magmas au sein de la croûte supérieure égéenne semble s'être limitée dans un intervalle de 15 à 9 Ma, soit plusieurs millions d'années après le début de l'extension arrière-arc et les premières stades d'exhumation des dômes métamorphiques. Ce calendrier implique que le magmatisme cycladique ne peut être considéré comme un candidat pour la genèse des MCCs. Ce magmatisme syn-extensif serait au contraire le produit d'un environnement thermique plus chaud au cours de l'amincissement lithosphérique, ainsi qu'au cours du retrait et la déchirure du panneau plongeant. Il est dès lors possible que la migration des produits magmatiques syn-extensifs générés au sein de la lithosphère profonde ait été au cours de leur remontée en partie guidée par les gradients de pressions engendrés par l'extension et les zones d'intense déformation, jusqu'à atteindre le cœur des MCCs déjà formés.

Cependant, les diverses observations structurales et relations géométriques attestent d'une interaction étroite entre intrusions et développement de détachements. Tous ces complexes magmatiques, placés structuralement sous les détachements les plus superficiels, enregistrent divers niveaux d'intensité de la déformation depuis les prémices d'une structuration syn-magmatique jusqu'à la mylonitisation à l'approche des détachements, voire

même une déformation cassante-cataclastique le long de ces discontinuités. Ces continuums témoignent ainsi d'une localisation progressive de la déformation extensive le long de leur marge intrusive. En conséquence, j'ai proposé un schéma généralisable à l'ensemble de ces MCCs (voir chapitre IV), dans lequel le développement séquentiel de détachements résulte de l'interaction locale et transitoire avec une intrusion magmatique. Dans ce scenario, les intrusions inhibent l'activité de détachements en les perforant et modifiant ainsi la position des plus forts contrastes rhéologiques. La déformation extensive, redistribuée le long des marges intrusives, se localise avec le temps au travers de détachements nouvellement formés, achevant l'exhumation des dômes métamorphiques. Ainsi, ce scénario dans lequel le magmatisme impacte dynamiquement l'évolution tardive des dômes métamorphiques implique que les corps magmatiques, considérés comme des instabilités thermo-mécaniques ponctuelles, sont capables d'introduire des contrastes rhéologiques drastiques de courte durée.

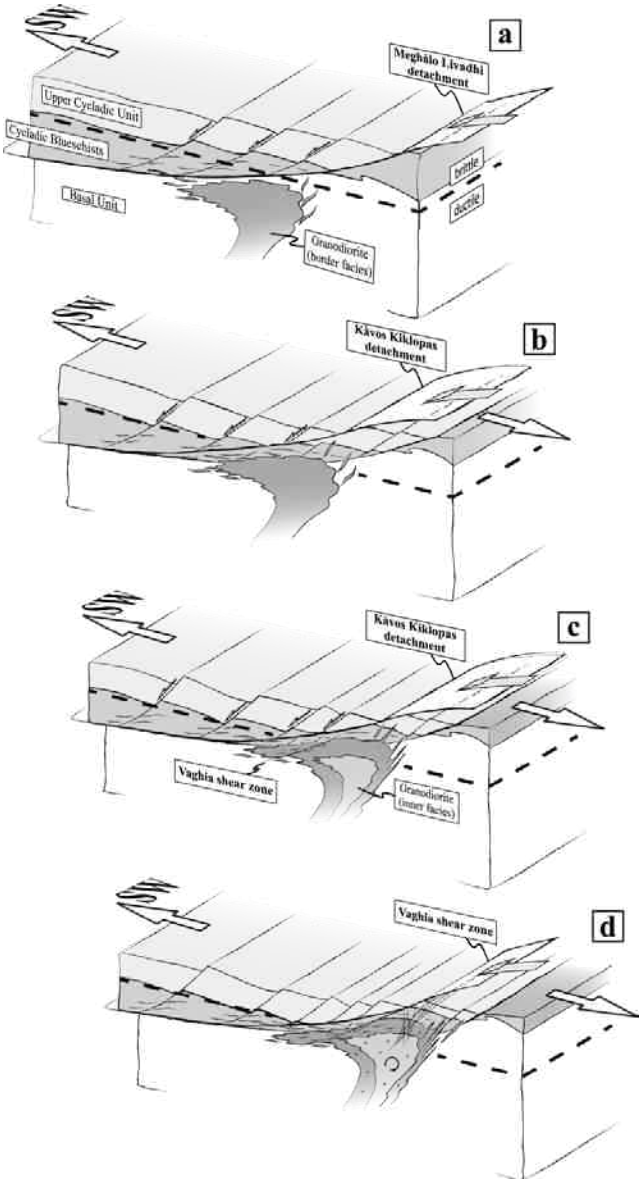

Figure VI-1: *modèle d'interaction entre magmatisme et détachements crustaux au cours de l'évolution d'un MCC cycladique*

B : Quels sont les vecteurs de localisation de la déformation dans les magmas partiellement cristallisés ?

Par l'étude expérimentale du comportement structural de magmas partiellement cristallisés réalisée au cours de cette thèse, deux mécanismes à l'origine de la localisation de la déformation dans les corps magmatiques peuvent être supposés :

a : Les filons syn-plutoniques, retour sur les observations de terrain à partir des expériences.

La comparaison entre les résultats de l'expérience à haute cristallinité et les observations de terrain sur des corps intrusifs interagissant avec des détachements. Le transfert d'échelle est sans doute délicat à faire car les viscosités absolues et les contrastes de viscosité entre les magmas et leur encaissant puissent être directement comparés mais les ressemblances géométriques et en terme de localisation de la déformation nous conduisent à penser qu'il faut travailler dans cette direction.

La Figure VI-2 montre une image de l'ensemble de la zone de cisaillement observée au sommet de l'expérience à haute cristallinité associée à une photographie du détachement de Livada sur l'île de Mykonos.

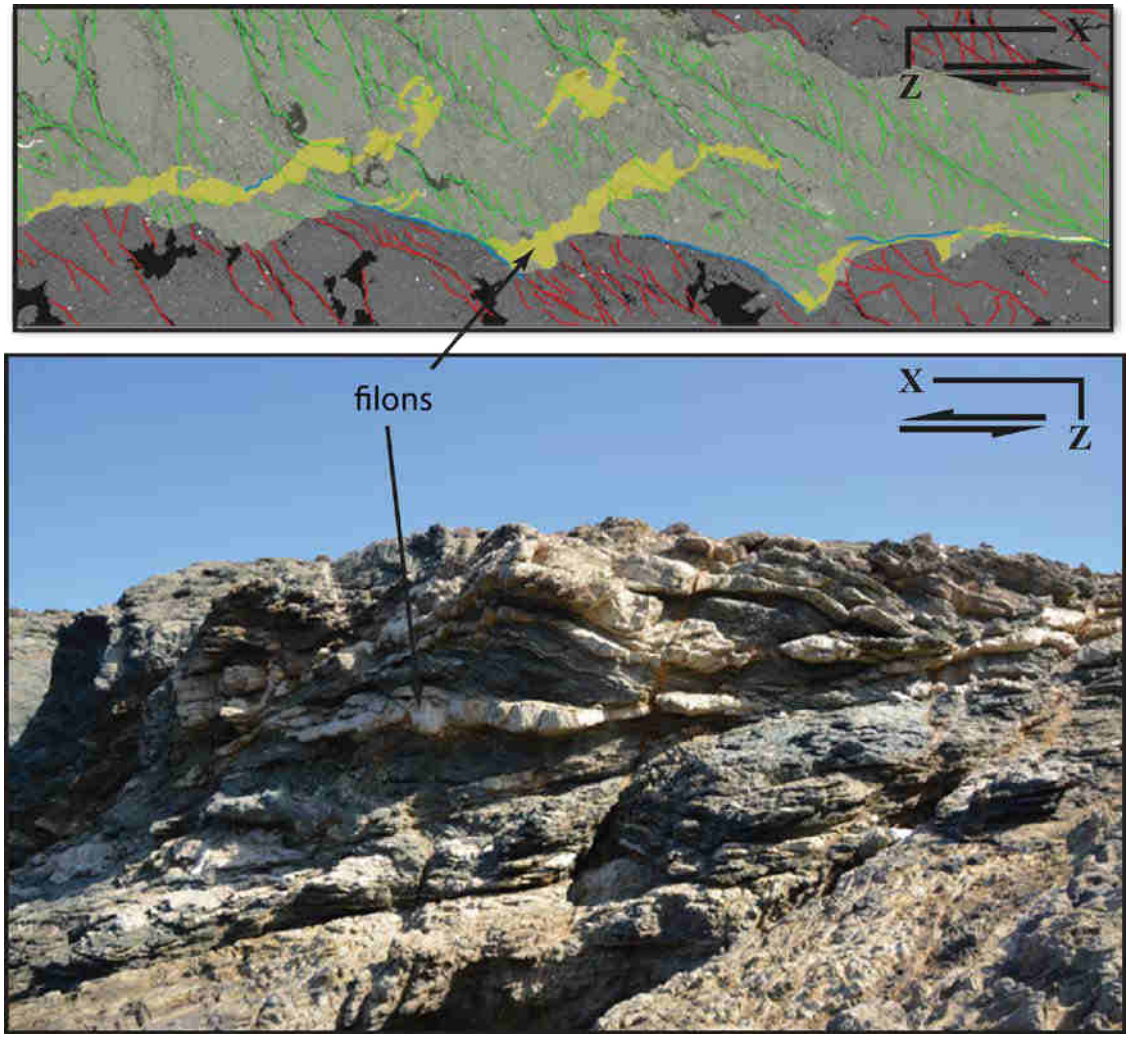

Figure VI-2: *analogie entre expérience et terrain ; haut : zone de cisaillement dans l'échantillon expérimentalement déformé. Bas : filons aplitiques sur l'île de Mykonos*

La position des filons aplitiques à Mykonos dans la zone de cisaillement à la base de l'Unité supérieure des Cyclades et celle des filons dans la zone de cisaillement expérimentale est identique par rapport au sens de cisaillement imposé. Dans le cas naturel, les intrusions aplitiques sont des sills aplatis dans le plan [xy] (le plan de la foliation). La même observation a été faite de manière systématique à Mykonos dans la détachement de Livada et également sur l'île de Tinos. Cette géométrie peut donc être considérée comme significative des interactions

entre les magmas et le jeu du détachement. Dans le cas de l'expérience Paterson, la géométrie 3D des injections magmatiques n'est pas exactement connue mais l'image en section [xz] est identique à celle que nous observons sur le terrain. Nous pouvons donc envisager, sous réserve de travailler encore sur la géométrie 3D de ces filons expérimentaux, que dans les deux cas, les injections magmatiques issues du corps intrusif se propagent dans le plan perpendiculaire à l'aplatissement tectonique et s'étalent dans ce plan. Ceci serait compatible avec la relativement faible déformation des filons naturels, à Tinos comme à Mykonos.

La Figure VI-3 montre une autre analogie entre le terrain et les expériences, cette fois avec un changement d'échelle moins drastique. Nous avons vu que les filons injectés dans la zone de cisaillement expérimentale sont localement déformés de manière intense quand ils sont parallélisés avec les bords de la zone de cisaillement. Cette déformation est ductile sur les bords du filon et dans l'encaissant et cassante à l'intérieur du filon, les cristaux étant cataclasés.

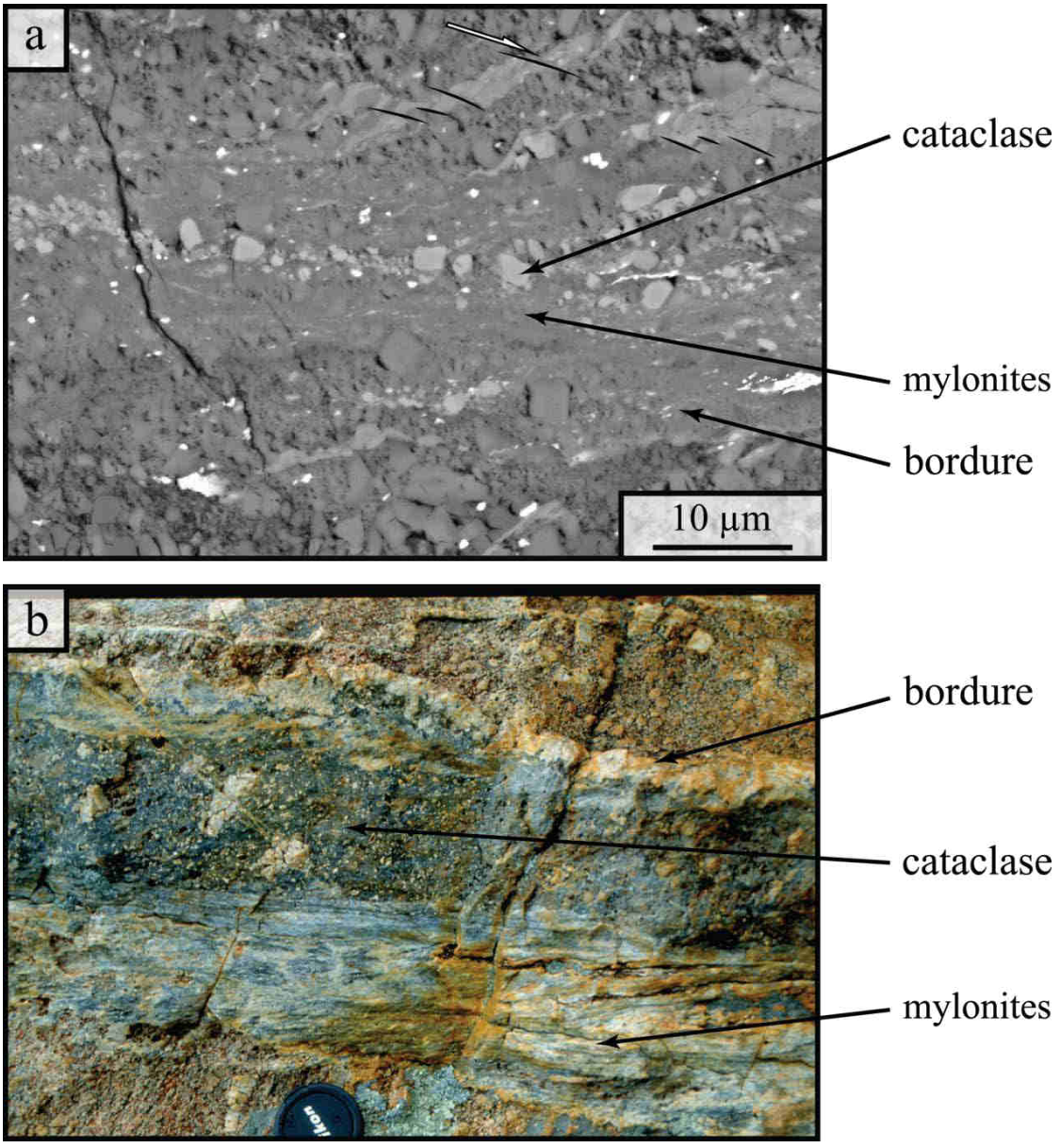

Figure VI-3: *analogie entre expérience et terrain ; (a): filon déformé expérimentalement. (b): filon déformé (Monte Cristo)*

La Figure VI-4 montre également une photographie d'un filon granitique tardif dans le corps magmatique syn-extensif de l'île de Monte Cristo dans l'archipel Toscan. Cette intrusion s'est mise en place au Miocène supérieur pendant l'amincissement crustal du nord de la Mer Tyrrhénienne en contexte arrière-arc sous une série de détachements à pendage est [*Jolivet et al.*, 1998]. On voit sur cette photographie la concomitance de la déformation ductile avec un cisaillement vers l'est clair dans les mylonites en bordure du filon et la cataclase dans le filon. Une autre image des filons naturels de Monte Cristo montrent la très forte intensité du cisaillement ductile dans une autre portion de ce filon comme dans certaines parties de l'expérience en Presse Paterson. Ces filons se comportent donc de la même façon au premier ordre dans le cas naturel et dans l'expérience.

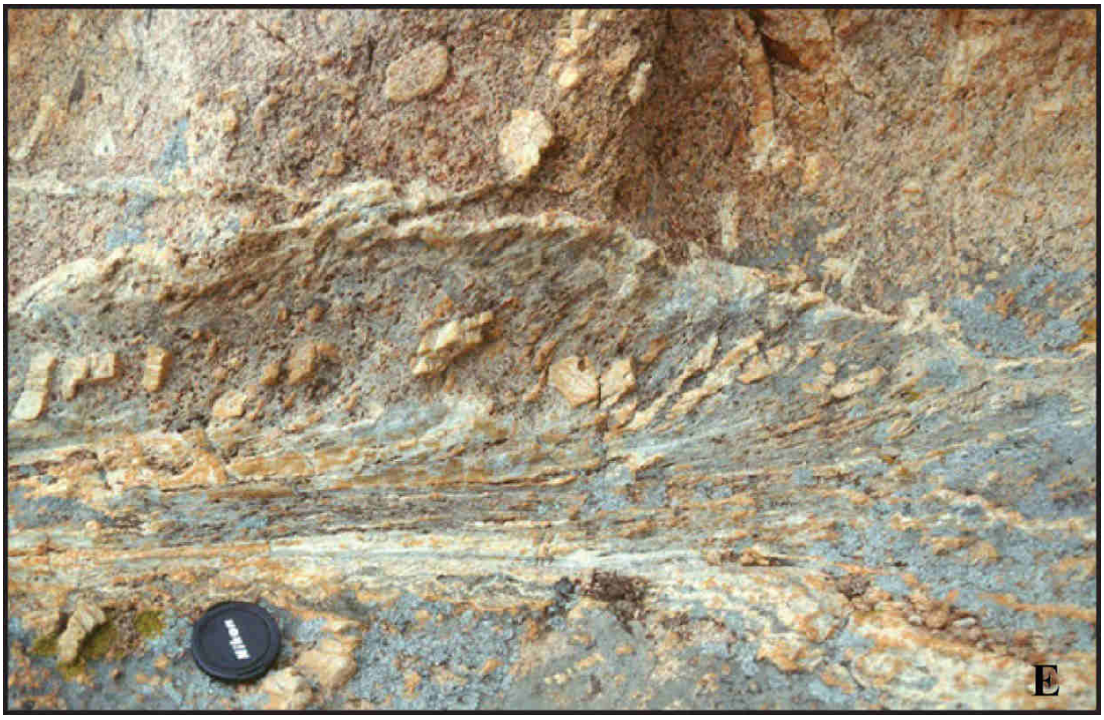

Figure VI-4: *f ilons déformé (Monte Cristo), cisaillement vers l'est*

Cette expérience montre donc à une échelle réduite des similitudes importantes avec le cas naturel. Sans oublier le saut important d'échelle, ces ressemblances suggèrent que les mécanismes mis en jeu sont en partie identiques. Elles donnent un cadre physique aux interprétations que nous avons faites sur le terrain, les filons seraient donc bien injectés dans la zone de cisaillement à partir du réservoir de magma du corps intrusif sous-jacent pendant la déformation. Il reste un travail important à faire pour mieux caractériser la géométrie des filons dans l'expérience et sans doute pour modéliser ces processus numériquement, mais ces aspects sortent du cas de ce mémoire.

b : L'effet de l'inhomogénéité texturale des magmas sur la localisation de la déformation

Dans les expériences Paterson, nous avons pu voir qu'aux moyennes fractions cristallines la présence d'hétérogénités texturales (i.e., la présence de glomérphyres) pertube

l'écoulement du liquide silicaté, aboutissant au développement d'une fabrique semi-pénétrative aux propriétés directionnelles inhomogènes (Figure VI-5). Cette constatation est majeure dans le sens où, dans un milieu physiquement homogène, sans hétérogénéités structurales (fractures préexistantes) ou compositionnelles (mélanges de magmas : filons, enclaves), la localisation de la déformation peut s'initier à la faveur de faibles variations texturales dans l'espace. Autrement dit, la présence d'amas de minéraux cristallisés au sein d'un magma non consolidé soumis à une contrainte différentielle peut aboutir à des couloirs de déformation plus intense où les minéraux baignant dans un liquide silicaté vont pouvoir s'orienter et créer des plans préférentiels le long desquelles la déformation se localise puis s'accumule au cours du temps (Figure VI-5).

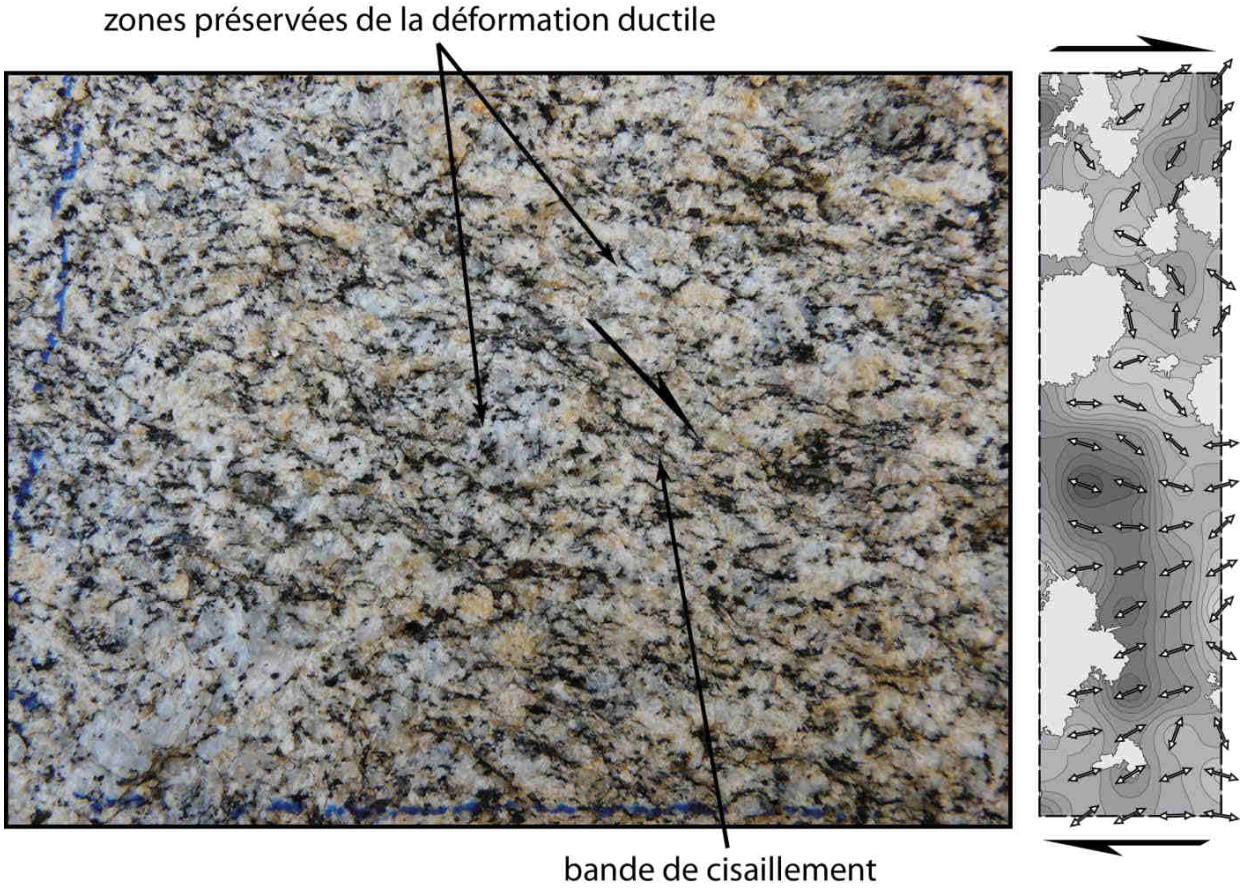

Figure VI-5: analogie entre expérience et terrain ; monzogranite de Naxos faiblement déformée montrant la localisation de la déformation entre des zones dépourvue de déformation. Droite : résultat de l'expérience de déformation de moyenne cristallinité montrant la tortuosité des fabriques locales. Les zones entre les glomérophyres peuvent constituer des couloirs de déformation

Les variations spatiales de concentration de minéraux, inhomogènes dans une suspension magmatique, peuvent engendrer des gradients de résistance suffisamment élevés pour localiser des sites où les minéraux vont être déformés ou être concentrés. Ainsi, les minéraux précocement formés dans la séquence de cristallisation d'un granite, typiquement les

ferromagnésiens ou les feldspaths, s'orienteront selon certains plans préférentiels et subiront une quantité de déformation plus importante. La composition minéralogique et la manière dont se distribuent les phases dans la suspension magmatique peuvent donc être à l'origine de variations spatiales de résistance au sein d'une même roche magmatique. La géométrie et l'intensité de cette anisotropie de fabrique, face à un état de contrainte donné, peut donc conduire à l'initiation d'une déformation localisée.

Le passage continue de la déformation précoce, observée alors qu'il reste du liquide silicaté dans le bâti, comme nous l'observons à distance du détachement à Ikaria, Naxos ou Mykonos à la déformation mylonitique sub-solidus quand on approche du détachement posait un problème : comment peut-on localiser de la déformation dans un milieu a priori aussi faible. Il semble que, dans les premiers stades de ce refroidissement, l'hétérogénéité du magma soit suffisante pour localiser de la déformation cisaillante, en rapprochant les expériences à moyenne cristallinité et les observations loin des détachements. La genèse pendant le refroidissement des fabriques de type S/C dans les granites syn-cinématiques pourrait ainsi être la conséquence des hétérogénéités de cristallinité dans le magma pendant son refroidissement, pour les tous premiers stades de la déformation.

Ce travail offre donc des perspectives nouvelles sur les interactions entre tectonique et mise en place d'intrusions magmatiques. Une analyse d'autres corps magmatiques, ou une analyse plus poussée des géométries des hétérogénéités précoces dans les magmas syn-tectoniques loin des détachements sous lesquels ils se mettent en place serait utile pour aller plus loin. Le cas du corps intrusif de l'île d'Elbe est un candidat particulièrement favorable par la granulométrie exceptionnelle des feldspaths alcalins dans la zone la moins déformée.

Annexe A

Article: Interrelations between extensional shear zones and synkinematic intrusions: The example of Ikaria Island (NE Cyclades, Greece)

Publié dans dans la revue *Tectonophysics*, 2015

Valentin Laurent [1,2,3], Alexandre Beaudoin [1,2,3], Laurent Jolivet [1,2,3], Laurent Arbaret [1,2,3], Romain Augier [1,2,3], **Aurélien Rabillard** [1,2,3], Armel Menant [1,2,3]

(1) Université d'Orléans, ISTO, UMR 7327, 45071, Orléans, France
(2) CNRS/INSU, ISTO, UMR 7327, 45071 Orléans, France
(3) BRGM, ISTO, UMR 7327, BP 36009, 45060 Orléans, France

Tectonophysics 651–652 (2015) 152–171

Contents lists available at ScienceDirect

Tectonophysics

journal homepage: www.elsevier.com/locate/tecto

Interrelations between extensional shear zones and synkinematic intrusions: The example of Ikaria Island (NE Cyclades, Greece)

Valentin Laurent *, Alexandre Beaudoin, Laurent Jolivet, Laurent Arbaret, Romain Augier, Aurélien Rabillard, Armel Menant

Université d'Orléans, ISTO, UMR 7327, 45071 Orléans, France
CNRS/INSU, ISTO, UMR 7327, 45071 Orléans, France
BRGM, ISTO, UMR 7327, BP 36009, 45060 Orléans, France

ARTICLE INFO

Article history:
Received 30 January 2015
Received in revised form 25 March 2015
Accepted 29 March 2015
Available online 12 April 2015

Keywords:
Backarc extension
Metamorphic core complexes
Detachment
Intrusions
Aegean
Ikaria Island

ABSTRACT

The Aegean extensional backarc domain is an ideal place to investigate the interrelations between syntectonic intrusions and large-scale detachments, understanding whether the intrusions have a triggering effect on the inception of metamorphic core complex formation or not. A new field study of Ikaria Island (NE Cyclades, Greece) in two Miocene granitoid plutons intruding a high-temperature metamorphic dome, namely the Raches and Karkinagrion granites, leads to the identification of a major structure that has been omitted in previous studies: the Gialiskari Detachment. This regional-scale detachment is correlated with the North Cycladic Detachment System. Structural fieldwork at the scale of the entire Raches and Karkinagrion intrusions allows us to propose a map of strain intensity in these granites. This map, based on macrostructural criteria, highlights a strong strain gradient in both intrusions from base to top, when approaching the Gialiskari Detachment. Along the strain gradient, a continuum of top-to-the north shearing deformation is recognized, including i) syn-magmatic deformation, ii) high-temperature ductile deformation at submagmatic state, iii) mylonitic to ultramylonitic deformation, and iv) low-temperature brittle deformation. A scenario of the interactions between the detachment and the Raches and Karkinagrion intrusions during their emplacement is proposed. We show that these granites were emplaced while the exhumation of the Ikaria metamorphic dome was already underway. We conclude that these plutons do not initially localize detachments, and instead that detachments localize and control the ascent of plutons. Intrusions then interact with detachments, accommodating their upward migration in the crust. This scenario is described on other Cycladic islands such as on Tinos or Mykonos. At a larger scale, the final emplacement of plutons may result from the flow of molten crust toward metamorphic core complex during extension.

1. Introduction

Metamorphic Core Complexes (MCCs) are crustal-scale structures exhumed by major shallow-dipping extensional shear zones, or detachments. They result from the intense thinning of a previously thickened continental crust in post-orogenic extensional context (Dewey, 1988). First described in the Basin and Range Province (Crittenden et al., 1980; Davis and Coney, 1979; Wernicke, 1981) these structures were later recognized throughout the world in young mountain belts (e.g. Papua New Guinea, Baldwin et al., 1993; Lister and Baldwin, 1993; Himalayas, Aoya et al., 2005) or more ancient belts (French Variscanides, Burg et al., 1994; Turrillot et al., 2011; Norwegian Caledonides, Andersen et al., 1991; Labrousse et al., 2002). MCC development is often spatially and temporally associated with intense magmatic activity (Baldwin et al., 1993; Crittenden et al., 1980; Hill et al., 1992; Jolivet and Brun, 2010) and the development of detachments often interacts with syntectonic intrusions. On the one hand, detachments may either be seen as conduits for ascending magmas or as barriers limiting their rise (Brown, 1994; Brown and Solar, 1998; D'lemos et al., 1992; Hutton and Reavy, 1992). On the other hand, field studies and thermomechanical modeling have shown that shear zones can nucleate within partly crystallized plutons that introduce a local, yet drastic rheological heterogeneity in the crust (Aoya et al., 2005; Foster et al., 2001; Lister and Baldwin, 1993; Neves et al., 1996). Therefore, the role of detachments in the emplacement of magmatic intrusions, or conversely, the role of intrusions to localize deformation remains not clearly understood.

Series of MCCs have been described in the Mediterranean region, notably in the Aegean domain (Gautier et al., 1993; Jolivet et al., 2004a, 2004b; Lister et al., 1984), where some of the Cycladic islands (e.g. Mykonos, Naxos, Ios, Tinos, Serifos, Andros and Paros) expose the

* Corresponding author.
E-mail addresses: valentin.laurent@univ-orleans.fr (V. Laurent), alexandre.beaudoin@univ-orleans.fr (A. Beaudoin), laurent.jolivet@univ-orleans.fr (L. Jolivet), laurent.arbaret@univ-orleans.fr (L. Arbaret), romain.augier@univ-orleans.fr (R. Augier), aurelien.rabillard@univ-orleans.fr (A. Rabillard), armel.menant@cnrs-orleans.fr (A. Menant).

http://dx.doi.org/10.1016/j.tecto.2015.03.020
0040-1951/

relations between MCCs and intrusions (Avigad and Garfunkel, 1989; Buick, 1991; Denèle et al., 2011; Faure and Bonneau, 1988; Gautier and Brun, 1994; Gautier et al., 1993; Grasemann and Petrakakis, 2007; Lee and Lister, 1992; Lister et al., 1984; Rabillard et al., 2015; Urai et al., 1991; Vandenberg and Lister, 1996). Indeed, these MCCs, characterized by series of ductile-then-brittle detachment systems, are often intruded by syntectonic Miocene plutons (Jolivet et al., 1994, 2010; Lecomte et al., 2010; Lister and Baldwin, 1993; Rabillard et al., 2015). These detachment systems comprise the North Cycladic Detachment System (NCDS), the West Cycladic Detachment System (WCDS) and the Paros–Naxos Detachment (PND) and have accommodated the exhumation of these MCCs (Grasemann et al., 2012; Jolivet et al., 2010).

The geometrical and kinematic relations between plutons and detachments have been described on Naxos and Mykonos with quite some details (Andriessen et al., 1979; Buick, 1991; Denèle et al., 2011; Gautier et al., 1993; Keay et al., 2001; Lecomte et al., 2010; Urai et al., 1991) but the largest Cycladic pluton (Raches pluton on Ikaria Island) has so far not been studied in detail. In this paper, we study the geometrical kinematic setting of the emplacement of intrusions on Ikaria Island and their evolution through time. Combining these data with recent studies of the metamorphic part of the island, we discuss the large-scale interrelations between the extensional structures, the Ikaria MCC and the synkinematic intrusions, from the scale of the island up to the Aegean domain.

2. Geological setting

2.1. Tectonic evolution of the Cycladic Archipelago

Located in the eastern part of the Mediterranean area, the Aegean domain (Fig. 1a) corresponds to a collapsed segment of the Hellenic belt above a north-plunging subduction (Jolivet and Faccenna, 2000; Jolivet et al., 1994; Le Pichon and Angelier, 1981). The Aegean domain underwent a complex Alpine history that can be summarized in two main successive steps: 1) the late Cretaceous–Eocene formation of the Hellenides–Taurides belt resulted from the convergence between Africa and Eurasia plates. During this episode, a series of oceanic and continental nappes entered the subduction zone and was thrust on top of each other in a high-pressure and low-temperature (HP–LT) metamorphic context (Bonneau and Kienast, 1982), 2) the inception and acceleration of African slab retreat from 30 to 35 Ma led to the crustal collapse in the backarc domain, the dislocation of the nappe stack and the formation of MCCs (Jolivet et al., 2004a, 2013; Le Pichon and Angelier, 1981; Lister et al., 1984). North–south (N–S) extension in the backarc domain was characterized by a distributed deformation over a wide region covering the entire Aegean Sea, part of western Anatolia and the Rhodope massif in the north. The extensional tectonic regime was also characterized by more localized deformation with the development of MCCs where the exhumation of HP–LT units was

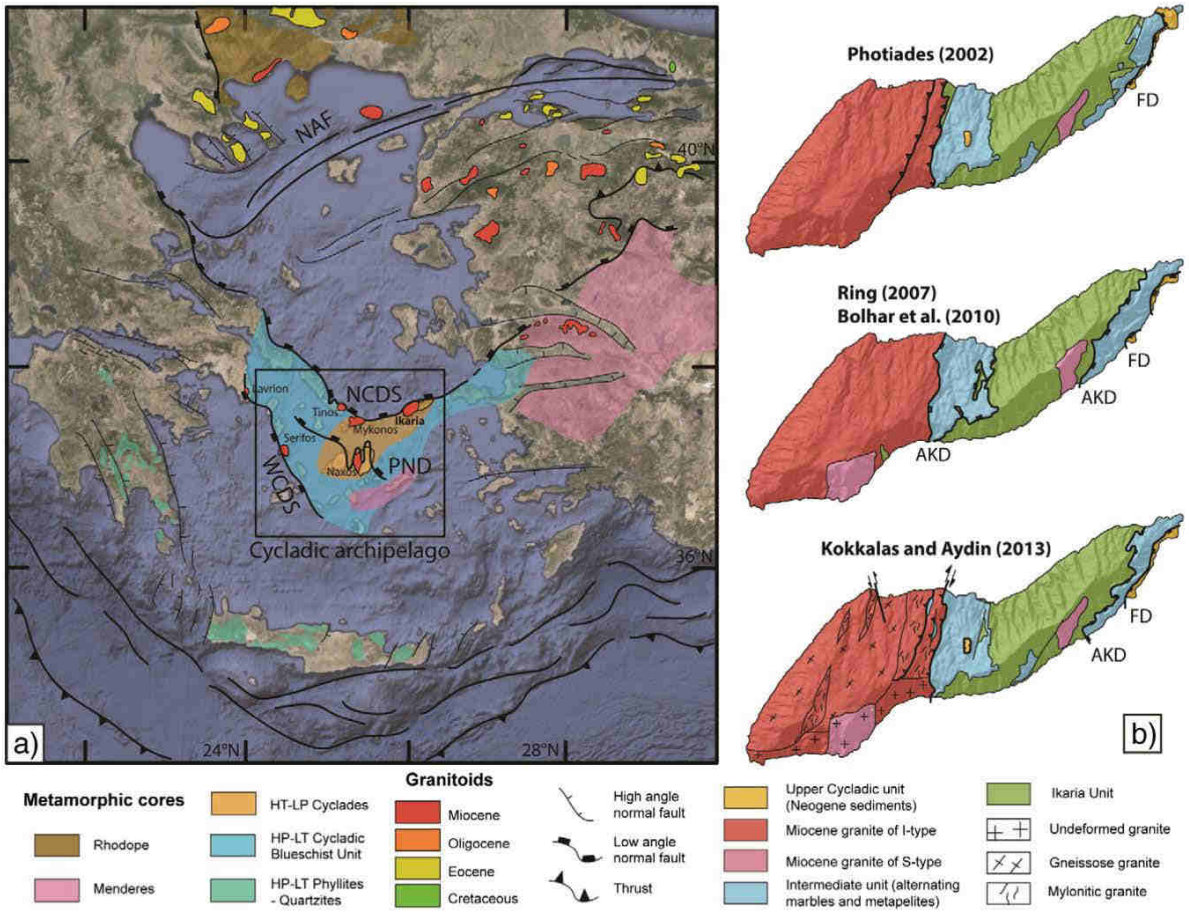

Fig. 1. Localization of the studied area and conflicting previous works. a) Tectonic map of the Aegean domain showing the distribution of metamorphic cores and granitoids and their link with major tectonic structures such as the North Cycladic Detachment System (NCDS), the West Cycladic Detachment System (WCDS), the Paros–Naxos Detachment (PND) and the North Anatolian Fault (NAF). b) Representation of the different author interpretations of the structures composing the island of Ikaria, especially on the ambiguous nature of the contact between the granite and the metamorphic dome and on the geometry of major tectonic contacts such as the Fanari Detachment (FD) and the Agios Kirykos Detachment (AKD).

completed in a low-pressure and high-temperature (LP–HT) environment (Fig. 1a; Jolivet and Patriat, 1999).

The Cycladic archipelago is located in the center of the Aegean domain and corresponds to the deepest exhumed parts of the Hellenides–Taurides belt (Fig. 1a). Three tectonic units are traditionally recognized in the Cyclades (Bonneau, 1984; Jolivet et al., 2004b), 1) the Upper Cycladic (UC) unit corresponds to the shallowest part of the nappe stack. It is composed of non-metamorphic Permian to Mesozoic sediments, some minor, mainly Cretaceous, orthogneisses, ophiolites and rocks metamorphosed under greenschist-facies to amphibolite-facies conditions, 2) the Cycladic BlueSchist unit (CBS) is structurally positioned below the UC unit. It is composed of metapelites, quartzites, marbles and various amounts of metabasites all equilibrated in blueschist- or eclogite-facies conditions (e.g. Avigad and Garfunkel, 1989; Blake et al., 1981; Bonneau, 1984). The CBS unit experienced a complex Alpine tectonometamorphic evolution, with an early burial in HP–LT conditions reaching ~18–20 kbar and 500–550 °C (Augier et al., 2015; Bröcker and Enders, 2001; Dürr et al., 1978; Parra et al., 2002; Tomaschek et al., 2003; Trotet et al., 2001) during the Eocene, followed by a greenschist to amphibolite overprint of variable intensity during the Oligocene and the Miocene (Altherr et al., 1982; Buick, 1991; Duchene et al., 2006; Keay et al., 2001; Wijbrans and McDougall, 1986), 3) the Cycladic Continental Basement (CCB) crops out on different islands from the center to the south of the Cyclades (e.g. Paros, Naxos, Ios or Sikinos) and is structurally positioned beneath the CBS (e.g. Andriessen et al., 1987; Huet et al., 2009). This unit is composed of Variscan orthogneisses mantled by metasediments that locally retain metamorphic relics of amphibolite-facies assemblages suggesting a complex pre-Alpine history (e.g. Andriessen et al., 1987; Bonneau and Kienast, 1982; Keay, 1998; Photiades and Keay, 2003). Late exhumation stages of both the CBS and the CCB were accompanied by the emplacement of syntectonic Miocene intrusions (Fig. 1a; e.g. Tinos, Mykonos, Ikaria, Naxos, Serifos or even Lavrion; Altherr and Siebel, 2002; Altherr et al., 1982; Bolhar et al., 2010; Denèle et al., 2011; Faure et al., 1991; Grasemann and Petrakakis, 2007; Jansen, 1973; Lee and Lister, 1992; Pe-Piper et al., 2002; Lecomte et al., 2010; Stouraiti et al., 2010). These intrusions are of two types: 1) S-type per-aluminous two-mica leucogranites and granites and 2) I-type granites resulting from lower crust and mantle partial melting (Altherr and Siebel, 2002; Pe-Piper et al., 2002). In the entire Aegean domain, magmatic intrusions were all dated between 15 and 10 Ma while volcanic rocks yielded ages between 11 and 6 Ma (Altherr et al., 1982; Baltatzis et al., 2009; Bolhar et al., 2010; Brichau et al., 2007; Keay, 1998; Keay et al., 2001; Liati et al., 2009; Weidmann et al., 1984). The southward younging emplacement ages of both volcanic and magmatic rocks highlight the southward migration of the magmatic arc in relation to the retreating African slab (Fig. 1a).

2.2. Geology of Ikaria

Ikaria Island is located in the northeastern part of the Cyclades, near the west coast of Turkey and close to the island of Samos. Three tectonic units are recognized (Fig. 1b; Altherr et al., 1982; Kumerics et al., 2005; Papanikolaou, 1978; Photiades, 2002), from top to bottom:

1) The non-metamorphic Fanari unit, correlated with the UC unit corresponds to series of Miocene to Pliocene sandstones, conglomerates and ophiolitic molasses (Photiades, 2002).
2) The intermediate unit consists of alternating marble and metapelite layers, metamorphosed in greenschist-facies conditions (Altherr et al., 1982; Kumerics et al., 2005). Recently, based on structural and metamorphic criteria, Beaudoin et al. (2014) have reinterpreted the geometry of this unit, called Messaria unit by Kumerics et al. (2005), and renamed it as the Agios Kirykos unit. This term is then used hereafter in this study.
3) The Ikaria unit is composed of an up to 1 km-thick association of metasediments including micaschist and marble layers and minor metabasite occurrences (Photiades, 2002). Rocks of this unit were equilibrated in amphibolite-facies conditions (e.g. Altherr et al., 1982; Kumerics et al., 2005; Martin et al., 2011) at ca. 6–8 kbar and 600–650 °C. Peak-metamorphic conditions were retrieved from the basal parts of the succession (Kumerics et al., 2005; Martin, 2004; Martin et al., 2011).

Recent studies in the metamorphic dome (Kumerics et al., 2005; Ring, 2007) show the presence of two low-angle ductile shear zones on Ikaria: 1) the Fanari Detachment cropping out in the northeastern part of the island shows a continuum of deformation from ductile to brittle conditions. This detachment is located at the contact between the Agios Kirykos and Fanari (UC) units, except for its northern part where it juxtaposes directly the Fanari and Ikaria units (Fig. 2), 2) the second low-angle ductile shear zone corresponds to the Agios Kirykos Detachment located between the Ikaria and the Agios Kirykos units. Conversely to the Fanari Detachment, this detachment became inactive in the ductile regime and does not show any brittle deformation imprint.

Three main granitic intrusions are recognized on Ikaria Island (Fig. 2; Bolhar et al., 2010; Kokkalas and Aydin, 2013; Ring, 2007): two small-scale S-type intrusions (Xylosyrtis and Karkinagrion) and the large I-type Raches intrusion that constitutes the largest magmatic intrusion of the whole Cycladic archipelago (Altherr et al., 1982; Kumerics et al., 2005; Photiades, 2002).

The S-type Xylosyrtis granite intrudes the Ikaria unit on the southeastern coast of the island. The intrusion consists of a two-mica granite with a uniformly fine grain-size and characterized by a mineral assemblage of feldspar, plagioclase, quartz, biotite and muscovite. Minor and accessory phases are green hornblende, apatite, zircon, tourmaline, magnetite and cassiterite (Altherr et al., 1982; Photiades, 2002). Emplacement of this granitic pluton was dated by U/Pb method in zircon at 14.63 ± 0.67 Ma (Bolhar et al., 2010).

The Raches granite composes the western part of the island. This I-type granite of calc-alkaline composition belongs to the Miocene magmatic arc of potassic plutons parallel to the Hellenic Trench (Altherr et al., 1982). Mineral assemblage consists of feldspar phenocrysts, zoned plagioclase, quartz, biotite and hornblende with accessory phases such as red allanite, apatite, sphene, titanomagnetite, zircon, tourmaline or garnet (Altherr et al., 1982). The emplacement of this granite was dated by U/Pb method in zircon at 13.33 ± 0.17 Ma (Bolhar et al., 2010).

Due to its recent discovery (Ring, 2007), the S-type Karkinagrion granite has been little studied. Two statistically distinct ages were retrieved by the U/Pb method in zircon at 13.73 ± 0.29 Ma and 16.67 ± 0.64 Ma. Although the youngest age is slightly older than the one obtained for the emplacement of the Raches granite and without obvious evidence, Bolhar et al. (2010) concluded that the Karkinagrion granite intruded the I-type Raches granite.

At variance with the Xylosyrtis intrusion that displays a clear intrusive character within metamorphic series, the nature of the Raches granite contact with the metamorphic dome remains highly controversial. This contact was mapped so far as intrusive (Papanikolaou, 1978), as a detachment (Kumerics et al., 2005) or as a thrust (Fig. 1b; Boronkay and Doutsos, 1994; Kokkalas and Aydin, 2013; Photiades, 2002).

Deformation in intrusions remains poorly studied. Faure et al. (1991) described for the first time a widespread mylonitic foliation, a N–S stretching lineation and a preferred top-to-the north sense of shear in the Raches granite. These authors stated that magmatic deformation is seldom preserved on Ikaria and only mylonitic, subsolidus deformation is currently observable. Besides, Kokkalas and Aydin (2013) elaborated a deformation map of the Raches granite and concluded that the strain increases from west to east when approaching the contact between the granite and metamorphic units, described as a large thrust with an oblique dextral motion (Fig. 1b).

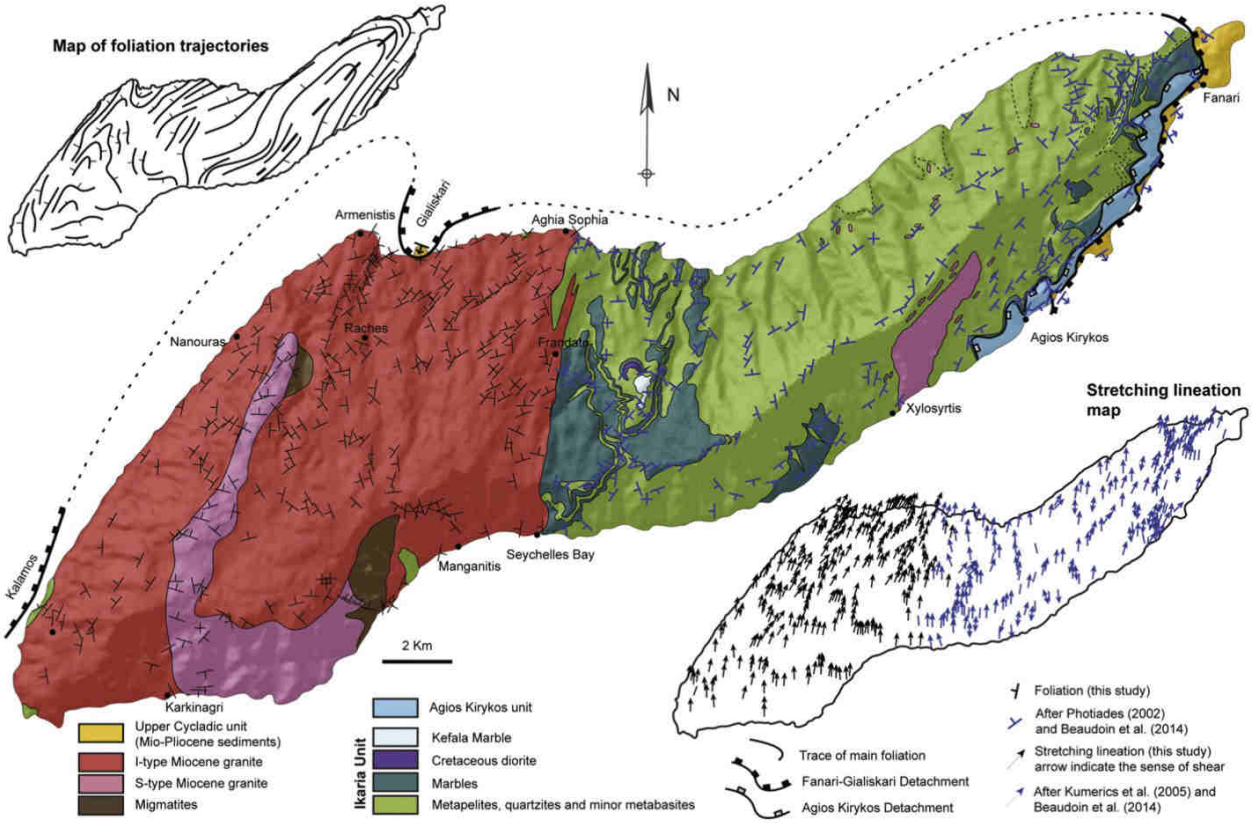

Fig. 2. New geological map of Ikaria Island showing the tectonic units, the two Gialiskari and Agios Kirykos detachments, foliation trajectories, stretching lineation measurements and localities cited in the text.

It appears that the structure of the intrusive granitic bodies and their relation with the metamorphic host rock of Ikaria Island still remain poorly understood. However, this is crucial to address the feedback relationships between intrusions, detachments and the formation of MCC. In order to study these interrelations, we have reconsidered these discrepancies. An extensive field study on Ikaria Island was performed, including primarily new geological mapping of the geometry of the Raches and Karkinagrion plutons combined with a detailed study of the strain intensity affecting these intrusions. The detailed structural study shows contrasting results with respect to previously published papers. Main changes and their implications are shown below.

3. Methods

In order to start from a clear geometrical context the whole island has been remapped based on field observations and satellite images. The finite strain pattern has been studied and the result is given as maps of the foliation and stretching lineations in the metamorphic dome and in the intrusions. Kinematic indicators have been systematically observed all over the island and reported on the map of stretching lineations. In order to obtain an image of the strain gradients within the intrusions, a scale of strain intensity with seven grades, adapted to the Raches granite, was constructed and the deformation grade reported on the map. Aiming at quantifying the strain intensity affecting the intrusions in more details, eight samples were selected all around the Raches granite in order to reconstruct the strain ellipsoid by image analysis, based on the shape fabric of biotite aggregates. Biotite was selected as strain indicator because it is easy to segment on images due to its strong color contrast with the felsic background. The protocol, similar to Launeau and Robin (2005), was first to cut rock samples along three orthogonal sections, one section in the XY plane of the finite strain ellipsoid parallel to foliation and lineation, one YZ section perpendicular to the lineation and one XZ section perpendicular to the foliation and parallel to the lineation. Then, 2D images of the three sections XY, XZ and YZ of each sample were treated. This step was performed using GIMP 2 software and consisted of image enhancement (filters) and segmentation of the biotite phase. Filters and segmentation were adapted for each sample. Segmented images were then analyzed with the 2003 Intercept software (Launeau and Robin, 2005; Launeau et al., 2010). Analyses were conducted with the intercept method that allows finding the preferential direction of biotite. This direction corresponds to the minimum number of intercepts (contact between the analyzed phase and the matrix). Finally, the 3D fabric ellipsoid was calculated by using the 2D analyses performed on the three orthogonal faces of our sample (Launeau et al., 2010).

Moreover, in this work chemical analyses of hornblende crystals have been performed in order to determine the pressure emplacement of the Raches intrusion using the experimental calibration of Schmidt (1992): $P\ (\pm 0.6\ \text{kb}) = -3.01 + 4.76\ \text{Al Tot}$. A Cameca SX50 electron probe microanalyzer at the University "Pierre et Marie Curie" (Paris VI) was used to acquire spot analyses of hornblendes. Analytical conditions for spot analyses were 15 kV accelerating voltage and 10 nA beam current. Standards used were Fe_2O_3 (Fe), $MnTiO_3$ (Mn, Ti), diopside (Mg, Si), CaF_2 (F), orthoclase (Al, K), anorthite (Ca), albite (Na), and vanadinite (Cl). The counting time was 10 s for all elements.

4. Field observations

4.1. Nature of contact zones with intrusions

A new field study of Ikaria Island was conducted and resulted in the proposition of a new geological map (Fig. 2). Our survey shows that the Karkinagrion two-mica intrusion occupies a much larger volume than initially proposed by Bolhar et al. (2010) and we highlight for the first time the presence of migmatites closely associated to this S-type granite (Fig. 2). In this section, we explore and describe the different contact zones between the western set of intrusions and the wall-rocks forming the Ikaria MCC.

4.1.1. Contact between the Raches intrusion and the Ikaria MCC

The contact between the Raches intrusion and the Ikaria MCC is often hidden on land but is spectacularly exposed on the coast. The contact is described along strike from south to north.

The intrusive nature of the contact between the Raches granite and the metamorphic dome is well exposed along the southern coast of Ikaria near Seychelles Beach (Fig. 3a). Folded synplutonic dikes cutting the vertical foliation of the marble are observed. Two distinctive foliations, within the granite and the metamorphic dome, show a clear intrusive relation between these units. The marble unit appears strongly deformed with vertical foliation planes, while granitic dikes show only a weak folded foliation showing that the metamorphic rocks were already

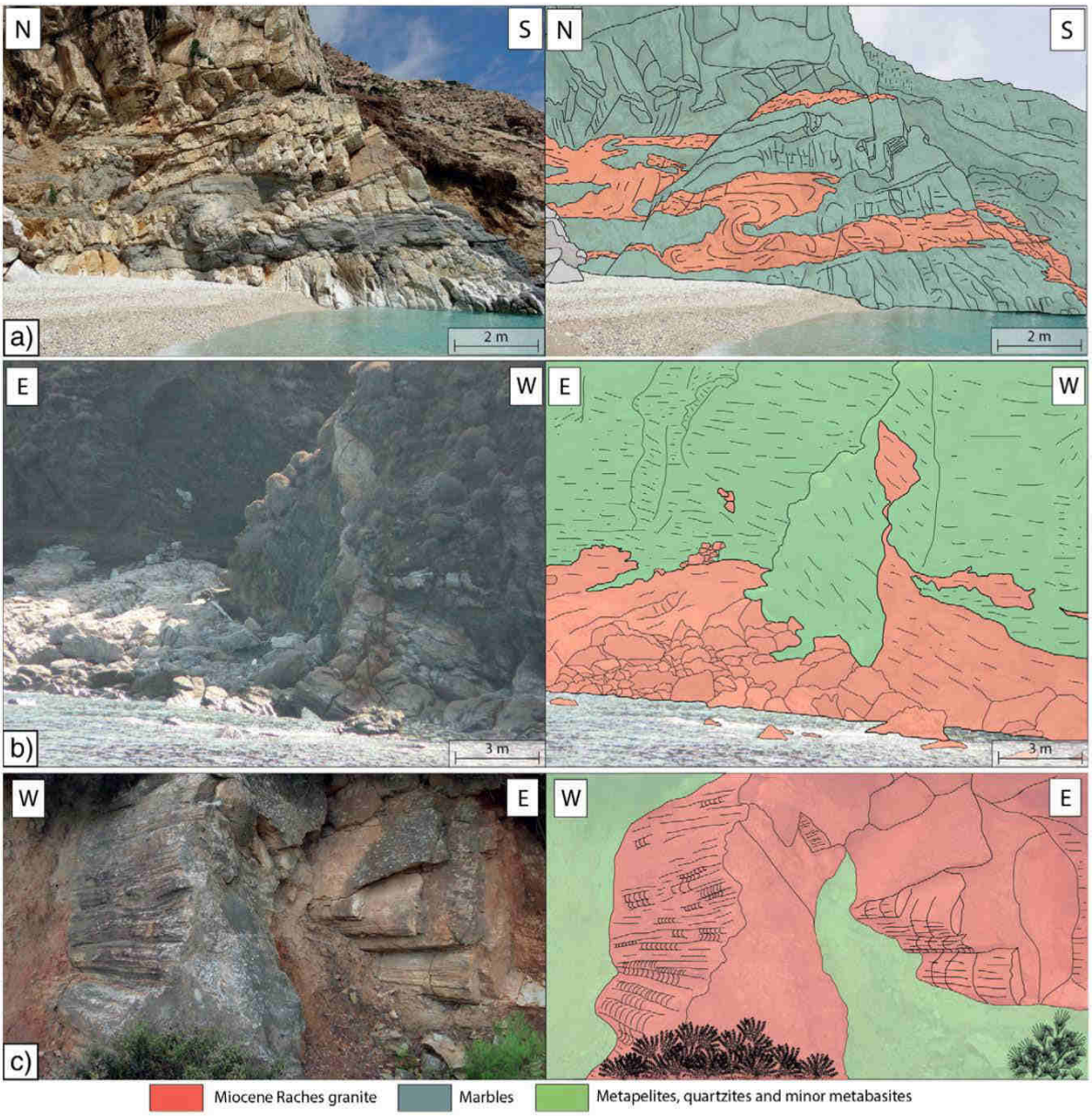

Fig. 3. Photographs showing the intrusive nature of the contact between the Raches granite and metamorphic rocks. a) Southern part of the contact, where poorly deformed granitic dikes intruded highly deformed metamorphic units. b and c) Northern part of the contact, where granitic dikes intruded metamorphic host rocks. Rocks of both sides of this contact have been deformed as a single unit after the emplacement of the Raches granite.

deformed when the intrusion emplaced. Thereby, the southern part of the contact is intrusive and rocks near this southern contact have been poorly deformed after the emplacement of the intrusion.

In the northern part of the contact, near Aghia Sophia chapel (see location in Fig. 2), the intrusive nature of the contact is clearly observed at large-scale in the landscape: near Frandato village, a several hundred meter-long branch of the granite intrudes the metamorphic unit (Fig. 2). Moreover, on the northern coast, granitic dikes intrude the host rocks (Fig. 3b). At the scale of the island, the contact is almost vertical and it undulates at small scale due to folding, as observed near Frandato village (Fig. 2) where other granitic dikes penetrate the host metamorphic rocks (Fig. 3c). The contact between these dikes and the host rock appears folded with N–S axes, parallel to the regional stretching lineation, and with horizontal axial planes. Rocks on both sides of this contact appear strongly deformed, with both granitic and metamorphic foliation planes being transposed at the contact. The northern contact geometry thus shows a clear intrusive relation and not the tectonic contact described by Boronkay and Doutsos (1994), Kokkalas and Aydin (2013), Kumerics et al. (2005), Photiades (2002) or Ring (2007). Rocks on either side of the northern part of the contact have been afterward deformed as a single unit. In contrast to the southern part of the contact, it is not possible to determine whether the metamorphic unit was already deformed before the emplacement of the Raches granite.

4.1.2. Contact between the Raches and Karkinagrion intrusions

Thanks to good outcrop conditions at the top of the reliefs (Fig. 4a), the contact between Raches and Karkinagrion intrusions can be studied near Raches village (see location in Fig. 2). There, the Karkinagrion granite occurs structurally above the Raches granite (Fig. 4b). At the contact, mylonitic foliation planes in both granites are parallel. Our new mapping reveals a much larger volume of the Karkinagrion granite than previously described by Bolhar et al. (2010 and Ring (2007); Figs. 1 and 2). We also report the presence of large-scale migmatite massifs near Manganitis and Raches, found at the contact with the Karkinagrion granite (Figs. 2 and 4c). A gradual transition from migmatites to this two-mica granite is observed, implying that the granite is closely associated and then coeval with migmatites. Therefore, the emplacement scenario first proposed by Bolhar et al. (2010) must be redefined. It is here concluded that the Raches granite intruded the lower parts of the Ikaria MCC made of migmatites and in-situ granites such as the Karkinagrion intrusion. These observations are furthermore in agreement with available radiometric ages (Bolhar et al., 2010).

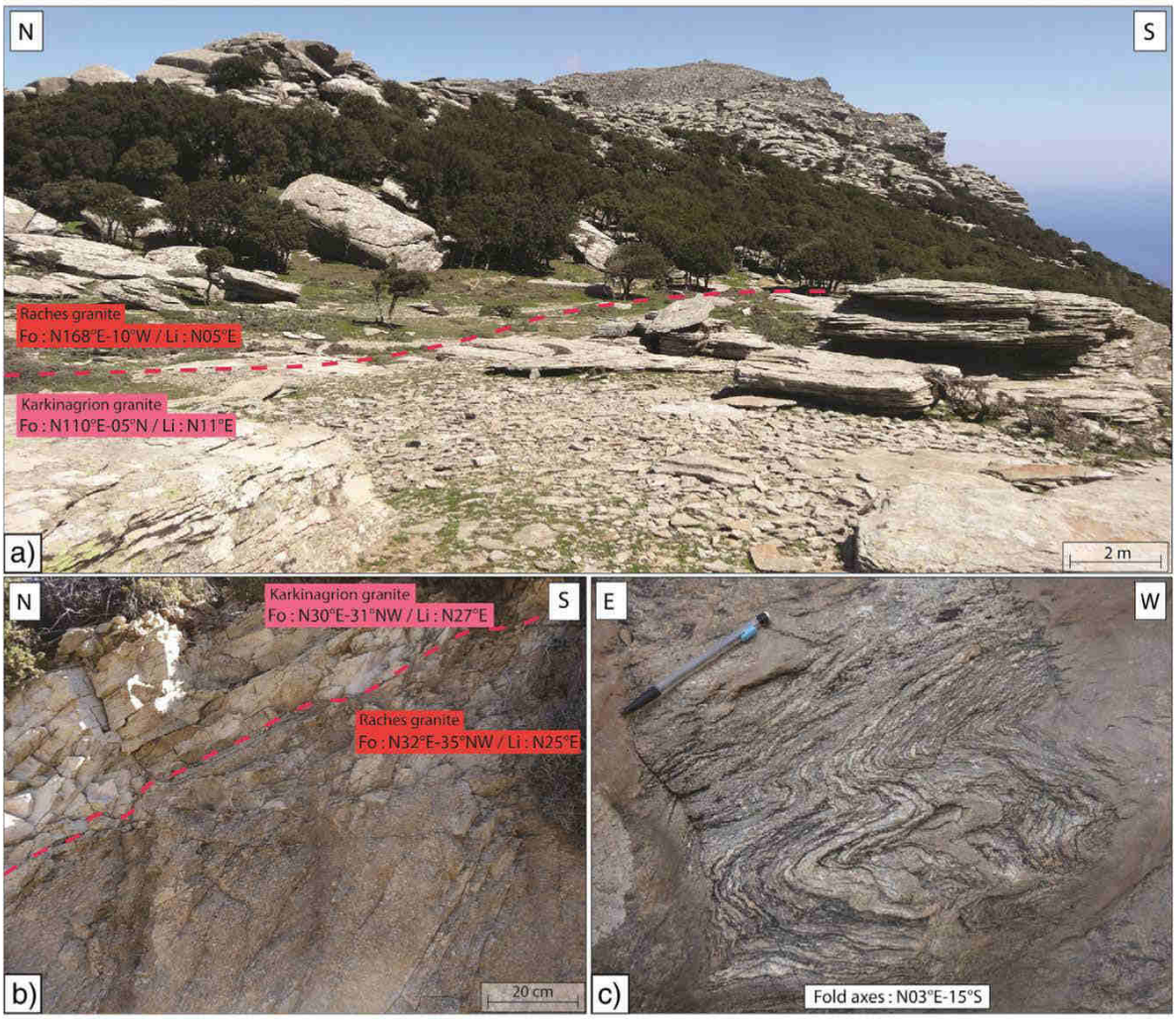

Fig. 4. Photographs showing the contact between the Raches and Karkinagrion granites. a) Large-scale field view of this contact. b) At the contact, these two granites have parallel foliation (Fo) and lineation (Li). c) Migmatites were found in close contact with the Karkinagrion granite, with a progressive transition from S-type granitic to migmatitic composition.

4.1.3. Contact between the Raches granite and a Mio-Pliocene sedimentary unit

As observed in the NE part of the island, the Pliocene sedimentary unit, regionally correlated with the UC unit, occurs in the northern part of the Raches intrusion near the village of Gialiskari (Fig. 5a). Here, this unit is made of Miocene sandstones and conglomerates fed by the Pelagonian unit. As observed in the metamorphic dome near Fanari, this unit is separated from the underlying Raches intrusion by a major tectonic contact (Fig. 2). Despite its importance, this contact has been omitted in recent studies (Bolhar et al., 2010; Kokkalas and Aydin, 2013; Kumerics et al., 2005; Ring, 2007) and remains currently not described in detail. The contact zone between the granite and the sedimentary unit is marked by a shallow-dipping (10–15°) mylonitic foliation carrying a N30°E stretching lineation (Figs. 2 and 5b). A widespread S–C fabric points to a clear top-to-the north sense of shear (Fig. 2). In addition, the contact itself is marked by a thick cataclastic band reaching ca. 10 m in thickness that partially reworks the mylonites and ultramylonites (Fig. 5c). Conversely, the Mio-Pliocene sedimentary unit is affected only by two conjugate sets of north- and south-dipping brittle normal faults with N–S to NE–SW oriented displacements, consistent with the ductile stretching direction in the granite (Fig. 5d).

4.2. Recognition of four deformation styles (D_1 to D_4)

In order to investigate the interrelations between intrusions and the Ikaria MCC, an extensive field survey including structural observations on 266 sites was performed over the Raches and Karkinagrion granites. These intrusions recorded, at least locally, a strong ductile and then

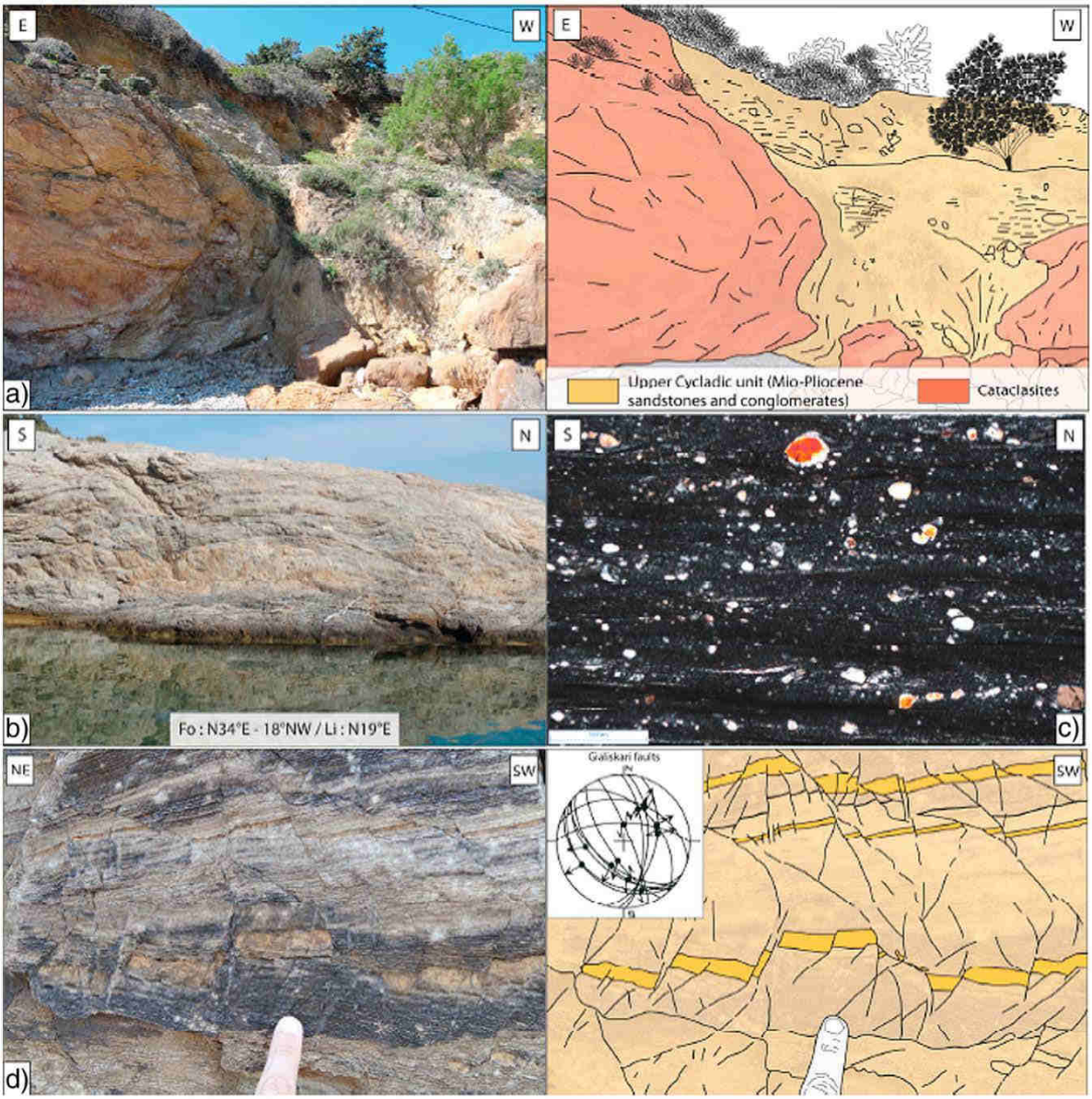

Fig. 5. Photographs showing the contact between the Raches intrusion and a Mio-Pliocene sedimentary unit. This major tectonic contact superposed a non-metamorphic sedimentary unit above the Raches granite. At the contact, the Raches granite is strongly deformed: a) ten meters of cataclasites, b) mylonites associated to a stretching lineation oriented N10°E to N30°E, c) microphotography illustrating the grain size reduction associated with ultramylonites, and d) the non-metamorphic sedimentary unit revealed only brittle deformation plotted on a stereogram.

brittle deformation as attested by the presence of ultramylonites and cataclasites (Fig. 5). The most obvious feature of our field study is that the whole Raches and Karkinagrion intrusions are affected by a top-to-the north asymmetric deformation, consistent with our observations near Gialiskari (Fig. 2). Moreover, intrusions show evidence for four distinct deformation structures (D_1 to D_4) that probably occurred during a single continuum of top-to-the north shearing deformation, i.e. the same progressive tectonic event through strain localization.

The first deformation feature (D_1) is recorded in the poorly deformed rocks of intrusions and is characterized by homogeneous sub-horizontal mineral lineation oriented N–S and a sub-vertical foliation (Fig. 6a). Feldspar phenocrysts are all aligned but not internally deformed (Fig. 6b). These crystals had to be free to rotate within the magma when they became oriented. D_1 can thus be considered as a magmatic fabric.

On incipiently deformed rocks, microfractures are observed in potassium feldspar, reflecting the D_2 set of structures (Fig. 7). Bouchez et al. (1992) describe three conditions to consider microfractures in feldspar as indicating submagmatic state deformation: 1) microfractures should not intersect more than one grain to ensure that each crystal has been in contact with the magma and 2) mineral phases filling microfractures should have the same magmatic composition and should be in crystallographic continuity with mineral phases outside the fracture. In these samples, the two conditions were met (Fig. 7) and D_2 can thus be considered as a submagmatic state deformation.

The third set of structures (D_3) is characterized by a less steep foliation (15–30°) and a stretching lineation oriented N10°E to N30°E. All kinematic indicators show a top-to-the northeast ductile shear sense (Figs. 2 and 6c, d). D_3 is characterized by unevenly distributed protomylonitic, mylonitic and ultramylonitic facies. The grain size of crystals, and especially feldspar phenocrysts, is reduced with the increase of strain (Figs. 5c and 6c).

While deformation styles D_1, D_2 and D_3 qualified a magmatic, submagmatic or ductile deformation, the D_4 deformation features are characterized by pure brittle deformation recorded throughout the granite. North-dipping low-angle normal fault planes are observed with striations parallel to the stretching lineation in mylonites (Fig. 8a). Moreover, normal steeply dipping brittle faults oriented E–W are observed consistently with a N–S extension (Fig. 8b).

Near the village of Nanouras, some striated planes have been observed. These planes have a consistent NE–SW orientation with sub-horizontal striations (Fig. 8c). The lack of kinematic indicators on fault planes does not allow firmly concluding on the motion sense. Thus, relationships between these structures and the regional top-to-the north ductile shearing remain unclear.

Structurally just below the northern contact between the Raches granite and the Gialiskari sedimentary unit, about 10 m-thick cataclasites are observed. Cataclasites are also found on the southwest coast, near the village of Kalamos. These cataclasites represent the last brittle increment of the deformation.

4.3. Distribution of the magmatic and ductile deformation (D_1, D_2 and D_3)

4.3.1. Field mapping of deformation intensity

Our study of the deformation has shown that in the whole Raches and Karkinagrion intrusions, the ductile deformation is geometrically unevenly distributed. Indeed, these intrusions show a distinct shallow-dipping foliation carrying a N10°E to N30°E trending stretching lineation above a core of less deformed granite characterized by a subvertical foliation and a N–S lineation (Figs. 2 and 6). Moreover, all kinematic indicators in tectonically deformed rocks such as S–C fabric, rotated porphyroclasts and sigmoidal foliation, show top-to-the north sense of shear, suggesting the presence of a thick north-dipping mylonitic shear zone deforming the upper part of granites, especially the Raches granite near the northern contact with the upper sedimentary unit at Gialiskari. Open folds furthermore deform the foliation with axes parallel to the stretching lineation. Because of shallow dip toward

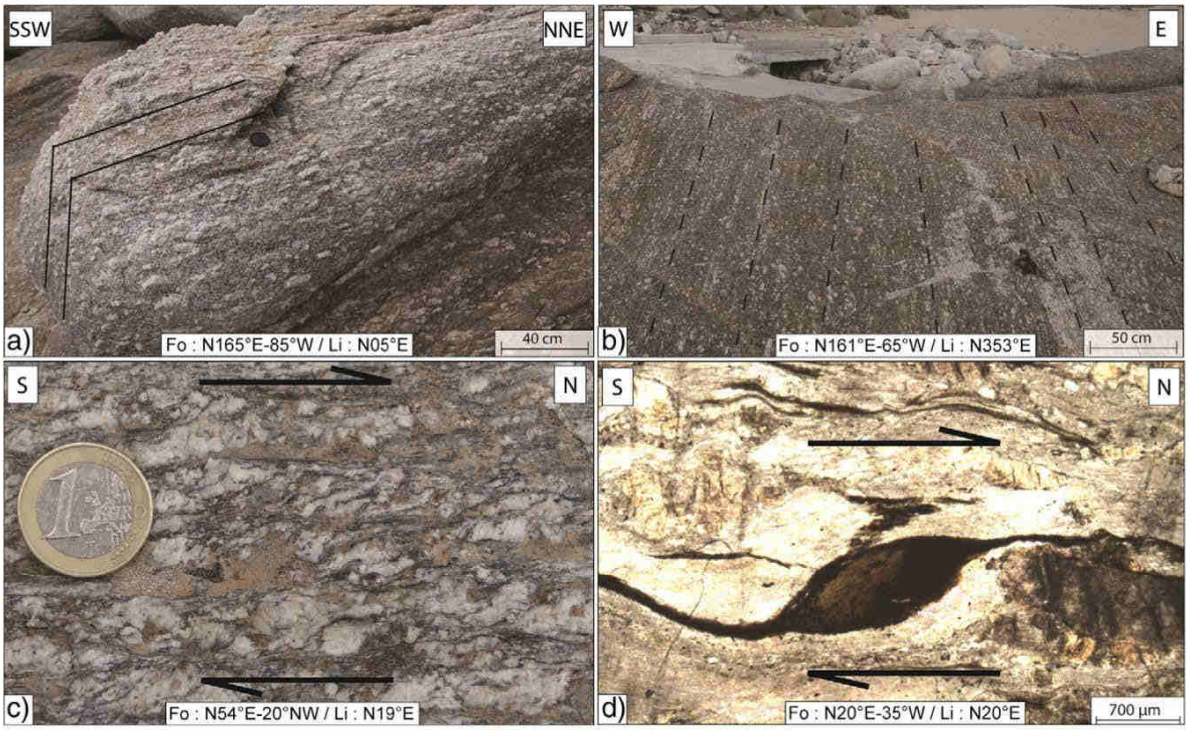

Fig. 6. Photographs showing field evidence of an unequal distribution of ductile deformation in the intrusive. a) and b) Poorly deformed Raches granite with preserved vertical foliation and north–south mineral lineation characterizing the D_1 deformation structure. c) and d) All kinematic indicators in mylonites, such as S–C shear bands or sigmoidal biotite, show top-to-the north sense of shear. These mylonites, characteristic of the D_3 deformation feature, are characterized by a low dipping foliation and a stretching lineation oriented N10°E to N30°E.

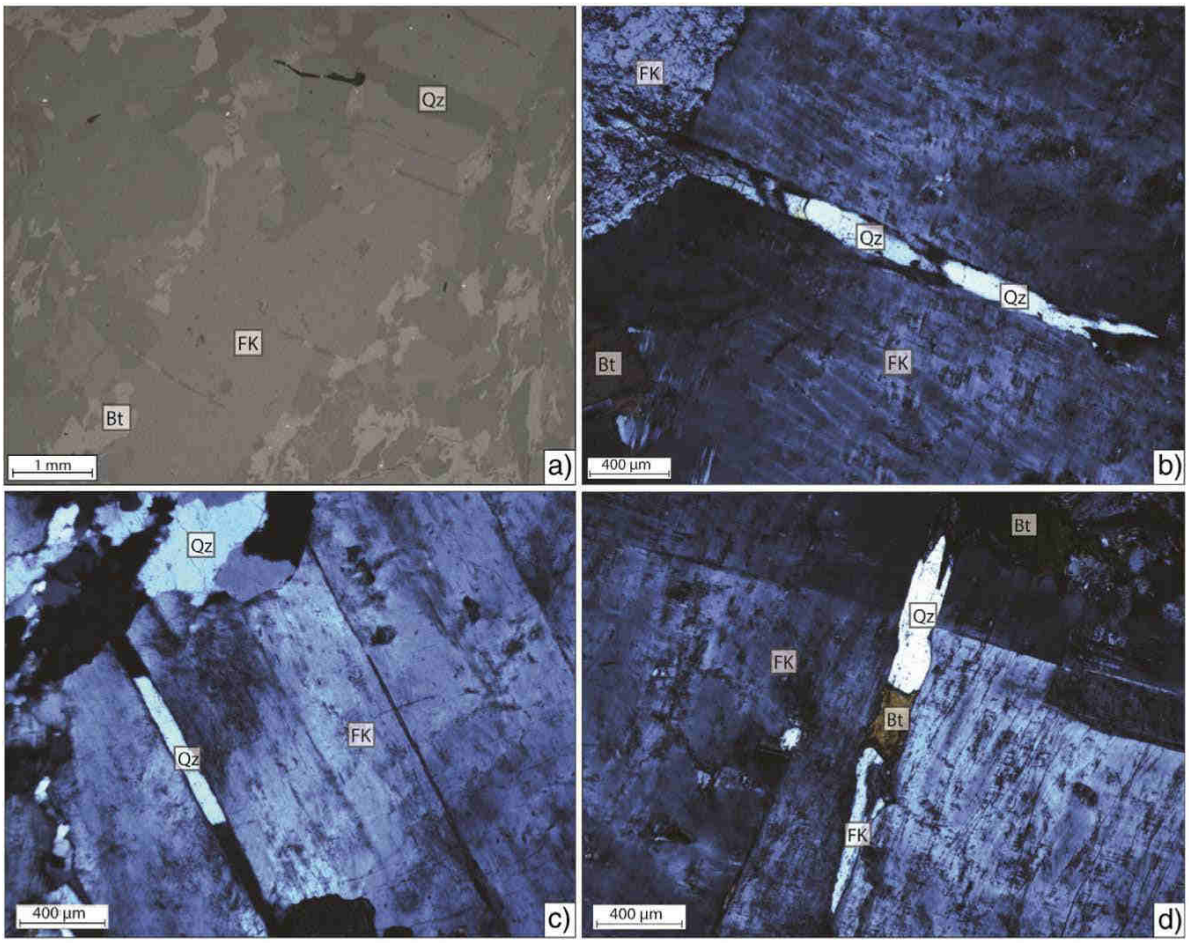

Fig. 7. Photographs showing the D_2 deformation style characterized by submagmatic microfractures in potassic feldspar (FK). a) Back scattered Scanning Electron Microscope (SEM) micrograph showing several microfractures in a single FK crystal. b) and c) Mineral phases filling the microfractures are in crystallographic continuity with mineral phases outside the fracture and not deformed. d) Microfracture with a coherent magmatic composition of FK + biotite (Bt) + quartz (Qz).

the north of these late fold axes, a south to north transect crosses the strain gradient upward, i.e. toward the most deformed structural part of the granite. In order to characterize the distribution of this ductile deformation, the intensity of finite deformation was mapped at high resolution. The strain gradient that affected the orthogneisses, resulting from the deformation of the same granitic protoliths, was characterized by defining seven strain facies of ductilely deformed granites as proposed by Charles et al. (2011) or Huet et al. (2009; Fig. 9). Each grade of deformation was defined on macro-structural criteria adapted to fieldwork, such as the shape and size of the main minerals but also the succession of microstructures developing during progressive deformation. The seven strain facies were defined as follows:

Grade 0 corresponds to an isotropic magmatic fabric. The term "magmatic fabric" is used in the mechanical sense, so when there is no direct interaction (contact) in the magma between phenocrysts (Vernon, 2000) and no magmatic preferred orientation develops. The granite shows neither foliation nor lineation and minerals are not deformed (Fig. 9a).

Grade 1 corresponds to an anisotropic magmatic fabric. Minerals are not deformed but an incipient foliation and/or lineation can be observed (Fig. 9b).

Grade 2 can no longer be considered as a pure magmatic fabric. Feldspar megacrysts start to be deformed, which suggests interactions between phenocrysts in the magma. Some FK are not deformed while others are stretched, boudinaged and sheared (Fig. 9c). Elongated clusters of biotite mark the stretching lineation.

Grade 3 is marked by the appearance of a weak foliation, a clear stretching lineation, a few penetrative shear bands that affect large volume of rocks, grain-size reduction and clear quartz ribbons (Fig. 9d). This fabric can be qualified as protomylonitic.

Grade 4 is characterized by a strong foliation and lineation with increasing number of shear bands associated with stretched biotite and quartz ribbons (Fig. 9e). This fabric can be qualified as mylonitic.

Grade 5 shows the presence of ultramylonite bands in addition to the mylonitic shear bands of grade 4 (Fig. 9f). The average thickness of these bands varies from a few centimeters to ten centimeters.

Grade 6 is characterized by a few meters of massive ultramylonites (Fig. 9g).

Field observations across the entire intrusive bodies allow us to propose a qualitative map depicting the distribution of the magmatic and ductile deformation in granites (Fig. 10a). This map shows a gradual increase in the intensity of deformation from south to north, or from base to top. The least deformed rocks (grades 0, 1 and 2) are found in the southern part of the two granites (Fig. 10a). In contrast, in the northern part, approaching the contact with the Gialiskari sedimentary unit, the two granites are strongly deformed (grades 3, 4, 5 and 6). A strong increase in strain intensity is also locally observed in the southwestern

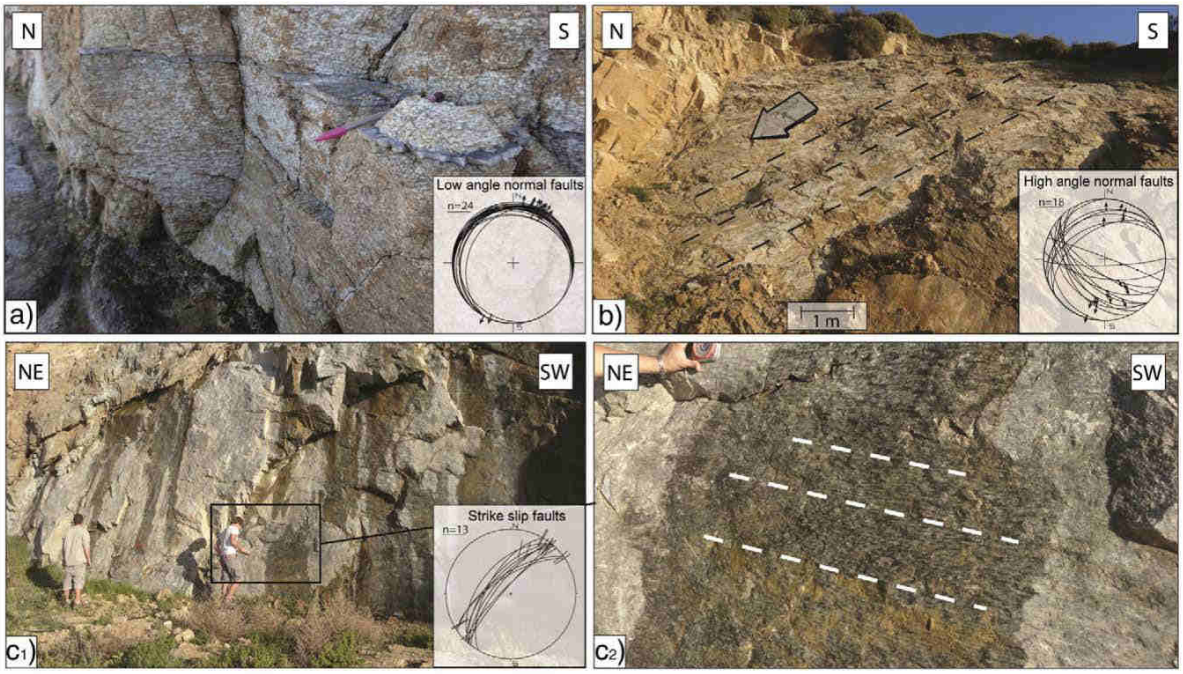

Fig. 8. Photographs showing the brittle D_4 style of deformation in the Raches granite. This deformation was characterized by both low-angle (a) and steeply dipping (b) normal faults. In addition to normal faults, the brittle deformation was marked by large strike-slip fault planes with ambiguously sense motion not taken in consideration (c).

part of the island, near the village of Kalamos (Fig. 10a). A N–S cross-section crossing the strain gradient upward, i.e. toward the most deformed granite (Fig. 10b), shows the attitude of the north-dipping shear zone revealed by these observations. All kinematic indicators show a consistent top-to-the north shear sense compatible with the regional variation of the foliation dip that draws a sigmoid at the scale of ca. 10 km (Fig. 10b).

4.3.2. Quantification of ductile deformation

This section documents quantitatively the strain gradient across the deformed granitic bodies by a detailed study of selected outcrops given in Fig. 10a. The Raches granite was targeted because it shows all strain grades. The reconstruction of the strain ellipsoid (following the protocol described in Section 2) allows calculating the degree of anisotropy (P′) and the shape parameter (T) of biotite fabric for each sample (Borradaile and Werner, 1994; Launeau and Robin, 2005). P′ refers to the eccentricity of the 3D fabric ellipsoid and can be correlated with the intensity of biotite preferred orientation. T refers to the symmetry of the 3D fabric ellipsoid. Three cases can be considered: i) if T is lower than −0.2, the lineation is dominant (L > S) and the ellipsoid is prolate, ii) if T is comprised between −0.2 and 0.2, the lineation and foliation parameters are close to each other (L = S) and iii) if T is comprised between 0.2 and 1, foliation is dominant (S > L) and the ellipsoid is oblate.

The results of the quantitative analysis are shown in the deformation map and the P′–T graph (Fig. 10a and c). The P′ = f(T) diagram presents the relationship between the shape parameter and the degree of anisotropy (Fig. 10c). A good correlation is observed between the degree of anisotropy (P′) and the qualitative strain map elaborated in the field. Indeed, grade 0 corresponds to a very low degree of anisotropy (P′ = 1.10), whereas grade 5 has the highest degree of anisotropy (P′ = 1.62). The foliation is dominant in the least deformed zones and a gradual evolution is observed toward plano-linear, or even a pure linear fabric, in the most deformed zones. Therefore, the degree of anisotropy and the shape parameter correlates well with strain intensity observed in the field.

5. The Gialiskari detachment

The strain gradient observed when approaching the base of the Gialiskari sedimentary unit (Fig. 10a) points to the existence of a shallow north-dipping top-to-the north shear zone. Associated to this shear zone, a clear reorientation from subvertical magmatic foliations to subhorizontal mylonitic foliations has been observed in the field. Furthermore, this shear zone evolves from ductile to brittle through time, the thick cataclasites being the brittle expression of the shear zone continuing motion in the brittle regime. The shear zone brings into close contact the ductilely deformed granites and the non-metamorphosed basin and its normal faults. All these features are characteristic of an exhuming shallow-dipping normal shear zone, hereafter named the Gialiskari Detachment (Fig. 11). The study of this structure together with the map of deformation grades in the granites shows an undulated ductile and then brittle plane, undulation particularly well illustrated by the strain gradient between Armenistis and Gialiskari and the orientation of foliation in this area (Fig. 11).

In the southwest of the island, near the village of Kalamos, a strong increase in strain intensity is also locally observed with a mylonitic foliation oriented N41°E-33°NW and a very well marked stretching lineation oriented N12°E (Fig. 12). Ultramylonites are also present, as well as cataclasites. A schematic 3D representation in Fig. 12 shows the relative disposition of structures. The ultramylonites are located at the interface between the Raches granite and the lower boundary of a metamorphic rock septa. These ultramylonites form in the landscape a very well defined and continuous surface (Fig. 12a). Approaching the ultramylonites, the granite becomes more deformed with increasingly stretched mineral grains and aggregates (Fig. 12b). There, the seven grades of strain intensity are condensed within a few hundreds of meters (Fig. 10a). S–C shear bands and mica fishes indicate top-to-the

V. Laurent et al. / Tectonophysics 651–652 (2015) 152–171

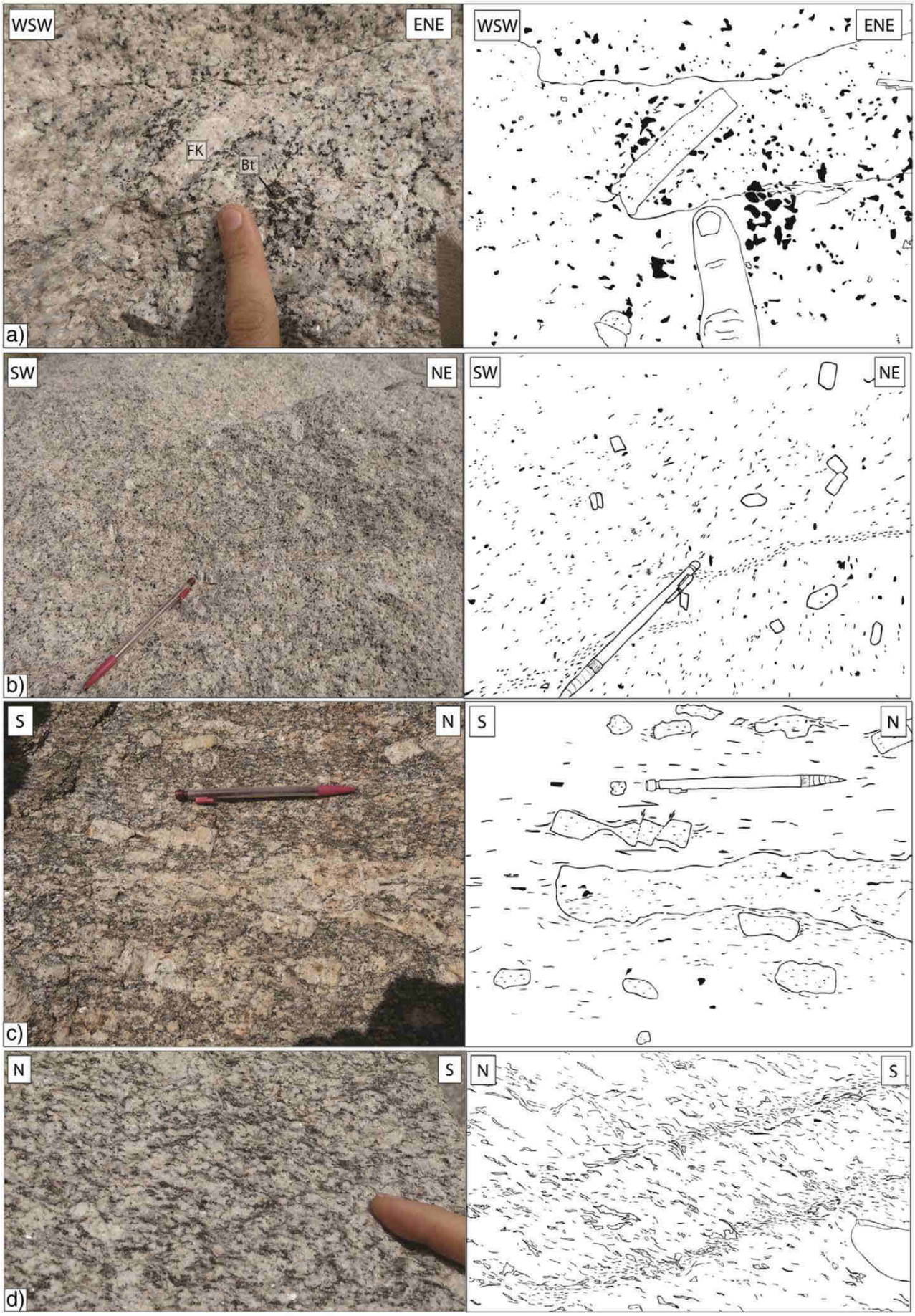

Fig. 9. Structural field scale of strain facies. The seven grades of deformation are described in the text.

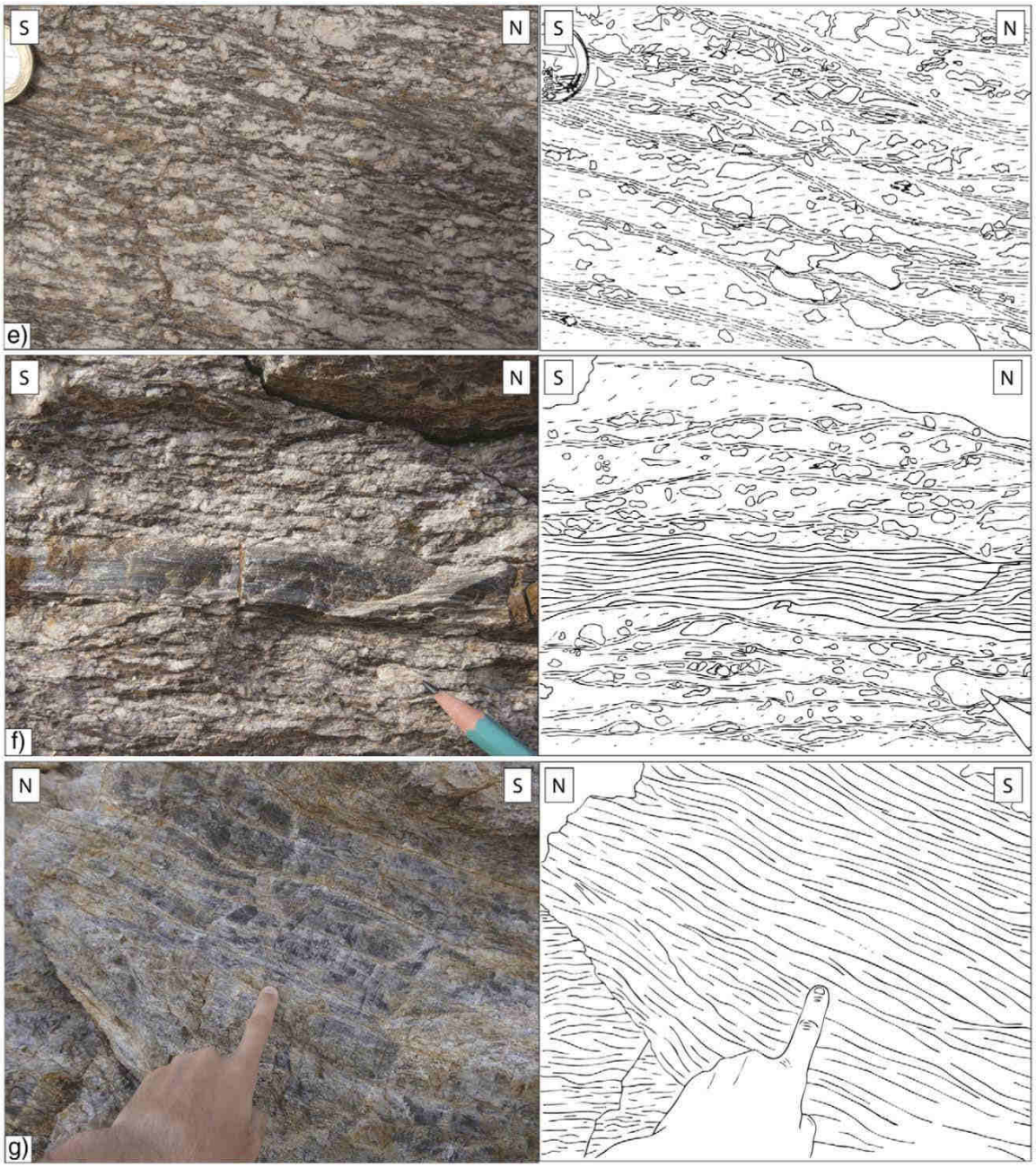

Fig. 9 (*continued*).

north sense of shear (Fig. 12b). The septa consist of highly deformed metasediments including metapelites and marble traversed by granitic dikes carrying also top-to-the north shear sense criteria (Fig. 12c). A ca. 20 m-thick cataclasites are observed above the septa (Fig. 12a). The general structure of this zone is similar to the one described at Gialiskari, except for the absence of the Mio-Pliocene sedimentary unit that may occur further offshore (Fig. 12d).

6. Emplacement depth of the Raches granite

The emplacement depth of an intrusion, i.e. the depth at which the magma crystallizes, is generally not easy to retrieve accurately. Two approaches are generally used. The first approach is based on the petrologic study of metamorphic assemblages that result from the metamorphic transformation of adjacent country rocks, and the second one on the intrinsic mineralogy of the intrusion (Nédélec and Bouchez, 2011). The polyphase character of the metamorphic rocks hosting the intrusion hindered the use of the first method (Altherr et al., 1982; Kumerics et al., 2005; Martin et al., 2011). Conversely, the general framework of I-type granitoids enables us to use hornblende chemical composition as a geobarometer. Hammarstrom and Zen (1986) describe the existence of linear relationship between the total number of aluminium atoms (Al Tot) in hornblende and crystallization depth of a pluton. This barometer was defined for conditions similar to those found in the Raches

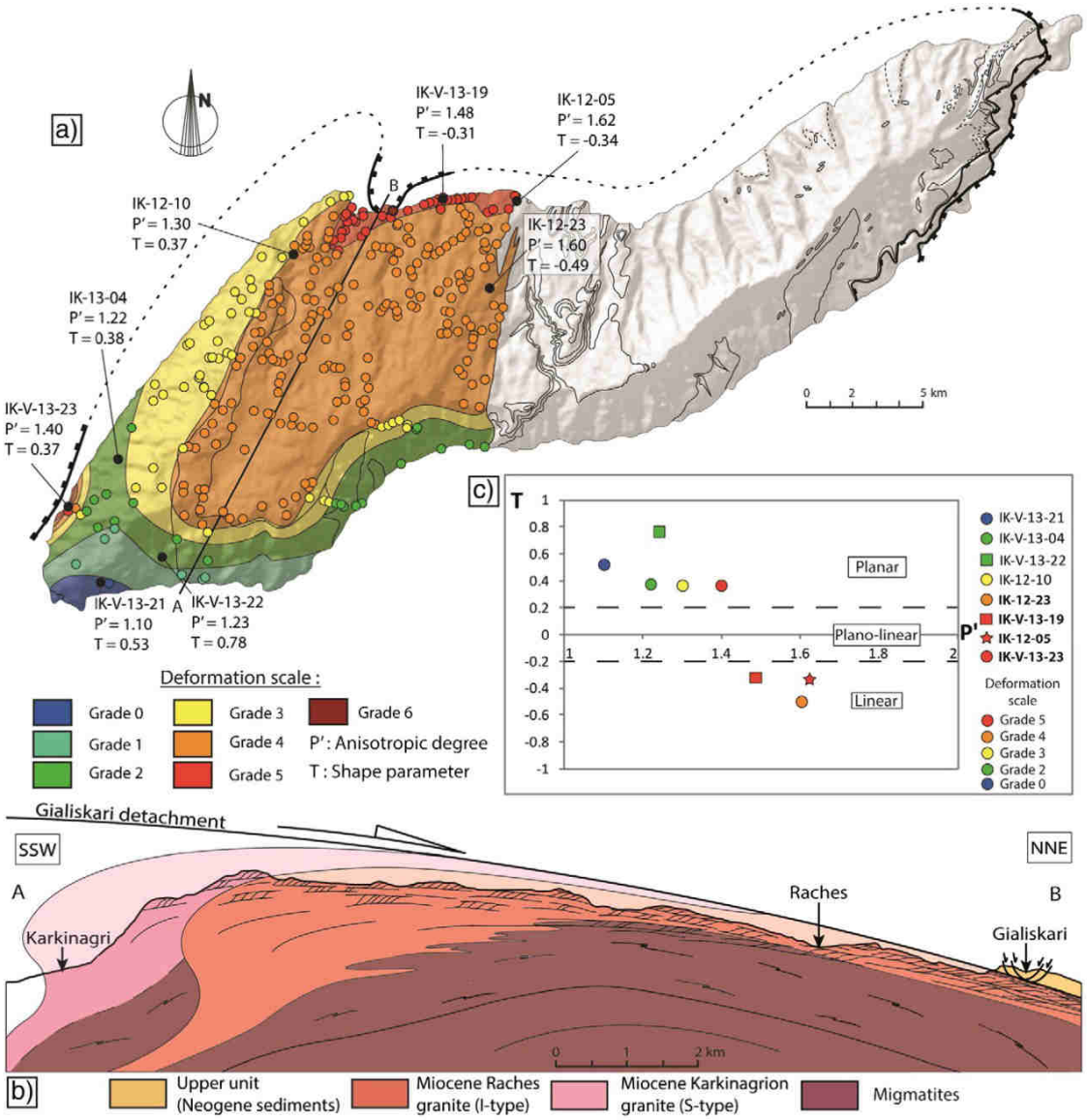

Fig. 10. Characterization of a strain gradient in Raches and Karkinagrion intrusions. a) Semi-quantitative map of deformation showing the heterogeneous distribution of the ductile deformation in both intrusions. Location of analyzed samples and position of the geological section AB are also represented. b) Geological section AB through the Raches and Karkinagrion intrusions indicating their relative structure (Raches granite intruding the Karkinagrion granite and the migmatites) and their relations with the Gialiskari Detachment (the structurally uppermost parts of intrusions are the most deformed ones). c) Diagram representing the shape parameter (T) vs. the anisotropic degree (P′) for samples localized in figure (a).

granite. Indeed, it is valid for a classical assemblage of I-type granitoids, including FK, quartz, plagioclase, biotite, hornblende, sphene and Fe–Ti oxides (ilmenite and/or Ti-magnetite).

To test the criticism of Anderson (1996) about the temperature sensibility of this barometer, both cores and rims of amphiboles have been analyzed. No chemical variations were observed between these analyses (Fig. 13a). Our results revealed the presence of two different types of amphibole: ferrohornblende and magnesiohornblende (Fig. 13b). Ferrohornblendes crystallize at higher pressure than magnesiohornblende with a crystallization depth of ferrohornblendes comprised in the range 9–15 km and 5–10 km for magnesiohornblendes (Fig. 13c). We interpret the crystallization depth of ferrohornblendes as representing a good estimate of the crystallization depth of the Raches granite. Moreover, the crystallization history of the Raches granite was probably further complicated by the injection of several magmatic pulses as suggested by Altherr et al. (1982), which may explain why magnesiohornblendes crystallized at shallower depth. The geodynamic consequences of these results are discussed in the following.

7. Interpretation and discussion

7.1. Continuity of deformation in the Raches granite from magmatic to solid state

The Raches and Karkinagrion granites can be considered asymmetrical laccolithic intrusions (Fig. 10b). The presence of the Karkinagrion granite in the southern part of the island, the top-to-the north sense of shear affecting both granites, as well as the Xylosyrtis granite intruding the southern part of the metamorphic dome, suggest that the magma injection zone was situated in the southern part of the island (Fig. 14).

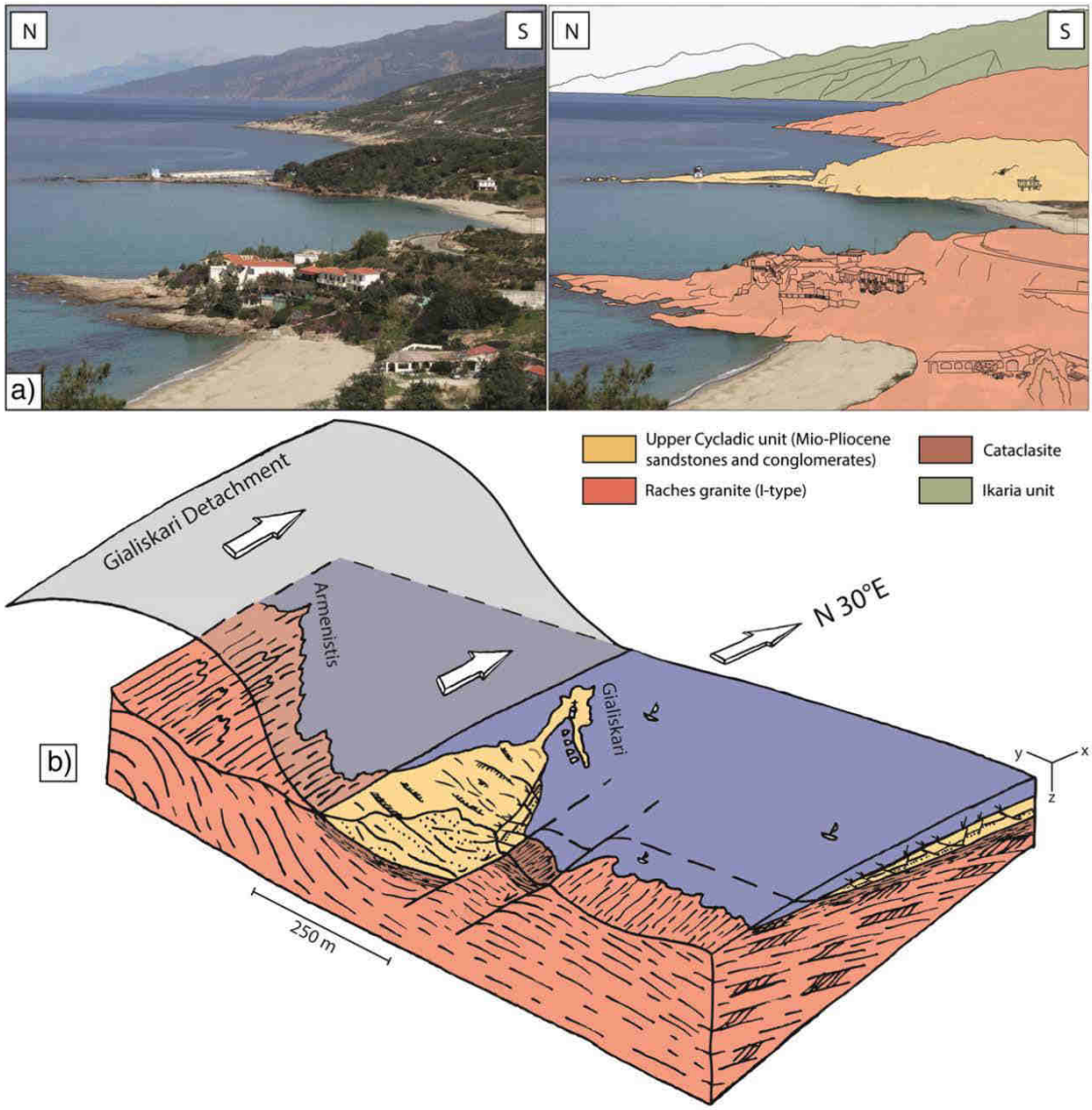

Fig. 11. The Gialiskari Detachment structure. a) View of the Gialiskari Detachment near the Gialiskari peninsula, where a non-metamorphic Mio-Pliocene sedimentary unit is superposed on the Raches granite. b) 3D block diagram highlighting the undulated geometry of the Gialiskari Detachment near the Gialiskari peninsula.

The Raches and Karkinagrion granites show evidence for four deformation styles (D_1 to D_4, Figs. 6, 7 and 8). D_1 reflects a magmatic deformation related to the early emplacement stage of the intrusion. The first style of deformation is recorded in the least deformed rocks (grades 1 and 2) and is characterized by a planar fabric disposed subvertical and a stretching lineation oriented N–S (Fig. 14). The map of stretching lineations (Fig. 2) shows a progressive rotation from this N–S oriented lineation to the N30°E trending one in the northern part of the granite.

The second set of structures (D_2) is characterized by the presence of microfractures in stretched potassic feldspars. According to Bouchez et al. (1992), these microfractures are characteristic of the submagmatic state deformation. To form these microfractures, a sufficiently high shear stress has been imposed on the crystal framework of the Raches pluton that remained partially molten. Once formed, these microfractures were instantaneously filled by the magma (Fig. 7). Thereby, the observation of this submagmatic deformation shows that Raches and Karkinagrion plutons are therefore syntectonic intrusions. These microfractures were not observable in the most deformed samples because the later solid-state deformation overprinted and erased the submagmatic deformation.

D_3 deformation features formed once the Raches and Karkinagrion granites had totally crystallized. It is marked by top-to-the northeast ductile shearing deformation, as also observed within the metamorphic dome (Figs. 2 and 14), suggesting that D_3 was related to the same regional extension. Strain intensity increases with the approach of the northern contact between the Raches granite and the Gialiskari sedimentary unit and a gradual transition from protomylonitic to mylonitic and also ultramylonitic facies is observed when approaching the Gialiskari Detachment at Gialiskari or at Kalamos (Fig. 14).

The last event of deformation (D_4) characterizing the Raches and Karkinagrion granites is brittle, as shown by cataclasites just below the Gialiskari Detachment and normal faults in various places in both granites (Figs. 5, 11 and 12).

The four deformation styles (D_1 to D_4) observed in the Raches and Karkinagrion granites show an evolution in deformation regime from magmatic to submagmatic, ductile and then brittle deformation. This

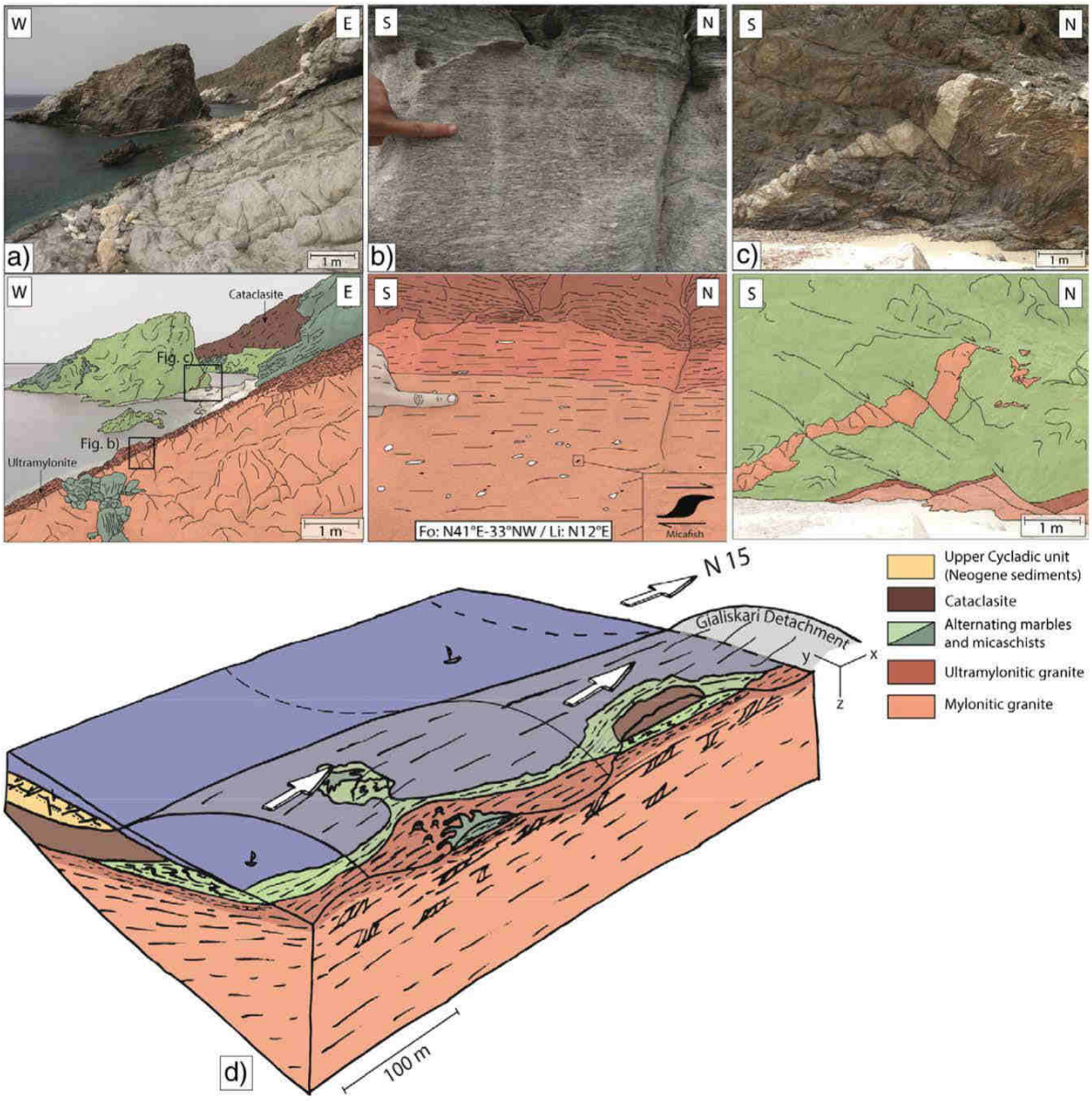

Fig. 12. Photographs showing the Gialiskari Detachment structure near the village of Kalamos. a) Base to top view of the mylonitic to ultramylonitic Raches granite, a septa composed by highly deformed metamorphic micaschists and marbles, and on top, a ca. 20 m-thick cataclasite. b) Highly deformed mylonites and ultramylonites in the Raches granite. Mica fish indicates top-to-the north sense of shear. c) Top-to-the north shearing in the metamorphic septa. d) 3D block summarizing the relative position of the structures and their link with the Gialiskari Detachment.

evolution demonstrates that these granites emplaced during top-to-the north shearing. Although we have described this evolution as a succession of four different sets of small-scale structures, from D_1 to D_4, these structures simply express a continuum of deformation with progressive strain localization along the main detachment from ductile to brittle conditions.

7.2. Localization of deformation during cooling and late-exhumation of the Raches granite

The Gialiskari Detachment is located along the contact between the Upper Cycladic unit and the Raches granite (Fig. 14). Emplacement, mylonitization and cooling of the Raches and Karkinagrion granites were contemporaneous with top-to-the northeast ductile shear observed along the Gialiskari Detachment. This structure passed over time through the ductile–brittle transition during exhumation (Fig. 15). The intrusive contact with the metamorphic dome is parallel to the shearing direction and is strongly folded with fold axes parallel to the same direction. The contact of the pluton with the host rocks has been totally transposed to end parallel to the regional shearing direction in most deformed parts. In agreement with our geobarometry results, this folding is an argument for a deep emplacement of granites in a ductile host rock (Fig. 15: step 1). Indeed, geobarometry results have shown that ferrohornblende crystallized at high pressure (ca. 3–5 kbar). It thus seems that the geometry of intrusions as a whole, the shape of the intrusive contact and the deformation during the entire cooling period were controlled by the activity of the Gialiskari Detachment.

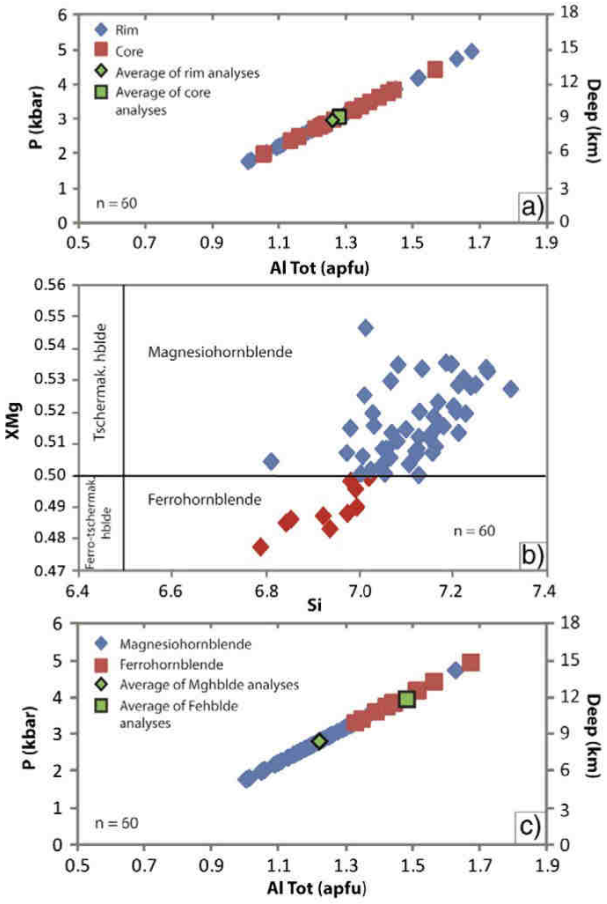

Fig. 13. Estimation of emplacement depth of the Raches granite. a) Diagram showing the pressure emplacement of amphibole vs. the aluminium atoms number for both core and rim analyses (calibration of Schmidt, 1992). Note that the average of core and rim analyses is similar. b) Chemistry of amphiboles showing the presence of both magnesio and ferrohornblende in samples. c) Diagram showing the two different pressure emplacements between the ferrohornblende (ca. 4 kbar) and magnesiohornblende (ca. 3 kbar).

From the depth of final emplacement, the Raches and Karkinagrion intrusions and the host metamorphic dome were sheared during cooling and a thick ductile shear zone developed below the UC unit. The whole system was then gradually exhumed while deformation progressively localized when approaching the ductile–brittle transition (Fig. 15: step 2). The strain was then accommodated by ultramylonitic and finally cataclastic deformation, still under an extensional regime oriented N30°E (Fig. 15: step 3).

7.3. Granite intrusions and development of metamorphic core complexes in the Cyclades

The Fanari and Gialiskari detachments, together with the ductile Agios Kirykos Detachment, make the eastern extension of the North Cycladic Detachment System (NCDS; Fig. 1a; Jolivet et al., 2010) running across Andros, Tinos, Mykonos and then Ikaria. The foliation that formed during top-to-the north shearing deformation below the Agios Kirykos Detachment was then intruded by the Raches granite, which shows that in the metamorphic units of Ikaria, the activity of the NCDS had started in the metamorphic units of Ikaria before the emplacement of intrusions. The geological evolution of the dome is summarized on a set of reconstructions (Fig. 16). On these reconstructions, the spacing between the main extensional structures is taken from Jolivet et al. (2010). As suggested by Jolivet et al. (2004a) extensional deformation in the Aegean involves a component of boudinaged at all scales, from the outcrop to the crust. Spacing of faults is mainly a consequence of the wavelength of such boudinaged, which itself depends upon crustal thickness.

At 30–35 Ma, acceleration of slab retreat initiated extensional tectonics in the Aegean backarc domain (Fig. 16; Jolivet and Faccenna, 2000). Crustal thickness before the period of extension (ca. 50 km) is taken from Jolivet and Brun (2010) for their geodynamic reconstructions of the Aegean domain. Being a major inherited structure, the base of the UC unit was then reactivated as a large detachment zone, the NCDS (Jolivet et al., 2010). Slab retreat was accompanied by a southward displacement of the volcanic arc, influx of hot asthenosphere and relaxation of HP–LT thermal regime established during subduction (Jolivet and Brun, 2010; Jolivet et al., 1994, 2013). This thermal relaxation involved a temperature increase in the lower crust that locally began to melt, forming migmatites (Fig. 16). These migmatites have been described on several Cycladic islands such as Mykonos, Delos, Rhenia, Naxos, Paros (Denèle et al., 2011; Jansen, 1973; Keay et al., 2001; Seward et al., 2009; Vanderhaeghe, 2004) and now Ikaria Island. The upper crust was then heavily fractured and faulted, leading to the formation of crustal-scale high-temperature metamorphic domes in-between, like the Ikaria MCC. These MCCs are delimited by crustal-scale structures, ductile in the lower crust, brittle in the upper crust (Fig. 16).

The age of the high-temperature event on Ikaria is currently not precisely known. Following up on the comparison with the northern part of the Menderes Massif, a late Oligocene–Early Miocene age can be proposed. Dating of the Simav Detachment, an eastern extension of the NCDS exhuming the northern Menderes Massif, suggests that the activity occurred between 30 and 8 Ma reaching high-temperature

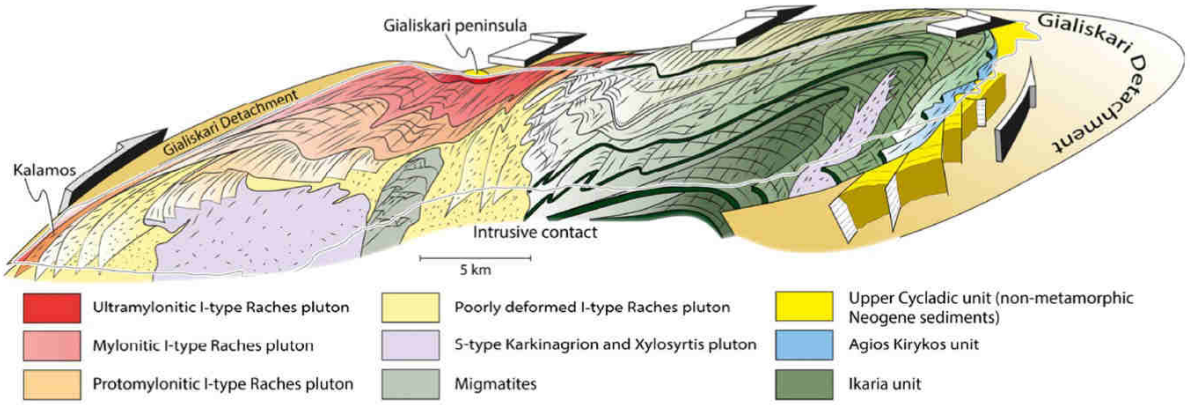

Fig. 14. 3D bloc showing the geological architecture of Ikaria Island, integrating and summarizing all the structural information.

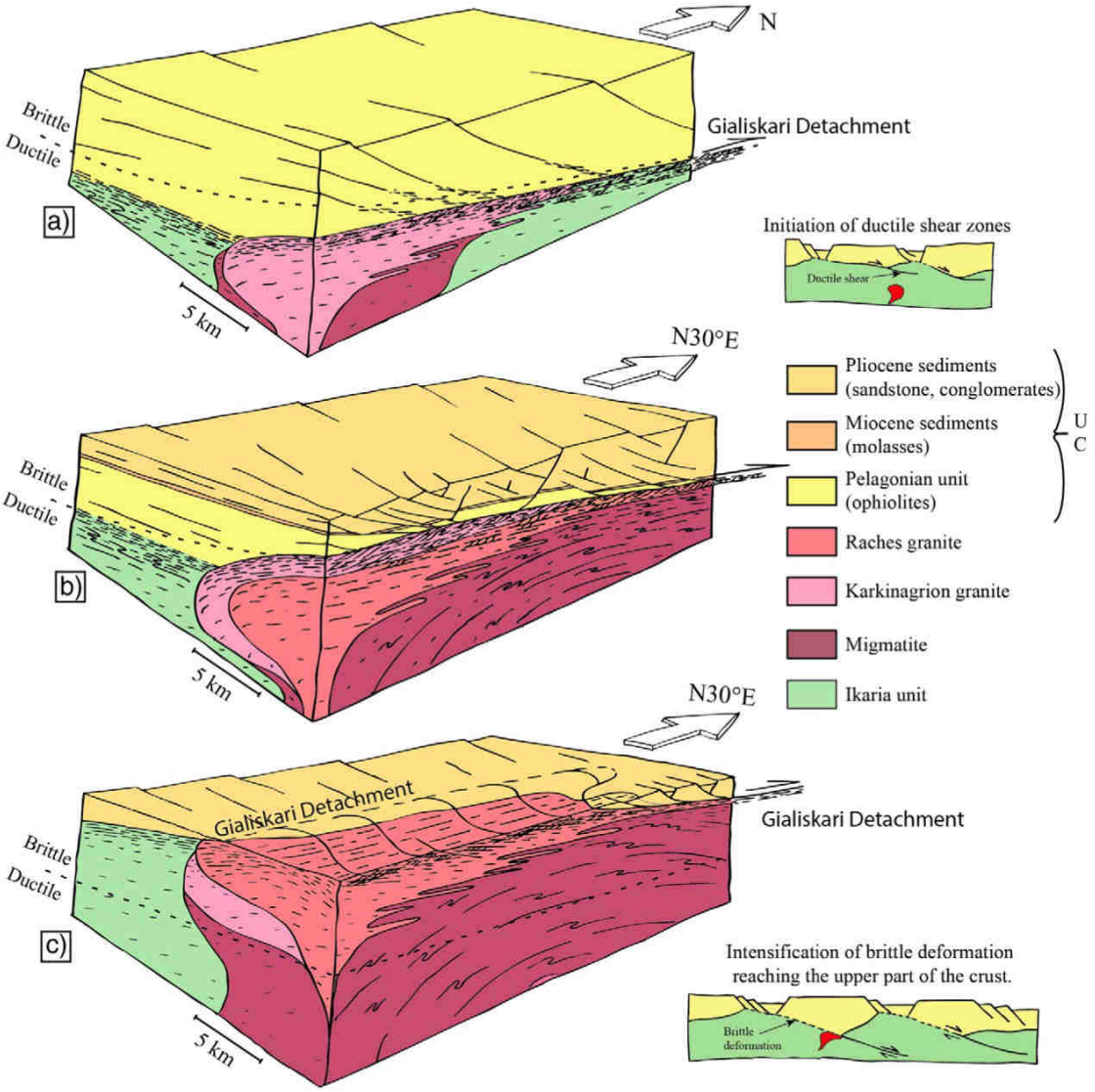

Fig. 15. Scenario at intrusion scale showing the evolution of the Gialiskari Detachment system. a) Inception of localization of the ductile deformation within the Gialiskari Detachment located between the Karkinagrion granite related to migmatites and the Upper Cycladic (UC) unit. b) Evolution of the deformation through the brittle–ductile transition. Cataclasis becomes the dominant deformation process when strain localizes in the Gialiskari Detachment. c) Intensive localization of cataclastic deformation in the Gialiskari Detachment overprints previous ductile fabrics.

conditions before 18 Ma (Bozkurt et al., 2011). This timing would make the Ikaria metamorphic dome coeval in age with the migmatitic dome of Naxos (Altherr et al., 1982; Duchene et al., 2006; Keay et al., 2001). The close association of migmatites with the two-micas Karkinagrion granite with a diffuse contact and the presence of the S-type Xylosyrtis granite, both dated around 14–13 Ma (Bolhar et al., 2010), reinforce the conclusion that the high-temperature event and crustal partial melting in Ikaria date back to the Miocene. Moreover, the Raches granite, dated at 13.33 ± 0.17 Ma by U/Pb method on zircon (Bolhar et al., 2010), results from a partial mixing of melted continental felsic crust and mantellic or mafic magma as described by Altherr and Siebel (2002) and Pe-Piper et al. (2002). It intrudes the earlier migmatites and the related Karkinagrion granite and also the Ikaria unit at a depth estimated between 10 and 15 km (Fig. 15: step 1). This emplacement may coincide with the period during which deformation migrated from the Agios Kirykos Detachment to the Gialiskari Detachment (Fig. 16).

This study provides new data on the debated triggering effect of magmatic intrusions in the development of MCCs. On Ikaria, emplacement of the Raches and Karkinagrion granites postdates the initiation of the MCC exhumation below the Agios Kirykos Detachment. We assume that the pluton had pierced the lower ductile Agios Kirykos Detachment. Contemporaneously, the northeast extensional deformation migrated upward in the crust, along the upper Gialiskari Detachment, where the pluton roof was subsequently sheared by a NNE-directed non-coaxial flow from magmatic to solid-state conditions. A similar sequence of events is described on Mykonos, Tinos and Serifos for the NCDS and the WCDS (Brichau et al., 2007; Denèle et al., 2011; Rabillard et al., 2015) as well as on Naxos (Gautier et al., 1993; Urai et al., 1991). On Mykonos, the intrusion postdates the initiation of the Rhenia migmatitic dome (Denèle et al., 2011). On Naxos Island, intrusion of the granodioritic pluton into the roof of the migmatitic dome is dated around 12 Ma (Andriessen et al., 1979; Keay et al., 2001;

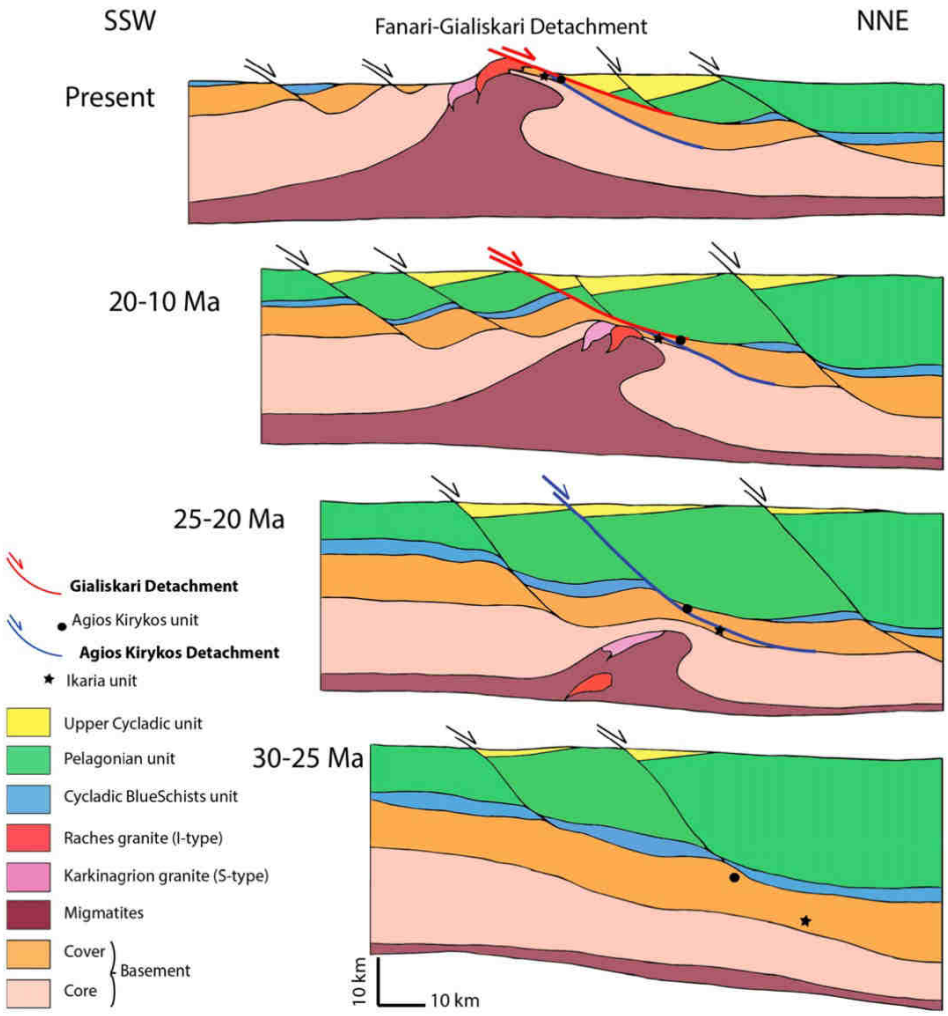

Fig. 16. Probable crustal scale scenario of the evolution of structures in Ikaria Island. See text for explanations.

Wijbrans and McDougall, 1986), while the development of this dome is estimated around 20–21 Ma by U/Pb dating on zircon from migmatitic samples (Keay et al., 2001; Martin et al., 2006). Initiation of top-to-the northeast ductile shear within the greenschist facies dome of Tinos was estimated at 30 Ma (Parra et al., 2002), while this dome and the Tinos Detachment are intruded by the pluton around 14–15 Ma (Avigad and Garfunkel, 1989; Brichau et al., 2007).

These observations show that intrusions emplaced while the MCC was already in an advanced stage of development and thus that the Cycladic plutons did not play a dominant role in the initiation of MCCs, as already proposed by Denèle et al. (2011). It appears that detachments instead controlled the emplacement of granites as described by Brown (1994), Brown and Solar (1998a), D'lemos et al. (1992) and Hutton and Reavy (1992). It thus seems that major inherited structures allow localizing extensional deformation in the crust during exhumation. The close association of plutons and detachments in the Cyclades then indicates that MCCs are preferential sites for pluton emplacement. Flow of partially molten crust toward the core of the dome induced by crustal-scale boudinage may explain this association (Augier et al., 2015; Gautier et al., 1993; Huet et al., 2011a, 2011b; Tirel et al., 2004).

On the other hand, plutons may help localizing shear zones. When the Raches and Karkinagrion granites intruded the Agios Kirykos Detachment, the motion jumped on a structurally higher position along the Gialiskari Detachment. The same scenario has been observed on other Cycladic islands. For examples, when the Tinos granite intruded the Tinos Detachment, the deformation migrated upward along the Livada Detachment (Brichau et al., 2007; Jolivet and Patriat, 1999). Or even, when the Mykonos granite intruded the Livada Detachment the deformation localized on a structurally higher position along the Mykonos Detachment (Denèle et al., 2011; Lecomte et al., 2010). The Meghalo Livadhi detachment cropping out on Serifos Island was also intruded by an I-type granodiorite, itself sheared by the upper Kavos Kiklopas and Agios Sostis detachments (Rabillard et al., 2015). Upward migration of the actively deformed zone is therefore a consequence of the intrusion that lifts up the ductile–brittle transition (Caggianelli et al., 2014; Jolivet and Patriat, 1999). This is consistent with several models suggesting that crystallizing plutons are capable of producing, at least locally, weak rheological heterogeneities where shear zones can nucleate along the contact with more resistant host rocks (Aoya et al., 2005; Caggianelli et al., 2014; Foster et al., 2001; Lister and Baldwin, 1993; Neves et al., 1996).

8. Conclusion

This contribution analyzes the interrelations between syntectonic intrusions and the development of metamorphic core complexes. An extensive field study of the structure of the Raches and Karkinagrion

granites in Ikaria was conducted, resulting in a new geological map that changes drastically from previous works in the area particularly in three key points: i) the Raches granite is an intrusive body within the Ikaria metamorphic dome although the contact appears intensely deformed and locally folded, ii) the Karkinagrion granite can now be considered as an *in-situ* two-mica granite closely associated with migmatites of the core of Ikaria MCC, and iii) the Gialiskari Detachment is a major, regional scale top-to-the north shear zone, part of the North Cycladic Detachment System, responsible for exhumation of the Ikaria MCC and the ascent of intrusions in its hanging-wall.

The emplacement of the Karkinagrion and Raches intrusions postdates the initiation of the Ikaria MCC. The exhumation of the metamorphic dome involved the Agios Kirykos Detachment during the first stages, before plutons intruded the detachment and deformation migrated upward. It is concluded that plutons do not nucleate the detachments, but instead detachments localize and control the ascent of plutons.

Acknowledgments

This study is a contribution of the ERC RHEOLITH project (ERC advanced grant no. 290864) and Labex VOLTAIRE. The authors are indebted to IGME and especially to Nikolas Carras and Adonis Photiades for their help. We are grateful to S. Janiec and J.G. Badin (ISTO) for the preparation of thin sections. Sergio Llana-Fúnez and an anonymous reviewer are thanked for their constructive reviews and suggestions that were helpful to prepare the final version.

References

Altherr, R., Siebel, W., 2002. I-type plutonism in a continental back-arc setting: Miocene granitoids and monzonites from the central Aegean Sea, Greece. Contrib. Mineral. Petrol. 143, 397–415. http://dx.doi.org/10.1007/s00410-002-0352-y.

Altherr, R., Kreuzer, H., Wendt, I., Lenz, H., Wagner, G.A., Keller, J., Harre, W., Hohndorf, A., 1982. A late Oligocene/early Miocene high temperature belt in the Attic–Cycladic crystalline complex (SE Pelagonian, Greece). Geol. Jahrb. E 23, 97–164.

Andersen, T.B., Jamtveit, B., Dewey, J.F., Swensson, E., 1991. Subduction and eduction of continental crust: major mechanisms during continent–continent collision and orogenic extensional collapse, a model based on the south Norwegian Caledonides. Terra Nova 3, 303–310.

Anderson, J.L., 1996. Status of thermobarometry in granitic batholiths. Geol. Soc. Am. Spec. Pap. 315, 125–138. http://dx.doi.org/10.1130/0-8137-2315-9.125.

Andriessen, P.A.M., Banga, G., Hebeda, E.H., 1987. Isotopic age study of pre-Alpine rocks in the basal units on Naxos, Sikinos and Ios, Greek Cyclades. Geol. Mijnb. 66, 3–14.

Andriessen, P.A.M., Boelrijk, N., Hebeda, E.H., Priem, H.N.A., Verdurmen, E.A., Verschure, R.H., 1979. Dating the events of metamorphism and granitic magmatism in the Alpine Orogen of Naxos (Cyclades, Greece). Contrib. Mineral. Petrol. 69, 215–225.

Aoya, M., Wallis, S.R., Terada, K., Lee, J., Kawakami, T., Wang, Y., Heizler, M., 2005. North–south extension in the Tibetan crust triggered by granite emplacement. Geology 33, 853–856.

Augier, R., Jolivet, L., Gadenne, L., Lahfid, A., Driussi, O., 2015. Exhumation kinematics of the Cycladic Blueschists unit and back-arc extension, insight from the Southern Cyclades (Sikinos and Folegandros Islands, Greece). Tectonics 34. http://dx.doi.org/10.1002/2014TC003664.

Avigad, D., Garfunkel, Z., 1989. Low-angle faults above and below a blueschist belt—Tinos Island, Cyclades, Greece. Terra Nova 1, 182–187.

Baldwin, S.L., Lister, G.S., Hill, E., Foster, D.A., McDougall, I., 1993. Thermochronologic constraints on the tectonic evolution of active metamorphic core complexes, D'Entrecasteaux Islands, Papua New Guinea. Tectonics 12, 611–628.

Baltatzis, E., Kostopoulos, D., Godelitsas, A., Zachariadis, P., Papanikolaou, D., 2009. Pliocene tourmaline rhyolite dykes from Ikaria Island in the Aegean back-arc region: geodynamic implications. Geodin. Acta 22, 189–199.

Beaudoin, A., Laurent, V., Augier, R., Jolivet, L., Lahfid, A., Arbaret, L., Rabillard, A., 2014. Geometry, thermal structure and kinematics of the metamorphic dome of Ikaria (eastern Cyclades, Greece): implication for Aegean tectonics. in: EGU General Assembly Conference Abstracts, p. 12128.

Blake, M.C., Bonneau, M., Geyssant, J., Kienast, J.R., Lepvrier, C., Maluski, H., Papanikolaou, D., 1981. A geological reconnaissance of the Cycladic blueschist belt, Greece. Geol. Soc. Am. Bull. 92, 247–254.

Bolhar, R., Ring, U., Allen, C.M., 2010. An integrated zircon geochronological and geochemical investigation into the Miocene plutonic evolution of the Cyclades, Aegean Sea, Greece: part 1: geochronology. Contrib. Mineral. Petrol. 160, 719–742.

Bonneau, M., 1984. Correlation of the Hellenide nappes in the south-east Aegean and their tectonic reconstruction. Geol. Soc. Lond. Spec. Publ. 17, 517–527.

Bonneau, M., Kienast, J.R., 1982. Subduction, collision et schistes bleus; l'exemple de l'Egée (Grece). Bull. Soc. Geol. Fr. 7, 785–791.

Boronkay, K., Doutsos, T., 1994. Transpression and transtension within different structural levels in the central Aegean region. J. Struct. Geol. 16, 1555–1573.

Borradaile, G.J., Werner, T., 1994. Magnetic anisotropy of some phyllosilicates. Tectonophysics 235, 223–248.

Bouchez, J.L., Delas, C., Gleizes, G., Nédélec, A., Cuney, M., 1992. Submagmatic microfractures in granites. Geology 20, 35–38.

Bozkurt, E., Satır, M., Buğdaycıoğlu, Ç., 2011. Surprisingly young Rb/Sr ages from the Simav extensional detachment fault zone, northern Menderes Massif, Turkey. J. Geodyn. 52, 406–431.

Brichau, S., Ring, U., Carter, A., Monié, P., Bolhar, R., Stockli, D., Brunel, M., 2007. Extensional faulting on Tinos Island, Aegean Sea, Greece: how many detachments? Tectonics 26, TC4009. http://dx.doi.org/10.1029/2006TC001969.

Bröcker, M., Enders, M., 2001. Unusual bulk-rock compositions in eclogite-facies rocks from Syros and Tinos (Cyclades, Greece): implications for U–Pb zircon geochronology. Chem. Geol. 175, 581–603.

Brown, M., 1994. The generation, segregation, ascent and emplacement of granite magma: the migmatite-to-crustally-derived granite connection in thickened orogens. Earth Sci. Rev. 36, 83–130.

Brown, M., Solar, G.S., 1998. Shear-zone systems and melts: feedback relations and self-organization in orogenic belts. J. Struct. Geol. 20, 211–227.

Buick, I.S., 1991. The late Alpine evolution of an extensional shear zone, Naxos, Greece. J. Geol. Soc. 148, 93–103.

Burg, J.-P., Van Den Driessche, J., Brun, J.-P., 1994. Syn- to post-thickening extension: mode and consequences. C. R. Acad. Sci., Ser. IIa: Sci. Terre Planets 319, 1019–1032.

Caggianelli, A., Ranalli, G., Lavecchia, A., Liotta, D., Dini, A., 2014. Post-emplacement thermo-rheological history of a granite intrusion and surrounding rocks: the Monte Capanne pluton, Elba Island, Italy. Geol. Soc. Lond. Spec. Publ. 394, 129–143.

Charles, N., Gumiaux, C., Augier, R., Chen, Y., Zhu, R., Lin, W., 2011. Metamorphic Core Complexes vs. synkinematic plutons in continental extension setting: insights from key structures (Shandong Province, eastern China). J. Asian Earth Sci. 40, 261–278.

Crittenden, M.D., Coney, P.J., Davis, G.H., Davis, G.H., 1980. Cordilleran metamorphic core complexes. Mem. Geol. Soc. Am. 1–490.

D'Iemos, R.S., Brown, M., Strachan, R.A., 1992. Granite magma generation, ascent and emplacement within a transpressional orogen. J. Geol. Soc. 149, 487–490.

Davis, G.H., Coney, P.J., 1979. Geologic development of the Cordilleran metamorphic core complexes. Geology 7, 120–124.

Denèle, Y., Lecomte, E., Jolivet, L., Lacombe, O., Labrousse, L., Huet, B., Le Pourhiet, L., 2011. Granite intrusion in a metamorphic core complex: the example of the Mykonos laccolith (Cyclades, Greece). Tectonophysics 501, 52–70.

Dewey, J.F., 1988. Extensional collapse of orogens. Tectonics 7, 1123–1139.

Duchene, S., Aissa, R., Vanderhaeghe, O., 2006. Pressure–temperature–time evolution of metamorphic rocks from Naxos (Cyclades, Greece): constraints from thermobarometry and Rb/Sr dating. Geodin. Acta 19, 301–321.

Dürr, S., Altherr, R., Keller, J., Okrusch, M., Seidel, E., 1978. The median Aegean crystalline belt: stratigraphy, structure, metamorphism, magmatism. In: Cloos, H., Roeder, D., Schmidt, K. (Eds.), Alps, Apennines, Hellenides. I.U.G.S. Rep. 38, pp. 455–477

Faure, M., Bonneau, M., 1988. Données nouvelles sur l'extension néogène de l'Egée: la déformation ductile du granite miocène de Mykonos (Cyclades, Grèce). C. R. Acad. Sci., Ser. II: Mec., Phys., Chim., Sci. Terre Univers 307, 1553–1559.

Faure, M., Bonneau, M., Pons, J., 1991. Ductile deformation and syntectonic granite emplacement during the late Miocene extension of the Aegean (Greece). Bull. Soc. Geol. Fr. 5, 3–11.

Foster, D.A., Schafer, C., Fanning, C.M., Hyndman, D.W., 2001. Relationships between crustal partial melting, plutonism, orogeny and exhumation: Idaho–Bitterroot batholith. Tectonophysics 342, 313–350.

Gautier, P., Brun, J.P., 1994. Ductile crust exhumation and extensional detachments in the central Aegean (Cyclades and Evvia Islands). Geodin. Acta 7, 57–85.

Gautier, P., Brun, J.-P., Jolivet, L., 1993. Structure and kinematics of upper Cenozoic extensional detachment on Naxos and Paros (Cyclades Islands, Greece). Tectonics 12, 1180–1194.

Grasemann, B., Petrakakis, K., 2007. Evolution of the Serifos metamorphic core complex. Inside the Aegean Core Complexes. In: Lister, G., Foster, M. (Eds.), Inside the Aegean Core Complexes. Journal of the Virtual Explorer, Electronic Edition.

Grasemann, B., Schneider, D.A., Stockli, D.F., Iglseder, C., 2012. Miocene bivergent crustal extension in the Aegean: evidence from the western Cyclades (Greece). Lithosphere L164-1.

Hammarstrom, J.M., Zen, E., 1986. Aluminum in hornblende; an empirical igneous geobarometer. Am. Mineral. 71, 1297–1313.

Hill, R.I., Campbell, I.H., Davies, G.F., Griffiths, R.W., 1992. Mantle plumes and continental tectonics. Science 256, 186–193.

Huet, B., Labrousse, L., Jolivet, L., 2009. Thrust or detachment? Exhumation processes in the Aegean: insight from a field study on Ios (Cyclades, Greece). Tectonics 28, TC3007. http://dx.doi.org/10.1029/2008TC002397.

Huet, B., Le Pourhiet, L., Labrousse, L., Burov, E., Jolivet, L., 2011a. Formation of metamorphic core complex in inherited wedges: a thermomechanical modelling study. Earth Planet. Sci. Lett. 309, 249–257.

Huet, B., Le Pourhiet, L., Labrousse, L., Burov, E., Jolivet, L., 2011b. Post-orogenic extension and metamorphic core complexes in a heterogeneous crust: the role of crustal layering inherited from collision. Application to the Cyclades (Aegean domain). Geophys. J. Int. 184, 611–625.

Hutton, D.H.W., Reavy, R.J., 1992. Strike-slip tectonics and granite petrogenesis. Tectonics 11, 960–967.

Jansen, J.B.H., 1973. Geological Map of Naxos (1/50 000). Nation. Inst. Geol. Mining Res, Athens.

Jolivet, L., Brun, J.-P., 2010. Cenozoic geodynamic evolution of the Aegean. Int. J. Earth Sci. 99, 109–138.

Jolivet, L., Faccenna, C., 2000. Mediterranean extension and the Africa–Eurasia collision. Tectonics 19, 1095–1106.
Jolivet, L., Patriat, M., 1999. Ductile extension and the formation of the Aegean Sea. Geol. Soc. Lond. Spec. Publ. 156, 427–456.
Jolivet, L., Daniel, J.M., Truffert, C., Goffé, B., 1994. Exhumation of deep crustal metamorphic rocks and crustal extension in arc and back-arc regions. Lithos 33, 3–30.
Jolivet, L., Famin, V., Mehl, C., Parra, T., Aubourg, C., Hébert, R., Philippot, P., others, 2004a. Progressive strain localisation, boudinage and extensional metamorphic complexes, the Aegean Sea Case, in Whitney DL, Teyssier C. and Siddoway CS, Gneiss domes in orogeny: Boulder, Colorado. Geol. Soc. Am. Spec. Pap. 380, 185–210.
Jolivet, L., Rimmelé, G., Oberhänsli, R., Goffé, B., Candan, O., 2004b. Correlation of syn-orogenic tectonic and metamorphic events in the Cyclades, the Lycian nappes and the Menderes massif. Geodynamic implications. Bull. Soc. Geol. Fr. 175, 217–238.
Jolivet, L., Lecomte, E., Huet, B., Denèle, Y., Lacombe, O., Labrousse, L., Le Pourhiet, L., Mehl, C., 2010. The North Cycladic Detachment System. Earth Planet. Sci. Lett. 289, 87–104.
Jolivet, L., Faccenna, C., Huet, B., Labrousse, L., Le Pourhiet, L., Lacombe, O., Lecomte, E., Burov, E., Denèle, Y., Brun, J.-P., others, 2013. Aegean tectonics: strain localisation, slab tearing and trench retreat. Tectonophysics 597, 1–33.
Keay, S., 1998. The Geological Evolution of the Cyclades, Greece: Constraints From SHRIMP U–Pb Geochronology. (Ph.D. thesis), Australian National University, Canberra (337 pp.).
Keay, S., Lister, G., Buick, I., 2001. The timing of partial melting, Barrovian metamorphism and granite intrusion in the Naxos metamorphic core complex, Cyclades, Aegean Sea, Greece. Tectonophysics 342, 275–312.
Kokkalas, S., Aydin, A., 2013. Is there a link between faulting and magmatism in the south-central Aegean Sea? Geol. Mag. 150, 193–224.
Kumerics, C., Ring, U., Brichau, S., Glodny, J., Monié, P., 2005. The extensional Messaria shear zone and associated brittle detachment faults, Aegean Sea, Greece. J. Geol. Soc. 162, 701–721.
Labrousse, L., Jolivet, L., Agard, P., Hébert, R., Andersen, T.B., 2002. Crustal-scale boudinage and migmatization of gneiss during their exhumation in the UHP province of western Norway. Terra Nova 14, 263–270.
Launeau, P., Robin, P.-Y.F., 2005. Determination of fabric and strain ellipsoids from measured sectional ellipses implementation and applications. J. Struct. Geol. 27, 2223–2233.
Launeau, P., Archanjo, C.J., Picard, D., Arbaret, L., Robin, P.-Y., 2010. Two- and three-dimensional shape fabric analysis by the intercept method in grey levels. Tectonophysics 492, 230–239.
Le Pichon, X., Angelier, J., 1981. The Aegean Sea. Philos. Trans. R. Soc. Lond. A 300, 357–372.
Lecomte, E., Jolivet, L., Lacombe, O., Denèle, Y., Labrousse, L., Le Pourhiet, L., 2010. Geometry and kinematics of a low-angle normal fault on Mykonos island (Cyclades, Greece): evidence for slip at shallow dip. Tectonics 29, TC5012. http://dx.doi.org/10.1029/2009TC002564.
Lee, J., Lister, G.S., 1992. Late Miocene ductile extension and detachment faulting, Mykonos, Greece. Geology 20, 121–124.
Liati, A., Skarpelis, N., Pe-Piper, G., 2009. Late Miocene magmatic activity in the Attic–Cycladic Belt of the Aegean (Lavrion, SE Attica, Greece): implications for the geodynamic evolution and timing of ore deposition. Geol. Mag. 146, 732–742.
Lister, G.S., Baldwin, S.L., 1993. Plutonism and the origin of metamorphic core complexes. Geology 21, 607–610.
Lister, G.S., Banga, G., Feenstra, A., 1984. Metamorphic core complexes of Cordilleran type in the Cyclades, Aegean Sea, Greece. Geology 12, 221–225.
Martin, L., 2004. Signification des âges U–Pb sur zircon dans l'histoire métamorphique de Naxos et Ikaria (Cyclades, Grèce). (Phd thesis), Université Henri Poincaré, Nancy I (288 pp.).
Martin, L., Duchêne, S., Deloule, E., Vanderhaeghe, O., 2006. The isotopic composition of zircon and garnet: a record of the metamorphic history of Naxos, Greece. Lithos 87, 174–192.
Martin, L., Ballevre, M., Boulvais, P., Halfpenny, A., Vanderhaeghe, O., Duchêne, S., Deloule, E., 2011. Garnet re-equilibration by coupled dissolution–reprecipitation: evidence from textural, major element and oxygen isotope zoning of "cloudy" garnet. J. Metamorph. Geol. 29, 213–231.
Nédélec, A., Bouchez, J.-L., 2011. Pétrologie des granites: structure, cadre écologique. Vuibert.
Neves, S.P., Vauchez, A., Archanjo, C.J., 1996. Shear zone-controlled magma emplacement or magma-assisted nucleation of shear zones? Insights from northeast Brazil. Tectonophysics 262, 349–364.
Papanikolaou, D.J., 1978. Contribution to the geology of Ikaria Island, Aegean Sea. Ann. Géol. Pays Hellén. 29, 1–28.
Parra, T., Vidal, O., Jolivet, L., 2002. Relation between the intensity of deformation and retrogression in blueschist metapelites of Tinos Island (Greece) evidenced by chlorite–mica local equilibria. Lithos 63, 41–66.
Pe-Piper, G., Piper, D.J., Matarangas, D., 2002. Regional implications of geochemistry and style of emplacement of Miocene I-type diorite and granite, Delos, Cyclades, Greece. Lithos 60, 47–66.
Photiades, A.D., 2002. The ophiolitic molasse unit of Ikaria Island (Greece). Turk. J. Earth Sci. 11, 27–38.
Photiades, A., Keay, S., 2003. Geological and geochronological data for Sikinos and Folegandros metamorphic units (Cyclades, Greece): their tectono-stratigraphic significance. Bull. Geol. Soc. Greece 35, 35–45.
Rabillard, A., Arbaret, L., Jolivet, L., Le Breton, N., Gumiaux, C., Augier, R., Grasemann, B., 2015. Interactions between plutonism and detachments during Metamorphic Core Complex formation, Serifos Island (Cyclades, Greece). Tectonics (accepted for publication).
Ring, U., 2007. The Geology of Ikaria Island: the Messaria extensional shear zone, granites and the exotic Ikaria nappe: inside the Aegean Metamorphic Core Complexes. In: Gordon Lister, M.F., Ring, U. (Eds.), Journal of the Virtual Explorer, Electronic Edition 27. http://dx.doi.org/10.3809/jvirtex.2007.00171 (paper 3).
Schmidt, M.W., 1992. Amphibole composition in tonalite as a function of pressure: an experimental calibration of the Al-in-hornblende barometer. Contrib. Mineral. Petrol. 110, 304–310.
Seward, D., Vanderhaeghe, O., Siebenaller, L., Thomson, S., Hibsch, C., Zingg, A., Holzner, P., Ring, U., Duchêne, S., 2009. Cenozoic tectonic evolution of Naxos Island through a multi-faceted approach of fission-track analysis. Geol. Soc. Lond. Spec. Publ. 321, 179–196.
Stouraiti, C., Mitropoulos, P., Tarney, J., Barreiro, B., McGrath, A.M., Baltatzis, E., 2010. Geochemistry and petrogenesis of late Miocene granitoids, Cyclades, southern Aegean: nature of source components. Lithos 114, 337–352.
Tirel, C., Brun, J.-P., Burov, E., 2004. Thermomechanical modeling of extensional gneiss domes. Geol. Soc. Am. Spec. Pap. 380, 67–78.
Tomaschek, F., Kennedy, A.K., Villa, I.M., Lagos, M., Ballhaus, C., 2003. Zircons from Syros, Cyclades, Greece recrystallization and mobilization of zircon during high-pressure metamorphism. J. Petrol. 44, 1977–2002.
Trotet, F., Vidal, O., Jolivet, L., 2001. Exhumation of Syros and Sifnos metamorphic rocks (Cyclades, Greece): new constraints on the PT paths. Eur. J. Mineral. 13, 901–902.
Turrillot, P., Faure, M., Martelet, G., Chen, Y., Augier, R., 2011. Pluton-dyke relationships in a Variscan granitic complex from AMS and gravity modelling. Inception of the extensional tectonics in the South Armorican Domain (France). J. Struct. Geol. 33, 1681–1698.
Urai, J.L., Schuiling, R.D., Jansen, J.B.H., 1991. Alpine deformation on Naxos (Greece). Geol. Soc. Lond. Spec. Publ. 54, 509–522.
Vandenberg, L.C., Lister, G.S., 1996. Structural analysis of basement tectonites from the Aegean metamorphic core complex of Ios, Cyclades, Greece. J. Struct. Geol. 18, 1437–1454.
Vanderhaeghe, O., 2004. Structural development of the Naxos migmatite dome. Geol. Soc. Am. Spec. Pap. 380, 211–227.
Vernon, R.H., 2000. Review of microstructural evidence of magmatic and solid-state flow. Vis. Geosci. 5, 1–23.
Weidmann, M., Solounias, N., Drake, R.E., Curtis, G.H., 1984. Neogene stratigraphy of the eastern basin, Samos island, Greece. Geobios 17, 477–490.
Wernicke, B., 1981. Low-angle normal faults in the Basin and Range Province: nappe tectonics in an extending orogen. Nature 291, 645–648.
Wijbrans, J.R., McDougall, I., 1986. $^{40}Ar/^{39}Ar$ dating of white micas from an Alpine high-pressure metamorphic belt on Naxos (Greece): the resetting of the argon isotopic system. Contrib. Mineral. Petrol. 93, 187–194.

Annexe B

Article: The Ikaria high-temperature Metamorphic Core Complex (Cyclades, Greece): Geometry, kinematics and thermal structure

Publié dans dans la revue *Journal of Geodynamics*, 2015

Alexandre Beaudoin [1,2,3], Romain Augier [1,2,3], Valentin Laurent [1,2,3], Laurent Jolivet [1,2,3], Abdeltif Lahfid [2,3], Valérie Bosse [4], Laurent Arbaret [1,2,3], **Aurélien Rabillard** [1,2,3], Armel Menant [1,2,3]

(1) Université d'Orléans, ISTO, UMR 7327, 45071, Orléans, France
(2) CNRS/INSU, ISTO, UMR 7327, 45071 Orléans, France
(3) BRGM, ISTO, UMR 7327, BP 36009, 45060 Orléans, France
(4) Université Blaise Pascal, Laboratoire Magmas & Volcans, CNRS, UMR 6524, 63000 Clermont-Ferrand, France

Journal of Geodynamics 92 (2015) 18–41

Contents lists available at ScienceDirect

Journal of Geodynamics

journal homepage: http://www.elsevier.com/locate/jog

The Ikaria high-temperature Metamorphic Core Complex (Cyclades, Greece): Geometry, kinematics and thermal structure

Alexandre Beaudoin[a,b,c,*], Romain Augier[a,b,c], Valentin Laurent[a,b,c], Laurent Jolivet[a,b,c], Abdeltif Lahfid[b,c], Valérie Bosse[d], Laurent Arbaret[a,b,c], Aurélien Rabillard[a,b,c], Armel Menant[a,b,c]

[a] Université d'Orléans, ISTO, UMR 7327, 45071 Orléans, France
[b] CNRS/INSU, ISTO, UMR 7327, 45071 Orléans, France
[c] BRGM, ISTO, UMR 7327, 45060 Orléans, France
[d] Université Blaise Pascal, Laboratoire Magmas & Volcans, CNRS, UMR 6524, 63000 Clermont-Ferrand, France

ARTICLE INFO

Article history:
Received 29 January 2015
Received in revised form
18 September 2015
Accepted 28 September 2015
Available online 11 October 2015

Keywords:
Structural analysis
RSCM geothermometry
U–Th–Pb geochronology
Metamorphic Core Complex
Ikaria
North Cycladic Detachment System

ABSTRACT

This work attempted at clarifying the structure of Ikaria using primarily intensive geological mapping combined with structural analysis and a geothermometry approach of Raman spectrometry of carbonaceous material. Foliation over the whole island defines a structural dome cored by high-grade to partially molten rocks. Its exhumation was completed by two top-to-the-N ductile extensional shear zones, operating in the ductile and then the brittle fields, through a single extensional event coeval with progressive strain localization. The thermal structure of the dome with regard to position of ductile shear zones was retrieved using the Raman spectroscopy of carbonaceous material. Peak-metamorphic temperatures range from 390 °C in the upper parts of the structure down to 625 °C in the core of the dome in the vicinity of migmatites and S-type granite. Pioneer in situ U–Th–Pb analyses on monazite performed on the leucosome parts of these rock yielded a 15.7 ± 0.2 Ma age. Ikaria Island thus completes the series of Miocene migmatite-cored Metamorphic Core Complex in the central part of the Aegean domain where a genuine high-temperature zone can be defined as the central Aegean HT zone. There, the extreme stretching of the continental crust is associated with dominantly top-to-the-N kinematics.

1. Introduction

In the Mediterranean realm, the retreat of oceanic slabs triggered the initiation of back-arc extension (i.e. large-scale extension in the upper plate of a subduction zone), leading to the collapse of previously thickened continental lithosphere (Le Pichon and Angelier, 1979; Malinverno and Ryan, 1986; Dewey, 1988; Platt and Vissers, 1989; Royden, 1993; Jolivet and Faccenna, 2000; Rosenbaum et al., 2002; Faccenna et al., 2004; Jolivet et al., 2008). This post-orogenic evolution (i.e. crustal thinning by extension-related normal faulting after an episode of crustal thickening) resulted in the formation of series of extensional domains or wide-rift systems (Lister et al., 1984; Buick, 1991; Corti et al., 2003) such as the Alboran Sea, the Tyrrhenian Sea, the Pannonian Basin and the Aegean Sea. Lateral evolution from the central parts of the extensional domains to the bounding non-collapsed orogenic segments implies drastic lateral gradients of finite extension and suggests highly non-cylindrical structures. In the Aegean Sea, along with the drastic decrease in topography and crustal thickness, the main orogenic structures of the Hellenic belt are increasingly reworked by extension from continental Greece to Naxos, in the center of the Aegean Sea. Extensional structures related to back-arc crustal stretching evolve from essentially brittle steep and shallow-dipping normal faults in continental Greece to shallow-dipping ductile shear zones in the center of the Aegean domain (Jolivet and Patriat, 1999; Jolivet et al., 2010). Furthermore, a straightforward correlation between the degree of non-coaxiality of the back-arc domain and the amount of stretching of the continental crust is observed at the scale of the entire Aegean domain (e.g. Augier et al., 2015). Marginal areas that connect to non-collapsed orogenic segments display symmetrically arranged detachment systems. In the western parts of the Aegean domain, both the West Cycladic Detachment System (WCDS) and the North Cycladic Detachment System (NCDS) exhume a horst-shaped domain, where orogenic features are still nicely preserved, depicting bivergent extension

* Corresponding author at: ISTO, 1A rue de la Férollerie, 45071 Orléans, France. Tel.: +33 2 38 49 25 73.
E-mail address: alexandre.beaudoin@univ-orleans.fr (A. Beaudoin).

http://dx.doi.org/10.1016/j.jog.2015.09.004
0264-3707/

(e.g. Jolivet et al., 2010; Grasemann et al., 2012). Conversely, in the center of the Aegean domain, deformation remains highly asymmetric from Mykonos in the north, all the way to Sikinos in the south (e.g. Gautier et al., 1993; Kumerics et al., 2005; Denèle et al., 2011; Augier et al., 2015). There, orogenic features are particularly overprinted or even locally erased by the combined effects of intense top-to-the-N shearing and partial-melting. Migmatite-cored Metamorphic Core Complexes (MCCs), associated with Miocene intrusions, roofed by major top-to-the-N crustal-scale detachments, are described on Naxos, in the center (e.g. Lister et al., 1984; Urai et al., 1990; Buick, 1991; Gautier and Brun, 1994; Jolivet et al., 2004a; Vanderhaeghe, 2004) and Mykonos in the north of the Aegean domain (Lecomte et al., 2010; Denèle et al., 2011). Concentrating a large part of the total amount of stretching, recognition of MCCs therefore appears of prime importance. Similarly, asymmetry of crustal thinning at the regional-scale is another key-question for understanding back-arc extension dynamics. However, the current understanding of back-arc dynamics in the Aegean domain is hindered by the severe lack of knowledge for the bulk of its eastern part.

One of the largest Aegean islands, displaying the largest intrusion of the Aegean Sea, located between the northern Cyclades and western Turkey, Ikaria Island has been the focus of several recent studies. However, the first order structural architecture of this island remains conflicting and the existing geological maps of Ikaria present marked discrepancies. Besides, the current knowledge of the metamorphic record and particularly the thermal structure of Ikaria remain fragmentary. These problems were reconsidered after an extensive field survey, including primarily new geological mapping and structural analysis. The position and importance of the various tectonic contacts as well as the bulk thermal architecture of the island were further constrained using the geothermometry approach of Raman Spectrometry of Carbonaceous Material (RSCM). Following their recent discovery, the migmatites described in the core of the structure were dated by U–Th–Pb LA-ICPMS analyses on monazite.

2. Geological setting

2.1. Geodynamic context

The Aegean domain (Fig. 1) corresponds to the collapsed segment of the Hellenides-Taurides belt, developed as the result of the convergence between Apulian and European plates, in the eastern Mediterranean, since the Late Cretaceous (e.g. Aubouin and Dercourt, 1965; Brunn et al., 1976; Bonneau and Kienast, 1982; Bonneau, 1984; van Hinsbergen et al., 2005; Jolivet and Brun, 2010; Ring et al., 2010). During this period, a south-verging crustal-scale orogenic wedge was formed by subduction and accretion of several Apulia-derived continental blocks separated by oceanic basins. Post-orogenic extension of the Hellenic thickened crust started in the Early Oligocene (Jolivet and Faccenna, 2000; Jolivet et al., 2008) or the Early Miocene (Ring et al., 2010) by a combination of gravitational collapse and back-arc extension during the southward retreat of the African slab (e.g. Jolivet and Faccenna, 2000; Jolivet and Brun, 2010). Intense crustal stretching of the upper plate leads to the formation of a series of MCCs (Lister et al., 1984; Avigad and Garfunkel, 1989, 1991; Gautier and Brun, 1994; Jolivet et al., 2004a). Despite the importance of the post-orogenic overprint on the orogenic architecture, the original vertical superposition of tectonic units in the nappe stack is often preserved at the scale of the whole Aegean domain (e.g. Bonneau, 1984; van Hinsbergen et al., 2005). Three main tectonometamorphic units are classically recognized (e.g. Bonneau, 1984; Ring et al., 2010) (Fig. 1):

1. The Upper Cycladic unit corresponds to a lateral equivalent of the Pelagonian nappe (e.g. Bonneau, 1984; Jolivet et al., 2004a) recognized in continental Greece. This unit generally crops out as isolated klippes or rafts in the Cyclades, essentially made of ophiolitic material such as in Andros, Tinos, Mykonos, Kea, Kythnos, Serifos and Samos (e.g. Ring et al., 1999; Jolivet et al., 2010; Grasemann et al., 2012). Rocks preserve a Cretaceous *HT-LP* metamorphic imprint but escaped both the Eocene *HP-LT* and the Oligocene-Miocene *HT-LP* tectonometamorphic events (Katzir et al., 1996). Syn-tectonic detrital shallow-marine and continental sediments locally form the uppermost unit on Mykonos, Paros, Naxos and Ikaria (e.g. Angelier, 1976; Photiades, 2002a; Sanchez-Gomez et al., 2002; Kuhlemann et al., 2004; Lecomte et al., 2010). Conglomerates mostly contain pebbles derived from the Upper Cycladic nappe and reworked magmatic rocks as young as 10 Ma (e.g. Sanchez-Gomez et al., 2002).
2. The Cycladic Blueschists unit crops out as a composite unit including locally a significant component of metabasic rocks interleaved with metapelites and marbles, all equilibrated in blueschist-facies conditions (e.g. Blake et al., 1981; Bonneau, 1984; Avigad and Garfunkel, 1991; Keiter et al., 2004). This unit experienced a complex alpine tectonometamorphic evolution, with an early burial in *HP-LT* conditions reaching blueschist to eclogite-facies conditions during the Eocene, followed by a greenschist overprint of variable intensity during the Oligocene and the Miocene (Altherr et al., 1979, 1982; Wijbrans et al., 1990; Parra et al., 2002; Duchêne et al., 2006; Augier et al., 2015). On Ikaria, despite the lack of reliable *HP* index minerals, the Messaria unit (Kumerics et al., 2005) was correlated with the Ampelos nappe recognized on Samos that experienced metamorphic conditions of the order of 15 kbar and 500 °C (Will et al., 1998).
3. The lower units crop out in tectonic windows. The Cycladic Basement unit crops out in the central and southern Cyclades (i.e. on Naxos, Paros, Sikinos and Ios) (e.g. Andriessen et al., 1987). It is composed of Variscan granitoids mantled by micaschists that retain either metamorphic relics of amphibolite-facies assemblages or inherited radiometric ages suggesting a complex prealpine history (e.g. Henjes-Kunst and Kreuzer, 1982; Andriessen et al., 1987; Keay and Lister, 2002). It is sometimes covered by Mesozoic marbles that may represent a *HP* equivalent of the Gavrovo unit cropping out in continental Greece (Jolivet et al., 2004b). Just as the Cycladic Blueschists unit, the Cycladic Basement unit shows a complex alpine tectonometamorphic evolution, with an initial subduction-related burial in *HP-LT* conditions during the Eocene whose trace has been obscured by an Oligocene-Miocene local overprint (van der Maar et al., 1981; Vandenberg and Lister, 1996; Baldwin and Lister, 1998; Augier et al., 2015). On Naxos and Paros, it experienced a partial-melting stage in amphibolite to granulite-facies conditions (i.e. Jansen and Schuiling, 1976; Buick and Holland, 1989; Vanderhaeghe, 2004; Duchêne et al., 2006).

Rocks of the Cycladic Blueschists and the lower units were exhumed during two distinctive stages in two contrasted geodynamic settings. The first stage occurred in the Hellenic subduction context, during the Eocene, with burial and synorogenic exhumation (by shortening-related normal faulting) of blueschist to eclogite-facies assemblages in an extrusion wedge structure (e.g. Altherr et al., 1979; Wijbrans et al., 1990; Trotet et al., 2001a,b; Groppo et al., 2009; Ring et al., 2007; Jolivet and Brun, 2010). The second stage occurred in the Oligocene-Miocene with the post-orogenic exhumation in the back-arc domain of the Cycladic Blueschists and the lowers units as metamorphic domes or migmatite-cored MCCs (Lister et al., 1984) below a series of detachments (e.g. Avigad and Garfunkel, 1989; Buick and Holland, 1989; Buick, 1991; Faure et al., 1991; Lee and Lister, 1992; Gautier et al.,

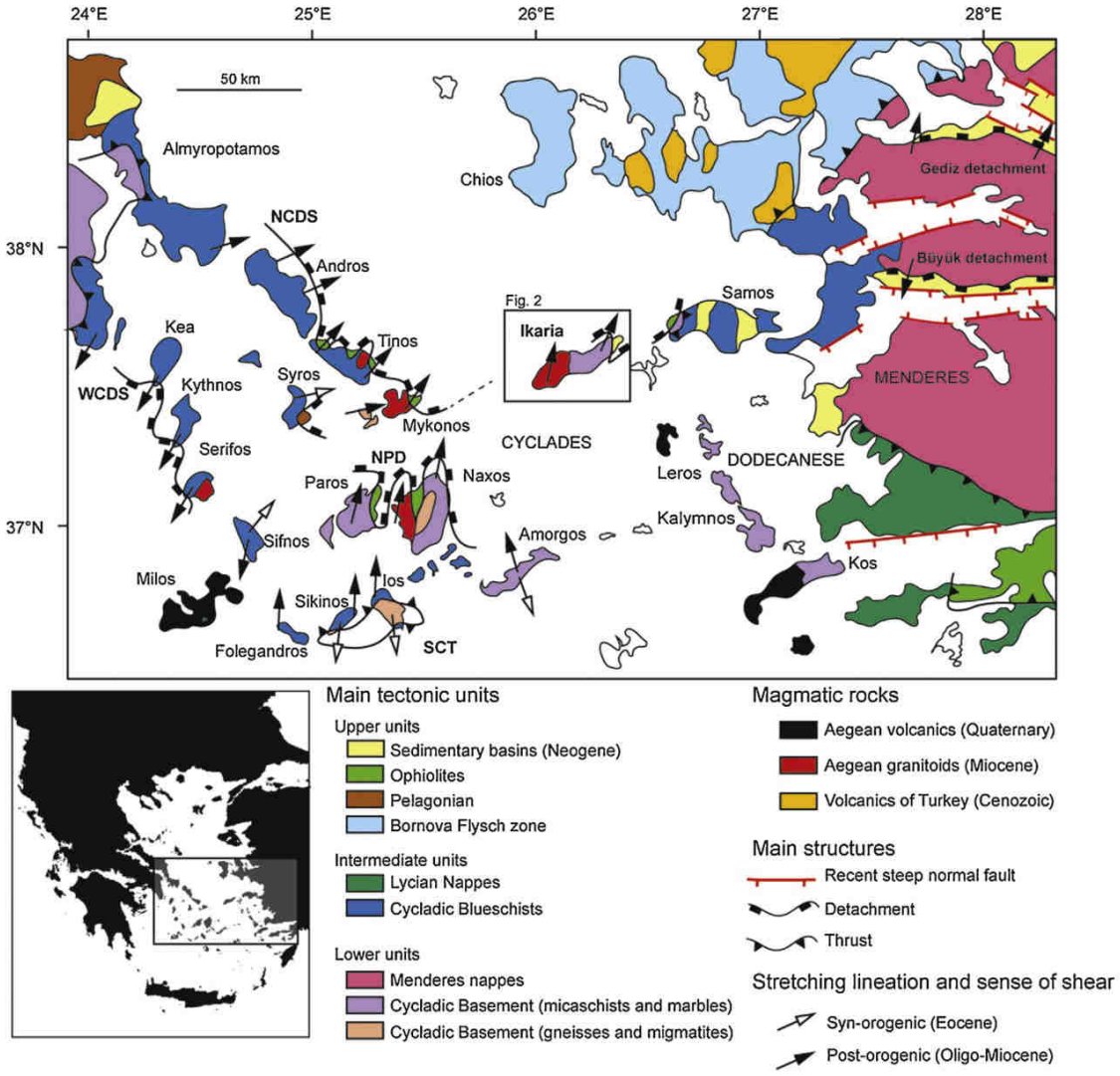

Fig. 1. Tectonic map of the Aegean domain. Tectonic map of the Aegean domain showing the main geological units and structures related to both synorogenic and postorogenic episodes, modified after Jolivet et al. (2013) and references therein. Original map has been modified incorporating recent works (Ring et al., 1999; Kumerics et al., 2005; Rosenbaum et al., 2007; Huet et al., 2009; Grasemann et al., 2012; Augier et al., 2015). NCDS: North Cycladic Detachment System; WCDS: West Cycladic Detachment System; NDP: Naxos-Paros Detachment; SCT: South Cycladic Thrust.

1993; Gautier and Brun, 1994; Jolivet and Patriat, 1999; Keay et al., 2001; Vanderhaeghe, 2004; Kumerics et al., 2005; Mehl et al., 2005, 2007; Denèle et al., 2011; Augier et al., 2015). In the northern Cyclades, these detachments were recently grouped in a single large-scale top-to-the-N structure running over 130 km to form the NCDS (Fig. 1; Jolivet et al., 2010). A similar set of detachments with opposed, top-to-the-S or SW kinematics, was identified in the western Cyclades (Grasemann and Petrakakis, 2007; Iglseder et al., 2009, 2011; Tschegg and Grasemann, 2009; Brichau et al., 2010) and recently mechanically linked to form the WCDS (Grasemann et al., 2012). The Naxos-Paros Detachment (NDP) completes those series of detachment systems in the center of the Aegean domain (Buick and Holland, 1989; Buick, 1991; Gautier and Brun, 1994; Kruckenberg et al., 2011). Another major shear zone over which top-to-the-N kinematics rework top-to-the-S shear sense occurs in the southern Cyclades on the islands of Sikinos and Ios (e.g. Vandenberg and Lister, 1996; Forster and Lister, 2009; Huet et al., 2009; Thomson et al., 2009; Augier et al., 2015). Extension on this shear zone starts to exhume rocks near the Early Miocene (Thomson et al., 2009). Here, top-to-the-S kinematics was first considered as extensional (Vandenberg and Lister, 1996; Forster and Lister, 2009; Thomson et al., 2009) and later correlated with the WCDS (Ring et al., 2011). Another study reinterpreted this shear zone as a top-to-the-S thrust reworked by top-to-the-N extension (the South Cycladic Thrust, SCT) (Huet et al., 2009). The same interpretation is made on Sikinos where the SCT crops out (Augier et al., 2015). Late exhumation stages along extensional systems were accompanied by the emplacement of syn-tectonic Miocene I and S-type granites (i.e. Tinos, Mykonos, Naxos, Serifos and Ikaria; Fig. 1) (Faure et al., 1991; Lee and Lister, 1992; Altherr and Siebel, 2002; Grasemann and Petrakakis, 2007; Ring, 2007; Iglseder et al., 2009; Bolhar et al., 2010; Laurent et al., 2015). The activity of detachments is also constrained by syn-tectonic deposition of sediments over the Upper Cycladic unit (e.g. Sanchez-Gomez et al., 2002; Kuhlemann et al., 2004; Lecomte et al., 2010; Menant et al., 2013).

Although part of these features of the Cycladic geology are found further east within the Menderes massif (Fig. 1), type, distribution and timing of metamorphism appear less clear. The Cycladic Blueschists unit and the Lycian Nappe that experienced *HP-LT* metamorphic conditions rest on top of the structure to the north and to the south of the massif (Oberhansli et al., 1998; Rimmelé et al., 2003a,b; Pourteau et al., 2010). *HP-LT* metamorphic conditions are dated from Late Cretaceous to Eocene (Oberhansli et al., 1998; Pourteau et al., 2013). Crustal stretching responsible for the final exhumation of the metamorphic part of the Menderes massif under shallow-dipping shear zones (e.g. Rimmelé et al., 2003b; Bozkurt, 2007; van Hinsbergen, 2010; Bozkurt et al., 2011) is very similar to the Cyclades one. Detachments juxtapose Neogene syn-tectonic sediments on metamorphic rocks that are strongly retrograded in the greenschist facies during the Miocene (Hetzel et al., 1995a; Lips et al., 2001). Here again, crustal thinning is accompanied by the emplacement of syn-tectonic granites (Ring and Collins, 2005; Glodny and Hetzel, 2007).

2.2. Geology of Ikaria

Ikaria is a 40 km-long island located in the eastern Aegean Sea between Mykonos and Samos. A recent map coverage was performed by the Greek Institute of Geology and Mineral Exploration (G-IGME) (Photiades, 2002b), complemented by independent geological maps presenting highly conflicting interpretations (Papanikolaou, 1978; Kumerics et al., 2005; Ring, 2007; Bolhar et al., 2010; Kokkalas and Aydin, 2013).

At first glance, the geology of Ikaria consists in an equal distribution of a metamorphic domain to the east and a large-scale magmatic complex to the west, bounded by sedimentary rocks (Fig. 2). The metamorphic part consists in a 1500 m-thick tectonometamorphic succession made of metasediments including metapelites, metaquartzites, marbles and minor metabasites occurrences passing upward to finely alternating metapelites and marbles (Photiades, 2002a,b; Kumerics et al., 2005). The metamorphic grade decreases upward from widespread amphibolite-facies associations (i.e. staurolite-garnet-biotite in metapelites and hornblende-plagioclase in metabasites) to greenschists-facies associations in the uppermost parts of the succession (e.g. Altherr et al., 1982; Kumerics et al., 2005; Martin et al., 2011). Peak-metamorphic conditions, as retrieved from pseudo-section approaches, yielded 6–8 kbar for 600–650 °C conditions for the basal parts of the tectonometamorphic succession (Kumerics et al., 2005; Martin et al., 2011), fringing partial-melting conditions assuming water saturation conditions (Weinberg and Hasalová, 2015). While similar quantitative P–T estimates are currently lacking for the upper parts of the succession, a localized change in the metamorphic grade has however been proposed within the upper parts (Papanikolaou, 1978; Altherr et al., 1982; Kumerics et al., 2005). Besides, it is noteworthy that traces of an initial *HP* imprint is currently lacking on Ikaria, at variance with neighboring islands (Altherr et al., 1982; Photiades, 2002a; Kumerics et al., 2005; Ring, 2007).

Three main magmatic intrusions were recognized on Ikaria (Papanikolaou, 1978; Photiades, 2002b; Ring, 2007); two small-scale, less than 10 km^2 S-type two-mica leucogranite intrusions (i.e. the Xylosyrtis and the Karkinagrion intrusions) and a large-scale I-type intrusion (i.e. the Raches intrusion). Along with a related pervasive pegmatite dyke array (Photiades, 2002b; Hezel et al., 2011), the Xylosyrtis pluton displays a clear intrusive character within the metamorphic series. Conversely, the nature of the Raches granite contact remains highly controversial and was mapped so far as intrusive (Papanikolaou, 1978; Laurent et al., 2015), as a detachment (Kumerics et al., 2005) or as a thrust (Photiades, 2002a,b; Kokkalas and Aydin, 2013). Emplacement of the main intrusions occurred in a narrow 15–13 Ma age-range (Bolhar et al., 2010).

Metamorphic and intrusive rocks experienced an intense top-to-the-N shearing in both ductile and then brittle regimes (Kumerics et al., 2005; Ring, 2007). The Raches intrusion in the west thus shows a top-to-the-N strain gradient toward the upper structural levels, from proto-mylonites to ultra-mylonites, and finally cataclasites (Laurent et al., 2015). Prior to this study, two main tectonic contacts, along which deformation is concentrated, were distinguished: the Messaria and Fanari detachments (Kumerics et al., 2005). According to Kumerics et al. (2005), the Messaria detachment corresponds to a mylonite zone later partly overprinted by cataclastic deformation. At variance, the Fanari detachment is currently regarded as a purely brittle contact roofing the metamorphic rocks and bounding the sediments of the upper unit (Kumerics et al., 2005; Ring, 2007). This unit, regionally known as the Fanari unit, consists in sandstones, siltites and conglomerates containing clasts of red cherts and ophiolitic rocks of Early Cretaceous age and large-scale olistoliths of Triassic recrystallized limestones (Papanikolaou, 1978) reminding typically rocks of Pelagonian affinity (Pe-Piper and Photiades, 2006). Ages of those sediments spread from Oligocene to Pliocene (Photiades, 2002a,b). In the center of the island, the recrystallized limestone of Kefala, inferred as Triassic, is sometimes described as a klippe of the upper unit of Ikaria (Papanikolaou, 1978; Photiades, 2002a,b; Pe-Piper and Photiades, 2006). The main argument for the presence of the Pelagonian unit relies on the description of a diorite intrusive body that yielded Cretaceous K/Ar ages on hornblende (Altherr et al., 1994).

Precise age-constraints on peak-metamorphic conditions and the accurate timing for the onset of extensional motions along main shear zones are currently lacking on Ikaria. First record of cooling, below 550 °C (Villa, 1998), is scattered between 25 and 17 Ma (K/Ar on hornblende; Altherr et al., 1982). Late exhumation stages are, in turn, well constrained after 15 Ma by varied thermochronological tools (Altherr et al., 1982; Kumerics et al., 2005). The K/Ar and Ar/Ar ages on both fabric-forming white mica and biotite yield numerous 12 to 9 Ma ages. In metamorphic rocks, these ages are interpreted as both cooling or deformation ages during exhumation while they are considered as cooling ages for granites (Altherr et al., 1982; Kumerics et al., 2005). Fission-track (FT) analyses yielded 10.3 ± 0.3 to 7.1 ± 0.3 Ma ages for zircon and 8.4 ± 0.8 to 5.9 ± 0.8 Ma ages for apatite (Kumerics et al., 2005). Final cooling stages were constrained by U–Th/He analyses on apatite that yielded symmetrically arranged 6 Ma ages for both flanks and a 3 Ma age for the core of the structure (Kumerics et al., 2005). Cooling rates therefore exceeded 100 °C/Ma from the ductile to brittle transition (i.e. 300–400 °C, Stöckhert et al., 1999; Imber et al., 2001) and temperatures as low as 70 °C between 10 and 6 Ma.

3. A new geological map of Ikaria

An extensive field survey was carried out on Ikaria including new field mapping in order to complement the existing G-IGME geological map (Photiades, 2002b). The result is presented in Fig. 2; readers are referred to existing maps showing very conflicting interpretations to appreciate the modifications (Papanikolaou, 1978; Photiades, 2002b; Kumerics et al., 2005; Ring, 2007; Bolhar et al., 2010; Kokkalas and Aydin, 2013).

For clarity, the lithostratigraphic subdivisions of Photiades (2002b) were kept as much as possible. Three main lithologies, including marbles, micaschists (including calcschists and minor metaquartzites and metabasites occurrences) and granitic rocks derived from three main intrusive bodies were mapped (Fig. 2). Definition of the main tectonic units changed as the result of the

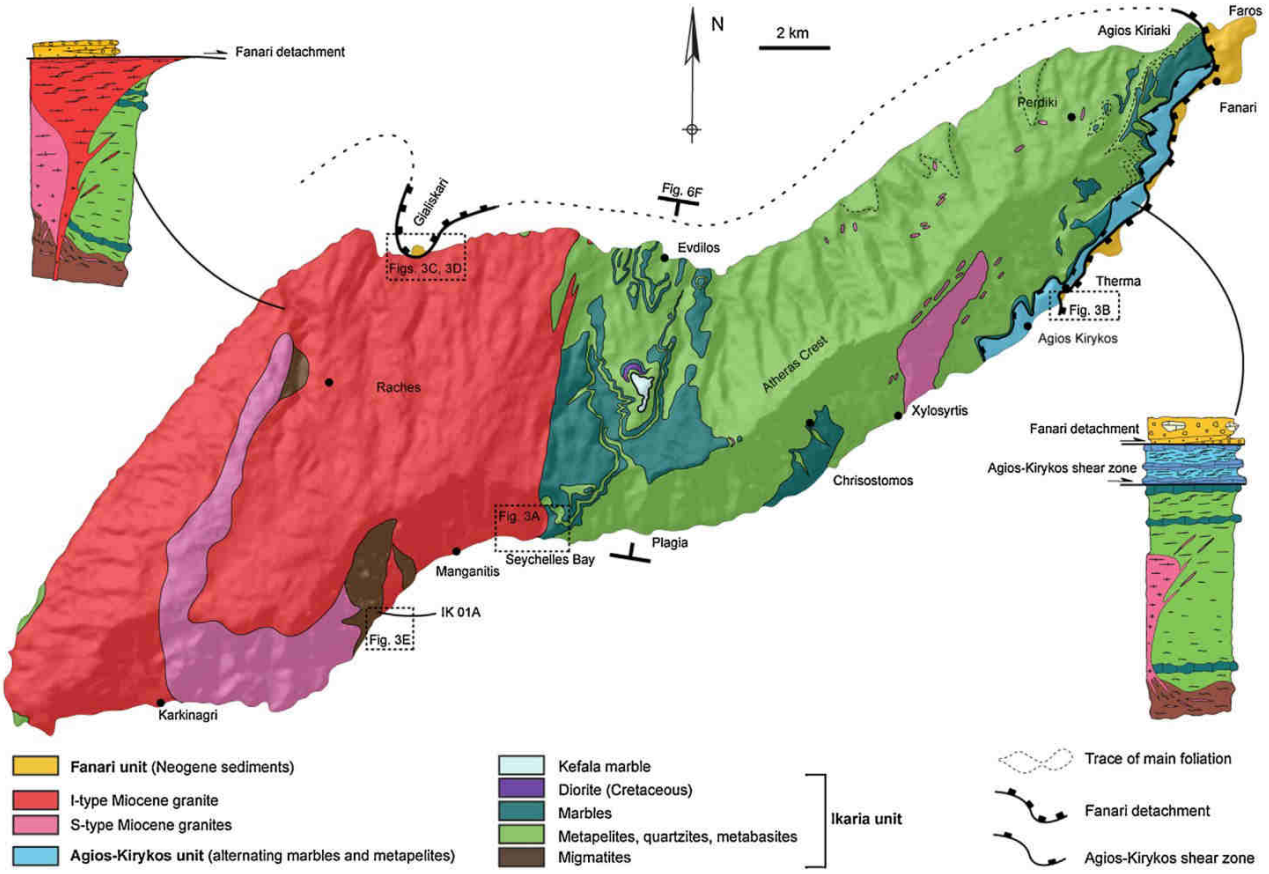

Fig. 2. Geological map of Ikaria. (a) New geological map of Ikaria proposed in this study. Lithologic outlines correspond to new field observations and a compilation of existing maps (e.g. Papanikolaou, 1978; Photiades, 2002b; Kumerics et al., 2005; Ring, 2007). Also indicated are two representative tectonometamorphic piles for the eastern and the western parts of Ikaria.

modification and the reinterpretation of their boundaries, particularly the tectonic and intrusive contacts. Three main tectonic units, from bottom to top: the Ikaria, Agios-Kirykos and Fanari units, limited by two major shear zones, are now distinguished. The main tectonic features having a map-scale expression were also reported in detail. These structures consist primarily in the Agios-Kirykos and the Fanari ductile shear zones developed as ramp-flat extensional structures either at shallow-angle to the compositional layering as décollement zones or cutting down-section. The Fanari shear zone even presents evidence for subsequent displacements in the brittle field superimposed on ductile features. On the map, the Fanari detachment clearly cuts across the whole Agios-Kirykos unit and the Agios-Kirykos shear zone. Other shear zones or brittle contacts put forward on previous maps were abandoned. The basal contact below Kefala marble (e.g. Papanikolaou, 1978; Altherr et al., 1994; Photiades, 2002a,b; Pe-Piper and Photiades, 2006) is considered less important than in previous studies since no metamorphic gap is backed up by published data. Moreover, detailed mapping of this zone indicate that the diorite is intrusive in Ikaria unit. However, a panorama on the Kefala marble seen suggests the presence of a tectonic contact at its base (Papanikolaou, 1978). Although probably minor, this contact might be a late brittle expression of the system of detachments. Similarly, the nature of the eastern contact of the Raches granite considered either as the lateral equivalent of the Messaria detachment (Kumerics et al., 2005; Ring, 2007) or a major thrust contact (Photiades, 2002a,b; Kokkalas and Aydin, 2013) was re-evaluated. Field work in the vicinity of the contact of the Raches granite unambiguously shows, despite ductile deformation, the clear intrusive character of the granite within Ikaria unit (Fig. 3a) as suggested in earlier studies (e.g. Papanikolaou, 1978; Laurent et al., 2015). Along with the Fanari detachment, the Fanari sedimentary unit of Kumerics et al. (2005) was extended further southwest (Fig. 3b). This sedimentary unit was correlated to sediments recognized on the northern part of Ikaria at Gialiskari (Fig. 3c) as initially proposed by Photiades (2002a,b) and recently reinforced by Laurent et al. (2015). There, the Fanari sedimentary unit lies on top of a thick cataclastic body (Fig. 3c and d) superimposed over a 300–500 m-thick ductile strain gradient developed within both the Raches and Karkinagrion granites (Laurent et al., 2015). Besides, the initial geological outline of the Karkinagrion granite (Ring, 2007) was significantly modified and extended toward the north (Fig. 2). Detailed field work within and around this granite massif allows the recognition of a large-scale migmatite complex closely associated with this S-type granite (see recent description in Laurent et al., 2015) (Fig. 3e).

4. Structural analysis of the ductile deformation in metamorphic rocks

4.1. Main planar fabrics

All metamorphic rocks and most of magmatic lithologies from Ikaria are pervasively foliated. In most cases, compositional

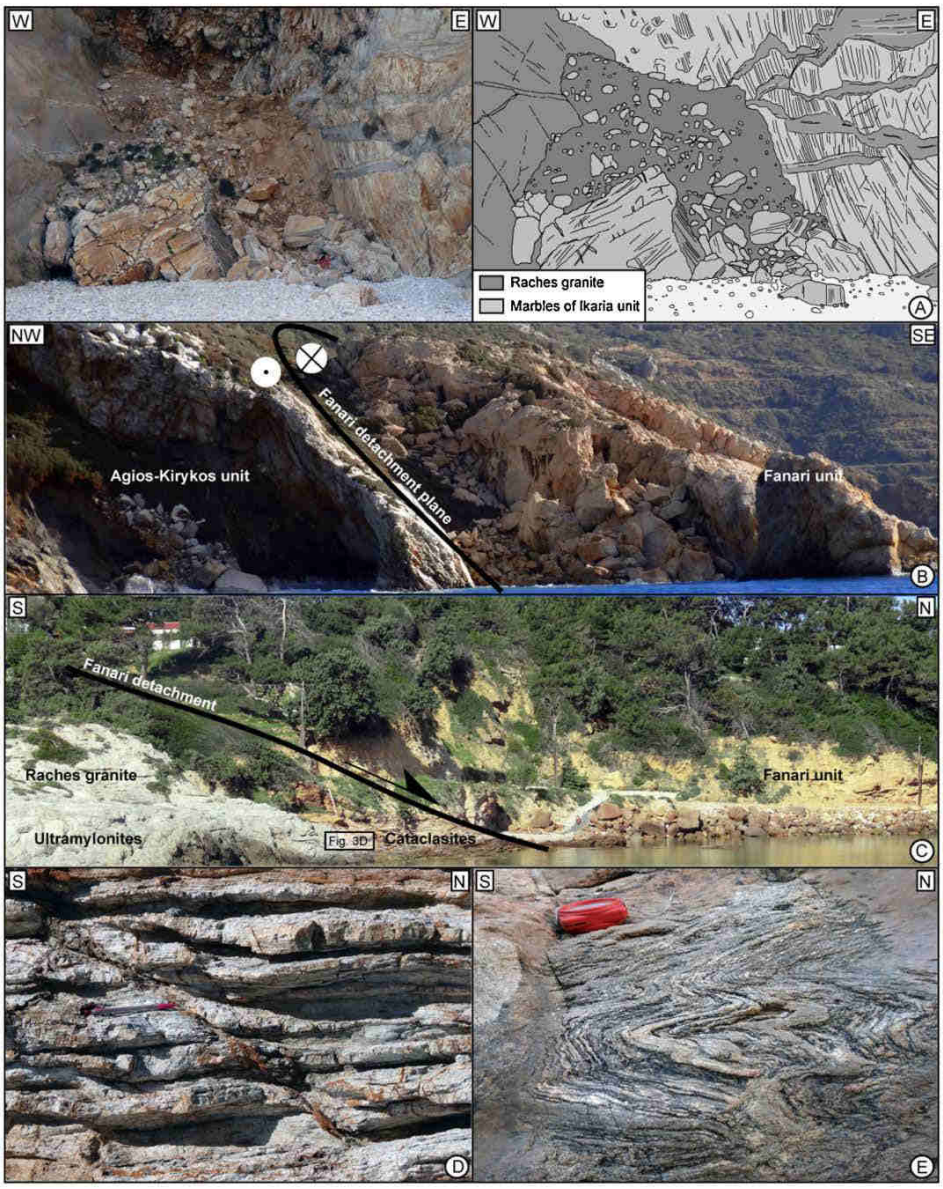

Fig. 3. New geological features and precisions about nature of contacts. (a) The intrusive contact between Raches granite and marbles of Ikaria unit is clearly marked by the presence of granitic dykes within marbles. (b) Southward extension of the Fanari detachment at Therma, separating conglomerates of Fanari unit and metasediments of Agios-Kirykos unit. (c) Panorama of the Fanari detachment at Gialiskari between sediments of Fanari unit and the Raches granite. (d) Close-up view of granite-derived cataclasites beneath the Fanari detachment at Gialiskari. (e) Details of migmatites from the lower parts of Ikaria unit preserved in the south of Raches granite. See Fig. 2 for location.

layering in the metasediments has been transposed into a main, generally shallow-angle foliation.

221 foliation planes were measured in all lithologies of the two metamorphic units. Besides, bedding was measured in Fanari unit. Measurements, statistical analysis and foliation trajectories are reported in Fig. 4a–c, respectively. The dip of foliation planes displays a large range of variation between 10° and 50° for a mean value at 20–25° (Fig. 4b). Smoothing out these small-scale dip variations, the main foliation planes commonly dip away from the long axis of the island. The strike of foliation therefore shows a fairly concentric pattern depicting a NE-SW elongated structural dome (Fig. 4c), which ends in the northeast. The dome axis, issued from the inversion of field measurements, trends N037° E, which corresponds to the main orientation of regional foliation (Fig. 4b and c). Additionally, this dome presents a marked asymmetry with a steeper, 30–40° dipping southeastern flank (Fig. 4b). The deeper parts of the dome crop out in the central part of the southern coast of the island, close to the contact with the Raches granite. Toward the southwest, the axis extends seaward and turns to a more E-W orientation to finally show up again across the main occurrence of migmatites (Fig. 4c). Strike and dip of the main foliation are generally discontinuous across intrusive contact of the Raches intrusion, particularly to the south. Conversely, foliation trajectories are more continuous to the north where both the granite and the wall-rocks locally present an ultramylonitic fabric (Fig. 4c).

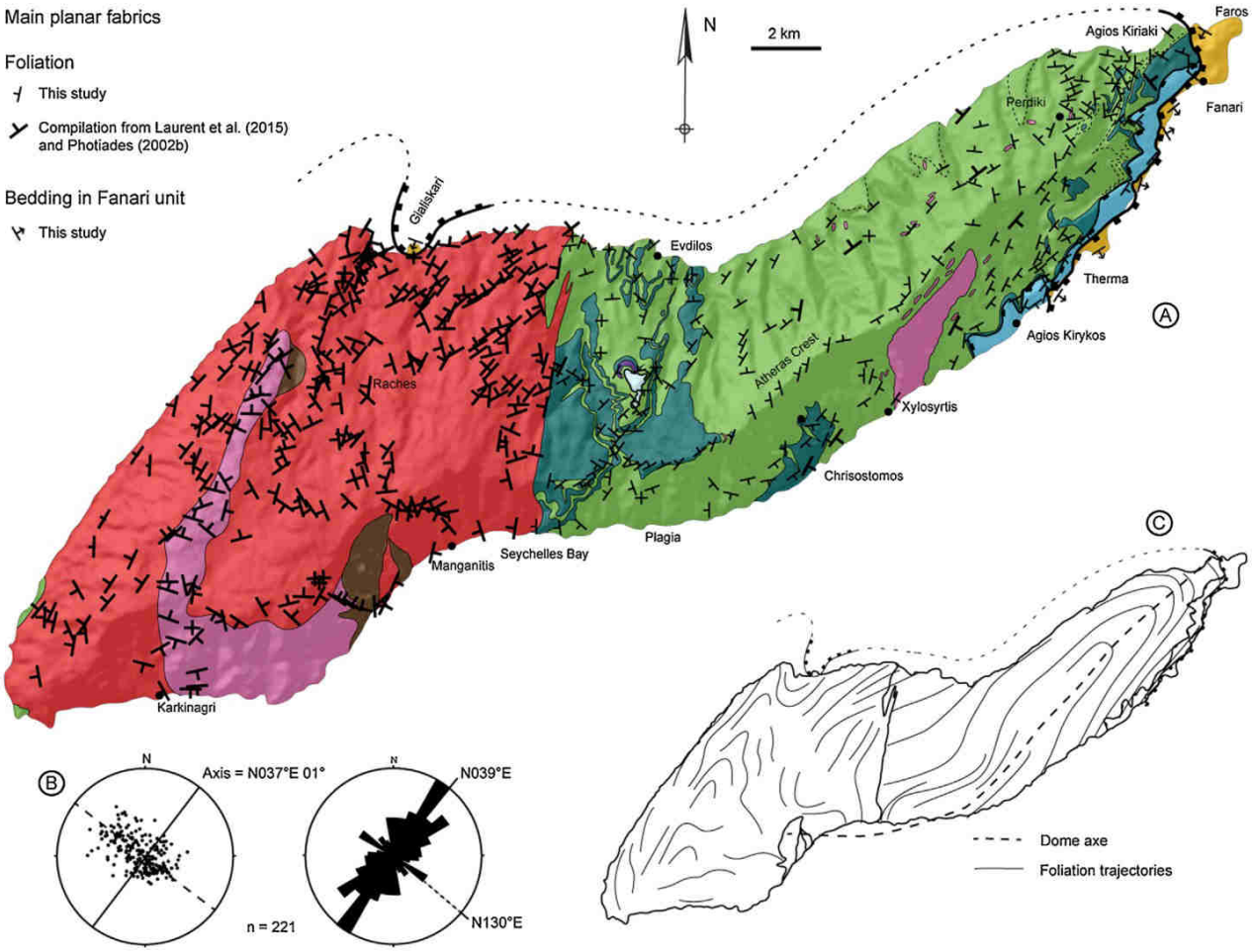

Fig. 4. Main planar fabrics. (a) Foliation-map of Ikaria. Geometry of sedimentary bedding in Fanari unit is also showed. (b) Statistics of the main foliation geometry. Poles of foliation are presented in Schmidt's lower hemisphere equal-area projection and preferred orientations of foliation is given by the rose-diagram. The elongation of the cloud allows retrieving the geometry of the dome axis. Also note that the asymmetry of the cloud calls for the asymmetry of the dome with a steeper southeast flank. (c) Simplified geological map showing foliation trajectories and traces of the main shear zones.

4.2. Stretching lineation

Stretching lineation is carried by the foliation plane in most metamorphic rocks, while it may sometimes occur as the unique strain marker in the intrusive rocks. It is marked by various indicators, depending on lithology, metamorphic grade and strain intensity. In calcite and dolomite marbles, it is defined by very fine-grained mica slates and the elongation of graphite-rich inclusions. In metapelites, it is generally defined by elongated quartz rods and phyllosilicate aggregates. It is also sometimes marked by the elongation and the truncation of epidote or tourmaline in granitic rocks. Evidence for stretching is also recorded by the preferred elongation and the brittle truncation of clasts in conglomeratic layers at the base of Fanari unit, just above the Fanari detachment.

202 stretching lineations have been measured in the field in all metamorphic rocks. Data are all reported in Fig. 5 together with some first-order statistics. At first glance, the trend of lineation shows very little dispersion. It is centered on an average value of N008°E ranging from N160°E and N020°E (Fig. 5b). Wrapped around the dome, the lineation plunges to the north in the northwestern flank of the island and to the south in the southeastern flank. At large-scale, the trend of stretching lineation describes slightly curved patterns from N-S to more NNE-SSW directions. The spatial rotation of the stretching lineation can be correlated with the relative structural position; NNE-SSW orientations are observed in the uppermost parts of the metamorphic succession and particularly in the vicinity of the Fanari shear zone, in the northeast of Ikaria or at Gialiskari (Fig. 5a).

4.3. Asymmetry of ductile deformation

The whole volume of the metamorphic succession and a great part of the magmatic intrusions of Ikaria are pervasively affected by a top-to-the-N to -NNE ductile deformation (Fig. 5a). Kinematics indicators of top-to-the-N deformation are very common and often unambiguous, particularly toward the top of Ikaria unit and in the bulk of Agios-Kirykos unit. Differing in terms of style, asymmetry and physical conditions of deformation, descriptions in Ikaria and Agios-Kirykos units are presented separately.

4.3.1. Top-to-the-N shearing gradient in Ikaria unit

Shear bands accompanied by asymmetric boudinage are the most common kinematic indicators in Ikaria unit (Fig. 6). Top-to-the-N shear bands are particularly abundant in metapelite layers interleaved with more competent rocks such as marbles, metaquartzites or metabasites. Due to asymmetric dome-shaped

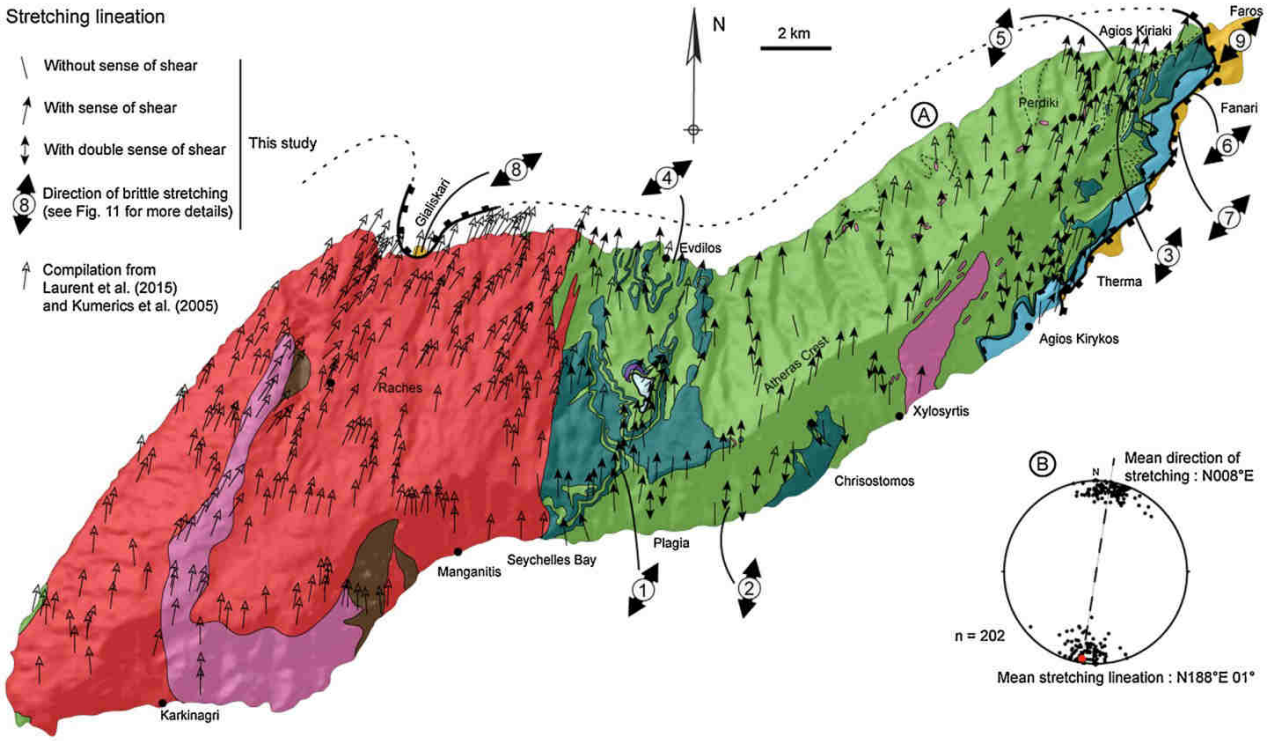

Fig. 5. Stretching lineation. (a) Stretching lineation-map of Ikaria. Note that the trend of the lineation shows very little dispersion. It is noteworthy that the strike of the stretching lineation describes slightly curved patterns from N-S to more NNE-SSW directions. Indicated are the results of the fault-slip data inversion. (b) Statistics on the preferred orientation of stretching lineation presented in Schmidt's lower hemisphere equal-area projection.

architecture of the island, shear bands display, in their present position, gentle to moderate north-westward dips and normal-sense displacements on the northwestern flank of the island while they often present flat or even "reverse" geometry on the southeastern flank. Boudinage occurs at various scales in alternating lithologies such as metapelites interleaved with marbles, metaquartzites or metabasites. Boudins frequently show asymmetric shapes consistent with a northward asymmetry. However, antithetic bookshelf structures compatible with a top-to-the-N sense of shear can be developed within marble at different scales as observed by Ring (2007).

Top-to-the-N ductile deformation appears unevenly distributed within Ikaria unit, primarily controlled by the relative structural position. Evolution of its asymmetry can be studied along a composite cross-section from the deepest parts to the top of this unit from Plagia to Evdilos. The deepest parts crop out on the southeastern coast between Chrisostomos and Plagia. There, the most typical structural feature is an intense folding of the primary compositional layering (Fig. 6a). Folds display a wide range of morphologies but all share common subhorizontal axial planes consistent with vertical flattening. A N-S stretching lineation is only developed in metapelitic or sometimes quartzitic layers while other lithologies display more randomly oriented intersection lineations. Sense of shear is often ambiguous with the presence of both top-to-the-N and top-to-the-S shear criteria suggesting a strong flattening component. Upward, the development of meter-scale decimeter-thick shear bands marks the appearance of a clear asymmetry. Shear bands delimit asymmetric boudins that preserve more ductile deformation as tight recumbent to isoclinal folds, or only as detached fold hinges (Fig. 6b). However, at variance with deeper levels of the unit, fold axes trend parallel to the stretching lineation arguing for a significant component of shearing in the direction of stretching (Fig. 6c). Upward, along with the multiplication of shear bands, the decreasing size of shear domains and boudins, metapelitic rocks become more homogeneous. Lenses of metabasites, dolomitic marbles and remains of metaquartzites occur as sigma or more rarely delta-type porphyroclasts systems consistent with an overall top-to-the-N sense of shear (Fig. 6d). Intense shear strain has turned the rocks into fine-grained mylonites (Fig. 6e). The resulting cross-section shows a first-order strain gradient, where asymmetric stretching is more and more systematic toward the highest structural levels of the unit (Fig. 6f).

Metamorphic conditions that prevailed during deformation also depend on structural position. Amphibolite-facies assemblages and gneisses are generally well preserved in the deepest parts of Ikaria unit. There, first retrogression stages are clearly synkinematic, as exemplified by the crystallization of biotite around stable garnets forming sigma-type porphyroclasts system (Fig. 7a). Upward, developed during garnet breakdown, asymmetric strain shadows around garnet contain chlorite and white-micas. Biotite, still metastable in the bulk of the rock is retrograded to chlorite in shear bands. Associated with the crystallization of large amounts of synkinematic chlorite and albite, top-to-the-N shearing in the highest levels was clearly recorded within greenschist-facies metamorphic conditions (Fig. 7b).

4.3.2. Deformation in Agios-Kirykos unit and along Fanari shear zone

The Agios-Kirykos unit can be studied along a series of foliation-orthogonal valleys from Therma to Agios Kiriaki (see location in Fig. 2). It consists in the alternation of marble and dark metapelites layers reaching 150–200 m of structural thickness. On most outcrops, top-to-the-NNE ductile shearing is clear. Greenschist-facies shear bands are abundant and display a clear upward evolution

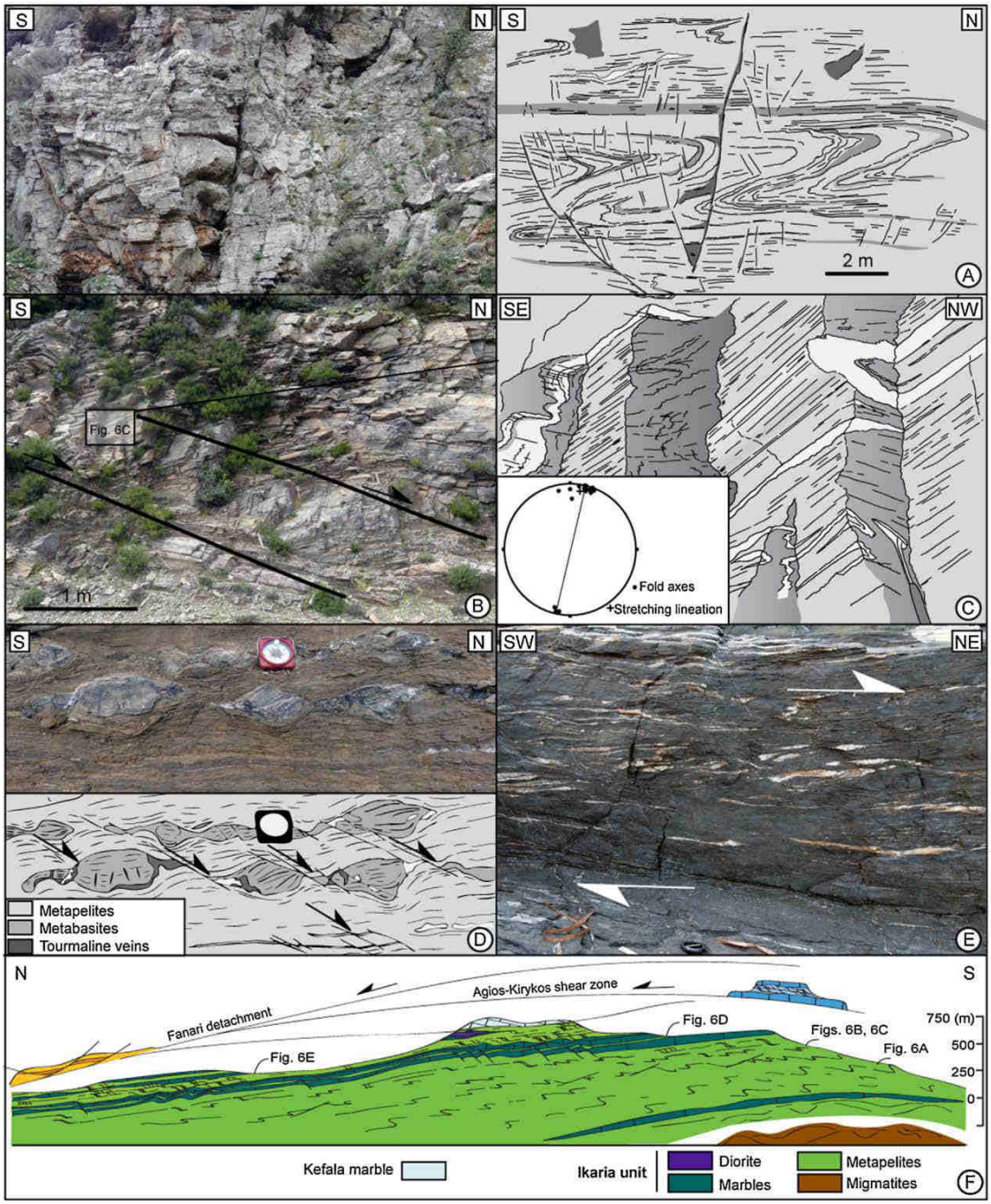

Fig. 6. Upward strain gradient within Ikaria unit. (a) Incomplete transposition of the compositional layering into a main, flat-lying penetrative foliation within the deepest parts of the structure. (b) More advanced transposition of the compositional layering into the flat-lying penetrative foliation. Note that boudin-shaped volume of rocks preserved isoclinal folds between decameter-scale top-to-the-N shear bands. (c) Close-up view of the cross-cutting relationships compositional layering and the main foliation. Note that fold axes are now mostly parallel to the stretching direction. (d) Mylonitic deformation of the upper parts of Ikaria unit. The foliation dips gently toward the north. Metabasites form asymmetric pinch-and-swell boudinage indicating top-to-the-N kinematics. (e) Typical mylonites from the uppermost parts of Ikaria unit, near Evdilos. Quartz veins have been transposed and stretched into the shear direction and forming asymmetric sigmoids indicating top-to-the-NNE kinematics. (f) Composite cross section showing the first-order strain gradient and the structural position of outcrops of Fig. 6. Trace is represented in Fig. 2.

to more localized or even cataclastic flow (compare Fig. 8a and b). The core of Fanari shear zone, developed at the expense of the uppermost parts of Ikaria unit, is well exposed in the western part of Agios Kiriaki harbor (Fig. 8c). While the contact itself is hidden by the airport runaway, Fanari unit crops out directly to the northeast, 100 m apart (Fig. 8c). There, rocks present a northeast-dipping mylonitic fabric and carry a N035°E stretching lineation marked by numerous quartz rods and boudins of all sizes from a few

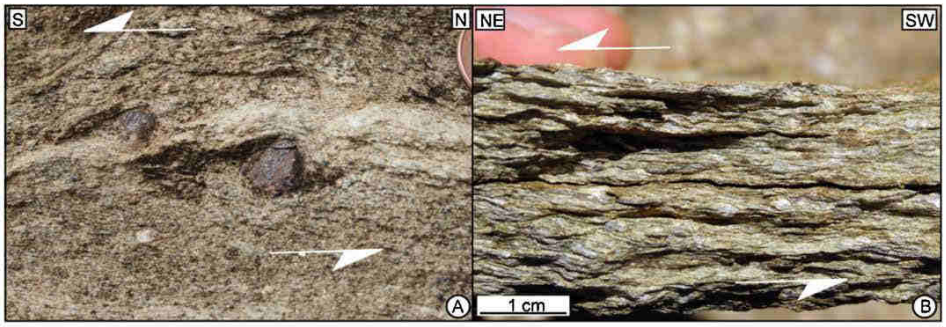

Fig. 7. Physical conditions of the deformation within Ikaria unit. (a) Small-scale top-to-the-S shear bands operating in the lower parts of Ikaria unit. The volume of rocks involved in the deformation is quite large and the amphibolite-facies associations are quite well preserved. Note that in these incipiently deformed rocks, deformation is rather symmetrical and local top-to-the-S kinematics are sometimes observed. (b) Close-up view of syn-greenschist-facies mylonites from the core of the Agios-Kirykos shear zone in the upper parts of Ikaria unit.

centimeters to several meters. Marble layers are stretched and boudinaged within the metapelitic matrix. The internal deformation of marbles displays successive stages of symmetric boudinage, evolving from ductile to brittle (Fig. 8d). Metapelite levels show a clear non-coaxial component of shearing consistent with an overall top-to-the-NNE kinematics (Fig. 8e). These layers, generally thinned to 1 m or even less, display a single and penetrative set of shear bands locally obliterating the main foliation. Spacing between

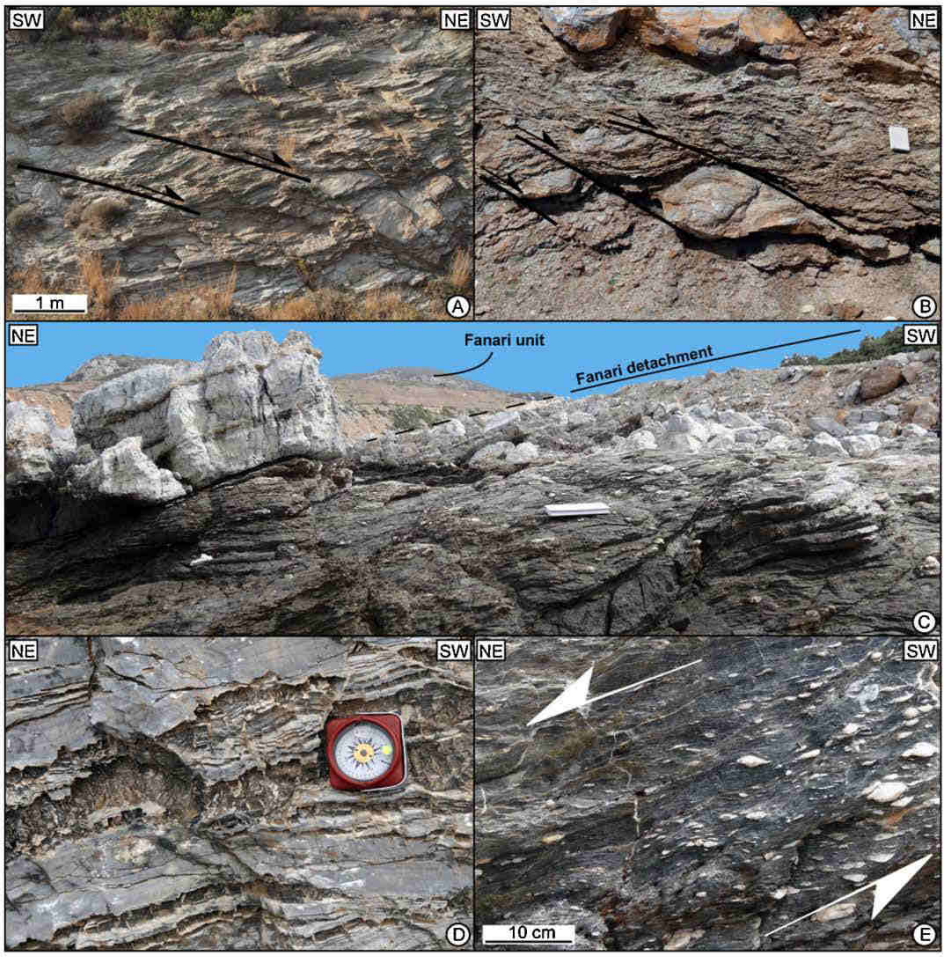

Fig. 8. Deformation in Agios-Kirykos unit. Outcrop pictures of rather weak (a) and intense (b) top-to-the-NE asymmetric deformation in Agios-Kirykos unit. Note that shearing, developed in the greenschist-facies conditions, displays a clear evolution to more localized or even cataclastic flow. (c) Large-scale view of the core of the Fanari shear zone at Agios Kiriaki. Exposed are the mylonites of the uppermost parts of Ikaria unit, on the first plane, while sediments of Fanari unit crop out in the background. Close-up views of the deformation of (d) marble and (e) metapelite layers. Marble layers display successive stages of symmetric boudinage, ranging from ductile to strictly brittle while metapelite levels show a strong non-coaxial component consistent with an overall top-to-the-NE kinematics.

shear bands, controlled by the presence of quartz lenses is locally as small as 1–3 cm (Fig. 8e). Chlorite is abundant within these rocks and adopts a clear synkinematic character in the vicinity of shear bands. The brittle expression of the Fanari shear zone is not exposed there but occurs spectacularly near Fanari, 1 km further south along the coast (Fig. 9). The Fanari detachment is described in the next section.

5. Brittle deformation analysis

Ikaria presents either large to meso-scale brittle structures or locally pervasive networks of small-scale brittle faults systems developed from the ductile-brittle transition to the brittle field. Brittle structures of all scales are first described. Results of the paleostress analysis are then presented. It must be noted here that some NNE-SSW lineaments, visible on satellite images, do not have any particular expression in the field.

5.1. Description of brittle structures

The Fanari detachment is the only large-scale structure that was active under both ductile and subsequent brittle conditions. Displacement in the brittle regime over the Fanari detachment is attested by the development of cataclasites particularly well exposed along the southeastern coast of the island as a series of several hundreds of meters of continuous outcrops (Fig. 9). There, the detachment plane appears stripped of its sedimentary cover over a large surface revealing large-scale corrugations and crescent-shaped structures that remind the Cape Evros outcrop on Mykonos (Lecomte et al., 2010; Menant et al., 2013) or the Platy Gialos outcrop on Serifos (Grasemann and Petrakakis, 2007). Breccias, locally reaching more than 2 m, are mainly developed at the expense of Agios-Kirykos unit but also from the very first decimeters of Fanari unit. Cataclastic rocks often show typical clasts size ranging from 1 to 20 cm embedded in reddish-brownish cement supposed to be composed of Fe-rich oxy-hydroxides and carbonates. The detachment plane displays a NE-SW strike and a 60° southeast-dip. It carries shallow-dipping, southwest-plunging, large-scale corrugations consistent with the opening of perpendicular cracks. Variable types of kinematics indicators of top-to-the-NNE brittle deformation in the detachment footwall unambiguously ascribe a left-lateral reverse sense of displacement. A secondary discrete striae indicates locally a reverse sense of displacement. At the scale of the map, kinematics of brittle motion over Fanari detachment indicates northeast-directed displacement consistent with the kinematics of the last increments of ductile deformation (compare kinematics given in Fig. 9 with the last ductile stretching lineation in Fig. 5). In its current position, the detachment plane is offset by a set of NW-SE vertical faults carrying oblique striations.

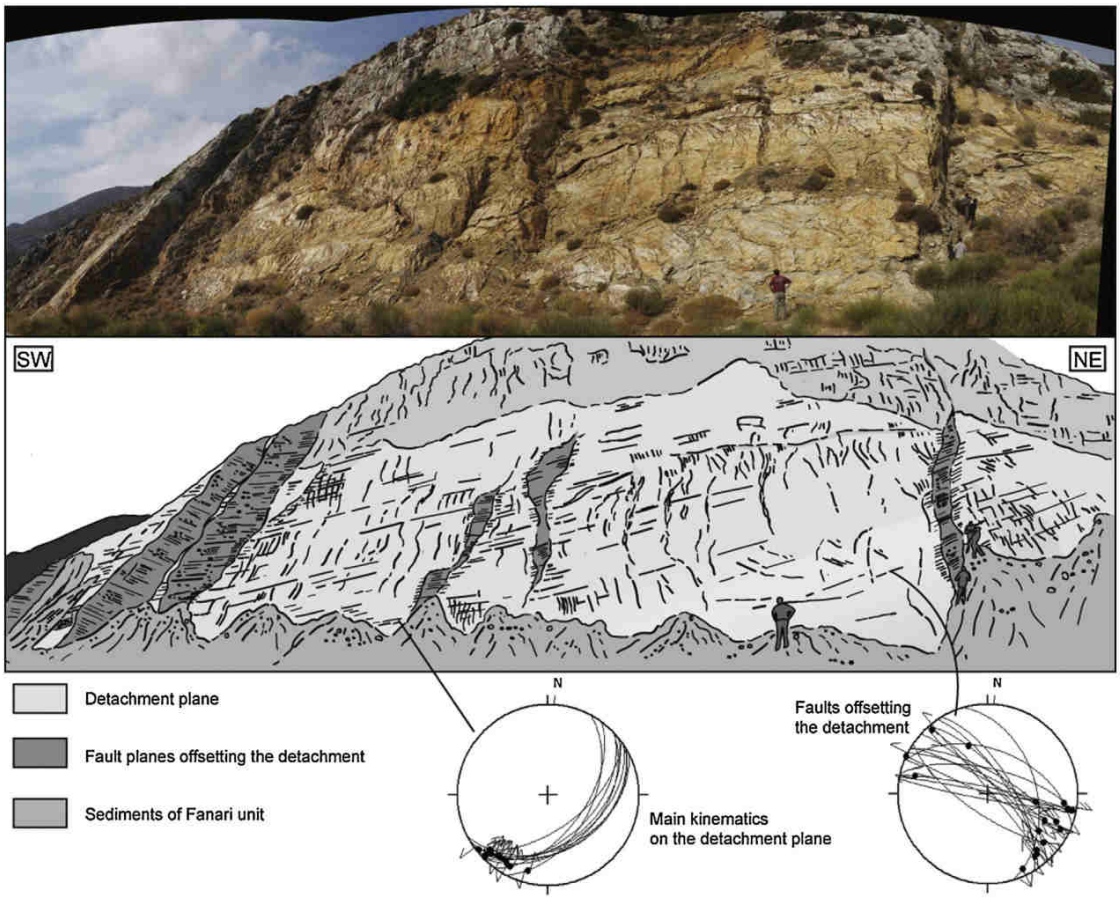

Fig. 9. The Fanari detachment plane. Large-scale representative view of the Fanari detachment plane at Fanari. The detachment plane is stripped of its sedimentary cover over several hundreds of square meters. Sediments that are almost vertical are preserved in the incised gullies and all along the coast from Fanari to Agios-Kirykos. The plane carries series of large-scale corrugations and crescent-shaped structures indicating a consistent top-to-the-NNE kinematics. Note that the detachment plane is cut across by series of high-angle faults carrying sub-horizontal striations. Also are represented stereographic projections of striations and kinematics of both the detachment plane and the faults that offset the plane.

Cataclastic rocks also occur on the northern part of Ikaria at Gialiskari (Fig. 3c and d). They overprint the uppermost parts of a 500 m-thick strain gradient developed exclusively at the expense of the underlying Raches granite (Laurent et al., 2015). Here, they bound again a tectonic unit considered as the lateral equivalent of Fanari unit exposed further east. Sediments, consisting on alternating gray sandstones, conglomerates and brownish limestones are heavily affected by extensional features. WNW-ESE normal faults are organized in conjugate sets accompanied by a dense array of subvertical WNW-ESE veins that both overprint a gently south-dipping bedding.

Beside this major brittle structure, small-scale brittle features mostly correspond to late W-E to NW-SE conjugate faults systems developed in all lithologies (Figs. 10 and 11). Displacement on faults ranges typically from a few centimeters to a few meters and can generally be constrained in the field using marker-levels. In the entire studied area, the fault population is dominated by dihedral orientations arguing for the formation of newly formed conjugate sets of faults rather than reactivated shear planes. Normal faults are often accompanied by subvertical joints and tension gashes filled with quartz, chlorite, iron oxy-hydroxides in the metamorphic rocks, quartz, chlorite or even epidote and tourmaline in granites and mostly calcite in the sediments. The close association between faults and joints often displays contradictory intersection relationships and thus argues for a contemporaneous development.

5.2. Inversion of fault-slip data

Paleostress orientation patterns were evaluated by the Win-Tensor computer-aided inversion software (Delvaux and Sperner, 2003). The reduced paleostress tensor consists in the identification of orientation of the three principal stress axes and the axial ratio of stress ellipsoid. Determination of the paleostress axes was completed by the analysis of accompanying brittle structures such as joints, tension gashes or stretched pebbles. Brittle structure analysis was conducted over 9 main sites scattered over the island (see Fig. 5 for location). Results are presented in the next two sections.

5.2.1. Using microstructures to unfold the Fanari detachment

Although the Fanari detachment consistently exhibits top-to-the-NE kinematics, it currently crops out with the geometry of southeast-dipping left-lateral reverse fault zone, a quite rare configuration in the Aegean domain (Fig. 9). A detailed study of geometrical relationships between detachment, sediments of Fanari unit and attitude of small-scale brittle structures affecting either the sediments or the detachment plane, allows proposing a restoration scenario of the initial geometry of the Fanari detachment (Fig. 10a). Two reference outcrops (6 and 7) were selected 2 km apart within sediments of Fanari unit along the detachment (see position in Fig. 5) with contrasting spatial relationships between structures. Outcrop of station 7 (Fig. 10b), which presents almost vertical bedding, displays a conjugate set of subvertical faults affecting alternating sandstones and conglomeratic layers. N030°E to N160°E faults present consistent sinistral kinematics while N070°E to N130°E faults present dextral kinematics. Part of these faults even cuts across the Fanari detachment causing 1–5 m offsets of the plane. Outcrop of station 6 also presents two sets of faults that affect a 40° dipping bedding further southeastward. The dominant set of faults displays subvertical fault planes carrying both normal and reverse kinematics. This set is accompanied by a subordinate set of flat to gently dipping fault planes that also present both normal and reverse kinematics (Fig. 10b). In their present geometry, this heterogeneous fault set requires the superimposition of two distinct stress regimes. Back-tilting of those systems of faults about a horizontal axis, in order to obtain a horizontal bedding, permits to get a coherent stress regimes for both sites 6 and 7. Maximum principal stress axis becomes vertical and the two others become horizontal, compatibly with a NE-SW extension for both sites. It strongly suggests that faults form before an unequal tilting of the different outcrops. This assumption is confirmed further to the southwest where both the detachment plane and the bedding of sediments are subhorizontal (i.e. less than 20° toward the southwest) while tension-gashes are now subvertical and all faults appear as a single conjugate normal fault set preserved in its initial attitude. Importantly, back-tilting of the whole system, including the Fanari detachment, results in a system where the detachment plane operates at shallow angle, 10–15° to the northwest, with normal-dextral-sense kinematics and cuts the sediments down-section as observed in the neighboring island of Mykonos (e.g. Lecomte et al., 2010; Menant et al., 2013). In this restored position (Fig. 10a), sediments are pervasively affected by normal faulting consistent with a unique and common NNE-SSW to NE-SW extension (Fig. 10b). This paleostress solution is consistent with the paleostress field deduced from other stations throughout the island and previous studies (e.g. Kumerics et al., 2005). This point is discussed below. The causes of the Fanari detachment tilting and the more general arching of the ductile to brittle fabrics at the scale of the whole island are addressed in the discussion section.

5.2.2. Large-scale consistency of the paleostress inversions

Despite the local coexistence of both N80-110°E and N130-160°E trending normal faults, results present rather small internal dispersion (Fig. 11). At most stations, stress tensor analysis shows a consistent subvertical orientation for the maximum principal stress axis (σ_1). In other stations (e.g. sites 6 and 7 in Fig. 10b), σ_1 was restored using horizontal-axis back-tilting rotation. The minimum principal stress axis (σ_3) is horizontal or very gently dipping with a consistent NNE-SSW to more NE-SW direction of extension. In turn, the overall consistency of the direction of σ_3 prevents from significant vertical-axis large-scale block rotations. Planes of joint and tension gashes correspond to the calculated σ_1–σ_2 plane, and their poles therefore appear scattered around the σ_3 axis. Brittle structures recorded during the last exhumation stages present a marked consistency of a NE-SW stretching direction occurring in an extensional regime.

6. Thermal structure

The RSCM method is based on the quantitative study of the degree of organization of carbonaceous material (CM), which is a reliable indicator of metamorphic temperature (e.g. Pasteris and Wopenka, 1991; Beyssac et al., 2002; Lahfid et al., 2010). Because of the irreversible character of graphitization, CM structure is not sensitive to the retrograde reactions and permits to determine peak temperature conditions (T_{max}) reached during metamorphism, using an area ratio (R2 ratio) of different peak of Raman spectra (Beyssac et al., 2002). T_{max} can be determined in the 300–640 °C range with an accuracy of ±50 °C related with the precision and the dispersion of petrological data used for the method calibration (Beyssac et al., 2002). Relative uncertainties on T_{max} are however much smaller, around 10–15 °C and relative variations of that order of magnitude can be detected (e.g. Gabalda et al., 2009; Vitale Brovarone et al., 2013; Augier et al., 2015). Sampling was performed in order to quantitatively describe the large-scale thermal structure of Ikaria to complement the few existing, punctual P–T estimates (Kumerics et al., 2005; Martin et al., 2011). Sampling was therefore regularly distributed within the tectonometamorphic succession of Ikaria and a more systematic sampling was carried out in the vicinity of possible second-order thermal effects such as intrusions and

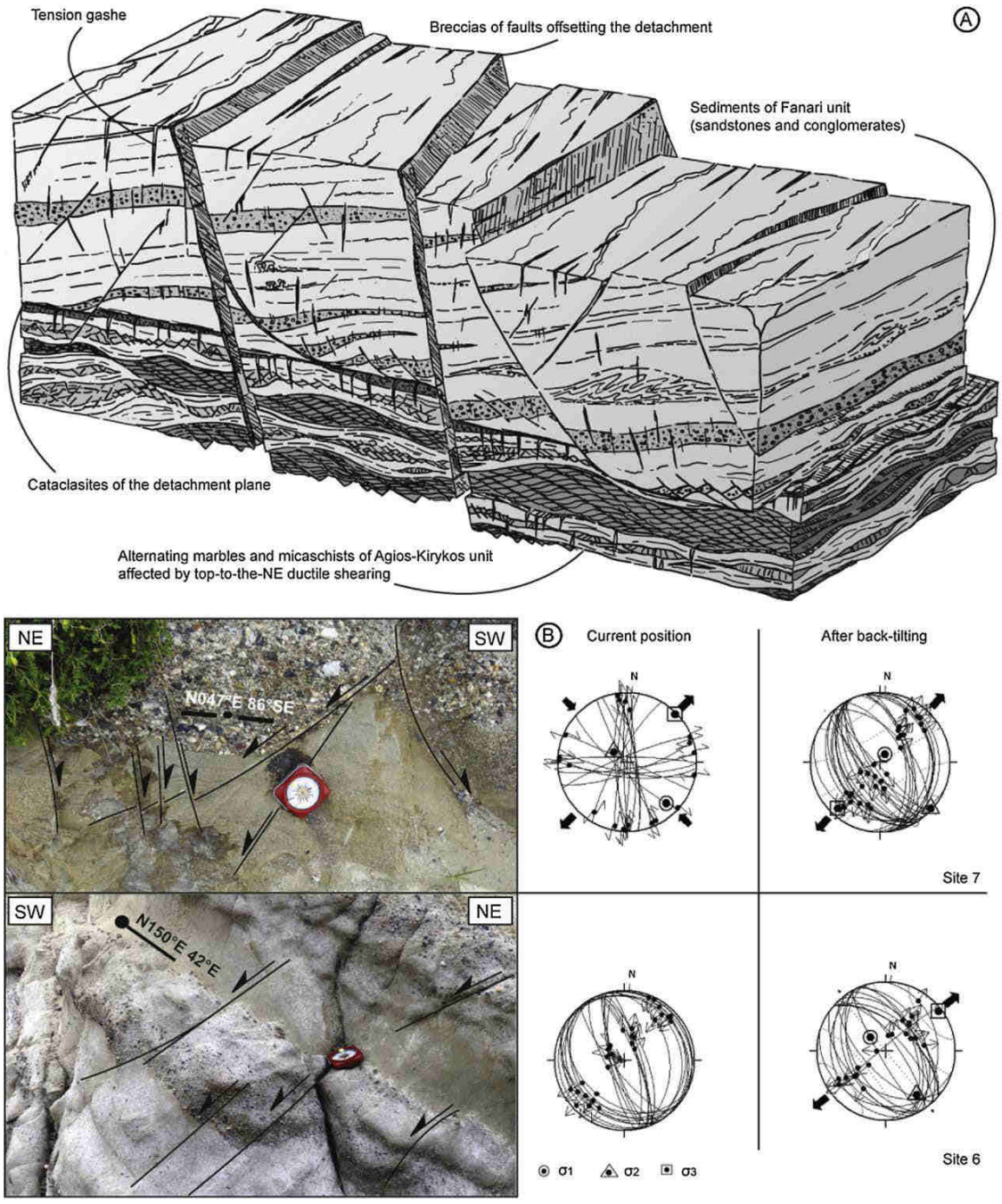

Fig. 10. Using microstructures to unfold the Fanari detachment. (a) Sketch depicting the probable geometry of the Fanari detachment prior to its tilting together with the whole system (see Fig. 9). The result is a system where the detachment plane operates at shallow angle with dextral-normal-sense. In the restored position, sediments appear pervasively affected by a single set of conjugate normal faults. (b) Outcrop pictures and stereographic projections of fault systems before and after back-tilting rotation for sites 6 and 7 (see Fig. 5 for location). In this restored position, paleostress solutions are all consistent with a unique and common NNE-SSW to NE-SW extensional stretching. This orientation is consistent with the paleostress field deduced from other stations throughout the island (see Fig. 11). Note that, conversely, three successive stress states are required to account for the heterogeneous fault populations present in their current position.

tectonic contacts. 35 samples consisting of CM-bearing metasediments were collected (see Fig. 12 for location). In order to bring out and possibly smooth out the inner structural heterogeneity of CM within samples, 13–20 spectra were recorded for each sample. Detailed results, including R2 ratio, number of spectra, T_{max} and standard deviation are presented in Table 1. In addition, RSCM temperatures are all reported in Fig. 12.

RSCM results embrace a wide range of temperature from 391 to 625 °C (Table 1). At first glance, T_{max} presents a correlation with the relative structural position. 625 °C was indeed recorded for the deepest parts of the structural dome with gneisses while 390 °C was retrieved for the uppermost parts of the metamorphic succession where low-crystallinity micaschists crop out. Ikaria therefore appears as a metamorphic dome in which temperature

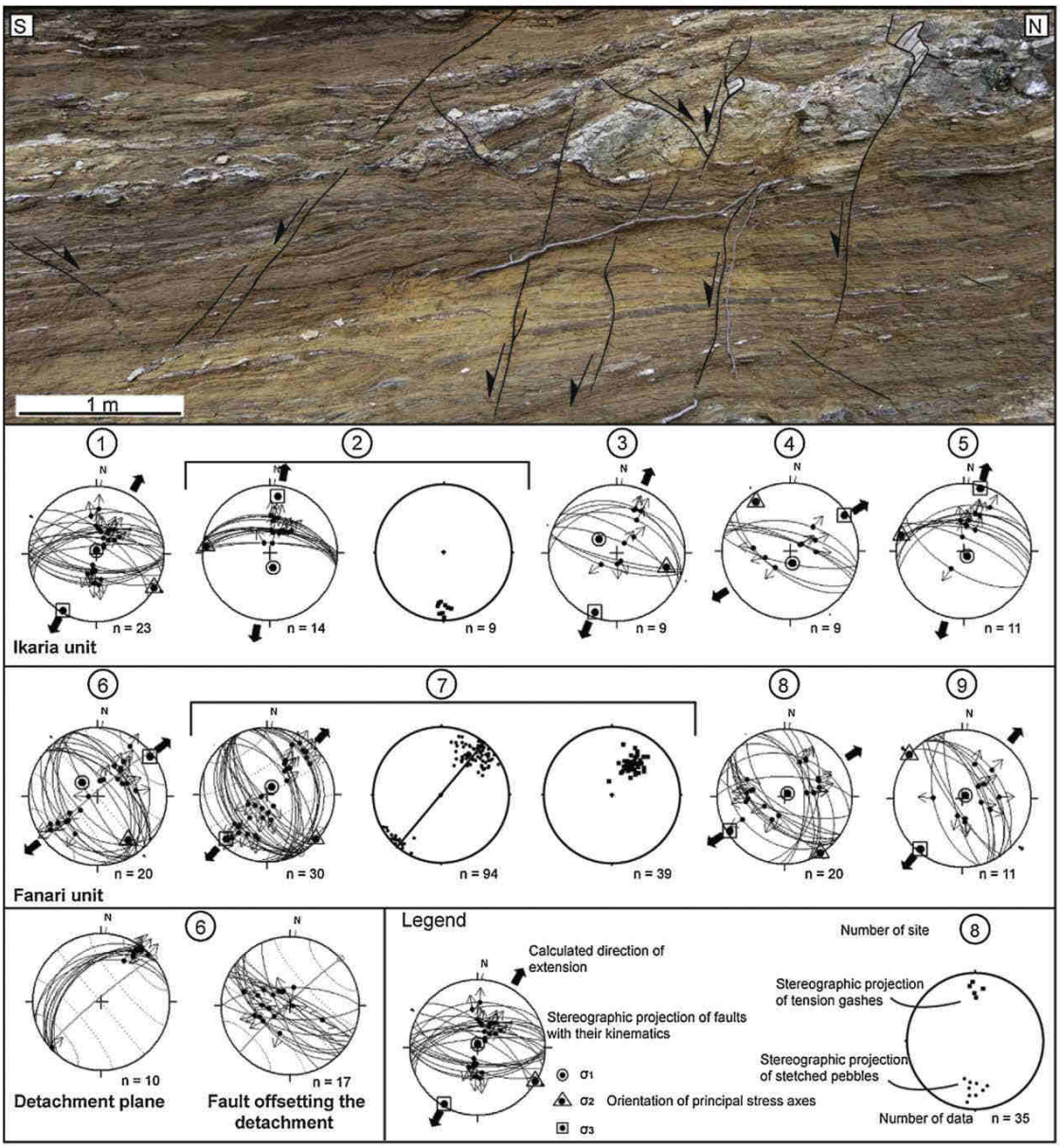

Fig. 11. Small-scale brittle structures. Detailed results of the fault-slip data inversion. Fault planes, associated striae and results of inversion were plotted using WinTensor software in Schmidt's lower hemisphere equal-area projection (Delvaux and Sperner, 2003). Also is presented a representative outcrop recognized as demonstrative of a brittle stage subsequently developed after the ductile one (site 1; see location in Fig. 5). Faults occur as a dense array of rather steep normal faults. Note the consistency of the NNE-SSW to NE-SW direction of extension all over the island.

increases down-section (Fig. 12a and b). Samples from Ikaria unit show rather high T_{max}, from 625 to 500 °C, presenting an important scatter. The 550 °C temperatures for the volume of Ikaria unit are moreover consistent with the amphibolite-facies metamorphic associations. Samples from Agios-Kirykos unit display lower temperature ranging between 450 and 390 °C (Table 1). Two main sets of temperatures can then be identified separated by a 50 °C temperature gap (Fig. 12a and b). This gap of temperature corresponds to the position of the Agios-Kirykos shear zone, independently recognized on the basis of structural criteria. This particular feature was studied in the east of Ikaria, and particularly along a foliation-orthogonal cross-section upstream of Therma valley (Fig. 12b). There, T_{max} shows a regular temperature decrease from 600 to 400 °C accompanied by a 50 °C normal-sense metamorphic gap. Among the causes of temperature variation in Ikaria unit, local heating by intrusive rocks has been tested in the vicinity of the Raches granite (Fig. 12c). Samples were picked at decreasing distance from the intrusive contact for almost the same relative structural position. Results show regularly decreasing temperatures from 580 °C to 520 °C, in accordance with the intrusive character of the Raches granite (Fig. 3a). Accordingly, smaller intrusive bodies as the Kefala diorite or small-scale pegmatite dykes that are only partly mapped (Fig. 2) may be responsible of erratic, isolated high T_{max} results.

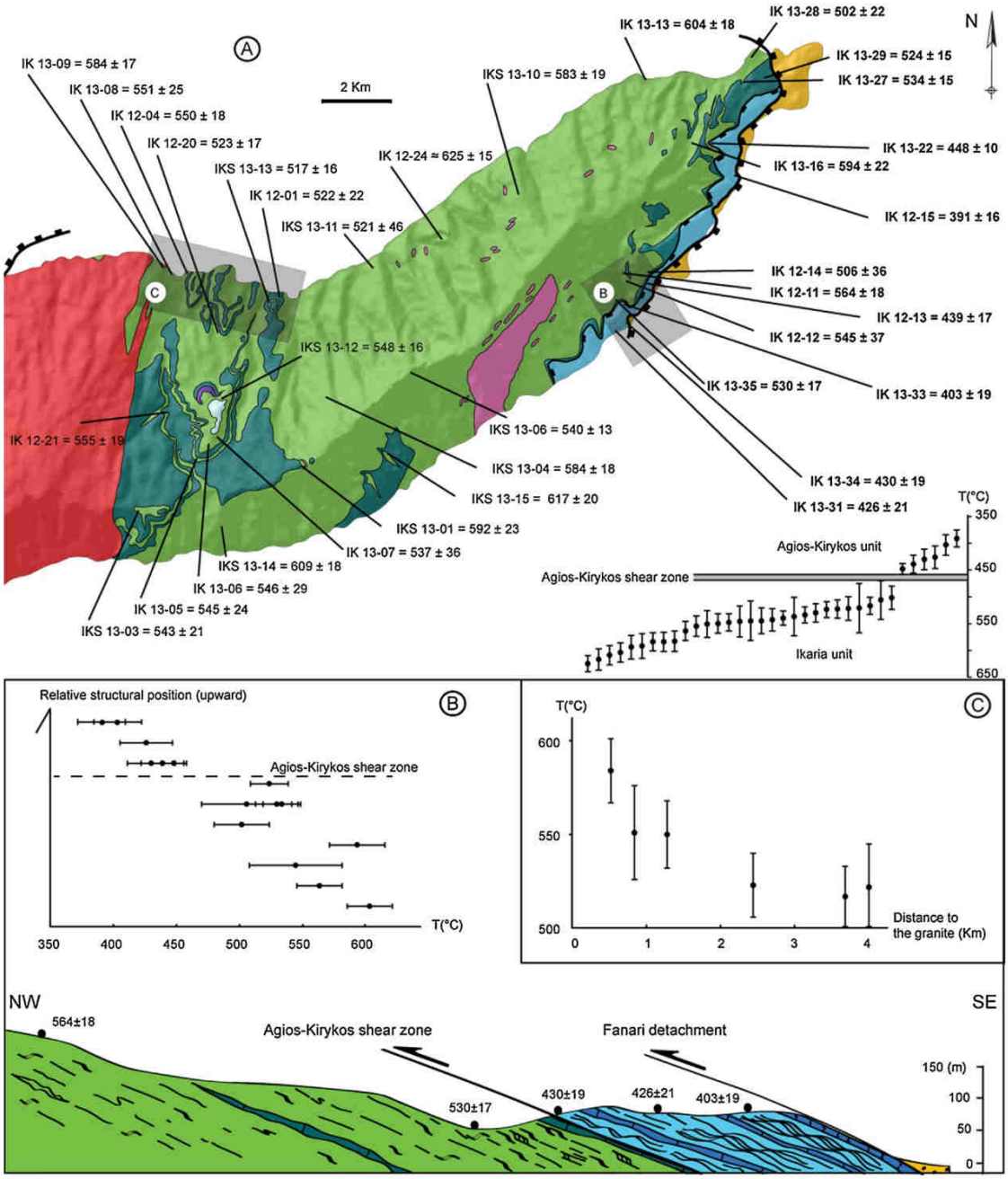

Fig. 12. RSCM peak temperature results. (a) Sampling map used for the RSCM study. In the bottom right corner, T_{max} are sorted by increasing temperature, where errors brackets correspond to intra-sample heterogeneity standard deviation. Note that temperature is comparable for two samples, positioned side by side in the chart, for Ikaria unit on one hand, and for AgiosKirykos unit on the other hand. But the two units are characterized by clearly differentiable bulk temperature. (b) T_{max} vs structural position for the northeastern part (samples used for (b) are written in bold on the map). Note the gap of temperature near the Agios-Kirykos shear zone, quite clear on the Therma cross section. (c) Increasing temperature approaching the Raches granite.

7. Age constraints on the partial melting event

7.1. Analytical methods

Analyses were performed in thin section by laser ablation inductively coupled plasma spectrometry (LA-ICPMS) at the Laboratoire Magmas et Volcans (LMV), Clermont-Ferrand (France). The ablation is performed using a Resonetics Resolution M-50E system equipped with an ultra-short pulse (<4 ns) ATL excimer 193 nm wavelength laser. This laser system is coupled with Agilent 7500 cs ICP-MS equipped with a pumping system to enhance the sensitivity. Spot diameter of 9 μm was used with a 1 Hz repetition rates. Ablated material is transported using a helium flux, and then mixed with nitrogen and argon before being injected into the plasma source. Analytical procedures for monazite dating are reported in details in Didier et al. (2013, 2014) and Paquette and

Table 1
RSCM peak temperature results. RSCM results classified by increasing temperatures. For each sample are indicated the GPS position, the total number of Raman spectra (n) performed, the mean R2 ratio and temperature calculated, both associated with their standard deviation (SD) related to the intra-sample heterogeneity. Location of samples and Tmax results are given in Fig. 12.

Sample	Coordinates (UTM 35 N)	*n*	*R2*		*T* (°C)	
			Mean	SD	Mean	SD
Agios-Kirykos unit						
IK 12-15	441548 4168007	21	0.562	0.036	391	16
IK 13-33	438478 4163867	19	0.535	0.043	403	19
IK 13-31	438178 4163625	20	0.482	0.049	426	21
IK 13-34	438453 4164338	19	0.473	0.044	430	19
IK 12-13	439086 4164923	19	0.453	0.037	439	17
IK 13-22	440733 4168835	14	0.433	0.023	448	10
Ikaria unit						
IK 13-28	441898 4171296	19	0.312	0.049	502	22
IK 12-14	439237 4165283	20	0.303	0.082	506	36
IKS 13-13	428570 4164441	17	0.278	0.035	517	16
IKS 13-11	431485 4165492	21	0.269	0.104	521	46
IK 12-01	428758 4164611	23	0.266	0.051	522	22
IK 12-20	427111 4163553	18	0.264	0.038	523	17
IK 13-29	442324 4170727	13	0.262	0.034	524	15
IK 13-35	438248 4164495	15	0.251	0.039	530	17
IK 13-27	441743 4170619	15	0.241	0.033	534	15
IK 13-07	426986 4160696	21	0.233	0.081	537	36
IKS 13-06	432513 4162583	16	0.228	0.029	540	13
IKS 13-03	424903 4158649	16	0.219	0.047	543	21
IK 12-12	438723 4164980	20	0.216	0.082	545	37
IK 13-05	426436 4160041	15	0.216	0.055	545	24
IK 13-06	426795 4160494	16	0.213	0.065	546	29
IKS 13-12	427145 4161730	16	0.209	0.035	548	16
IK 12-04	426177 4165286	16	0.204	0.040	550	18
IK 13-08	425761 4165301	18	0.202	0.057	551	25
IK 12-21	425535 4161591	13	0.194	0.044	555	19
IK 12-11	438363 4165292	19	0.174	0.041	564	18
IKS 13-10	435557 4167534	13	0.130	0.042	583	19
IK 13-09	425573 4165499	17	0.129	0.045	584	20
IKS 13-04	430168 4161819	11	0.129	0.041	584	18
IKS 13-01	429434 4159919	17	0.110	0.051	592	23
IK 13-16	440281 4168893	18	0.107	0.051	594	22
IK 13-13	439031 4170692	15	0.083	0.040	604	18
IKS 13-14	427196 4158256	13	0.072	0.041	609	18
IKS 13-15	431859 4160264	14	0.054	0.045	617	20
IK 12-24	433322 4166192	18	0.037	0.034	625	15

Tiepolo (2007). Following isotopes ^{204}(Pb + Hg), ^{206}Pb, ^{207}Pb, ^{208}Pb, ^{232}Th and ^{238}U were acquired. Data disturbed by inclusions, fractures or age mixing (between different areas of a single grain) were not taken into account for calculation. The occurrence of initial Pb in the sample can be monitored by the evolution of the ^{204}(Pb + Hg) signal intensity, but no Pb correction was applied. Elemental fractionation and mass bias were corrected making repeated analyses on Trebilcock monazite (272 ± 2 Ma, Tomascak et al., 1996). Analyses on the Moacyr monazite (Cruz et al., 1996; Seydoux-Guillaume et al., 2002; Gasquet et al., 2010; Fletcher et al., 2010) at the beginning and at the end of each session, treated as unknowns, verify the reproducibility, especially for the ^{208}Pb/^{232}Th ages, and the accuracy of the corrections. Data reduction was carried out with GLITTER® software package (van Achterbergh et al., 2001; Jackson et al., 2004). Calculated ratios were exported and age diagrams were generated using Isoplot software package by Ludwig (2001).

In this study, ^{208}Pb/^{232}Th ages are preferably used because: (1) U decay series could be in disequilibrium in young monazites (Schärer, 1984), resulting in overestimated ^{206}Pb/^{238}U ages; (2) ^{232}Th is so abundant that ^{208}Pb originating from initial Pb is negligible compared to radiogenic ^{208}Pb (Janots et al., 2012; Didier et al., 2013). However, in this study, ^{206}Pb/^{238}U ages are fully consistent with the ^{208}Pb/^{232}Th ages suggesting the absence of disequilibrium in the U decay series. Slight common Pb contamination is suggested by the Tera Wasserburg diagram, enhanced by the large uncertainty of the ^{207}Pb/^{235}U ages due to very low ^{207}Pb content in young monazite ages.

7.2. Results

Fourteen monazites have been analyzed for U–Th–Pb in situ dating in thin section from one migmatite sample (IK01A; see Fig. 2 for localization; Qz, Pl, Afs, Bt, Sil and Zrn). Monazites often appear as inclusions in biotite or set at grain boundaries and occur as large pristine crystals (Fig. 13a; between 60 and 100 μm) showing in few cases irregular boundaries. Besides, most of the crystals present a clear core and rim texture (Fig. 13b) which represents variable Y and U contents: the core is Y and U-poor (Y_2O_3 between 0.3 and 1.6 wt% and UO_2 between 0.2 and 0.8 wt%) whereas the rim is Y and U-rich (Y_2O_3 between 1.7 and 4.2 wt% and UO_2 up to 3.7 wt%).

Thirty two analyses have been performed in the different domains of the monazite grains. ^{208}Pb/^{232}Th analyses yielded ages between 14.9 ± 0.5 and 16.4 ± 0.5 Ma, with a weighted mean age at 15.7 ± 0.2 Ma (MSWD = 4,1; *N* = 32). All ages appear always concordant with the ^{206}Pb/^{238}U ages (Fig. 13c). The U–Pb ages are mostly discordant and define a linear trend crosscutting the Concordia at 15.1 ± 0.2 Ma in a Tera Wasserburg diagram (Fig. 13d). This suggests a slight common Pb contamination and the large uncertainty of the ^{207}Pb/^{235}U ages due to the very low ^{207}Pb content in young monazite. For this reason, only ^{208}Pb/^{232}Th ages are considered here (see details in analytical methods).

The scattering of the ^{208}Pb/^{232}Th ages (high MSWD) is broadly correlated to the core to rim zonation, the Y and U-poor cores yielding older ages than the Y and U-rich rims (Fig. 13b). However, the small difference between the ages measured in the cores and in

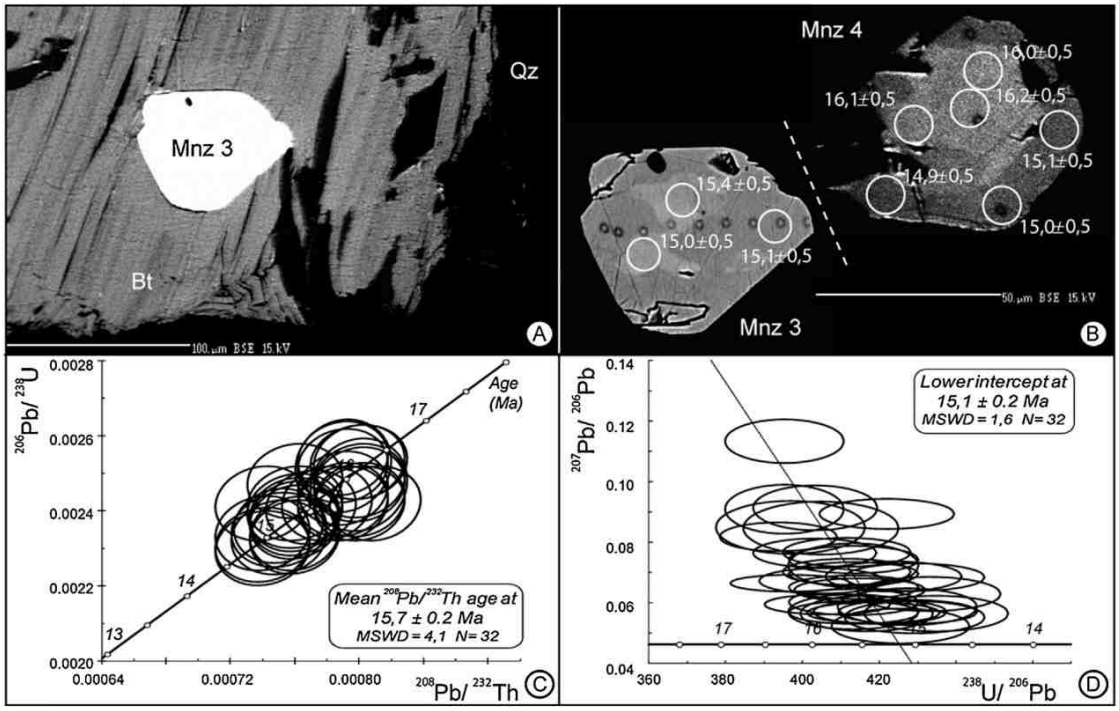

Fig. 13. U–Th–Pb analyses on monazite from migmatite sample IK01A. (a) Typical textural relationships between monazite (Mnz) crystals and the magmatic paragenesis as explored by BSE mean. Mnz 3 is included into biotite (Bt). (b) Details of the internal texture of Mnz 3 and Mnz 4 monazite crystals. BSE image reveal a clear core-rim textures. Is also shown the location of ICPMS laser ablation analysis (9 μm) and their corresponding $^{208}Pb/^{232}Th$ ages (2σ level). Note the correlation between ages and the core-rim textures. (c) $^{206}Pb/^{238}U$ vs $^{208}Pb/^{232}Th$ diagram for all data showing a $^{208}Pb/^{232}Th$ age of 15.7 ± 0.2 Ma concordant with the $^{206}Pb/^{238}U$ ages. (d) Tera-Wasserburg diagram for all analyses, intercepting the Concordia at 15.1 ± 0.2 Ma. Discordant U/Pb ages suggest a slight common Pb contamination and the uncertainty of the $^{207}Pb/^{235}U$ ages due to the low ^{207}Pb content of young monazites. In this study, only the $^{208}Pb/^{232}Th$ ages were considered (inset c). Mineral abbreviations are after Whitney and Evans (2010).

the rim of the monazite grains (less than 1.5 Ma) does not enable a clear distinction between two age groups. Because (i) the monazite is well known to be an efficient chronometer in dating the high temperature metamorphic processes, and (ii) no inheritance (suggesting the recording of older metamorphic event) has been observed, these results clearly establish a Langhian age for the partial melting event that affected the infrastructure of Ikaria Island.

8. Discussion

8.1. An overall top-to-the-N sense of shear as the main deformation record

The whole tectonometamorphic succession of Ikaria is pervasively affected by top-to-the-N to -NNE ductile deformation whose intensity increases toward the top of the structure (Figs. 6f and 14a). While the deepest parts of the tectonometamorphic succession exhibits rather symmetrical deformation dominated by flattening, top-to-the-N shearing deformation shows a large-scale strain gradient toward the Fanari shear zone along which most of the strain is concentrated, with an upward evolution toward a more top-to-the-NNE kinematics (Fig. 5). Characterized by a subordinate top-to-the-NNE strain gradient, the Agios-Kirykos shear zone is furthermore responsible for a 50 °C gap of normal sense, as retrieved by RSCM analyses (Fig. 12). These embedded gradients are accompanied by greenschist-facies retrogression gradients quite obvious at the scale of the outcrop or hand-specimen (Fig. 7). Crossing the ductile to brittle transition, the Fanari shear zone has even recorded increments of motion in brittle conditions responsible for the development of thick cataclasite bodies (Figs. 3 and 9). The direction of ductile stretching and markers of later brittle extensional motions on the detachment planes show a continuum of NNE-SSW stretching and top-to-the-NNE shearing, consistent, in a broad sense, with extensional direction in both metamorphic and sedimentary rocks (Fig. 11). This evolution is interpreted as an evidence of continuous stretching from middle to upper crustal levels through the ductile-brittle transition and continuous shearing along a major detachment localizing deformation.

Low-temperature geochronology pointed out a clear northward younging of ZFT ages (10.3 ± 0.3 to 7.1 ± 0.3 Ma) and AFT ages (8.4 ± 0.8 to 5.9 ± 0.8 Ma) consistent with an overall top-to-the-N unroofing with apparent slip-rates over the Fanari detachment of 10–8 km/Ma (Fig. 14b; Kumerics et al., 2005). U–Th/He analyses on apatite for both flanks of the dome yielded similar 6 Ma ages. Motion over the Fanari detachment seems stop near 6 Ma. These ages constrain, in turn, the maximum age for the onset of passive "folding" of the Fanari detachment plane around the dome, which postdates the last brittle motions of the detachment and even the brittle normal faulting that affects sediments.

A progressive rotation of the stretching and shearing direction is observed from the core to the outer flanks of the domes (Fig. 5). As suggested by the structural study, the shearing strain has progressively localized through time upward from a distributed flow, recorded in the amphibolite-facies conditions, to mylonites, ultramylonites and then cataclasites in the vicinity of Fanari detachment (Figs. 3 and 9). Accordingly, the N-S trending lineation preserved in the core is older than the NNE-SSW trending one at the top along the main shear zones. The core of the dome has therefore rotated 35° counterclockwise during its exhumation before the final doming that seems to be the latest event recorded on Ikaria. This late event tends to confer to the dome the geometry of an a-type dome where the stretching direction is parallel to the dome axis (Jolivet

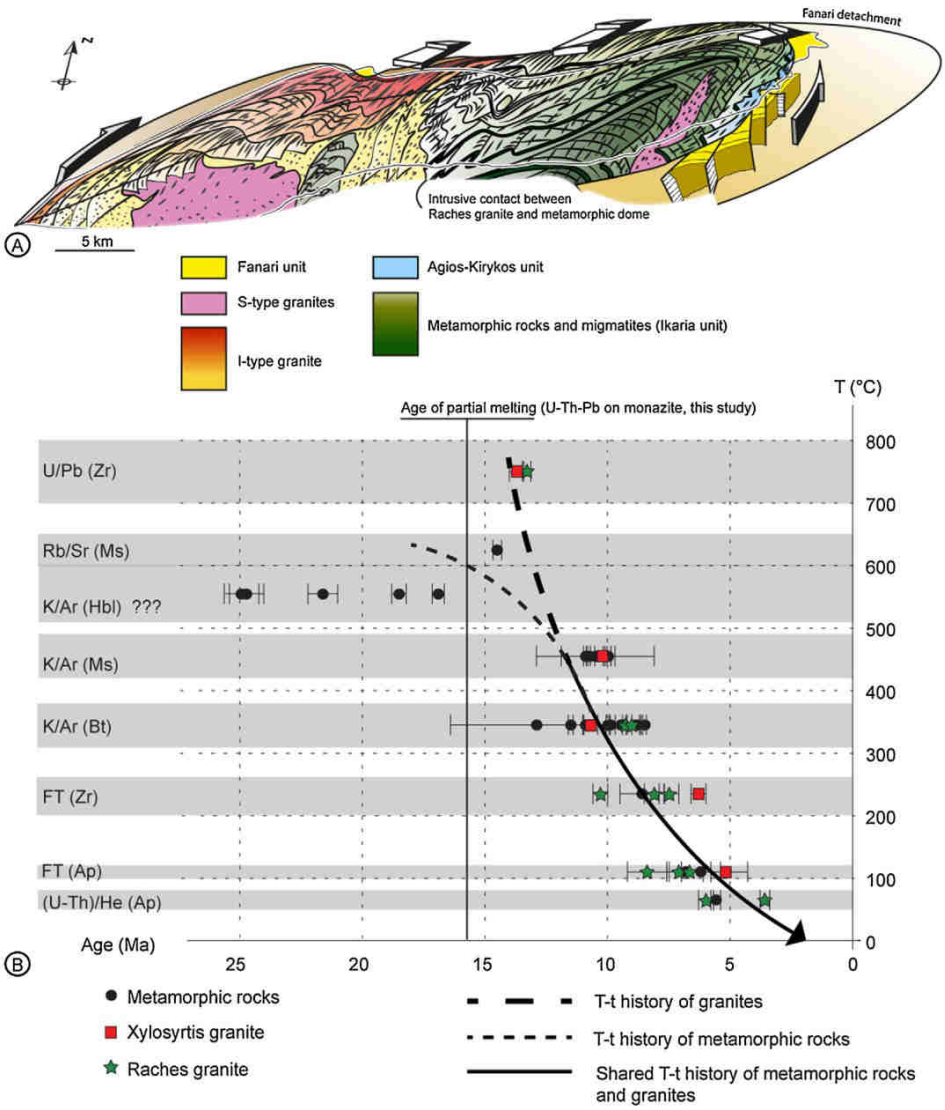

Fig. 14. Large-scale structure and available time-constraints. (a) Three-dimensions large-scale sketch of Ikaria depicting the relationships between the structural dome, the synkinematic intrusions and the major shear zones. (b) Time-chart compiling all geochronological constraints available for Ikaria. Note that both the metamorphic dome and the late intrusions share a common fast cooling from 11 to 10 Ma onward. U/Pb ages on zircon (Zrn) are from Bolhar et al. (2010); K/Ar ages on muscovite (Ms) and biotite (Bt), Rb/Sr ages on muscovite and FT ages on apatite (Ap) are from Altherr et al. (1982) and Kumerics et al. (2005). (U–Th)/He ages on apatite and FT ages on zircon are from Kumerics et al. (2005); K/Ar ages on hornblende (Hbl) are from Altherr et al. (1982). Mean closure temperature are from Harrison (1981), Steck and Hunziker (1994), Grove and Harrison (1996), Brandon et al. (1998), Ketcham et al. (1999), Farley (2000), Cherniak and Watson (2001) and Harrison et al. (2009). K/Ar, Ar/Ar and Rb/Sr ages on metamorphic rocks could reflect deformation-assisted crystallization (Kumerics et al., 2005) or cooling (Altherr et al., 1982). Same ages on granites are interpreted as cooling ages (Altherr et al., 1982; Kumerics et al., 2005). The new age of partial melting from this study is also showed. Question mark is associated with ages which are discussed in the text.

et al., 2004a) and which can suggests an oblique component of shearing during doming (Le Pourhiet et al., 2012). A significant component of E-W shortening is currently recorded in the deformation of the northern Aegean domain as a result of westward motion of Anatolia along the North Anatolian Fault (NAF) (e.g. Le Pichon and Kreemer, 2010). If the NAF has reached the northern Aegean some 6 Ma ago as a localized crustal-scale fault zone (Armijo et al., 1999; Melinte-Dobrinescu et al., 2009), it has been suggested that dextral movements has been active since 12 Ma (Sengör et al., 2005). In the field, consequences of an E-W shortening are clearly recorded in the northern Cyclades, all the way to western Turkey (Angelier, 1976; Buick, 1991; Bozkurt and Park, 1997; Ring et al., 1999; Avigad et al., 2001; Menant et al., 2013). This context, showing a combination of exhumation, strike-slip and contemporaneous E-W shortening and N-S crustal stretching, suggests a component of transtension during the last evolution stages (Le Pourhiet et al., 2012; Fossen et al., 2013). This oblique component fits the hypothesis of a left-lateral transfer zone from the Menderes massif to the Cyclades proposed by Ring et al. (1999) and recently reassessed by Gessner et al. (2013). Detailed studies on the timing of the formation of stretching directions across the dome coupled with the timing of doming are necessary to go any further.

8.2. *Eastern extension of the North Cycladic Detachment System*

Obvious structural and metamorphic similarities of the series of detachments from Andros to Mykonos, with coeval top-to-the-N to -NNE kinematics, led Jolivet et al. (2010) to mechanically merge

them in a single crustal-scale extensional structure, called NCDS. A probable correlation of the Fanari detachment of Kumerics et al. (2005) with the NCDS was even proposed (Jolivet et al., 2010). The existence on Ikaria of two detachments, one purely ductile and the other evolving from ductile to brittle conditions and the presence of the synkinematic granite piercing through the dome are indeed reminiscent of the anatomy of the NCDS as described on Andros, Tinos and Mykonos (Jolivet et al., 2010). On Tinos (e.g. Jolivet and Patriat, 1999; Jolivet et al., 2004a; Brichau et al., 2007) as well as on Mykonos (e.g. Faure et al., 1991; Lecomte et al., 2010; Denèle et al., 2011; Menant et al., 2013), increments of ductile and then brittle deformation are recorded by synkinematic intrusions emplaced into the main extensional shear zones. The Tinos Detachment is mostly ductile and is pierced by the Tinos intrusion. Conversely, the Livada Detachment shows ductile then brittle deformation and affects the Tinos intrusion (Brichau et al., 2007). This last detachment is then pierced by the Mykonos intrusion. The more superficial Mykonos Detachment that clearly post-dates all intrusions, operated only in purely brittle conditions and carries syn-extension sediments (e.g. Lecomte et al., 2010; Menant et al., 2013). These three detachments that operate sequentially form the NCDS. A similar evolution is observed on Ikaria. Exclusively operating in the ductile field, the Agios-Kirykos shear zone is later cut down-section by the Fanari detachment that evolves from ductile to brittle and even controls the deposition of syn-tectonic sediments in the hangingwall.

Along with the current lack of precise time-constraints on synkinematic minerals, timing of extensional deformation onset is still unclear on Ikaria. If partial melting occurred at ca. 15.5 Ma, as showed in this study, the signification of the 25–17 K/Ar ages on hornblende (Altherr et al., 1982) are questioned. These ages may reflect either Ar inheritance from an earlier tectonometamorphic event or simply excess argon (i.e. extraneous argon), as suggested by the strong scattering of these ages. Then, onset of extension might starts at or just after ca. 15.5 Ma. The 12–9 Ma K/Ar and Ar/Ar ages obtained on fabric-forming white-micas and biotite are believed to record either a fast cooling or last recrystallizations during mylonitization (see compilation in Fig. 14b; Altherr et al., 1982; Kumerics et al., 2005). In parallel, the three intrusions (Raches, Karkinagrion and Xylosyrtis) that crystallized at 14–13 Ma therefore synkinematically emplace within the Fanari shear zone (U–Pb on zircon; Bolhar et al., 2010; Laurent et al., 2015). Intrusions all underwent a common fast cooling to temperatures close to the ductile to brittle transition (Stöckhert et al., 1999; Imber et al., 2001) at ca. 10 Ma (K/Ar and Ar/Ar on micas; Altherr et al., 1982; Kumerics et al., 2005). Being only active in the ductile field, the Agios-Kirykos therefore probably ceased to be active some 10 Ma ago. Displacement and further strain localization were thus transferred to the Fanari shear zone, responsible for the final exhumation, in the ductile and then the brittle field. The last exhumation stages were characterized by fast (100–80 °C/Ma) cooling rates and ended at around 6 Ma (Fig. 14b; FT and U–Th/He on zircon and apatite; Kumerics et al., 2005). As a comparison, crystallization and cooling of the Mykonos pluton occurred between 13.5 Ma and 9 Ma as a result of the fast exhumation related to the activity of the Livada and Mykonos detachments (e.g. Brichau et al., 2008; Lecomte et al., 2010; Jolivet et al., 2010). Low-temperature ages even suggest that motions over the Fanari detachment continued until 6 Ma and are thus the last top-to-the-N to -NNE detachment active in the Aegean domain. These similarities in terms of geometries, kinematics and timing of the Ikaria detachments and the various branches of the NCDS confirm the proposed eastward extension of the NCDS all the way to the eastern end of Ikaria in the Agios-Kirykos and Fanari shear zones (Fig. 15).

Similarly to Mykonos, the detachment system of Ikaria, does not exhume *HP-LT* metamorphic rocks belonging to the Cycladic Blueschists unit, at variance with Tinos and Andros. Indeed, along with the structural position and the lithostratigraphic succession, the apparent lack of any *HP-LT* imprint either in Ikaria and Agios-Kirykos units precludes correlations with the Cycladic Blueschists unit. The Ikaria and Agios-Kirykos units are characterized by the same monotonous lithologies and a similar 80–100 °C/km thermal field gradient, it is proposed that both units were equilibrated along a single, warm gradient rooting in partially molten rocks.

Correlated with the Upper Cycladic unit, in a broad sense, the Fanari unit reworks large amount of Pelagonian detritus shed into the extensional basins (Photiades, 2002a). While deposition of sediments on the Upper Cycladic unit started around 23 Ma throughout the Aegean domain (Angelier, 1976; Sanchez-Gomez et al., 2002; Kuhlemann et al., 2004), sediments preserved on Ikaria are attributed to Late Oligocene to Early Pliocene (Papanikolaou, 1978; Photiades, 2002a,b). This rather recent deposition age is consistent with last denudation ages ascribed to last extensional motions over the Fanari detachment (Kumerics et al., 2005), which may be responsible for maintaining a significant tectonic subsidence.

8.3. Definition of the Ikaria MCC and the central Aegean *HT* zone

The structure of Ikaria is composed of two main parts separated by a detachment system consisting in shallow-dipping extensional ductile to brittle shear zones connecting surficial to mid-crustal levels (e.g. Fig. 2). The bulk finite architecture of the footwall consists in an elongated structural dome roofed by a partly eroded mylonite, ultramylonite and cataclasite carapace (Fig. 4). This geometrical dome is paired with a fairly concentric distribution metamorphic zones of decreasing grade from migmatites and 625 °C in the core to 390 °C in the externals parts (Fig. 12). The dome flanks display 500-m thick strain gradient evolving upward to mylonites characterized by the uniformity of shear sense from one limb to the other. They are partially overprinted by cataclasites and fault-rocks in the Fanari detachment zone (Figs. 3 and 9). The detachment itself is marked by a clear-cut fault plane carrying evidences for large-scale displacements in the brittle field (Fig. 9). The hangingwall unit, exclusively composed sediments, is only characterized by brittle deformation (Fig. 10). Following this description, Ikaria dome shares all attributes of a typical migmatite-cored MCC (see Platt et al., 2014, for review) firstly described in the Basin and Range of western United States (Davis and Coney, 1979; Crittenden et al., 1980; Wernicke, 1981, 1985), and then in other Alpine (e.g. Lister et al., 1984; Dewey, 1988; Gautier et al., 1993; Gautier and Brun, 1994; Jolivet and Patriat, 1999; Vanderhaeghe, 2004) and Variscan or Caledonian orogenic belts (e.g. Norton, 1986; Andersen et al., 1991).

Partial melting is a key factor that controls the strength of the continental crust. The recent discovery of migmatites in the infrastructure of the Ikaria MCC dome may have important implications for the behavior of the Hellenic continental crust during Oligo-Miocene extension. Several high-grade gneiss and migmatite massifs have already been described in the Aegean realm. However, most of these occurrences of *HT* rocks are basement rocks inherited from ancient tectonometamorphic events. An early Paleozoic *HT* event is known in the Menderes (e.g. Gessner et al., 2004) and in the East of the Aegean Sea, particularly on Ikaria (Kumerics et al., 2005; Ring et al., 2007). There, a ca. 460 Ma age retrieved form a pegmatite dyke may reflect a minimum age for *HT* metamorphism (Kumerics et al., 2005). A Variscan inheritance is also well described in the Cycladic basement unit in the Southern Cyclades (e.g. Henjes-Kunst and Kreuzer, 1982; Andriessen et al., 1987; Keay and Lister, 2002). On these islands, a ca. 320 Ma granite and amphibolite facies gneisses are partially overprinted by the Eocene HP imprint (e.g. Henjes-Kunst and Kreuzer, 1982; Andriessen et al.,

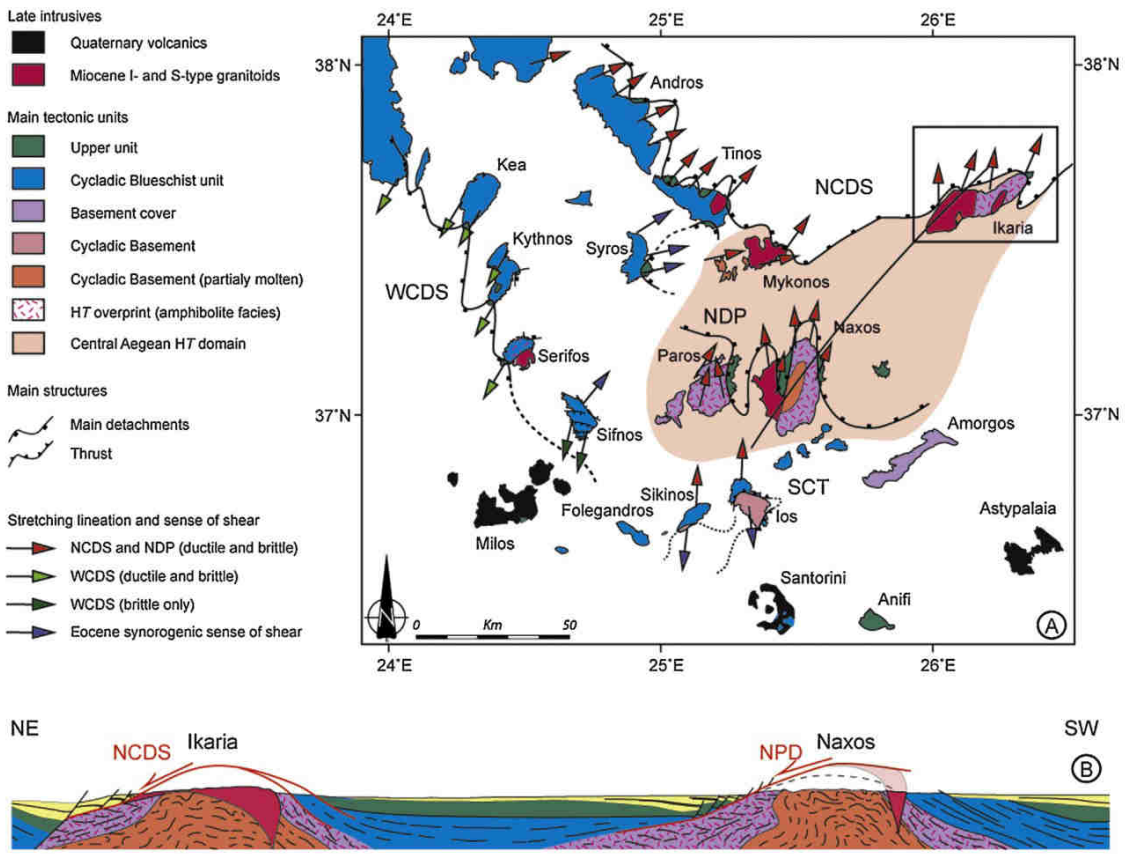

Fig. 15. Large-scale implications. Tectonic map of synorogenic and postorogenic structures in the Aegean domain showing (i) how far the back-arc postorogenic extension remains highly asymmetric in the center of the domain and (ii) the footprint of the central Aegean HT zone where MCCs are described. Red and green arrows indicate the ductile sense of shear associated to the Oligo-Miocene extensional episode associated with the NCDS, the WCDS and the NDP (Lister et al., 1984; Faure et al., 1991; Gautier and Brun, 1994; Vandenberg and Lister, 1996; Jolivet and Patriat, 1999; Mehl et al., 2005, 2007; Huet et al., 2009; Grasemann et al., 2012; Augier et al., 2015). On Syros and Sifnos islands, the synorogenic top-to-the-ENE sense of shear is associated to the synorogenic Vari detachment of Syros (Trotet et al., 2001a,b). (b) Stretching-parallel cross-section through the central Aegean HT zone where intensity of stretching and asymmetry of the deformation are maximum.

1987; Keay and Lister, 2002; Huet et al., 2009; Augier et al., 2015). The only Oligo-Miocene migmatites crop out in the core of the Naxos MCC, the first that has been described in the Aegean domain (e.g. Lister et al., 1984). There, the age of the partial melting is quite constrained by U–Pb analyses on zircon yielding series of ages ranging from 21 to 17 Ma (Keay et al., 2001). The age of migmatites recently discovered on Ikaria is therefore of prime importance. In this study, pioneer U–Th–Pb analyses on monazites from a leucosome of the migmatites yielded an age of 15.7 ± 0.2 Ma (Fig. 13). This result falls in the same age-range than the recent U–Pb age on zircon ascribed to the Karkinagrion S-type granite (Bolhar et al., 2010) together with closely associated migmatites (Laurent et al., 2015). Clearly associated with the same large scale partial melting event that affected the Hellenic continental crust, anatexis at the latitude of Ikaria appears slightly younger than further south on Naxos. Along with Naxos, Mykonos and Ikaria, HT MCCs all cluster in the central part of the Aegean domain. It is here proposed to define the central Aegean HT zone as a large-scale extensional tectonic window of high-grade, partially molten rocks (Fig. 15), of Early-Middle Miocene age (Keay et al., 2001; this study) (Fig. 15). There, intense stretching leads to the complete tectonic omission of the Cycladic Blueschists unit that is observed in colder MCCs further west in Syros, Andros or Tinos (e.g. Trotet et al., 2001a; Mehl et al., 2007), to the east in Samos (e.g. Ring et al., 1999) or to the south in Ios, Folegandros and Sikinos (e.g. Huet et al., 2009; Augier et al., 2015). This gradient of finite stretching toward the center and east of the Cyclades is attested by the joint evolution of the topography, the crustal thickness and the first order transition from brittle to ductile deformation from marginal areas to the center of the Aegean domain (e.g. Jolivet et al., 2010). Uprise of partially molten materials in-between less-extended Cycladic Blueschists unit evokes crustal-scale equivalents of the scar folds that result from "boudins" separation in the process of boudinage (Tirel et al., 2008). This simple model should however be adapted as three distinctive detachment bounding smaller-scale MCCs are currently observed (Fig. 15). The NCDS (Jolivet et al., 2010) exhumes Andros, Tinos, Mykonos and Ikaria in the north while the NDP exhumes Naxos and Paros in the center (Buick, 1991; Gautier et al., 1993; Vanderhaeghe, 2004; Duchêne et al., 2006; Kruckenberg et al., 2011). Both are associated with top-to-the-N shear. Finally, further southwest, the alignment of Kea, Kythnos and Serifos shows another row of small-scale domes exhumed by the top-to-the-SW WCDS (Grasemann et al., 2012). If top-to-the-S criteria on Ios and Sikinos are related to a thrust (Huet et al., 2009; Augier et al., 2015) and not to a detachment (Vandenberg and Lister, 1996; Forster and Lister, 2009; Thomson et al., 2009; Ring et al., 2011) then extensional top-to-the-N shearing is systematically observed from north to south of the central Aegean (Fig. 15). This result contrasts with the more symmetric deformation recognized in marginal areas, where symmetrically arranged detachment systems depict more

bivergent extensional systems either to the west (Grasemann et al., 2012) or east in Samos (Ring et al., 1999) or in the Menderes massif (Hetzel et al., 1995b; Gessner et al., 2001). A correlation between the amount of stretching of the crust and the degree of non-coaxiality is therefore proposed. Just as the Tyrrhenian or the Alboran back-arc systems, the causes of this regional-scale non-coaxial extension in the Aegean back-arc domain is a first-order question that is outside the focus of this paper but may pertain to the interactions between the upper plate, the retreating subducting slab and the flowing asthenospheric mantle (Jolivet et al., 2009; Sternai et al., 2014).

9. Conclusions

Although Ikaria is one of the largest Aegean islands and paves the way between the Cyclades and the Menderes massif, its geology and tectonic evolution remain poorly understood since recent studies lead to very conflicting maps and interpretations. This paper reports a detailed 3D study of the geometry and the thermal structure of Ikaria. The structural study shows that the *HT-LP* foliation is arched, forming a NE-SW trending structural dome cored by partially molten rocks and intruded by late intrusive granitic bodies. Lineation shows a N-S to NNE-SSW ductile stretching associated with an overall top-to-the-N to -NNE sense of shear. Final exhumation of the dome was completed by Miocene extensional system made of two main top-to-the-N to -NNE shear zones, operating in the ductile and then the brittle fields. The thermal structure revealed by the RSCM approach strengthened the subdivision of the metamorphic succession in two main metamorphic units (Ikaria and Agios-Kirykos units) with an upward decrease of maximum temperature, separated by the Agios-Kirykos shear zone. The Fanari detachment permits to juxtapose the sedimentary Fanari unit directly on metamorphic rocks. The distribution of RSCM temperatures within the dome and the presence of migmatites of ca. 15.5 Ma age in the western part of the island fit the description of a *HT* MCC such as Naxos or Mykonos. The proposed tectono-metamorphic evolution of the dome is consistent with the evolution of the northern Aegean area controlled by the eastern extension of the NCDS. Definition of Ikaria as a *HT* MCC allows the definition of the geographic extent of the central Aegean *HT* zone associated with strictly asymmetric top-to-the-N ductile shearing and an Early-Middle Miocene partial melting event. A correlation between the amount of stretching of the crust and the degree of non-coaxiality is therefore proposed.

Acknowledgements

Uwe Ring and Berhnard Grasemann are thanked for their constructive comments and suggestions that improved the manuscript. This work has received funding from the European Research Council (ERC) under the Seventh Framework Programme of the European Union (ERC Advanced Grant, grant agreement No. 290864, RHEOLITH) as well as Institut Universitaire de France. It is a contribution of the Labex VOLTAIRE. The authors are grateful to S. Janiec and J.G. Badin (ISTO) for the preparation of thin sections.

Appendix A. Supplementary data

Supplementary data associated with this article can be found, in the online version, at http://dx.doi.org/10.1016/j.jog.2015.09.004.

References

Altherr, R., Kreuzer, H., Lenz, H., Wendt, I., Harre, W., Dürr, S., 1994. Further evidence for a late cretaceous low-pressure high-temperature Terrane in the Cyclades, Greece – petrology and geochronology of crystalline rocks from the Islands of Donoussa and Ikaria. Chemie Der Erde 54, 319–328.

Altherr, R., Kreuzer, H., Wendt, I., Lenz, H., Wagner, G.A., Keller, J., Harre, W., Höhndorf, A., 1982. A late oligocene/early Miocene high temperature belt in the attic-cycladic crystalline complex (SE Pelagonian, Greece). Geol. Jahrb. 23, 97–164.

Altherr, R., Schliestedt, M., Okrusch, M., Seidel, E., Kreuzer, H., Harre, W., Lenz, H., Wendt, I., Wagner, G.A., 1979. Geochronology of high-pressure rocks on Sifnos (cyclades, Greece). Contrib. Mineral. Petrol. 70, 245–255.

Altherr, R., Siebel, W., 2002. I-type plutonism in a continental back-arc setting: Miocene granitoids and monzonites from the central Aegean Sea, Greece. Contrib. Mineral. Petrol. 143, 397–415.

Andersen, T.B., Jamtveit, B., Dewey, J.F., Swensson, E., 1991. Subduction and eduction of continental crust: major mechanisms during continent–continent collision and orogenic extensional collapse, a model based on the south Norwegian Caledonides. Terra Nova 3, 303–310.

Andriessen, P.A.M., Banga, G., Hebeda, E.H., 1987. Isotopic age study of pre-Alpine rocks in the basal units on Naxos, Sikinos and Ios, Greek Cyclades. Geol. Mijnb. 66, 3–14.

Angelier, J., 1976. Sur l'alternance mio-plio-quaternaire de mouvements extensifs et compressifs en Egée orientale: l'île de Samos (Grèce). Comp. Rend. Acad. Sci. Paris 283, 463–466.

Armijo, R., Meyer, B., Hubert, A., Barka, A., 1999. Westward propagation of the North Anatolian fault into the northern Aegean: timing and kinematics. Geology 27, 267–270.

Aubouin, J., Dercourt, J., 1965. Sur la géologie de l'Egée: regard sur la Crète. Bull. Soc. Geol. France 7, 787–821.

Augier, R., Jolivet, L., Gadenne, L., Lahfid, A., Driussi, O., 2015. Exhumation kinematics of the Cycladic Blueschists unit and back-arc extension, insight from the Southern Cyclades (Sikinos and Folegandros Islands, Greece). Tectonics 34, 152–185.

Avigad, D., Garfunkel, Z., 1989. Low-angle faults above and below a blueschist belt: Tinos Island, Cyclades, Greece. Terra Nova 1, 182–187.

Avigad, D., Garfunkel, Z., 1991. Uplift and exhumation of high-pressure metamorphic terrains: the example of the Cycladic blueschist belt (Aegean Sea). Tectonophysics 188, 357–372.

Avigad, D., Ziv, A., Garfunkel, Z., 2001. Ductile and brittle shortening, extension-parallel folds and maintenance of crustal thickness in the central Aegean (Cyclades, Greece). Tectonics 20, 277–287.

Baldwin, S.L., Lister, G.S., 1998. Thermochronology of the South Cyclades Shear Zone, Ios, Greece: effects of ductile shear in the argon partial retention zone. J. Geophys. Res. 103, 7315–7336.

Beyssac, O., Goffé, B., Chopin, C., Rouzaud, J.N., 2002. Raman spectra of carbonaceous material in metasediments: a new geothermometer. J. Metamorph. Geol. 20, 859–871.

Blake, M.C., Bonneau, M., Geyssant, J., Kienast, J.R., Lepvrier, C., Maluski, H., Papanikolaou, D., 1981. A geologic reconnaissance of the Cycladic blueschist belt, Greece. Geol. Soc. Am. Bull. 92, 247–254.

Bolhar, R., Ring, U., Allen, C.M., 2010. An integrated zircon geochronological and geochemical investigation into the Miocene plutonic evolution of the Cyclades, Aegean Sea, Greece: Part 1: Geochronology. Contrib. Mineral. Petrol. 160, 719–742.

Bonneau, M., 1984. Correlation of the Hellenic nappes in the south-east Aegean and their tectonic reconstruction. In: Dixon, J.E., Robertson, A.H.F. (Eds.), The Geological Evolution of the Eastern Mediterranean, vol. 17. Geological Society, London, Special Publications, pp. 517–527.

Bonneau, M., Kienast, J.R., 1982. Subduction, collision et schistes bleus: exemple de l'Egée, Grèce. Bull. Soc. Geol. France 24, 785–791.

Bozkurt, E., 2007. Extensional v. contractional origin for the southern Menderes shear zone, SW Turkey: tectonic and metamorphic implications. Geol. Mag. 144, 191–210.

Bozkurt, E., Park, R.G., 1997. Evolution of a mid-Tertiary extensional shear zone in the southern Menderes massif, western Turkey. Bull. Soc. Geol. France 168, 3–14.

Bozkurt, E., Satir, M., Bugdaycioglu, C., 2011. Surprisingly young Rb/Sr ages from the Simav extensional detachment fault zone, northern Menderes Massif, Turkey. J. Geodyn. 52, 406–431.

Brandon, M.T., Roden-Tice, M.K., Garver, J.I., 1998. Late Cenozoic exhumation of the Cascadia accretionary wedge in the Olympic Mountains, northwest Washington State. Geol. Soc. Am. Bull. 110, 985–1009.

Brichau, S., Ring, U., Carter, A., Bolhar, R., Monié, P., Stockli, D., Brunel, M., 2008. Timing, slip rate, displacement and cooling history of the Mykonos detachment footwall, Cyclades, Greece, and implications for the opening of the Aegean Sea basin. J. Geol. Soc. 165, 263–277.

Brichau, S., Ring, U., Carter, A., Monié, P., Bolhar, R., Stockli, D., Brunel, M., 2007. Extensional faulting on Tinos Island, Aegean Sea, Greece: how many detachments? Tectonics 26, TC4009.

Brichau, S., Thomson, S., Ring, U., 2010. Thermochronometric constraints on the tectonic evolution of the Serifos detachment, Aegean Sea, Greece. Int. J. Earth Sci. 99, 379–393.

Brunn, J.H., Argyriadis, I., Ricou, L.E., Poisson, A., Marcoux, J., de Graciansky, P.C., 1976. Eléments majeurs de liaison entre Taurides et Hellénides. Bull. Soc. Geol. France 18, 481–497.

Buick, I.S., 1991. The late Alpine evolution of an extensional shear zone, Naxos, Greece. J. Geol. Soc. London 148, 93–103.

Buick, I.S., Holland, T.J.B., 1989. The P–T–t path associated with crustal extension, Naxos, Cyclades, Greece. Geol. Soc. Lond. Spec. Publ. 43, 365–369.

Cherniak, D.J., Watson, E.B., 2001. Pb diffusion in zircon. Chem. Geol. 172, 5–24.

Corti, G., Bonini, M., Conticelli, S., Innocenti, F., Manetti, P., Sokoutis, D., 2003. Analogue modelling of continental extension: a review focused on the relations between the patterns of deformation and the presence of magma. Earth-Sci. Rev. 63, 169–247.

Crittenden, M.D., Coney, P.J., Davis, G.H., 1980. Cordilleran metamorphic core complexes. Geol. Soc. Am. Mem. 153, 271–279.

Cruz, M.J., Cunha, J.C., Merlet, C., Sabaté, P., 1996. Dataçao pontual das monazitas da regiao de Itambe, Bahia, através da microssonda electrônica. In: XXXIX Congresso Brasileiro de Geologia, pp. 206–209.

Davis, G.H., Coney, P.J., 1979. Geologic development of the Cordilleran metamorphic core complexes. Geology 7, 120–124.

Delvaux, D., Sperner, B., 2003. New aspects of tectonic stress inversion with reference to the TENSOR program. In: Nieuwland, D.A. (Ed.), New Insights into Structural Interpretation and Modelling, vol. 212. Geological Society, London, Special Publications, pp. 75–100.

Denèle, Y., Lecomte, E., Jolivet, L., Lacombe, O., Labrousse, L., Huet, B., Le Pourhiet, L., 2011. Granite intrusion in a metamorphic core complex: The example of the Mykonos laccolith (Cyclades, Greece). Tectonophysics 501, 52–70.

Dewey, J.F., 1988. Extensional collapse of orogens. Tectonics 7, 1123–1139.

Didier, A., Bosse, V., Boulvais, P., Bouloton, J., Paquette, J.L., Montel, J.M., Devidal, J.L., 2013. Disturbance versus preservation of U–Th–Pb ages in monazite during fluid-rock interaction: textural, chemical and isotopic in situ study in microgranites (Velay Dome, France). Contrib. Mineral. Petrol. 165, 1051–1072.

Didier, A., Bosse, V., Cherneva, Z., Gautier, P., Georgieva, M., Paquette, J.L., Gerdjikov, I., 2014. Syn-deformation fluid-assisted growth of monazite during renewed high-grade metamorphism in metapelites of the Central Rhodope (Bulgaria, Greece). Chem. Geol. 381, 206–222.

Duchêne, S., Aïssa, R., Vanderhaeghe, O., 2006. Pressure-temperature-time evolution of metamorphic rocks from Naxos (Cyclades, Greece): constraints from thermobarometry and Rb/Sr dating. Geodinam. Acta 19, 299–313.

Faccenna, C., Piromallo, C., Crespo-Blanc, A., Jolivet, L., Rossetti, F., 2004. Lateral slab deformation and the origin of the western Mediterranean arcs. Tectonics 23, TC1012.

Farley, K.A., 2000. Helium diffusion from apatite: general behavior as illustrated by Durango fluorapatite. J. Geophys. Res. 105, 2903–2914.

Faure, M., Bonneau, M., Pons, J., 1991. Ductile deformation and syntectonic granite emplacement during the late Miocene extension of the Aegea (greece). Bull. Soc. Geol. France 162, 3–11.

Fletcher, I.R., McNaughton, N.J., Davis, W.J., Rsmussen, B., 2010. Matrix effects and calibration limitations in ion probe U–Pb and Th–Pb dating of monazite. Chem. Geol. 270, 31–44.

Forster, M., Lister, G., 2009. Core-complex-related extension of the Aegean lithosphere initiated at the Eocene-Oligocene transition. J. Geophys. Res. 114, B02401.

Fossen, H., Teyssier, C., Whitney, D.L., 2013. Transtensional folding. J. Struct. Geol. 56, 89–102.

Gabalda, S., Beyssac, O., Jolivet, L., Agard, P., Chopin, C., 2009. Thermal structure of a fossil subduction wedge in the Western Alps. Terra Nova 21, 28–34.

Gasquet, D., et al., 2010. Miocene to Messinian deformation and hydrothermalism in the Lauzière Massif (French Western Alps): new U–Th–Pb and Argon ages. Bull. Soc. Geol. France 181, 227–241.

Gautier, P., Brun, J.-P., 1994. Ductile crust exhumation and extensional detachments in the central Aegean (Cyclades and Evvia Islands). Geodinam. Acta 7, 57–85.

Gautier, P., Brun, J.-P., Jolivet, L., 1993. Structure and kinematics of upper cenozoic extensional detachment on Naxos and Paros (cyclades islands, Greece). Tectonics 12, 1180–1194.

Gessner, K., Collins, A.S., Ring, U., Güngör, T., 2004. Structural and thermal history of poly-orogenic basement: U–Pb geochronology of granitoid rocks in the southern Menderes Massif, Western Turkey. J. Geol. Soc. Lond. 161, 93–101.

Gessner, K., Gallardo, L.A., Markwitz, V., Ring, U., Thomson, S.N., 2013. What caused the denudation of the Menderes Massif: Review of crustal evolution, lithosphere structure, and dynamic topography in southwest Turkey. Gondwana Res. 24, 243–274.

Gessner, K., Ring, U., Johnson, C., Hetzel, R., Passchier, C.W., Güngör, T., 2001. An active bivergent rolling-hinge detachment system: Central Menderes metamorphic core complex in western Turkey. Geology 29, 611–614.

Glodny, J., Hetzel, R., 2007. Precise U–Pb ages of syn-extensional Miocene intrusions in the central Menderes Massif, western Turkey. Geol. Mag. 144, 235.

Grasemann, B., Petrakakis, K., 2007. Evolution of the Serifos Metamorphic Core Complex. In: Lister, G., Foster, M., Ring, U. (Eds.), Inside the Aegean Core Complexes. , Journal of the Virtual Explorer, 27.

Grasemann, B., Schneider, D.A., Stöckli, D.F., Iglseder, C., 2012. Miocene bivergent crustal extension in the Aegean: evidence from the western Cyclades (Greece). Lithosphere 4, 23–39.

Groppo, C., Forster, M., Lister, G., Compagnoni, R., 2009. Glaucophane schists and associated rocks from Sifnos (Cyclades, Greece): new constraints on the P–T evolution from oxidized systems. Lithos 109, 254–273.

Grove, M., Harrison, T.M., 1996. Ar-40* diffusion in Fe-rich biotite. Am. Mineral. 81, 940–951.

Harrison, T.M., 1981. Diffusion of 40Ar in hornblende. Contrib. Mineral. Petrol. 78, 324–331.

Harrison, T.M., Célérier, J., Aikman, A.B., Hermann, J., Heizler, M.T., 2009. Diffusion of 40Ar in muscovite. Geochim. Cosmochim. Acta 73, 1039–1051.

Henjes-Kunst, F., Kreuzer, H., 1982. Isotopic dating of pre-Alpidic rocks from the island of Ios (Cyclades, Greece). Contrib. Mineral. Petrol. 80, 245–253.

Hetzel, R., Passchier, C.W., Ring, U., Dora, Ö.O., 1995a. Bivergent extension in orogenic belts: the Menderes massif (southwestern Turkey). Geology 23, 455–458.

Hetzel, R., Ring, U., Akal, C., Troesch, M., 1995b. Miocene NNE-directed extensional unroofing in the Menderes Massif, southwestern Turkey. J. Geol. Soc. Lond. 152, 639–654.

Hezel, D.C., Kalt, A., Marschall, H.R., Ludwig, T., Meyer, H.-P., 2011. Major-element and Li, Be compositional evolution of tourmaline in an S-type granite-pegmatite system and its country rocks: an example from Ikaria, Aegean Sea, Greece. Can. Mineral. 49, 321–340.

Huet, B., Labrousse, L., Jolivet, L., 2009. Thrust or detachment? Exhumation processes in the Aegean: insight from a field study on Ios (Cyclades, Greece). Tectonics 28, TC3007.

Iglseder, C., Grasemann, B., Rice, A.H.N., Petrakakis, K., Schneider, D.A., 2011. Miocene south directed low-angle normal fault evolution on Kea Island (West Cycladic Detachment System, Greece). Tectonics 30, TC4013.

Iglseder, C., Grasemann, B., Schneider, D.A., Petrakakis, K., Miller, C., Klötzli, U.S., Thöni, M., Zámolyi, A., Rambousek, C., 2009. I and S-type plutonism on Serifos (W-Cyclades, Greece). Tectonophysics 473, 69–83.

Imber, J., Holdsworth, R.E., Butler, C.A., Strachan, R.A., 2001. A reappraisal of the Sibson-Scholz fault zone model: the nature of the frictional to viscous ("brittle–ductile") transition along a long-lived, crustal-scale fault, Outer Hebrides, Scotland. Tectonics 20, 601–624.

Jackson, S.E., Pearson, N.J., Griffin, W.L., Belousova, E.A., 2004. The application of laser ablation-inductively coupled plasma-mass spectrometry to in situ U–Pb zircon geochronology. Chem. Geol. 211, 47–69.

Janots, E., Berger, A., Gnos, E., 2012. Constraints on fluid evolution during metamorphism from U–Th–Pb systematics in Alpine hydrothermal monazite. Chem. Geol. 326–327, 61–71.

Jansen, J.B.H., Schuiling, R.D., 1976. Metamorphism on Naxos-Petrology and geothermal gradients. Am. J. Sci. 276, 1225–1253.

Jolivet, L., et al., 2013. Aegean tectonics: strain localisation, slab tearing and trench retreat. Tectonophysics 597, 1–33.

Jolivet, L., Augier, R., Faccenna, C., Negro, F., Rimmelé, G., Agard, P., Robin, C., Rossetti, F., Crespo-Blanc, A., 2008. Subduction, convergence and the mode of backarc extension in the Mediterranean region. Bull. Soc. Geol. France 179, 525–550.

Jolivet, L., Brun, J.-P., 2010. Cenozoic geodynamic evolution of the Aegean. Int. J. Earth Sci. 99, 109–138.

Jolivet, L., Faccenna, C., 2000. Mediterranean extension and the Africa-Eurasia collision. Tectonics 19, 1095–1106.

Jolivet, L., Faccenna, C., Piromallo, C., 2009. From mantle to crust: stretching the Mediterranean. Earth Planet. Sci. Lett. 285, 198–209.

Jolivet, L., Famin, V., Mehl, C., Parra, T., Aubourg, C., Hébert, R., Philippot, P., 2004a. Progressive strain localisation, boudinage and extensional metamorphic complexes, the Aegean Sea case. In: Whitney, D.L., Teyssier, C., Siddoway, C.S. (Eds.), Gneiss Domes in Orogeny, vol. 380. Geological Society of America Special Papers, pp. 185–210.

Jolivet, L., Lecomte, E., Huet, B., Denèle, Y., Lacombe, O., Labrousse, L., Le Pourhiet, L., Mehl, C., 2010. The North Cycladic Detachment System. Earth Planet. Sci. Lett. 289, 87–104.

Jolivet, L., Patriat, M., 1999. Ductile extension and the formation of the Aegean Sea. In: Durand, B., Jolivet, L., Horváth, F., Séranne, M. (Eds.), The Mediterranean Basins: Tertiary Extension Within the Alpine Orogen, vol. 156. Geological Society, London, Special Publications, pp. 427–456.

Jolivet, L., Rimmelé, G., Oberhänsli, R., Goffé, B., Candan, O., 2004b. Correlation of syn-orogenic tectonic and metamorphic events in the Cyclades, the Lycian nappes and the Menderes massif. Geodynamic implications. Bull. Soc. Geol. France 175, 217–238.

Katzir, Y., Matthews, A., Garfunkel, Z., Schliestedt, M., Avigad, D., 1996. The tectono-metamorphic evolution of a dismembered ophiolite (Tinos, Cyclades, Greece). Geol. Mag. 133, 237–254.

Keay, S., Lister, G., 2002. African provenance for the metasediments and metaigneous rocks of the Cyclades, Aegean Sea, Greece. Geology 30, 235–238.

Keay, S., Lister, G., Buick, I., 2001. The timing of partial melting, Barrovian metamorphism and granite intrusion in the Naxos metamorphic core complex, Cyclades, Aegean Sea, Greece. Tectonophysics 342, 275–312.

Keiter, M., Piepjohn, K., Ballhaus, C., Lagos, M., Bode, M., 2004. Structural development of high-pressure metamorphic rocks on Syros island (Cyclades, Greece). J. Struct. Geol. 26, 1433–1445.

Ketcham, R.A., Donelick, R.A., Carlson, W.D., 1999. Variability of apatite fission-track annealing kinetics: III. Extrapolation to geological time scales. Am. Mineral. 84, 1235–1255.

Kokkalas, S., Aydin, A., 2013. Is there a link between faulting and magmatism in the south-central Aegean Sea? Geol. Mag. 150, 193–224.

Kruckenberg, S.C., Vanderhaeghe, O., Ferré, E.C., Teyssier, C., Whitney, D.L., 2011. Flow of partially molten crust and the internal dynamics of a migmatite dome, Naxos, Greece. Tectonics 30, TC3001.

Kuhlemann, J., Frisch, W., Dunkl, I., Kázmér, M., Schmiedl, G., 2004. Miocene siliciclastic deposits of Naxos Island: geodynamic and environmental implications for the evolution of the southern Aegean Sea (Greece). In: Bernet, M., Spiegel, C. (Eds.), Detrital Thermochronology-Provenance Analysis, Exhumation, and Landscape Evolution of Mountain Belts., vol. 378. Geological Society of America Special Papers, pp. 51–65.

Kumerics, C., Ring, U., Brichau, S., Glodny, J., Monié, P., 2005. The extensional Messaria shear zone and associated brittle detachment faults, Aegean Sea, Greece. J. Geol. Soc. 162, 701–721.

Lahfid, A., Beyssac, O., Deville, E., Negro, F., Chopin, C., Goffé, B., 2010. Evolution of the Raman spectrum of carbonaceous material in low-grade metasediments of the Glarus Alps (Switzerland). Terra Nova 22, 354–360.

Laurent, V., Beaudoin, A., Jolivet, L., Arbaret, L., Augier, R., Rabillard, A., Menant, A., 2015. Interrelations between extensional shear zones and synkinematic intrusions: the example of Ikaria Island (NE Cyclades, Greece). Tectonophysics 651–652, 152–171.

Lecomte, E., Jolivet, L., Lacombe, O., Denèle, Y., Labrousse, L., Le Pourhiet, L., 2010. Geometry and kinematics of Mykonos detachment, Cyclades, Greece: evidence for slip at shallow dip. Tectonics 29, TC5012.

Lee, J., Lister, G.S., 1992. Late Miocene ductile extension and detachment faulting, Mykonos, Greece. Geology 20, 121–124.

Le Pichon, X., Angelier, J., 1979. The Hellenic arc and trench system: a key to the neotectonic evolution of the eastern Mediterranean area. Tectonophysics 60, 1–42.

Le Pichon, X., Kreemer, C., 2010. The Miocene-to-present kinematic evolution of the eastern mediterranean and Middle East and its implications for dynamics. Annu. Rev. Earth Planet. Sci. 38, 323–351.

Le Pourhiet, L., Huet, B., May, D.A., Labrousse, L., Jolivet, L., 2012. Kinematic interpretation of the 3D shapes of metamorphic core complexes. Geochem. Geophys. Geosyst. 13, Q09002.

Lips, A.L.W., Cassard, D., Sözbilir, H., Yilmaz, H., Wijbrans, J.R., 2001. Multistage exhumation of the Menderes Massif, western Anatolia (Turkey). Int. J. Earth Sci. 89, 781–792.

Lister, G.S., Banga, G., Feenstra, A., 1984. Metamorphic core complexes of Cordilleran type in the Cyclades, Aegean Sea, Greece. Geology 12, 221–225.

Ludwig, K.R., 2001. Isoplot/Ex rev. 2.49 – A Geochronological Toolkit for Microsoft Excel. Berkeley Geochronology Canter. Special Publication, No. 1a.

Malinverno, A., Ryan, W.B.F., 1986. Extension in the Tyrrhenian Sea and shortening in the Apennines as result of arc migration driven by sinking of the lithosphere. Tectonics 5, 227–245.

Martin, L.A.J., Ballèvre, M., Boulvais, P., Halfpenny, A., Vanderhaeghe, O., Duchêne, S., Deloule, E., 2011. Garnet re-equilibration by coupled dissolution-reprecipitation: evidence from textural, major element and oxygen isotope zoning of "cloudy" garnet. J. Metamorph. Geol. 29, 213–231.

Mehl, C., Jolivet, L., Lacombe, O., 2005. From ductile to brittle: evolution and localization of deformation below a crustal detachment (Tinos, Cyclades, Greece). Tectonics 24, TC4017.

Mehl, C., Jolivet, L., Lacombe, O., Labrousse, L., Rimmele, G., 2007. Structural evolution of Andros island (Cyclades, Greece): a key to the behaviour of a flat detachment within an extending continental crust. In: Taymaz, T., Dilek, Y., Yilmaz, Y. (Eds.), The Geodynamics of the Aegean and Anatolia, vol. 291. Geological Society, London, Special Publications, pp. 41–73.

Melinte-Dobrinescu, M.C., et al., 2009. The Messinian Salinity Crisis in the Dardanelles region: chronostratigraphic constraints. Palaeogeogr. Palaeoclimatol. Palaeoecol. 278, 24–39.

Menant, A., Jolivet, L., Augier, R., Skarpelis, N., 2013. The North Cycladic Detachment System and associated mineralization, Mykonos, Greece: insights on the evolution of the Aegean domain. Tectonics 32, 433–452.

Norton, M.G., 1986. Late Caledonide Extension in western Norway: a response to extreme crustal thickening. Tectonics 5, 195–204.

Oberhansli, R., Monie, P., Candan, O., Warkus, F.C., Partzsch, J.H., Dora, O.O., 1998. The age of blueschist metamorphism in the Mesozoic cover series of the Menderes Massif. Schweiz. Mineral. Petrogr. Mitt. 78, 309–316.

Papanikolaou, D., 1978. Contribution to the geology of Ikaria island, Aegean sea. Ann. Géol. Pays Hellén. 29, 1–28.

Paquette, J.L., Tiepolo, M., 2007. High resolution (5 μm) U–Th–Pb isotope dating of monazite with excimer laser ablation (ELA)-ICP-MS. Chem. Geol. 240, 222–237.

Parra, T., Vidal, O., Jolivet, L., 2002. Relation between the intensity of deformation and retrogression in blueschist metapelites of Tinos Island (Greece) evidenced by chlorite-mica local equilibria. Lithos 63, 41–66.

Pasteris, J.D., Wopenka, B., 1991. Raman-spectra of graphite as indicators of degree of metamorphism. Can. Mineral. 29, 1–9.

Pe-Piper, G., Photiades, A., 2006. Geochemical characteristics of the Cretaceous ophiolitic rocks of Ikaria island, Greece. Geol. Mag. 143, 417–429.

Photiades, A.D., 2002a. The ophiolitic molasse unit of Ikaria Island (Greece). Turk. J. Earth Sci. 11, 27–38.

Photiades, A.D., 2002b. Geological Map of Greece Scale: 150,000: Island of Ikaria. Institute of Geology and Mineral Exploration.

Platt, J.P., Behr, W.M., Cooper, F.J., 2014. Metamorphic core complexes: windows into the mechanics and rheology of the crust. J. Geol. Soc.

Platt, J.P., Vissers, R.L.M., 1989. Extensional collapse of thickened continental lithosphere: a working hypothesis for the Alboran Sea and Gibraltar arc. Geology 17, 540–543.

Pourteau, A., Candan, O., Oberhänsli, R., 2010. High-pressure metasediments in central Turkey: constraints on the Neotethyan closure history. Tectonics 29, TC5004.

Pourteau, A., Sudo, M., Candan, O., Lanari, P., Vidal, O., Oberhänsli, R., 2013. Neotethys closure history of Anatolia: insights from ^{40}Ar–^{39}Ar geochronology and P–T estimation in high-pressure metasedimentary rocks. J. Metamorph. Geol. 31, 585–606.

Rimmelé, G., Jolivet, L., Oberhänsli, R., Goffé, B., 2003b. Deformation history of the high-pressure Lycian Nappes and implications for tectonic evolution of SW Turkey. Tectonics 22, 1007.

Rimmelé, G., Oberhänsli, R., Goffé, B., Jolivet, L., Candan, O., Cetinkaplan, M., 2003a. First evidence of high-pressure metamorphism in the "Cover Series" of the southern Menderes Massif. Tectonic and metamorphic implications for the evolution of SW Turkey. Lithos 71, 19–46.

Ring, U., 2007. The Geology of Ikaria Island: the Messaria extensional shear zone, granites and the exotic Ikaria nappe. In: Lister, G., Foster, M., Ring, U. (Eds.), Inside the Aegean Core Complexes. , Journal of the Virtual Explorer, 27.

Ring, U., et al., 2007. Early exhumation of high-pressure rocks in extrusion wedges: cycladic blueschist unit in the eastern Aegean, Greece, and Turkey. Tectonics 26, TC2001.

Ring, U., Collins, A.S., 2005. U–Pb SIMS dating of synkinematic granites: timing of core-complex formation in the northern Anatolide belt of western Turkey. J. Geol. Soc. 162, 289–298.

Ring, U., Glodny, J., Will, T.M., Thomson, S., 2011. Normal faulting on Sifnos and the South Cycladic Detachment System, Aegean Sea, Greece. J. Geol. Soc. 168, 751–768.

Ring, U., Glodny, J., Will, T., Thomson, S., 2010. The hellenic subduction system: high-pressure metamorphism, exhumation, normal faulting, and large-scale extension. In: Jeanloz, R., Freeman, K.H. (Eds.), Annual Review of Earth, Planetary Sciences. Annual Reviews, Palo Alto, pp. 45–76.

Ring, U., Laws, S., Bernet, M., 1999. Structural analysis of a complex nappe sequence and late-orogenic basins from the Aegean Island of Samos, Greece. J. Struct. Geol. 21, 1575–1601.

Rosenbaum, G., Lister, G.S., Duboz, C., 2002. Relative motions of Africa, Iberia and Europe during Alpine orogeny. Tectonophysics 359, 117–129.

Rosenbaum, G., Ring, U., Kühn, A., 2007. Tectonometamorphic evolution of high-pressure rocks from the island of Amorgos (Central Aegean, Greece). J. Geol. Soc. Lond. 164, 425–438.

Royden, L.H., 1993. Evolution of retreating subduction boundaries formed during continental collision. Tectonics 12, 629–638.

Sanchez-Gomez, M., Avigad, D., Heimann, A., 2002. Geochronology of clasts in allochthonous Miocene sedimentary sequences on Mykonos and Paros Islands: implications for back-arc extension in the Aegean Sea. J. Geol. Soc. Lond. 159, 45–60.

Schärer, U., 1984. The effect of initial ^{230}Th disequilibrium on young U–Pb ages: the Makalu case, Himalaya. Earth Planet. Sci. Lett. 67, 191–204.

Sengör, A.M.C., Tüysüz, O., İmren, C., Sakınç, M., Eyidoğan, H., Görür, N., Le Pichon, X., Rangin, C., 2005. The North Anatolian fault: a new look. Annu. Rev. Earth Planet. Sci. 33, 37–112.

Seydoux-Guillaume, A.M., Paquette, J.L., Wiedenbeck, M., Montel, J.M., Heinrich, W., 2002. Experimental resetting of the U–Th–Pb systems in monazite. Chem. Geol. 240, 222–237.

Steck, A., Hunziker, J., 1994. The Tertiary structural and thermal evolution of the Central Alps-compressional and extensional structures in an orogenic belt. Tectonophysics 238, 229–254.

Sternai, P., Jolivet, L., Menant, A., Gerya, T., 2014. Driving the upper plate surface deformation by slab rollback and mantle flow. Earth Planet. Sci. Lett. 405, 110–118.

Stöckhert, B., Brix, M.R., Kleinschrodt, R., Hurford, A.J., Wirth, R., 1999. Thermochronometry and microstructures of quartz – a comparison with experimental flow laws and predictions on the temperature of the brittle-plastic transition. J. Struct. Geol. 21, 351–369.

Thomson, S.N., Ring, U., Brichau, S., Glodny, J., Will, T.M., 2009. Timing and nature of formation of the Ios metamorphic core complex, southern Cyclades, Greece. In: Ring, U., Wernicke, B. (Eds.), Extending a Continent: Architecture, Rheology and Heat Budget, vol. 321. Geological Society, London, Special Publications, pp. 139–167.

Tirel, C., Brun, J.-P., Burov, E., 2008. Dynamics and structural development of metamorphic core complexes. J. Geophys. Res. 113, B04403.

Tomascak, P.B., Krogstad, E.J., Walker, R.J., 1996. U–Pb monazite geochronology of granitic rocks from Maine: implications for Late Paleozoic tectonics in the northern Appalachians. J. Geol. 104, 185–195.

Trotet, F., Jolivet, L., Vidal, O., 2001a. Tectono-metamorphic evolution of Syros and Sifnos islands (Cyclades, Greece). Tectonophysics 338, 179–206.

Trotet, F., Vidal, O., Jolivet, L., 2001b. Exhumation of Syros and Sifnos metamorphic rocks (Cyclades, Greece). New constraints on the P–T paths. Eur. J. Mineral. 13, 901–920.

Tschegg, C., Grasemann, B., 2009. Deformation and alteration of a granodiorite during low-angle normal faulting (Serifos, Greece). Lithosphere 1, 139–154.

Urai, J.L., Schuiling, R.D., Jansen, J.B.H., 1990. Alpine deformation on Naxos (Greece). In: Knipe, R.J., Rutter, E.H. (Eds.), Deformation Mechanisms, Rheology and Tectonics, vol. 54. Geological Society, London, Special Publications, pp. 509–522.

van Achterbergh, E., Ryan, C.G., Jackson, S.E., Griffin, W.L., 2001. Data reduction software for LA-ICP-MS. In: Sylvester, P. (Ed.), Laser ablation-ICP-MS in the Earth Science, vol. 29. Mineralogical Association of Canada, pp. 239–243.

Vandenberg, L.C., Lister, G.S., 1996. Structural analysis of basement tectonites from the Aegean metamorphic core complex of Ios, Cyclades, Greece. J. Struct. Geol. 18, 1437–1454.

Vanderhaeghe, O., 2004. Structural development of the Naxos migmatite dome. In: Whitney, D.L., Teyssier, C., Siddoway, C.S. (Eds.), Gneiss Domes in Orogeny. Geological Society of America Special Papers, pp. 211–227.
van der Maar, P.A., Feenstra, A., Manders, B., Jansen, J.B.H., 1981. The petrology of the island of Sikinos, Cyclades, Greece, in comparison with that of the adjacent island of Ios. Neues Jahrb. Mineral.-Abh. 10, 459–469.
van Hinsbergen, D.J.J., 2010. A key extensional metamorphic complex reviewed and restored: the Menderes Massif of western Turkey. Earth-Sci. Rev. 102, 60–76.
van Hinsbergen, D.J.J., Hafkenscheid, E., Spakman, W., Meulenkamp, J.E., Wortel, R., 2005. Nappe stacking resulting from subduction of oceanic and continetal lithosphere below Greece. Geology 33, 325–328.
Villa, I.M., 1998. Isotopic closure. Terra Nova 10, 42–47.
Vitale Brovarone, A., Beyssac, O., Malavieille, J., Molli, G., Beltrando, M., Compagnoni, R., 2013. Stacking and metamorphism of continuous segments of subducted lithosphere in a high-pressure wedge: the example of Alpine Corsica (France). Earth-Sci. Rev. 116, 35–56.
Weinberg, R.F., Hasalová, P., 2015. Water-fluxed melting of the continental crust: a review. Lithos 212–215, 158–188.
Wernicke, B., 1981. Low-angle normal faults in the Basin and Range Province: nappe tectonics in an extending orogen. Nature 291, 645–648.
Wernicke, B., 1985. Structural discordance between Neogene detachments and frontal Sevier thrusts, central Mormon Mountain, southern Nevada. Tectonics 4, 213–246.
Whitney, D.L., Evans, B.W., 2010. Abbreviations for names of rock-forming minerals. Am. Mineral. 95, 185–187.
Wijbrans, J.R., Schliestedt, M., York, D., 1990. Single grain argon laser probe dating of phengites from the blueschist to greenschist transition on Sifnos (Cyclades, Greece). Contrib. Mineral. Petrol. 104, 582–593.
Will, T., Okrusch, M., Schmädicke, E., Chen, G.L., 1998. Phase relations in the greenschist–blueschist–amphibolite–eclogite facies in the system Na_2O–CaO–FeO–MgO–Al_2O_3–SiO_2–H_2O (NCFMASH), with application to metamorphic rocks from Samos, Greece. Contrib. Mineral. Petrol. 132, 85–102.

Aurélien RABILLARD

Interactions magmas-détachements : du terrain (Mer Égée, Grèce) à l'expérimentation

Les intrusions magmatiques au sein d'une lithosphère soumise aux contraintes tectoniques sont souvent considérées comme des instabilités thermomécaniques à même de stimuler transitoirement et localement la localisation de la déformation. Dans le but de tester ce modèle et de déterminer les possibles mécanismes gouvernant l'initiation d'une déformation localisée au contact et au sein de corps magmatiques en cours de consolidation, ce travail de thèse se propose de coupler une étude de terrain à une approche expérimentale. Les Cyclades (Mer Égée, Grèce) constituent un domaine de croûte continentale en extension dans lequel se sont mises en place au cœur de cinq dômes métamorphiques extensifs (MCCs) des intrusions magmatiques, elles-mêmes coiffées par des systèmes de détachements. Les diverses campagnes de terrain, combinées aux données de la bibliographie, ont permis de proposer un modèle d'interaction régional dans lequel ces corps magmatiques impactent l'évolution tardive de MCCs cycladiques. Au vu des âges de mise en place des intrusions (15-9 Ma), soit plusieurs millions d'années après le début de l'extension et les premiers stades d'exhumation de roches métamorphiques, le magmatisme dans les Cyclades ne peut être considéré comme un candidat réel pour la genèse de MCCs. Néanmoins, les continuums de la déformation enregistrés en bordure des intrusions (depuis l'état magmatique jusqu'aux conditions ductile/cassant) et les relations géométriques avec les détachements laissent supposer un rôle majeur des complexes magmatiques dans les processus de redistribution et de localisation de la déformation, notamment sur le développement séquentiel de détachements. Les vecteurs de localisation de la déformation au sein de magmas partiellement cristallisés ont été en parallèle recherchés par la voie expérimentale. L'étude du comportement structural de magmas, chimiquement et texturalement proches de systèmes naturels, a permis d'une part de confirmer que la déformation se localise préférentiellement le long d'interfaces à rhéologie contrastée tels aux abords de filons syn-plutoniques. Il est d'autre part montré que la présence initiale d'inhomogénéités texturales (e.g. concentration de cristaux en amas) au sein de magmas moyennement cristallisés peut de manière drastique influencer le degré de localisation de la déformation au cours des stades de refroidissement ultérieurs.

Mots clés : magmas ; dômes métamorphiques extensifs ; détachements ; localisation de la déformation

Magmas-detachments interactions: from field (Aegean Sea, Greece) to experimental work

Magma intrusions within the lithosphere are often considered as thermomechanical instabilities capable to locally and transiently stimulate strain localization. With the aim of testing this model and determining possible mechanisms that govern the initiation of localized deformation at the contact and within magmatic bodies, this thesis combine a fieldwork with an experimental approach. The Cyclades (Aegean Sea, Greece) form a highly extended continental domain in which five metamorphic core complexes (MCCs) were intruded by magmatic complexes, themselves capped by detachment systems. All collected structural and kinematic data, combined with previous investigations, converge toward a regional scheme in which magmatic bodies dynamically impacted the late evolution of the Cycladic MCCs. Granitoids were emplaced in relatively short time period (15-9 Ma) while metamorphic domes were largely exhumed after more than 10 Myrs of extension. None of those intrusions thereby proves to be a real candidate for the genesis of MCCs. However, continuums of deformation recorded within granitoids (magmatic to ductile/brittle states) as well as geometrical relationships with detachments suggest a pivotal role of magmatic complexes in redistribution and localization processes of the deformation, with in particular the sequential development of detachments. Precursors of strain localization within partially cristallized magmas have been concurrently deciphered by an experimental study. The investigation of the structural behavior of magmas, chemically and texturally similar to natural systems, corroborates that strain localization is efficiently activated along interfaces with contrasting rheology such as in the vicinity of synplutonic dikes. It has been also shown that the initial presence of textural inhomogeneities (e.g. like clusters) in medium-crystallized magmas can drastically influence the degree of strain localization during subsequent cooling stages.

Key words: magmas; metamorphic core complexes; detachments; strain localization

Institut des Sciences de la Terre d'Orléans
1A rue de la Férollerie – 45071 Orléans Cedex 2